V. 122, NO. 1
JANUARY 2025

ACI STRUCTURAL JOURNAL

A JOURNAL OF THE AMERICAN CONCRETE INSTITUTE

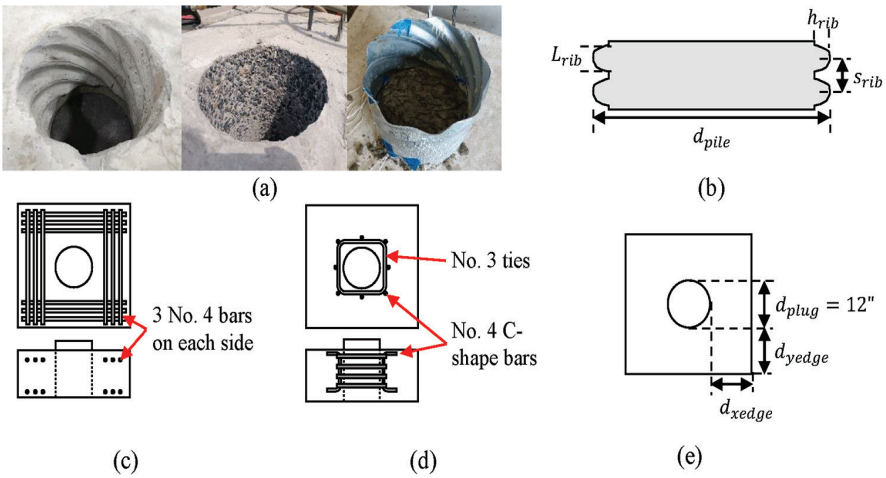

American Concrete Institute

CONTENTS

ACI Structural Journal

January 2025, V. 122, No. 1

A JOURNAL OF THE AMERICAN CONCRETE INSTITUTE
AN INTERNATIONAL TECHNICAL SOCIETY

Contents continued on next page

The *ACI Structural Journal* (ISSN 0889-3241) is published bimonthly by the American Concrete Institute. Publication office: 38800 Country Club Drive, Farmington Hills, MI 48331. Periodicals postage paid at Farmington, MI, and at additional mailing offices. Subscription rates: $210 per year, payable in advance. POSTMASTER: Send address changes to: *ACI Structural Journal*, 38800 Country Club Drive, Farmington Hills, MI 48331.

Canadian GST: R 1226213149.

Direct correspondence to 38800 Country Club Drive, Farmington Hills, MI 48331. Telephone: +1.248.848.3700. Facsimile (FAX): +1.248.848.3701. **Website: http://www.concrete.org.**

PRINTED WITH SOY INK

CONTENTS

ON COVER: 122-S01, p. 5, Fig. 2—Variables used in the experimental testing: (a) interface surface condition; (b) corrugation spacing and depth; (c) typical longitudinal reinforcement details; (d) typical confining reinforcement details; and (e) edge distance.

Contributions to *ACI Structural Journal*

The *ACI Structural Journal* is an open forum on concrete technology and papers related to this field are always welcome. All material submitted for possible publication must meet the requirements of the "American Concrete Institute Publication Policy" and "Author Guidelines and Submission Procedures." Prospective authors should request a copy of the Policy and Guidelines from ACI or visit ACI's website at **www.concrete.org** prior to submitting contributions.

Papers reporting research must include a statement indicating the significance of the research.

The Institute reserves the right to return, without review, contributions not meeting the requirements of the Publication Policy.

All materials conforming to the Policy requirements will be reviewed for editorial quality and technical content, and every effort will be made to put all acceptable papers into the information channel. However, potentially good papers may be returned to authors when it is not possible to publish them in a reasonable time.

Discussion

All technical material appearing in the *ACI Structural Journal* may be discussed. If the discussion is received within four months of the paper's print publication, it will appear in the issue dated ten months from this journal's date. Discussion material received after specified dates will be considered individually for publication or private response. ACI Standards published in ACI Journals for public comment have discussion due dates printed with the Standard. Discussion should be complete and ready for publication, including finished, reproducible illustrations. Discussion must be confined to the scope of the paper and meet the ACI Publication Policy.

Follow the style of the current issue. Discussions should not exceed 1800-word equivalents (illustrations and tables count as 300 words each). References should be complete. Do not repeat references cited in original paper; cite them by original number. Numbering of additional references, figures, tables, and equations should follow sequentially from the original manuscript throughout the discussion. The discusser must indicate the month, year, volume number, issue number, authors' names, and manuscript number of the original manuscript. Closures responding to a single discussion should not exceed 1800-word equivalents in length, and to multiple discussions, approximately one half of the combined lengths of all discussions. Closures are published together with the discussions.

Discuss the paper, not some new or outside work on the same subject. Use references wherever possible instead of repeating available information.

Discussion offered for publication should offer some benefit to the general reader. Discussion which does not meet this requirement will be returned or referred to the author for private reply.

Send manuscripts to:
http://mc.manuscriptcentral.com/aci
Send discussions to:
Journals.Manuscripts@concrete.org

ACI STRUCTURAL JOURNAL TECHNICAL PAPER

Title No. 122-S01

Evaluation of Shear-Friction Behavior of Cylindrical Pocket Connections

by Fatima Vieira, Bruno Vasconcelos, and David B. Garber

An experimental investigation was conducted to evaluate the shear-friction capacity of cylindrical pocket connections without reinforcement crossing the interface, which is a common connection detail between precast concrete substructure elements. Current Code expressions for shear-friction capacity include components for cohesion or aggregate interlock and contribution from steel crossing the interface or a clamping force. These expressions were primarily derived and calibrated based on pushoff tests with reinforcement crossing the shear plane, which do not represent the behavior of the shear plane in a cylindrical pocket connection. Thirty-four large-scale specimens were built and tested to investigate the shear friction of the cylindrical pocket connection without reinforcing steel crossing the shear plane. This experimental study showed that current Code expressions provided conservative estimates for this connection. A revised proposed theory is presented that more accurately predicts the shear-friction capacity of this connection without interface steel.

Keywords: accelerated bridge construction; precast concrete; prefabricated elements and systems; shear friction; substructure connections.

INTRODUCTION

Shear friction is a term used to describe the shear transfer mechanism along an interface between two concrete members that were cast at different times or two adjacent members that can slip relative to each other.[1] Shear friction is typically critical either at cold joints or geometric discontinuities, where a small piece of concrete enters a large concrete region. Some examples of shear friction found in practice are[2]:

- Repairing or strengthening an existing reinforced concrete member through adding new concrete layers;
- Supplementing precast elements with concrete cast on the site;
- Casting new concrete against concrete that has been completely hardened because the erection process was interrupted;
- Post-installations of concrete elements attached to existing members for introduction of loads (for example, corbels); and
- Field connection of precast elements using cast-in-place concrete connections.

The shear-friction capacity of an interface is dependent on cohesion or aggregate interlock, friction, reinforcement crossing the interface, concrete strength, and curing conditions, which are factors that have been studied by numerous researchers.[3-9]

The effects of cohesion and friction in the interface are directly related to the surface preparation and surface roughness. At the same time, these parameters with the concrete strength will impact the adhesive bonding and mechanical interlocking of the interface. The desired roughness can be achieved by preparing the interface surface with some of these technologies: paste retarder painting, high-pressure water-jetting (HPW), milling, shot-blasting, or sandblasting.[7] The curing condition of the joint material has also been suggested to influence the transfer of stresses between concrete surfaces.[8] Improper curing of the joint material can lead to excessive shrinkage, which will introduce a tensile stress between layers and can cause loss of adhesion and cracking at the interface prior to any load being applied.

The mechanical interlocking will decrease as the adhesive bonding fails. This is when the reinforcement crossing the interface will be engaged if present. The reinforcement crossing the interface plays two important roles when transmitting stresses between interfaces:

1. Once in tension due to the surfaces separating, the reinforcement provides a clamping force to act normal to the concrete and provide a friction component to the resistance.
2. Sliding of the elements will create bending stress in the reinforcement, which leads to crushing of the concrete in the bending angle.[3]

When there is no reinforcement crossing the interface, the shear-friction capacity will be achieved by the bond strength between the two elements in contact and the frictional resistance force. This behavior requires more investigation as this construction technique is being more implemented in today's construction practice.

Typical test methods

There have been numerous studies investigating the shear-friction capacity of interfaces with reinforcement crossing the interfaces.[4,6,10-12] There are two principal test methods that have been used to evaluate the capacity of interfaces with reinforcement present: 1) pushoff test; and 2) push-through test.

The pushoff test is the most common test used by researchers to evaluate the shear-friction capacity of interfaces. Normally, the pushoff test involves first casting an L-shaped specimen and allowing it to harden. This L-shaped

ACI Structural Journal, V. 122, No. 1, January 2025.
MS No. S-2021-287.R6, doi: 10.14359/51743289, received July 25, 2022, and reviewed under Institute publication policies.

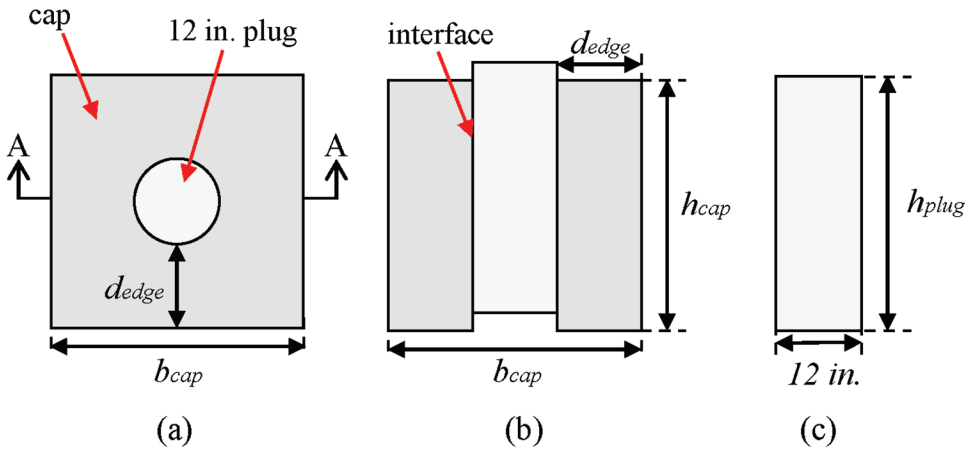

Fig. 1—General geometry of experimental specimens: (a) plan view; (b) Section A-A; and (c) elevation of plug. (Note: 1 in. = 25.4 mm.)

specimen will have reinforcement to strengthen the L-shaped component itself and reinforcement that will cross the interface plane. After the first L-shaped component sufficiently hardens, the second L-shaped component is formed and cast. This second L-shaped component typically has the same geometry and reinforcement as the first L-shaped component. After the second L-shaped component is hardened, the specimen is tested. A normal force can be applied perpendicular to the shear plane to provide a clamping force if desired.

The "push-through" test was first proposed and used by Williams et al.[12] to evaluate both the shear-friction capacity and the bond strength in the interface between two concrete cast at different times, simulating the splice region in post-tensioned spliced girders. The casting and testing procedure are similar to the pushoff test, with the difference that in the push-through test, two outer elements are cast at the same time and an inner element is then cast later directly between the other two elements. Reinforcing steel is included in each element themselves and between the interfaces. More details of the casting and testing procedure for the push-off and push-through tests are provided in Appendix A.*

Prefabricated substructure connection details

Prefabricated bridge elements and systems (PBES) are one of the primary techniques used in accelerated bridge construction. The prefabrication of these elements or systems improves the quality of the members themselves, as they are generally cast at precast plants with better quality control than on-site construction. Prefabricated bridge elements require on-site connections between elements, which often become the critical component of the overall bridge design. Over the years, many types of connections in precast elements have been evaluated to ensure the monolithic behavior of the entire structure. The details of these connections vary depending on which elements are being connected.

Pocket and socket connections are two commonly used connections between precast substructure elements. In a pocket connection, the precast pile does not extend into the pocket in the precast pile cap. Reinforcement is extended from the precast pile into the pocket in the pile cap and cast-in-place (CIP) concrete or grout is placed to fill the pocket, develop the reinforcement, and connect the two members. A corrugated metal pipe is often used to form the void to enhance the mechanical interlock between the CIP concrete or grout and the precast pile cap. A socket connection consists of one of the precast members (for example, pile) extending into a large void in the other precast element; CIP concrete or grout is cast to fill in the remaining space in the void.

This type of connection does not have reinforcement crossing the interface, so it at least partially relies on the shear-friction capacity between the CIP connection and the precast element. The shear-friction capacity of interfaces without steel crossing the interface has not previously been studied. The purpose of the research summarized in this paper was to investigate the behavior of shear interfaces without reinforcement crossing the interface, such as those found in pocket and socket connections.

RESEARCH SIGNIFICANCE

Previous experimental shear friction testing has been conducted and code equations developed based on members with reinforcement crossing the shear plane. This previous research does not adequately represent the shear friction behavior of cylindrical pocket connections without shear reinforcement, which is the mechanism commonly used to connect precast substructure elements. The objective of this research was to determine the shear-friction capacity and behavior of cylindrical pocket interfaces without reinforcement. This research is significant as there has been little previous research on this type of shear friction interface without reinforcement crossing the interface plane.[4,6,10-12]

EXPERIMENTAL INVESTIGATION

Thirty-four large-scale specimens were experimentally tested to evaluate the shear-friction capacity of cylindrical pocket interfaces without steel crossing them. Due

*The Appendix is available at **www.concrete.org/publications** in PDF format, appended to the online version of the published paper. It is also available in hard copy from ACI headquarters for a fee equal to the cost of reproduction plus handling at the time of the request.

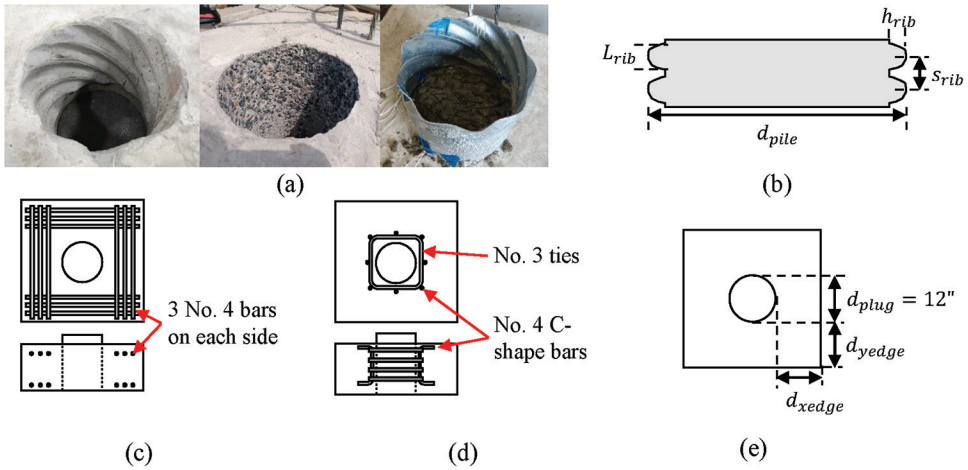

Fig. 2—Variables used in the experimental testing: (a) interface surface condition; (b) corrugation spacing and depth; (c) typical longitudinal reinforcement details; (d) typical confining reinforcement details; and (e) edge distance. (Note: 1 in. = 25.4 mm.)

Table 1—Experimental variables

Experimental variable	Values for test matrix
Interface surface condition	Corrugated pipe left in place; sandblasted concrete finish (1/16 in. roughness), exposed aggregate concrete finish (1/4 in. roughness)
Corrugation spacing and depth	Smooth; corrugated plastic duct (h_{rib} = 0.875 in., L_{rib} = 1 in., s_{rib} = 2 in.); corrugated metal duct (h_{rib} = 0.5 in., L_{rib} = 0.75 in.) with different spacing (2.67 and 5.33 in.)
Reinforcement around pocket and in cap	Different amounts of reinforcement around the pocket (confinement reinforcement) and in the longitudinal direction crossing the splitting plane
Edge distance (d_{edge})	$1d_{plug}$, $0.75d_{plug}$, $0.5d_{plug}$

Note: 1 in. = 25.4 mm.

to limitations of time and resources, only one test was conducted for most combinations of variables. A modified push-through test was designed for this project, because the traditional push-through test does not capture possible pocket concrete expansion that may happen. The base and general geometry for the specimens is shown in Fig. 1. Four different variables were investigated through the experimental investigation: 1) interface surface condition; 2) corrugation spacing and depth; 3) reinforcement around pocket; and 4) edge distance, as shown in Fig. 2 and Table 1. The investigation was divided into two series of specimens, in which different groups of variables were experimentally evaluated.

Series A was designed to investigate the first two variables: 1) effect of the interface surface condition; and 2) corrugation spacing and depth. The interface surface condition was investigated as it was thought to influence the cohesion component of the interface behavior and the corrugation spacing and depth was investigated to see its influence on the interlock along the interface after cohesion was overcome. Several different interface surface conditions and corrugation spacings and depths were investigated as defined in Table 1, including a monolithically cast specimen which was used as a baseline comparison for this series (A-22). The main interface surface condition and corrugation spacing, and depth are shown in Fig. 2(a). A smooth cylindrical form was used to create the void in some specimens; this form was removed, and the surface prepared to either 1/16 or 1/4 in. (1.6 or 6.4 mm) roughness. A corrugated metal pipe was used to create the void in some of the specimens; the pipe was left in place for some specimens (Fig. 2(a)) and removed in others to allow for a 1/16 in. (1.6 mm) roughness surface preparation. This is further explained in the "Specimen details and construction" section. Definitions for the rib length (L_{rib}), height (h_{rib}), and spacing (s_{rib}) are provided in Fig. 2(b). The base reinforcement used in this series is defined in Fig. 2(c) and (d). The base reinforcement included three No. 4 ties in each direction on each side of the plug, called longitudinal reinforcement in this study. These bars were typically spaced at 2 in. (51 mm) on center with 2 in. (51 mm) cover on the exterior face. No. 3 ties were provided around the pocket as confinement reinforcement with No. 4 C-shaped bars used to keep the ties in place during casting. The No. 3 confining ties were typically spaced at 2 in. (51 mm) on center. Typical reinforcement in the plug included eight No. 8 straight bars and No. 3 confining (ring shape) bars at 2 in. (51 mm) spacing.

Specimens in Series A had $1d_{plug}$ (12 in. [305 mm]) edge distance on all sides and used the base reinforcement described previously.

Series B tests were designed to investigate two additional important variables that became apparent through Series A tests: 1) reinforcement around the pocket and in the cap; and 2) edge distance between the edge of the pocket and edge of the cap, as shown in Fig. 2(c), (d), and (e). The reinforcement surrounding the pocket (confinement reinforcement)

Fig. 3—Construction process for the modified push through: (a) formwork before casting; (b) caps already hardened; and (c) specimens after second placement.

and other reinforcement crossing the failure splitting cracks (longitudinal reinforcement) were both found to engage during testing of specimens in Series A. Confinement reinforcement and longitudinal reinforcement amounts were varied to see their effect on the shear-friction capacity and behavior.

Typical confinement reinforcement around the pocket was used for the specimens evaluating the effect of the longitudinal reinforcement. The different longitudinal reinforcement configurations used for these specimens are shown in Appendix A. Specimen B-1 had no longitudinal reinforcement on the cap and Specimen B-3 had only 2 of the No. 4 longitudinal bars in each face spaced 4 in. (102 mm) center to center. In both cases, regular confinement and plug reinforcement was used.

These specimens were all 14 in. (356 mm) deep, had $1d_{plug}$ edge distance on all sides, and had a corrugated interface with 1/16 in. (1.6 mm) concrete surface finish.

When evaluating the confinement reinforcement around the pocket, typical longitudinal reinforcement around the pocket was used in all these specimens. Three different confinement reinforcement configurations were used in these specimens. Typical confinement reinforcement included No. 3 ties around the plug spaced at 2 in. (51 mm) on center and eight No. 4 C-shaped bars at corners and middle of ties. The half-spacing configuration included two No. 3 ties around the plug spaced at 4 in. (102 mm) on center and the same eight No. 4 C-shaped bars. There were also specimens without any confinement reinforcement. Half of these specimens had a corrugated interface with 1/16 in. (1.6 mm) concrete surface finish and half had the corrugated metal pipe left in place to see if the corrugated metal pipe provided similar restraint as the confinement reinforcement, as was previously observed by Restrepo et al.[13] More details are provided in Appendix A.

Finally, because splitting cracks were observed along the height of the specimens extending from the edge of the pocket to edge of the cap in Series A, the edge distance was also a variable to evaluate if decreasing edge distances would decrease strength. The edge distance is the distance between the edge of the plug and the edge of the cap. All specimens tested in this comparison had a corrugated interface with 1/16 in. (1.6 mm) surface roughness. The reinforcement was also kept consistent in specimens in this comparison, with one No. 7 longitudinal bar on the face with the decreasing dimension, three No. 4 longitudinal bars on the other faces, and the typical No. 4 confining bars around the pocket. A similar specimen tested in Series A with three No. 4 longitudinal bars in all faces (A-11) is used as a baseline for comparison.

Specimen details and construction

The procedure for constructing the modified push-through test specimens was as follows: 1) casting a cube with an inner void in the middle (Fig. 3(a)); 2) removing the pipe that was used to create the void and prepare the surface accordingly (2 to 3 days after casting); 3) create a 3 in. (76 mm) blockout in the bottom of the void to allow sliding on the plug when the interface fails and 3 in. (76 mm) cylindrical form on top of the void (Fig. 3(b)); and 4) place concrete in the void and remove formwork used to create the top cylinder and the bottom blockout (Fig. 3(c)). The interface surface was prewet for specimens where the concrete pipe was removed using wet burlap or equivalent to achieve a saturated surface-dry (SSD) condition.

Details of specimens and all combinations of the variables evaluated and tested are provided for Series A and B in Appendix B. The variables not listed in the tables were not varied for each series, respectively. All specimens in Series A had the same 36 in. (914 mm) base for the cap and the same cap and plug reinforcement and edge distances, which were 12 in. (305 mm) on each direction (x- and y-direction). All specimens in Series B had 14 in. (356 mm) height. All the specimens in Series A and B had a plug diameter of 12 in. (305 mm). For all specimen in Series A and B, Grade 60 reinforcing bars were used as a reinforcement and the concrete strength at the day of testing is provided in Appendix B.

The age of the cap concrete at time of plug casting and age of plug concrete at time of testing varied between specimens. Specimens A-1 to A-7 had plugs cast when the cap concrete was an average of 31 days old and were tested when the plug concrete was approximately 28 days old. Specimens A-8 to A-13 had plugs cast when the cap concrete was approximately 5 days old and were tested when the plug concrete was approximately 28 days old. Specimens A-1 to A-13 were cast at the Florida Department of Transportation (FDOT) Structures Research Center (SRC), and from A-14 to A-20 and all Series B precast at the facilities of a precast manufacturer in Miami, FL. Specimens A-14 to A-20 had plugs cast when the cap concrete was 7 days old and were

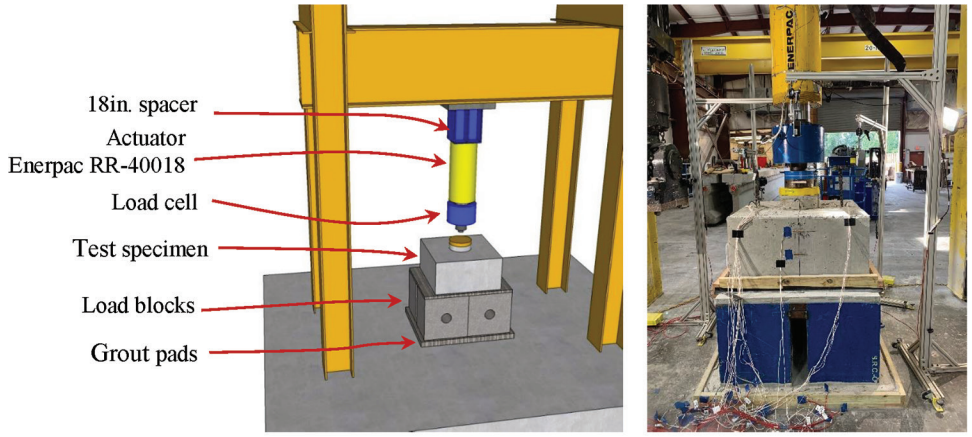

Fig. 4—(a) Schematic; and (b) photograph of test setup. (Note: 1 in. = 25.4 mm.)

tested when the plug concrete was approximately 150 days old. Specimens A-22 and all Series B specimens had plugs cast when the cap concrete was 7 days old and were tested when the plug concrete was approximately 35 days old. Specimen A-21 was cast specifically to investigate the effect of additional time between casting of the cap and plug; the plug was cast when the cap concrete was 163 days old, and the specimen tested when the plug was 16 days old. More details are provided in Appendix B. Sensitivity of the casting procedure was seeing mainly on the behavior of specimens that were cast in the different locations and had smooth surface and sandblasted (1/16 in. [1.6 mm] of roughness) interface preparation. The reason might have been that for those specimens built by the precast manufacturer, the sandblasted preparation was not properly done and the surface was not prewetted.

Testing protocol

The load was applied to the specimens using a 750 kip (3336 kN) hydraulic jack and load cell attached to a load frame with a 1000 kip (4448 kN) capacity. The specimens were placed on top of two load blocks for testing, as shown in Fig. 4. The load blocks were separated 2 to 3 in. (51 to 76 mm) apart to leave room for a laser displacement transducer to measure the deflection of the bottom of the plug.

All specimens were tested using the same loading procedure. The load was applied at a rate of 0.2 kip (0.9 kN) per second. At 200 kip (890 kN) load, the testing was stopped while the specimens were inspected for cracks; cracks were marked, labeled, and documented. Load was then applied at the same load rate (0.2 kip [0.9 kN] per second) until failure of the interface or maximum capacity of the actuator (750 kip [3336 kN]). Cracks were marked on all sides (including the bottom) of the specimens after they were removed from the test frame.

EXPERIMENTAL RESULTS

Summary of results

The measured compressive strengths, cracking loads, ultimate loads, and normalized ultimate loads are summarized and provided in Appendix B for all the specimens tested in Series A and B. An analysis of these results is provided in the following sections.

A normalization based on *AASHTO LRFD Guide Specifications for Accelerated Bridge Construction* (ABC)[14] was used to analyze the data for Series A and Series B and is identify as k normalization. The *AASHTO LRFD Guide Specifications for ABC*[14] is calibrated to k equal to 0.13, which was evaluated using the experimental results in this research

$$V_n = 0.13\sqrt{f_{cp}'}A_{cv} \qquad \text{(3.6.6.6-1) (1)}$$

$$k = \frac{V_{ni,ex}}{\sqrt{f_{cp}'}A_{cv}} \qquad k \text{ normalization (2)}$$

The interface area in both equations is

$$A_{cv} = \pi d_v h_v$$

The currently recommended value for k in the *AASHTO LRFD Guide Specification for ABC* is 0.13.

Analysis of failure mechanism

A similar failure mechanism and progression to failure was seen in most of the specimens. First cracking would occur on one face or parallel faces between 16 and 70% of the ultimate capacity, with an average of 32% of ultimate capacity; the variety in cracking load was a result of the different interface conditions and specimen geometry. The first cracking load could be clearly determined from reinforcing bar strain gauge (RSG) and concrete strain gauge (CSG) readings; sample RSG readings from the longitudinal reinforcement are shown in Fig. 5(a). RSG and CSG readings would remain linear until first cracking (indicated by the red circle in Fig. 5(a)). At first cracking, strain in RSGs would greatly increase (as the reinforcement engaged after cracking), as shown in Fig. 5(a). The CSG would abruptly change from tensile strains to compression strains (if the crack occurred next to the gauge) or have a dramatic increase in tensile strain (if the crack extended through the CSG). The

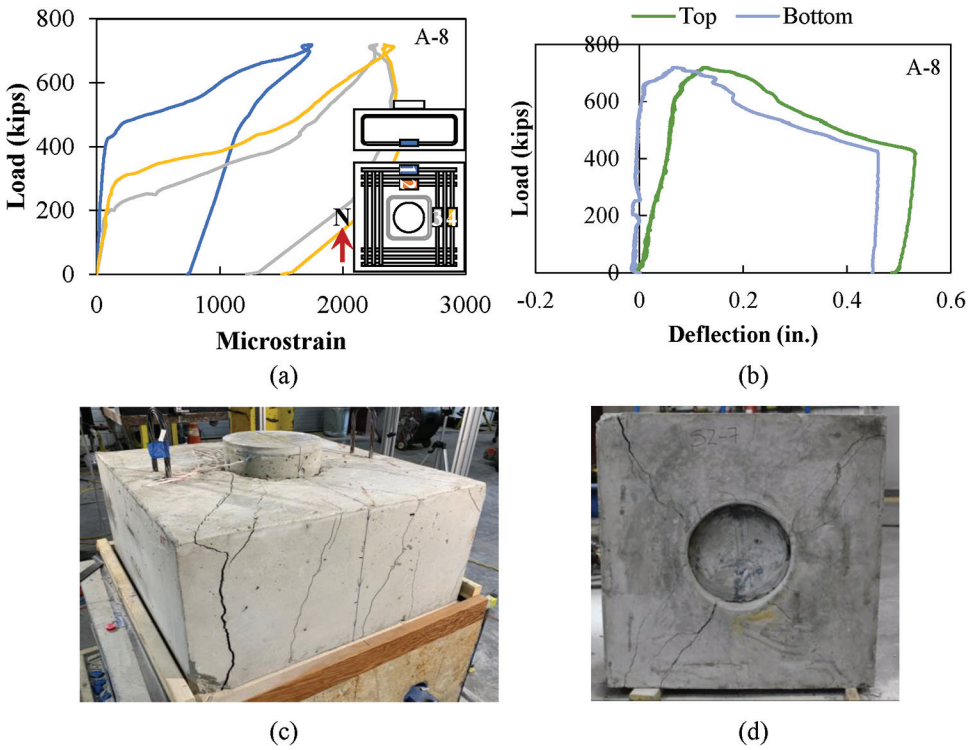

Fig. 5—Example failure mechanism for Specimen A-8: (a) reinforcing bar strain gauges of longitudinal reinforcement; (b) load-deflection curve; and (c) and (d) typical crack pattern. (Note: 1 kip = 4.45 kN; 1 in. = 25.4 mm.)

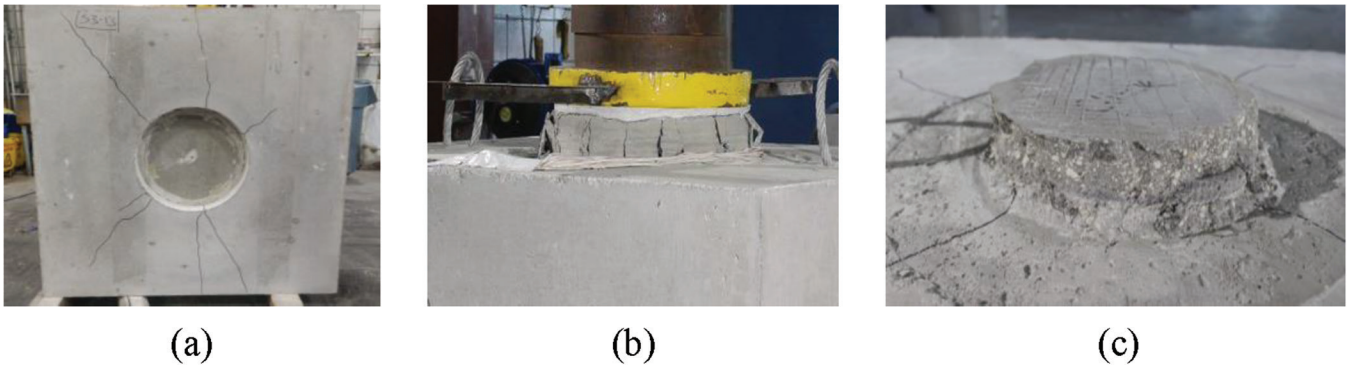

Fig. 6—Failure details on: (a) bottom; (b) plug detail during testing; and (c) top of plug after testing for Specimen A-22.

average cracking loads between CSG and RSG readings for all the specimens are provided in Appendix B.

The load-deflection curve would typically remain linear-elastic until extensive cracking would develop in the cap (typically accompanied by several large cracks), which was then typically followed by sliding of the plug. Deflection occurred at both the top and bottom of the plug when the plug began to slide. The maximum applied failure loads are provided in Appendix B.

Monolithic concrete specimen (A-22)

Although there was no cold joint, the monolithic cast specimen (A-22) also experienced a sliding failure along the same interface between the plug and cap as the other specimens. Cracking began in the specimen at a normalized load k of 0.139 (125 kip [556 kN]), which was close to the average normalized cracking load k_{avg} of 0.132 for all the specimens tested. The observed crack pattern was similar to the typical crack pattern seen in the other specimens (Fig. 5(c) and (d)). One difference was that concrete on the sides of the extended plug progressively spalled off during testing, as shown in Fig. 6. The spalling of the extended plug during failure did not appear to impact the sliding of the plug as similar displacements were measured on the top and bottom of the plug during failure. Displacement in the bottom of the plug began at approximately the same time first cracking occurred in the sides of the specimen (125 kip [556 kN]). After this, there was similar displacement measured on the top and bottom of the plug until sliding began at the failure load of 387.5 kip (1754 kN). The monolithic specimen was used as a baseline comparison in the following sections. Several specimens had a normalized capacity greater than that of the monolithically cast specimen, which is inconsistent with the current shear-friction estimation procedures in ACI 318-19[15] and *AASHTO LRFD Bridge Design Specification*.[16] This may have been a result of the concrete strength

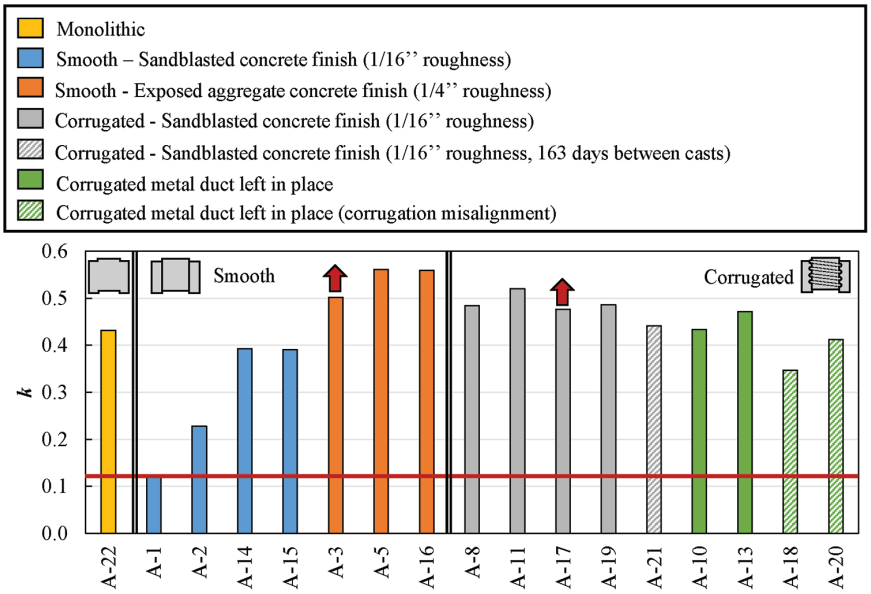

Fig. 7—Comparisons for Series A of specimens based on interface surface condition. Red arrows indicate higher failure load (specimens did not fail due to test setup limitations); red line is at current AASHTO LRFD Guide Specification for ABC recommended value of 0.13. (Note: 1 in. = 25.4 mm; full-color PDF is available at www.concrete.org.)

for A-22 being noticeably lower than the other specimens in Series A.

Effect of interface surface condition

The interface surface condition directly influenced the cohesion component of the shear-friction capacity. A comparison of the normalized failure loads between the specimen with different interface surface conditions is shown in Fig. 7. The red line indicates the current recommended value for k (0.13) in *AASHTO LRFD Guide Specification for ABC*. Red arrows in Fig. 7 indicate that the normalized load for those specimens was higher than shown since the specimens did not fail. The conditions that were evaluated for this variable were: sandblasted concrete (1/16 in. [1.6 mm] of roughness); corrugated pipe left in place (metal finish); and exposed aggregate concrete finish (1/4 in. [6.4 mm] of roughness). These interface surface conditions were evaluated using smooth and corrugated plugs in configurations that are practical for actual use (for example, exposed aggregate with smooth form but not exposed aggregate with corrugated plug). The normalized strength of the specimen with a monolithically cast plug (A-22) is also shown in Fig. 7 for comparison.

The smooth interface (without corrugations) with sandblasted finish (1/16 in. [1.6 mm] of roughness) had the lowest normalized strength of the specimens and a lower normalized strength than the monolithic specimen. The variation in the behavior observed in these specimens was likely due to the sensitivity of these specimens to the casting procedure, geometry, and concrete strength. Specimens A-1 and A-2 were both cast at the FDOT SRC, while Specimens A-14 and A-15 were both precast by the precast manufacturer. The casting procedure did not have as significant an effect on the specimens with the 6.4 mm (1/4 in.) exposed aggregate finish, as A-5 (cast at SRC) and A-16 (cast at the manufacturer) both had very similar behavior. Additionally, Specimen A-1 had a 36 in. (914 mm) height (compared to 14 and 18 in. [356 and 457 mm] height for other specimens) and higher concrete compressive strength than the other specimens; these differences likely contributed to the lower normalized failure load than the other three specimens with a similar interface. Specimen A-2 also had a higher concrete compressive strength than specimens A-14 and A-15. The exposed aggregate concrete finish (1/4 in. [6.4 mm] roughness) (A-3, A-5, and A-16) increased the strength compared to the sandblasted concrete finish (1/16 in. [1.6 mm] roughness) (A-1, A-2, A-14, and A-15) when using a smooth pipe and had the highest normalized strength among all the different finishes and corrugations, also shown in Fig. 7. The sandblasted concrete finish (1/16 in. [1.6 mm] roughness) had a higher normalized failure load than when the corrugated metal duct was left in place for the specimens with a corrugated interface.

The normalized load (k) versus deflection plots for the specimens with no corrugation and 1/16 and 1/4 in. (1.6 and 6.4 mm) surface roughness are shown in Fig. 8(a) and (b), respectively. The response of the specimen with a monolithically cast plug (A-22) is also shown in Fig. 8 for comparison. A-3 could not be failed due to the capacity of the load cell being used for testing; this plot is shown as a dotted line in Fig. 8(b). The cohesion is related to the negative slope following the maximum load. After cohesion is overcome, it is assumed the load will have a sharp decrease and then level out at a load related to the kinetic coefficient of friction between the plug and cap.

The increased roughness of the exposed aggregate concrete finish (1/4 in. [6.4 mm] roughness) (A-3, A-5, and A-16) improved both the cohesion and friction components of the interface capacity leading to the higher strength, steeper decline following the maximum failure load, and higher sustained load during sliding of the plug as compared

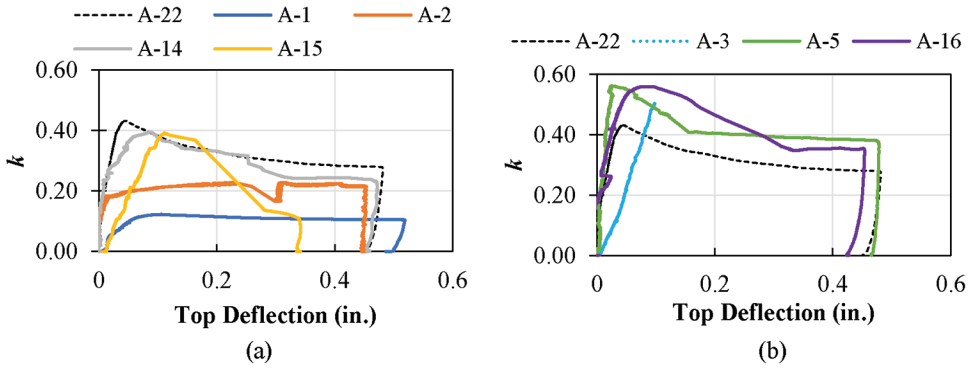

*Fig. 8—Normalized load (*k*) versus top deflection plots for specimens with no corrugations with: (a) 1/16 in. (1.6 mm); and (b) 1/4 in. (6.4 mm) interface surface roughness. (Note: 1 in. = 25.4 mm.)*

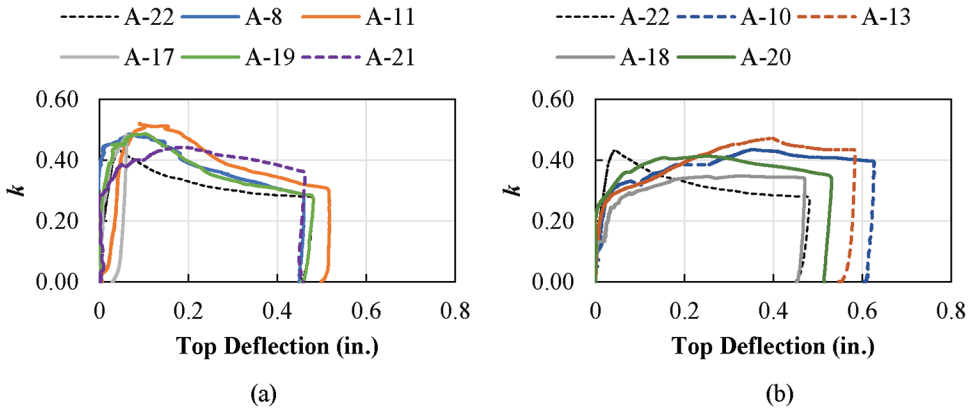

*Fig. 9—Normalized load (*k*) versus top deflection plots for specimens with corrugations with: (a) 1/16 in. (1.6 mm) concrete finish; and (b) concrete to metal interface. (Note: 1 in. = 25.4 mm.)*

to the sandblasted concrete finish (1/16 in. [1.6 mm] roughness) (A-1, A-2, A-14, and A-15) when using a smooth pipe.

1/16 in. (1.6 mm) concrete versus steel (corrugated)

All specimens with corrugation and the 1/16 in. (1.6 mm) surface roughness concrete finish reached their peak load and then decreased in load as the plug pushed through, as shown in Fig. 9(a). A-8, A-11, and A-19 all gradually decreased in load as the plug pushed through, while A-17 had a sudden failure when the cohesion was overcome. A-21 had less cohesion (that is, nonlinear response prior to reaching the maximum load and a less dramatic drop in strength following the maximum load) than the other specimens with the 1/16 in. (1.6 mm) finish; this was likely due to the longer time between casting of the cap and plug (163 days compared to 5 to 7 days for the other specimens). The specimens with corrugation and the 1/16 in. (1.6 mm) surface roughness all reached a higher capacity than the monolithically cast specimen (A-22).

The metal finish had a lower cohesion and strength than 1/16 in. (1.6 mm) concrete roughness, as shown in Fig. 9(b). The normalized load versus displacement in the top of the plug began nonlinear behavior between k of 0.25 and 0.3. After this, the load continued to increase while the plug was pushing through.

Effect of corrugation spacing and depth

The corrugation spacing and depth influenced the interlock and friction components between the plug and cap after cohesion had been overcome. Several different corrugation configurations were investigated in Series A: smooth, single large rib at the bottom of the plug; double large rib at the bottom of the plug; half-spacing of the corrugated ribs along the plug length; and full corrugations. All these specimens had the corrugated metal pipe removed and a 1/16 in. (1.6 mm) roughness finish on the concrete surface. The normalized failure loads for all specimens in this comparison are shown in Fig. 10. All specimens with the interface were cast at FDOT SRC other than A-14 and A-15, which were cast by the precast manufacturer; these are differentiated in Fig. 10.

The specimens with full corrugation (created using the corrugated metal pipe) had the highest normalized strength, which was also comparable with the strength of the monolithically cast specimen. Comparing only the specimens cast at FDOT SRC, the specimens with variations of corrugation had normalized strengths greater than the smooth interface but less than the full corrugations. As mentioned earlier, the smooth specimens cast by the precast manufacturer had a higher strength than those cast at FDOT SRC due to the sensitivity of the behavior of these specimens to casting procedure. More cracking and larger cracks were observed in specimens with corrugation compared to those with smooth interfaces.

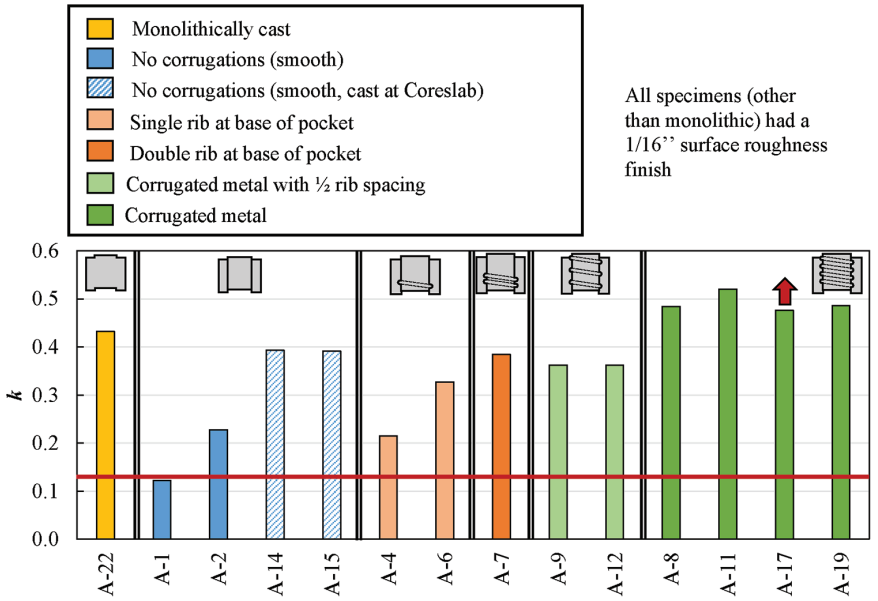

Fig. 10—Comparison for Series A specimens based on corrugation spacing and depth. Red arrow indicates higher failure load (specimen did not fail due to test setup limitations); red line is at current AASHTO LRFD Guide Specification for ABC recommended value of 0.13. (Note: 1 in. = 25.4 mm; full-color PDF is available at www.concrete.org.)

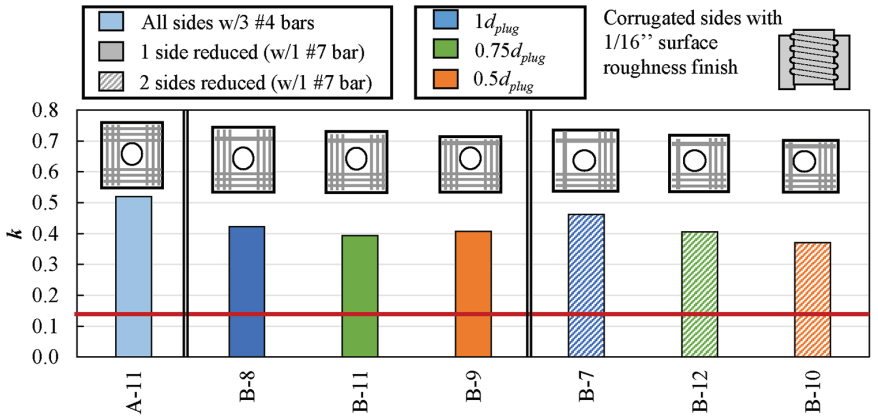

Fig. 11—Comparison graph for specimen while varying edge distance; red line is at current AASHTO LRFD Guide Specification for ABC recommended value of 0.13.

Effect of edge distance

The specimen used as a baseline for Series B and to analyze the effects of edge distance, longitudinal and confinement reinforcement was A-11 because it had the same interface height and surface condition and was fully reinforced. The normalized strength of all specimens in the edge distance comparison are shown in Fig. 11, grouped by specimens with decreasing edge distance on one side and two sides. There was a drop in normalized strength when one No. 7 bar was used in place of the three No. 4 bars in one or two faces. There was approximately a 7% drop in strength when the edge distance was decreased in one direction (from $1d_{plug}$ to $0.75d_{plug}$ or $0.5d_{plug}$). There was a 12.3% drop in strength when the edge distance was reduced in two directions from $1d_{plug}$ to $0.75d_{plug}$, and an additional 8.9% drop when reduced from $0.75d_{plug}$ to $0.5d_{plug}$.

The normalized load versus top of plug deflection curves for all the edge distance specimens are shown in Fig. 12. All specimens saw a relatively linear-elastic response until cohesion was overcome along the interface and sliding of the plug began. Specimen A-11 had a higher strength than the other specimens with similar edge distance on all sides and one No. 7 bar on one (B-8) or two faces (B-7). The crack patterns became more extensive and more concentrated toward the corner between the two shorter edges as the edge distance was decreased.

Effect of longitudinal reinforcement

The normalized failure load and normalized load versus deflection of the top of the plug for specimens with various amounts of longitudinal reinforcement are shown in Fig. 13. The normalized strength decreased in specimens with less longitudinal reinforcement. All specimens had a linear response until reaching the maximum load and then had a drop in strength as the cohesion was overcome. The drop in strength immediately following the maximum failure load was steeper in specimens with less longitudinal reinforcement. The specimen with no longitudinal reinforcement

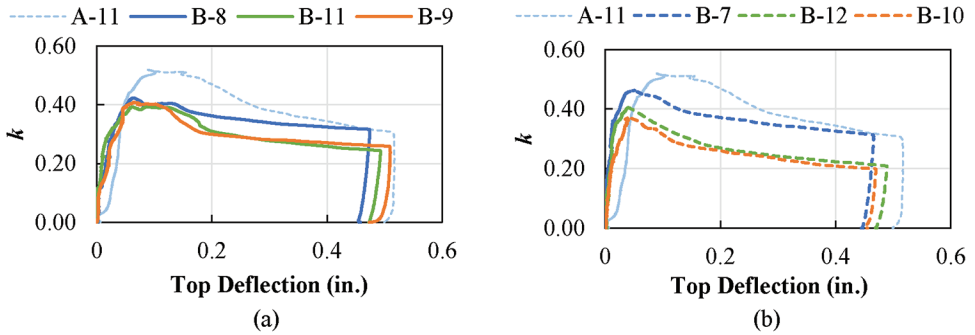

Fig. 12—Normalized load (k) versus top deflection plots for specimens with corrugations, 1.6 mm (1/16 in.) concrete finish, and varying edge distance in: (a) one direction; and (b) two directions. (Note: 1 in. = 25.4 mm.)

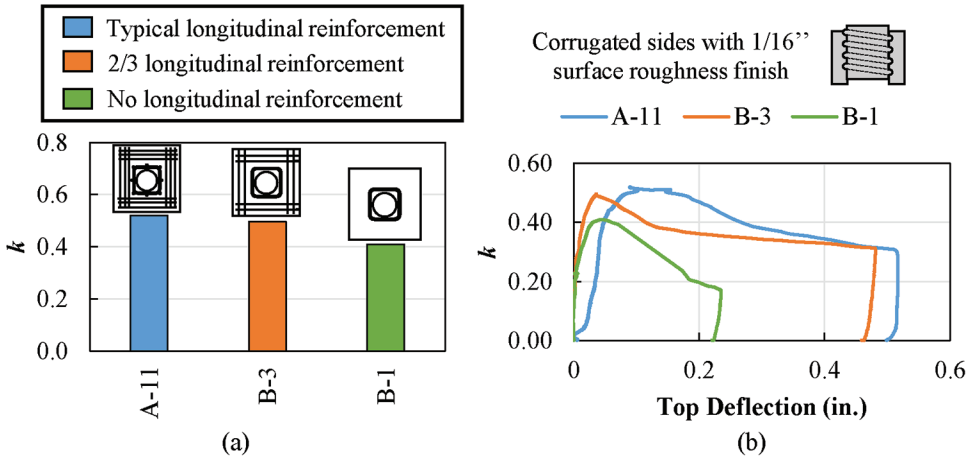

Fig. 13—(a) Normalized failure loads; and (b) normalized versus top of plug displacement curves for specimens with varying longitudinal reinforcement. (Note: 1 in. = 25.4 mm.)

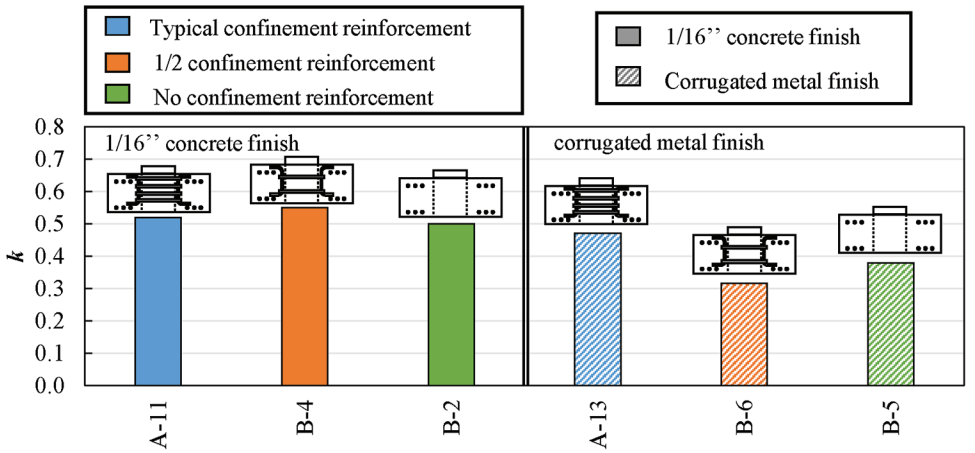

Fig. 14—Comparison graph for specimens with varying confinement reinforcement around pocket. (Note: 1 in. = 25.4 mm.)

around the pocket (B-1) experienced a more sudden failure after reaching the ultimate load. The other specimens (A-11 and B-3) held load as the pocket slid along the interface.

Effect of confinement reinforcement

The normalized failure loads for all specimens with different amounts of confinement reinforcement for specimens with a 1/16 in. (1.6 mm) concrete finish and a corrugated metal pipe finish are shown in Fig. 14. For the specimens with 1/16 in. (1.6 mm) concrete finish on the interface, the specimen with no confinement reinforcement had 4% lower strength than the full confinement reinforcement and 9% lower strength than the half-confinement reinforcement specimen.

The specimens with the corrugated metal pipe finish and either no or half the confinement reinforcement had between 19 and 33% lower strength than the equivalent specimens with full confinement reinforcement. Specimen A-13 experienced rotation of the plug as the plug pushed through, compared with specimens B-6 and B-7, which only experienced minor rotation of the plug.

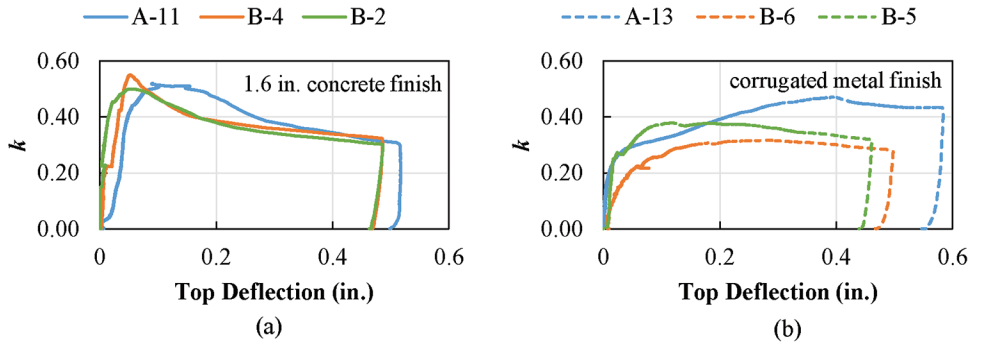

Fig. 15—Normalized load versus top of plug displacement for specimens with varying confinement reinforcement around the pocket and: (a) 1/16 in. (1.6 mm) concrete finish; and (b) corrugated metal finish. (Note: 1 in. = 25.4 mm.)

The normalized load versus top plug deflection curves for specimens with varying amounts of confinement reinforcement with a 1/16 in. (1.6 mm) concrete finish and corrugated metal pipe finish are shown in Fig. 15. The specimens with a 1/16 in. (1.6 mm) concrete finish, Fig. 15(a), all had a relatively linear response until overcoming the cohesion and reaching the failure load. The specimens with less confinement reinforcement seemed to have a more dramatic decrease in strength after reaching the ultimate capacity. Specimens with the corrugated metal pipe finish also had similar responses with a nonlinear response before reaching the ultimate capacity and then maintaining of load as the plug was pushed through, Fig. 15(b).

Plug rotation in specimens with corrugated metal pipe

Two of the specimens with the corrugated metal duct left in place (A-10 and A-13) experienced clear rotation of the plug as the plug was pushed through (following the angle of rotation). For specimens A-18 and A-20, the metal duct was cut at middepth and rotated to make the corrugations discontinuous at the cut to try and prevent the rotation of the plug during testing. Only slight rotation was observed in these specimens, but they did end up failing at lower normalized loads than the specimens where clear rotation was observed. Refer to the details of rotation in Appendix A.

COMPARISON WITH ESTIMATION PROCEDURES FROM CODES AND SPECIFICATIONS

Three different currently available estimation procedures were used to estimate the ultimate loads for the specimens described in this paper.

1. *AASHTO LRFD Bridge Design Specification 8th Edition*[16] (AASHTO LRFD)
2. *AASHTO LRFD Guide Specifications for Accelerated Bridge Construction 1st Edition*[14] (AASHTO ABC)
3. Building Code Requirements for Structural Concrete and Commentary[15] (ACI 318-19)

A fourth estimation procedure was developed based on the AASHTO LRFD BDS; this is called the Proposed Modified Theory and is described in detail in this section.

A summary of these procedures is shown in Table 2. There are additional upper limits to the expression from AASHTO BDS that did not control for the specimens described in this paper.

Table 2—Shear-friction estimation in different codes

Design code	Shear-friction capacity	Equation details
AASHTO LRFD Bridge Design Specification (2017)	$V_{ni} = cA_{cv} + \mu(A_{vf}f_y + P_c)$	Eq. (1) AASHTO BDS (5.7.4.3-3)
AASHTO LRFD Guide Specification for ABC (2018)	$V_{ni} = 0.13\sqrt{f'_{cp}}A_{cv}$	Eq. (2) AASHTO ABC (3.6.6.6-1)
ACI 318-19	$V_{ni} = \mu A_{vf}f_y$	Eq. (3) ACI 318-19 (22.9.4.2)
Proposed Modified Theory based on AASHTO LRFD BDS	$V_{ni} = V_{ni,c} + V_{ni,f}$	Eq. (4)

Proposed Modified Theory based on AASHTO LRFD BDS

The current AASHTO LRFD BDS[16] assumes that the shear-friction capacity is made up of a cohesion component (dependent on the cohesion coefficient and the area of the interface) and a friction component (dependent on the coefficient of friction and clamping force), as shown in Eq. (3)).

$$V_{ni} = V_{ni,c} + V_{ni,f} \quad (3)$$

The cohesion component of the shear-friction capacity is likely dependent on whether the shear plane is through the corrugation (monolithic) or along the interface between cap and plug (non-monolithic). The failure crack will extend through a combination of the interface and corrugations, as shown in Fig. 16(a). The exact location of the failure crack would depend on the concrete strength of each portion in addition to the characteristics of the corrugation (spacing and depth).

The cohesion term of the shear-friction capacity can be found based on the area of the interface that is monolithic and non-monolithic along the failure plane, shown in Eq. (4). When the void is created using corrugated pipes, the areas are calculated using the corrugation sizes.

$$V_{ni,c} = c_m A_{cv,m} + c_r A_{cv,r} \quad (4)$$

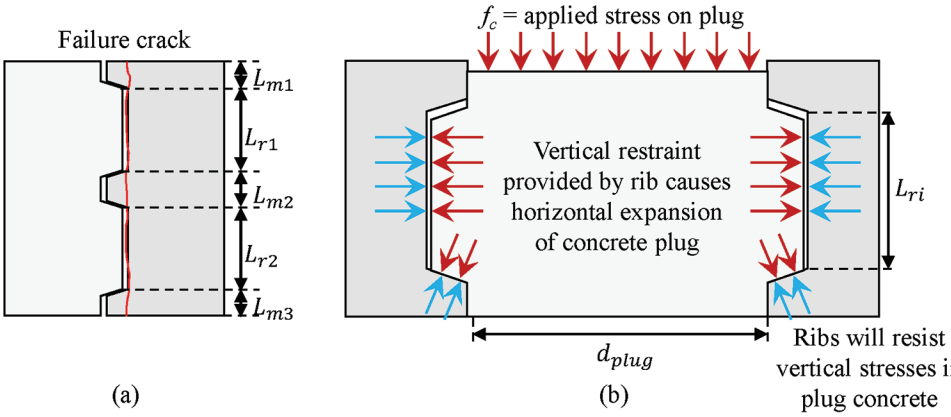

Fig. 16—(a) Area to consider for cohesion component of shear-friction capacity; and (b) ribs restrain vertical movement, resulting in expansion of plug.

The cohesion component for the non-monolithic part varied depending on the surface preparation that was experimentally used. All the cohesion values were found based on AASHTO LRFD BDS.[16] A cohesion factor of 0.24 was used for interfaces with 1/4 in. (6.4 mm) surface roughness and 0.1575 for specimens with 1/16 in. (1.6 mm) of roughness, which is an average between the cohesion factor for 1/4 in. (6.4 mm) surface roughness and when the surface is not intentionally roughened (0.075). A cohesion factor of 0.025 was used for interfaces where the corrugated metal pipe was left in place.

The friction component of the current AASHTO LRFD BDS[16] is shown in Eq. (5). The equation is made up of the coefficient of friction (μ) and normal force ($A_{cv}f_y + P_c$).

$$V_{ni,f} = \mu(A_{vf}f_y + P_c) \quad (5)$$

There is no steel crossing the interface in these specimens, so A_{vf} will equal zero. The normal force P_c may not be equal to zero due to plug expansion during testing. When the vertical stress (f_c) is applied on a plug with a corrugated interface, the corrugation will help to resist vertical stresses in the concrete, which will cause a horizontal displacement and horizontal stresses, shown in Fig. 16(b). The vertical stress can be related to the horizontal stress through Poisson's ratio, and the horizontal stress related to the normal force by the interface area, as shown in Eq. (6)

$$P_c = (\upsilon_c \varepsilon_v) E_c A_r = \upsilon_c \left(\frac{f_c}{E_c}\right) E_c A_r = \upsilon_c f_c (\pi d_{plug}) L_{ri} \quad (6)$$

The actual behavior will be more complicated for several reasons. First, the aforementioned relationship assumes that all the vertical displacement is restrained at the location of the bottom rib. The vertical restrain of the plug is likely spread across multiple ribs. A solution to this is to determine an effective or average depth over which to find the average strain to use in Eq. (6). The effective or average depth can be used as the L_r component of Eq. (6). This value was assumed as the distance from the top of the interface to the mid-height of the corrugated interface ($0.5h_v$).

Another complication to the equation is that the Poisson's ratio for concrete does not remain constant as the stress increases and is dependent on the material properties. The Poisson's ratio for concrete generally remains close to 0.20, but will dramatically increase as the concrete approaches its ultimate strength. The maximum vertical strains observed during the experimental program in the reinforcement in the plug was about 700 με compression. This maximum strain suggests that using a Poisson's ratio of 0.20 will be reasonable for these specimens.

Additionally, the applied stress (f_c) will increase during the test, which means that the normal force component will increase during the test. The maximum stress that the plug will see is the compressive strength (f_c'). The compressive strength of the concrete (f_c') was used in the equation for simplicity.

A coefficient of friction of 1.4 was used for corrugated interfaces with 1/16 in. (1.6 mm) roughened surface and non-corrugated interfaces with a 1/4 in. (6.4 mm) roughened surface, 1.0 for corrugated interfaces where the metal pipe was left in place, and 0.8 for non-corrugated interfaces with 1/16 in. (1.6 mm) roughened surface.

Measured versus estimated results

The measured ultimate loads and ultimate loads normalized by estimated loads are shown in Table 3. The normalized load for each estimated procedure is found by dividing the experimental capacity by the estimated capacity found using each procedure. For example, as shown in Table 3, for specimen A-1, Measured/AASHTO = 429.7 kip (1911 kN)/298.6 kip (1328 kN) = 1.44. A normalized ultimate load greater than or equal to 1.0 is conservative and less than 1.0 is unconservative. Because there was no steel crossing the interface, the shear-friction capacity estimated using ACI 318-19 would be 0 for all the specimens; this estimate was not included in the following analyses.

On average, the AASHTO LRFD BDS, the AASHTO LRFD Guide Specification for ABC, and the Proposed Modified Theory based on AASHTO LRFD BDS provided conservative estimates, with the proposed theory being more accurate (with an average closer to 1.0) and precise (with lower coefficient of variation).

There were several specimens that had an estimated capacity less than the measured capacity or closer to the measured capacity (depending on the procedure); these

Table 3—Measured and estimated failure loads and ultimate loads normalized by estimated loads

Specimen	Ultimate load, kip				Normalized ultimate load		
	Measured	AASHTO	ABC	Proposed theory	AASHTO	ABC	Proposed theory
A-1	429.7	298.6	457.4	557.9	1.44	0.94	0.77
A-2	339.0	135.7	193.7	434.7	2.50	1.75	0.78
A-3	>750	135.7	194.2	688.3	—	—	—
A-4	320.2	135.7	193.7	413.7	2.36	1.65	0.77
A-5	615.4	99.5	142.4	504.8	6.18	4.32	1.22
A-6	356.0	99.5	141.7	305.0	3.58	2.51	1.17
A-7	418.6	99.5	141.7	327.0	4.21	2.95	1.28
A-8	719.5	135.7	193.2	677.8	5.30	3.72	1.06
A-9	553.5	135.7	198.5	542.8	4.08	2.79	1.02
A-10	662.2	135.7	198.5	470.3	4.88	3.34	1.41
A-11	575.4	99.5	143.7	508.7	5.78	4.00	1.13
A-12	399.8	99.5	143.7	375.5	4.02	2.78	1.06
A-13	521.6	99.5	143.7	352.5	5.24	3.63	1.48
A-14	605.6	135.7	200.2	335.2	4.46	3.02	1.81
A-15	441.3	99.5	146.7	310.8	4.43	3.01	1.42
A-16	631.2	99.5	146.7	529.1	6.34	4.30	1.19
A-17	>750	135.7	204.8	581.3	—	—	—
A-18	533.3	135.7	200.0	385.5	3.93	2.67	1.38
A-19	569.2	99.5	152.2	558.6	5.72	3.74	1.02
A-20	482.6	99.5	152.2	388.2	4.85	3.17	1.24
A-21	666.0	135.7	196.0	543.6	4.91	3.40	1.23
A-22	387.5	165.9	116.6	437.6	2.34	3.32	0.89
B-1	364.1	99.5	115.5	362.4	3.66	3.15	1.00
B-2	444.6	99.5	115.5	362.4	4.47	3.85	1.23
B-3	440.9	99.5	115.5	362.4	4.43	3.82	1.22
B-4	493.8	99.5	116.6	367.6	4.96	4.23	1.34
B-5	340.7	99.5	116.6	251.8	3.42	2.92	1.35
B-6	283.8	99.5	116.6	251.8	2.85	2.43	1.13
B-7	413.6	99.5	116.3	365.9	4.16	3.56	1.13
B-8	379.3	99.5	116.6	367.6	3.81	3.25	1.03
B-9	364.6	99.5	116.3	365.9	3.66	3.14	1.00
B-10	330.7	99.5	116.3	365.9	3.32	2.84	0.90
B-11	352.4	99.5	116.6	367.6	3.54	3.02	0.96
B-12	363.2	99.5	116.3	365.9	3.65	3.12	0.99
				Average =	4.14	3.14	1.14
				Standard deviation =	1.12	0.74	0.24
				Coefficient of variation =	0.271	0.236	0.194

Note: 1 kip = 4.45 kN.

included A-1, A-2, A-4, A-22, B-10, B-11, and B-12. A-1 and A-2 were both smooth interfaces with sandblasted finishes. A-4 had a smooth interface with sandblasted finish, other than a single rib at the bottom of the plug. The smooth interfaces did not provide as significant a friction component after the cohesion was overcome, which is the reason for the lower capacities. B-10, B-11, and B-12 all had reduced edge distances in one or both faces. The reduced edge distance led to the surrounding cap not being able to provide as much restraint to the normal force from the expanding plug as the other specimens. This led to the decreased capacity compared to the estimation procedures. These lower conservative estimates can be avoided by providing corrugated

interfaces or exposed aggregate finishes and edge distances at least equal to the pocket diameter.

CONCLUSIONS

Several preliminary conclusions and experimental observations can be made based on the shear-friction testing described in this report:

1. All specimens with the 12 in. (305 mm) diameter plug failed due to a shear-friction failure at the interface between the plug and cap. Even the monolithically cast specimen failed due to a shear-friction failure at the interface. Most of the shear-friction failures were preceded by radial cracking extending out of the plug toward the exterior surfaces of the cap.

2. Normalizing by interface area and the square root of concrete strength was found to be a reasonable approach for normalizing the results (that is, similar results were observed between specimens where only interface area and concrete strength varied).

3. Specimens with an exposed aggregate finish with 1/4 in. (6.4 mm) surface roughness had the highest normalized strength among all specimens tested (higher than corrugated interface with 1/16 in. [1.6 mm] surface roughness). This is based on testing of 12 in. (305 mm) diameter plugs and should be verified with larger diameter plugs.

4. Specimens with a smooth interface and 1/16 in. (1.6 mm) surface roughness are sensitive to the casting procedure (for example, time between casts, surface preparation, specific concrete properties). Normalized strengths varied from k of 0.122 (specimen cast at the Florida Department of Transportation Structures Research Center [FDOT SRC]) to 0.393 (specimen cast by precast manufacturer). Specimens with a corrugated interface had less variability in normalized strength between casting location.

5. The corrugated metal pipe surface condition provides only minor cohesion between the plug concrete and metal pipe and failed at lower loads than specimens with the corrugated interface with 1/16 in. (1.6 mm) surface roughness concrete finish. The plug rotated during testing when a continuous pipe was provided. Cutting the pipe at midheight helped to restrict the rotation but led to lower capacities.

6. The corrugation size and spacing affects the strength of the interface. Providing single or double ribs at the base of the pocket increased the normalized strength of specimens compared to those with a smooth interface (comparing only specimens cast at FDOT SRC). Half spacing of the corrugations still had a lower normalized strength than the full corrugations.

7. Edge distance (between the edge of the plug and edge of cap) had a noticeable effect on the normalized strength only when the edge distance was decreased in two directions. Large failure cracks typically extended diagonally out of the plug toward the corner of the cap. Decreasing the edge distance in one direction did not have as significant an effect on this diagonal distance as decreasing the edge distance in two directions.

8. The confinement reinforcement saw higher strains in specimens with smaller edge distances in two directions. This shows that as there is less concrete area to resist the splitting cracks, the confinement reinforcement becomes more important.

9. Decreasing the longitudinal reinforcement in the cap decreased the normalized strength of the specimens. Changing the confinement reinforcement did not have a significant effect on the strength of the specimens with $1d_{plug}$ edge distance. However, it is assumed that the confinement reinforcement would influence the strength for smaller edge distances.

10. The current procedures available to estimate the strength of this interface (*AASHTO LRFD Bridge Design Specification 8th Edition* and *AASHTO LRFD Guide Specification for Accelerated Bridge Construction 1st Edition*) were found to conservatively estimate the ultimate capacity of the interface for the specimens tested. A proposed theory based on AASHTO LRFD BDS was presented and shown to be more accurate and precise than currently available estimation procedures.

AUTHOR BIOS

Fatima Vieira *is a PhD Student and Graduate Research Assistant at Florida International University (FIU), Miami, FL. She received her BSc from Santa Maria University, Caracas, Venezuela, in 2016, and her MSc in civil engineering from FIU in 2018. Currently, she is working on a Florida Department of Transportation project under the supervision of D. Garber. In her research, she is evaluating the shear-friction capacity of corrugated pipe connection in precast footings.*

Bruno Vasconcelos *is a Senior Structural Engineer for the Federal Highway Administration (FHWA) Resource Center. He received his BS from Johns Hopkins University, Baltimore, MD, and his MS and PhD from The University of Texas at Austin, Austin, TX. His research interests include the design and analysis of prestressed concrete structures, ultra-high-performance concrete, and accelerated bridge construction.*

ACI member **David B. Garber** *is a Senior Structural Engineer for Federal Highway Administration's Resource Center. He previously served as Associate Professor and Interim Department Chair at Florida International University before joining FHWA. He received his BS from Johns Hopkins University and his MS and PhD from The University of Texas at Austin. His research interests include the design and analysis of prestressed concrete structures, ultra-high performance concrete, and accelerated bridge construction.*

ACKNOWLEDGMENTS

The research presented in this project was supported by the Florida Department of Transportation (FDOT). The authors would like to thank FDOT for their financial support and the team of engineers and staff at the Structures Research Center for their assistance in constructing and testing the specimens. The authors would also like to thank Coreslab Structures (Miami), Inc., for their construction of 20 of the specimens tested for this research. The opinions, findings and conclusions expressed in this publication are those of the author(s) and not necessarily those of the Florida Department of Transportation or the U.S. Department of Transportation.

NOTATION

A_{cv}	=	area of shear plane
$A_{cv,m}$	=	concrete interface area for monolithic component (using corrugation sizes found in Table 1 and Fig. 2)
$A_{cv,r}$	=	concrete interface area for non-monolithic component
A_r	=	interface area to use for friction component calculation in proposed theory
A_{vf}	=	area of reinforcement crossing plane
c	=	cohesion factor
c_m	=	cohesion coefficient for monolithic concrete
c_r	=	cohesion coefficient for non-monolithic concrete
d_{edge}	=	distance between edge of cylindrical pocket and edge of cube or cap
d_{plug}	=	diameter of cylindrical pocket or plug
d_v	=	inside diameter of pocket
E_c	=	modulus of elasticity for concrete
f_c	=	vertical stress in plug concrete during testing

f_c' = concrete compressive strength
f_{cp}' = concrete compressive strength of plug concrete
f_y = yield strength of reinforcement
h_{cap} = height of cap or cube
h_{rib} = height of rib in corrugated interface
h_v = effective height of the pocket or interface
k = normalization factor based on *AASHTO LRFD Guide Specification for ABC*
L_m = length of monolithic portion of interface
L_{ri} = average interface length to use for friction component calculation in proposed theory (assumed as $0.5h_v$)
L_{rib} = length of rib in corrugated interface
P_c = compressive force perpendicular to shear plane
s_{rib} = spacing of ribs in corrugated interface
V_{ni} = nominal interface shear resistance
$V_{ni,c}$ = cohesion portion of nominal interface shear resistance
$V_{ni,ex}$ = experimental interface shear capacity
$V_{ni,f}$ = friction portion of nominal interface shear resistance
ε_v = vertical strain in plug
v_c = Poisson's ratio for concrete
μ = friction coefficient

REFERENCES

1. Rahal, K., "Shear-Transfer Strength of Reinforced Concrete," *ACI Structural Journal*, V. 107, No. 4, July-Aug. 2010, pp. 419-426.

2. *fib*, "*fib* Model Code 2010 Final Draft, Volume 1," International Federation for Structural Concrete, Lausanne, Switzerland, 2010.

3. Ali, M., and White, R., "Enhanced Contact Model for Shear Friction of Normal and High-Strength Concrete," *ACI Structural Journal*, V. 96, No. 3, May-June 1999, pp. 348-360.

4. Hofbeck, J.; Ibrahim, O.; and Mattock, A., "Shear Transfer in Reinforced Concrete," *ACI Journal Proceedings*, V. 66, No. 2, Feb. 1969, pp. 119-128.

5. Júlio, E. N. B. S.; Branco, F. A. B.; and Silva, V. D., "Concrete to Concrete Bond Strength. Influence of the Roughness of the Substrate Surface," *Construction and Building Materials*, V. 18, No. 9, 2004, pp. 675-681. doi: 10.1016/j.conbuildmat.2004.04.023

6. Mohamad, M. E.; Ibrahim, I. S.; Abdullah, R.; Abd. Rahman, A. B.; Kueh, A. B. H.; and Usman, J., "Friction and Cohesion Coefficients of Composite Concrete to Concrete Bond,"," *Cement and Concrete Composites*, V. 56, 2015, pp. 1-14. doi: 10.1016/j.cemconcomp.2014.10.003

7. Randl, N., "Design Recommendations for Interface Shear Transfer in *fib* Model Code 2010," *Structural Concrete*, V. 14, No. 3, 2013, pp. 230-241. doi: 10.1002/suco.201300003

8. Santos, P. M. D.; Júlio, E. N. B. S.; and Silva, V. D., "Correlation Between Concrete to Concrete Bond Strength and the Roughness of the Substrate Surface," *Construction and Building Materials*, V. 21, No. 8, 2007, pp. 1688-1695. doi: 10.1016/j.conbuildmat.2006.05.044

9. Santos, P. M. D., and Júlio, E. N. B. S., "Factors Affecting Bond between New and Old Concrete," *ACI Structural Journal*, V. 108, No. 4, July-Aug. 2011, pp. 449-456.

10. Mattock, A. H.; Li, W. K.; and Wang, T. C., "Shear Transfer in Lightweight Reinforced Concrete," *PCI Journal*, V. 21, No. 1, 1976, pp. 20-39. doi: 10.15554/pcij.01011976.20.39

11. Mattock, A. H., and Hawkins, N. M., "Shear Transfer in Reinforced Concrete - Recent Research," *PCI Journal*, V. 17, No. 2, 1972, pp. 55-75. doi: 10.15554/pcij.03011972.55.75

12. Williams, C. S.; Massey, J. B.; Bayrak, O.; and Jirsa, J. O., "Investigation of Interface Shear Transfer Using Push-Through Tests," *ACI Structural Journal*, V. 114, No. 1, Jan.-Feb. 2017, pp. 173-185.

13. Restrepo, J.; Tobolski, M.; and Matsumoto, E., "Development of a Precast Bent Cap System for Seismic Regions," NCHRP Report 681, National Cooperative Highway Research Program, Washington, DC, 2011, 115 pp.

14. Culmo, M. P.; Marsh, L.; Stanton, J.; and Mertz, D., "Recommended AASHTO Guide Specifications for ABC Design and Construction," NHCRP Project No. 12-102, National Cooperative Highway Research Program, Washington, DC, 2018, 219 pp.

15. ACI Committee 318, "Building Code Requirements for Structural Concrete (ACI 318-19) and Commentary (ACI 318R-19) (Reapproved 2022)," American Concrete Institute, Farmington Hills, MI, 2019, 624 pp.

16. AASHTO, *AASHTO LRFD Bridge Design Specification, Customary U.S. Units, 8th Edition*, American Association of State Highway and Transportation Officials, Washington, DC, 2017.

ACI STRUCTURAL JOURNAL TECHNICAL PAPER

Title No. 122-S02

Axial Load-Bearing Concrete Confined with Ultra-High-Performance Concrete Jackets and Basalt Fiber-Reinforced Polymer Grids

by Yail J. Kim and Yordanos Dinku

This paper presents the behavior of unreinforced cylindrical concrete elements confined with a hybrid system, consisting of an ultra-high-performance concrete (UHPC) jacket and basalt fiber-reinforced polymer (BFRP) grids. For exploring the feasibility of the proposed strengthening scheme, a series of tests are conducted to evaluate material properties and to obtain results related to interfacial bond, load-bearing capacity, axial responses, and failure modes. To understand the function of the individual components, a total of 57 cylinders are loaded under augmented confining conditions, including plain cores with ordinary concrete (CONT), plain cores with UHPC jackets (Type A), and plain cores with UHPC jackets plus BFRP grids (Type B). By preloading the cores at up to 60% of the control capacity (60%f_c') before applying the confinement system, the repercussions of inherent damage that can take place in vertical members on site are simulated. The compressive strength of UHPC rapidly develops within 7 days, whereas its splitting strength noticeably ascends after 14 days. The adhesion between the ordinary concrete and UHPC increases over time. While the Type B specimens outperform their Type A counterparts in terms of axial capacity by more than 18%, reliance on the BFRP grids is reduced with the growth of UHPC's strength and adhesion because of the interaction between the hardened UHPC and the core concrete. The adverse effects of the preloading are noteworthy for both types, especially when exceeding a level of 30%f_c'. The BFRP grid-wrapping alleviates the occurrence of a catastrophic collapse in the jacketed cylinders, resulting from a combination of the axial distress and lateral expansion of the core. Analytical models explain the load-carrying mechanism of the strengthened concrete, including confinement pressure and BFRP stress. Through parametric investigations, the significance of the constituents is clarified, and design recommendations are suggested.

Keywords: fiber-reinforced polymer (FRP); rehabilitation; retrofit; strengthening; ultra-high-performance concrete (UHPC).

INTRODUCTION

The demand for upgrading the functionality of existing structures has increased in modern society as the condition of constituents deteriorates over time. Such degradation can be attributed to a number of causes—for example, aging, aggressive environments, excessive live load, and physical damage.[1] On account of constrained funding and resources, rehabilitation may be preferred to reconstruction for the restoration of intended performance, enhanced safety, and extended service life.[2] External confinement is an effective solution to improve the capacity of a concrete member subjected to axial compression.[3] The mechanics associated with confinement is that the lateral dilation of a section is restrained and thus, its structural integrity is preserved under a load exceeding initial design requirements. When a jacket is installed and loaded in compression, the confined concrete undergoes triaxial stresses and is protected from the ingress of detrimental chemicals, which is beneficial from capacity, failure mode, and durability perspectives.[4] Various forms of jackets are used, including concrete, ferrocement, steel shells, fiber-reinforced polymer (FRP) sheets, and hybrid materials.[5-9] The activation of jackets, unless prestressed, demands substantial damage and transverse expansions in the core; accordingly, this type of strengthening is referred to as passive confinement and size effect is generally deemed insignificant.[10,11]

Hybrid configurations in strengthening concrete provide several advantages in terms of strength, stiffness, energy dissipation, ductility, and cost.[12] Rousakis[13] attempted to confine concrete using a combination of glass FRP (GFRP) sheets and polypropylene ropes. The inelastic deformation and post-peak dilation of the confined cylinders were resisted by the sheets and ropes, respectively, so that abrupt failure of the cylinders was mitigated. Koutas et al.[14] reported a review of textile-reinforced mortars and discussed confinement methods, the behavior and failure of textiles and mortars, and the effects of assorted parameters. The properties of binding resins dominated the effectiveness of such a hybrid-strengthening concept. Mohammed et al.[15] tested concrete columns repaired with hybrid jackets, made of GFRP shells and a cementitious grout. The strength of the infill grout was crucial to increasing the capacity of the confined concrete and, considering stress concentrations, the jackets were more appropriate for circular cross sections than square sections. Overall, hybrid confinement is a promising technique and further research is warranted with emerging materials.

Ultra-high-performance concrete (UHPC) is recognized as a state-of-the-art cementitious composite and has been adopted for numerous projects around the world.[16] The water-cement ratio (w/c) of UHPC is lower than 0.25 to formulate a dense mixture along with optimized granular

ACI Structural Journal, V. 122, No. 1, January 2025.

MS No. S-2021-479.R2, doi: 10.14359/51743290, received March 6, 2024, and reviewed under Institute publication policies.

gradations, leading to favorable durability, strength, and energy absorption.[17,18] Despite the recent acceptance of UHPC in the construction industry,[19] applications are largely unknown as a repair and rehabilitation material. A few laboratory experiments were carried out to examine the feasibility of UHPC jackets as a means for confining concrete.[20,21] Compared with a high compressive strength varying from f_c' = 120 to 150 MPa (17.4 to 21.8 ksi), the tensile resistance of UHPC is limited even with the presence of reinforcement.[18,22] For this reason, supplementary elements may be added to withstand the splitting stress of UHPC jackets in the circumferential direction and to preclude the regional spalling of the jackets. Among other types of FRP composites, basalt FRP (BFRP) is gaining attention because of the strength, acid resistance, water absorption, non-combustibility, and affordable expense.[23] Basalt fibers, extracted from volcanic rocks, are environmentally friendly and innocuous.[24] Preliminary efforts were made to assess the applicability of BFRP sheets in confining concrete,[25-27] whereas an inorganic matrix such as UHPC cannot be impregnated with such continuum basalt fabrics and hence, another conformation may be sought.

This paper experimentally investigates the behavior of cylindrical concrete specimens confined with a hybrid system incorporating UHPC jackets and BFRP grids when subjected to axial compression. Factors of interest are constituent properties, ameliorated capacities, axial responses, and failure characteristics. Through analytical modeling, parameters influencing the confining pressure and BFRP stress of the proposed system are identified, and practical recommendations are proposed.

RESEARCH SIGNIFICANCE

Although traditional materials are dominant in confining concrete, their long-term effectuality is questionable in matters of consistency, preservation, and reliability. As a result, the necessity of an alternative arises to prolong the operable period of load-bearing concrete that fulfills modified expectations. In the present research, a conceptual examination is performed to explore the potential of a new confinement system for improving the axial capacity of concrete and to ascertain how each component carries external loadings. For the convenience of laboratory experiments, rather than contemplating infinitely many combinations of possible scenarios in the field, representative load levels are employed to simulate the ramifications of pre-damaged concrete cores without reinforcement. Upon substantiating the validity of the hybrid strengthening approach with UHPC and BFRP, transformative knowledge is furnished for the rehabilitation community to assimilate.

EXPERIMENTAL INVESTIGATION

This section outlines a test program to provide information on materials, confining schemes, and loading protocols, which are necessary for understanding the efficacy of a strengthening system comprising a UHPC jacket and BFRP grids.

Materials

Concrete—The specified compressive strength of ordinary concrete (ready mix) was 25 MPa (3625 psi). Complying with the instruction manual, a patented UHPC product was mixed in the laboratory at room temperature, which contained sulfate-resistant cement, finely graded sand, carbon nanofibers, and others (detailed information cannot be released for proprietary reasons). The following properties are reported by the manufacturer: autogeneous shrinkage < 0.01%; density = 2350 kg/m^3 (147 lb/ft^3); flow diameter = 280 mm (11 in.) per ASTM C230/C230M[28]; and 28-day compressive strength = 120 MPa (17,400 psi).

BFRP—Commercially available BFRP grids, consisting of basalt fibers and an epoxy resin, were employed as a confining material. The mesh-opening size of the grids was 10 x 10 mm (0.4 x 0.4 in.), and the apparent width and thickness of a single grid were 2 and 0.65 mm (0.079 and 0.025 in.), respectively, on average (Fig. 1(a)). The density of BFRP was 2.7 g/cm^3 (0.1 lb/in.^{3}). The grids were bonded to a concrete substrate using a two-part epoxy adhesive (a hardener and a resin to be mixed at a mass ratio of 1:3). After complete curing at room temperature (6 to 7 days), the nominal properties of the hardened epoxy are: tensile strength = 30 MPa (4350 psi); elastic modulus = 1.5 GPa (220 ksi); and ultimate strain = 1.5%.

Specimens and preloading

Using the ordinary concrete, a total of 57 unreinforced cylinders were cast, with dimensions of 100 mm (4 in.) in diameter by 200 mm (8 in.) in depth, and moisture-cured for 28 days. Pursuant to ASTM C39/C39M,[29] three cylinders were tested and an average compressive strength of f_c' = 25.4 MPa (3680 psi) was obtained. For the purpose of simulating possible damage in on-site concrete, the cylinders were preloaded at 0, 30, and 60% of f_c' (18 cylinders each and 54 cylinders in total) under a force-control mode with a rate of 2.5 kN/s (0.56 kip/s). Such an experimental technique is frequently used to emulate deteriorated structural concrete in tandem with microcracking and the weakened bond between a binder and aggregates,[30] as well as to comprehend the full-range response of the confined concrete.

Strengthening scheme

The prepared cylinders were classified into two categories (Fig. 1(a) and Table 1): plain concrete with a UHPC jacket (Type A), and plain concrete with a UHPC jacket plus a single layer of BFRP grids (Type B). These augmented strengthening schemes were intended to clarify the role of each confining element. The Type A cylinders had 25 mm (1 in.) thick UHPC jackets surrounding the cores (fully cured, preloaded, and surface-cleaned cylinders). As instructed by the UHPC manufacturer, prepackaged dry components were stirred with water until a homogeneous mixture was obtained; then, the wet UHPC was placed into a plastic mold (150 mm [6 in.] in diameter) containing the core to produce a jacketed cylinder (Type A in Fig. 1(a)). One day after UHPC casting, the heterogeneous specimens were stripped and additionally cured for up to 28 days at room temperature (27 cylinders in Table 1). The Type B cylinders were

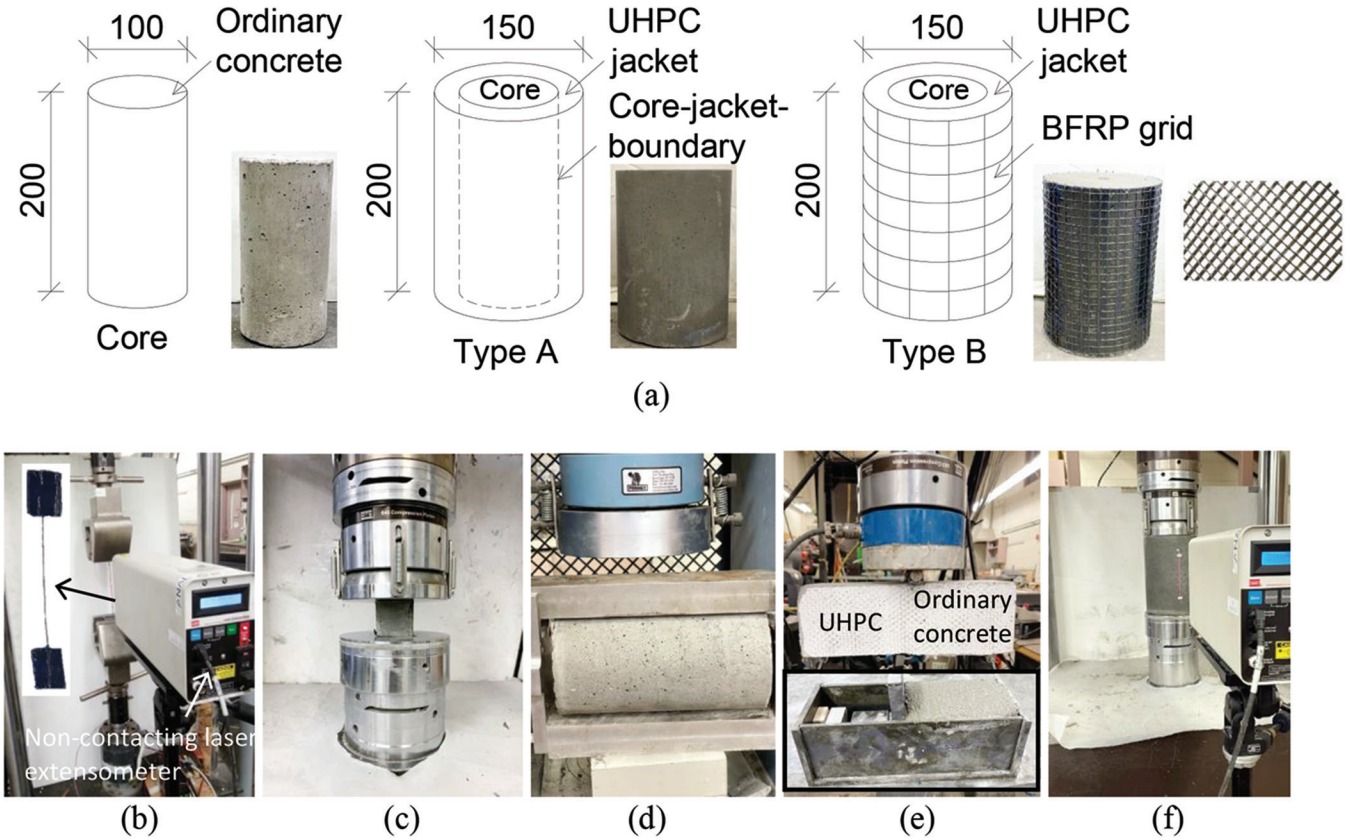

Fig. 1—Specimen details: (a) schematic of cylinders; (b) BFRP coupon; (c) UHPC cube; (d) UHPC splitting; (e) prism under three-point bending; and (f) axial compression.

produced in a similar manner to their Type A counterparts. The mixed epoxy was pasted to precut BFRP grids (200 mm [8 in.] wide by 546 mm [21.5 in.] long), which completely enclosed UHPC-jacketed cylinders (1-day cured) with an overlapping length of 75 mm (3 in.), and the BFRP-bonded specimens (27 cylinders in Table 1) were cured in the same manner as the Type A cylinders. To understand the implications of time-dependent UHPC strength, the confined cylinders were loaded to failure at 7, 14, and 28 days of curing (three cylinders, each, in agreement with ASTM C39/C39M [29]).

Test methods

Material properties—Three BFRP coupons were cut from the grid for a tension test (Fig. 1(b)) and the effective cross-sectional area of the individual BFRP strands was 0.118 mm^2 (0.0002 in.^{2}). To prevent slippage, both ends of the BFRP coupon were tapped with epoxy-impregnated composite sheets (Fig. 1(b), inset). In accordance with ASTM C109/C109M[31] and C496/C496M,[4] the compressive and splitting strengths of UHPC were attained by testing 50 mm (2 in.) cubes and cylinders (100 mm [4 in.] in diameter by 200 mm [8 in.] in depth), respectively. As pictured in Fig. 1(c) and (d), 18 specimens were loaded at 7, 14, and 28 days of UHPC curing (three cubes and three cylinders, each).

Bond—Due to the absence of a standard bond test method for UHPC, custom-made interface specimens were used (Fig. 1(e)): the purpose of the interfacial test was to characterize the bond performance between the ordinary concrete and UHPC, rather than to directly examine their interactions in shear. The specimen was composed of two blocks (100 x 100 x 150 mm [4 x 4 x 6 in.], each). A 28-day-cured ordinary concrete block was placed in a steel mold (Fig. 1(e), inset) and UHPC was added to produce a prism set. Upon curing for 7, 14, and 28 days at room temperature, nine prisms (three specimens times three curing periods) were loaded per ASTM C78/C78M[32] at a support-to-support length of 250 mm (10 in.). The specimens were painted in white to better monitor a cracking pattern. The applied load and displacement at midspan were measured by a load cell and a linear potentiometer, respectively. The digital image correlation technique was used to visually evaluate the failure characteristics of the interface.

Axial capacity—The confined cylinders were located to a universal testing machine and monotonically loaded until failure at a rate of 5 mm (0.2 in.)/min. (Fig. 1(f)): the compression load was shared by the core concrete and the jacketing system like the load-bearing mechanism of upgraded columns in a typical field application. For the measurement of concrete deformation, reflection tapes were attached at a gauge length of 100 mm (4 in.) and a non-contacting laser extensometer logged axial displacements, which were synchronized with load-cell readings. A computer system controlled all data acquisition processes and recorded the response of the specimens.

Table 1—Test matrix and axial capacity

Category	UHPC curing	Preload	Effective stress, MPa		Category	UHPC curing	Preload	Effective stress, MPa	
			Ind.	Ave.				Ind.	Ave.
Type A	7 days	0%f_c'	34.1	30.6	Type B	7 days	0%f_c'	32.9	34.3
Type A	7 days	0%f_c'	27.7		Type B	7 days	0%$f_{c\,v}'$	33.9	
Type A	7 days	0%f_c'	30.1		Type B	7 days	0%f_c'	36.2	
Type A	7 days	30%f_c'	19.2	25.0	Type B	7 days	30%f_c'	26.2	29.0
Type A	7 days	30%f_c'	26.5		Type B	7 days	30%f_c'	31.5	
Type A	7 days	30%f_c'	29.2		Type B	7 days	30%f_c'	29.3	
Type A	7 days	60%f_c'	20.8	22.4	Type B	7 days	60%f_c'	25.9	23.6
Type A	7 days	60%f_c'	22.9		Type B	7 days	60%f_c'	18.3	
Type A	7 days	60%f_c'	23.5		Type B	7 days	60%f_c'	26.5	
Type A	14 days	0%f_c'	39.5	38.1	Type B	14 days	0%f_c'	47.9	48.9
Type A	14 days	0%f_c'	37.0		Type B	14 days	0%$f_{c\,v}'$	52.2	
Type A	14 days	0%f_c'	37.7		Type B	14 days	0%f_c'	46.8	
Type A	14 days	30%f_c'	33.6	34.4	Type B	14 days	30%f_c'	48.8	41.1
Type A	14 days	30%f_c'	35.9		Type B	14 days	30%f_c'	45.6	
Type A	14 days	30%f_c'	33.6		Type B	14 days	30%f_c'	29.0	
Type A	14 days	60%f_c'	26.9	25.3	Type B	14 days	60%f_c'	40.0	37.5
Type A	14 days	60%f_c'	25.3		Type B	14 days	60%f_c'	42.4	
Type A	14 days	60%f_c'	23.8		Type B	14 days	60%f_c'	30.0	
Type A	28 days	0%f_c'	43.8	44.3	Type B	28 days	0%f_c'	56.0	55.2
Type A	28 days	0%f_c'	43.1		Type B	28 days	0%$f_{c\,v}'$	54.4	
Type A	28 days	0%f_c'	46.1		Type B	28 days	0%f_c'	55.2	
Type A	28 days	30%f_c'	35.2	36.1	Type B	28 days	30%f_c'	43.8	43.7
Type A	28 days	30%f_c'	35.7		Type B	28 days	30%f_c'	42.6	
Type A	28 days	30%f_c'	37.3		Type B	28 days	30%f_c'	44.7	
Type A	28 days	60%f_c'	30.4	31.3	Type B	28 days	60%f_c'	36.9	36.7
Type A	28 days	60%f_c'	30.3		Type B	28 days	60%f_c'	35.0	
Type A	28 days	60%f_c'	33.3		Type B	28 days	60%f_c'	38.3	

Note: Effective stress is ultimate load/cross-sectional area of core; Ind. is individual; Ave. is average; 1 MPa = 145 psi.

RESULTS AND DISCUSSION

Experimental outcomes are delineated with an emphasis on the material properties, interfacial strength, load-bearing capacity, axial responses, and failure of concrete cylinders confined with a UHPC-BFRP system. Statistical techniques characterize the ability of resisting external load for the strengthened concrete subjected to inherent core damage.

Strength of constituents

The constitutive behavior of BFRP is given in Fig. 2(a). The response was linear until abrupt fracture occurred at an average stress of f_{fu} = 2104 MPa (305 ksi) with an elastic modulus of E_f = 101 GPa (14,650 ksi). Although these values cannot be appraised against the contents shown in the manufacturer's data sheet, which only states a maximum capacity of the grid mesh (24 kN/m [1650 lb/ft]), an article documents the following property ranges[23]: 656 MPa (95 ksi) ≤ f_{fu} ≤ 3470 MPa (503 ksi) and 35 GPa (5100 ksi) ≤ E_f ≤ 103 GPa (14,900 ksi). The average compressive strength of UHPC at 7 days of curing was 110 MPa (16.0 ksi) and it reached to 120 MPa (17.4 ksi) at 28 days, conforming to the manufacturer's design strength of 120 MPa (17.4 ksi). The rapid growth of the early-age strength is attributable to the agglomerated cement grains without interruption by coarse aggregates, which facilitated the formation of continuous calcium silicate hydrate (C-S-H) gels with a high packing density.[33] Figure 2(c) exhibits the splitting strength of UHPC over time. Contrary to the case of the axial compression (Fig. 2(b)), the development of the splitting strength was pronounced after 14 days: 0.08 MPa (11.6 psi)/day between 7 and 14 days versus 0.33 MPa (47.9 psi)/day between 14 and 28 days. Given that the tensile cohesion of a cement

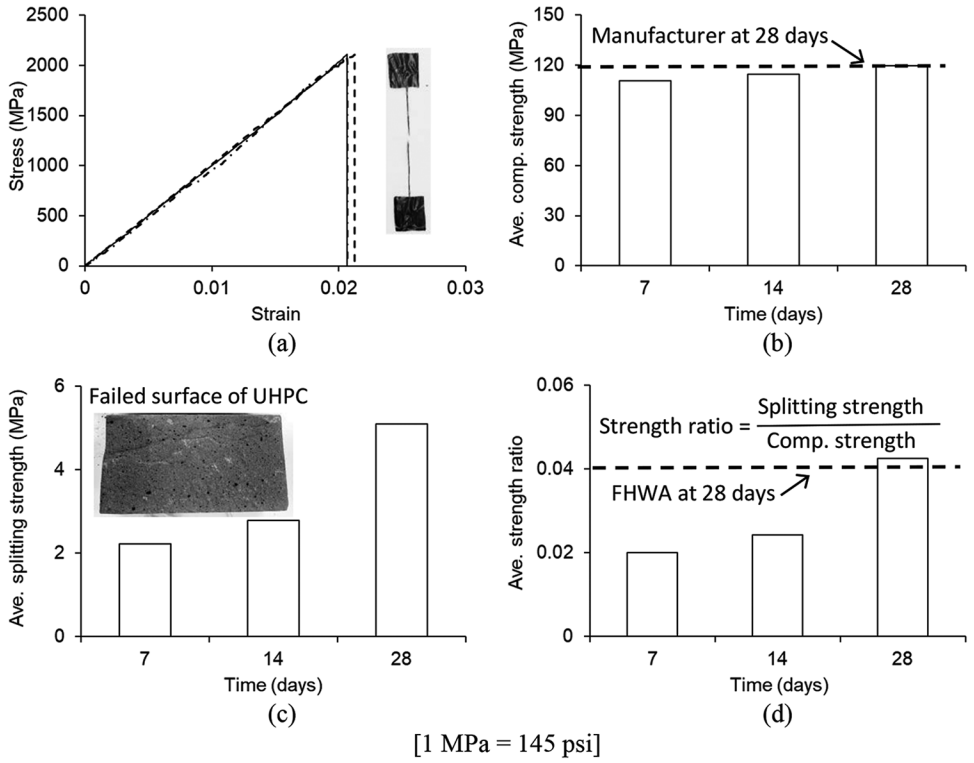

Fig. 2—Ancillary test results: (a) tensile strength of BFRP; (b) compressive strength of UHPC; (c) splitting strength of UHPC; and (d) strength ratio of UHPC.

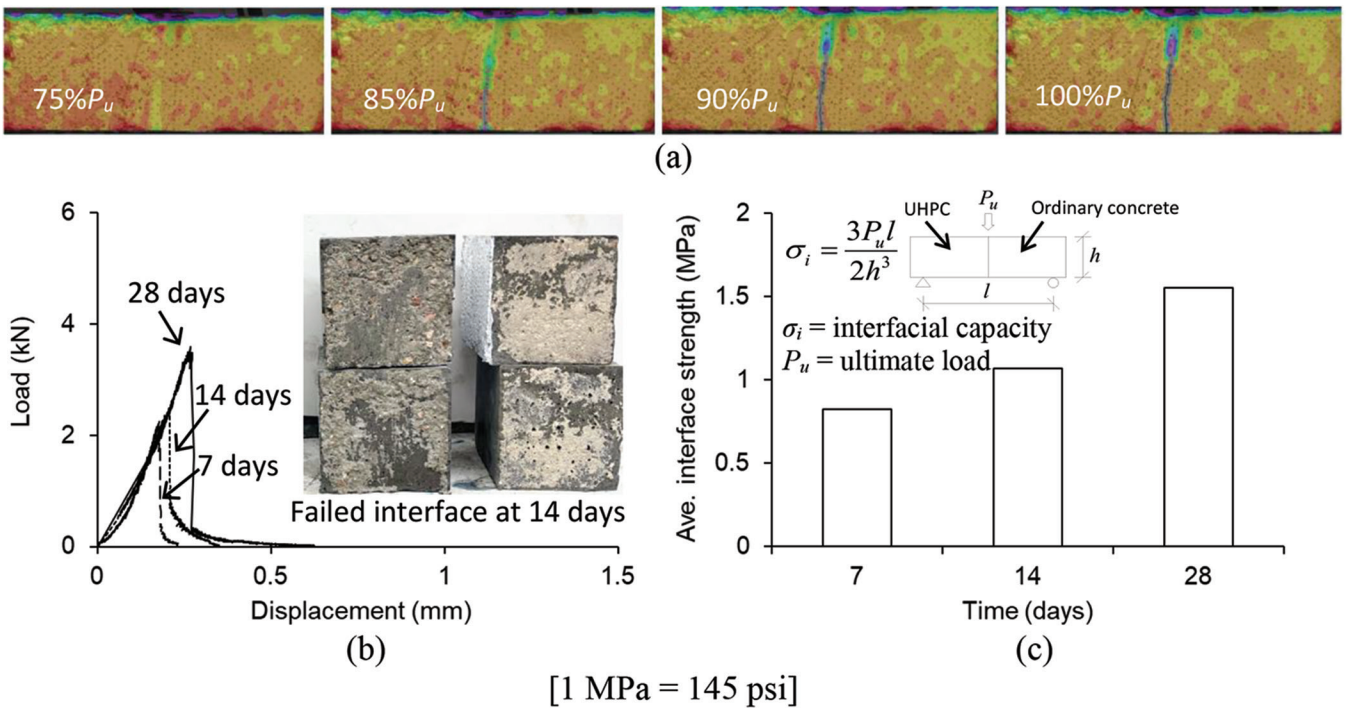

Fig. 3—Bond test results: (a) sequential cracking on brink of interfacial failure at 28 days of curing; (b) load-displacement; and (c) interface strength.

paste is concerned with attractive electrostatic forces and interlayer water in the C-S-H gels,[34] the nonuniform evolution of the splitting strength appears to be the result of irregularly consumed water with the progression of hydration, influencing the bond of the silicate chains. Shown in Fig. 2(d) is a ratio between the splitting and compressive strengths of UHPC. The experimentally determined ratio at 28 days was close to the recommended ratio of FHWA[35]; however, because the strength ratio doubled from 0.020 to 0.043 at 7 and 28 days, respectively, the linear equation of FHWA ($f_{jr} = 0.04f_c'$, in which f_{jr} is the tensile strength of UHPC) should need an improvement to cover the full range

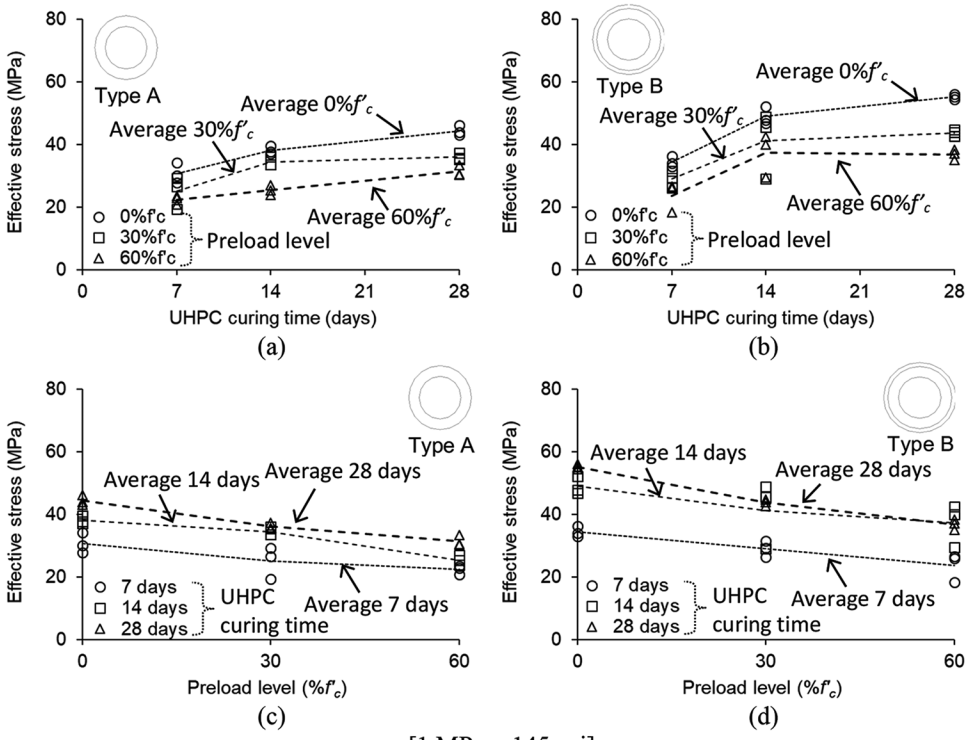

Fig. 4—Load-carrying capacity: (a) curing time for Type A; (b) curing time for Type B; (c) preload level for Type A; and (d) preload level for Type B.

of strength variations until complete curing of the densely mixed cementitious composite.

Interfacial bond

Figure 3(a) pictures the sequential cracking of the bonded prism (28-day curing is shown for brevity and other cases were similar). The specimen was pristine prior to 75% of the ultimate load (P_u); afterward, a crack initiated at the interface and progressed swiftly. A previous study based on scanning electron microscopy[36] explains that the fine particle gradation of UHPC inhibits bleeding bubbles on a contact plane to ordinary concrete; consequently, the failure path did not wobble. The load-displacement relationship of the prisms was linear with a marginal stiffness variation (Fig. 3(b)). As visible in the inset of Fig. 3(b), the evenly dispersed cement residues on the failed surface confirm that the bond of the two blocks was adequate, which is desirable to warrant the acceptable performance of the strengthening system from a practical standpoint. Analogous to the aforementioned splitting strength, the average interfacial capacity of UHPC (σ_i) gradually ascended with time (Fig. 3(c))

$$\sigma_i = \frac{3P_u l}{2h^3} \quad (1)$$

where l and h are the span length and depth of the prism, respectively. The increasing adhesion is ascribed to the mutual interaction between the silicon dioxide (SiO_2) in UHPC and the calcium hydroxide ($Ca(OH)_2$) in the ordinary concrete.[37]

Axial capacity

Effective stress—The influence of curing time and preload levels in the axial strength of the confined concrete is graphed in Fig. 4. For comparison, effective stress was defined as the maximum resistance of the core concrete (ultimate load divided by cross-sectional area), so that all test specimens were evaluated regardless of confinement system. With the increased curing time, the average effective stress of Type A (UHPC, Fig. 4(a)) went up consistently; however, the stress of Type B (UHPC+BFRP, Fig. 4(b)) rose between 7 and 14 days and the escalation rate slowed down between 14 and 28 days (Fig. 4(b)). This fact indicates that the reliance of BFRP tended to decline when the strength and adhesion of UHPC made progress; in other words, the hardened UHPC jackets with the enhanced adhesion to the core concrete carried more loads and the degree of stress transfer to the BFRP grids was reduced after 14 days of curing. Figures 4(c) and (d) corroborate the downside of the preload-induced damage in lowering the effective stress of the cylinders. Due to the contribution of BFRP, the average stress lines of Type B (Fig. 4(d)) were positioned higher than those of Type A (Fig. 4(c)); nonetheless, their degradation slopes were essentially alike (discussions continue in the next section).

Efficacy of confinement—Figures 5(a) and (b) display the curing-dependent effective stress ratio of the confined cylinders (f_{cc}') to the baseline strength of the unconfined control cylinders (f_c'). During the curing period of 28 days, the stress ratios were scaled up and Type B with a combination of UHPC and BFRP (Fig. 5(b)) outperformed Type A with the UHPC jackets only (Fig. 5(a)). Regarding the impairment of the core concrete, the 28-day effective stress ratio of the

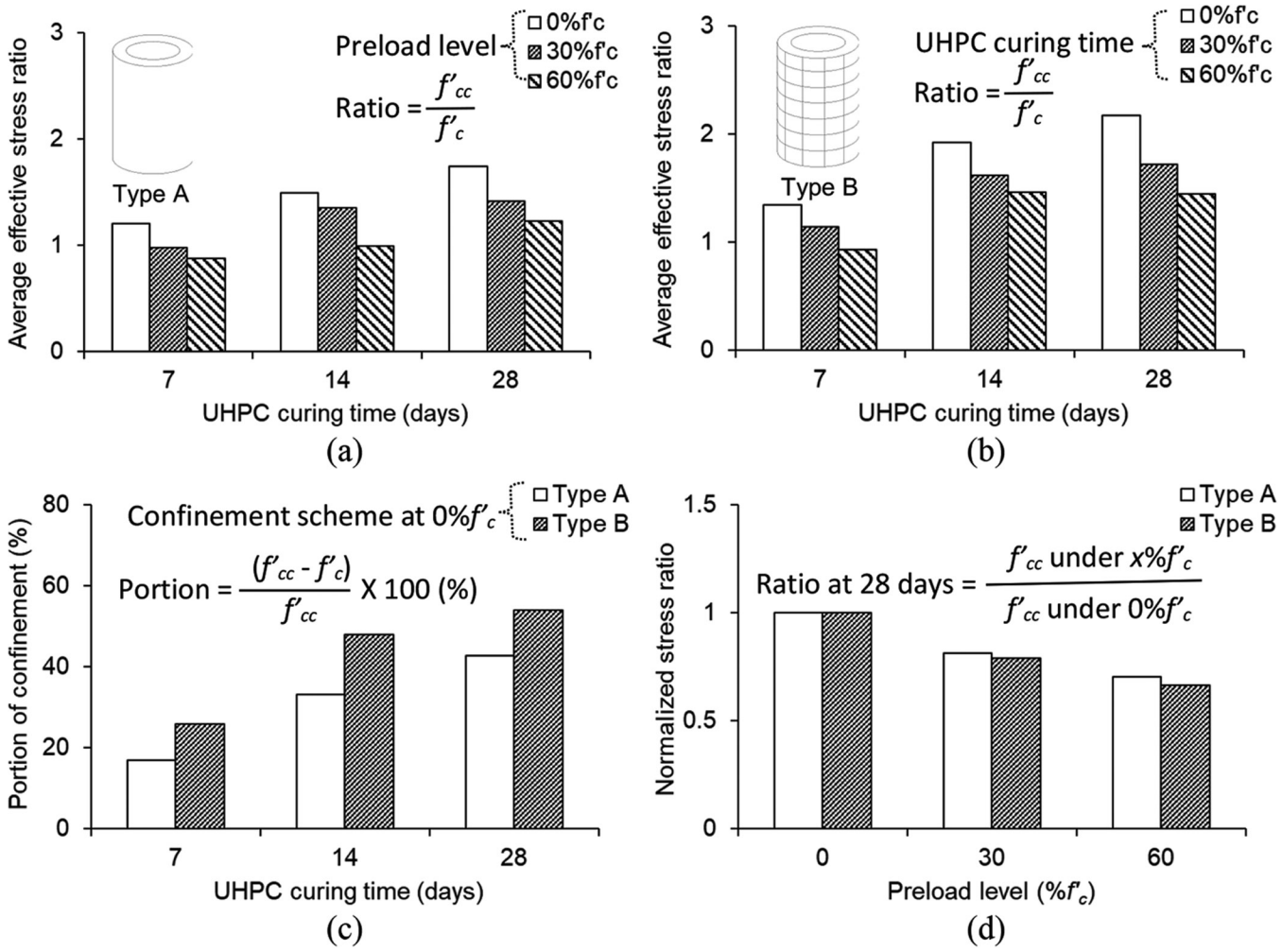

Fig. 5—Efficacy of proposed confinement system: (a) effective stress ratio with UHPC curing time for Type A; (b) effective stress ratio with UHPC curing time for Type B; (c) portion of confinement components; and (d) preload effect at 28 days.

confined concrete under a preload level of 60%f_c' was equivalent to the 7-day stress ratio without core damage (0%f_c'): f_{cc}'/f_c' = 1.23 and 1.45 for Types A and B under 60%f_c' at 28 days, respectively, versus f_{cc}'/f_c' = 1.21 and 1.35 for Types A and B under 0%f_c' at 7 days, respectively. As demonstrated in Fig. 5(c), the BFRP-grid wrapping raised the load-bearing portion of the confinement system (0%f_c') by 28.7%, on average. The normalized stress plotted in Fig. 5(d) reveals that, whether the UHPC-jacketed concrete was confined by BFRP or not, there was a subtle difference in the reduction of the effective stress once the core was damaged before strengthening. This is a salient facet for handling extensively deteriorated members. The lower stress ratio of Type B relative to that of Type A, albeit insignificant, illustrates the sensitivity of the UHPC-BFRP interactions in resisting the applied loads.

Statistical characterization—A two-factor analysis of variance (ANOVA) was conducted to test equality in the axial capacities of the confined specimens at three significance levels (α = 0.05, 0.10, and 0.25). The established hypotheses were H_0: all capacities are equal in each category and H_1: at least one capacity is not equal. As depicted in Fig. 6(a), if a calculated value on the F distribution is greater than a preset limit ($F \geq F_{limit}$), H_0 is rejected (the background of ANOVA and specific equations are available in a statistics text[38]). Table 2 enumerates the source of variation, sum of squares, degrees of freedom, mean square, and F statistics. The F values for the curing time and preload damage of Types A and B exceeded the limits; therefore, the capacities of the conditioned cylinders were concluded to be statistically different. The interaction of these two variables generated substantially low F values (Fig. 6(b)), reaffirming mutual independence between the internal (curing) and external (preloading) attributes. It should be noted that, considering the result of Type A at $F_{0.25}$ ($F = 2.0 > F_{limit} = 1.48$ in Table 2), the 75% confidence interval (α = 0.25) seems to be too wide for strengthening application. Figures 6(c) and (d) provide the t-test[38] results of the confined cylinders against the 28-day-cured control ones at a 90% confidence interval (α = 0.1). This approach renders reliable statistical information on individual variables when the number of specimens is small (less than 30).[39] On the whole, the t-values of Types A and B pertaining to the curing periods of 7 and 14 days were within or slightly outside the 90% confidence zone. By contrast, the confined concrete at 28 days under the preload levels of 0%f_c' and 30%f_c' was apparently away from the 90% zone, particularly for the Type B case, which manifests the notable efficaciousness of the UHPC+BFRP system in

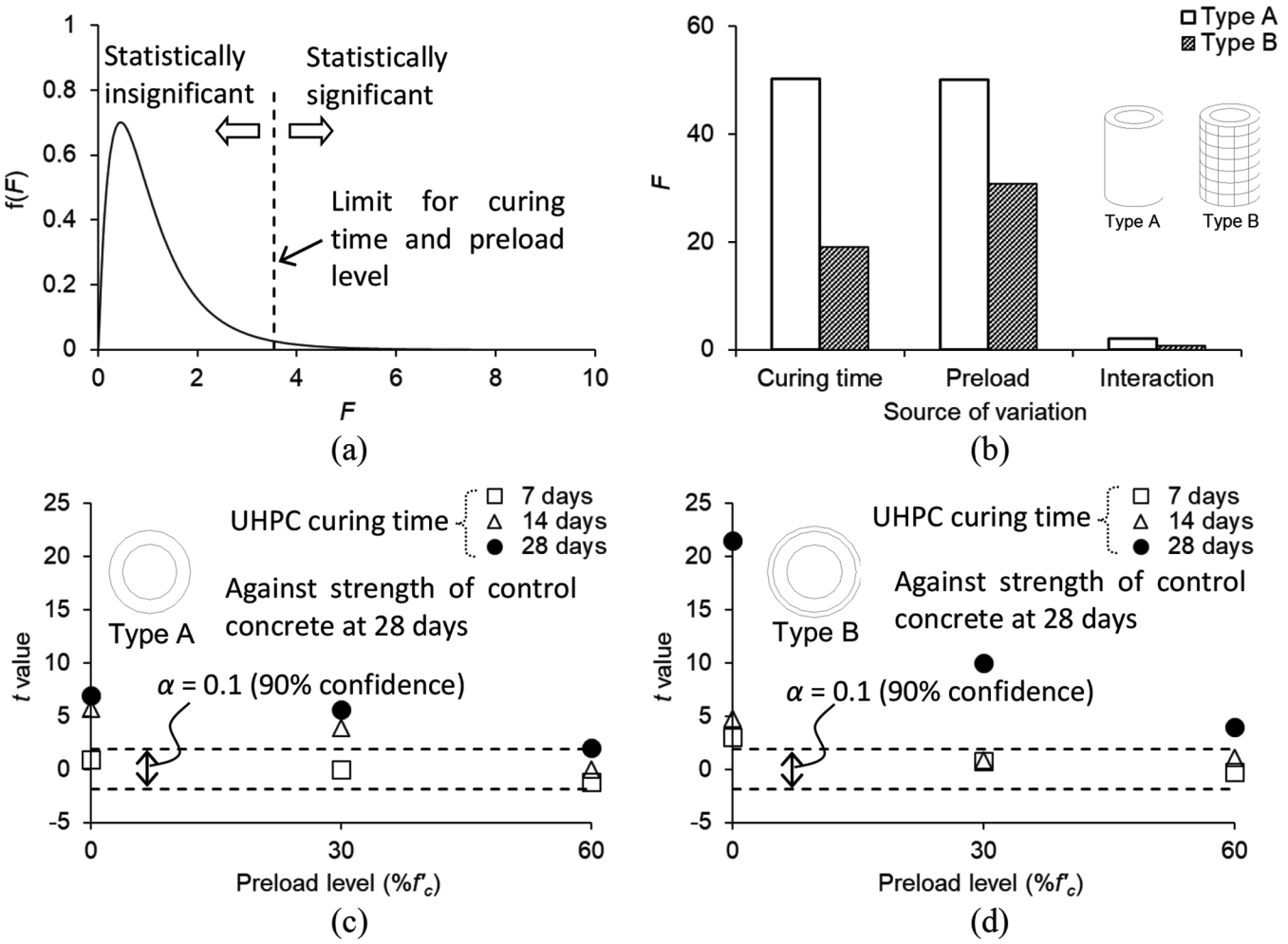

Fig. 6—Statistical characterization: (a) F *distribution; (b)* F *statistics; (c)* t*-test for Type A; and (d)* t*-test for Type B.*

Table 2—Analysis of variance

Cylinder	Source of variation	Sum of squares	Degrees of freedom	Mean square	F	Critical limit					
						$F_{0.05}$		$F_{0.10}$		$F_{0.25}$	
						Value	Sig.	Value	Sig.	Value	Sig.
Type A	Curing	577.1	2	288.6	50.3	3.55	S	2.62	S	1.50	S
	Preload	574.6	2	287.3	50.1	3.55	S	2.62	S	1.50	S
	Interaction	46.5	4	11.6	2.0	2.93	I	2.29	I	1.48	S
	Error	103.3	18	5.7	—	—	—	—	—	—	—
	Total	1301.5	26	—	—	—	—	—	—	—	—
Type B	Curing	841.9	2	420.9	18.9	3.55	S	2.62	S	1.50	S
	Preload	1364.6	2	682.3	30.8	3.55	S	2.62	S	1.50	S
	Interaction	60.8	4	15.2	0.7	2.93	I	2.29	I	1.48	I
	Error	399.4	18	22.2	—	—	—	—	—	—	—
	Total	2666.8	26	—	—	—	—	—	—	—	—

Note: Sig. is significance; S is significant; I is insignificant.

improving the load-bearing capacity with feasible damage levels in the field (≤30%f_c').

Load-displacement

The load-displacement curves of the tested cylinders are described in Fig. 7. The pre-peak behavior of the 7-day specimens in Type A was almost identical, irrespective of core damage, whereas their post-peak responses revealed a tendency of becoming flattened with the preload level (Fig. 7(a)). The applied stress was redistributed from the deteriorated core to the UHPC jacket; hence, the rapid load drop with 0%f_c' changed to the plateau-like deformation

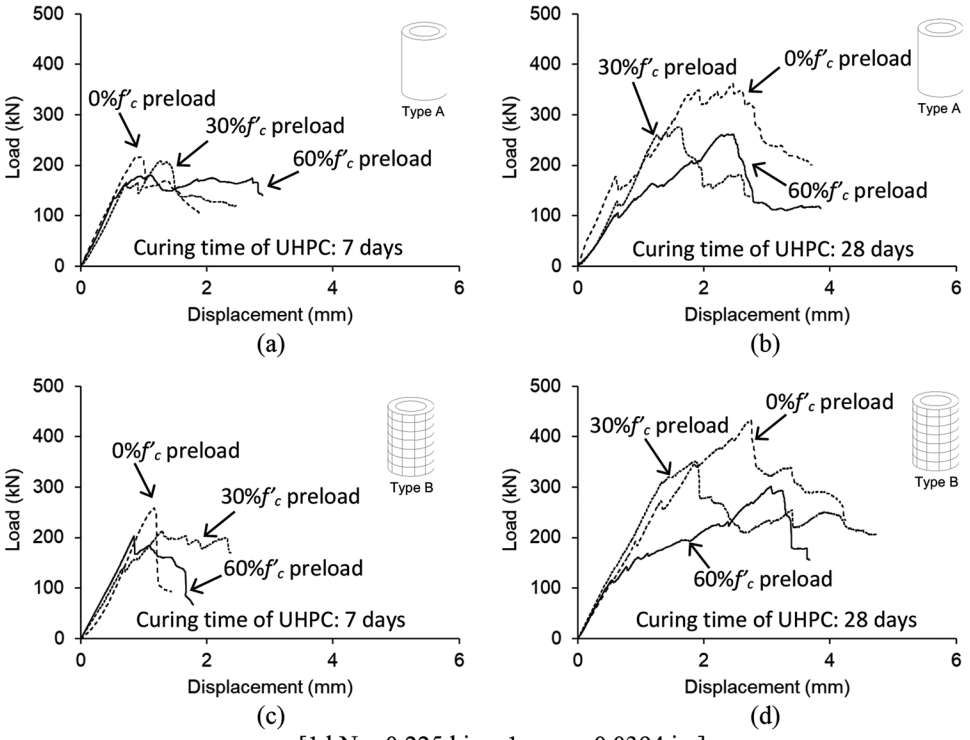

Fig. 7—Load-displacement behavior in axial direction: (a) curing time of 7 days for Type A; (b) curing time of 28 days for Type A; (c) curing time of 7 days for Type B; and (d) curing time of 28 days for Type B.

with 60%f_c'. When the curing time progressed to 28 days (Fig. 7(b)), a remarkable divergence was noticed in terms of the capacity and response. Unlike the specimens subjected to the preload levels of 0%f_c' and 30%f_c', the prepeak stiffness of the cylinder with 60%f_c' dwindled because of the insufficient load-sharing between the core concrete and UHPC. The post-peak behavior of the specimen without core damage (0%f_c') was steady before it collapsed; on the other hand, the behavior of those under 30%f_c' and 60%f_c' was brittle. The Type B cylinders at 7 days in Fig. 7(c) demonstrated linear responses up to the peak loads; then, the previously explained stress redistribution was observed, meaning that the BFRP grids did not significantly alter the load-carrying mechanism with the partially developed adhesion between the core and the UHPC jacket. Care should thus be exercised when the BFRP grid system is used in practice. The constantly rising load of the 28-day specimens in Type B (Fig. 7(d)), except for the 60%f_c' case, supports that BFRP stabilized the response of the jacketed concrete. The stiffness variation of the cylinders prior to reaching the ultimate loads was due to the local debonding of the grids, which was of little importance since the confinement nature is not bond-critical.[10]

Failure mode

Figure 8 shows the failure mode of the cylinders. The unconfined specimen exhibited a few cracks and crushed (Fig. 8(a)), while the axial distress combined with an outward pressure resulting from the expanded core concrete caused cracking in the UHPC jacket, parallel to the loading direction (Fig. 8(b)). As the preload level was increased, the extent of the stress redistribution from the core to the jacket became apparent and multiple cracks were seen (0%f_c' versus 60%f_c' in Fig. 8(b)). It is worth noting that the widened crack width disrupted the transfer of radial and circumferential stresses in the jacket; subsequently, the degradation process of the confinement system was exacerbated at a high level of the preload. Aligning with the interface test results (Fig. 3), the curing time of UHPC intensified the bond against the concrete substrate (Fig. 8(c)); accordingly, the 7-day specimen failed by localized delamination representing a disproportionate bond (Fig. 8(c), left), which was distinct from the 28-day specimen exhibiting a circumferential failure plane (Fig. 8(c), right). In contrast to the catastrophic collapse of the Type A cylinders (Fig. 8(c)), the failure of those confined by the UHPC+BFRP system was modest (Fig. 8(d)). Notwithstanding the ruptured grids owing to the excessive hoop-directional tensile stresses, BFRP was instrumental in preserving the morphology of the core and the UHPC jacket.

ANALYTICAL MODELING

A procedure is developed to predict the theoretical response of concrete confined with a UHPC jacket and BFRP grids. In principle, the jacket hinders the dilation of the core in a passive fashion, which is analytically reproduced by a uniform pressure surrounding the concrete circumference via force equilibrium. The consequences of variable parameters are studied to understand the performance of the proposed strengthening system.

Development

The load-carrying capacity of confined concrete (f_{cc}') is conventionally expressed as

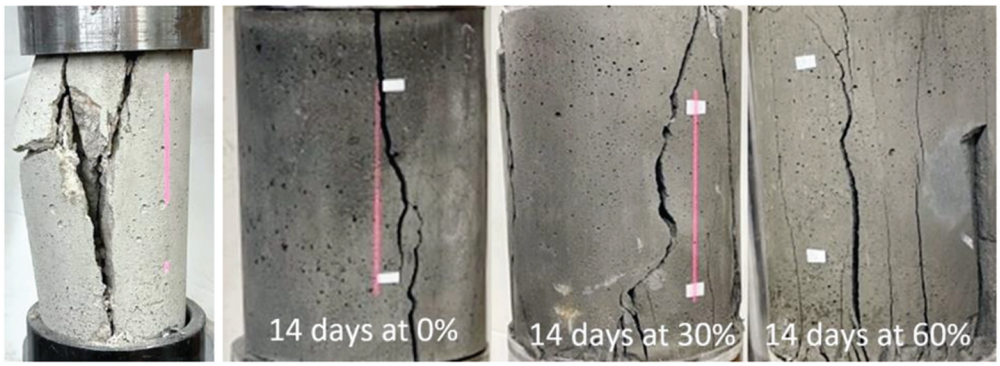

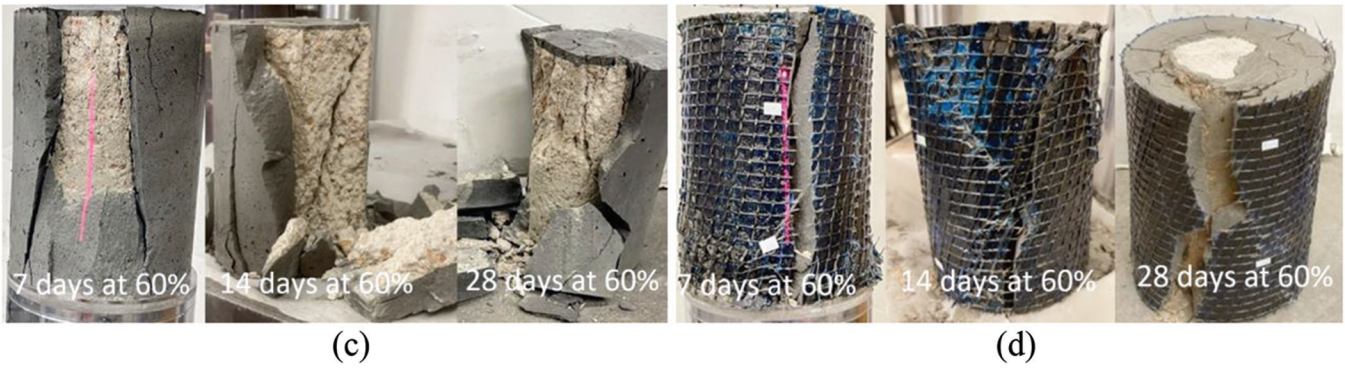

Fig. 8—Failure mode (time = curing period of UHPC jacket; percentage = fraction of f_c'*): (a) control with preload level; (b) Type A with preload level immediately before failure; (c) Type A with curing time; and (d) Type B with curing time.*

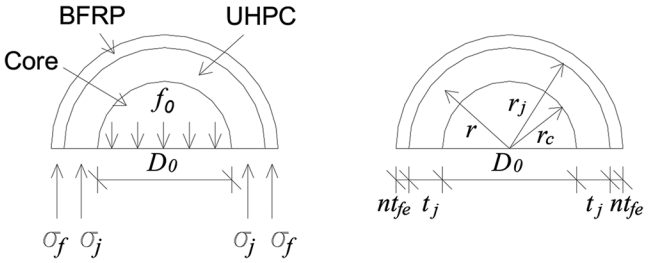

Fig. 9—Analytical model.

$$f_{cc}' = f_c' + \kappa f_0 \tag{2}$$

where f_c' is the core strength; κ is an empirical confinement factor; and f_0 is the confining pressure, which may be derived from force equilibrium among the core, UHPC, and BFRP (Fig. 9)

$$f_0 = \frac{2(t_j \sigma_j + n t_{fe} \sigma_f)}{D_0} \tag{3}$$

where t_j and σ_j are the thickness and tensile stress of the UHPC jacket, respectively; n, t_{fe}, and σ_f are the layer number, equivalent thickness, and stress of the BFRP grids, respectively; and D_0 is the core diameter. Upon confining the concrete, the core's ability is ameliorated in matters of accommodating large deformations until the jacket system ruptures—that is, the strengthened cylindrical element dissipates a considerable amount of plastic strain energy up to failure. Because the confining effect of the grids differs from that of continuum sheets covering the entire surface of the UHPC jacket, Eq. (4) was adopted for the equivalent thickness of BFRP[40]

$$t_{fe} = \frac{n A_g}{s_g + b_g} \tag{4}$$

where A_g and s_g are the cross-sectional area and mesh spacing of the grids, respectively; and b_g is the width of a single grid. Knowing the confining pressure, which is equated to be an interface pressure between the core and the jacket,[41] circumferential stresses around the UHPC jacket (σ_θ) are calculated by the theory of elasticity[42]

$$\sigma_\theta = \frac{f_0 r_c^2}{r_j^2 - r_c^2}\left(1 + \frac{r_j^2}{r^2}\right) \tag{5}$$

where r_c and r_j are the radii of the core and the jacketed cylinder, respectively; and r is the radial distance from the center of the core (Fig. 9).

Implementation

When the circumferential stress (σ_θ) of the UHPC jacket at $r = r_j$ in Eq. (5) (equivalent to σ_j in Eq. (3)) reaches the cracking strength ($f_{jr} = 0.04 f_c'$ according to FHWA[35]), the jacket is assumed to fail. Likewise, if the σ_θ of the BFRP grids at $r = r_j$ (equivalent to σ_j in Eq. (3)) equals σ_{fe}, the grids fracture, in which σ_{fe} is the effective stress. Conforming to ACI 440.2R-17[10].

$$\sigma_{fe} = \kappa_\varepsilon f_{fu} \tag{6}$$

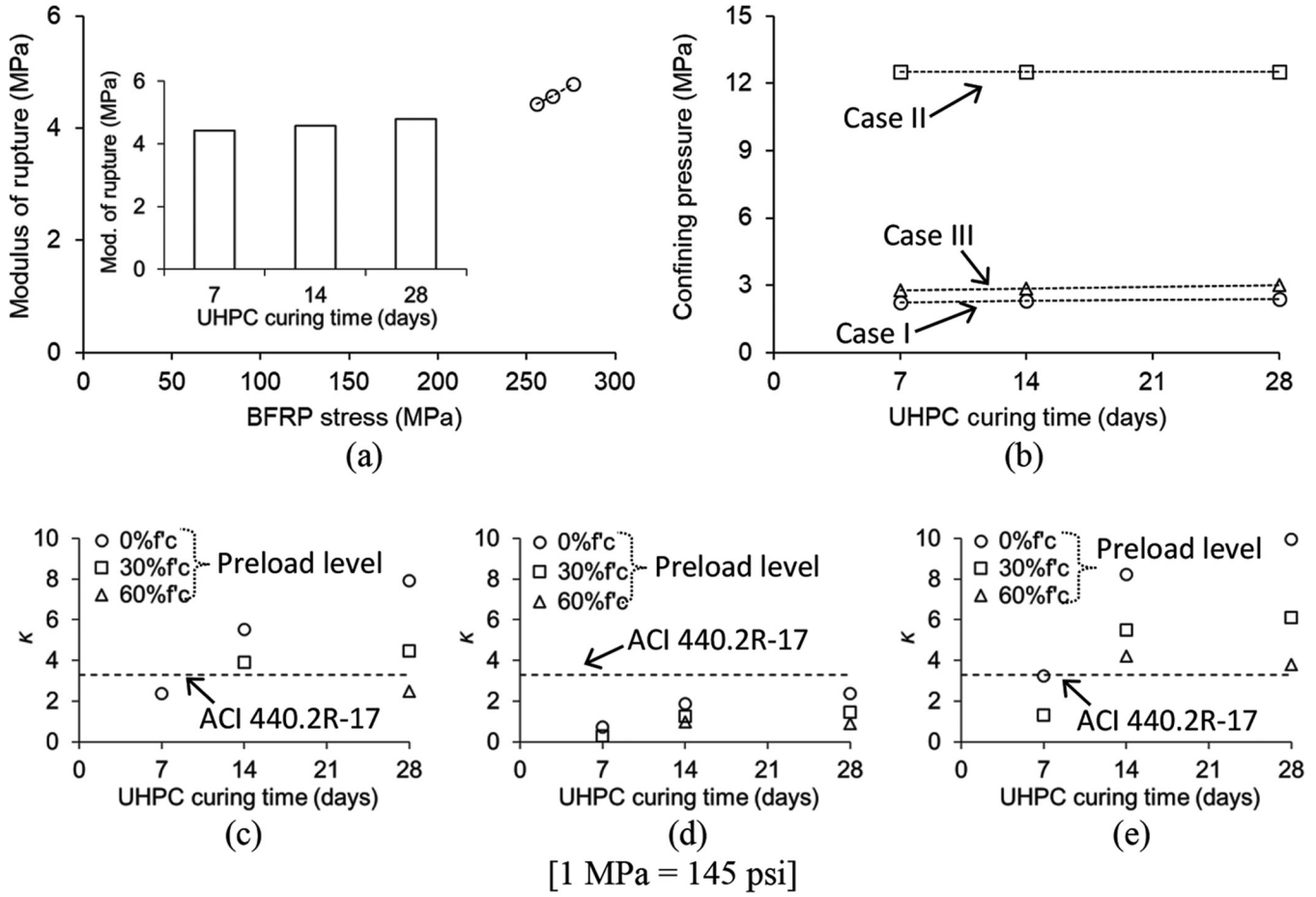

Fig. 10—Theoretical interpretation of test data: (a) relationship between UHPC and BFRP; (b) confining pressure; (c) confining factor for Case I; (d) confining factor for Case II; and (e) confining factor for Case III.

where κ_ε is the efficiency factor related to the core dilation (κ_ε = 0.55). Depending upon the failure of the confining system, three scenarios are expected in conjunction with Eq. (3).

1. UHPC ruptures (Case I): σ_j becomes f_{jr}. This instance is applicable to UHPC jacketing without the BFRP grids.

2. BFRP fractures before UHPC ruptures (Case II): σ_f is equal to σ_{fe}, and σ_j is calculated by σ_θ at $r = r_j$

$$\sigma_j = \frac{2n\,t_{fe}\,\sigma_{fe}}{D_0\left(\frac{r_j^2 - r_c^2}{2\,r_c^2}\right) - 2\,t_j} \le f_{ir} \tag{7}$$

3. UHPC ruptures before BFRP fractures (Case III): σ_j is replaced by f_{jr}, and σ_f is determined at $r = r_j$ using an approach similar to Eq. (7)

$$\sigma_f = \frac{f_{jr}}{n\,t_{fe}}\left(\frac{D_0\left(r_j^2 - r_c^2\right)}{4\,r_c^2} - t_j\right) \le \sigma_{fe} \tag{8}$$

After calculating f_0 (Eq. (3)) associated with one of the three possible failure situations, the κ factor in Eq. (2) is determined alongside the test results of f_{cc}' and f_c'

$$\kappa = \frac{f_{cc}' - f_c'}{f_0} \tag{9}$$

Application

Figure 10 systematically interprets the experimental data of the confined cylinders. The development of the BFRP stress was proportional to the modulus of rupture of UHPC (Fig. 10(a)), verifying that the adjoining components acted together in the strengthening system. Given in Fig. 10(b) is the confining pressure of the cylinders (f_0). While the rupture of the Type A jacket was obvious in Case I (Fig. 8(b)), the failure sequence of UHPC and BFRP was not clearly discernible during the test of Type B (Fig. 8(d)); as such, Cases II and III were simultaneously presented for the sake of numerical investigations. The confining pressure of Case II was constant in all curing periods because the failure was dominated by the fracture of BFRP, whereas the pressures of Cases I and III slightly increased with the time (Δf_0 = 0.008 MPa [1.2 psi]/day and 0.011 MPa [1.6 psi]/day, respectively). An increasing propensity was attained for the confinement factor (κ) as the curing of UHPC progressed (Fig. 10(c) to (e)); negative factors induced by the inordinate preload $f_{cc}' < f_c'$ were omitted). The Case II scenario with BFRP-fracture brought about lower confinement factors (Fig. 10(d)), relative to other cases (Fig. 10(c) and (e)), which implies the significance of the BFRP configurations in the proposed strengthening scheme (additional examinations are imparted later). The factor of ACI 440.2R-17[10] without a 5% reduction for design (κ = 3.3) was reasonably usable for the cases with the core damage under 30%f_c', accompanied

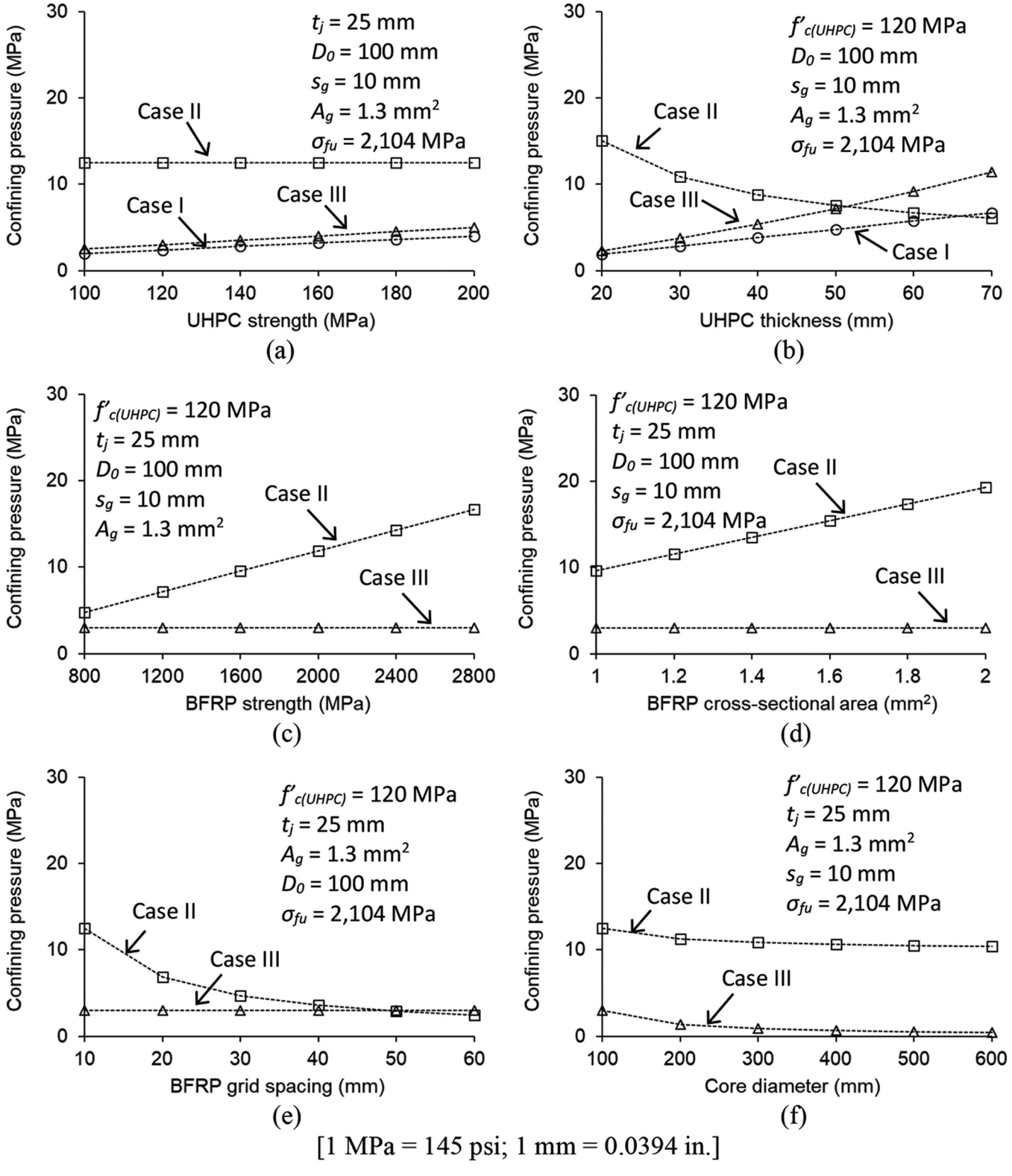

Fig. 11—Confining pressure of strengthened concrete: (a) UHPC strength; (b) UHPC thickness; (c) BFRP strength; (d) BFRP cross-sectional area; (e) BFRP grid spacing; and (f) core diameter.

by the 28-day-cured jackets, except if BFRP fractured before the failure of UHPC.

Parametric study

Sensitivity analysis was carried out to elucidate the repercussions of the constituting parameters for the behavior of the confined concrete at 28 days of curing. Unless otherwise stated, the properties of the experimental program were taken as the default.

Confining pressure—With an increase in the UHPC strength from f_c' = 100 to 200 MPa (14.5 to 29 ksi), the confining pressure of Cases I and III ascended by up to 100% (Fig. 11(a)); contrarily, that of Case II controlled by the BFRP strength was constant. The thickening of the jacket

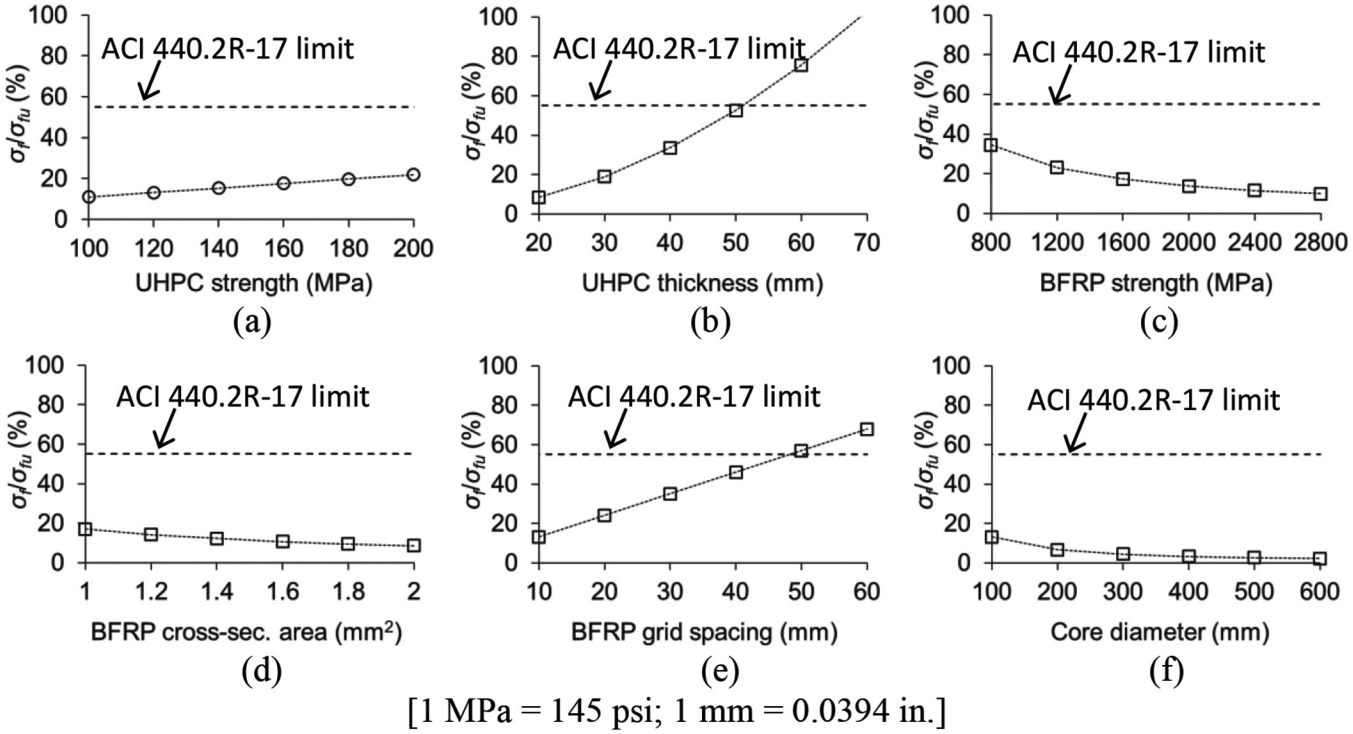

Fig. 12—BFRP stress of strengthened concrete: (a) UHPC strength; (b) UHPC thickness; (c) BFRP strength; (d) BFRP cross-sectional area; (e) BFRP grid spacing; and (f) core diameter.

retarded the failure of UHPC (Fig. 11(b)), thereby raising the pressure of Cases I and III (the inclusion of the BFRP grids in Case III generated higher values). The declining pressure of Case II was ascribed to the fracture of BFRP, which was accelerated as the jacket thickness increased (stress levels are analyzed in the subsequent section). The tensile strength and cross-sectional area of BFRP played an important role in increasing the confining pressure under the circumstance of Case II (Fig. 11(c) and (d)); meanwhile, when the rupture of UHPC governed the failure of the cylinders (Case III), these BFRP properties were not influential. Wide grid spacings reduced the confining pressure of Case II (Fig. 11(e)) and, over a spacing of 50 mm (2 in.), the usable pressures of Cases II and III were basically the same. It is, thus, recommended that grid spacings be narrower than a threshold limit (50 mm [2 in.] in the present study, preferably less than 20 mm [0.8 in.]). The impact of variable core diameters was inappreciable in altering the confining pressure of Cases II and III (Fig. 11(f)), confirming that the size effect of FRP-confined concrete is negligible.[43,44]

BFRP stress—In line with the foregoing parameters (Fig. 11), the stress levels of BFRP (σ_f, Eq. (8)) were calculated and compared against the limit of ACI 440.2R-17 (Eq. (6))[10] to assess the premature failure of the grids (Fig. 12). The strengths of most UHPC and BFRP products available in market were usable for the proposed confinement system (Fig. 12(a) and (c)); however, the jacket thickness greater than about 50% of the core diameter prompted a stress level exceeding the limit (Fig. 12(b)). As shown in Fig. 12(d) and (e), when selecting BFRP grid geometries, attention should be paid to the spacing between the integrated grids (Fig. 12(e)), rather than the cross-sectional area of the individual grids (Fig. 12(d)). The BFRP stresses below 20% of the ultimate strength in Fig. 12(f) denote that the performance of the grids would be independent of the core diameter.

Design proposal—The results of the parametric study were collated, and Eq. (2) was rearranged to solve for the confinement factor at a target strength-increase ratio spanning from $f_{cc}'/f_c' = 1.05$ to 1.4

$$\kappa = \frac{f_{cc}'/f_c' - 1}{f_0/f_c'} \tag{10}$$

Contemplating practical application, the UHPC+BFRP system (Cases II and III) was adopted. Figure 13(a) demonstrates the growth of the κ factor with the f_{cc}'/f_c' related to the UHPC strength parameter (Fig. 11(a)). The factors developed in a linear manner and the variation of Case III was wider than that of Case II where BFRP fracture controlled the failure. Shown in Fig. 13(b) are the calculated factors normalized by the factor of ACI 440.2R-17 ($\kappa = 3.3$). Even if the ACI design factor conservatively enveloped most occasions, except for some values over $f_{cc}'/f_c' = 1.35$, a refinement appeared necessary to avoid large discrepancies; especially below $f_{cc}'/f_c' = 1.3$. The maximum factors associated with the individual parameters at selected f_{cc}'/f_c' are charted in Fig. 13(c) and (d), excerpted from the graphs similar to those given in Fig. 13(a). The grid spacing of BFRP necessitated high κ factors in Case II (Fig. 13(c)); on the contrary, all parameters demanded reasonably uniform factors in Case III (Fig. 13(d)). For implementation, the peak factors in Fig. 13(c) and (d) were gathered and listed in Table 3. The factor of ACI 440.2R-17 was equivalent to an f_{cc}'/f_c' of 1.3. It is suggested that a κ factor be selected, depending upon the target strengthening level of f_{cc}'/f_c'.

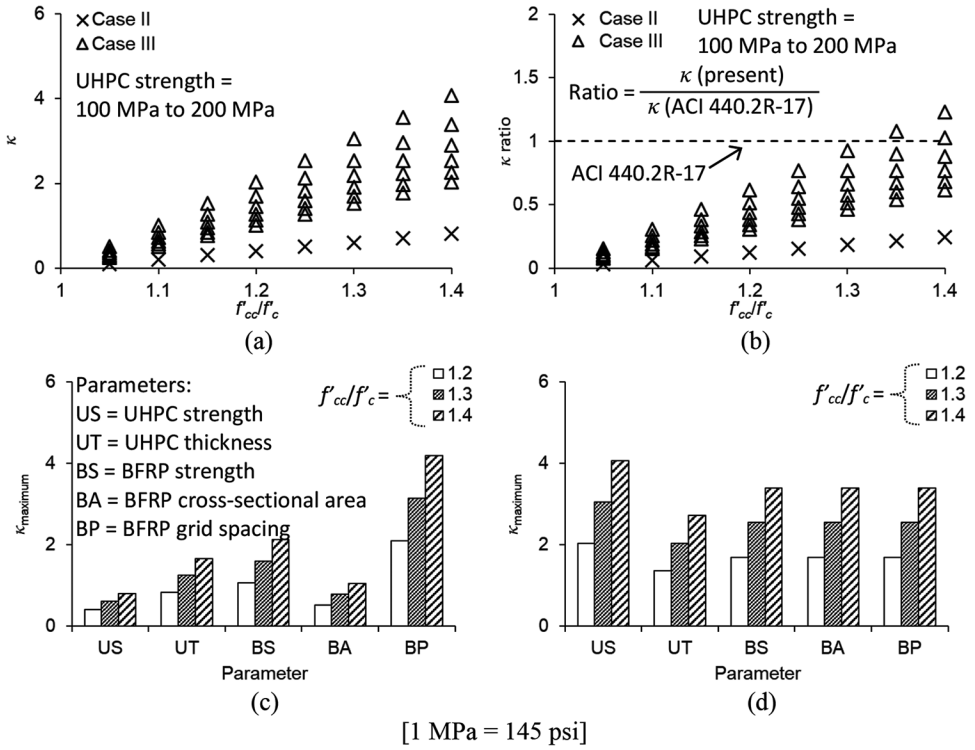

Fig. 13—Determination of confinement factor: (a) UHPC strength; (b) confinement factor ratio; (c) maximum confinement factor for Case II; and (d) maximum confinement factor for Case III.

Table 3—Proposed confinement factor

UHPC+BFRP system	Target ratio of f_{cc}'/f_c'			Applicable range
	1.2	1.3	1.4	
Confinement factor (κ)	2.2	3.3	4.4	100 MPa ≤ UHPC strength ≤ 200 MPa 20 mm ≤ UHPC thickness ≤ 60 mm 800 MPa ≤ BFRP strength ≤ 2800 MPa 1 mm^2 ≤ BFRP cross-sectional area ≤ 2 mm^2 10 mm ≤ BFRP grid spacing ≤ 60 mm

Note: 1 MPa = 145 psi; 1 mm = 0.0394 in.; 1 mm^2 = 0.0016 in.^{2}.

SUMMARY AND CONCLUSIONS

This paper investigated the potential of a hybrid confining method, consisting of an ultra-high-performance concrete (UHPC) jacket and basalt fiber-reinforced polymer (BFRP) grids, to enhance the capacity of concrete subjected to axial compression. The adverse effects of possible damage in the field were simulated by preloading cores at up to 60%f_c', and the performance of the confinement system was evaluated from load bearing to failure modes. Analytical modeling complemented the findings of the laboratory test, and the established approach was used to conduct parametric investigations, leading to design recommendations. For the verification of the promising outcomes, structural-scale column testing should be a future research topic with a specific goal of implementing the proposed strengthening concept to alleviate the likelihood of failure (both monotonic and cyclic loadings are of interest for a potential application in seismic regions, including investigations into ductility and slenderness, so that the universal adaptiveness of the hybrid retrofit technique can be assured). The following conclusions are drawn:

- The compressive strength of UHPC rapidly grew to 110 and 120 MPa (16.0 and 17.4 ksi) at 7 and 28 days, respectively, while the development of the splitting strength became conspicuous by 0.33 MPa (47.9 psi)/day after 14 days. The adhesion between the ordinary concrete and UHPC increased with time and a crack quickly progressed along the interface on the brink of the bond failure.
- The load-bearing capacity of the confined concrete with and without BFRP differed, and the dependency of the grids was reduced as the strength and adhesion of the enclosed UHPC layer rose. Regardless of jacketing scheme, the preload-induced damage abated the capacity of the strengthened concrete. The confidence interval of 90% ($\alpha = 0.1$) was appropriate to characterize the statistical significance of the cylinder capacities.
- For both cases of Types A and B at 7-day curing, the load-displacement relationship was linear within the pre-peak region, after which stress redistributions were noticed between the core concrete and the jackets, contingent upon preload intensity. The BFRP grids

stabilized the axial behavior of the confined concrete under 28-day curing.

- The axial compression synergized with the lateral expansion of the core was responsible for cracking the UHPC jacket. When the crack width enlarged, the extent of a stress transfer within the jacket diminished and the failure of the confining system was accelerated. The catastrophic failure of the Type A specimens was inhibited by the wrapping of BFRP in Type B.
- In consonance with UHPC curing, the confining pressure of the concrete ascended over time, unless the fracture of BFRP took place. As the strength, jacket thickness, and cross-sectional area of UHPC and BFRP increased, the core concrete was subjected to augmented confining pressures. Wide grid spacings (≥50 mm [2 in.]) weakened the pressure and the influence of core diameters was insignificant in altering the pressure. The proposed confinement factor, varying from $\kappa = 2.2$ to 4.4, can cover a target strength-increase ratio of $f_{cc}'/f_c' = 1.2$ to 1.4.

AUTHOR BIOS

Yail J. Kim, *FACI, is President of the Bridge Engineering Institute, An International Technical Society, and a Professor in the Department of Civil Engineering at the University of Colorado Denver, Denver, CO. He is past Chair of ACI Committee 345, Concrete Bridge Construction and Preservation and ACI Subcommittee 440-I, FRP-Prestressed Concrete. He is a member of ACI Committees 342, Evaluation of Concrete Bridges and Bridge Elements; 377, Performance-Based Structural Integrity and Resilience of Concrete Structures; 440, Fiber-Reinforced Polymer Reinforcement; and Joint ACI-ASCE Committee 343, Concrete Bridge Design. He received the Chester Paul Siess Award for Excellence in Structural Research in 2019. His research interests include advanced composite materials for rehabilitation; structural informatics; complex systems; and science-based structural engineering including statistical, interfacial, and quantum physics.*

Yordanos Dinku *is a Master's Student in the Department of Civil Engineering at the University of Colorado Denver, where she received her BS in 2020. Her research interests include the application of ultra-high-performance concrete.*

ACKNOWLEDGMENTS

The authors gratefully acknowledge support from the U.S. Department of Transportation through the Mountain-Plains Consortium Program. P. Weber at ceEntek donated the UHPC material used for this research. Proprietary information such as product names was not included to avoid commercialism.

REFERENCES

1. Li, F., *Durability Design of Concrete Structures, Phenomena, Modeling, and Practice*, first edition, John Wiley & Sons, Singapore, 2016, 288 pp.

2. Costa, A.; Arede, A.; and Varum, H., *Strengthening and Retrofitting of Existing Structures*, Springer, Singapore, 2018.

3. Tijani, I. A.; Wu, Y.-F.; and Lim, C. W., "Effects of Pre-Damage on Stress-Strain Relationship of Partially Confined Concrete," *ACI Structural Journal*, V. 118, No. 1, Jan. 2021, pp. 61-72.

4. ASTM C496/C496M-17, "Standard Test Method for Splitting Tensile Strength of Cylindrical Concrete Specimens," ASTM International, West Conshohocken, PA, 2017, 4 pp.

5. Vandoros, K. G., and Dritsos, S. E., "Concrete Jacket Construction Detail Effectiveness When Strengthening RC Columns," *Construction and Building Materials*, V. 22, No. 3, 2008, pp. 264-276. doi: 10.1016/j.conbuildmat.2006.08.019

6. Li, B.; Lam, E. S.-S.; Wu, B.; and Wang, Y.-Y., "Effect of High Axial Load on Seismic Behavior of Reinforced Concrete Beam-Column Joints With and Without Strengthening," *ACI Structural Journal*, V. 112, No. 6, Nov.-Dec. 2015, pp. 713-723. doi: 10.14359/51687938

7. Lai, M.; Li, C.; Ho, J. C. M.; and Chen, M.-T., "Experimental Investigation on Hollow-Steel-Tube Columns With External Confinements," *Journal of Constructional Steel Research*, V. 166, 2020, p. 105865. doi: 10.1016/j.jcsr.2019.105865

8. Zhou, J.; Tian, Y.; Bi, F.; and Zhao, X., "Size Effect on Strength of Reinforced Concrete Cylinders Confined by Carbon Fiber-Reinforced Polymer and Transverse Stirrup Reinforcement," *ACI Structural Journal*, V. 118, No. 2, Mar. 2021, pp. 263-272.

9. Wang, Y.; Chen, G.; Wan, B.; Han, B.; and Ran, J., "Axial Compressive Behavior and Confinement Mechanism of Circular FRP-Steel Tubed Concrete Stub Columns," *Composite Structures*, V. 256, 2021, p. 113082. doi: 10.1016/j.compstruct.2020.113082

10. ACI Committee 440, "Guide for the Design and Construction of Externally Bonded FRP Systems for Strengthening Concrete Structures (ACI 440.2R-17)," American Concrete Institute, Farmington Hills, MI, 2017, 122 pp.

11. De Lorenzis, L., and Tepfers, R., "Comparative Study of Models on Confinement of Concrete Cylinders with Fiber-Reinforced Polymer Composites," *Journal of Composites for Construction*, ASCE, V. 7, No. 3, 2003, pp. 219-237. doi: 10.1061/(ASCE)1090-0268(2003)7:3(219)

12. Mirmiran, A., and Shahawy, M., "Behavior of Concrete Columns Confined by Fiber Composites," *Journal of Structural Engineering*, ASCE, V. 123, No. 5, 1997, pp. 583-590. doi: 10.1061/(ASCE)0733-9445(1997)123:5(583)

13. Rousakis, T., "Hybrid Confinement of Concrete by Fiber-Reinforced Polymer Sheets and Fiber Ropes Under Cyclic Axial Compressive Loading," *Journal of Composites for Construction*, ASCE, V. 17, No. 5, 2013, pp. 732-743. doi: 10.1061/(ASCE)CC.1943-5614.0000374

14. Koutas, L.; Tetta, Z.; Bournas, D. A.; and Triantafillou, T. C., "Strengthening of Concrete Structures with Textile Reinforced Mortars: State-of-the-Art Review," *Journal of Composites for Construction*, ASCE, V. 23, No. 1, 2019, p. 03118001. doi: 10.1061/(ASCE)CC.1943-5614.0000882

15. Mohammed, A. A.; Manalo, A. C.; Maranan, G. B.; Zhuge, Y.; Vijay, P. V.; and Pettigrew, J., "Behavior of Damaged Concrete Columns Repaired With Novel FRP Jacket," *Journal of Composites for Construction*, ASCE, V. 23, No. 3, 2019, p. 04019013. doi: 10.1061/(ASCE)CC.1943-5614.0000942

16. Graybeal, B.; Bruhwiler, E.; Kim, B.-S.; Toutlemonde, F.; Voo, Y. L.; and Zaghi, A., "International Perspective on UHPC in Bridge Engineering," *Journal of Bridge Engineering*, ASCE, V. 25, No. 11, 2020, p. 04020094. doi: 10.1061/(ASCE)BE.1943-5592.0001630

17. ACI Committee 239, "Ultra-High-Performance Concrete: An Emerging Technology Report (ACI 239R-18)," American Concrete Institute, Farmington Hills, MI, 2018, 21 pp.

18. Hung, C.-C.; El-Tawil, S.; and Chao, S.-H., "A Review Of Developments and Challenges for UHPC in Structural Engineering: Behavior, Analysis, and Design," *Journal of Structural Engineering*, ASCE, V. 147, No. 9, 2021, p. 03121001. doi: 10.1061/(ASCE)ST.1943-541X.0003073

19. Middendorf, B.; Fehling, E.; and Wetzel, A., "Ultra-High-Performance Concrete and High-Performance Construction Materials," *Proceedings of the 5th International Symposium on Ultra-High Performance Concrete and High Performance Construction Materials*, HiPerMat, Kassel, Germany, 2020.

20. Xie, J.; Fu, Q.; and Yan, J.-B., "Compressive Behavior of Stub Concrete Column Strengthened with Ultra-High Performance Concrete Jacket," *Construction and Building Materials*, V. 204, 2019, pp. 643-658. doi: 10.1016/j.conbuildmat.2019.01.220

21. Tong, T.; Lei, H.; Yuan, S.; and Liu, Z., "Experimental Investigation and Seismic Vulnerability Assessment of Low Flexural Strength Rectangular Bridge Piers Retrofitted with Ultrahigh-Performance Concrete Jackets," *Engineering Structures*, V. 206, 2020, p. 110132. doi: 10.1016/j.engstruct.2019.110132

22. Perry, V. H., and Zakariasen, D., "First Use of Ultra-High-Performance Concrete for an Innovative Train Station Canopy," *Concrete Technology Today*, V. 25, No. 2, 2004, 1-8 pp.

23. Monaldo, E.; Nerilli, F.; and Vairo, G., "Basalt-Based Fiber-Reinforced Materials and Structural Applications in Civil Engineering," *Composite Structures*, V. 214, 2019, pp. 246-263. doi: 10.1016/j.compstruct.2019.02.002

24. Fiore, V.; Scalici, T.; Bella, G. D.; and Valenza, A., "A Review on Basalt Fiber and Its Composites," *Composites Part B: Engineering*, V. 74, 2015, pp. 74-94. doi: 10.1016/j.compositesb.2014.12.034

25. Suon, S.; Saleem, S.; and Pimanmas, A., "Compressive Behavior of Basalt FRP-Confined Circular and Non-Circular Concrete Specimens," *Construction and Building Materials*, V. 195, 2019, pp. 85-103. doi: 10.1016/j.conbuildmat.2018.11.039

26. Ahmad, J.; Yu, T.; and Hadi, M. N. S., "Basalt Fiber-Reinforced Polymer-Confined Geopolymer Concrete," *ACI Structural Journal*, V. 118, No. 1, Jan. 2021, pp. 289-300.

27. Song, J.; Gao, W.-Y.; Ouyang, L.-J.; Zeng, J.-J.; Yang, J.; and Liu, W.-D., "Compressive Behavior of Heat-Damaged Square Concrete Prisms

Confined with Basalt Fiber-Reinforced Polymer Jackets," *Engineering Structures*, V. 242, 2021, p. 112504. doi: 10.1016/j.engstruct.2021.112504

28. ASTM C230/C230M-20, "Standard Specification for Flow Table for Use In Tests of Hydraulic Cement," ASTM International, West Conshohocken, PA, 2020.

29. ASTM C39/C39M-18, "Standard Test Method for Compressive Strength of Cylindrical Concrete Specimens," ASTM International, West Conshohocken, PA, 2018.

30. Ma, G.; Chen, X.; Yan, L.; and Hwang, H.-J., "Monotonic and Cyclic Axial Compressive Properties and Modeling of Basalt FRP-Retrofitted Predamaged Short Columns," *Journal of Composites for Construction*, ASCE, V. 24, No. 4, 2020, p. 04020023. doi: 10.1061/(ASCE)CC.1943-5614.0001034

31. ASTM C109/C109M-12, "Standard Test Method for Compressive Strength of Hydraulic Cement Mortars," ASTM International, West Conshohocken, PA, 2012, 11 pp.

32. ASTM C78/C78M-10, "Standard Test Method for Flexural Strength of Concrete Using Simple Beam with Third-Point Loading," ASTM International, West Conshohocken, PA, 2010, 5 pp.

33. Abdulkareem, O. M.; Fraj, A. B.; Bouasker, M.; and Khelidj, A., "Mixture Design and Early Age Investigations of More Sustainable UHPC," *Construction and Building Materials*, V. 163, 2018, pp. 235-246. doi: 10.1016/j.conbuildmat.2017.12.107

34. Murray, S. J.; Subramani, V. J.; Selvam, R. P.; and Hall, K. D., "Molecular Dynamics to Understand the Mechanical Behavior of Cement Paste," *Transportation Research Record: Journal of the Transportation Research Board*, V. 2142, No. 1, 2010, pp. 75-82. doi: 10.3141/2142-11

35. FHWA, Design and Construction of Field-Cast UHPC Connections, Report No. FHWA-HRT-14-084, Federal Highway Administration, Washington, DC, 2014

36. Zhang, Y.; Zhu, P.; Liao, Z.; and Wang, L., "Interfacial Bond Properties Between Normal Strength Concrete Substrate and Ultra-High-Performance Concrete as a Repair Material," *Construction and Building Materials*, V. 235, 2020, p. 117431. doi: 10.1016/j.conbuildmat.2019.117431

37. Tayeh, B. A.; Bakar, B. H. A.; Johari, M. A. M.; and Zeyad, A. M., "Microstructural Analysis of the Adhesion Mechanism Between Old Concrete Substrate and UHPFC," *Journal of Adhesion Science and Technology*, V. 28, No. 18, 2014, pp. 1846-1864. doi: 10.1080/01694243.2014.925386

38. Montgomery, D. C., *Design and Analysis of Experiments*, eighth edition, John Wiley and Sons, Hoboken, NJ, 2013, 688 pp.

39. Chase, W., and Bown, F., *General Statistics*, third edition, John Wiley and Sons, New York, NY, 1997.

40. Wang, W.; Sheikh, M. N.; and Hadi, M. N. S., "Axial Compressive Behavior of Concrete Confined with Polymer Grid," *Materials and Structures*, V. 49, No. 9, 2016, pp. 3893-3908. doi: 10.1617/s11527-015-0761-9

41. Becque, J.; Patnaik, A. K.; and Rizkalla, S. H., "Analytical Models for Concrete Confined with FRP Tubes," *Journal of Composites for Construction*, ASCE, V. 7, No. 1, 2003, pp. 31-38. doi: 10.1061/(ASCE)1090-0268(2003)7:1(31)

42. Ugural, A. C., and Fenster, S. K., *Advanced Strength and Applied Elasticity*, third edition, Prentice-Hall, Englewood Cliffs, NJ, 1995.

43. Thériault, M.; Neale, K.W.; and Claude, S."Fiber-Reinforced Polymer-Confined Circular Concrete Columns: Investigation of Size and Slenderness Effects," *Journal of Composites for Construction*, ASCE, V. 8, No. 4, 2004, pp. 323-331. doi: 10.1061/(ASCE)1090-0268(2004)8:4(323)

44. Silva, M. A. G., and Rodrigues, C. C., "Size and Relative Stiffness Effects on Compressive Failure of Concrete Columns Wrapped with Glass FRP," *Journal of Materials in Civil Engineering*, ASCE, V. 18, No. 3, 2006, pp. 334-342. doi: 10.1061/(ASCE)0899-1561(2006)18:3(334)

ACI STRUCTURAL JOURNAL TECHNICAL PAPER

Title No. 122-S03

Reinforced Concrete Coupling Beams with Axial Restraint

by Baha'a Al-Khateeb and Christopher J. Motter

Seven one-half-scale reinforced concrete coupling beams, designed using ACI 318-19, were tested with constant stiffness axial restraint. The test variables were the span-depth ratio, reinforcement configuration (conventional or diagonal), primary reinforcement ratio and bar diameter, and level of axial restraint. Six beams consisted of three nominally identical pairs, with the two beams in each pair tested at a different level of axial restraint. The two conventionally reinforced beams reached peak strength at 2.0 and 3.0% chord rotation and experienced rapid post-peak strength degradation with the opening of diagonal cracks and the formation of splitting cracks along the longitudinal reinforcement. Strength degradation in diagonally reinforced beams initiated with buckling of diagonal reinforcement, and variation in axial restraint on identical pairs of beams did not lead to a significant difference in deformation capacity. Deformation capacity was larger for beams with a larger diagonal bar diameter, which corresponded to a larger reinforcement ratio and a larger ratio of transverse reinforcement spacing to diagonal bar diameter (s/d_b). For the diagonally reinforced test beams, the maximum measured shear strength reached as high as 2.4 times the nominal shear strength computed using ACI 318-19 and exceeded the $0.83\sqrt{f_c'}A_{cw}$ MPa ($10\sqrt{f_c'}A_{cw}$ psi) limit on nominal shear strength by more than a factor of 2.0 in the test with the smallest span-depth ratio. Based on strut-and-tie behavior, modifications to the ACI 318-19 equation to include axial load were examined. When the location of the compressive strut and tension tie at the beam ends was consistent with nominal moment calculations, the resulting ratio of the average maximum measured shear strength in the positive and negative loading directions to shear strength calculated using the modified equation ranged from 1.16 to 1.33. For the diagonally reinforced beams, a larger span-depth ratio, bar size, and reinforcement ratio were associated with larger rotation at yielding and larger effective flexural rigidity.

Keywords: axial restraint; coupling beam; earthquake; link beam; reinforced concrete; seismic; shear wall; structural wall.

INTRODUCTION

Structural walls are used in buildings to resist seismic and wind loads. Two adjacent walls in the same plane may be connected by coupling beams at the top of each story. When a coupled wall is subjected to lateral load, the shear demands in the beams are transferred to the walls as axial load, such that an axial tension-compression couple forms in the walls. Coupled wall systems have higher stiffness, strength, and energy dissipation capacity than single cantilever wall systems due to the coupling action provided by the coupling beams. Coupling beams are intended to respond to seismic loads in a ductile manner to provide energy dissipation.

Coupling beams are typically designed to yield and form plastic hinges before the walls. Following the 2010-2011 Canterbury Earthquake Sequence in New Zealand, the Canterbury Earthquakes Royal Commission (CERC 2012) investigated damaged and collapsed buildings. CERC determined that coupled walls did not behave as intended, as the plastic hinges concentrated at the base of the walls, and the coupling beams did not form plastic hinges. CERC (2012) suggested that axial compressive restraint from walls and floors may have increased the strength of the coupling beams. If not accounted for in the design, the additional strength of the beams could alter the behavior of the coupled walls by preventing yielding in the beams and providing larger axial forces to the walls.

Previous research on the influence of coupling beam axial restraint on coupled wall behavior has included analytical studies. Mohr (2007) used VecTor2 (2006) to develop nonlinear finite element models of coupling beams that were calibrated to tests and then used in pushover analysis of a 10-story coupled wall designed in accordance with the International Building Code (IBC) Structural/Seismic Design Manual (ICC 2006). The resulting behavior was not as intended in design, as coupling beams at the first two stories did not form plastic hinges. It was determined that a reduction in beam strength to 25% of the design strength allowed the formation of plastic hinges at the ends of these beams prior to the walls. Barbachyn et al. (2012) developed strut-and-tie models for diagonally reinforced concrete coupling beams using OpenSees (Mazzoni et al. 2009) and validated the models using existing test data. Barbachyn et al. (2012) modeled coupled walls and determined that the level of axial restraint was dependent on the location, with beams at lower stories having higher axial restraint. Barbachyn et al. (2012) reported that axial restraint may cause crushing of the compression strut. Malcolm (2015) used VecTor2 (2011) to develop nonlinear finite element models that were calibrated to the Naish et al. (2013a) tests and then used to model coupled walls. Malcolm (2015) reported that axial restraint increased beam strength by two to three times the design strength and that coupled walls designed in accordance with the New Zealand standard NZS 3101.1&2:2006 (2006) behaved as a single cantilever wall rather than a coupled wall due to the increase in coupling beam strength.

Limited experimental studies have been conducted on individual reinforced concrete coupling beams subjected to axial restraint. Tegos and Penelis (1988) tested 24 coupling beams, 21 of which had constant axial load. Three were diagonally reinforced, three were conventionally

ACI Structural Journal, V. 122, No. 1, January 2025.

MS No. S-2022-249.R3, doi: 10.14359/51742135, received May 25, 2024, and reviewed under Institute publication policies.

reinforced, and 18 had rhombic reinforcement. The beams had a span-depth ratio of 2.0 to 4.0 and axial load ranging from zero to $0.35A_g f_{c,test}'$, where $f_{c,test}'$ is the tested concrete compressive strength. Galano and Vignoli (2000) tested 15 coupling beams with a span-depth ratio of 1.5 and full axial restraint. Four were conventionally reinforced, seven were diagonally reinforced, and four had rhombic reinforcement. The axial forces developed in the beams were not measured. The beams tested in both of these studies had a level of transverse reinforcement less than that required by ACI 318-19 (ACI Committee 318 2019). The influence of axial restraint on coupling beam behavior was not emphasized in the data and analysis presented by Tegos and Penelis (1988) or Galano and Vignoli (2000). Gonzalez (2001) tested a diagonally reinforced coupling beam with axial restraint provided by high-strength rods. The strength was reported to be twice the ultimate strength reported using CSA A23.3-94 (1994), noting that this beam was not tested to failure. Breña and Ihtiyar (2011) tested four conventionally reinforced coupling beams with wall segments that had pin connections and rotation imposed during testing. Breña and Ihtiyar (2011) reported an estimated maximum coupling beam axial load of $0.06A_g f_c'$, where A_g is the gross cross-sectional area of the beam, and f_c' is the specified 28-day compressive strength of concrete, and noted this was less than the limit of $0.10A_g f_c'$ in ACI 318-08 (ACI Committee 318 2008) to neglect axial force in strength calculations. Setkit (2012) tested five fiber-reinforced concrete coupling beams and one diagonally reinforced coupling beam with conventional concrete, with steel links used to apply axial force. The maximum measured axial force was reported to be 6.5% of the axial compressive strength for the fiber-reinforced beams and 5.0% for the beam with conventional concrete. Naish et al. (2013a) tested diagonally reinforced coupling beams that included a portion of a floor slab and reported that the slab restrained the axial elongation of the beam and increased the shear strength by roughly 20%. Seo et al. (2017) tested four conventionally reinforced coupling beams with a span-depth ratio of 1.68 and full axial restraint. The beams were reported to have developed strength over 1.5 times the design strength determined using the strut-and-tie model per the Korea Concrete Institute (KCI) standard (KCI 2012). Fisher et al. (2017) tested four conventionally reinforced coupling beams with a span-depth ratio of 2.67. Axial restraint was provided by segments of the wall that were included in the test specimens, although boundary conditions did not restrain the rotation of wall piers to impose full axial restraint. It was reported that the ratio of peak measured strength to predicted strength was 1.05 and 1.45 on average using CSA A23.3-14 (2014) and ACI 318-14 (ACI Committee 318 2014), respectively. Poudel et al. (2018) tested a diagonally reinforced coupling beam with axial restraint and compared the results to an identical coupling beam tested by Ameen et al. (2017) without axial restraint. Axial restraint was provided by high-strength threaded rods, and the reported stiffness was not constant. It was reported that strength increased by roughly 30% for the axially restrained beam relative to the unrestrained beam. Park et al. (2021) tested two conventionally reinforced coupling beams with a span-depth ratio of 2.0, one with axial restraint provided by actuators controlled through hybrid simulation and the other without axial restraint. It was reported that the initial shear stiffness and shear capacity were larger for the beam with axial restraint.

This study was motivated by the limited previous studies on ACI 318-19-compliant diagonally reinforced concrete coupling beams with axial restraint. In this study, seven reinforced concrete coupling beams, designed using ACI 318-19, were tested with constant axial compressive stiffness within each test. Test variables included span-depth ratio, reinforcement configuration (longitudinal or diagonal), longitudinal and transverse reinforcement ratio, bar diameter of primary reinforcement, and transverse reinforcement spacing. The results were used to assess the impact of axial restraint on coupling beam behavior.

RESEARCH SIGNIFICANCE

Previous studies (Mohr 2007; CERC 2012; Barbachyn et al. 2012; Malcolm 2015) have highlighted the potential for axial restraint on coupling beams to alter the behavior of coupled walls relative to that expected in design. This research addresses the need for experimental study on Code-compliant coupling beams subjected to measured axial restraint. Results of the study highlight the potential for significant strength increase in coupling beams due to axial restraint, suggesting the need for strength design of coupled walls in ACI 318. The study provides data needed for the calibration of nonlinear numerical coupling beam models that may be used for future modeling efforts of coupled wall behavior.

EXPERIMENTAL PROGRAM

Test beams

Seven one-half-scale reinforced concrete coupling beams, designed using ACI 318-19, were constructed and tested. The test matrix is provided in Table 1. The seven beams included three nominally identical pairs, of which one pair was conventionally reinforced, and two pairs were diagonally reinforced. The two beams in each pair were tested at different levels of constant stiffness axial restraint, k_{axial}. Additional test variables included span-depth (aspect) ratio (L/h) and quantity of longitudinal or diagonal reinforcement, which varied with bar diameter. For beams with diagonal reinforcement, the longitudinal reinforcement ratio (ρ_s) was calculated by multiplying the area of diagonal reinforcement by the cosine of the angle of the bars relative to the longitudinal. Test variables were reflected in the beam names. The first letter indicates the reinforcement configuration, with "C" for conventionally reinforced and "D" for diagonally reinforced. The first numerical value indicates the size of the primary reinforcement using the U.S. designation. The second numerical value indicates the span-depth ratio of the beam. The last numerical value indicates the level of applied axial stiffness normalized to $A_g f_c'$, where A_g is the gross area of the beam cross section, and f_c' is the specified concrete compressive strength. The axial stiffness was 43.8, 87.6, or 175.2 kN/mm (250, 500, or 1000 kip/in.), which corresponded to $0.014A_g f_c'$, $0.027A_g f_c'$, or $0.055A_g f_c'$ mm

Table 1—Test matrix

Beam name	L/h	α	Primary reinforcement	ρ	k_{axial}, kN/mm (kip/in.)
C(#5)-3.0-0.69	3	0	(4) 15.9 mm (No. 5) conventional	0.0075	87.6 (500)
C(#5)-3.0-0.35			(4) 15.9 mm (No. 5) conventional	0.0075	43.8 (250)
D(#4)-3.0-0.69		12.7	(6) 12.7 mm (No. 4) diagonal	0.0071	87.6 (500)
D(#4)-3.0-1.39			(6) 12.7 mm (No. 4) diagonal	0.0071	175.1 (1000)
D(#6)-3.0-0.69			(6) 19.1 mm (No. 6) diagonal	0.0158	87.6 (500)
D(#6)-3.0-1.39			(6) 19.1 mm (No. 6) diagonal	0.0158	175.1 (1000)
D(#6)-1.5-0.69	1.5	24.5	(6) 19.1 mm (No. 6) diagonal	0.0148	87.6 (500)

Note: 1 mm = 0.039 in.

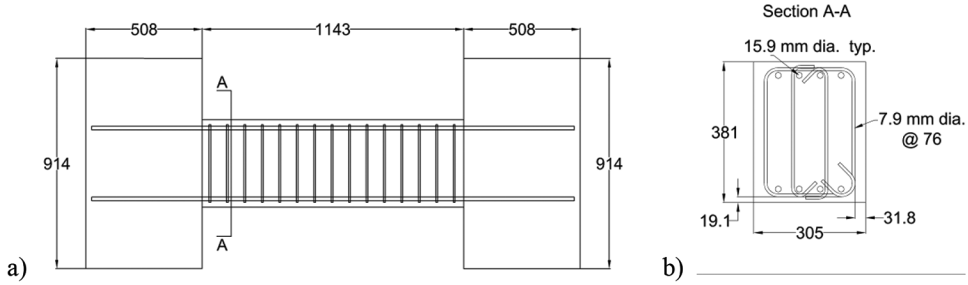

Fig. 1—C(#5)-3.0-0.69 and C(#5)-3.0-0.35: (a) elevation view; and (b) beam cross section. (Note: All dimensions in mm; 1 mm = 0.039 in.)

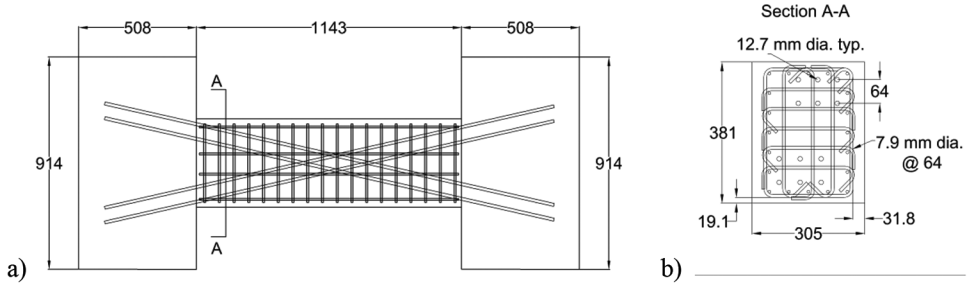

Fig. 2—D(#4)-3.0-0.69 and D(#4)-3.0-1.39: (a) elevation view; and (b) beam cross section. (Note: All dimensions in mm; 1 mm = 0.039 in.)

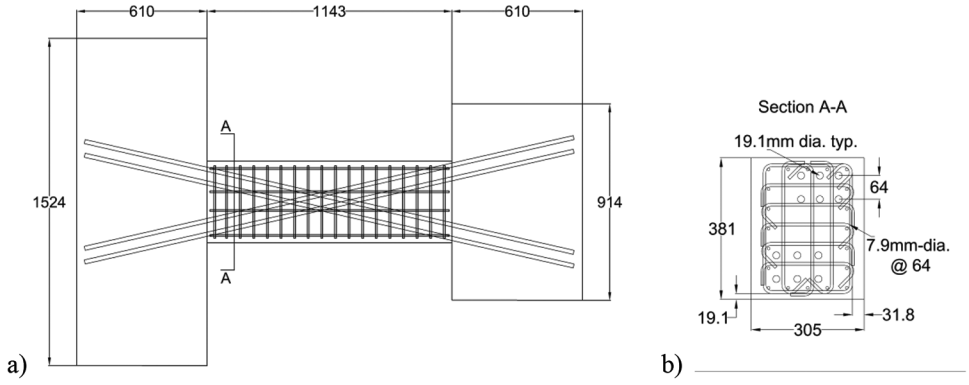

Fig. 3—D(#6)-3.0-0.69 and D(#6)-3.0-1.39: (a) elevation view; and (b) beam cross section. (Note: All dimensions in mm; 1 mm = 0.039 in.)

($0.35A_g f_c'$, $0.69A_g f_c'$, or $1.39A_g f_c'$ in.), respectively, for f_c' = 27.6 MPa (4.0 ksi). These values were selected to provide a range of values within the capacity of the actuators used to apply the loads based on estimates of axial elongation from previous data from Naish et al. (2013a) on unrestrained diagonally reinforced concrete coupling beams.

Drawings of the beams are provided in Fig. 1 through 4. The beams were considered half-scale and had a 305 x 381 mm (12 x 15 in.) cross section. For the full-scale beams, primary reinforcement was assumed to range from 25.4 to 35.8 mm (1 to 1.4 in.) in diameter (No. 8 to 11), with six bars in each diagonal bundle. The diagonal reinforcement in the

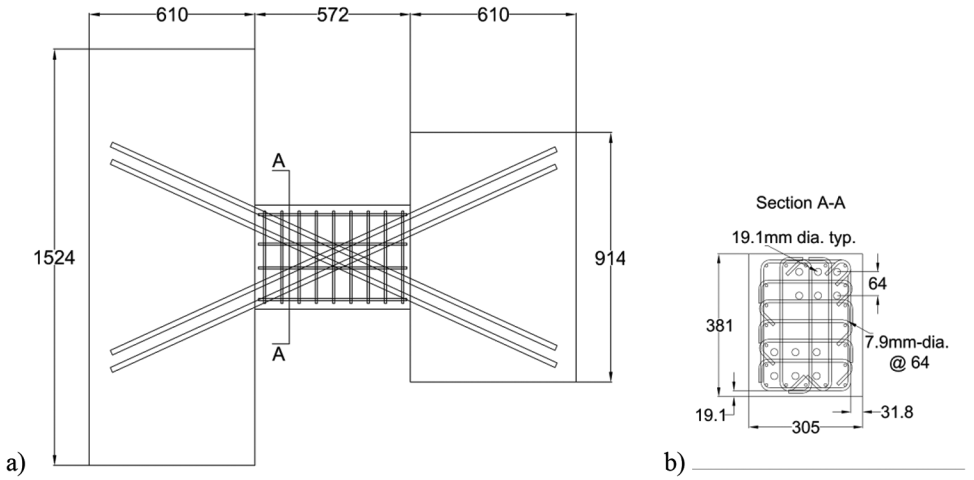

Fig. 4—D(#6)-1.5-0.69: (a) elevation view; and (b) beam cross section. (Note: All dimensions in mm; 1 mm = 0.039 in.)

test beams was six 19.1 mm (0.75 in.) diameter (No. 6) or six 12.7 mm (0.5 in.) diameter (No. 4) in each diagonal bar bundle. The resulting longitudinal reinforcement ratios were 0.0071, 0.0148, and 0.0158, which were deemed to reasonably cover the range of 0.0027 to 0.0217, as reported by Mohr (2007) for a survey of sample buildings. The conventionally reinforced beams had four 15.9 mm (0.63 in.) (No. 5) longitudinal reinforcements, both top and bottom. The resulting longitudinal reinforcement ratio of 0.0075 fell within the range of 0.0046 to 0.0116 reported by Mohr (2007) for conventionally reinforced coupling beams. The span-depth ratio was 3.0 for the conventionally reinforced beams and was either 1.5 or 3.0 for the diagonally reinforced beams. These values fell within the ranges reported by Mohr (2007), which were 2.7 to 3.4 for conventionally reinforced and 1.1 to 3.2 for diagonally reinforced. Transverse reinforcement, as well as longitudinal reinforcement in diagonally reinforced beams, was a 7.9 mm (0.31 in.) diameter ASTM A36/A36M smooth bar due to the lack of availability of ASTM A706/A615 deformed bar in this size. All other reinforcement in the test beams was ASTM A706/A615 Grade 60. The clear cover to transverse reinforcement was larger at the sides than at the top and bottom due to the position of the longitudinal reinforcement in the conventionally reinforced beams and the diagonal reinforcement in the diagonally reinforced beams, which, in practice, may be developed as straight bars into a wall with potentially the same width as the coupling beam and with reinforcement near the perimeter of the cross section.

For the two conventionally reinforced beams, the design of the transverse reinforcement satisfied ACI 318-19, Section 18.6.5, per ACI 318-19, Section 18.10.7.3. Although the beams were tested with axial restraint applied, axial load was not included in the computation of the probable flexural strength, M_{pr}, for strength design for shear. Gravity load was not applied to the test beams, so w_u was zero. The nominal shear strength of concrete was taken as zero per ACI 318-19, Section 18.6.5.2. Nominal shear strength was computed using the expected yield strength of 372 MPa (54 ksi) for ASTM A36/A36M reinforcement (PEER TBI 2017). Although this is inconsistent with design practice, it was used here due to the large difference in expected versus specified strength for ASTM A36/A36M relative to ASTM A615/A615M. For the diagonally reinforced beams, the design of transverse reinforcement satisfied ACI 318-19, Section 18.10.7.4, which specifies transverse reinforcement for each diagonal bar group or the full cross section. Full cross-section transverse reinforcement was used for the test beams.

As shown in Fig. 1 through 4, each test beam included two concrete blocks at the beam ends. The blocks enabled the anchorage of the beam specimen to the laboratory strong floor and the loading beam. Polyvinyl chloride (PVC) pipes were installed in the top and bottom blocks to create voids for anchor rods. For the beams with 19.1 mm (0.75 in.) diameter (No. 6) diagonal reinforcement, the blocks were larger at one end to facilitate the use of additional anchor rods, noting that the spacing of anchor rods in the strong floor differed from that in the loading beam. The provided embedment length into the blocks of the longitudinal reinforcement in the conventionally reinforced beams and the diagonal reinforcement in the diagonally reinforced beams was sufficient to develop $1.25f_y$ in accordance with ACI 318-19, Section 18.10.2.5, where f_y is the specified yield strength of reinforcement. The longitudinal reinforcement in the diagonally reinforced beams was terminated 12.7 mm (0.5 in.) from the beam ends, so it was not embedded into the blocks, consistent with the recommendation of Barbachyn et al. (2012) and the recommendation of ANSI/AISC 341-22 (2022), Section H4.5b.2(c), for longitudinal reinforcement in steel-reinforced concrete (SRC) coupling beams, rather than embedded a short distance, as shown in ACI 318-19, Fig. R18.10.7b. The test specimens were constructed with the beams in the horizontal position, such that the beam had a free concrete surface during concrete placement, which is typical for coupling beams.

Material properties

Tensile testing was conducted on reinforcement samples for the beam reinforcement. Measured values for the tested yield strength, $f_{y,test}$, and tested ultimate strength, $f_{u,test}$, are provided in Table 2. Compression testing was conducted on 152 x 305 mm (6 x 12 in.) concrete cylinders cast during concrete placement. A different batch of concrete was used

Table 2—Measured yield and ultimate strength of reinforcement

Reinforcement		
Bar diameter, mm (in.)	$f_{y,test}$, MPa (ksi)	$f_{u,test}$, MPa (ksi)
12.7 (0.5000)	478 (69.3)	757 (109.8)
15.9 (0.6250)	441 (64.0)	703 (101.9)
19.1 (0.7500)	454 (65.8)	742 (107.6)
7.9 (0.3125)	541 (78.4)	574 (83.3)

for C(#5)-3.0-0.69, C(#5)-3.0-0.35, D(#4)-3.0-0.69, and D(#4)-3.0-1.39 than that used for D(#6)-3.0-0.69, D(#6)-3.0-1.39, and D(#6)-1.5-0.69. At the time of beam testing, three compression tests were conducted for each of C(#5)-3.0-0.69, C(#5)-3.0-0.35, D(#4)-3.0-0.69, D(#4)-3.0-1.39, with results provided in Table 3 and an overall average value of 23.8 MPa (3.45 ksi). Due to minimal variation in strength with time, this value was used for the tested compressive strength of concrete, $f_{c,test}'$, for these four tests. After testing D(#6)-3.0-0.69, D(#6)-3.0-1.39, and D(#6)-1.5-0.69, three compression tests were conducted, and the average value of 21.0 MPa (3.05 ksi) was used for $f_{c,test}'$ for these three tests.

Test setup

A schematic and photo of the test setup are provided in Fig. 5. The beams were tested in the vertical orientation. Three actuators were used during testing. A laterally oriented actuator with ±254 mm (±10 in.) stroke and 890 kN (200 kip) capacity was aligned with the beam midlength and used to apply reversed-cyclic loading. Two vertically oriented actuators with ±914 mm (±36 in.) stroke and 1334 kN (300 kip) capacity were used to apply axial restraint. Two 610 mm (24 in.) tall concrete spacers were used to elevate the test specimen from the ground to accommodate the length of the vertical actuators. The bottom block of the test specimen was post-tensioned to the strong floor. The top block of the test specimen and the actuators were post-tensioned to the structural steel loading frame. A 17.8 kN (4 kip) plate was attached to the end of the horizontal member of the loading frame to counter the weight of the vertical member of the loading frame and the lateral actuator. Two frames oriented in the out-of-plane direction were used to prevent out-of-plane movement of the horizontal member of the loading frame near the two ends. Each frame comprised two structural steel columns, a structural steel beam, and two shorter-length structural steel columns. The two longer columns had a steel beam spanning between them and welded base plates that were anchored to the laboratory strong floor. The two short columns were connected to the steel beam with a 6.35 mm (0.25 in.) gap between the columns and the horizontal member of the loading frame.

Loading protocol

The test beam was subjected to both axial and lateral loads. The two vertical actuators were programmed to apply a total load that was proportional to the measured axial elongation of the beam while maintaining zero rotation over the height of the actuators. This programming was achieved through

Table 3—Concrete strength

Beam name	Specified compressive strength f_c', MPa (ksi)	Concrete age, days	Average tested compressive strength $f_{c,test}'$, MPa (ksi)
C(#5)-3.0-0.69	27.6 (4.0)	217	23.6 (3.42)
C(#5)-3.0-0.35		228	24.1 (3.49)
D(#4)-3.0-0.69		247	23.8 (3.45)
D(#4)-3.0-1.39		259	23.7 (3.44)
D(#6)-3.0-0.69		288	—
D(#6)-3.0-1.39		302	—
D(#6)-1.5-0.69		355	21.0 (3.05)

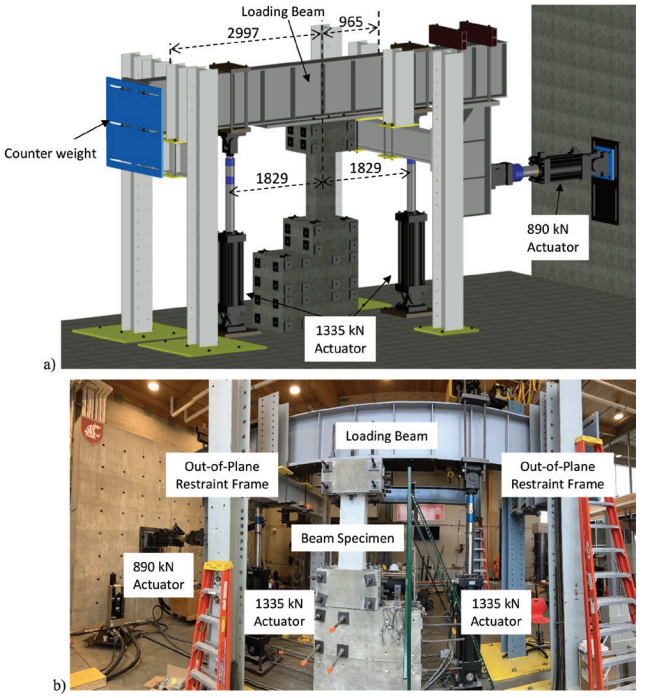

Fig. 5—Test setup: (a) schematic; and (b) photo. (Note: All dimensions in mm; 1 mm = 0.039 in.; 1 kN = 0.2248 kip.)

two control equations: one that specified equal displacement in the actuators, and one that specified total force in the actuators equal to the product of axial stiffness and measured axial elongation. Measured axial elongation was an input into the control program. Axial elongation in each test beam was measured using linear variable differential transformers (LVDTs) that spanned from the top of the bottom block to the bottom of the top block and were located as shown in Fig. 6. For C(#5)-3.0-0.69, C(#5)-3.0-0.35, D(#4)-3.0-0.69, D(#4)-3.0-1.39, and D(#6)-3.0-0.69, the measurement from one LVDT, V4, which was not aligned with beam centerline in the plane of loading, was used to control the applied axial load. Asymmetry in the axial load versus coupling beam chord rotation was measured for D(#4)-3.0-1.39 and D(#6)-3.0-0.69, with more information provided in the section "Axial elongation and axial restraint." Out of consideration that this asymmetry could have resulted from deformation in the top and/or bottom block, the average measurement from two LVDTs, V3 and V4, which were aligned with the beam

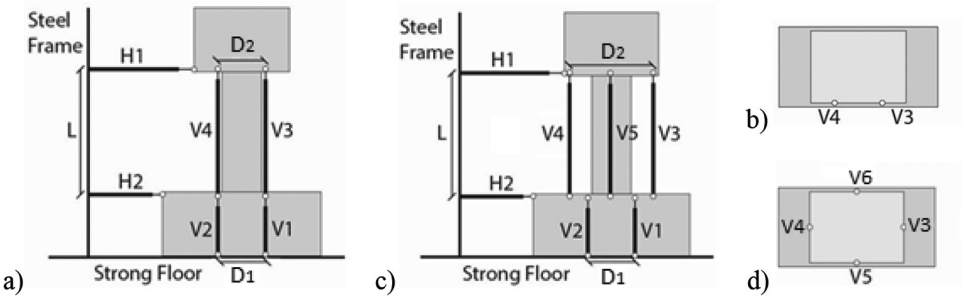

Fig. 6—LVDT layout: (a) elevation view; (b) plan view for C(#5)-3.0-0.69, C(#5)-3.0-0.35, D(#4)-3.0-0.69, D(#4)-3.0-1.39, and D(#6)-3.0-0.69; (c) elevation view; and (d) plan view for D(#6)-3.0-1.39 and D(#6)-1.5-0.69.

centerline in the plane of loading and located on opposite sides of the beam, was used to control the applied axial load for the remaining tests, D(#6)-3.0-1.39 and D(#6)-1.5-0.69. For all tests, the measured axial elongation was taken as the change in the length of the sensors, so it was elongation of the chord rather than elongation in the vertical direction.

Fully reversed-cyclic lateral loading was applied using the lateral actuator to apply displacement-controlled cycles in terms of chord rotation. Chord rotation was computed as the ratio of the difference in lateral displacement between the top and bottom of the beam to the length of the beam, with the lateral displacement at the top and bottom of the beam measured using LVDTs H1 and H2, respectively, as shown in Fig. 6. Three cycles each were applied at 0.125, 0.25, 0.375, 0.50, 0.75, 1.0, 1.5, 2.0, and 3.0% chord rotation, followed by two cycles each at 4.0, 6.0, 8.0, and 10.0% chord rotation. Starting with the cycles at 0.50% chord rotation, this loading protocol matched that used by Naish et al. (2013a) for testing diagonally reinforced concrete coupling beams without axial restraint. Prior to 0.50% chord rotation, displacement-controlled cycles were used due to axial restraint, rather than load-controlled cycles at increments of the yield strength as used by Naish et al. (2013a). During testing, the chord rotation was corrected for translation and rotation of the bottom block and for half of the rotation measured over the length of the beam, resulting in a chord rotation, θ, used to control the test of

$$\theta = \frac{\Delta_{H1} - \Delta_{H2}}{L} - \frac{\Delta_{V2} - \Delta_{V1}}{D_1} - \frac{\Delta_{V4} - \Delta_{V3}}{2D_2} \quad (1)$$

where Δ_{H1}, Δ_{H2}, Δ_{V1}, Δ_{V2}, Δ_{V3}, and Δ_{V4} are displacement measurements from the LVDTs shown in Fig. 6; L is the length of the beam; D_1 is the distance between vertical sensors $V1$ and $V2$ shown in Fig. 6; and D_2 is the distance between vertical sensors $V3$ and $V4$ shown in Fig. 6. D_1 was 457 mm (18 in.) for all beams. D_2 was 914 mm (36 in.) for D(#6)-3.0-1.39 and D(#6)-1.5-0.69 and 457 mm (18 in.) for the other five beams.

TEST RESULTS

Observed damage

Damage photos for the test beams at 3.0% and 6.0% chord rotation are provided in Fig. 7 and 8, respectively. The cycles at which damage states were first observed for each beam are summarized in Table 4. Flexural cracks refer to those perpendicular to the beam length and initiating at the extreme fibers (that is, the top and bottom faces for a beam in standard position). Shear cracks refer to diagonal cracks crossing the centerline of the beam. Flexural cracking initiated in all test beams at 0.125% rotation. For C(#5)-3.0-0.69, compared to C(#5)-3.0-0.35, the onset of shear cracking occurred at larger chord rotation, and the onset of concrete crushing and spalling occurred at smaller chord rotation. Shear crack width increased with deformation demand for both C(#5)-3.0-0.69 and C(#5)-3.0-0.35.

Of the four diagonally reinforced beams with a span-depth ratio of 3.0, D(#6)-3.0-1.39 was expected to have the largest compression demands at a given drift level based on section equilibrium for the combination of larger axial load and a larger quantity of diagonal reinforcement. Conversely, D(#4)-3.0-0.69 was expected to have the smallest compression demands. Concrete crushing was observed to initiate at 1.5% for D(#6)-3.0-1.39 and 2.0% for the other three beams. Concrete spalling was observed to initiate at 2.0% for D(#6)-3.0-1.39 and 3.0% for the other three beams. For these four beams, concrete spalling and diagonal reinforcement buckling and fracture concentrated at the ends, where moment demand was largest. For the beam with a span-depth ratio of 1.5, concrete spalling and buckling and fracture of diagonal reinforcement spread over the length of the beam. Buckling of diagonal reinforcement was first observed at 6.0% rotation for the two beams with No. 4 diagonal reinforcement and 10.0% rotation for the three beams with No. 6 diagonal reinforcement. The beams with No. 6 diagonal reinforcement had larger ρ_s and a larger ratio of transverse reinforcement spacing to diagonal bar diameter, s/d_b. Previous research (Rodriguez et al. 1999) has demonstrated an increased likelihood of bar buckling as s/d_b is increased. The difference in axial stiffness and the associated effect on the strain history in the reinforcement had little impact on the initiation of bar buckling relative to the change in ρ_s and s/d_b.

Load-deformation

The load-deformation response of each test beam is provided in Fig. 9. Peak shear force, V_{max}, chord rotation at peak shear force, $\theta@V_{max}$, and chord rotation at lateral failure, $\theta@0.8V_{max}$, are provided in Table 5. Lateral failure, which was determined independently in each loading direction, was defined to occur at the first instance of a cycle peak at which strength at the cycle peak and for the remainder of the test did not exceed 80% of V_{max}.

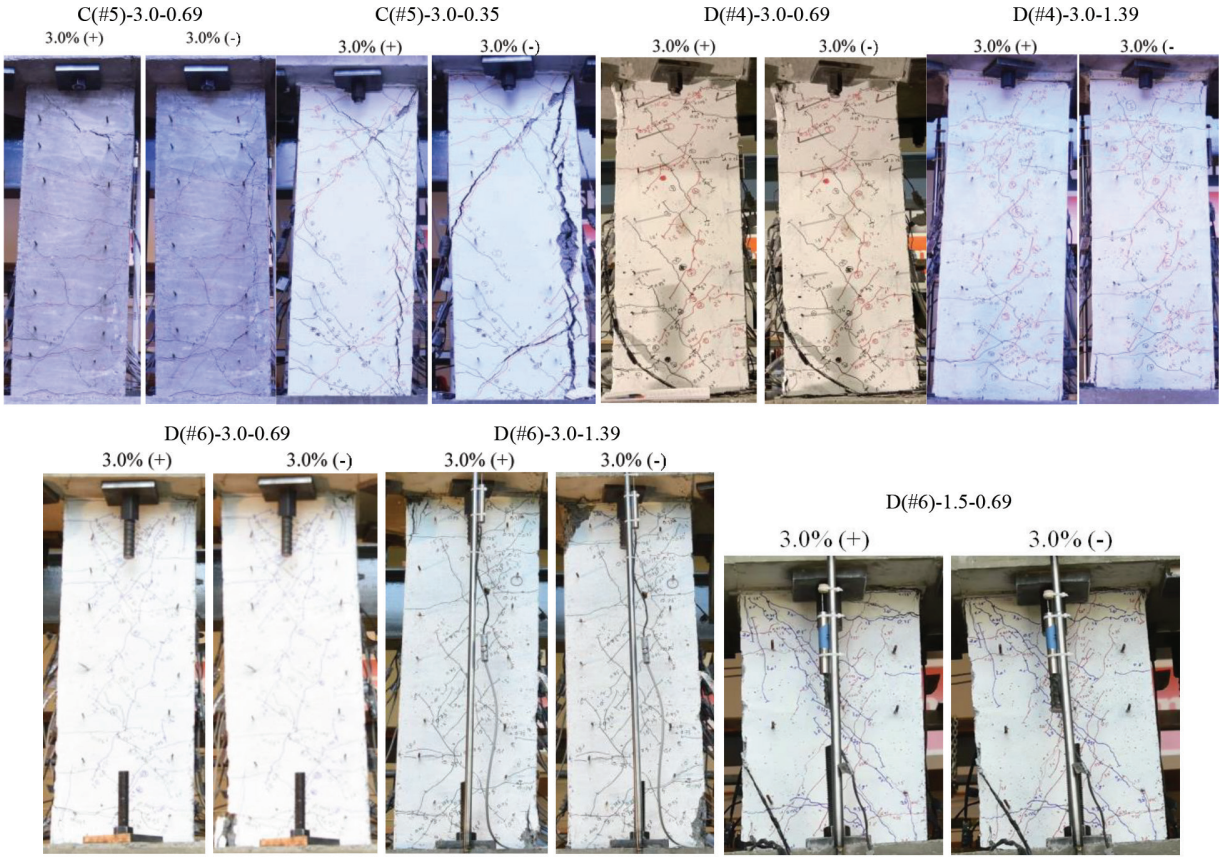

Fig. 7—Damage photos at 3.0% chord rotation.

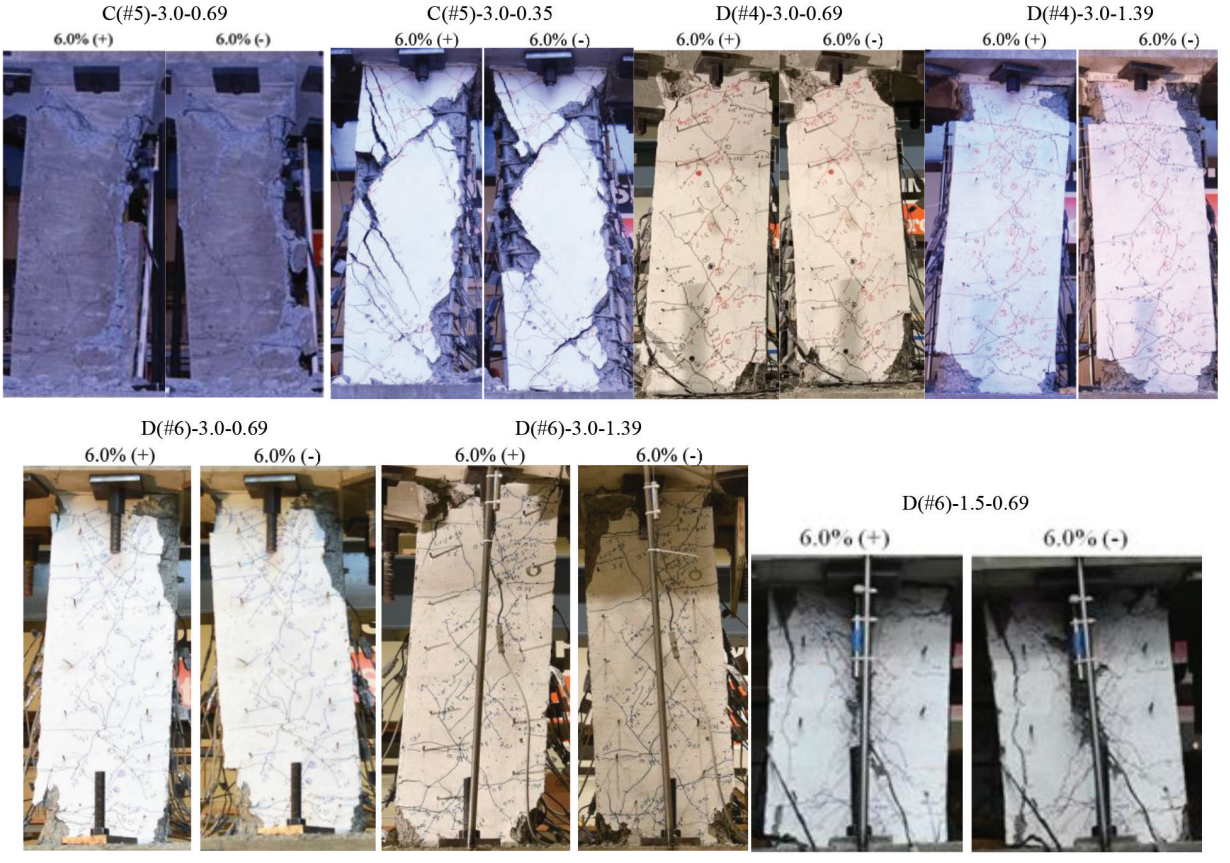

Fig. 8—Damage photos at 6.0% chord rotation.

Table 4—Chord rotation at which damage state was first observed

Beam name	First flexure crack at interface	First flexure crack within beam span	First shear crack	Concrete crushing	Concrete spalling	Bar buckling	Bar fracture
C(#5)-3.0-0.69	0.125%	0.125%	0.75%	2.0%	3.0%	None	None
C(#5)-3.0-0.35	0.125%	0.125%	0.25%	3.0%	4.0%	None	None
D(#4)-3.0-0.69	0.125%	0.125%	0.375%	2.0%	4.0%	6.0%	8.0%
D(#4)-3.0-1.39	0.125%	0.125%	0.375%	2.0%	3.0%	6.0%	6.0%
D(#6)-3.0-0.69	0.125%	0.125%	0.375%	2.0%	3.0%	10.0%	10.0%
D(#6)-3.0-1.39	0.125%	0.125%	0.25%	1.5%	2.0%	10.0%	12.0%
D(#6)-1.5-0.69	0.125%	0.125%	0.25%	2.0%	3.0%	10.0%	10.0%

In comparing the two conventionally reinforced beams, $\theta@V_{max}$ was reached at 3.0% chord rotation for C(#5)-3.0-0.69 and 2.0% chord rotation for C(#5)-3.0-0.35. Post-peak strength degradation was rapid. $\theta@0.8V_{max}$ occurred at the second cycle of 3.0% for both beams. Both beams experienced opening of shear cracks in addition to the formation of splitting cracks along longitudinal reinforcement at one face, as shown in Fig. 7 and 8. For the conventionally reinforced beams relative to the diagonally reinforced beams, $\theta@0.8V_{max}$ was significantly lower, and the rate of strength degradation and the level of pinching in the load-deformation response was larger. Strength degradation was more pronounced for C(#5)-3.0-0.69 than C(#5)-3.0-0.35. $\theta@0.8V_{max}$ for the conventionally reinforced beams, with opening of shear cracks and formation of splitting cracks along longitudinal reinforcement, was less than that of previous tests on flexure-yielding conventionally reinforced beams, such as FB33 (Naish et al. 2013a) with $\theta@0.8V_{max}$ of 4.0% and HB3-6L-T100 (Xiao et al. 1999) with $\theta@0.8V_{max}$ of 3.7%.

For the diagonally reinforced beams, $\theta@0.8V_{max}$ was more heavily influenced by reinforcing bar size than the level of axial restraint, as evident in Table 5. For beams with the same level of axial restraint, those with 19.1 mm (0.75 in.) diameter (No. 6) diagonal reinforcement had significantly larger $\theta@0.8V_{max}$ than those with 12.7 mm (0.5 in.) diameter (No. 4) diagonal reinforcement. This is consistent with the occurrence of bar buckling and fracture at lower rotation levels for the beams with 12.7 mm (0.5 in.) diameter (No. 4) diagonal reinforcement. Strength degradation primarily occurred due to buckling and fracture of diagonal reinforcement rather than crushing of confined concrete. Greater pinching is evident in the load-deformation response of the beams with 12.7 mm (0.5 in.) diameter (No. 4) diagonal reinforcement than those with 19.1 mm (0.75 in.) diameter (No. 6) diagonal reinforcement due to buckling of 12.7 mm (0.5 in.) diameter (No. 4) diagonal reinforcement at lower levels of deformation demand.

Strength

Values for V_{max} in Table 5 are provided relative to the nominal shear strength, V_n; the shear at nominal moment, $V@M_n$, calculated at $P@V_{max}$ and zero axial load; and $\sqrt{f_c'}A_{cw}$, where $P@V_{max}$ is the measured axial force at V_{max}, and A_{cw} is the area of the concrete section resisting shear. V_n for conventionally reinforced beams was calculated with $V_c = 0$ in accordance with ACI 318-19, Section 18.6.5.2, where V_c is the nominal shear strength of concrete. V_n for diagonally reinforced beams was calculated in accordance with ACI 318-19, Section 18.10.7.4 as

$$V_n = 2A_{vd}f_y\sin(\alpha) \le 0.83\sqrt{f_c'}A_{cw} \text{ (MPa)}$$
$$V_n = 2A_{vd}f_y\sin(\alpha) \le 10\sqrt{f_c'}A_{cw} \text{ (psi)} \quad (2)$$

where A_{vd} is the total reinforcement area of one bundle of the diagonal reinforcement; f_y is the yield stress of the reinforcement; α is the angle of inclination of the diagonal reinforcement; and f_c' is the specified concrete compressive strength. M_n was calculated using a uniform magnitude (Whitney) stress block for concrete per ACI 318-19 and an elastic-perfectly-plastic stress-strain relationship for steel reinforcement with an elastic modulus of 200,000 MPa (29,000 ksi). For the diagonally reinforced beams, M_n was calculated at the beam ends using the longitudinal component of the force in the diagonal bars and neglecting the longitudinal reinforcement, which was not embedded into the concrete blocks. Because gravity load was not applied to the coupling beams during testing, shear at nominal moment, $V@M_n$, was computed for a fixed-fixed beam, so the shear span was half the beam length. The values of V_n and M_n reflected in Table 5 were computed for each test beam using $f_{c,test}'$ in place of f_c' and $f_{y,test}$ in place of f_y.

V_{max} of the conventionally reinforced beams was less than V_n, as shown in Table 5. The lack of ribs on the transverse reinforcement may have affected the anchorage of the transverse reinforcement, as these bars did not fracture despite the opening of significant diagonal crack widths. Relative to deformed ASTM A706/A615 Grade 60 reinforcement, reduced anchorage strength and the reduced difference between $f_{u,test}$ and $f_{y,test}$, as evident from the values in Table 2, may have led to a reduction in shear strength. The splitting crack along the longitudinal reinforcement may have also led to reduced strength. ACI 318-19, Section 18.7.4.3, applies to columns but not coupling beams. The provision, which specifies that $1.25l_d$ should not exceed $l_u/2$, was not satisfied for these two beams, where l_d is the development length, and l_u is the clear span. The ratio of $1.25l_d$ to $l_u/2$ was 1.19 for C(#5)-3.0-0.69 and 1.17 for C(#5)-3.0-0.35, with l_d calculated using ACI 318-19, Section 25.4.2.4, and using $f_{c,test}'$ in place of f_c' and $f_{y,test}$ in place of f_y.

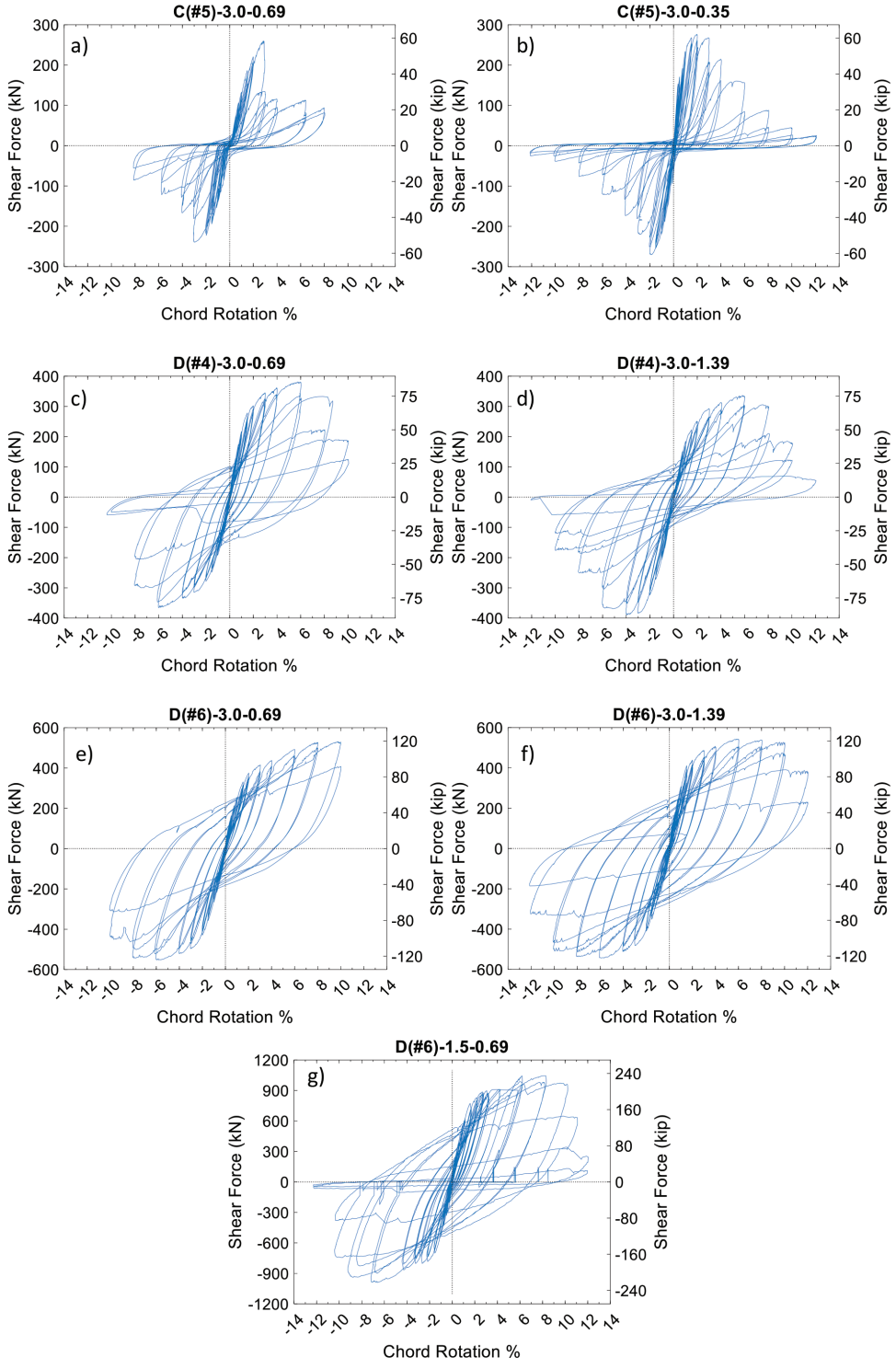

Fig. 9—Load-deformation responses.

For the diagonally reinforced test beams, V_{max}/V_n ranged from 1.56 to 2.40, regardless of whether the $0.83\sqrt{f_c'}A_c$ MPa ($10\sqrt{f_c'}A_{cw}$ psi) limit was included. The shear strength specified in ACI 318-19, which was provided in Eq. (2), is consistent with the strut-and-tie truss model shown in Fig. 10(a) for the beam. In this model, the ratio of flexural resistance to shear resistance at any location in the beam is equal to the longitudinal distance from the midspan, which is consistent with the ratio of flexural demand to shear demand for a fixed-fixed beam. This formulation of beam strength does not consider the influence of axial restraint. If the influence of axial restraint is included, as shown in Fig. 10(b), the modified V_n, referred to as $V_{n,mod.}$, is

$$V_{n,mod.} = 2A_{vd}f_y\sin(\alpha) + P\tan(\alpha) \quad (3)$$

where P is the axial load, with positive load reflecting compression. Values for $V_{max}/V_{n,mod.}$ are provided in Table 5, with $V_{n,mod.}$ computed for $P@V_{max}$ and computed with and without inclusion of the $0.83\sqrt{f_c'}A_{cw}$ MPa ($10\sqrt{f_c'}A_{cw}$ psi)

Table 5—Peak strength, deformation at peak strength, and deformation capacity

	V_{max}				$\theta@V_{max}$, %		$\theta@0.8V_{max}$, % [cycle number]		V_{max}/V_n				$V_{max}/V_{n,mod.}$				$V_{max}/V@M_n = V_{max}/V_{n,prop.}$				$V_{max}/\sqrt{f_{c,test}'}A_{cw}$			
	kN		kip						with		without		with		without		M_n for $P@V_{max}$		M_n for $P = 0$		kPa		psi	
									$0.83\sqrt{f_{c,test}'}A_{cw}$				$0.83\sqrt{f_{c,test}'}A_{cw}$											
Beam name	(+)	(–)	(+)	(–)	(+)	(–)	(+)	(–)	(+)	(–)	(+)	(–)	(+)	(–)	(+)	(–)	(+)	(–)	(+)	(–)	(+)	(–)	(+)	(–)
C(#5)-3.0-0.69	258	240	58	54	3.0	3.0	3.0 [2]	3.0 [2]	0.55	0.51	0.53	0.49	—	—	—	—	1.01	0.96	1.38	1.28	38	35	5.5	5.1
C(#5)-3.0-0.35	276	271	62	61	2.0	2.0	3.0 [2]	3.0 [2]	0.59	0.58	0.57	0.56	—	—	—	—	1.07	1.05	1.48	1.45	41	40	5.9	5.8
D(#4)-3.0-0.69	374	365	84	82	6.0	6.0	8.0 [2]	8.0 [2]	2.30	2.24	2.30	2.24	0.98	1.05	0.98	1.05	1.18	1.16	2.15	2.10	54	54	7.9	7.8
D(#4)-3.0-1.39	338	391	76	88	6.0	4.0	8.0 [2]	6.0 [2]	2.08	2.40	2.08	2.40	1.14	0.86	1.14	0.86	1.18	1.27	1.94	2.25	50	57	7.2	8.3
D(#6)-3.0-0.69	529	552	119	124	10.0	6.0	10.0 [2]	10.0 [2]	1.56	1.62	1.56	1.62	1.32	1.25	1.32	0.90	1.33	1.30	1.52	1.59	83	86	12	12.5
D(#6)-3.0-1.39	543	543	122	122	6.0	6.0	12.0 [1]	12.0 [1]	1.60	1.60	1.60	1.60	1.23	1.23	0.99	0.99	1.21	1.21	1.56	1.56	85	85	12.3	12.3
D(#6)-1.5-0.69	1045	983	235	221	8.0	7.0	10.0 [2]	10.0 [1]	2.36	2.22	1.63	1.53	2.36	2.22	1.10	1.08	1.21	1.21	1.60	1.51	163	153	23.6	22.2

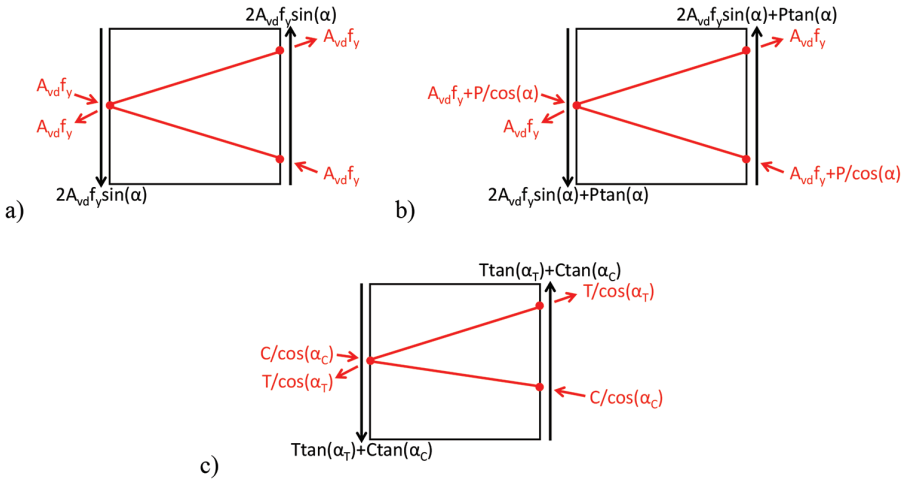

Fig. 10—Strut-and-tie model for half-length diagonally reinforced concrete coupling beam for: (a) no axial load; (b) axial compressive load located at centroid of diagonal reinforcement; and (c) resultant compression and tension based on M_n *at end of beam.*

limit. $V_{max}/V_{n,mod.}$ ranged from 0.86 to 1.32 when excluding the $0.83\sqrt{f_c'}A_{cw}$ MPa ($10\sqrt{f_c'}A_{cw}$ psi) limit, with the average of the positive and negative values for each beam ranging from 0.99 to 1.11. Axial compression increased the shear strength beyond V_n to values closer to $V_{n,mod}$.

$V@M_n$ and $V_{n,mod.}$ are equal when the resultant compression force for M_n is at the location of the centroid of the diagonal reinforcement, consistent with the computation of $V_{n,mod.}$ reflected by the model in Fig. 10(b). Deviation of the resultant compression force in the M_n calculation from the centroid of the diagonal reinforcement toward the centerline of the beam cross section will lead to a reduction in $V@M_n$ relative to $V_{n,mod.}$. If the computation of M_n at the end of the beam is used to determine the location of the resultant compression and tension forces, the location of these forces and the orientation of the compression strut and tension tie could be adjusted accordingly, as shown in Fig. 10(c). This brings the strut-and-tie model into agreement with the calculation of M_n, with $V_{n,prop.}$ for this model differing from the calculation of $V_{n,mod.}$ in Eq. (3) and becoming

$$V_{n,prop.} = V@M_n = \frac{2M_n}{L} = T\tan(\alpha_T) + C\tan(\alpha_C) \quad (4)$$

where L is the beam length; T and C are the resultant tension and compression forces from computation of M_n; and α_T and α_C are the angles of the tension tie and compression strut, respectively, relative to the longitudinal. For the five diagonally reinforced beams, $V_{max}/V_{n,prop.} = V_{max}/V@M_n$ ranged from 1.16 to 1.33 when M_n was computed with $P@V_{max}$ and from 1.51 to 2.25 when M_n was computed with zero axial load. As evident in Table 5, values of $V_{n,prop.} = V@M_n$ for $P = 0$ were slightly larger than V_n, while values of $V_{n,prop.} = V@M_n$ for $P@V_{max}$ were smaller than $V_{n,mod.}$ from Eq. (3). The discrepancy between $V_{n,prop.} = V@M_n$ and $V_{n,mod.}$ was larger for larger values of $P@V_{max}$ due to migration of the resultant compression force in the M_n calculation toward

the centerline of the cross section, noting that M_n was compression-controlled for larger values of $P@V_{max}$. Although Eq. (3) represents an improvement over Eq. (2) by including the influence of axial load, Eq. (4) represents an improvement over Eq. (3) by creating consistency in the computation of nominal moment strength and nominal shear strength. It is evident from the values in Table 5 that V_{max} for the diagonally reinforced beams with No. 6 bars exceeded $0.83\sqrt{f_c'}A_{cw}$ MPa ($10\sqrt{f_c'}A_{cw}$ psi), with V_{max} reaching more than twice this limit for D(#6)-1.5-0.69. As such, this limit was excluded from Eq. (3) and (4).

Increased coupling beam strength from axial restraint creates additional demands on the walls, noting that the effect of axial restraint is typically excluded when coupling beams are designed in practice. In this study, the constant axial compressive stiffness applied to the diagonally reinforced beams ranged from $0.027A_gf_c'$ to $0.055A_gf_c'$ mm ($0.69A_gf_c'$ to $1.39A_gf_c'$ in.). Additional research is needed to characterize typical levels of axial restraint for coupling beams. ACI 318-19 does not explicitly recommend strength design for coupled walls. It is recommended that an upper bound for coupling beam strength be used to determine wall demands, similar to the use of probable beam strength for the design of columns in special moment frames. If the probable moment strength of a coupling beam was computed in the same manner as a special moment frame beam (that is, using $1.25f_y$), additional strength may be created by axial restraint, as evident from the tests. Although further research is needed to better characterize the level of overstrength, results from this study provide experimentally derived values of overstrength for the range of constant stiffness axial restraint levels considered.

Axial elongation and axial restraint

Plots of axial elongation and axial compressive load versus chord rotation are provided in Fig. 11 with peak axial compressive force, P_{max}; peak axial elongation, Δ_{max}; and chord rotation at peak axial compressive force, $\theta@P_{max}$, provided in Table 6. Responses were roughly linear-elastic prior to reaching 90% of the peak axial load, and elongation at cycle peaks decreased as chord rotation increased for chord rotations larger than $\theta@P_{max}$. At the largest applied deformation levels, many of the beams had shortened due to damage, such that axial tension was applied. For each of the three pairs of nominally identical beams, the average of the positive and negative P_{max} was larger for the beam with larger axial stiffness. Due to asymmetry, this was not the case in the positive and negative directions for D(#4)-3.0-1.39 and D(#6)-3.0-0.69. The asymmetry could have resulted from deformation in the top and/or bottom block, which would have influenced the axial elongation sensor used to control the applied axial load. $\theta@P_{max}$ was 3.0% for the two conventionally reinforced beams, and there was extensive shear cracking at this level. Beyond 3.0% rotation, axial shortening was more gradual for C(#5)-3.0-0.35 than C(#5)-3.0-0.69. The axial elongation of the conventionally reinforced beams was less than the diagonally reinforced beams, as the conventionally reinforced beams were observed to experience opening of shear cracks. In comparing the diagonally reinforced beams, $\theta@P_{max}$ was 4.0% for D(#4)-3.0-1.39 and at least 7.2% for the other four beams. $P_{max}/(f_{c,test}'A_g)$ was 0.35 to 0.51 for beams with a span-depth ratio of 3.0 and 0.27 for D(#6)-1.5-0.69 with a span-depth ratio of 1.5, as shorter beam length led to reduced axial elongation. Despite the high levels of peak axial compressive stress, fracture of transverse reinforcement associated with crushing failure of confined core concrete was not observed. Comparing beams that were nominally identical other than bar size and associated differences in ρ_s and s/d_b (that is, comparing D(#4)-3.0-1.39 to D(#6)-3.0-1.39 and comparing D(#4)-3.0-0.69 to D(#6)-3.0-0.69), the beams with larger bar size (and with larger ρ_s and smaller s/d_b) had a 14 to 15% increase in the average positive and negative P_{max} and more gradual axial shortening beyond $\theta@P_{max}$.

Effective stiffness

The effective secant stiffness plots provided in Fig. 12 were determined assuming all deformation was due to flexure. This is consistent with the approach used by Naish et al. (2013b) to report stiffness for reinforced concrete coupling beams without axial restraint, as the majority of the deformation in the Naish et al. (2013a) tests was determined to be from flexure. Values of effective secant stiffness in Fig. 12 were determined at the peak displacement of the first cycle for each loading level. The effective secant stiffness is provided as flexural rigidity, $(EI)_{sec}$, determined by assuming fixity at the beam ends. $(EI)_{sec}$ was normalized to E_cI_g, where E_c is the modulus of elasticity of concrete, and I_g is the moment of inertia of the gross concrete section. E_c was computed as $4730\sqrt{f_{c,test}'}$ MPa ($57\sqrt{f_{c,test}'}$ ksi) per ACI 318-19. Section 19.2.2.1.

Significant variation in $(EI)_{sec}/(E_cI_g)$ versus chord rotation is evident from Fig. 12. The diagonally reinforced beams generally had larger $(EI)_{sec}/(E_cI_g)$ values than the conventionally reinforced beams, with a larger reinforcement ratio corresponding to larger $(EI)_{sec}/(E_cI_g)$ for the diagonally reinforced beams. The influence of axial restraint on $(EI)_{sec}/(E_cI_g)$ was less than that of reinforcement configuration and reinforcement ratio. The shorter beam, D(#6)-1.5-0.69, had significantly lower $(EI)_{sec}/(E_cI_g)$ than the corresponding longer beam, D(#6)-3.0-0.69. This is likely due to the lower longitudinal reinforcement ratio for the greater diagonal bar inclination and the increased deformation from shear and bond slip relative to deformation from flexure for a shorter span. $(EI)_{sec}/(E_cI_g)$ varied from 0.21 for D(#6)-3.0-1.39 to 0.05 for C(#5)-3.0-0.69 at 0.25% chord rotation and 0.10 for D(#6)-3.0-1.39 to 0.024 for D(#6)-1.5-0.69 at 1.0% chord rotation. C(#5)-3.0-0.69 and D(#4)-3.0-1.39 were cracked during the test setup, which may have contributed to the lower $(EI)_{sec}/(E_cI_g)$ values than C(#5)-3.0-0.35 and D(#4)-3.0-0.69, respectively.

For each test, an effective stiffness was estimated using a backbone fitting procedure, with a sample shown in Fig. 13. A linearized backbone of the load-displacement test data was formulated by connecting the peaks of the first cycle of each chord rotation increment, and a bilinear backbone model was fit to the test data backbone up to V_{max}, similar to the backbone model described in ASCE/SEI 41-13 (2014),

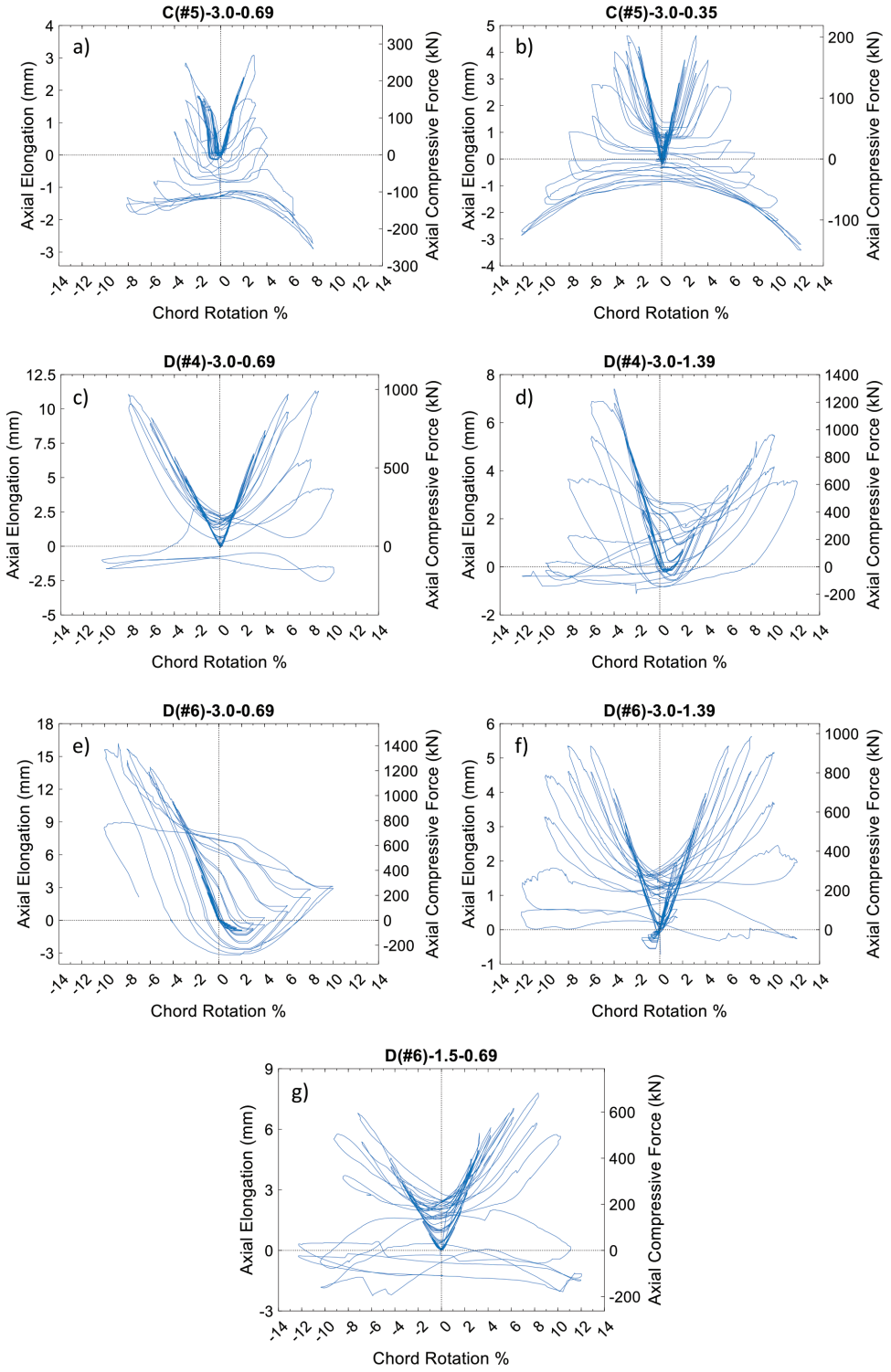

Fig. 11—Axial elongation and axial compressive load versus deformation responses. (Note: 1 mm = 0.039 in.; 1 kN = 0.2248 kip.)

Section 7.4.3.2.4. For the bilinear backbone model, the first line connected the origin to the predicted yield force and intersected the test data backbone at 0.6 of the predicted yield force. The second line connected the predicted yield force to the peak shear force and displacement at the peak shear force. The predicted yield force was determined such that the area under the test data backbone and model backbone were equal up to the peak shear force.

The effective stiffness and yield rotation, θ_y, values from the backbone models are provided in Table 7. Similar to $(EI)_{sec}$, the effective stiffness is provided as flexural rigidity, $(EI)_{eff}$, and was normalized to E_cI_g. For the conventionally reinforced beams, θ_y was significantly larger for the beam with larger axial restraint. For the diagonally reinforced beams, minimal difference in θ_y was associated with variation in axial restraint, while larger span-depth ratio, bar size, and reinforcement ratio were associated with larger θ_y and

Table 6—Maximum axial elongation, maximum axial load, and chord rotation at maximum axial load and elongation

	Δ_{max}				P_{max}						$P_{max}/(f_{c,test}'A_g)$			$\theta@P_{max}$, %	
	mm		in.		kN			kip							
Beam name	(+)	(–)	(+)	(–)	(+)	(–)	Average	(+)	(–)	Average	(+)	(–)	Average	(+)	(–)
C(#5)-3.0-0.69	3.1	2.8	0.12	0.11	269	249	259	60.5	56.0	58.2	0.096	0.088	0.092	3.0	3.0
C(#5)-3.0-0.35	4.6	4.6	0.18	0.18	202	202	202	45.4	45.4	45.4	0.072	0.072	0.072	3.0	3.0
D(#4)-3.0-0.69	11.0	11.3	0.43	0.44	965	992	979	216.9	223.0	220.1	0.346	0.352	0.349	8.4	8.0
D(#4)-3.0-1.39	5.5	7.4	0.22	0.29	961	1294	1128	216.0	290.9	253.6	0.342	0.462	0.402	10.0	4.0
D(#6)-3.0-0.69	3.1	16.2	0.12	0.64	271	1419	845	60.9	319.0	190.0	0.096	0.506	0.301	9.8	8.8
D(#6)-3.0-1.39	5.6	5.4	0.22	0.21	939	988	961	211.1	222.1	216.0	0.333	0.351	0.342	8.0	8.0
D(#6)-1.5-0.69	7.7	6.8	0.30	0.27	672	596	632	151.1	134.0	142.1	0.274	0.244	0.259	8.3	7.2

Table 7—Parameters determined from backbone modeling

	$(EI)_{eff}/(E_cI_g)$			θ_y, %			Predicted yield force						Post-yield stiffness/ effective stiffness		
							kN			kip					
Beam name	(+)	(–)	Average	(+)	(–)	Average	(+)	(–)	Average	(+)	(–)	Average	(+)	(–)	Average
C(#5)-3.0-0.69	0.048	0.051	0.0495	1.2	1.2	1.20	171	191	181	38.4	42.9	40.7	0.365	0.181	0.273
C(#5)-3.0-0.35	0.118	0.092	0.105	0.6	0.7	0.65	218	201	209.5	49.0	45.2	47.1	0.119	0.217	0.168
D(#4)-3.0-0.69	0.076	0.072	0.074	1.3	1.2	1.25	310	268	289	69.7	60.2	65.0	0.066	0.095	0.081
D(#4)-3.0-1.39	0.067	0.072	0.0695	1.2	1.4	1.30	248	311	279.5	55.8	69.9	62.8	0.092	0.147	0.120
D(#6)-3.0-0.69	0.084	0.086	0.085	1.6	1.7	1.65	417	461	439	93.7	103.6	98.7	0.054	0.084	0.069
D(#6)-3.0-1.39	0.111	0.083	0.097	1.3	1.8	1.55	434	453	443.5	97.6	101.8	99.7	0.070	0.089	0.80
D(#6)-1.5-0.69	0.029	0.051	0.04	1.3	1.3	1.30	839	722	780.5	188.6	162.3	175.5	0.045	0.079	0.062

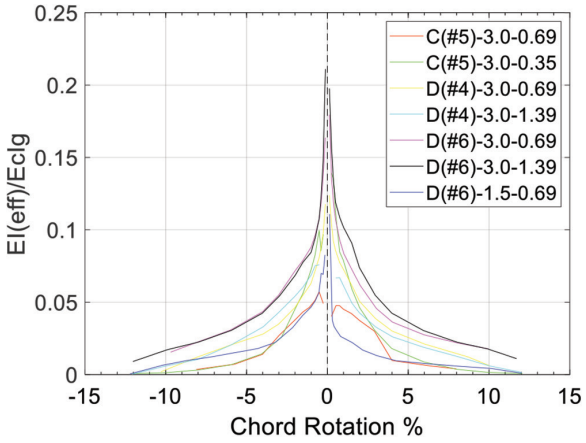

Fig. 12—Effective secant stiffness.

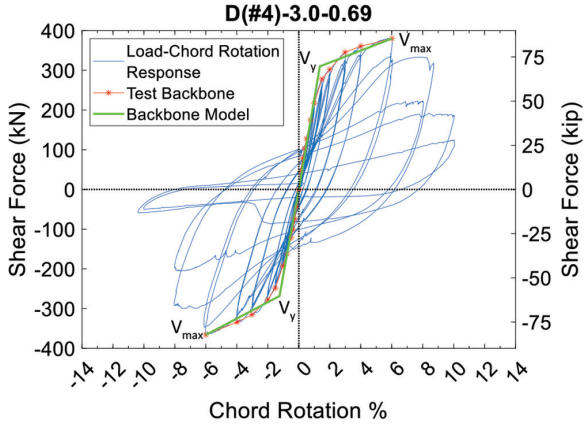

Fig. 13—Sample of bilinear backbone model fit to data.

larger $(EI)_{eff}/(E_cI_g)$. θ_y for all of the beams except C(#5)-3.0-0.35 was more than 1.0%, while Naish et al. (2013b) reported values at roughly 1.0% for the beams without axial restraint tested in that study. Axial restraint likely contributed to the increase in θ_y. $(EI)_{eff}/(E_cI_g)$ of D(#6)-3.0-1.39 was larger than D(#6)-3.0-0.69, as expected due to the higher level of axial restraint, while $(EI)_{eff}/(E_cI_g)$ of D(#4)-3.0-1.39 was slightly less than D(#6)-3.0-0.69.

SUMMARY AND CONCLUSIONS

Seven one-half-scale reinforced concrete coupling beams were designed, constructed, and tested to failure under constant stiffness axial restraint and fully reversed-cyclic lateral loading. The beams were designed to comply with ACI 318-19 provisions. Test variables were reinforcement configuration (longitudinal or diagonal), span-depth ratio, primary reinforcement bar size and reinforcement ratio, ratio of transverse reinforcement spacing to primary reinforcement bar diameter (s/d_b), and axial stiffness. The test beams included three pairs of nominally identical beams tested under varying levels of constant stiffness axial restraint. One of the pairs was conventionally reinforced, while the other two were diagonally reinforced. The following conclusions were reached:

- The two conventionally reinforced beams reached peak strength at 2.0 and 3.0% chord rotation and experienced rapid post-peak strength degradation with opening of diagonal cracks and the formation of splitting cracks along longitudinal reinforcement. The deformation capacity of these beams was less than that of flexure-yielding conventionally reinforced beams from other studies.
- Strength degradation in the diagonally reinforced beams was associated with buckling and fracture of diagonal reinforcement. For beams with an aspect ratio of 3.0, damage concentrated at the ends of the beam, while, for the beam with an aspect ratio of 1.5, the damage spread over the length of the beam. The chord rotation at the onset of bar buckling was more sensitive to changes in reinforcement ratio and s/d_b than the level of axial restraint. The beams with 12.7 mm (0.5 in.) diameter (No. 4) diagonal reinforcement had s/d_b of 5.0 and longitudinal reinforcement ratio of 0.0071, and buckling initiated at 6.0% chord rotation. In comparison, the beams with 19.1 mm (0.75 in.) diameter (No. 6) diagonal reinforcement had s/d_b of 3.33 and longitudinal reinforcement ratio of 0.0158, and buckling initiated at 10.0% chord rotation. The longitudinal reinforcement ratio was determined as the product of the area of steel in one bundle of diagonal reinforcement and the angle of the bar inclination relative to the longitudinal.
- Axial elongation was nearly proportional to chord rotation until significant damage was observed, at which stage the axial elongation decreased. Advanced levels of deformation and damage resulted in axial shortening, resulting in the application of axial tension. The diagonally reinforced beams developed high levels of axial compressive stress, with peak values ranging from $0.35P_{max}/f_{c,test}'A_g$ to $0.51P_{max}/f_{c,test}'A_g$ for a span-depth ratio of 3.0, and a peak value of $0.27P_{max}/f_{c,test}'A_g$ for the beam with a span-depth ratio of 1.5, where P_{max} is the maximum axial load measured in the test, $f_{c,test}'$ is the tested strength of concrete, and A_g is the gross concrete area of the cross section. Axial elongation increased with an increase in span-depth ratio and longitudinal reinforcement ratio. The conventionally reinforced beams experienced less axial elongation than the diagonally reinforced beams, as strength degradation in the conventionally reinforced beams was associated with opening of shear cracks rather than damage patterns characteristic of flexural failure.
- The equation for nominal shear strength, V_n, of diagonally reinforced concrete coupling beams provided by ACI 318-19 is based on the contribution of diagonal reinforcement to shear strength. The peak shear forces recorded for the diagonally reinforced beams were greater than V_n computed using the ACI 318-19 equation by factors ranging from 1.56 to 2.40. The ACI 318-19 equation is consistent with strut-and-tie behavior that considers only the diagonal reinforcement and does not consider the influence of axial restraint. The influence of axial restraint was included in the formulation of Eq. (3) and (4). In Eq. (4), the computation of nominal moment at the ends of the beam was used to determine the location of the resultant compression and tension forces in the strut-and-tie model. This brings the strut-and-tie model into agreement with the calculation of nominal moment, such that the nominal shear strength becomes equal to the shear at nominal moment strength. When using Eq. (4), with axial load taken as the measured value at peak measured shear strength, the resulting ratios of average peak measured shear strength in the positive and negative loading directions to computed nominal shear strength were 1.16 to 1.33. V_n in ACI 318-19 is limited to $0.83\sqrt{f_c'}A_{cw}$ MPa ($10\sqrt{f_c'}A_{cw}$ psi). The maximum measured shear for the diagonally reinforced beams with No. 6 bars exceeded this limit, with measured peak shear forces reaching more than twice this limit for the beam with a span-depth ratio of 1.5. As such, this limit was excluded from Eq. (3) and (4).
- When modeling flexibility as being solely due to flexure, the diagonally reinforced beams generally had larger effective flexural rigidity values than the conventionally reinforced beams, with a larger reinforcement ratio corresponding to a larger effective secant flexural rigidity for the diagonally reinforced beams. Based on backbone models formulated for the test beams, the yield rotation for the conventionally reinforced beams increased with an increase in axial compression. For the diagonally reinforced beams, the beams with larger bar size had greater yield rotation and effective flexural rigidity, while the effect of axial restraint was minimal.
- For the diagonally reinforced beams tested in this study, constant axial compressive stiffness ranging from $0.027A_gf_c'$ to $0.055A_gf_c'$ mm ($0.69A_gf_c'$ to $1.39A_gf_c'$ in.) led to peak compressive stresses of 0.27 to $0.51P_{max}/f_c'A_g$. ACI 318-19 does not explicitly recommend strength design for coupled walls. It is recommended that an upper bound for coupling beam strength be used to determine wall demands. If the probable moment strength of a coupling beam was computed in the same manner as a special moment frame beam (that is, using $1.25f_y$), additional strength may be created by axial restraint. Although further research is needed to better characterize the level of overstrength from axial restraint, results from this study provide experimentally derived values for the levels of axial demand considered. Additional research is also needed to characterize typical levels of axial restraint for coupling beams.

AUTHOR BIOS

Baha'a Al-Khateeb *is a PhD Student in the Department of Civil and Environmental Engineering and Earth Sciences at the University of Notre Dame, Notre Dame, IN. He received his BS from The University of Jordan, Amman, Jordan, and his MS from Washington State University, Pullman, WA. His research interests include the behavior and design of reinforced concrete structures subjected to seismic demands.*

ACI member **Christopher J. Motter** *is an Assistant Professor in the Department of Civil and Environmental Engineering at Washington State University. He received his BS and MS from The Pennsylvania State University, University Park, PA, and his PhD from the University of California, Los Angeles, Los Angeles, CA. He is Secretary of ACI Committee 374, Performance-Based Seismic Design of Concrete Buildings, and a member*

of ACI Subcommittee 318-1W, Wind Provisions. His research interests include the behavior and design of reinforced concrete structures subjected to seismic and wind demands.

ACKNOWLEDGMENTS

This research was supported by funding from the ACI Foundation. The authors express their gratitude to the ACI Foundation. Any opinions, findings, and conclusions expressed in this material are those of the authors and do not necessarily reflect those of the ACI Foundation. Thanks are extended to S. Lewis, J. Jennings, D. Dolan, K. Maloney, S. McGuiness, A. Hill, J. Forbes, J. Hatt, M. Jarrah, A. Islam, M. Wagemann Herrera, C. Moen, J. Divelbiss, R. Dombrowski, T. Walters, and Z. Kylany for assistance with laboratory testing. The authors would like to thank four anonymous reviewers for providing insightful comments on earlier versions of the manuscript that have led to the improvement of the manuscript.

REFERENCES

ACI Committee 318, 2008, "Building Code Requirements for Structural Concrete (ACI 318-08) and Commentary (ACI 318R-08)," American Concrete Institute, Farmington Hills, MI, 473 pp.

ACI Committee 318, 2014, "Building Code Requirements for Structural Concrete (ACI 318-14) and Commentary (ACI 318R-14)," American Concrete Institute, Farmington Hills, MI, 520 pp.

ACI Committee 318, 2019, "Building Code Requirements for Structural Concrete (ACI 318-19) and Commentary (ACI 318R-19) (Reapproved 2022)," American Concrete Institute, Farmington Hills, MI, 624 pp.

Ameen, S.; Lequesne, R. D.; Lepage, A.; Weber-Kamin, A.; and Huq, S., 2017, "Behavior Of Diagonally-Reinforced Concrete Coupling Beams With High-Strength Steel Bars," 16th World Conference on Earthquake Engineering, Santiago, Chile, 2017.

ANSI/AISC 341-22, 2022, "Seismic Provisions for Structural Steel Buildings," American Institute of Steel Construction, Chicago, IL, 546 pp.

ASCE/SEI 41-13, 2014, "Seismic Evaluation and Retrofit of Existing Buildings," American Society of Civil Engineers, Reston, VA, 554 pp.

Barbachyn, S. M.; Kurama, Y. C.; and Novak, L. C., 2012, "Analytical Evaluation of Diagonally Reinforced Concrete Coupling Beams under Lateral Loads," *ACI Structural Journal*, V. 109, No. 4, July-Aug., pp. 497-507.

Breña, S. F., and Ihtiyar, O., 2011, "Performance of Conventionally Reinforced Coupling Beams Subjected to Cyclic Loading," *Journal of Structural Engineering*, ASCE, V. 137, No. 6, June, pp. 665-676. doi: 10.1061/(ASCE)ST.1943-541X.0000316

Canterbury Earthquakes Royal Commission, 2012, Final Report Volumes 1-7, New Zealand Government, Christchurch, New Zealand. doi: 978-0-478-39558-7

CSA A23.3-94 (R2000), 1994, "Design of Concrete Structures (Reaffirmed in 2000)," CSA Group, Toronto, ON, Canada, 199 pp.

CSA A23.3-14, 2014, "Design of Concrete Structures," CSA Group, Toronto, ON, Canada, 297 pp.

Fisher, A. W.; Bentz, E. C.; and Collins, M. P., 2017, "Response of Heavily Reinforced High-Strength Concrete Coupling Beams," *ACI Structural Journal*, V. 114, No. 6, Nov.-Dec., pp. 1483-1494. doi: 10.14359/51689501

Galano, L., and Vignoli, A., 2000, "Seismic Behavior of Short Coupling Beams with Different Reinforcement Layouts," *ACI Structural Journal*, V. 97, No. 6, Nov.-Dec., pp. 876-885.

Gonzalez, E., 2001, "Seismic Response of Diagonally Reinforced Slender Coupling Beams," master's thesis, The University of British Columbia, Vancouver, BC, Canada, 164 pp.

ICC, 2006, "2006 IBC Structural/Seismic Design Manual," Structural Engineers Association of California, Sacramento, CA, and International Code Council, V. 3, Washington, DC.

KCI, 2012, "Korea Structural Concrete Design Code and Commentary," Korea Concrete Institute, Seoul, South Korea. (in Korean)

Malcolm, R. C., 2015, "Seismic Performance of Reinforced Concrete Coupled Walls," master's thesis, University of Auckland, Auckland, New Zealand, 181 pp.

Mazzoni, S.; McKenna, F.; and Fenves, G., 2009, "Open System for Earthquake Engineering Simulation (OpenSees)," Version 2.1.0, Pacific Earthquake Engineering Research Center, University of California, Berkeley, Berkeley, CA.

Mohr, D. S., 2007, "Nonlinear Analysis and Performance Based Design Methods for Reinforced Concrete Coupled Shear Walls," master's thesis, University of Washington, Seattle, WA, 255 pp.

Naish, D.; Fry, A.; Klemencic, R.; and Wallace, J., 2013a, "Reinforced Concrete Coupling Beams—Part I: Testing," *ACI Structural Journal*, V. 110, No. 6, Nov.-Dec., pp. 1057-1066.

Naish, D.; Fry, A.; Klemencic, R.; and Wallace, J., 2013b, "Reinforced Concrete Coupling Beams—Part II: Modeling," *ACI Structural Journal*, V. 110, No. 6, Nov.-Dec., pp. 1067-1075.

NZS 3101.1&2:2006, 2006, "Concrete Structures Standard," Standards New Zealand, Wellington, New Zealand, 754 pp.

Park, J.; Strepelias, E.; Stathas, N.; Kwon, O.-S.; and Bousias, S., 2021, "Application of Hybrid Simulation Method for Seismic Performance Evaluation of RC Coupling Beams Subjected to Realistic Boundary Condition," *Earthquake Engineering & Structural Dynamics*, V. 50, No. 2, Feb., pp. 375-393. doi: 10.1002/eqe.3335

PEER TBI, 2017, "Guidelines for Performance-Based Seismic Design of Tall Buildings," PEER Report No. 2017/06, Tall Buildings Initiative, Pacific Earthquake Engineering Research Center, University of California, Berkeley, Berkeley, CA, 147 pp.

Poudel, A.; Lequesne, R. D.; and Lepage, A., 2018, "Diagonally Reinforced Concrete Coupling Beams: Effects of Axial Restraint," SL Report 18-3, The University of Kansas Center for Research, Inc., Lawrence, KS, 48 pp.

Rodriguez, M. E.; Botero, J. C.; and Villa, J., 1999, "Cyclic Stress-Strain Behavior of Reinforcing Steel Including Effect of Buckling," *Journal of Structural Engineering*, ASCE, V. 125, No. 6, June, pp. 605-612. doi: 10.1061/(ASCE)0733-9445(1999)125:6(605)

Seo, S.-Y.; Yun, H.-D.; and Chun, Y.-S., 2017, "Hysteretic Behavior of Conventionally Reinforced Concrete Coupling Beams in Reinforced Concrete Coupled Shear Wall," *International Journal of Concrete Structures and Materials*, V. 11, No. 4, Dec., pp. 599-616. doi: 10.1007/s40069-017-0221-8

Setkit, M., 2012, "Seismic Behavior of Slender Coupling Beams Constructed with High-Performance Fiber-Reinforced Concrete," PhD dissertation, University of Michigan, Ann Arbor, MI, 261 pp.

Tegos, I. A., and Penelis, G. G., 1988, "Seismic Resistance of Short Columns and Coupling Beams Reinforced with Inclined Bars," *ACI Structural Journal*, V. 85, No. 1, Jan.-Feb., pp. 82-88.

VecTor Analysis Group, 2006, "VecTor2 - Finite Element Analysis of Reinforced Concrete," Version 2.3.

VecTor Analysis Group, 2011, "VecTor2 - Finite Element Analysis of Reinforced Concrete." Version 3.5.

Xiao, Y.; Esmaeily-Ghasemabadi, A.; and Wu, H., 1999, "High-Strength Concrete Short Beams Subjected to Cyclic Shear," *ACI Structural Journal*, V. 96, No. 3, May-June, pp. 392-400.

ACI in Your Classroom

Integrate ACI into your classroom!

To support future leaders, ACI has launched several initiatives to engage students in the Institute's activities and programs – select programs that may be of interest to Educators are:

- **Free student membership –** encourage students to sign up
- **Special student discounts on *ACI 318 Building Code Requirements for Structural Concrete*, *ACI 530 Building Code Requirements and Specification for Masonry Structure*, & *Formwork for Concrete* manual.**
- **Access to *Concrete International* –** free to all ACI student members
- **Access to *ACI Structural Journal* and *ACI Materials Journal* –** free to all ACI student members
- **Free sustainability resources –** free copies of Sustainable Concrete Guides provided to universities for use in the classroom
- **Student competitions –** participate in ACI's written and/or team-based competitions
- **Scholarships and fellowships –** students who win awards are provided up to $15,000 and may be offered internships and paid travel to attend ACI's conventions
- **ACI Award for University Student Activities –** receive local and international recognition for your University's participation in concrete-related activities
- **Free access to the *ACI Collection of Concrete Codes, Specifications, and Practices* –** in conjunction with ACI's chapters, students are provided free access to the online ACI Collection
- **ACI online recorded web sessions and continuing education programs –** online learning tools ideal for use as quizzes or in-class study material

https://www.concrete.org/educatorsandresearchers/aciinyourclassroom.aspx

ACI STRUCTURAL JOURNAL TECHNICAL PAPER

Title No. 122-S04

Deep-Learning-Informed Design Scheme for Prediction of Interfacial Concrete Shear Strength

by Tarutal Ghosh Mondal, Nikkolas Edgmond, Lesley H. Sneed, and Genda Chen

Current design provisions pertaining to the shear transfer strength of concrete-to-concrete interfaces, including those of the AASHTO LRFD design specifications and ACI 318 Code, are based on limited physical test data from studies conducted decades ago. Since the development of these design provisions, many studies have been conducted to investigate additional parameters. In addition, modern concrete technology has expanded the range of materials available and often includes the use of high-strength concrete and high-strength reinforcing steel. Recent studies examined the applicability of current shear-friction design approaches to interfaces that comprise high-strength concrete and/or high-strength steel and identified a need for revision to the existing provisions. To this end, this study leveraged a comprehensive database of test results collected from the literature to propose a deep-learning-based predictive model for normalweight concrete-to-concrete interfacial shear strength. Additionally, a new computation scheme is proposed to estimate the nominal shear strength with a higher prediction accuracy than the existing AASHTO LRFD and ACI 318 design provisions.

Keywords: deep learning; interfacial shear strength; learning-informed design; neural additive models; neural network; reinforced concrete; shear friction.

INTRODUCTION

The shear-friction design concept is applicable in conditions where direct shear must be transferred across a structural concrete plane or interface, such as an existing crack or an interface between dissimilar materials or concretes cast at different times (that is, construction or cold joint). Shear-friction provisions are commonly used in the design of reinforced and precast-prestressed concrete elements/connections, including corbels, dapped double-tees, beam bearings, and diaphragms. These types of connections are critical because there is little or no redundancy, which makes them critical to the safety of the structure.

The existing shear-friction design provisions are largely empirical and are based on physical test data. In fact, the AASHTO LRFD Bridge Design Specifications[1] and ACI 318 Building Code Requirements for Structural Concrete[2] use different approaches to compute the shear transfer strength resulting in different shear-friction equations and maximum design values. The data used to develop these provisions are predominantly from experiments conducted decades ago. However, modern concrete construction has expanded the range of construction materials available, and recent studies on shear friction have included tests on advanced materials such as high-strength concrete,[3] high-performance concrete,[4,5] lightweight concrete,[6] and high-strength reinforcing steel.[7] Thus, the applicability of the design provisions to interfaces with high-strength concrete and/or high-strength reinforcing steel is worth investigating, especially as these materials become increasingly common in modern bridge and building structures.

Edgmond and Sneed[8] assembled a comprehensive database of shear-friction test results, enabling an in-depth statistical analysis to evaluate different shear-friction design provisions. The authors identified a critical need for revision to current design provisions to ensure safe and cost-effective designs. In this context, the present study proposes a deep-learning-based regression model to predict the interfacial shear strength in reinforced concrete. Deep learning has been used in the past to predict the compressive strength,[9,10] shear strength,[11,12] and elastic modulus[13] of concrete. However, it has not been used to predict the interfacial shear strength at normalweight concrete-to-concrete interfaces. This study aims to fill this information gap by investigating multilayer perceptron (MLP) and one-dimensional (1-D) convolutional neural network (1D-CNN)-based deep-learning models to predict the interfacial shear strength in reinforced concrete based on 12 input parameters. The proposed techniques were validated on an extensive database collected from literature spanning over five decades and were observed to outperform the existing design methods that rely on linear expressions as well as the traditional polynomial regression models. This study also went a step further and reduced the dimension of the parameter space from 12 to six by an iterative selection, elimination, and grouping of the original parameters. This was instrumental in developing a new learning-informed design (LID) scheme based on a state-of-the-art neural additive modeling approach[14] that was found to be more accurate than the existing AASHTO LRFD and ACI 318 design provisions. The proposed LID scheme is based on parameter-specific interpretable shape functions that conform with the physical understanding of shear-friction behavior at normalweight concrete-to-concrete interfaces. Therefore, it is believed that the findings of this work will help engender the long-sought changes in the current design provisions leading to a more safe and economical design of reinforced concrete structures.

ACI Structural Journal, V. 122, No. 1, January 2025.

MS No. S-2022-377.R3, doi: 10.14359/51743291, received March 20, 2024, and reviewed under Institute publication policies.

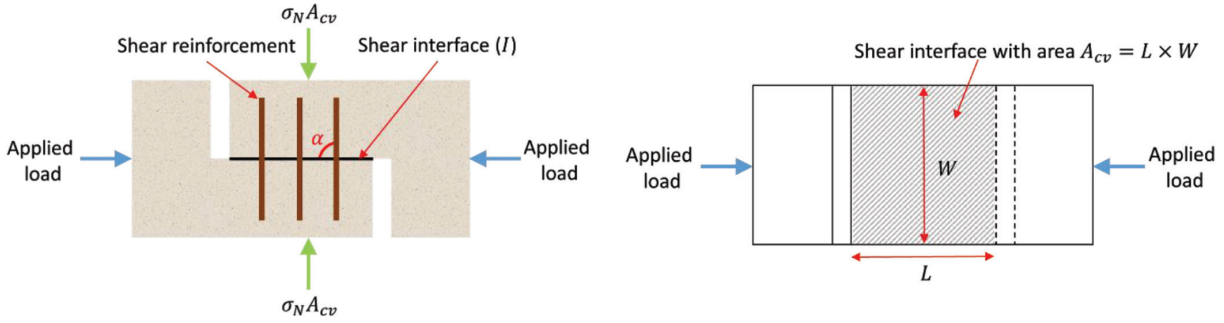

Fig. 1—Illustrative sketch of typical shear-friction test.

Table 1—Coefficients of friction μ for normalweight concrete interfaces as prescribed by ACI 318[2]

Contact surface condition	Coefficient of friction μ
Concrete placed monolithically	1.4
Concrete placed against hardened concrete that is clean, free of laitance, and intentionally roughened to a full amplitude of approximately 6 mm (1/4 in.)	1.0
Concrete placed against hardened concrete that is clean, free of laitance, and not intentionally roughened	0.6

RESEARCH SIGNIFICANCE

Design of interfaces between concrete members or parts of members that can slip relative to one another is commonly based on the shear-friction model. Shear-friction model parameters and other design limits (for example, upper limit on shear strength) have been determined by fitting test data. Advances in concrete technology have expanded the range of materials available, prompting reexamination of current shear-friction design provisions. The present study uses a deep-learning-based regression model to provide insight into the nature of parameters that influence the shear transfer strength. A new learning informed design scheme developed to predict the shear strength is more accurate than existing provisions.

EXISTING DESIGN EQUATIONS

The deep-learning techniques proposed in this study are benchmarked against the current AASHTO LRFD[1] and ACI 318[2] design provisions. The ACI 318 Code provides a shear-friction model that is based on a linear relationship between interfacial normal forces and shear strength that neglects the contribution of concrete cohesion. The ACI 318 Code equation for determining the nominal shear strength V_n of a given interface can be written in terms of nominal shear stress v_n as

$$v_n = \rho f_y(\mu \sin\alpha + \cos\alpha) + \mu\sigma_N \quad (1)$$

where v_n is V_n divided by the area of the interface. α is the acute angle between the shear-friction reinforcement and the shear interface (Fig. 1). The model does not apply if α is greater than 90 degrees. ρ is the ratio of area of shear-friction reinforcement crossing the shear plane to the area of the interface engaged in shear transfer. f_y is the yield strength

Table 2—Maximum v_n across shear plane as prescribed by ACI 318[2]

Condition	Maximum v_n, MPa (ksi)
Normalweight concrete placed monolithically or placed against hardened concrete intentionally roughened to full amplitude of approximately 6 mm (1/4 in.)	least of $\begin{cases} 0.2f_c' \\ 3.3(480) + 0.08f_c' \\ 11(1600) \end{cases}$
Other cases	least of $\begin{cases} 0.2f_c' \\ 5.5(800) \end{cases}$

Note: f_c' is compressive strength of monolithically cast concretes engaged in shear friction. If concretes on two sides of shear interface have different strengths, then lesser value of f_c' should be considered.

of shear-friction reinforcement (not to exceed 420 MPa [60 ksi]). μ is the coefficient of interfacial friction, as enumerated in Table 1. σ_N is the compressive normal stress applied to the shear interface, if present (σ_N is taken as positive for compression). In the case of net tension applied to the interface, a part of the reinforcement crossing the shear plane is used in resisting tension and provides no contribution to the shear strength. The residual reinforcement is considered for shear strength estimation as per Eq. (1) with σ_N taken as zero. The shear strength (v_n) is subject to the maximum limits prescribed by ACI 318 based on the condition of the concrete surface and the compressive strength of concrete f_c' (Table 2). If the concretes on two sides of the shear interface have different strengths, then the lesser value of f_c' should be considered.

Similar to the ACI 318 approach, the AASHTO LRFD model is also based on the linear relationship between interfacial normal forces and shear strength, but it considers an additional component of cohesion, as shown in the following equation written in terms of shear stress

$$v_n = c + \mu(\rho f_y + \sigma_N) \quad (2)$$

subject to the maximum limit of

$$v_{n,max} = \min\{K_1 f_c', K_2\} \quad (3)$$

where c is the cohesion factor; and K_1 and K_2 are friction factors dictated by the interface condition (Table 3). For brackets, corbels, and ledges, c should be taken as zero because the effectiveness of cohesion and aggregate interlock along a vertical crack interface is unreliable. Similar to

ACI 318, if the concretes on two sides of the shear interface have different strengths, then the lesser value of f_c' should be considered. It should be noted here that AASHTO LRFD does not specify how to deal with inclined reinforcement. However, the earlier equation can be extended for the case of inclined reinforcement based on the physical model enunciated in ACI 318. The treatment of the net tension case is identical with the requirements of ACI 318.

To evaluate the performance of these design provisions, the database of test results collected by Edgmond and Sneed[8] was examined. It should be mentioned in this context that a number of specimens in the original database were subjected to eccentric loading leading to combined bending and shear. The dataset also contained composite beam specimens tested under three- and four-point bending configurations. Such loading conditions were beyond the scope of the present study and were therefore eliminated from the revised data set. Additionally, the database comprised a number of specimens with inclined interfaces. These specimens were also not included in this study. The resulting data set contained 639 test results.

The shear strength values calculated by the design provisions are plotted against the test data in Fig. 2 and 3. Load and strength reduction factors are taken as 1.0. It should be noted here that the strength of concrete and reinforcing steel has increased over the years, extending beyond the experimental results on which the design equations were based. The current design specifications get around this by limiting the maximum steel yield strength and maximum nominal shear strength as a way to keep the design within the parameters of the empirical formulas. Therefore, the shear strength values calculated by disregarding the design limits are also plotted in the same figures for comparative evaluations. It was observed that the values calculated by AASHTO LRFD (coefficient of determination $R^2 = 0.62$) are more accurate than those by ACI 318 ($R^2 = 0.35$) when the design limits are employed. Also, the ACI 318 values tend to be more conservative (that is, test value larger than calculated value). These observations can be partly attributed to the fact that the AASHTO LRFD design provision takes into account the contribution of concrete cohesion, which ACI 318 neglects. As a consequence of this, ACI 318 predicts zero shear strength for specimens with no shear reinforcement, which is at odds with the experimental observations. The elimination of design limits increased the calculated strength of specimens made of high-strength materials. This is more prominent for specimens with high-strength steel reinforcement, as evident in Fig. 2 and 3. It should be noted in this context that concrete having compressive strength greater than 60 MPa (9 ksi) is designated in this study as high-strength concrete. On the other hand, steel reinforcement having yield strength greater than 420 MPa (60 ksi) is identified as high-strength steel. Withdrawal of the design limits resulted in an increase in accuracy for ACI 318 but a reduction in accuracy for AASHTO LRFD. For both provisions, it should be noted that removal of design limits resulted in a large number of calculated values that were overestimated (that is, unconservative) by a significant margin. Overall, AASHTO LRFD, along with the prescribed design limits, produced the most accurate results and is therefore considered in this study as a benchmark to assess the performance of the deep-learning techniques introduced later in this paper.

Table 3—Cohesion and friction factors for normalweight concrete interfaces as prescribed by AASHTO LRFD[1]

Description	c, MPa (ksi)	μ	K_1	K_2, MPa (ksi)
Concrete placed monolithically	2.8 (0.4)	1.4	0.25	10.3 (1.5)
Concrete placed against clean concrete surface, free of laitance with surface roughened to amplitude of 6 mm (1/4 in.)	1.9 (0.28)	1.0	0.3	12.4 (1.8)
Concrete placed against clean concrete surface, free of laitance, but not intentionally roughened	0.52 (0.075)	0.6	0.2	5.5 (0.8)

Note: For brackets, corbels, and ledges, c should be taken as zero.

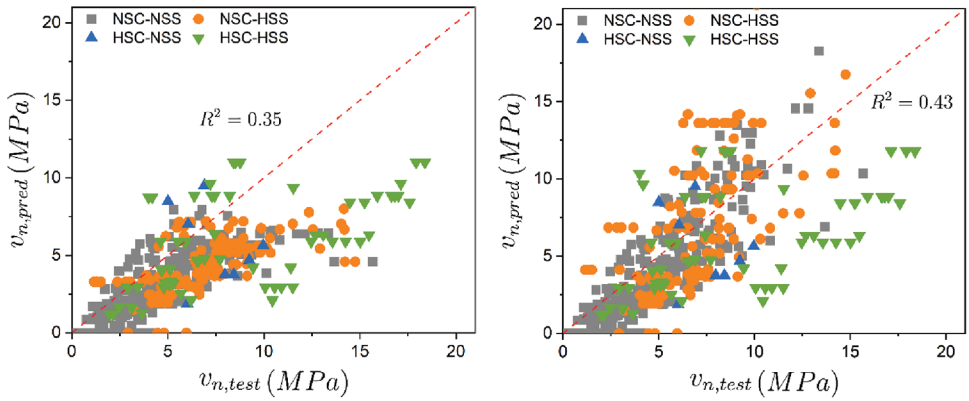

(a) With design limits **(b) Without design limits**

Fig. 2—Accuracy of ACI 318 shear-friction design provisions with and without prescribed design limits. $v_{n,test}$ *and* $v_{n,pred}$ *denote the experimental and predicted values of interfacial shear strength (in MPa), respectively. NSC, NSS, HSC, and HSS represent normal-strength concrete, normal-strength steel, high-strength concrete, and high-strength steel, respectively. Concrete having compressive strength greater than 60 MPa is designated herein as HSC. Steel reinforcement having yield strength greater than 420 MPa is identified as HSS. (Note: 1 MPa = 0.145 ksi.)*

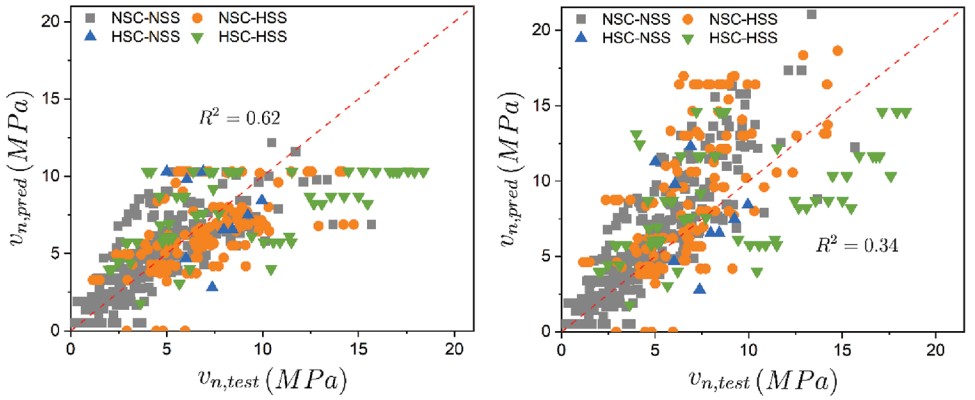

(a) With design limits **(b) Without design limits**

Fig. 3—Accuracy of AASHTO LRFD shear-friction design provisions with and without prescribed design limits. $v_{n,test}$ *and* $v_{n,pred}$ *denote the experimental and predicted values of interfacial shear strength (in MPa), respectively. NSC, NSS, HSC, and HSS represent normal-strength concrete, normal-strength steel, high-strength concrete, and high-strength steel, respectively. Concrete having compressive strength greater than 60 MPa is designated herein as HSC. Steel reinforcement having yield strength greater than 420 MPa is identified as HSS. (Note: 1 MPa = 0.145 ksi.)*

PROPOSED NEURAL NETWORK APPROACH

Prediction of interfacial shear strength

To predict the interfacial shear strength, this study examined two classes of deep-learning approaches—namely, MLP and 1D-CNN. An MLP is the simplest form of a neural network consisting of interconnected neurons organized in the form of input, hidden, and output layers.[15] Information flows from the input to the output layer in a feed-forward manner through the connections. The input layer takes in an input which is subsequently processed by the intermediate hidden layers through a series of linear and nonlinear operations. Finally, the prediction of the neural network is displayed in the output layer. The connections between nodes are characterized by weights that are learned through a supervised back-propagation training algorithm.[16] The input layer in the proposed MLP had 12 nodes corresponding to 12 input parameters, as shown in Table 4. It should be noted here that the interface type (I) was an ordinal variable assuming a value of 1, 2, or 3 for monolithic, intentionally roughened (herein referred to as "rough"), or not intentionally roughened (herein referred to as "smooth") surfaces, respectively. None of the design limits prescribed by the ACI 318 Code or the AASHTO LRFD design specifications were put into practice in any of the deep-learning-based approaches. It is also worth mentioning in this context that many of the parameters listed in Table 4 are disregarded by the existing design provisions. The number of nodes in the hidden layers are shown in Fig. 4. The output layer contained only one node, which corresponded to the interfacial shear strength.

A CNN, on the other hand, employs convolution operations to extract spatial features.[17] In this study, the 12 input parameters were arranged as a 1-D array and were passed through a series of convolution, batch normalization, and rectified linear unit (ReLU) layers (Fig. 5). The output from the last ReLU layer was flattened and was input to a fully connected layer to produce the final network output. In this study, the optimum network parameters were obtained by minimizing the mean squared error between the predicted and target interfacial shear strengths using an Adam-based optimizer.[18] The learning rate was set to 0.001, and a batch size of 16 was considered for training.

Table 4—List of parameters used as input to deep-learning models

Attribute	Symbol	Parameter
Interface	I	Interface type
	L	Length of shear plane
	W	Width of shear plane
Concrete	f_{c1}, f_{c2}	Experimental compressive strength of concrete on either side of shear plane
	f_{t1}, f_{t2}	Estimated tensile strength of concrete on either side of shear plane
Steel	α	Angle of inclination of shear-friction reinforcement relative to shear plane
	n_s	Number of reinforcing bar legs crossing shear interface
	d	Diameter of reinforcing bars crossing shear interface
	f_y	Yield strength of shear-friction reinforcement
Loading	σ_N	Normal stress applied to shear interface

To assess the performance of the proposed deep-learning techniques, three different evaluation metrics were considered in this study—namely, the coefficient of determination (R^2), mean absolute error (MAE), and root-mean-squared error (RMSE). R^2 is a measurement of goodness of fit. It is represented by a value ranging from 0 to 1. A value of 1.0 indicates a perfect fit and a highly reliable model, whereas a value of 0 implies that the model utterly fails to fit the data. On the other hand, MAE and RMSE are the two most common indicators used to measure the amount of error in model predictions. A larger value of the metrics means a higher error between the true and predicted values and vice versa.

Tenfold cross validation was conducted in this study to test the generalization ability of the trained models. At each

cross-validation round, 10% of the available data (64) were randomly chosen as the test set, and the remaining 90% of the data (575) were used to train the models. The performance indicators obtained from the cross-validation process are plotted in Fig. 6. The small squares inside the rectangular boxes represent mean values. The horizontal lines inside the boxes represent the median values. The upper and lower sides of the rectangular boxes denote one standard deviation on either side of the mean values, and the whiskers protruding out of the boxes represent the minimum and maximum values of the performance metrics. It was observed that the MLP (mean R^2: 0.89, mean MAE: 0.69 MPa [0.10 ksi], mean RMSE: 1.19 MPa [0.17 ksi]) outperformed the AASHTO LRFD design specifications (mean R^2: 0.62, mean MAE: 1.55 MPa [0.22 ksi], mean RMSE: 2.19 MPa [0.32 ksi]) with significantly large margins. The 1D-CNN exhibited an accuracy (mean R^2: 0.89, mean MAE: 0.67 MPa [0.10 ksi], mean RMSE: 1.20 MPa [0.17 ksi]) neck and neck with the MLP. However, the predictions of the MLP were more robust than the 1D-CNN, as indicated by the height of the corresponding rectangular boxes. Thus, the MLP is identified to be more suitable than the 1D-CNN-based approach and is considered for all subsequent analyses. The inclusion of a broader range of parameters and the inherent ability of deep-learning-based techniques to model nonlinear relations can be credited for the overall superiority of these methods compared to the existing provisions that were developed based on the evaluation of discrete sets of test data.

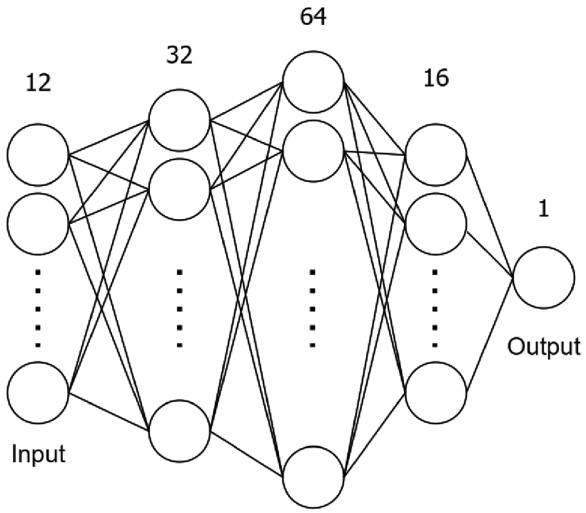

Fig. 4—Network architecture of MLP used for prediction of interfacial shear strength. Number above each layer denotes number of neurons in that layer.

Reduction of parameter space

Despite the proven advantage, deep-learning-based prediction models, unfortunately, have very few takers among structural engineers and designers. Therefore, it is improbable that these advanced modeling techniques will replace the prevailing design provisions anytime soon. Therefore, this study seeks to propose a new design scheme by striking a delicate balance between the accuracy of deep-learning models and the intuitive simplicity and physical understanding of the existing design models. As a stepping stone towards that objective, this section aims to reduce the dimension of the parameter space, which will be instrumental in enhancing the model simplicity. Subsequent to this, a recent advancement in deep learning is leveraged in the following section to propose a simple computation scheme as a more accurate alternative to the existing design provisions.

Backed by the physical understanding of the underlying principles, this study achieved a reduced parameter set by the iterative selection, elimination, and aggregation from the original list of parameters. At the end of the process, six key parameters are produced, indicating a 50% reduction in the parameter space dimension

$$x_1 = I \tag{4}$$

$$x_2 = LW \tag{5}$$

$$x_3 = \sqrt{\min(f_{c1}, f_{c2})} \tag{6}$$

$$x_4 = \frac{\pi d^2 n_s}{4LW} f_y \tag{7}$$

$$x_5 = \alpha \tag{8}$$

$$x_5 = \sigma_N \tag{9}$$

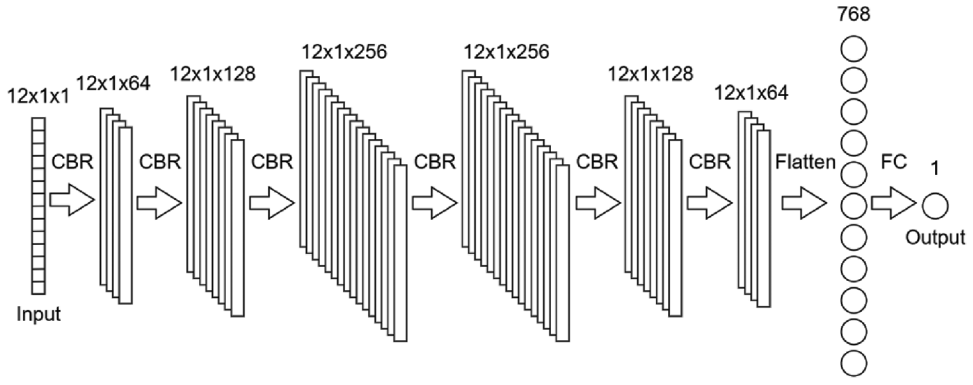

Fig. 5—Architecture of 1D-CNN used in this study for prediction of interfacial shear strength. CBR represents a sequence of 1-D convolution, batch normalization, and ReLU operations. FC denotes fully connected layer. Feature size at each layer is expressed as triad in H x W x C format, where H, W, and C denote height, width, and number of channels, respectively.

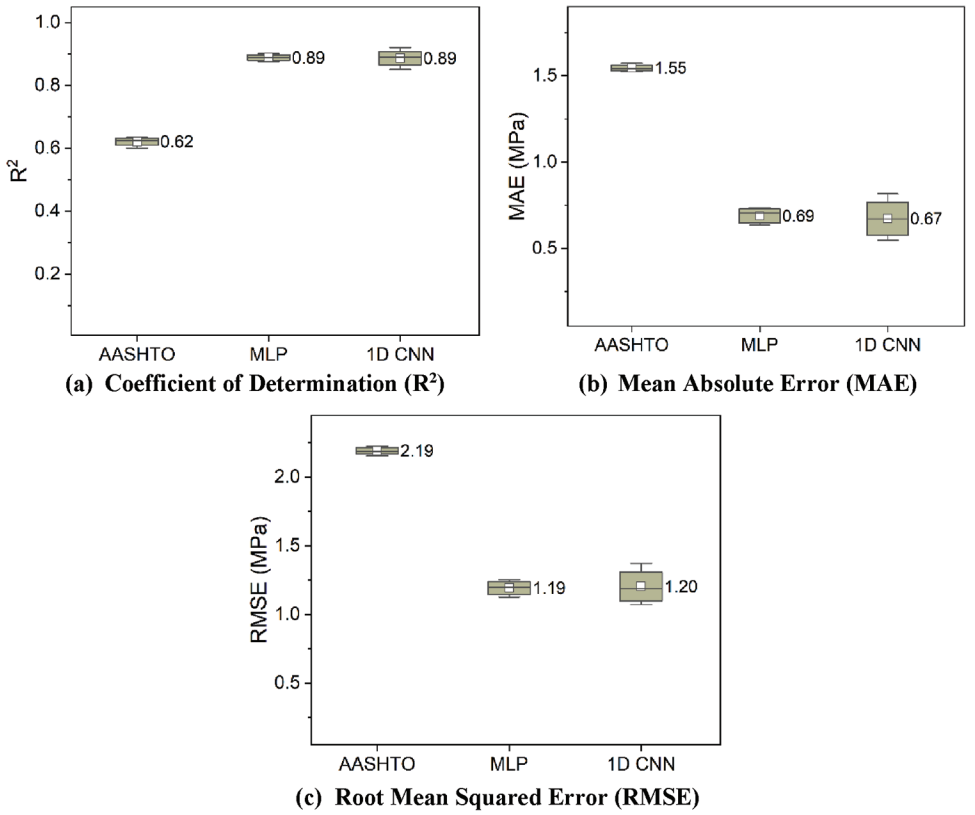

Fig. 6—Performance of proposed deep-learning approaches compared to AASHTO LFRD design provisions. (Note: 1 MPa = 0.145 ksi.)

It was observed that the reduction in the number of parameters slightly reduced the prediction accuracy of the MLP (Fig. 7). It produced a mean R^2 of 0.85, mean MAE of 0.83 MPa (0.12 ksi), and mean RMSE of 1.33 MPa (0.19 ksi), indicating a slight reduction in performance compared to the original 12-parameter model (mean R^2: 0.89, mean MAE: 0.69 MPa [0.10 ksi], mean RMSE: 1.19 MPa [0.17 ksi]).

Further, this study tested the efficacy of an ordinary polynomial regression model, which was based on a feature space that comprised all polynomial combinations of the parameters with degree less than or equal to a specified degree. The highest specified degree of the polynomial features was varied sequentially, and quadratic features were observed to produce the most accurate predictions (mean R^2: 0.74, mean MAE: 1.06 MPa [0.15 ksi], mean RMSE: 1.74 MPa [0.25 ksi]). Although the quadratic regression model considerably outperformed the design equation provided by the AASHTO LRFD specification (mean R^2: 0.62, mean MAE: 1.55 MPa [0.22 ksi], mean RMSE: 2.19 MPa [0.32 ksi]), it still did not perform as well as the MLP-based algorithm. This confirms the point that the traditional regression models are no match for the latest deep-learning-based techniques, particularly when accuracy is a key objective. On the whole, this signifies an important breakthrough that sets the stage for developing a new design scheme, as presented in the following section.

New LID scheme

This section is dedicated to the development of a new LID scheme that is more accurate and straightforward at the same time. To this end, this study leveraged a recent development in deep learning called neural additive models.[14] This additive modeling approach jointly trains a set of neural networks that attend to a single input parameter (Fig. 8). This study used six MLP blocks to handle the six input parameters identified in the previous section. The MLP blocks, apart from the input and output layers, contained three intermediate layers, comprising 16 neurons each. The MLP blocks can learn arbitrary complex shape functions, a combination of which produce the final model outputs, as shown in the following equation

$$y = \beta + \phi(s) \tag{10}$$

where

$$s = \sum_{i=1}^{6} f_i(\bar{x}_i) \tag{11}$$

$$\begin{aligned}\phi(s) &= \xi s + \frac{1-\xi}{\bar{y}^2}s^3,\ \xi \in [0,1] \\ &= \frac{-\xi}{\bar{y}^4}s^5 + \frac{1+\xi}{\bar{y}^2}s^3,\ \xi \in [-1,0]\end{aligned} \tag{12}$$

$\bar{x}_1, \bar{x}_2, \ldots, \bar{x}_6$ are normalized parameters given by

$$\bar{x}_i = \frac{x_i - x_{i,min}}{x_{i,max} - x_{i,min}} \tag{13}$$

$x_{i,max}$ and $x_{i,min}$ are the maximum and minimum values for the i-th parameter as enumerated in Table 5. $\bar{y}$ is the mean value

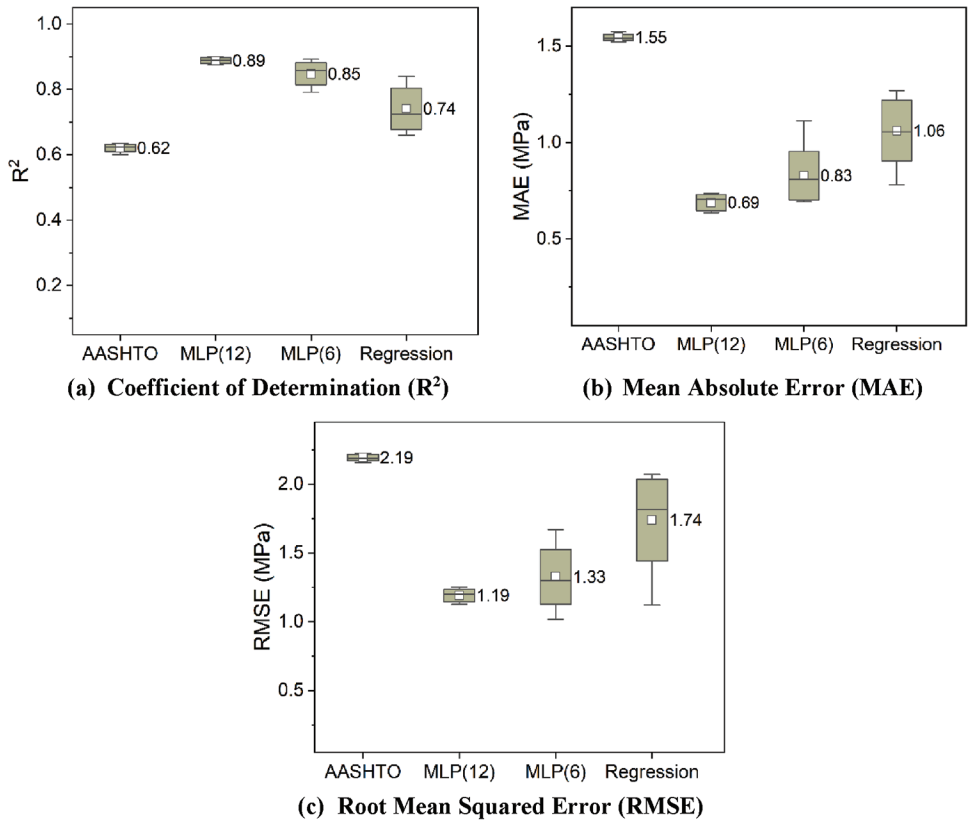

Fig. 7—Consequence of parameter reduction and comparison with polynomial regression. Original 1D-CNN based on 12 input parameters is denoted by MLP(12); MLP(6) represents modified MLP based on reduced set of six parameters. (Note: 1 MPa = 0.145 ksi.)

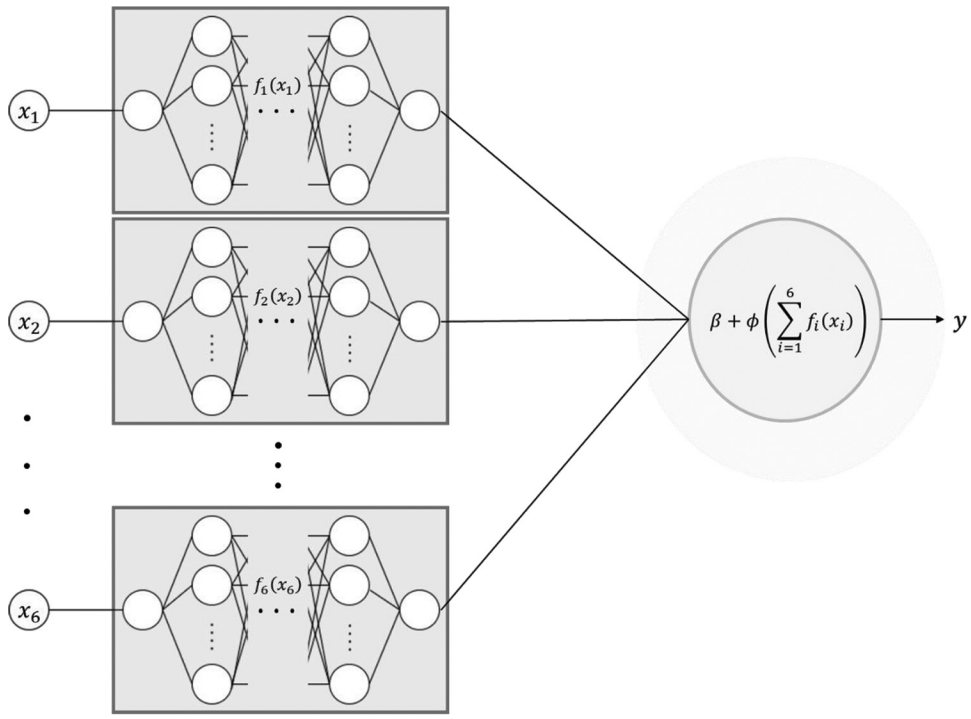

Fig. 8—Neural additive models.

of observed shear strength. ξ is a coefficient that regulates the mix proportion of linear and nonlinear terms. To estimate the optimum value of ξ, its value was incremented gradually from –1 to 1. An increment in the ξ value was followed by a training of the model by way of tenfold cross validation. The mean R^2 values obtained from 10 rounds of cross validation are plotted in Fig. 9 against the corresponding ξ values. It should be noted here that when $\xi = 0$, $\phi(s)$ is a cubic function

Table 5—Minimum and maximum values of input parameters

x_i	x_1	x_2, mm^2	x_3,$\sqrt{\text{MPa}}$	x_4, MPa	x_5, deg	x_6, MPa
$x_{i,min}$	1	20,645.12	3.86	0.00	0.00	–2.76
$x_{i,max}$	3	247,741.44	10.67	15.18	135.00	10.34

Note: 1 MPa = 0.145 ksi; 1 mm^2 = 0.00155 in.^{2}; deg is degrees.

of s. When $0 < \xi < 1$, $\phi(s)$ contains both linear and cubic terms. $\xi = 1$ gives rise to an entirely linear function of s. In the same token, $\phi(s)$ is an amalgam of cubic and quintic terms for $-1 < \xi < 0$. Lastly, $\xi = -1$ indicates a pure quintic function of s. Figure 9 reveals that the best performance is achieved when $\xi = 0$, implying that $\phi(s)$ is a cubic function of s. It can be mentioned in this context that a nonlinear function of s enables an interaction among various shape function components, which is otherwise nonviable in traditional additive modeling approaches where the shape functions are linearly combined. Therefore, a cubic $\phi(s)$ is chosen in this study for all subsequent analyses.

Once the training is complete, the shape functions can be plotted against the respective normalized parameter values. Each parameter produced 10 shape functions, corresponding to 10 cross-validation rounds. These shape functions were averaged to obtain a single shape function corresponding to each parameter

$$f_i(\overline{x}_i) = \frac{1}{10}\sum_{j=1}^{10} f_i^j(\overline{x}_i) \tag{14}$$

where $f_i^j(\overline{x}_i)$ denotes the shape function for the i-th parameter produced by the j-th cross-validation round. $f_i(\overline{x}_i)$ is the final aggregated shape function for the i-th parameter, as plotted in Fig. 10. It is to be noted here that x_1 is assigned an integer that can only be equal to 1, 2, or 3, which correspond to $\overline{x}_1$ of 0, 0.5, and 1, respectively. Thus, other values of this parameter are meaningless.

The shape functions in Fig. 10 are largely consistent with the physical understanding of the problem. As per classical shear-friction theory and recently developed models,[19,20] direct shear across a concrete-to-concrete interface is resisted by a combination of three mechanisms, namely cohesion, friction, and dowel action, which are affected by different parameters. These mechanisms do not reach their maximum contributions simultaneously, which adds to the complexity of the problem. Experimental evidence has shown that one of the important parameters that influences shear transfer is surface roughness.[21] A smoother surface leads to less aggregate interlocking and cohesion, resulting in reduced shear strength. This behavior is reflected in Fig. 10(a), where a significant dip in the shape plot was noticed for smooth surfaces. Another parameter that plays a major role in interfacial shear transfer is the concrete compressive strength. A number of previous studies have established that an increase in the concrete compressive strength results in an increase in the interfacial shear strength,[6,22] which is corroborated by the behavior depicted in Fig. 10(c). The figure also exhibits a softening effect towards the right, which is indicative of a diminishing return on increasing compressive strength. The clamping stress, which is defined as the product of the ratio and yield strength of shear reinforcement, is also known to impact the interfacial shear strength significantly.[21,23-25] It restrains crack dilation, develops aggregate interlocking, and thereby contributes positively to shear transfer strength through friction and dowel action. This is substantiated by the positive correlation exhibited in Fig. 10(d). The figure also exhibits a softening effect towards the right, which is indicative of a diminishing return on increasing reinforcement ratio, yield strength, or both. Previous studies have indicated that the presence of an external normal compressive stress can have an additive effect on the clamping stress leading to an enhanced shear-friction strength.[22] On the other hand, the presence of an external normal tensile stress is seen to reduce the interfacial shear strength.[26] The observations in Fig. 10(f) are in sync with this prior knowledge, facilitating the physical interpretation of the shape function plot. Interestingly, the behavior in Fig. 10(b) suggests that there is no consistent correlation between the interfacial area and shear strength. However, possible size effect on the different shear resisting mechanisms and on the interfacial shear strength requires further investigation.

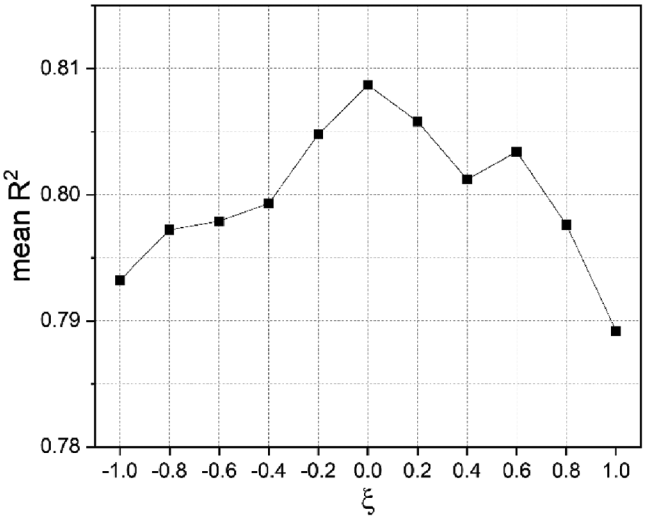

Fig. 9—R^2 produced by different values of ξ. Plotted values are mean R^2 obtained from tenfold cross validation.

The shape functions can also be presented in a tabular form, as shown in Table 6. This tabular presentation of shape plots forms the basis of the proposed LID scheme. To predict the interfacial shear strength of an interface, the known parameter values are first normalized according to Eq. (13). The shape function value corresponding to each normalized parameter is then interpolated from the two nearest entries in Table 6. In the end, all the estimated shape function values are combined to compute the interfacial shear strength ($\hat{y}$), as follows

$$\hat{y} = \beta + \left(\sum_{i=1}^{6} \hat{f}_i(\overline{x}_i)\right)^3 \tag{15}$$

$$\beta = 0.02 \tag{16}$$

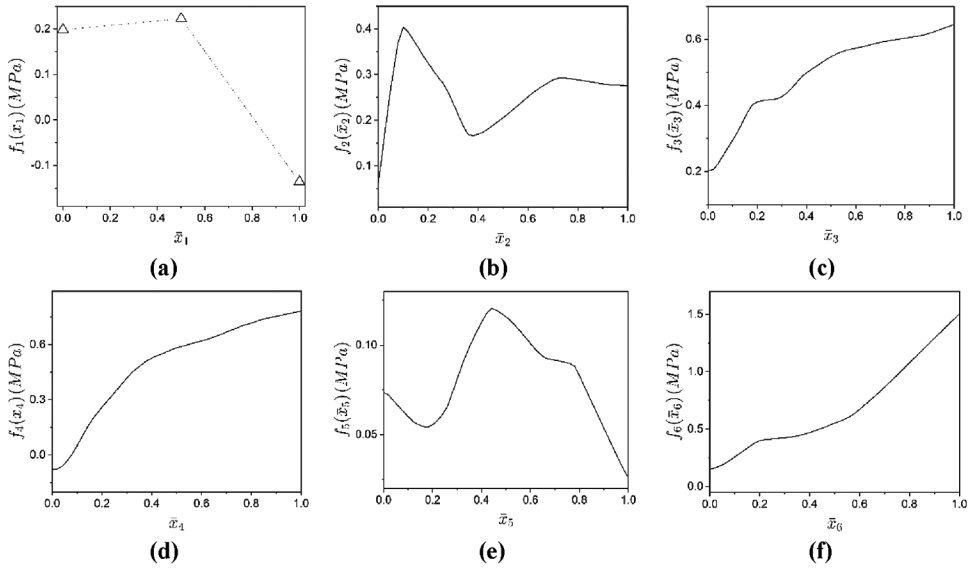

Fig. 10—Parameter-specific shape functions. (Note: 1 MPa = 0.145 ksi.)

where $\hat{f}_i(\bar{x}_i)$ is the interpolated shape function value corresponding to parameter i; and β is the bias term which is learned through network training, and the values obtained from different cross-validation rounds are averaged to produce the final β.

The proposed LID scheme can be illustrated with the help of an example. Consider specimen BRS12-4 from Hanson.[27] The specimen has a rough interface that is 304.8 mm (12.0 in.) long and 203.2 mm (8.0 in.) wide. The compressive strengths of concrete on either side of the shear interface are 21.7 and 26.7 MPa (3.1 and 3.9 ksi). Interfacial reinforcement in the form of two 12.7 mm (0.5 in.) diameter bars with a yield strength of 352 MPa (51 ksi) is oriented orthogonal to the interface. No compressive stress is applied normal to the interface. Accordingly, let

$$x = [2, 61{,}935.36, 4.66, 1.44, 90, 0] \tag{18}$$

be a set of parameters characterizing a shear interface under investigation. Normalization of the parameters as per Eq. (13) results in

$$\bar{x} = [0.50, 0.18, 0.12, 0.09, 0.67, 0.21] \tag{19}$$

Now, for $\bar{x}_1 = 0.50$, $\bar{x}_2 = 0.18$, and $\bar{x}_3 = 0.12$, the shape function values $\hat{f}_1(\bar{x}_1)$, $\hat{f}_2(\bar{x}_2)$, and $\hat{f}_3(\bar{x}_3)$ can be read directly from Table 6 as $\hat{f}_1(\bar{x}_1) = 0.22$, $\hat{f}_2(\bar{x}_2) = 0.34$, and $\hat{f}_3(\bar{x}_3) = 0.32$. Next, to estimate the shape function value corresponding to $\bar{x}_4 = 0.09$, the two nearest neighbors in the lookup table are identified as $u = 0.08$ and $v = 0.10$. The corresponding shape function values are $f_4(u) = 0.00$ and $f_4(v) = 0.05$. Therefrom, $\hat{f}_4(\bar{x}_4)$ can be computed by employing a simple linear interpolation as

$$\hat{f}_4(\bar{x}_4) = f_4(u) + \left(f_4(v) - f_4(u)\right) \times \frac{\bar{x}_4 - u}{v - u} \tag{20}$$

leading to $\hat{f}_4(\bar{x}_4) = 0.03$. In the same manner, the other shape function values can be estimated as shown in Table 7. Finally, these shape function values can be combined as per Eq. (15), resulting in an estimated interfacial strength of 2.79 MPa (0.40 ksi). This estimated shear strength compares favorably with (within 13.88% of) the test result of 2.45 MPa (0.36 ksi).[27] The AASHTO LRFD design provisions predict a shear strength of 3.34 MPa (0.48 ksi) for this specimen (36.33% larger than the test value), which is far less accurate than the proposed LID scheme.

In this way, the interfacial shear strength was obtained for all the specimens in the data set. The accuracy of the predicted values is compared with the AASHTO LRFD design specifications in terms of R^2, MAE, and RMSE in Fig. 11. It was observed that the proposed LID scheme produced significantly higher R^2 (0.79) and lower MAE (1.09 MPa [0.16 ksi]) and RMSE (1.61 MPa [0.23 ksi]) values compared to the AASHTO LRFD design specification (R^2: 0.62, MAE: 1.55 MPa [0.22 ksi], RMSE: 2.19 MPa [0.32 ksi]). The estimated interfacial shear strength values are plotted against the experimental observations in Fig. 12, which indicated a much closer correlation in case of the proposed LID scheme than the AASHTO LRFD design provision. It is also noticed that the relative superiority of the proposed LID scheme cuts across normal- and high-strength materials. This is a considerable advancement to the state-of-the-art, which structural engineers and designers can leverage for a more accurate prediction of the interfacial shear strength leading to a safer and more economical design of reinforced concrete members. However, there are still some unconservative predictions, particularly for specimens with high-strength concrete and high-strength steel. Therefore, future studies should aim to further reduce the extent of overestimation to address the needs of a conservative design paradigm.

SUMMARY AND CONCLUSIONS

This study identified the inaccuracy of the existing design provisions vis-à-vis the prediction of shear strength at the normalweight concrete-to-concrete interface. Two deep-learning models based on multilayer perceptron (MLP) and

Table 6—Tabular presentation of parameter-specific shape plots, MPa

$\bar{x}$	$f_1(\bar{x}_1)$	$f_2(\bar{x}_2)$	$f_3(\bar{x}_3)$	$f_4(\bar{x}_4)$	$f_5(\bar{x}_5)$	$f_6(\bar{x}_6)$
0.00	0.20	0.06	0.20	–0.08	0.07	0.15
0.02	—	0.15	0.21	–0.08	0.07	0.16
0.04	—	0.23	0.22	–0.06	0.07	0.18
0.06	—	0.31	0.25	–0.03	0.07	0.20
0.08	—	0.37	0.27	0.00	0.06	0.23
0.10	—	0.40	0.29	0.05	0.06	0.26
0.12	—	0.39	0.32	0.10	0.06	0.29
0.14	—	0.38	0.35	0.15	0.06	0.32
0.16	—	0.36	0.38	0.19	0.05	0.35
0.18	—	0.34	0.40	0.23	0.05	0.38
0.20	—	0.33	0.41	0.26	0.06	0.40
0.22	—	0.31	0.41	0.29	0.06	0.41
0.24	—	0.29	0.42	0.32	0.06	0.41
0.26	—	0.28	0.42	0.35	0.07	0.42
0.28	—	0.26	0.42	0.39	0.07	0.42
0.30	—	0.24	0.43	0.42	0.08	0.42
0.32	—	0.21	0.44	0.45	0.09	0.43
0.34	—	0.19	0.45	0.47	0.10	0.44
0.36	—	0.17	0.47	0.49	0.10	0.45
0.38	—	0.17	0.49	0.51	0.11	0.46
0.40	—	0.17	0.50	0.53	0.11	0.47
0.42	—	0.17	0.51	0.54	0.12	0.48
0.44	—	0.18	0.52	0.55	0.12	0.50
0.46	—	0.19	0.53	0.56	0.12	0.52
0.48	—	0.20	0.54	0.57	0.12	0.53
0.50	0.22	0.21	0.55	0.58	0.12	0.55
0.52	—	0.21	0.55	0.59	0.11	0.57
0.54	—	0.22	0.56	0.60	0.11	0.59
0.56	—	0.23	0.57	0.61	0.11	0.61
0.58	—	0.24	0.57	0.61	0.10	0.64
0.60	—	0.25	0.57	0.62	0.10	0.67
0.62	—	0.26	0.58	0.63	0.10	0.71
0.64	—	0.27	0.58	0.64	0.09	0.75
0.66	—	0.28	0.58	0.65	0.09	0.78
0.68	—	0.28	0.59	0.66	0.09	0.82
0.70	—	0.29	0.59	0.67	0.09	0.86
0.72	—	0.29	0.59	0.68	0.09	0.91
0.74	—	0.29	0.60	0.69	0.09	0.95
0.76	—	0.29	0.60	0.70	0.09	0.99
0.78	—	0.29	0.60	0.71	0.09	1.03
0.80	—	0.29	0.60	0.72	0.08	1.08
0.82	—	0.29	0.61	0.73	0.08	1.12
0.84	—	0.28	0.61	0.73	0.07	1.16
0.86	—	0.28	0.61	0.74	0.07	1.21
0.88	—	0.28	0.61	0.75	0.06	1.25
0.90	—	0.28	0.62	0.75	0.05	1.29
0.92	—	0.28	0.62	0.76	0.05	1.33
0.94	—	0.28	0.63	0.76	0.04	1.38
0.96	—	0.28	0.63	0.77	0.04	1.42
0.98	—	0.28	0.64	0.78	0.03	1.46
1.00	–0.14	0.28	0.64	0.78	0.03	1.50

Note: 1 MPa = 0.145 ksi.

Table 7—Numerical example to illustrate proposed LID scheme

$\bar{x}_i$	u	v	$f_i(u)$	$f_i(v)$	$\hat{f}_i(\bar{x}_i)$	$v_{n,LID}$	$v_{n,AASHTO}$	$v_{n,test}$
$\bar{x}_1 = 0.50$	0.50	0.50	0.22	0.22	0.22	2.79 (13.88%)	3.34 (36.33%)	2.45
$\bar{x}_2 = 0.18$	0.18	0.18	0.34	0.34	0.34			
$\bar{x}_3 = 0.12$	0.12	0.12	0.32	0.32	0.32			
$\bar{x}_4 = 0.09$	0.08	0.10	0.00	0.05	0.03			
$\bar{x}_5 = 0.67$	0.66	0.68	0.09	0.09	0.09			
$\bar{x}_6 = 0.21$	0.20	0.22	0.40	0.41	0.405			

Note: $\bar{x}_i$ indicates normalized value of parameter i. u and v signify normalized parameter values corresponding to two nearest entries in Table 6. The corresponding shape function values are represented as $f_i(u)$ and $f_i(v)$, respectively. $\hat{f}_i(\bar{x}_i)$ implies shape function value obtained by linear interpolation of nearest entries. $v_{n,LID}$ denotes interfacial shear strength estimated by the proposed LID scheme as per Eq. (15). $v_{n,AASHTO}$ connotes shear strength predicted by AASHTO LRFD design equations. The experimental shear strength for specimen under consideration is symbolized by $v_{n,test}$. All shear-strength values are reported in MPa (1 MPa = 0.145 ksi). Values inside parentheses indicate percentage errors relative to experimental result.

one-dimensional convolutional neural network (1D-CNN) were explored for a more accurate prediction of the interfacial shear strength. The proposed MLP, which is more robust than the 1D-CNN, was observed to considerably outperform both the AASHTO LRFD and ACI 318 design provisions. This is attributable to a neural network's superior ability to learn nonlinear functions. Subsequently, a neural additive model was leveraged to develop a novel learning-informed design (LID) scheme based on a reduced parameter space. The proposed LID scheme outperformed the existing design

equations with considerable margins. The effectiveness of any learning-based method relies on the quality of data used to train the model. In this study, to ensure reliable predictions, tenfold cross validation was conducted by splitting the data into different train-test sets. The model's ability to perform well on both the training and test sets indicates that it can generalize well to novel, unseen data without being overly influenced by potentially noisy training data. Overall, it is believed that this study will motivate the design community to consider such tools to help update the existing design provisions to benefit from some of the clear advantages that the latest deep-learning techniques can offer.

The timeframe of the database used in this study spanned over five decades, ranging from 1960 to 2017. To maintain the accuracy of the LID scheme, it will be imperative to calibrate the proposed model with new data as material strengths continue to evolve in the future. Moreover, this study did not account for the interplay between different design parameters, which is a scope for future work. Future studies should also look into a more granular gradation of the interface, taking into account the amplitude of roughness, aggregate properties, presence of a preexisting crack along the shear plane, and the time gap between the casting of the adjacent surfaces. In addition, quantifying the uncertainty and reliability of the predicted shear strength values is another important research area that merits attention from the scientific community.

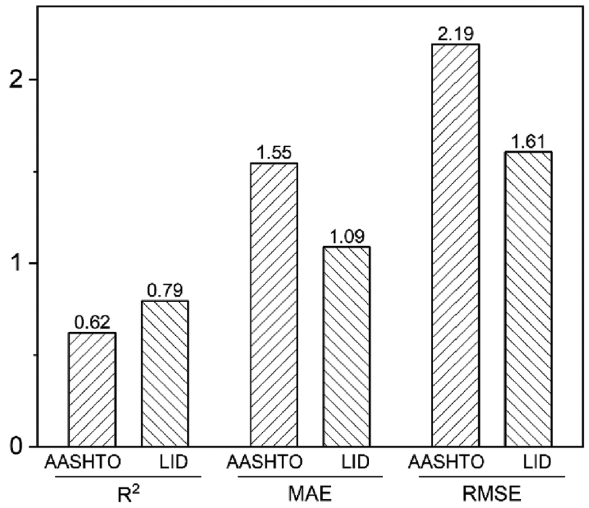

Fig. 11—Prediction accuracy of AASHTO LFRD design equations and the proposed LID scheme in terms of R^2, MAE, and RMSE. (Note: MAE and RMSE values in MPa; 1 MPa = 0.145 ksi.)

AUTHOR BIOS

Tarutal Ghosh Mondal *is an Assistant Professor in the School of Infrastructure at Indian Institute of Technology Bhubaneswar, Odisha, India. He received his PhD in civil engineering from Purdue University, West Lafayette, IN. His research interests include autonomous sensing and intelligent condition assessment of structures. He also works in the fields of computer vision, deep learning, and augmented reality to develop robust systems for the health monitoring of civil infrastructures.*

ACI member **Nikkolas Edgmond** *is an Engineering Intern at Genesis Structures in Kansas City, MO, and a PhD Candidate at Missouri University of Science and Technology (Missouri S&T), Rolla, MO, where he received his Bachelor of Science and Master of Science degrees in civil (structural) engineering.*

Lesley H. Sneed, *FACI, is a Professor of civil engineering at the University of Illinois Chicago, Chicago, IL. She is Chair of ACI Committee 549, Thin Reinforced Cementitious Products and Ferrocement, and a member of ACI Committee 318, Structural Concrete Building Code, and Joint Committee ACI-ASCE 445, Shear and Torsion. Her research interests include design, rehabilitation, and strengthening of reinforced and prestressed concrete structures.*

ACI member **Genda Chen** *is Professor and Robert W. Abbett Distinguished Chair in Civil Engineering at Missouri S&T, Director of the Center for Intelligent Infrastructure (CII), Director of INSPIRE University Transportation Center, and Associate Director of Mid-America Transportation Center.*

ACKNOWLEDGMENTS

Financial support to complete this study was provided by the U.S. Department of Transportation, Office of Assistant Secretary for Research and Technology under the auspices of Mid-America Transportation Center at the University of Nebraska–Lincoln (Grant No. 00065573).

REFERENCES

1. AASHTO, "AASHTO LRFD Bridge Design Specifications, 9th Edition," American Association of State Highway and Transportation Officials, Washington, DC, 2020.

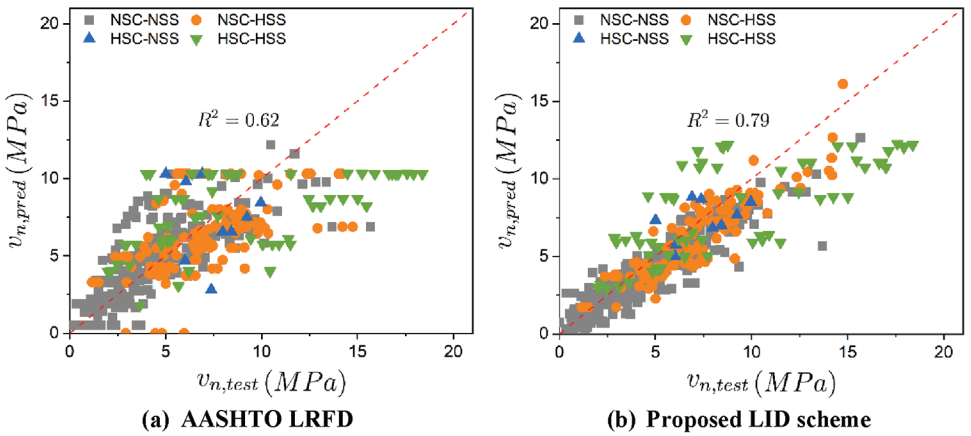

(a) AASHTO LRFD **(b) Proposed LID scheme**

Fig. 12—Comparison of the prediction accuracy of AASHTO LFRD design provisions (with design limits) and proposed LID scheme (no limits). NSC, NSS, HSC, and HSS represent normal-strength concrete, normal-strength steel, high-strength concrete, and high-strength steel, respectively. Concrete having compressive strength greater than 60 MPa is designated herein as HSC. Steel reinforcement having yield strength greater than 420 MPa is identified herein as HSS. (Note: 1 MPa = 0.145 ksi.)

2. ACI Committee 318, "Building Code Requirements for Structural Concrete (ACI 318-19) and Commentary (ACI 318R-19) (Reapproved 2022)," American Concrete Institute, Farmington Hills, MI, 2019, 624 pp.

3. Kahn, L. F., and Mitchell, A. D., "Shear Friction Tests with High-Strength Concrete," *ACI Structural Journal*, V. 99, No. 1, Jan.-Feb. 2002, pp. 98-103.

4. Hegger, J., and Görtz, S., "Nachträglich ergänzte Querschnitte mit horizontaler Fuge nach DIN 1045-1," *Beton- und Stahlbetonbau*, V. 98, No. 5, 2003, pp. 277-284. doi: 10.1002/best.200301450

5. Crane, C. K., "Shear and Shear Friction of Ultra-High Performance Concrete Bridge Girders," PhD dissertation, Georgia Institute of Technology, Atlanta, GA, 2010.

6. Shaw, D. M., and Sneed, L. H., "Interface Shear Transfer of Lightweight-Aggregate Concretes Cast at Different Times," *PCI Journal*, V. 59, No. 3, 2014, pp. 130-144. doi: 10.15554/pcij.06012014.130.144

7. Barbosa, A. R.; Trejo, D.; and Nielson, D., "Effect of High-Strength Reinforcement Steel on Shear Friction Behavior," *Journal of Bridge Engineering*, ASCE, V. 22, No. 8, 2017, p. 04017038. doi: 10.1061/(ASCE)BE.1943-5592.0001015

8. Edgmond, N. J., and Sneed, L. H., "Examination of Shear-friction design Provisions," Precast/Prestressed Concrete Institute (PCI), Chicago, IL, 2019, 147 pp.

9. Duan, Z.-H.; Kou, S.-C.; and Poon, C.-S., "Prediction of Compressive Strength of Recycled Aggregate Concrete Using Artificial Neural Networks," *Construction and Building Materials*, V. 40, 2013, pp. 1200-1206. doi: 10.1016/j.conbuildmat.2012.04.063

10. Dantas, A. T. A.; Batista Leite, M.; and de Jesus Nagahama, K., "Prediction of Compressive Strength of Concrete Containing Construction and Demolition Waste Using Artificial Neural Networks," *Construction and Building Materials*, V. 38, 2013, pp. 717-722. doi: 10.1016/j.conbuildmat.2012.09.026

11. Asteris, P. G.; Armaghani, D. J.; Hatzigeorgiou, G. D.; Karayannis, C. G.; and Pilakoutas, K., "Predicting the Shear Strength of Reinforced Concrete Beams Using Artificial Neural Networks," *Computers and Concrete, An International Journal*, V. 24, No. 5, 2019, pp. 469-488.

12. Bashir, R., and Ashour, A., "Neural Network Modelling for Shear Strength of Concrete Members Reinforced with FRP Bars," *Composites. Part B, Engineering*, V. 43, No. 8, 2012, pp. 3198-3207. doi: 10.1016/j.compositesb.2012.04.011

13. Demir, F., "Prediction of Elastic Modulus of Normal and High Strength Concrete by Artificial Neural Networks," *Construction and Building Materials*, V. 22, No. 7, 2008, pp. 1428-1435. doi: 10.1016/j.conbuildmat.2007.04.004

14. Agarwal, R.; Melnick, L.; Frosst, N.; Zhang, X.; Lengerich, B.; Caruana, R.; and Hinton, G. E., "Neural Additive Models: Interpretable Machine Learning with Neural Nets," *Advances in Neural Information Processing Systems*, V. 34, 2021, pp. 4699-4711.

15. Murtagh, F., "Multilayer Perceptrons for Classification and Regression," *Neurocomputing*, V. 2, No. 5-6, 1991, pp. 183-197. doi: 10.1016/0925-2312(91)90023-5

16. Hecht-Nielsen, R., "Theory of the Backpropagation Neural Network," *Neural Networks for Perception*, Elsevier, 1992, pp. 65-93.

17. O'Shea, K., and Nash, R., "An Introduction to Convolutional Neural Networks," *arXiv Preprint arXiv:1511.08458*, 2015.

18. Kingma, D. P., and Ba, J., "Adam: A Method for Stochastic Optimization," *arXiv Preprint arXiv:1412.6980*, 2014.

19. Palieraki, V.; Vintzileou, E.; and Silva, J. F., "Interface Shear Strength under Monotonic and Cyclic Loading," *ACI Structural Journal*, V. 119, No. 3, May 2022, pp. 17-28.

20. Palieraki, V.; Vintzileou, E.; and Silva, J., "Behavior of RC Interfaces Subjected to Shear: State-of-the Art Review," *Construction and Building Materials*, V. 306, 2021, p. 124855 doi: 10.1016/j.conbuildmat.2021.124855

21. Saemann, J., and Washa, G. W., "Horizontal Shear Connections between Precast Beams and Cast-in-Place," *ACI Journal Proceedings*, V. 61, No. 11, Nov. 1964, pp. 1383-1410.

22. Mattock, A. H., and Hawkins, N. M., "Shear Transfer in Reinforced Concrete—Recent Research," *PCI Journal*, V. 17, No. 2, 1972, pp. 55-75. doi: 10.15554/pcij.03011972.55.75

23. Hofbeck, J.; Ibrahim, I.; and Mattock, A. H., "Shear Transfer in Reinforced Concrete," *ACI Journal Proceedings*, V. 66, No. 2, Feb. 1969, pp. 119-128.

24. Bass, R. A.; Carrasquillo, R. L.; and Jirsa, J. O., "Shear Transfer across New and Existing Concrete Interfaces," *ACI Structural Journal*, V. 86, No. 4, July-Aug. 1989, pp. 383-393.

25. Echegaray-Oviedo, J.; Cuenca, E.; Navarro-Gregori, J.; and Serna, P., "Influence of the Fiber Reinforcement in Concrete under Direct Shear," *10th fib International PhD Symposium in Civil Engineering Proceedings*, 2014, pp. 415-424.

26. Chatterjee, P., "Shear Transfer in Reinforced Concrete," master's thesis, University of Washington, Seattle, WA, 1971.

27. Hanson, N. W., *Precast-Prestressed Concrete Bridges: 2. Horizontal Shear Connections*. Portland Cement Association, Research and Development Laboratories, Skokie, IL, 1960.

ACI STRUCTURAL JOURNAL TECHNICAL PAPER

Title No. 122-S05

Capacity Estimations for Three-Pile Caps with Size and Reinforcement Variations

by S. Mogili, S.-J. Hwang, K.-Y. Liu, T. Ichinose, L. Laughery, and K. Kasai

Past investigations showed that the one-way shear strength of reinforced concrete members exhibits "size effect," a phenomenon whereby shear strength does not increase in direct proportion to member size. However, it is unclear if the reduction in the two-way shear strength of reinforced concrete members due to size effect applies in the same magnitude as one-way shear strength. To investigate size effect in two-way shear, 12 three-pile caps were tested in three size groups: small, medium, and large. Specimens were doubly scaled from small to medium and medium to large groups, with all other key nondimensional structural parameters such as span-depth ratio, reinforcement ratio, and so on kept constant. The test results supported the existence of size effect in deep pile cap members, although the observed rate of unit shear strength reduction with depth was less severe than that predicted by size effect provisions in American and Japanese design codes. Capacity estimations made using sectional and strut-and-tie approaches prescribed by design codes, as well as the proposed analytical procedure using the softened strut-and-tie model, are presented. The proposed method produced reasonably accurate estimations at all size ranges, capturing the effect of reinforcement more efficiently resulting in an overall mean test-to-calculated capacity ratio of 1.15 with a low coefficient of variation of 11%.

Keywords: pile caps; punching; reinforced concrete; scaled testing; shear strength; size effect; softened strut-and-tie model; two-way shear.

INTRODUCTION

Reinforced concrete (RC) pile caps are deep foundation elements connecting columns to piles. Key parameters such as span-depth ratio, tension reinforcement (area and layout), and pile configuration have been reported to influence the strength and failure mode of pile caps.[1-4] Due to the brittle nature of failure, the shear behavior of pile caps is of particular interest to practicing engineers and researchers. Sectional methods used for shear design of pile cap members consist of strength verification using empirical equations derived based on experimental knowledge. The availability of new data provides an opportunity to recalibrate existing equations and include new factors as necessary for safety and economy. In this context, an important phenomenon known as "size effect" was introduced to ACI 318[5] in 2019 to account for the reduction in unit shear strength of reinforced concrete members with size. In this paper, an experimental study to quantify the size effect in two-way shear and validate the existing design provisions is presented. An efficient analytical procedure for capacity estimations of pile caps that is consistent with force transfer mechanisms is also introduced and compared with existing code provisions. A brief discussion of relevant design provisions from selected codes and their backgrounds is presented.

ACI 318-19 sectional method

American Concrete Institute design provisions (ACI 318-19[5]) for sectional method include one-way and two-way shear checks for the design of pile cap members. The critical section in one-way shear is considered at a distance of effective depth (d) away from the column face over the entire width of the pile cap. For two-way shear, a critical surface at a distance $d/2$ from column edges is considered. For pile cap members where transverse reinforcement is excluded, ACI 318-19[5] prescribes Eq. (1) and (2) for one-way shear capacity (V_{1w}) and two-way shear capacity (V_{2w}), respectively.

$$V_{1w} = 0.664 \times \lambda_s \times \rho^{1/3} \times \sqrt{f_c'} \times b_w d \ (f_c' \text{ in MPa}) \text{ or } 8 \times \lambda_s \times \rho^{1/3} \times \sqrt{f_c'} \times b_w d \ (f_c' \text{ in psi}) \quad (1)$$

$$V_{2w} = 0.332 \times \lambda_s \times \sqrt{f_c'} \times b_o d \ (f_c' \text{ in MPa}) \text{ or } 4 \times \lambda_s \times \sqrt{f_c'} \times b_o d \ (f_c' \text{ in psi}) \quad (2)$$

The phenomenon of concrete contribution to shear strength not increasing in direct proportion with member depth is defined as size effect. Size effect is a significant inclusion in ACI 318-19, applicable for both one-way and two-way shear strength estimations of reinforced concrete members. ACI 318-19 prescribes Eq. (3) for quantifying the size effect in shear members. The background of adopting Eq. (3) for one-way shear design provisions of ACI 318-19 has been described by Kuchma et al.[6]

$$\lambda_s = \sqrt{2/(1 + d/250)} \ (d \text{ in mm}) \text{ or } \sqrt{2/(1 + d/10)} \ (d \text{ in in.}) \leq 1.0 \quad (3)$$

The proportionality of the one-way size effect to $d^{-1/2}$ in Eq. (3) is well supported by Bažant et al.[7] in a statistical regression study using the data from 398 beams without stirrups over a broad range of sizes. It is thus reasonable to say that there is a sound theoretical and experimental basis for adopting Eq. (3) for one-way shear members such as deep

ACI Structural Journal, V. 122, No. 1, January 2025.
MS No. S-2022-432.R1, doi: 10.14359/51743292, received January 4, 2024, and reviewed under Institute publication policies.

beams. Although size effect is expected in two-way shear,[8] the extent of strength reduction due to increasing size must be separately quantified through evaluation of members tested experimentally in two-way shear. Indeed, such a study has been done: a detailed regression study[9] comprising 440 two-way slab specimens with and without transverse reinforcement supported the trend of the size effect proportional to $d^{-1/2}$. However, the maximum effective specimen depth in that study was only 668 mm (26.3 in.). Furthermore, after filtering to eliminate the effect of secondary variables such as geometry and longitudinal reinforcement ratios, only three specimens with an effective depth of more than 400 mm (15.7 in.) remained for the size effect regression study. To clarify, this filtering refers to the removal of outliers within each size group such that the resultant data subset contains nearly uniform means of variables not related to size. The purpose of said filtering was to ensure that the shear strength variation across various size intervals was solely due to the size. Therefore, it is reasonable to conclude that the accuracy of Eq. (3) for estimating the size effect in two-way shear members is yet to be verified. Test data from deeper two-way members is particularly important to verify the size effect, especially because the derivation of Eq. (3) was based only on beams loaded in one-way shear.

JSCE 2012 sectional method

The American Concrete Institute is not the only body to adopt a size effect factor. Notably, a size effect factor has been incorporated in the Japanese Design Code since 2012 (JSCE 2012[10]) for calculating shear compression capacity (Eq. (4)) through a factor β_d given by Eq. (5). Analogous to λ_s recommended by ACI 318-19, the size effect factor β_d suggested by the JSCE 2012 Code is given by Eq. (5).

$$V_{dd} = \beta_d \beta_p \beta_a f_{dd} b_w' d$$
$$\text{where } \beta_p = \frac{1 + \sqrt{100\rho}}{2} \leq 1.5;\ \beta_a = \frac{5}{1 + (a/d)^2}; \quad (4)$$

$$f_{dd} = 0.19\sqrt{f_c'}\ (f_c' \text{ in MPa}) \text{ or } 2.3\sqrt{f_c'}\ (f_c' \text{ in psi})$$
$$\beta_d = \sqrt[4]{1000/d}\ (d \text{ in mm}) \text{ or } \sqrt[4]{39/d}\ (d \text{ in in.}) \leq 1.5 \quad (5)$$

Equation (5) shows that JSCE 2012 adopts a depth effect factor proportional to $d^{-1/4}$, as opposed to a more conservative factor proportional to $d^{-1/2}$ adopted by ACI 318-19. The impact of such a difference on code-based strength estimations can be quite large, especially for deeper members. Nevertheless, the actual impact of size effect in two-way shear members has remained unclear due to a lack of controlled experimental data covering different size ranges. To address this gap, an experimental investigation of 12 RC three-pile caps for size effect in two-way shear was carried out as a collaborative effort[11] by the authors from Tokyo Institute of Technology and Nagoya Institute of Technology in Japan, and National Center for Research on Earthquake Engineering in Taiwan. Necessary information related to the size effect and observed capacities from the experimental study has been reviewed from Laughery et al.[11] and presented in this manuscript.

All test specimens were over-reinforced such that shear failure would occur prior to reinforcement yielding, making them relevant for the discussion of size effect in two-way shear members. To study the size effect, other dimensionless parameters such as tension reinforcement ratio, span-depth ratio, clear cover ratio, and so on, that affect shear strength in pile caps were kept constant. Besides size, tension reinforcement area was also varied within each size group to study its effect on two-way shear strength. Although current ACI 318-19 one-way provisions (Eq. (1)) for shear strength include a reinforcement ratio factor $\rho^{1/3}$ recognizing the beneficial effect of tension reinforcement on one-way shear strength, such a factor is not adopted for two-way shear (Eq. (2)). The test program can thus be used to assess the benefit to shear strength from adding tension reinforcement and emphasize the need (if any) for inclusion of a reinforcement area ratio factor in two-way shear strength estimation.

ACI 318-19 strut-and-tie method

The ACI 318-19 Code also recommends a strut-and-tie approach for pile cap design, especially when the shear span-depth ratios are lower than 2.5 due to predominant arch actions in load resistance. The strength of pile cap members is determined through analysis of an idealized three-dimensional truss comprising struts and ties. While shear failure is marked by crushing of concrete in the diagonal strut, flexural failure corresponds to tension tie yielding. ACI prescribes Eq. (6) and (7) for estimating the capacity of compression struts and tension ties, respectively

$$F_{ns} = 0.85\beta_c\beta_s f_c' \times A_{cs} \quad (6)$$

$$F_{nt} = f_y \times A_{ts} \quad (7)$$

where β_c and β_s are typically taken as 1.0 and 0.6, respectively, for pile caps.

The ACI strut-and-tie approach is generally regarded as superior and preferred by designers over sectional approaches for pile caps due to likely arch actions that are reasonably replicated by the strut-and-tie procedure. However, the strut-and-tie approach has been reported to be unconservative for pile cap members that failed in shear as opposed to failure by tension tie yielding.[12-14] This unconservatism for pile cap shear strength was reportedly attributed to an inaccurate assessment of strut strength using the ACI strut-and-tie approach.[12] Lack of guidelines on force distribution among different struts in asymmetric pile caps will further exemplify the inaccuracy of shear strength predictions.[13] Notably, the ACI strut-and-tie approach also cannot explain the observed improvement in the shear capacity of members with the addition of tension reinforcement.[12,13]

Another analytical procedure based on the softened strut-and-tie (SST) model is proven to address the foregoing shortcomings of the ACI strut-and-tie approach in estimating the strength of RC pile caps.[13] The term "softened" refers to the softening phenomenon of concrete due to the presence of transverse tensile strains within the strut. This term

gained popularity through the work of Hsu and Zhu[15] in the analysis of RC shear elements. In the proposed SST procedure, the area of diagonal strut resisting compression depends on the depth of flexural compression zone, which accounts for the variation in pile cap capacities with tension reinforcement. A comparative study[13] on the estimation of pile cap capacity showed that this approach can satisfactorily capture a wide range of parameters such as span-depth ratio, tension reinforcement, and pile configuration (symmetric or asymmetric). The SST model for pile caps uses a concept of effective loading width to capture the stress concentrations in the vicinity of column members. It was reported to provide better strength predictions than code-recommended sectional and strut-and-tie methods for both shear-dominant and flexure-dominant pile caps.[13]

Despite its improved accuracy for other parameters, due to a lack of relevant experimental data, the original SST analytical method for pile caps does not account for the size effect. Thus, the current experimental study can also help address the need for size effect inclusion in the analytical method. Discussion and application of the SST model to three-pile caps are presented in the latter sections. Comparative discussions on the overall accuracy of the SST model in capacity estimations of test specimens, relative to ACI 318-19 sectional and strut-and-tie provisions, and JSCE 2012 sectional provisions are subsequently presented.

RESEARCH SIGNIFICANCE

Experimental results of 12 three-pile cap specimens with different sizes and reinforcement ratios are presented in this manuscript in the context of evaluating code-based approaches for estimating the two-way shear strength of deep pile caps. This research work aims to study the efficacy of different approaches given variations in size, reinforcement ratio, and concrete strength. Experimental results supported the presence of size effect in pile caps, but the magnitude of strength reduction with size was smaller than what would be estimated by current design provisions. Possible revisions in the size effect provisions for two-way shear are subsequently discussed, particularly for very deep elements. Capacity estimates for the current test specimens using a proposed SST model are subsequently compared with estimates based on American and Japanese design provisions. Lastly, the effectiveness of the proposed analytical SST approach at capturing key parameters is also highlighted through capacity predictions of nine additional three-pile cap specimens from another study.[4]

EXPERIMENTAL DESIGN

The experimental program for studying size effect and reinforcement area was conceived and designed by researchers from Tokyo Institute of Technology and Nagoya Institute of Technology in Japan.[11] The test plan comprised 12 triangular three-way symmetrical reinforced concrete pile caps, each with one column (top plate) and three pile supports (bottom plates). They were divided into three size groups with four specimens each, labeled as small (S), medium (M), and large (L). Medium pile caps were twice as large as small pile caps, and large pile caps were twice as large as medium pile caps. Figure 1(a) shows geometric details and scaling of small, medium, and large specimens. Within each size group, three pile caps were heavily reinforced with three layers of tension reinforcement (labels include digit 3), and one pile cap was lightly reinforced with one layer of tension reinforcement (labels include digit 1) with identical bar diameters.

The reinforcement was provided in a bunched pattern over the piles in triangular form. In total, there were nine three-layer specimens and three one-layer specimens. Reinforcement ratios in all nine three-layer specimens were constant, despite size variation, as was the case in three one-layer specimens. The effective depth from the top of the pile cap to the centroid of reinforcement was the same for three-layer and one-layer reinforced specimens in each group. Reinforcement layouts in three-layer and one-layer specimens are illustrated in Fig. 1(b). Geometric scaling ensured that in all specimens, the horizontal distance between the column center to each pile center (denoted by a) was equal to the effective depth d. In other words, shear span-depth ratios (a/d) were equal to 1.0 for all specimens. All other key parameters were carefully scaled to keep associated dimensionless ratios constant such that observed strength variations could be definitively attributed to the size effect. Both geometric and reinforcement details of all test specimens are provided in Table 1.

Small- and medium-size specimens were cast in a single placement. However, large specimens were cast one at a time, leading to a slight variation in their concrete strength. To observe the effect of high-strength concrete on pile cap behavior, a single specimen (L3H) was cast from high-strength concrete. For small and medium groups of specimens, a baseline concrete compression strength was determined as the group mean of three cores taken from each specimen. As large specimens were cast in different placements, an average of three cylindrical cores in each specimen was taken to be representative of concrete compressive strength for these specimens. This is following the standard procedures outlined in ASTM C39/C39M-14.[16] Concrete compressive strengths measured this way for all test specimens are reported in Table 1.

All pile caps were built and tested at the National Center for Research on Earthquake Engineering (NCREE) in Taiwan. Uniaxial loading was applied monotonically on the top plate of each specimen using a Bi-Axial dynamic Testing System (BATS) at NCREE. Three bottom plates provided pile reactions to the whole setup. The vertical load on pile caps was measured throughout the test using the BATS system. Displacement transducers were mounted at various locations to measure the vertical and lateral deformations of pile caps. Strain gauges were attached to longitudinal reinforcing bars to monitor strains in tension reinforcement. A detailed discussion of these displacement and strain measurements is not within the scope of this paper. Instead, the focus of this paper is to understand and analyze the strength of two-way shear members; therefore, only vertical deformation at the center of the bottom face and the vertical load applied on the top plate for each specimen are reported in this manuscript. Readers are directed to refer to the companion paper[11] and

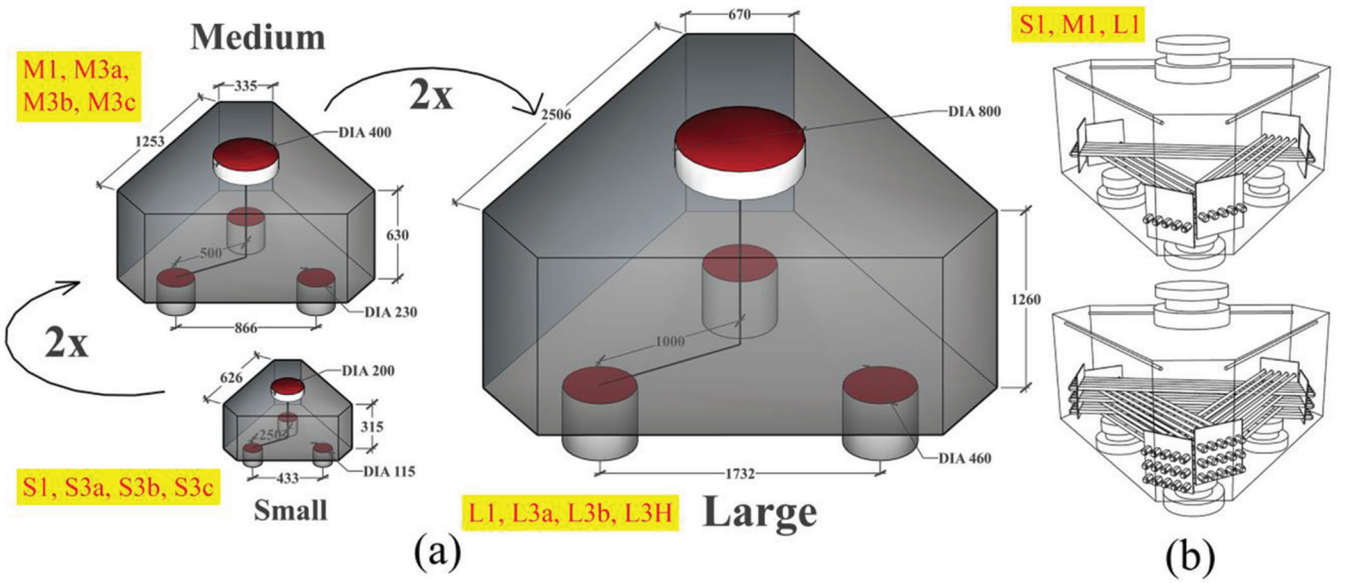

Fig. 1—(a) Geometric details showing scaling; and (b) typical reinforcement layouts in one-layered (top) and three-layered specimens (bottom). (Note: All units are in mm; 1 in. = 25.4 mm.)

Table 1—Details and experimental results of test specimens

Label	H, mm	a, mm	d, mm	b_{top}, mm	b_{bot}, mm	A_s, mm^2	ρ, %	f_y, MPa	f_c', MPa	P_u, kN	$v/\sqrt{f_c'}$, MPa$^{1/2}$
S3a	315	250	250	200	115	3207	1.48	758	42.1	1627	0.71
S3b										1713	0.75
S3c										1571	0.69
M3a	630	500	500	400	230	12,826	1.48	715	44.3	5691	0.61
M3b										6104	0.65
M3c										5787	0.62
L3a	1260	1000	1000	800	460	51,304	1.48	690	37.2	20,990	0.61
L3b									43.9	23,390	0.62
L3H									58.6	26,420	0.61
S1	315	250	250	200	115	1069	0.49	758	42.1	1157	0.50
M1	630	500	500	400	230	4275	0.49	715	44.3	3821	0.41
L1	1260	1000	1000	800	460	17,101	0.49	690	44.9	16,484	0.44

Note: ρ is calculated as $A_t/(2a \times d)$ assuming an effective width of $2a$, where $A_t = (A_s/3) \times 2\cos 30°$; 1 mm = 0.039 in.; 1 mm^2 = 0.00155 in.^{2}; 1 MPa = 145 psi; 1 kN = 0.225 kip.

other related publications[17-19] for a more detailed discussion of experimental design and results.

EXPERIMENTAL STRENGTH AND SIZE EFFECT

The vertical load on the top plate and deformation at the center of the bottom face throughout the loading and unloading stages are plotted in load-deformation responses of 12 specimens grouped based on their size in Fig. 2. All specimens exhibited substantial residual deformations even after the loading platen was detached from specimens indicative of significant inelastic damage. Sections of unloading branches of L1 and L3H were slightly erroneous and these are indicated through dashed lines. The observed capacity of each specimen is provided in Table 1 as P_u. With no difference in concrete strength, geometry, or reinforcement, the capacities of three-layer reinforced specimens within small and medium groups were expected to be similar. The test results showed good reproducibility with the peak loads for all three specimens in both small and medium groups within a 5% variation from the respective mean values. On the other hand, concrete strengths in large specimens varied in the range of (−)20% to (+)26% from the group mean value, resulting in a variation of capacities of three-layer reinforced large specimens in the order of (−)11% to (+)12% on average. As expected, L3H with high-strength concrete exhibited the largest capacity.

Unit shear strength (v) was calculated by dividing the peak load by the ACI two-way shear-critical area given by $\pi(b_{top} + d)$ multiplied with d. The concrete strength was subsequently normalized using $\sqrt{f_c'}$, which is consistent with ACI 318-19 recommendations. The resulting normalized shear strengths, represented by $v/\sqrt{f_c'}$, are calculated using Eq. (8) and listed

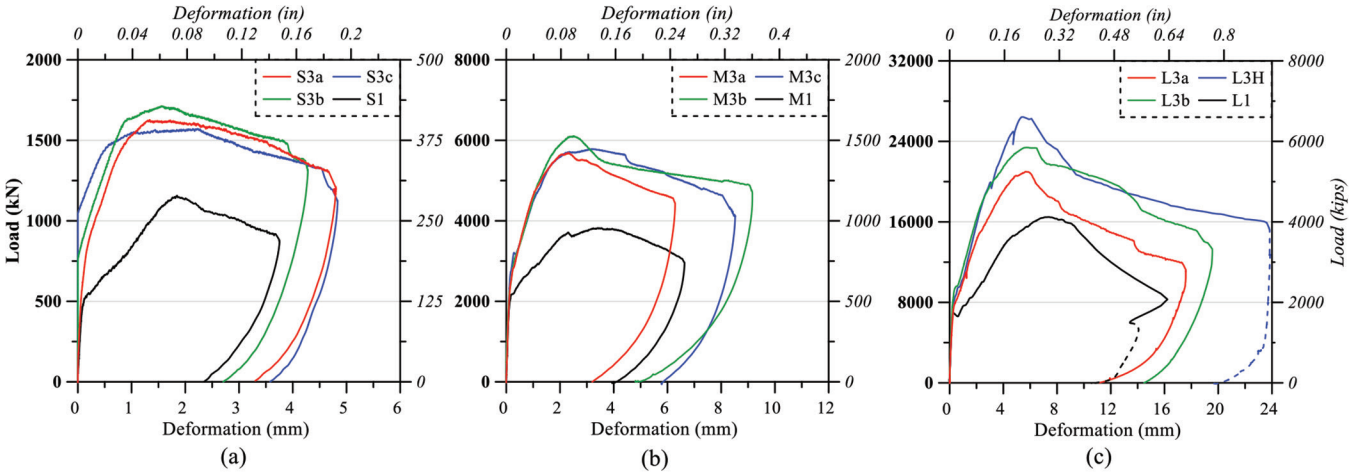

Fig. 2—Load-deformation behavior of: (a) small; (b) medium; and (c) large test specimens.

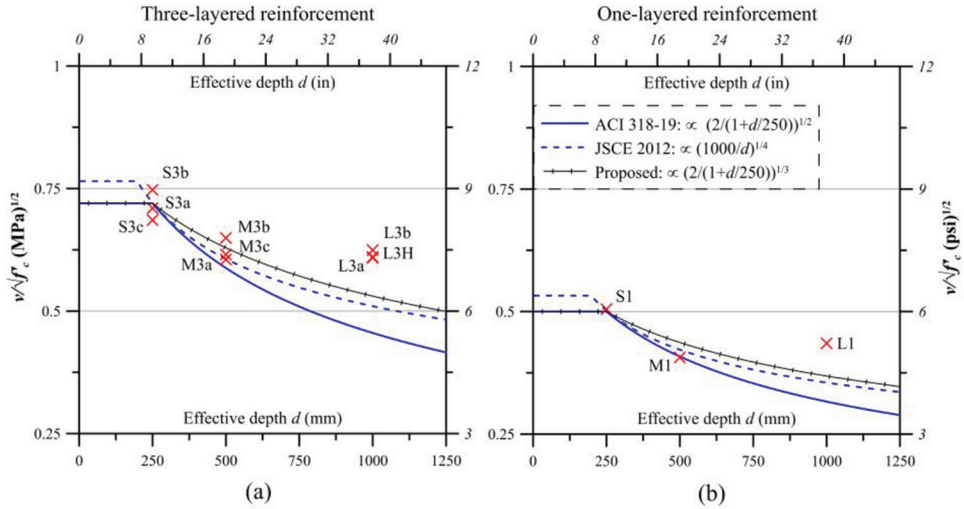

Fig. 3—Size effect in pile caps with tension reinforcement in: (a) three layers; and (b) one layer.

in Table 1 for all specimens. Results showed that higher $v/\sqrt{f_c'}$ was observed in three-layer specimens as compared with the one-layer specimen within the same size group. This indicated that tension reinforcement is favorable for strength even though the reinforcement did not yield. However, no normalization pertaining to tension reinforcing bar ratios was performed, primarily because ACI 318-19 design provisions do not consider the influence of the tension reinforcement ratio on two-way shear strength. Hence, visual comparisons of normalized shear strength varying with effective depth are presented separately for three-layered and one-layered specimens in Fig. 3. The size effect was observed in test results of both the three-layer and one-layer reinforced specimens, which showed a decrease of $v/\sqrt{f_c'}$ with an increase in effective depth. If there were no size effect on two-way shear strength, then $v/\sqrt{f_c'}$ values among different size groups would be similar.

$$\frac{v}{\sqrt{f_c'}} = \frac{P_u}{\pi(b_{top} + d)d\sqrt{f_c'}} \tag{8}$$

The accuracy of size effect provisions recommended by design codes depends on how closely the respective trendlines trace the observed variation in $v/\sqrt{f_c'}$. Accordingly, accuracies of size effect expressions adopted by ACI 318-19 and JSCE 2012 were assessed by overlaying the trendlines for Eq. (3) and (5), respectively, in Fig. 3. For the sake of comparison, intercepts (heights) of these trendlines were adjusted such that both ACI and JSCE trendlines pass through the mean value of $v/\sqrt{f_c'}$ for small specimens, under the assumption that there is no influence of size effect on small specimens in the current study (that is, at d equal to 250 mm [10 in.]). This assumption is consistent with the philosophy of ACI 318-19 that size effect is only expected in members with d above 250 mm (10 in.).

Figure 3 highlights clear evidence of the influence of size effect in both three-layer and one-layer groups as the size increases from small to medium. The trendlines for ACI 318-19 and JSCE 2012 can capture the strength reduction due to size effect from small to medium size reasonably well. In contrast, Fig. 3 indicates that no additional strength reduction due to size effect is observed from medium to large pile caps, despite ACI 318-19 and JSCE 2012 provisions suggesting a reduction of 23% and 16% respectively for such variation. Among the two codes, the JSCE depth effect factor, which is proportional to $d^{-1/4}$, provided better size

effect estimates for large members than the ACI depth effect factor, which is proportional to $d^{-1/2}$ with estimated-to-measured strength reduction ratios of 2.0 versus 2.5, respectively. Nonetheless, the JSCE expression still overestimates the size effect considerably, with a strength reduction ratio of 2.0, on shear strength for large members. Such a severe strength reduction due to size effect can have tremendous implications on design costs. For instance, the reductions due to size effect in ACI 318-19 and JSCE 2012 provisions in large specimens (d = 1000 mm [39 in.]) are 37% and 29%, respectively. In comparison, the experimental evidence showed that the strength reduction due to the size effect is only 15% (on average). This gap may be expected to further widen for larger pile caps, which are often encountered in practice. Thus, it is necessary to revisit the current size effect provisions for two-way shear to a milder version of that of one-way shear.

Based on experimental evidence from the current controlled study, the authors recommend a new expression for size effect in two-way shear members given by Eq. (9). This expression is a slight modification of the current ACI 318-19 expression for size effect. The trendline corresponding to the proposed expression is also plotted in Fig. 3. The unit strength reduction for large members of this study using Eq. (9) is 26%, as opposed to 37 and 29% reduction using ACI 318-19 and JSCE 2012 provisions.

$$\lambda_p = \sqrt[3]{2/(1 + d/250)}\ (d \text{ in mm})$$
$$\text{or } \sqrt[3]{2/(1 + d/10)}\ (d \text{ in in.}) \le 1.0 \quad (9)$$

The proposed size effect modification remains slightly over-conservative for the large members in the current study with 26% estimated strength reduction against 15% measured strength reduction. Admittedly, this suggestion is drawn from a handful number of medium and large specimens in this study. To enhance confidence in these findings, additional data from scaled studies involving larger sizes is necessary. Nevertheless, the suggestion underscores the observed need for quantifying the size effect in two-way shear differently from one-way shear.

It is also noteworthy that the test evidence through Fig. 3 indicates a possible saturation of size effect as the size is increased from medium to large. Based on this, a lower limit for the size effect factor in two-way shear can also be considered alternatively to Eq. (9). A similar idea was discussed for size effect studies on compressive strength in plain concrete cylinders[20] and bearing strength of concrete cubes.[21] This idea is not pursued in this paper. Nonetheless, there is a need for more experimental studies with deep specimens (d > 600 mm [24 in.]) to further improve the size effect provisions for two-way shear. Until such studies are carried out, conservatism offered by Eq. (9) can be considered sufficient, while offering a noticeable strength benefit for large two-way shear members.

OVERVIEW OF ANALYTICAL PROCEDURE

An analytical model based on the SST model for pile caps[13,22] is adopted to estimate the capacities of test specimens in this study. The SST model considers both geometric and reinforcement effects on the strength and failure mode of pile caps. The analytical model can accurately estimate both shear and flexural capacities of pile caps separately. The overall capacity (and failure mode) is taken as the smaller of the two. Vertical load on the column is resisted through struts (in shear) and equivalent beams (in flexure) which develop from the column towards each pile. A brief discussion of the SST model applied to the current test specimens is presented in this section. A more detailed discussion related to the application and scope of the SST model for pile caps with more complex layouts and reinforcement distributions is presented elsewhere.[13]

Figure 4 shows a typical strut formation (for shear) and an equivalent beam formation (for flexure) in a three-pile cap member. Shear capacity is calculated as the sum of the vertical components from the three struts. Similarly, flexural capacity is calculated as the sum of the contributions from the equivalent beams.

In the first step, an equivalent reinforcement tie area (A_t) along each loading path is calculated in the plane connecting the centers of the column to the respective pile as shown in Fig. 4. This tie area is used for both shear and flexural calculations. Next, the strut width and equivalent beam width, defined as "effective loading width" (b_e), is determined by considering simultaneous interactions of shear and flexural actions developed within the pile cap. Effective loading width marks the extent of the region with severe stress concentrations under punching. The flowchart for this procedure is shown in Fig. 5. This process can be summarized as follows: a flexural width (b_f) is assumed and the corresponding elastic neutral axis depth kd is estimated. A reasonable initial assumption for b_f is b_c + 0.5d. Next, the shear width (b_s) is calculated at a depth of kd/3, assuming that shear force is transmitted at a gradient of 1:2. Iterations are carried out by adjusting b_f until the resulting b_s is equal to the iterative width, which is selected as b_e.

After determining b_e, the area of the concrete diagonal strut (A_{str}) is estimated using Eq. (10), with the neutral axis calculated corresponding to a singly reinforced beam having tension reinforcement A_t and width b_e using Eq. (11).

$$A_{str} = b_e \times kd \quad (10)$$

$$kd = \left(\sqrt{(n\rho_f)^2 + 2n\rho_f} - n\rho_f\right) \times d \quad (11)$$

The capacity of a single strut is then estimated using Eq. (12). As mentioned earlier, the softening phenomenon[15,23] due to transverse tensile strains within the concrete strut is approximated using Eq. (13), which was proposed by Hwang and Lee in 2002.[24] The strut-and-tie index (K) is taken as 1.0 for pile caps without any transverse reinforcement. If transverse reinforcement is provided, it can reduce crack propagation and enhance the strut capacity, leading to a value of K greater than 1. To estimate K in those cases, Eq. (14) can be adopted[25]

$$C_d = K\zeta f_c' A_{str} \quad (12)$$

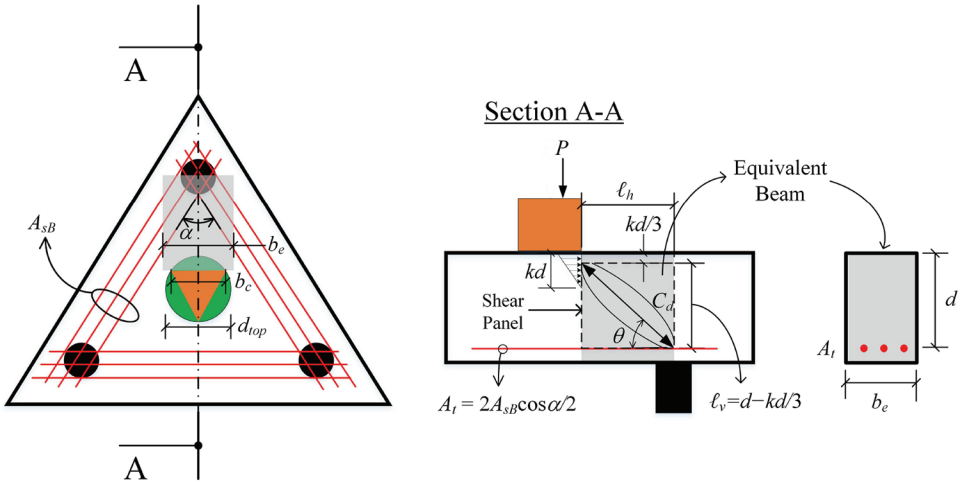

Fig. 4—SST formulation for three-pile caps.

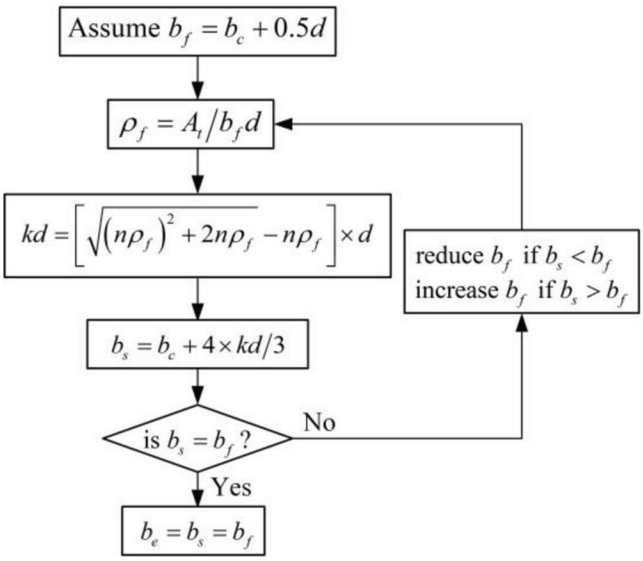

Fig. 5—Flowchart for effective loading width (b_e).

$$\zeta = 3.35/\sqrt{f_c'}\ (\text{MPa}) \text{ or } 40/\sqrt{f_c'}\ (\text{psi}) \le 0.52 \quad (13)$$

$$K = \tan^A\theta + \cot^B\theta - 1 + 0.14B \le 1.64 \quad (14)$$

where $A = 12\rho_t f_{yt}/f_c' \le 1.0$; and $B = 30\rho_t f_{yt}/f_c' \le 1.0$.

The angle of the diagonal strut θ is calculated using Eq. (15), where ℓ_h is the horizontal distance from the face of the inscribed equilateral triangle to the center of the pile, as shown in Fig. 4. It can be shown from geometry that the perpendicular distance from the center of the circle to the edge of an inscribed equilateral triangle is equal to one-fourth of the diameter. For three-way symmetric pile caps with circular columns in the current test program, ℓ_h is given by Eq. (16).

$$\theta = \tan^{-1}\ell_v/\ell_h = \tan^{-1}(d - kd/3)/\ell_h \quad (15)$$

$$\ell_h = a - b_{top}/4 \quad (16)$$

The pile cap shear capacity (P_s) is calculated by summing the vertical components of all strut capacities C_d. Due to the three-way symmetry in test specimens in this study, the capacities of all three struts are expected to be identical. Thus, the shear capacity is determined as

$$P_s = 3 \times C_d \times \sin\theta \quad (17)$$

Similarly, the flexural capacity is calculated by determining the vertical load required to generate the nominal bending moment capacity in equivalent singly reinforced beams with tension reinforcement equal to A_t.

$$P_f = 3 \times (M_n/\ell_h) \quad (18)$$

The overall capacity is then determined as the minimum of the shear and flexural capacities.

$$P_{SST} = \min(P_s, P_f) \quad (19)$$

In addition to punching capacity estimations, it is also of interest for engineers to estimate tensile strains in longitudinal bars at member capacity to check the yield condition of tension reinforcing bars. The SST model can also address this by predicting the strains in equivalent tension ties within the pile cap member at the peak load. Strain in tension ties can be estimated using Bernoulli sectional analysis of an equivalent beam with cross-sectional dimensions b_e and d for a given vertical load. The flexural moment (M_p) corresponding to vertical load P is determined through Eq. (20); this is illustrated in Fig. 6

$$M_p = (P/3) \times \ell_h \quad (20)$$

This bending moment is used to determine the strain in the tension tie using sectional analysis. This procedure can estimate strains regardless of whether the reinforcement is in an elastic or plastic state. In contrast, strain estimations given by conventional strut-and-tie models are appropriate only when the tension ties are in elastic state. The accuracy of reinforcement strain predictions at estimated capacities is

Table 2—Comparison of estimated pile cap capacities

	SST							ACI 318-19 Sectional			JSCE 2012 Sectional			ACI 318-19 Strut-and-tie			
Label	kd, mm	b_e, mm	λ_p	P_{SST} (no SE), kN	P_u/P_{SST} (no SE)	P_{SST}, kN	P_u/P_{SST}	λ_s	P_{ACISec}, kN	P_u/P_{ACISec}	β_d	$P_{JSCESec}$, kN	$P_u/P_{JSCESec}$	P_{ACIST} (no SE), kN	P_u/P_{ACIST} (no SE)	P_{ACIST}, kN	P_u/P_{ACIST}
S3a	106	314	1.00	1583	1.03	1583	1.03	1.00	761	2.14	1.41	1104	1.47	674	2.41	674	2.41
S3b					1.08		1.08			2.25			1.55		2.54		2.54
S3c					0.99		0.99			2.06			1.42		2.33		2.33
M3a	210	626	0.87	6424	0.89	5612	1.01	0.82	2549	2.23	1.19	3810	1.49	2836	2.01	2316	2.46
M3b					0.95		1.09			2.39			1.60		2.15		2.64
M3c					0.90		1.03			2.27			1.52		2.04		2.50
L3a	431	1267	0.74	23,155	0.91	17,060	1.23	0.63	7242	2.90	1.00	11,749	1.79	9536	2.20	6031	3.48
L3b	420	1253		25,638	0.91	18,891	1.24		7867	2.97		12,763	1.83	11,254	2.08	7118	3.29
L3H	401	1227		27,813	0.95	20,493	1.29		9089	2.91		14,746	1.79	15,022	1.76	9501	2.78
S1	73	270	1.00	961	1.20	961	1.20	1.00	761	1.52	1.41	848	1.36	674	1.72	674	1.72
M1	144	539	0.87	3894	0.98	3402	1.12	0.82	2549	1.50	1.19	2926	1.31	2836	1.35	2316	1.65
L1	288	1077	0.74	15,638	1.05	11,522	1.43	0.63	7956	2.07	1.00	9913	1.66	11,510	1.43	7280	2.26
AVG					0.99		1.15			2.27			1.57		2.00		2.51
CoV					0.09		0.11			0.20			0.11		0.18		0.20

Note: All 12 specimens were predicted to fail in shear using all four approaches outlined in this paper. Therefore, ACI 318-19 (both sectional and strut-and-tie) and JSCE 2012 sectional estimates included respective size effect (SE) factors. SST estimates, on the other hand, use proposed size effect factor p. In ACI strut-and-tie approach, area of strut A_{str} was calculated as $\sqrt{2} \times 0.25\pi b_{bot}^2$ toward bottom end of strut; 1 mm = 0.039 in.; 1 kN = 0.225 kip.

studied by comparing them to the observed strain at the peak load for all specimens. These comparisons for the current set of pile cap test specimens are presented in subsequent sections.

CAPACITY ESTIMATES FOR CURRENT TEST SPECIMENS

Capacity estimations for the test specimens using the aforementioned analytical method are presented in this section. The accuracy of the SST model is verified by comparing these estimates with the measured capacities of 12 test specimens. In addition, code-estimated capacities using ACI 318-19 and JSCE 2012 standards including their respective size effect provisions are presented. All estimated capacities and measured-to-estimated capacity ratios are listed in Table 2. Comparative discussions of the accuracy of pile cap capacity estimations using the four methods—proposed analytical method, ACI 318-19 sectional method, JSCE 2012 sectional method, and ACI 318-19 strut-and-tie method—are also presented.

Proposed analytical method (SST)

Measured-to-calculated capacity ratios (P_u/P_{SST}) for all 12 pile caps following the SST procedure described previously are outlined in Table 2. The estimates indicate that the analytical model is slightly unconservative for medium and large specimens, with an overall average capacity ratio of 0.99 and a coefficient of variation (CoV) of 9%. This slight overestimation, especially in medium and large specimens, can be attributed to size effect, emphasizing the need to include size effect for shear capacity estimations using the SST model. Accordingly, the authors introduced the proposed size effect factor λ_p as a multiplier to Eq. (17) for shear capacity calculations using the SST model. With inclusion of size effect, the resulting SST estimates are reasonably conservative with an average capacity ratio of 1.15 (CoV 11%). The capacity ratios with and without size effect inclusion are compared in Fig. 7. The comparison shows that with the inclusion of size effect in shear, the SST model provides reasonable accuracy and conservatism for the tested specimens. Hereon, the SST results discussed in this manuscript are with size effect inclusion unless explicitly stated otherwise.

Across all size groups, the larger capacities observed in three-layered pile caps versus one-layered pile caps are well-captured using the SST method. The increase in capacity with an increase in tension reinforcement area is captured in the SST method through the estimation of kd using Eq. (11), resulting in a larger neutral axis depth and greater strut area. As a result, the SST estimates are more consistent and accurate over different size groups in comparison with design methods as highlighted in Fig. 8. Comparative discussions based on the capacity ratios of SST, ACI 318-19, and JSCE 2012 methods are followed.

ACI 318-19 sectional method

Capacity estimates using ACI 318-19 two-way shear provisions using Eq. (2) were calculated for the 12 pile caps tested in this program. On average, the one-way shear estimates for the current test specimens were more severely underestimated as compared with the two-way shear estimates by a factor of 2. Notwithstanding, ACI one-way shear estimates are excluded from this manuscript as the pile caps predominantly exhibit two-way shear behavior, and thus, two-way shear provisions are more relevant. The ACI

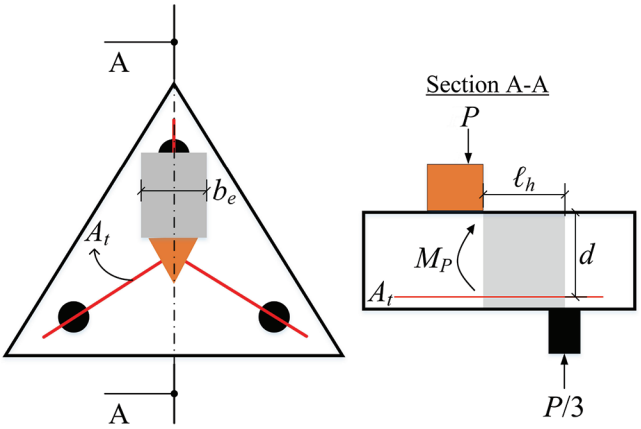

Fig. 6—Flexural moment on equivalent beam.

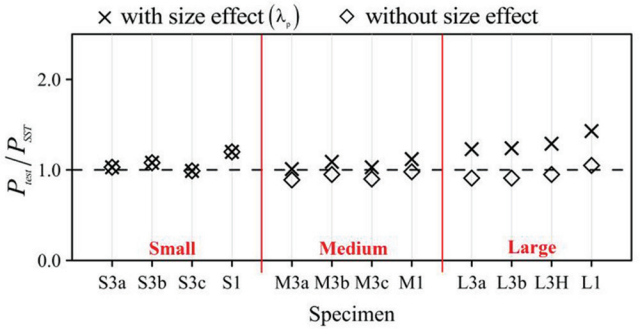

Fig. 7—Capacity estimations using SST model with and without size effect.

two-way shear estimates were conservative with an overall mean capacity ratio of 2.27 and a CoV of 20%. It should be noted that Eq. (2) already includes the ACI-specified size effect factor given by Eq. (3). Capacity of the largest specimens was severely underestimated by this approach, with mean test-to-estimated capacity ratios of 2.93 and 2.07 for three-layer and one-layer reinforced large specimens, respectively. A clear trend of increasing capacity ratios with size indicates current ACI 318-19 provisions for size effect underestimate the capacity for very large specimens loaded in two-way shear. For large specimens commonly encountered in practice, this severe strength underestimation can have tremendous cost implications. The proposed size-effect expression (Eq. (9)) can address this problem to some extent and improve the design of deep elements loaded in two-way shear, at least until more data at a large scale is available.

Furthermore, improvements in observed capacities with an increase in tension reinforcement within each size group are not captured using the current ACI two-way shear approach as Eq. (2) does not consider reinforcement ratio as one-way shear does. As a result, the ACI sectional capacity ratios are relatively higher (more conservative) in three-layer reinforced specimens as compared with the one-layer reinforced specimen within each size group. Therefore, it is recommended that a suitable factor for reinforcement ratio be included in the ACI two-way shear estimations. Analysis based on current test specimens indicates that a factor proportional to $\rho^{1/3}$ as in ACI one-way shear is appropriate for two-way shear.[11] This suggestion to include a

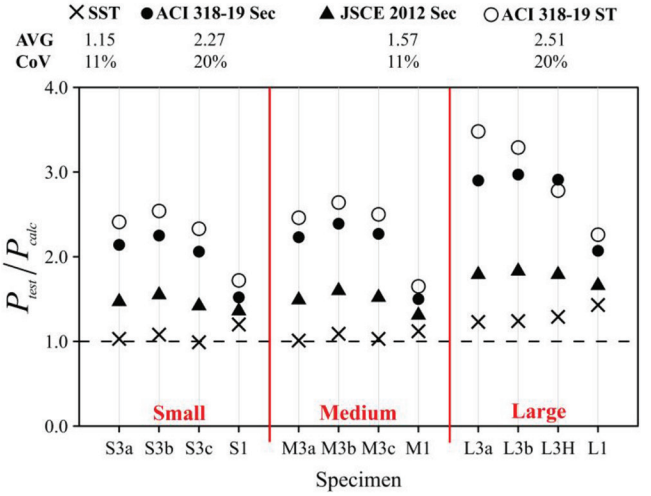

Fig. 8—Test-to-calculated capacity ratios for test specimens.

reinforcement factor of $(100\rho)^{1/3}$ for ACI two-way shear strength is also consistent with a recent study based on the analysis of 224 RC flat plates without shear reinforcement.[26]

JSCE 2012 sectional method

JSCE 2012 capacity estimates calculated using Eq. (4) fared better than ACI 318 sectional estimates for the specimens in this test program, with a mean capacity ratio of 1.57 (CoV of 11%). The differences between estimates for three-layer and one-layer specimens within each group are reduced as compared with the ACI 318-19 estimates. This can be attributed partly to the inclusion of an empirical factor β_p given by Eq. (4), which is proportional to $\rho^{1/2}$ for capturing the effect of tension reinforcement. In terms of size effect, capacity estimates were still over-conservative for medium and large specimens when compared with small specimens, indicating that the Japanese size effect provisions, similar to ACI size effect provisions, may be over-conservative for very deep members.

ACI 318-19 strut-and-tie method

The ACI 318-19 strut-and-tie method severely underestimated the capacities of the test specimens with an overall mean capacity ratio of 2.51 and CoV of 20%. This is despite the expected arch action in test specimens with low span-depth ratios. The ACI recommended size effect factor given by Eq. (3) was used for strut-and-tie estimations when the strength was controlled by strut failure. If such a size effect is not considered, the average improves to 2.00 (18%) as shown in Table 2. Although ACI does not explicitly prescribe size effect for the strut-and-tie model, as the current test specimens are predominantly shear dominant and the remaining three approaches compared include size effect, the ACI size effect is included for strut-and-tie calculations in this paper. The strut-and-tie capacity estimation in all 12 specimens was controlled by shear—that is, concrete crushing in the strut before tension tie yielding. Similar to the ACI 318-19 sectional method, the estimations for three-layer specimens were underestimated more severely than the one-layer specimen in all size groups. This is consistent with previous studies reporting more conservative strut-and-tie predictions

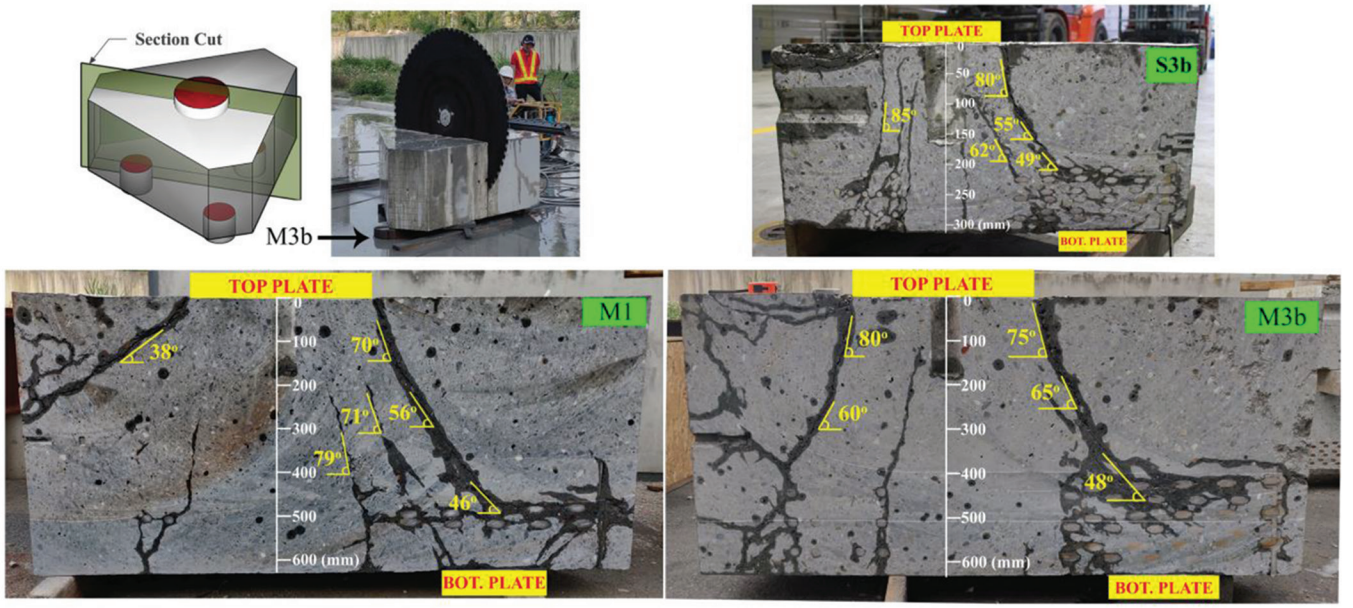

Fig. 9—Internal cracking in pile cap specimens. (Note: All units are in mm; 1 in. = 25.4 mm.)

in shear-dominant members with increased tension reinforcement areas.[12,14] Due to lack of tension reinforcing bar influence on two-way shear strength, the ACI-predicted shear capacity estimates for three- and one-layer specimens in small and medium size groups were identical.

Although the difference in f_c' within large specimens produced slight variation in shear capacity, the inability to capture the benefit to shear capacity with added tension reinforcement is apparent. Strikingly, this has also resulted in the strut-and-tie estimated capacity of L1 being higher than L3a and L3b, whereas the measured capacities of L1 were lower than L3a and L3b by 21% and 30%, respectively (refer to Table 2). This is overcome in the proposed analytical method as the influence of tension reinforcement is considered through the calculation of A_{str} as a function of kd. Consequently, the proposed method accurately captured the influence of tension reinforcement in the current test program with symmetric pile caps. A relevant study with pile caps comprising different span-depth ratios and pile configurations showed that the effects of tension reinforcement in bunched or distributed forms can be accounted for through the SST method.[13]

Further comments related to the strut behavior can be made through the sectional cuts of S3b, M1, and M3b as shown in Fig. 9. In all three sections, the most prominent crack originated from the edge of the top plate, with the region directly underneath the top plate showing no observable concrete cracking or crushing. The preservation of the region directly underneath the top plate could be attributed to beneficial confinement from triaxial compressive stresses improving the strength of concrete in this region significantly. Thus, it is reasonable to conclude that the failure of pile caps was caused by the crushing of the concrete near the periphery of the top plate and not by crushing in the region directly underneath the top plate. It can also be seen that no significant cracking is evident near the bottom plate, emphasizing that the crushing of diagonal struts resisting the applied load did not occur near the bottom end of the strut in these specimens. These observations are consistent with the proposed SST method where the strut area is calculated as a function of neutral axis depth estimated near the edge of the column.

Variation of code capacity estimates

Further comparisons of code provisions are carried out by plotting the variation of respective capacity estimates with tension reinforcement and concrete strength. Such a comparison for the four approaches outlined in this paper—that is, SST, ACI 318-19 Sectional, JSCE 2012 Sectional, and ACI 318-19 Strut-and-tie methods—is presented in Fig. 10. All four methods for comparison include respective size effect factors. The variation in tension reinforcement is represented through the number of layers of tension reinforcement with all other parameters held constant. The geometric and material parameters for small and medium pile caps in the current test program were used for Fig. 10(a) and (b), respectively. The effect of concrete strength on the estimated pile cap capacity is plotted in Fig. 10(c) with all other parameters held constant. Geometric details of three-layered large pile caps from the current test program were chosen for this exercise.

Comparisons through Fig. 10(a) and (b) show that SST model predictions can result in a nonlinear increase in capacity estimations with added tension reinforcement. The estimated magnitude of this increase in capacity is also accurate as compared with the measured capacities of small and medium specimens. Estimates using JSCE provisions also increased in a nonlinear fashion with tension reinforcement area through the factor β_p, as discussed previously. However, there is still a significant shortfall in the predicted versus observed capacities of the three-layer specimens in both small and medium size groups. Both ACI sectional and strut-and-tie capacities increased with tension reinforcement only when the controlling mode of failure is flexure. Shear

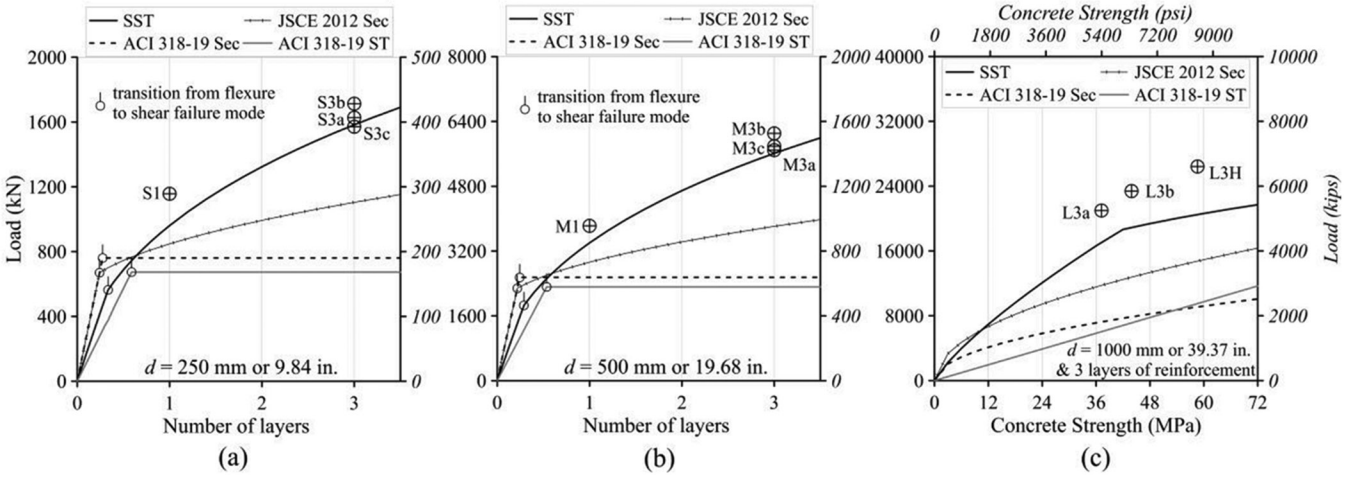

Fig. 10—Comparison of capacity estimates in: (a) small; (b) medium; and (c) large specimens.

capacity estimations for these methods do not include any parameter related to tension reinforcement. Consequently, these two methods exhibited no further increase in pile cap capacity, with reinforcement area resulting in the most severe underestimation for three-layer specimens in the current study.

Comparisons through Fig. 10(c) also show that all four methods exhibit an increase in estimated capacity with greater concrete strength. While ACI and JSCE sectional capacities are proportional to the square root of the concrete strength, the ACI strut-and-tie capacities exhibit a linear proportionality with concrete strength. The SST predictions, on the other hand, are influenced by concrete strength in three ways:

1. Concrete strength f_c' in Eq. (12) for the capacity of the strut;

2. Softening factor ζ given by Eq. (13), which is inversely proportional to the square root of the concrete strength with an upper limit of 0.52 that is effective when concrete strength is below 42 MPa (6100 psi); and

3. Neutral axis depth kd given by Eq. (11), which decreases with an increase in concrete strength, ultimately affecting both area and inclination of the diagonal strut through Eq. (10) and (15), respectively.

Finally, the observed increase in capacity with concrete strength is well replicated through the SST method showing that the effect of concrete strength on pile cap capacity is well captured. Although a minor trend of increasing capacities with concrete strength can be observed using the remaining methods, the underestimation is generally severe across all ranges of concrete strength. This can be attributed to the respective size effect considerations as well as their general inability to capture the effect of tension reinforcement.

To summarize, the proposed expression for size effect provided better estimates of strength than both ACI 318-19 and JSCE 2012, as highlighted in Fig. 3 and 8. However, the authors acknowledge and emphasize that more controlled studies on two-way members are needed, especially at large sizes (d > 600 mm [24 in.]), to further validate the proposed expression in determining the influence of size effect in two-way shear elements. In addition to size effect, the proposed analytical method can also address the benefit in shear strength associated with an increase in tension reinforcement, which is not captured through either the ACI sectional or strut-and-tie approaches.

STRAIN ESTIMATION AT CAPACITY FOR CURRENT TEST SPECIMENS

As discussed previously, the strains in tension ties were calculated by considering the flexural behavior in an equivalent beam with an effective width equal to b_e and spanning from the edge of the column to the center of the pile. The accuracy of this simplification can be assessed by comparing strains in tensile reinforcement with the average values of measured strain gauges at peak load. Both measured and calculated strains are presented in Table 3. The comparison shows that the estimated strains are reasonably close to measured strains in all specimens with an overall mean measured-to-calculated strain ratio of 1.10 and a low CoV of 11%. The larger measured strains in one-layered specimens compared to three-layered reinforced specimens are also captured in SST estimates. The overall accurate capacity and strain estimations show that b_e calculated by considering consistent shear and flexural interactions is reasonable for these pile caps.

MODEL EVALUATION AGAINST THREE-PILE CAPS WITH OTHER PARAMETERS

The parametric variations in the current experimental plan are limited to size and tension reinforcement ratio. To study more general applicability, the proposed model needs to be evaluated against results from tests where other parameters were varied. The authors selected another recent study in which three-pile cap specimens were tested monotonically to failure.[4] The main focus of the prior study was to investigate the influence of a/d and secondary reinforcement (in the form of distributed horizontal and transverse vertical reinforcement). Nine specimens were divided into three groups labeled A, B, and C for pile cap thicknesses of 250, 350, and 450 mm (10, 14, and 18 in.), respectively. The a/d of pile caps was constant within each group, but secondary reinforcement was varied: one pile cap had only longitudinal reinforcement, another had added horizontal distributed reinforcement, and the third had both added horizontal

Table 3—Estimation of strains in test specimens

Label	d, mm	A_t, mm^2	$\varepsilon_{s,test}^*$ ($\times 10^{-6}$)	$\varepsilon_{s,SST}$ ($\times 10^{-6}$)	$EPS_{s,test}$/ $EPS_{s,SST}$
S3a	250	1851	1320	1330	0.99
S3b			1490	1330	1.12
S3c			1600	1330	1.20
M3a	500	7405	1300	1350	0.96
M3b			1380	1350	1.02
M3c			1510	1350	1.12
L3a	1000	29,620	1100	1220	0.90
L3b			1800	1340	1.34
L3H			1430	1450	0.99
S1	250	617	2770	2300	1.20
M1	500	2468	2580	2330	1.11
L1	1000	9873	2810	2340	1.20
					AVG: 1.10 CoV: 0.11

*Average of measured strains from strain gauges on tension reinforcing bars at peak experimental load (rounded to nearest multiple of 10).

distributed and vertical transverse reinforcement. The longitudinal reinforcement, distributed horizontal reinforcement, and vertical transverse reinforcement areas in nine specimens are listed under A_{sB}, A_{sH}, and A_{sV}, respectively, in Table 4. Readers are recommended to refer to the original study for more details of the test plan.[4]

It was reported that the parametric variations resulted in significant behavior and capacity differences in pile caps. Specifically, a noticeable improvement in the capacity of pile caps was observed as a/d was reduced. Furthermore, within each group, the inclusion of secondary reinforcement was associated with increased capacity of pile caps. The capacity of pile caps with both horizontal distributed reinforcement and vertical transverse reinforcement was observed to be the highest within each group, indicating that the transverse reinforcement could have a beneficial effect on improving the pile cap capacity. Although effective depth varied among the test specimens, size effect can be considered negligible as this variation was only from 200 mm (7.9 in.) in A-series to 400 mm (15.7 in.) in C-series. However, the observed capacity variations associated with the inclusion of secondary reinforcement (both horizontal and vertical) and change in a/d were quite significant. For instance, within A-series, the addition of horizontal secondary reinforcement resulted in a 20% increase in capacity, whereas, the addition of both horizontal and transverse secondary reinforcement resulted in a 22% increase in capacity. The accuracy of the SST model can be evaluated by how well such variations are replicated in model estimates. Thus, the estimated capacities of these nine three-pile caps using the procedure outlined in this manuscript were calculated and compared with the observed peak loads. Additionally, in relation to strain estimations, vertical loads corresponding to the initial yielding of longitudinal reinforcement were estimated and compared with observed yield loads. Observed and estimated peak and yield loads for all nine pile caps are summarized in Table 4.

The capacity estimates of nine specimens show that the SST approach is reasonable and accurate with a mean measured-to-estimated capacity ratio of 1.22 and a CoV of 7%. The SST method was able to capture the increase in capacity associated with: a) reduction of a/d; b) addition of secondary horizontal reinforcement; and c) addition of vertical transverse reinforcement. The influence of the a/d was captured primarily through the strut inclination angle θ given by Eq. (15). The addition of horizontal reinforcement increases the effective tie area (A_t), which subsequently increases the neutral axis depth through Eq. (11), the strut area through Eq. (10), and the associated capacity. The effect of the addition of transverse reinforcement is also captured by the SST model through K defined as Eq. (14). As discussed previously, the presence of transverse reinforcement supporting the strut is reflected in the associated values of K greater than 1.0. Parameters A_t and K for the nine specimens are also listed in Table 4.

Furthermore, as the goal of that study was to investigate the influence of reinforcement, all specimens were designed such that yielding in longitudinal reinforcement was expected before failure. The experimental results indicated that all the specimens experienced yielding in tension reinforcement well before their respective capacities. This highlights that the pile cap capacity was not limited by the yielding of tension reinforcing bars, which is contrary to the philosophy of the ACI strut-and-tie model that limits the capacity to a load corresponding to the yielding of tension ties.

The SST analytical model can be used to estimate the yield load as the vertical load corresponding to the generation of yield moment in the equivalent beam highlighted in Fig. 6. Comparisons from Table 4 show that the yield load estimations through the proposed analytical model are also very reasonable with an overall mean measured-to-estimated yield load ratio of 0.89 (CoV of 12%). The yield load was slightly overestimated for A-series pile caps with an a/d of 1.68. The estimation of yield load is more accurate for B- and C-series pile caps with lower a/d. The capacity estimates, however, are accurate for all the pile caps including the A-series. This shows that the proposed method can capture the additional resistance offered by pile caps beyond the reinforcement tie yielding, a phenomenon that cannot be addressed by conventional strut-and-tie models, which is of great significance in pile caps with low tensile reinforcement ratios.

CONCLUSIONS

The effect of size on pile caps which are two-way shear members is studied through an experimental plan including 12 three-pile caps of three different sizes with reinforcement varied within each size group. Experimental evidence showed the presence of size effect in two-way shear through a reduction in normalized strength with size. Comparison with ACI 318-19 and JSCE 2012 provisions highlighted that current size effect provisions are over-conservative for very deep members of this test program loaded in two-way shear. Based on the limited experimental evidence from this

Table 4—SST model performance on pile caps reported by Miguel-Tortola et al.[4]

Label	f_c', MPa	d, mm	a/d	A_{sB}, mm^2	A_{sH}, mm^2	A_{sV}, mm^2	A_t, mm^2	kd, mm	b_e, mm	K^*	P_u, kN	$P_{SST}^\dagger$, kN	P_u/P_{SST}	$P_{y,test}$, kN	$P_{y,SST}$, kN	$P_{y,test}/P_{y,SST}$
3P-N-A1	23.3	250	1.68	452	—	—	784	74	316	1.00	445	381^S	1.17	395	518	0.76
3P-N-A2	22.8	250	1.68	452	236	—	862	77	319	1.00	534	392^S	1.36	433	558	0.78
3P-N-A2	23.7	250	1.68	452	236	302	862	76	319	1.23	573	494^S	1.16	433	562	0.77
3P-N-B1	24.7	350	1.12	305	—	—	528	79	322	1.00	660	535^S	1.23	586	572	1.02
3P-N-B2	26.3	350	1.12	305	151	—	578	81	324	1.00	709	586^S	1.21	553	626	0.88
3P-N-B3	26.5	350	1.12	305	151	302	578	80	324	1.10	713	639^F	1.12	567	626	0.91
3P-N-C1	24.0	450	0.84	236	—	—	408	83	327	1.00	800	615^F	1.30	602	596	1.01
3P-N-C2	26.4	450	0.84	236	151	—	458	85	330	1.00	796	691^F	1.15	593	669	0.89
3P-N-C3	28.5	450	0.84	236	151	302	458	84	328	1.06	910	693^F	1.31	689	669	1.03
AVG CoV	—	—	—	—	—	—	—	—	—	—	—	—	1.22 0.07	—	—	0.89 0.12

*Only stirrups that fall in loading path/strut are effective in strengthening strut. Thus, only two vertical legs of stirrups are considered for calculation of K using Eq. (14), where $\rho_t = (A_{sV}/3)/(b_e d)$.

†Shear and flexural failure modes are indicated through superscripts S and F, respectively.

Note: 1 mm = 0.039 in.; 1 mm^2 = 0.00155 in.^{2}; 1 MPa = 145 psi; 1 kN = 0.225 kip.

study, a new expression for the size effect factor for two-way shear is proposed to address this over-conservatism at large depths. More controlled studies are recommended to further understand the size effect phenomenon in two-way shear and validate the proposed expression.

Finally, the pile cap capacities estimated using ACI 318-19 and JSCE 2012 recommendations, as well as the softened strut-and-tie model (SST), were compared. Comparisons with test data showed that the SST model supplemented by the proposed size effect factor provided reasonable and safe estimates, with an average measured-to-estimated capacity ratio of 1.15 and coefficient of variation (CoV) of 11%. In contrast, ACI 318-19 and JSCE 2012 sectional provisions tended to underestimate strength, with mean capacity ratios of 2.27 (20%) and 1.57 (11%), respectively. Furthermore, the ACI 318-19 strut-and-tie model also underestimated the capacities with an overall mean ratio of 2.51 (20%) for 12 test specimens.

The accuracy of the SST model was further reinforced by comparisons with results from nine three-pile caps reported by Miguel-Tortola et al.,[4] who varied span-depth ratio (a/d) and secondary reinforcement. For these tests, the average measured-to-estimated capacity ratio was 1.22 with a CoV of 7%. Overall, results indicate that the SST model is effective in capturing capacity variations associated with changes in several key parameters such as a/d, longitudinal reinforcement ratio, and presence of stirrups.

AUTHOR BIOS

Srinivas Mogili *is an Assistant Professor at the Indian Institute of Technology, Delhi, India, and formerly a Postdoctoral Researcher at National Taiwan University, Taipei, Taiwan. He received his PhD from the Hong Kong University of Science and Technology, Clear Water Bay, Hong Kong. His research interests include the seismic design, analysis, and testing of reinforced concrete members.*

Shyh-Jiann Hwang, *FACI, is a Professor of civil engineering at the National Taiwan University. He received his PhD from the University of California, Berkeley, Berkeley, CA. His research interests include seismic behavior of reinforced concrete members and seismic retrofitting of reinforced concrete structures.*

Kuang-Yen Liu *is an Associate Professor at the National Cheng Kung University, Tainan, Taiwan. He received his PhD from National Taiwan University. His research interests include seismic design, assessment, and retrofit of reinforced concrete buildings and bridge structures.*

Toshikatsu Ichinose *is a Professor at Meijo University, Nagoya, Japan, and a Professor Emeritus at Nagoya Institute of Technology, Nagoya, Japan. He received his doctoral degree from the University of Tokyo, Tokyo, Japan. His research interests include seismic behavior and retrofit of reinforced concrete structures.*

Lucas Laughery *is a Senior Engineer at Exponent in Austin, TX. He received his PhD from Purdue University, West Lafayette, IN. He is a member of ACI Committee 133, Disaster Reconnaissance, and Joint ACI-ASCE Subcommittee 445-B, Seismic Shear. His research interests include design of structures for extreme environments and large-scale testing.*

Kazuhiko Kasai *is a Professor Emeritus at the Tokyo Institute of Technology, Tokyo, Japan. He received his PhD from the University of California, Berkeley. His research interests include large-scale structural testing, seismic design and analysis, steel structures, passive control systems, and base isolation systems.*

ACKNOWLEDGMENTS

The experimental research work was conducted collaboratively by Tokyo Institute of Technology (Tokyo Tech.) in Japan, Nagoya Institute of Technology in Japan, and National Center for Research on Earthquake Engineering (NCREE) in Taiwan. It was financially supported by NCREE and Kasai Laboratory (under the sponsorship of KYB Corp., SWCC Corp., Japan Iron and Steel Federation, Bridgestone Corp., and OILES Corp.) of Tokyo Tech. The reinforcing bars and anchor devices were provided by Kyoei-Seiko Corp. and Tokyo Tekko Corp. in Japan. Special thanks are given to C.-C. Lin, NCREE engineer who contributed in conducting tests. We also thank K.-Y. Liu and Y. Nakagami—former master's students from National Cheng Kung University in Taiwan and Nagoya Institute of Technology, respectively, for their excellent work of test preparation and data analysis.

NOTATION

A_{cs} = area of concrete strut in ACI 318-19 strut-and-tie method
A_s = total area of tension reinforcement in test specimens
A_{sB} = total area of bunched longitudinal tension reinforcement
A_{sH} = total area of horizontal transverse reinforcement
A_{str} = area of concrete strut in SST method
A_{sV} = total area of vertical (stirrup) transverse reinforcement
A_t = equivalent area of tension tie reinforcement in SST method
A_{ts} = area of tension tie reinforcement in ACI 318-19 strut-and-tie method
a = shear span length measured from column to pile centers

b_{bot} = diameter of bottom reaction plate in test specimens
b_c = dimension of column side perpendicular to the concerned concrete strut
b_e = effective loading width in SST method
b_f = flexural width in SST method
b_o = perimeter of two-way critical section as per ACI 318-19
b_s = shear width in SST method
b_{top} = diameter of top loading plate in test specimens
b_w = geometric width of pile cap at one-way critical section
b_w' = effective width of shear member as per JSCE 2012
C_d = compression capacity of concrete strut in SST method
d = effective depth of centroid of tension reinforcement from the compression face
F_{ns} = concrete strut capacity using ACI 318-19 strut-and-tie method
F_{nt} = tension tie capacity using ACI 318-19 strut-and-tie method
f_c' = concrete compressive strength measured using standard cylinders
f_{dd} = concrete strength factor in JSCE 2012
f_y = yield strength of longitudinal tension reinforcement
f_{yt} = yield strength of transverse reinforcement
H = geometric thickness of pile cap member
K = strut-and-tie index in SST method
kd = elastic neutral axis depth in flexure
ℓ_h = perpendicular distance between column side and the nearest support
ℓ_v = vertical distance between centroids of tension reinforcement and flexural compression
M_n = nominal bending moment capacity corresponding to a compression strain of 0.003 in extreme compression fiber
M_p = bending moment corresponding to a vertical load of P in pile caps
n = ratio of steel and concrete elastic moduli
P_{ACISec} = load capacity estimated using ACI 318-19 sectional method
P_{ACIST} = load capacity estimated using ACI 318-19 strut-and-tie method
$P_{JSCESec}$ = load capacity estimated using JSCE 2012 sectional method
P_f = flexural load capacity per SST method
P_{SST} = overall punching load capacity estimated using SST method
P_s = shear load capacity per SST method
P_u = peak observed punching load capacity of test specimens
$P_{y,SST}$ = SST estimated vertical load corresponding to yield moment in equivalent beams
$P_{y,test}$ = experimental load corresponding to first yielding in tension reinforcement
V_{dd} = shear compression capacity given by JSCE 2012
V_{1w} = one-way shear capacity estimated by ACI 318-19 sectional method
V_{2w} = two-way shear capacity estimated by ACI 318-19 sectional method
v = two-way shear strength calculated on ACI critical section
β_a = slenderness factor in JSCE 2012 derived from span-depth ratio
β_c = strut confinement factor in ACI 318-19 strut-and-tie method
β_d = size effect factor as given by JSCE 2012
β_p = reinforcement factor in JSCE 2012 derived from tension reinforcement ratio
β_s = strut strength coefficient in ACI 318-19 strut-and-tie method
$\varepsilon_{s,SST}$ = estimated strains at predicted load capacities using SST method
$\varepsilon_{s,test}$ = average of the observed strains in tension bars at peak experimental load
λ_p = proposed size effect factor in this paper
λ_s = size effect factor in ACI 318-19
θ = inclination of concrete strut with the horizontal plane
ρ = tension reinforcement ratio
ρ_f = equivalent tension tie reinforcement ratio given by $A_t/b_e d$
ρ_t = transverse reinforcement ratio
ζ = softening factor for concrete compression strut in SST method

REFERENCES

1. Sabnis, G. M., and Gogate, A. B., "Investigation of Thick Slab (Pile Cap) Behavior," *ACI Journal Proceedings*, V. 81, No. 1, Jan.-Feb. 1984, pp. 35-39.

2. Clarke, J. L., "Behaviour and Design of Pile Caps with Four Piles," Report No. 42.489, Cement and Concrete Association, London, UK, 1973, 19 pp.

3. Adebar, P.; Kuchma, D.; and Collins, M. P., "Strut-and-Tie Models for the Design of Pile Caps: An Experimental Study," *ACI Structural Journal*, V. 87, No. 1, Jan.-Feb. 1990, pp. 81-92.

4. Miguel-Tortola, L.; Pallarés, L.; and Miguel, P. F., "Punching Shear Failure in Three-Pile Caps: Influence of the Shear Span-Depth Ratio and Secondary Reinforcement," *Engineering Structures*, V. 155, 2018, pp. 127-143. doi: 10.1016/j.engstruct.2017.10.077

5. ACI Committee 318, "Building Code Requirements for Structural Concrete (ACI 318-19) and Commentary (ACI 318R-19) (Reapproved 2022)," American Concrete Institute, Farmington Hills, MI, 2019, 624 pp.

6. Kuchma, D. A.; Wei, S.; Sanders, D. H.; Belarbi, A.; and Novak, L. C., "Development of the One-Way Shear Design Provisions of ACI 318-19 for Reinforced Concrete," *ACI Structural Journal*, V. 116, No. 4, July 2019, doi: 10.14359/51716739

7. Bažant, Z. P.; Yu, Q.; Gerstle, W.; Hanson, J.; and Ju, J. W., "Justification of ACI 446 Code Provisions for Shear Design of Reinforced Concrete Beams," *ACI Structural Journal*, V. 104, No. 5, Sept.-Oct. 2007, pp. 601-610.

8. Bažant, Z. P., and Cao, Z., "Size Effect in Punching Shear Failure of Slabs," *ACI Structural Journal*, V. 84, No. 1, Jan.-Feb. 1987, pp. 44-53.

9. Dönmez, A., and Bažant, Z. P., "Size Effect on Punching Strength of Reinforced Concrete Slabs with and without Shear Reinforcement," *ACI Structural Journal*, V. 114, No. 4, 2017, pp. 875-886. doi: 10.14359/51689719

10. JSCE, "JSCE Standard Specifications for Concrete Structures [Design]," Japan Society of Civil Engineers, Tokyo, Japan, 2012.

11. Laughery, L.; Ichinose, T.; Kasai, K.; Mogili, S.; and Hwang, S.-J., "Experimental Investigation of Size Effect on Shear Strength of Reinforced Concrete Pile Caps," *ACI Structural Journal*, V. 121, No. 1, Jan. 2024, pp. 105-117.

12. Park, J. W.; Kuchma, D.; and Souza, R., "Strength Predictions of Pile Caps by a Strut-and-tie Model Approach," *Canadian Journal of Civil Engineering*, V. 35, No. 12, 2008, pp. 1399-1413. doi: 10.1139/L08-062

13. Mogili, S., and Hwang, S. J., "Softened Strut-and-Tie Model for Shear and Flexural Strengths of Reinforced Concrete Pile Caps," *Journal of Structural Engineering*, ASCE, V. 147, No. 11, 2021, p. 04021169. doi: 10.1061/(ASCE)ST.1943-541X.0003141

14. Adebar, P., and Zhou, L., "Design of Deep Pile Caps by Strut-and-Tie Models," *ACI Structural Journal*, V. 93, No. 4, July-Aug. 1996, pp. 437-448.

15. Hsu, T. T. C., and Zhu, R. R. H., "Softened Membrane Model for Reinforced Concrete Elements in Shear," *ACI Structural Journal*, V. 99, No. 4, July-Aug. 2002, pp. 460-469.

16. ASTM C39/C39M-14, "Standard Test Method for Compressive Strength of Cylindrical Concrete Specimens," ASTM International, West Conshohocken, PA, 2014, 7 pp.

17. Nakagami, Y., "Size Effect of Footing Under Two-Way Shear," Nagoya Institute of Technology, Nagoya, Japan, 2020.

18. Laughery, L.; Ichinose, T.; Kasai, K.; Liu, K.-Y.; Nakagami, Y.; and Matsunoshita, T., "Tests of Scaled Pile Caps Part 1 : Size Effect," 17th World Conference on Earthquake Engineering, 17WCEE, Sendai, Japan, 2020, pp. 1-10.

19. Ichinose, T.; Laughery, L.; Liu, K.-Y.; Komatsu S.; Nakagami Y.; Matsunoshita T.; and Kasai K., "Tests of Scaled Pile Caps Part 2 : Effect of Reinforcement Strain on Compressive Failure," 17th World Conference on Earthquake Engineering, 17WCEE, Sendai, Japan, 2020, pp. 1-12.

20. Kim, J. K.; Yi, S. T.; and Park, C. K., "Size Effect on Compressive Strength of Plain and Spirally Reinforced Concrete Cylinders," *ACI Structural Journal*, V. 96, No. 1, Jan.-Feb. 1999, pp. 88-94.

21. Ince, R., and Arici, E., "Size Effect in Bearing Strength of Concrete Cubes," *Construction and Building Materials*, V. 18, No. 8, 2004, pp. 603-609. doi: 10.1016/j.conbuildmat.2004.04.002

22. Mogili, S.; Hwang, S. J.; and Wu, P. W., "Estimating the Punching Shear Capacity of Reinforced Concrete Pile Caps," 17th World Conference on Earthquake Engineering, 17WCEE, Sendai, Japan, 2020, p. C002938.

23. Zhang, L. X., and Hsu, T. T. C., "Behavior and Analysis of 100 MPa Concrete Membrane Elements," *Journal of Structural Engineering*, ASCE, V. 124, No. 1, 1998, pp. 24-34. doi: 10.1061/(ASCE)0733-9445(1998)124:1(24)

24. Hwang, S. J., and Lee, H. J., "Strength Prediction for Discontinuity Regions by Softened Strut-and-Tie Model," *Journal of Structural Engineering*, ASCE, V. 128, No. 12, 2002, pp. 1519-1526. doi: 10.1061/(ASCE)0733-9445(2002)128:12(1519)

25. Hwang, S. J.; Tsai, R. J.; Lam, W. K.; and Moehle, J. P., "Simplification of Softened Strut-and-tie Model for Strength Prediction of Discontinuity Regions," *ACI Structural Journal*, V. 114, No. 5, Sept.-Oct. 2017, pp. 1239-1248. doi: 10.14359/51689787

26. Mogili, S.; Lin, H. Y.; and Hwang, S. J., "Vertical Punching Capacity of Reinforced Concrete Flat Plates without Shear Reinforcement," *ACI Structural Journal*, V. 121, No. 1, Jan. 2024, pp 171-184.

ACI STRUCTURAL JOURNAL TECHNICAL PAPER

Title No. 122-S06

Dual-Potential Capacity Model for Fiber-Reinforced Polymer-Reinforced Concrete Members Failed in Shear

by Deuckhang Lee and Min-Kook Park

Fiber-reinforced polymer (FRP) reinforcements have been used in versatile forms in recent construction practices to enhance durability performance and, consequently, to attain longevity of concrete structures. The shear strength of FRP-reinforced concrete (FRP-RC) beams holds significant importance in structural design. However, inherent analytical uncertainty exists concerning shear in concrete members due to the distinctive material characteristics of FRP bars compared to conventional steel reinforcements, such as their low axial stiffness and bond properties. This study aims to identify the shear-resistance mechanisms developed under combined actions between concrete and FRP reinforcements. To this end, the dual-potential capacity model (DPCM) was extended to FRP-RC beam members subjected to shear and flexure, and an attempt was also made to derive a simplified method. To validate the proposed approaches, a total of 437 shear test results from RC members incorporating FRP bars were used. Findings indicate that the proposed methods can provide an acceptable level of analytical accuracy. In addition, a significant shift in the shear failure mode of FRP-RC members with no stirrups was observed from the compression zone to the cracked tension zone as the FRP reinforcement ratios increased. Conversely, when FRP stirrups were added, the shear failure mode was mostly dominated by the compression zone.

Keywords: aggregate interlock; compression zone; dual-potential capacity model (DPCM); fiber-reinforced polymer (FRP); FRP bar; FRP stirrup; shear.

INTRODUCTION

Fiber-reinforced polymer (FRP) reinforcements have been used as one of the promising alternatives to improve the durability performance of reinforced concrete (RC) structures exposed to corrosive environments.[1-7] Key benefits of FRP composite materials include their light weight, high tensile strength, and excellent durability and fatigue performances. Meanwhile, their high price, low stiffness, and brittle material characteristics remain obstacles to widespread adoption in the recent construction industry. In flexural design,[1,2,6] unlike typical RC, because FRP bars exhibit linear-elastic-fracture stress-strain curves with high strength and no post-peak regime, FRP-RC members with a compression-controlled section overly reinforced in flexure (that is, a greater-than-balanced FRP reinforcement ratio, $\rho_{FRP} > \rho_b$) are treated as a slightly favorable failure mode rather than an under-reinforced design approach, and thus the higher strength reduction factor is recommended in ACI 440 design guidelines.[1] FRP-RC members with a tension-controlled section, characterized by a longitudinal reinforcement ratio ($\rho_{FRP} = A_{s,FRP}/b_w d_s$) lower than the balanced FRP reinforcement ratio (ρ_b), tend to exhibit a bit more brittle due to the non-ductile behavior of FRP bars in tension.[1,8] As a result, careful shear design becomes necessary when using FRP bars as longitudinal tension reinforcements, as the more brittle failure characteristics of FRP materials pose significant concerns compared to conventional RC members.[9-11] However, inevitable analytical uncertainty is usually involved in estimating the shear strength of concrete members.[12-22] To ensure safe design, a comprehensive understanding of the shear-resistance mechanism in FRP-RC members is essential. This understanding should encompass the unique material characteristics of FRP bars, such as their low axial stiffness and brittle nature, which directly influence the shear strength.[9,19] To examine the effect of FRP longitudinal and transverse reinforcements, existing test results of FRP-RC beams and conventional RC beams with and without shear reinforcements are directly compared against various key influential factors in Fig. 1 and 2, respectively. Note that the test results of the conventional RC members are from Lee et al.,[13,14] in which most of them were aligned with those data contained in the ACI 445 shear database,[23,24] and those of FRP-RC members are brought mostly from a well-established database attached in Appendixes B and C of Peng et al.[4] Detailed information will be presented later. For the cases with no shear reinforcement, the differences in data distributions are quite large between those two beam series (that is, FRP-RC and RC), especially in terms of the reinforcement index (that is, $\omega_s = \rho_s f_y/f_c'$ or $\rho_{FRP} f_{u,FRP}/f_c'$), where much lower normalized shear strength ($v_{test}/\sqrt{f_c'}$) was observed in FRP-RC members than in conventional RC members at the same level of the reinforcement index. In contrast, no clear difference in the distribution trend was observed against the axial stiffness ($\rho_s E_s$ or $\rho_{FRP} E_{FRP}$), member depth (that is, size effect), and shear span-depth ratio (a/d_s). Note that ρ_s and ρ_{FRP} are the tension reinforcement ratio, which can be estimated as $A_s/b_w d_s$ or $A_{s,FRP}/b_w d_s$, respectively; A_s and $A_{s,FRP}$ are the areas of conventional steel reinforcements and FRP reinforcements, respectively; a is the shear span length; b_w and d_s are the web width and effective depth of the concrete section; E_s and E_{FRP} are the elastic modulus of steel and FRP bars; f_y and $f_{u,FRP}$ are the yield strength of steel and tensile strength of FRP bars, respectively; and f_c' is the compressive strength of concrete.

ACI Structural Journal, V. 122, No. 1, January 2025.

MS No. S-2023-136.R1, doi: 10.14359/51743307, received August 27, 2023, and reviewed under Institute publication policies.

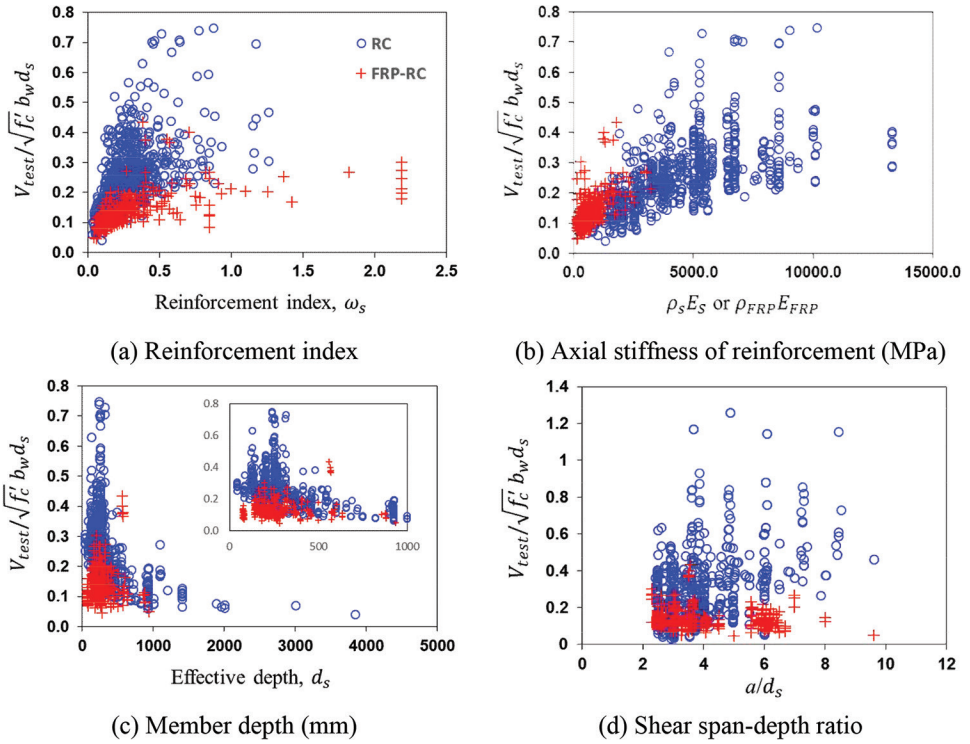

(a) Reinforcement index

(b) Axial stiffness of reinforcement (MPa)

(c) Member depth (mm)

(d) Shear span-depth ratio

Fig. 1—Comparison of shear test results of FRP-RC and RC members with no stirrups. (Note: 1 mm = 0.0394 in.; 1 MPa = 0.145 ksi.)

For the cases with shear reinforcements, where all the FRP-RC beams are reinforced in shear by using FRP stirrups, no sensitive trend was observed overall against the reinforcement index (ω_s), member depth (d_s), and shear span-depth ratio (a/d_s). However, as shown in Fig. 2(b) and (d), it appeared that the shear strengths are very different from each other, in accordance with the axial stiffness ($\rho_s E_s$ or $\rho_{FRP} E_{FRP}$) and shear reinforcement index ($\rho_v f_{vy}/f_c'$ or $\rho_{v,FRP} f_{vu,FRP}/f_c'$), where ρ_v and $\rho_{v,FRP}$ are the shear reinforcement ratio of steel and FRP stirrups, respectively, and f_{vy} and $f_{vu,FRP}$ are the yield strength and tensile strength of steel and FRP stirrups, respectively.

Overall, similar and consistent trends in the shear strengths and the geometric properties, such as the member depth and shear span-depth ratio, were observed when comparing RC and FRP-RC members with and without stirrups failed in shear. Still, quite insistent differences existed behind the shear-transfer mechanism depending on the material properties of the reinforcements between conventional RC and FRP-RC members, such as the effect of FRP tension reinforcement with low stiffness, the shear contribution of FRP stirrups, and perhaps bond properties.[4,11] To this end, the dual-potential capacity model (DPCM), which was originally developed for shear strength estimations of conventional RC members, is extended to be suitable for analyzing FRP-RC members failed in shear, and its simplified model is also presented in the current study.

RESEARCH SIGNIFICANCE

Continuous efforts have been made to elucidate the shear-transfer mechanism in various concrete members through the application of the DPCM, including conventional RC and prestressed concrete deep and slender beams, RC members strengthened in shear with FRP composites, steel fiber-reinforced concrete (SFRC), punching shear in flat-plate slabs, and unbonded post-tensioned members.[12-22] The objective of this study is to extend the model further to estimate the shear strengths of FRP-RC beam members without shear reinforcement and those reinforced in shear using FRP stirrups. Detailed formulations are presented in this paper, and an attempt is made to simplify the iterative calculation process for improved applicability. The proposed methods incorporated typical failure modes in concrete and also accounted for the effects of the bond mechanism, typical material and dimensional properties, and FRP stirrups.

FLEXURAL ANALYSIS

Figure 3(a) shows an FRP-RC beam member and its idealized cracked element for flexural analysis. Assuming the so-called crack stabilized state,[12-20,25-27] no increase in the number of cracks is expected, after which only flexural crack widths can increase. There are various expressions to estimate the flexural crack spacing (S_{mx}), but those usually require information that is unfortunately not available in the current shear database of the FRP-RC beams presented in Table 1. For this reason, this study adopts the following simple method as much as possible, based on Collins and Mitchell[26]

$$S_{mx} = 3c_{cv} \approx 3(h - d_s) \quad (1)$$

where c_{cv} is the thickness of the concrete cover, which can be approximated as $(h - d_s)$; h is the section height; and d_s is the distance between the extreme compression fiber

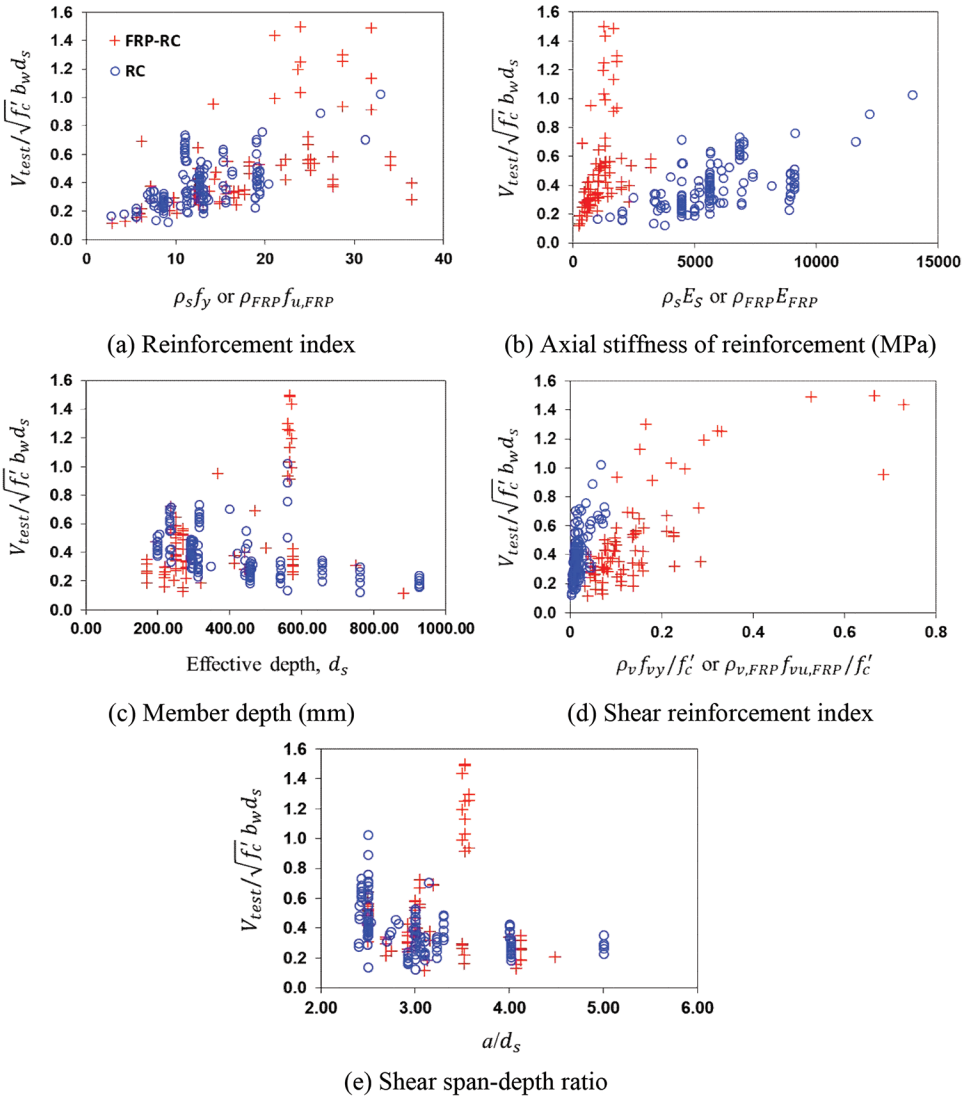

Fig. 2—Comparison of shear test results of FRP-RC and RC members with stirrups. (Note: 1 mm = 0.0394 in.; 1 MPa = 0.145 ksi.)

and centroidal axis of the longitudinal FRP bars. The fiber section approach is addressed to estimate a nonlinear flexural response of an FRP-RC section at the crack location (that is, $x = S_{mx}/2$ in Fig. 3). As presented in Fig. 3(b), the concrete strain at the extreme compression fiber of the RC section (ε_t) is chosen, and an arbitrary depth of the neutral axis (c) is assumed. Then, the linear strain profile in the concrete section can be assumed based on Bernoulli's principle, and thus, the strain in longitudinal tension reinforcements (ε_s) and the corresponding stresses can be determined. For this, the parabolic model proposed by Collins and Mitchell[26] was adopted for concrete in this study, as shown in Fig. 4(a), and the linear-elastic-brittle fracture model,[1-6,19] shown in Fig. 4(b), was adopted for FRP bars, where E_{FRP} is the elastic modulus of FRP bars. The normal compressive force of the concrete (C_c) and tensile force provided by the FRP reinforcing bar (T_s) can also be computed, respectively, where iterative calculations are essentially required by updating the neutral axis depth (c) until the sum of those normal forces satisfies the equilibrium condition in the longitudinal direction. When the convergence is obtained, a flexural response of the cracked section can be obtained at a certain strain level, and those computation processes are repeated by selecting a new concrete strain at the extreme compression fiber of the RC section (ε_t) until it reaches the maximum compressive strain of concrete ($\varepsilon_{cu} = 0.003$).[12-22] From the flexural analysis, the maximum stress in the longitudinal tension reinforcement ($f_{sx,max}$) and local stress increase (Δf_{sx}) at the crack interface of the cracked section ($x = S_{mx}/2$) for each load stage can also be determined, and this local stress is used as a key component in estimating the shear demands ($V_{ci,req}$, refer to Eq. (9a), presented later). As shown in Fig. 3(a), the bond mechanism is developed between the FRP reinforcement and surrounding concrete along the longitudinal direction,[27,28] and the tensile stress in the FRP bar subsequently increases locally at the crack surface.[1-3] The local stress increase in the longitudinal reinforcement (Δf_{sx}) between flexural cracks can be computed by taking the difference between the stress in FRP reinforcement estimated at the crack surface (that is, $f_{sx,max}$ at $x = S_{mx}/2$) and that estimated at the middle of two adjacent cracks (that is, $f_{sx,min}$ at $x = 0$), as presented in Fig. 3(a). The nonlinear distribution of

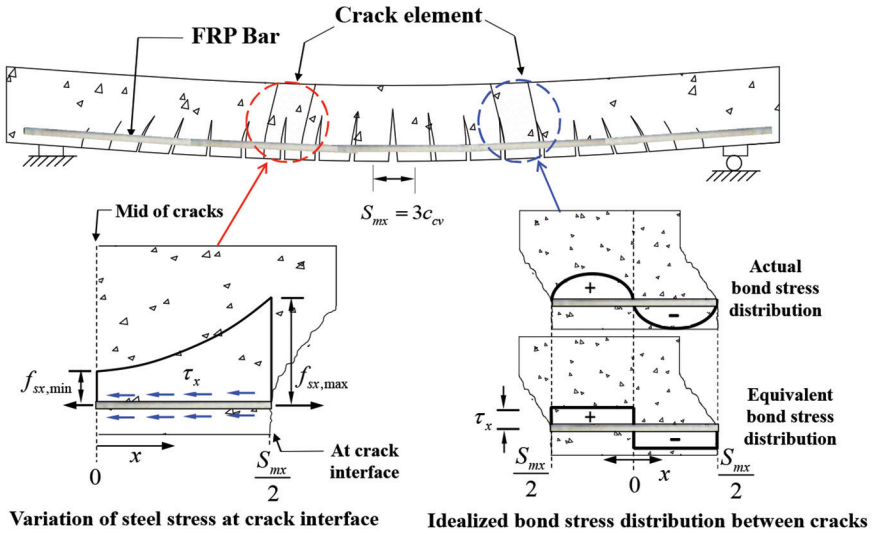

(a) Crack element and bond distribution

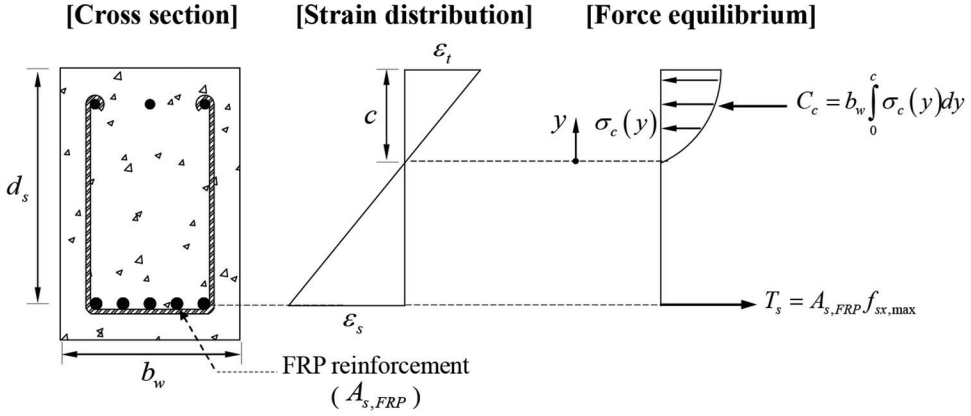

(b) Strain and stress profiles in section

Fig. 3—Flexural analysis model considering bond mechanism.

the bond stress is expected along the longitudinal direction of the tension reinforcement.[12-20] For the sake of simplicity, it was idealized as an equivalent uniform distribution (τ_x) in this study, based on previous studies.[27,29-31] Because the local stress increase in the longitudinal tension reinforcement (Δf_{sx}) is induced by the accumulated bond stress, the local stress increase of FRP bar (Δf_{sx}) can be taken as the sum of the equivalent bond stress (τ_x) as follows

$$\Delta f_{sx} = f_{sx,max} - f_{sx,min} = \frac{2\tau_x}{d_b} S_{mx} \quad (2)$$

where d_b is the diameter of the FRP bar. For the bond-slip relationship, the *fib* model is basically adopted,[25,32] but its post-peak plateau region was neglected, as presented in Fig. 4(c), to consider the splitting effect based on Jendele and Cervenka[33] as follows

$$\tau_x = \tau_{max}\left(\frac{s_x}{s_1}\right)^{0.4} \text{ (when } s_x \le s_1) \quad (3a)$$

$$\tau_x = \tau_{max} - (\tau_{max} - \tau_{min})\frac{s_x - s_2}{s_2 - s_1} \text{ (when } s_1 < s_x \le s_2) \quad (3b)$$

$$\tau_x = 0.15\tau_{max} \text{ (when } s_2 < s_x) \quad (3c)$$

where τ_{max} is the maximum bond strength between the FRP bar and surrounding concrete, which is taken as $14.7\sqrt{f_c'}/d_b$ based on Okelo and Yuan[34]; f_c' is the concrete compressive strength; and s_1 and s_2 are taken to be 0.6 mm (0.024 in.) and 1.0 mm (0.039 in.), respectively.[25,32] Relative slip between the longitudinal tension reinforcement and surrounding concrete at the crack interface (s_x), which is the main contributor to crack width, can be estimated by taking the difference between the elongation in concrete and FRP bar (that is, $e_s - e_c$) as follows

$$s_x = \frac{1}{2}(e_s - S_{mx}\varepsilon_r) = \frac{1}{2}\left(e_s - S_{mx}\frac{f_r}{E_c}\right) \quad (4a)$$

Table 1—Dimensions and material properties of collected test specimens

Reference No.	No. of specimens	d_s, mm	f_c', MPa	a/d_s	$f_{u,FRP}$, MPa	ρ_{FRP}[‡], %	$\rho_{v,FRP}$, %	Type of FRP[§]
FRP-RC test specimens with no stirrups								
2	2	104.0 to 154.0	63.2	6.5 to 9.6	692.0	0.77 to 0.95	N.A.	G
4[*]	303	73.0 to 937.0	20.0 to 102.0	2.5 to 8.0	476.0 to 2840.0	0.10 to 6.18	N.A.	CGBA
5	12	275.0 to 286.0	29.6 to 40.7	3.5 to 3.64	723.0	0.65 to 2.54	N.A.	G
6	12	196.7 to 200	13.0 to 33.5	2.3[†] to 3.0	770.0	0.30 to 0.91	N.A.	G
42	12	234.0 to 635.0	42.2 to 73.4	2.52 to 2.62	1089.0	0.71 to 2.69	N.A.	B
FRP-RC test specimens with FRP stirrups								
4[*]	84	170.0 to 883.0	20.0 to 102.0	2.5 to 4.5	476.0 to 2930.0	0.28 to 3.65	0.12 to 2.26	CGB (CGB[‖])

[*]Detailed information can be found in Appendixes B and C of Peng et al.[4]

[†]Six specimens had a/d_s less than 2.5.

[‡]Flange width was used in calculation of ρ_{FRP} for flanged sections.

[§]C is CFRP, G is GFRP, B is BFRP, and A is AFRP.

[‖]Material type of FRP stirrups (inside the bracket).

Note: 1 mm = 0.0394 in.; 1 MPa = 0.145 ksi. N.A. means data are not available.

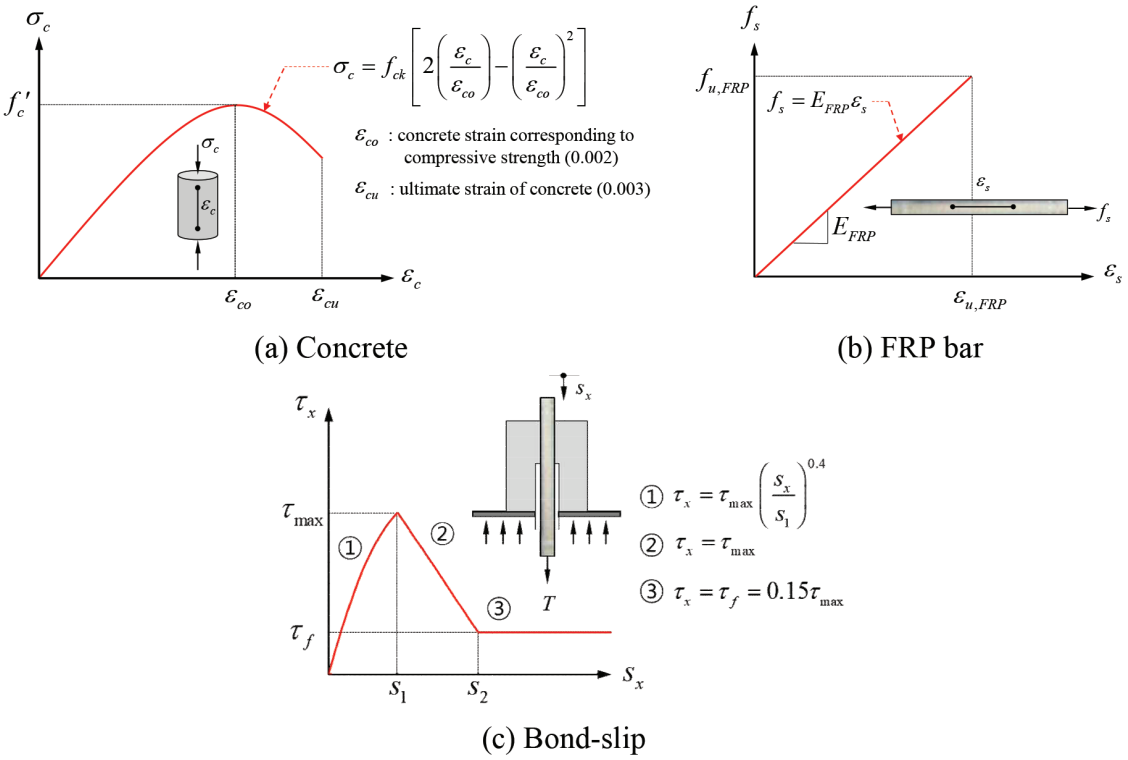

Fig. 4—Constitutive models of materials.

$$e_s = 2s_x + S_{mx}\frac{f_r}{E_c} \quad (4b)$$

where f_r and E_c are the modulus of rupture and elastic modulus of concrete, respectively, for which the material constants specified in ACI 318-19 were adopted in this study.[35] By combining Eq. (3) and (4), the elongation of longitudinal tension reinforcement (e_s) can be computed as follows

$$\tau_x = \left(f_{sx,max} - e_s\frac{E_{FRP}}{S_{mx}}\right)\frac{d_b}{S_{mx}} \quad (\text{when } f_{sx,max} \le f_{u,FRP}) \quad (5)$$

Herein, when the tensile stress in FRP bars is greater than their tensile strength (that is, $f_{sx,max} > f_{u,FRP}$), no bond failure occurs (that is, $\tau_x = 0$), and thus no local stress can be developed ($\Delta f_{sx} = 0$). Consequently, no shear demand (that is, aggregate interlock) is required in the cracked tension zone (that is, $V_{ci,req} = 0$; refer to Fig. 5 and Eq. (9), presented later), and the shear force estimated at the flexural strength calculated by using the tensile strength of FRP bars was taken as the shear strength of an FRP-RC member. Iterative calculations can be terminated when bond stresses obtained from the bond-slip relationships expressed in Eq. (3) and (5) are converged. On this basis, the flexural crack width at the centroidal axis of FRP bars (w_f) can be estimated as follows

$$w_f = e_s - e_c = \varepsilon_s S_{mx} - \varepsilon_r S_{mx} = 2s_x \quad (6)$$

This flexural crack width (w_f) is used as a key parameter to determine the potential shear capacity of the cracked tension zone ($V_{ci,cap}$, refer to Eq. (12), presented later).

DUAL-POTENTIAL CAPACITY MODEL

The DPCM has been successfully extended from conventional reinforced and prestressed concrete members to SFRC,[15,16] bonded prestressed concrete,[12,16] unbonded post-tensioned concrete beam members,[12] punching-shear problems,[17] web-shear problems of prestressed hollow-core slabs,[21] and the torsional strength model.[22] Furthermore, in recent years, its applicability was successfully confirmed for RC deep and short beams,[18] and also RC members strengthened in shear by using externally bonded FRP composites.[19] The same fundamental formulations are adopted in this study.

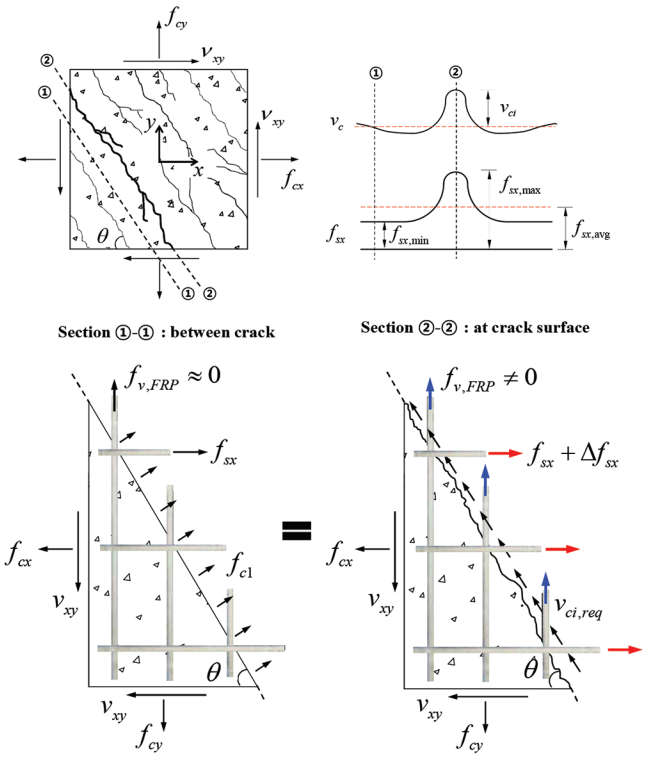

Fig. 5—Shear demand in cracked tension zone induced by bond and local stress increase.

As presented in Fig. 5, according to the equilibrium between stress distributions between adjacent cracks and local stress at the crack interface, the presence of the shear demand along the crack interface is mathematically required in the forms of so-called aggregate interlock and dowel action. This fact can be confirmed by the Modified Compression Field Theory (MCFT) and disturbed stress field model (DSFM).[36,37] On this basis, as shown in Fig. 6, the external shear force acting on the FRP-RC section (V_{tot}) can be divided into two shear demands of the aggregate interlock in the cracked tension zone and intact (uncracked) concrete in the compression zone above the neutral axis. Those shear demands can be defined as $V_{ci,req}$ and $V_{cc,req}$, respectively. It means the external shear force (V_{tot}) should be equal to the sum of $V_{ci,req}$ and $V_{cc,req}$ (that is, $V_{tot} = V_{ci,req} + V_{cc,req}$) to satisfy the equilibrium. Then, the corresponding potential capacity (that is, failure criterion) to each shear demand ($V_{ci,cap}$ and $V_{cc,cap}$) can also be defined, but it does not necessarily mean the external shear force (V_{tot}) is equal to the sum of the potential shear capacities (that is, $V_{tot} = V_{ci,cap} + V_{cc,cap}$). In the current method, when one mechanism dominates the shear failure mode (that is, $V_{ci,req} \geq V_{ci,cap}$ or $V_{cc,req} \geq V_{cc,cap}$), the shear contributions are provided from those two shear-transfer mechanisms ($V_n = V_{ci,req} + V_{cc,req}$ at $V_{ci,req} \geq V_{ci,cap}$ or $V_{cc,req} \geq V_{cc,cap}$). Thus, as shown in Fig. 7(a), two failure points can be obtained, and the minimum value between those two points can be taken as the shear capacity of the FRP-RC member. In detail, the external shear force acting on a critical section (V_{tot}) can be divided into two shear-resistance mechanisms as follows:

1. The shear demand to be resisted by the aggregate interlock mechanism in the cracked tension zone ($V_{ci,req}$) is inevitably induced by the local stress increase of longitudinal tension reinforcements at the crack location due to accumulated bond stress between cracks.

2. The shear demand of the compression zone in uncracked concrete ($V_{cc,req}$) is easily determined by taking the remaining shear force (that is, $V_{tot} - V_{ci,req}$).

Regardless of those shear demands, the potential shear capacities (that is, failure criteria) of the cracked tension

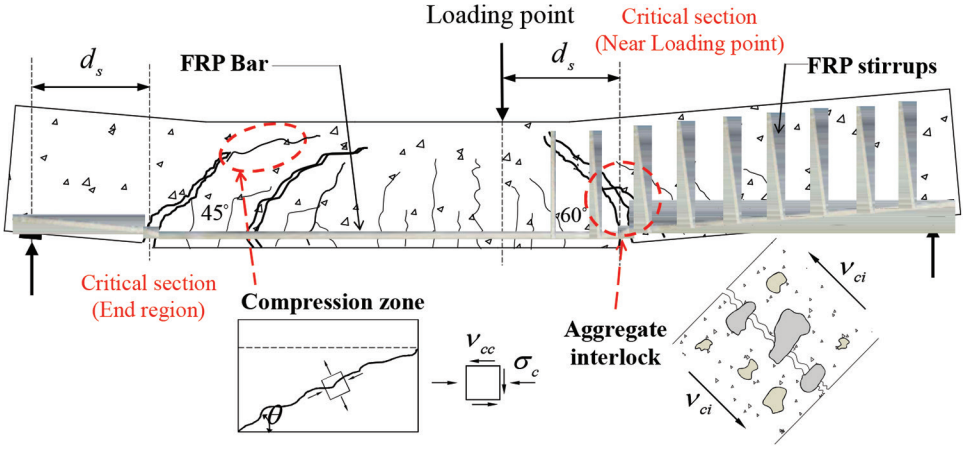

Fig. 6—Failure modes, critical sections, and shear crack angle.

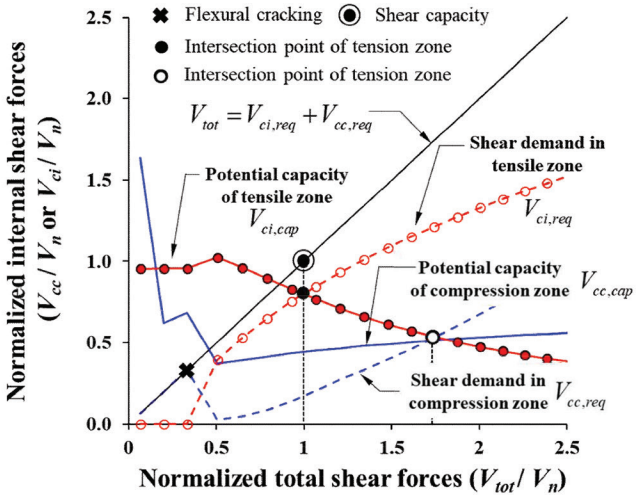

(a) Equilibrium in DPCM

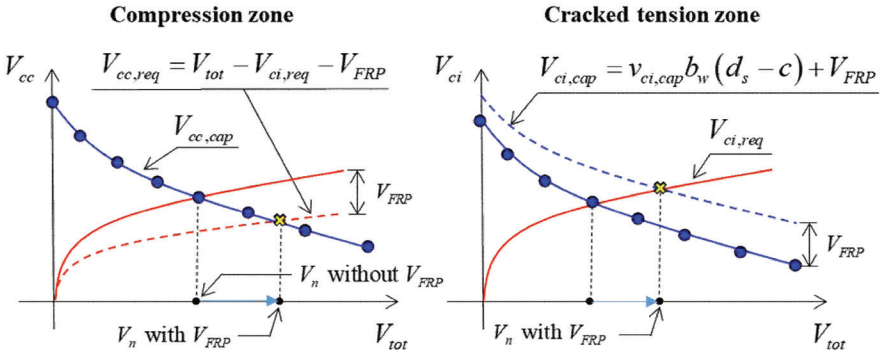

(b) Demand and potential capacity curves with no fracture in longitudinal FRP bars

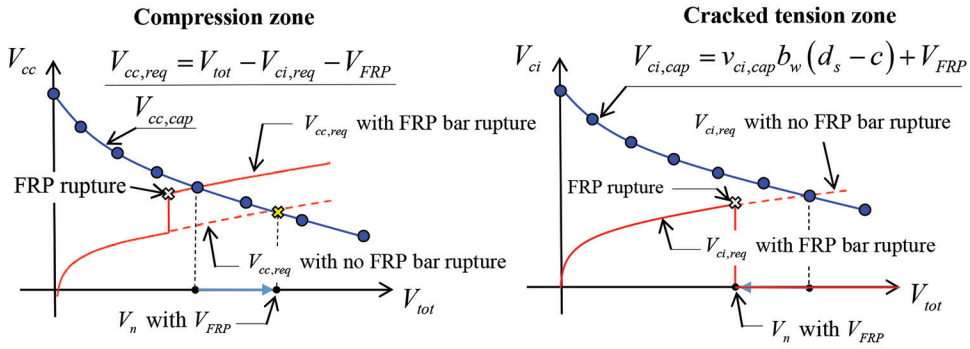

(c) Demand and potential capacity curves with fracture in longitudinal FRP bar

Fig. 7—Determination of shear strength in DPCM.

zone and uncracked compression zone ($V_{ci,cap}$ and $V_{cc,cap}$) corresponding to the demand curves ($V_{ci,req}$ and $V_{cc,req}$) can be defined separately. Note that those potential capacities decrease overall as the external load increases as a failure criterion because increasing crack width inevitably accompanies the decrease of aggregate interlock in the cracked tension zone ($V_{ci,cap}$). Moreover, the potential capacity of the compression zone ($V_{cc,cap}$) sharply decreases inevitably right after flexural cracking because its neutral axis depth is drastically shallower at flexural cracking, but it gradually increases again due to the beneficial effect of compressive stress above the neutral axis on the concrete plasticity (refer to Eq. (14), presented later). Based on this fact, the dominant failure mode can be determined when either of the shear demand curves ($V_{ci,req}$ or $V_{cc,req}$) exceeds the corresponding potential capacity curve ($V_{ci,cap}$ or $V_{cc,cap}$), at which the external shear force (V_{tot}) can be taken as the shear strength of an FRP-RC member.

Shear crack width

It is difficult to directly and accurately compute the shear crack width (w_s)[38]; thus, a semi-empirical factor, the so-called shear crack concentration factor (η), was addressed in this study, which was proposed in the authors' previous studies.[12-20] On this basis, the shear crack width (w_s) can then be calculated by multiplying the shear crack concentration factor (η) by the flexural crack width as follows

$$w_s = \eta w_f \tag{7}$$

where η can be defined as the ratio between the flexural crack spacing (S_{mx}) and the shear crack spacing ($S_{m\theta}$). For the sake of simplicity, by assuming the shear crack spacing ($S_{m\theta}$) to be $2d_s/\sin\theta$, the crack concentration factor (η) can be simplified[14] as follows

$$\eta = \frac{S_{m\theta}}{S_{mx}} = \frac{2\beta d_s}{3(h-d_s)\sin\pi/4} = \frac{0.94\beta d_s}{(h-d_s)} \tag{8}$$

where β is the crack control factor, which is taken to be 0.5 and 1.0 for FRP-RC members with and without shear reinforcements, respectively, to consider the reduced size effect in concrete members reinforced in shear.[14]

Shear demand curves of cracked tension zone and compression zone

Figure 5 shows the stress distribution between adjacent cracks and local stress distribution at the crack interface. As presented, the stress distributions between cracks and local stress distribution at the crack interface are different from each other due to the presence of the bond and cracking. Those two stress distributions should be statistically equivalent; thus, the equilibrium can be expressed as follows[12-20]

$$v_{ci,req} = (\rho_{s,eff}\Delta f_{sx} - \rho_{v,FRP}f_{v,FRP})\sin\theta\cos\theta \geq 0 \tag{9a}$$

$$V_{ci,req} = v_{ci,req}b_w(d_s - c) \tag{9b}$$

where $\rho_{s,eff}$ and $\rho_{v,FRP}$ are the effective longitudinal and transverse reinforcement ratios, which can be expressed as $A_{s,FRP}/[b_w(d_s - c)]$ and $A_{v,FRP}/(b_w s_v)$, respectively; $\rho_{v,FRP}$ is the FRP reinforcement ratio in the transverse direction; b_w is the web width; c is the neutral axis depth calculated from nonlinear flexural analysis; s_v is the spacing of FRP shear reinforcement; $A_{s,FRP}$ and $A_{v,FRP}$ are the areas of FRP reinforcements in the longitudinal and transverse directions, respectively; $f_{v,FRP}$ is the stress developed in FRP shear reinforcement; $f_{vu,FRP}$ is the tensile strength of the FRP stirrup, and θ is the inclination angle of the critical shear crack, for which 45 degrees ($\pi/4$) and 60 degrees ($\pi/3$) are taken for the critical sections located at d_s away from support and loading point, respectively, as shown in Fig. 6. Equation (9a) indicates that the shear force demand to be resisted in the cracked tension zone ($V_{ci,req}$) strongly relies on the magnitude of the local stress increases of the longitudinal bar (Δf_{sx}) at the crack location, which is obtained from the flexural analysis (Eq. (2)). The shear contribution of FRP stirrups (V_{FRP}) can be estimated by considering the number of FRP stirrups passing through the critical shear crack under the neutral axis depth (c)[12-20] as follows

$$V_{FRP} = n_v A_{v,FRP} f_{v,FRP} \tag{10a}$$

$$n_v = \frac{(d_s - c)}{s_v}\cot\theta \tag{10b}$$

where the stress in FRP stirrups ($f_{v,FRP}$) is taken to be $0.4f_{vu,FRP}$ based on Shehata et al.[11] Based on the interrelation method (IRM) proposed in the authors' previous study, shown in Fig. 7(b),[12,13] the shear force demand in the compression zone ($V_{cc,req}$) can be estimated as the net shear force by subtracting the shear resistances in the cracked tension zone, including stirrups, from the total shear force acting on the critical section as follows

$$V_{cc,req} = V_{tot} - V_{ci,req} - V_{FRP} \geq 0 \tag{11}$$

It shows that the shear contribution of FRP stirrups to the compression zone is indirectly reflected in the DPCM by reducing the shear demand.

Potential shear capacity curve of cracked tension zone

To estimate the shear strength of FRP-RC members, the shear demand curves of the tension and compression sides ($V_{ci,req}$ and $V_{cc,req}$) and corresponding potential strength curves of the tension and compression sides ($V_{ci,cap}$ and $V_{cc,cap}$) should be defined. For the potential shear strength curve of concrete in the cracked tension zone ($v_{ci,cap}$), the shear crack width (w_s) is the key influential parameter, which is magnified from flexural crack width by multiplying the shear crack concentration factor expressed in Eq. (7) and (8). On this basis, the potential shear capacity provided by aggregate interlock proposed by Vecchio and Collins[36] is adopted in this study as the failure criterion of cracked tension zone as follows

$$v_{ci,cap} = \frac{0.18\lambda\sqrt{f_c'}}{0.31 + \frac{24w_s}{a_{g,max} + 16}} \tag{12}$$

where $a_{g,max}$ is the maximum aggregate size (with zero used in the case of the lightweight aggregate concrete [LWAC]),[39,40] and $(a_{g,max} - 0.16f_c') \geq 0$ was taken when the compressive strength of normalweight concrete (NWC) was greater than 40.0 MPa (5.8 ksi); and λ is taken to be 1.0 and 0.75 for NWC and LWAC, respectively.[35] The total potential shear strength of the cracked tension zone ($V_{ci,cap}$) can be calculated by adding the contributions of FRP stirrups (V_{FRP}) estimated from Eq. (10) directly to the aggregate interlock resistance in the cracked concrete estimated from Eq. (12) as follows

$$V_{ci,cap} = v_{ci,cap}b_w(d_s - c) + V_{FRP} \tag{13}$$

where c is the depth of the neutral axis from the extreme top fiber of the concrete section, which is estimated from the flexural analysis.

Potential shear capacity of compression zone

As shown in Fig. 6, because the splitting failure mode in biaxial tension-compression is the dominant mechanism in the compression zone, the Rankine criterion was addressed in estimating the potential shear strength of the compression zone as follows

$$v_u(y) = \frac{1}{1+f_t/f_c'}\sqrt{f_t[f_t+\sigma_c(y)]\left[1-\frac{\sigma_c(y)}{f_c'}\right]} \quad (14)$$

where f_t is the tensile strength of concrete considering the effect of biaxial stress, for which $0.292\lambda\sqrt{f_c'}$ was taken[41]; and $\sigma_c(y)$ is the normal compressive stress induced by flexure in the critical section at y from the neutral axis, as shown in Fig. 3(b). By integrating Eq. (14) from the extreme top fiber of the critical section to the neutral axis depth (c), the potential shear capacity of the compression zone ($V_{cc,cap}$) can be estimated as follows

$$V_{cc,cap} = b\int_0^c v_u(y)dy \quad (15)$$

where b is the width of the compression zone, which is limited by ($b_w + 16t_f$) for the flanged section; and t_f is the flange thickness. In addition, according to Kani,[42] the calculated shear strength (V_{cal}) needs to be limited so that it cannot exceed the theoretical flexural strength (V_{flex}) obtained from the flexural analysis based on ACI 440.1R-15,[1] where V_{flex} is the shear force estimated at the flexural strength of an FRP-RC section.

Determination of shear strength

Figure 7 illustrates how the shear strength of an RC member with FRP bars is determined by the proposed method. The shear demand curves of both the compression and tension zones at the critical section ($V_{ci,req}$ and $V_{cc,req}$) can be calculated by using Eq. (9) and (11), respectively. The corresponding potential shear capacity curves of both the compression and tension zones ($V_{ci,cap}$ and $V_{cc,cap}$) are estimated from Eq. (13) and (15), respectively. The shear failure mode of an FRP-RC member is determined by comparing the shear demands ($V_{ci,req}$ or $V_{cc,req}$) with the corresponding potential shear capacities ($V_{ci,cap}$ or $V_{cc,cap}$). Whichever demand becomes greater governs the shear failure mode, at which the total external shear force acting on the section (V_{tot}) is taken as the shear strength of the FRP-RC member. As presented in Fig. 7(b), the IRM was used to reflect the shear contribution of FRP stirrups by increasing the potential capacity for the cracked tension zone and reducing the shear demand for the compression zone.

Meanwhile, if the stress in the FRP longitudinal reinforcement (f_s) reaches its tensile strength ($f_{u,FRP}$), as depicted in Fig. 7(c), the local stress increase (Δf_{sx}) and bond stress (τ_x) approach zero, and it is subsequently more realistic to take the shear demand of the cracked tension zone as zero (that is, $V_{ci,req} = 0$). For this case ($f_s = f_{u,FRP}$), the shear failure mode of an FRP-RC member is inevitably dominated by the compression zone, which also indicates that flexural failure dominates the failure mechanism.

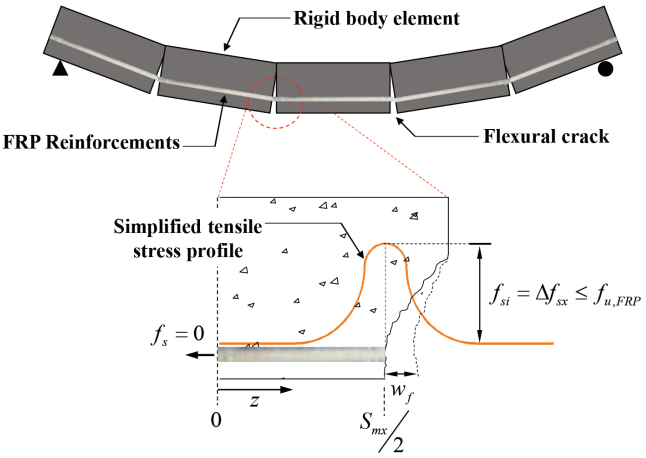

Fig. 8—Rigid-body model for simplification of DPCM.

SIMPLIFIED MODEL

Demand and capacity model for cracked tension zone

To simplify the detailed formulations of the DPCM, the rigid-body model is addressed, as presented in Fig. 8. On this basis, the local stress increase in the longitudinal FRP reinforcement (Δf_{sx}) at a given level of bending moment (M_u) can be approximated in a simple manner from Eq. (2)[14] as follows

$$f_{si} = \Delta f_{sx} = \frac{M_u}{A_{s,FRP}jd} \le f_{u,FRP} \quad (16)$$

where Δf_{sx} is the local stress increase of the longitudinal FRP bar at the crack surface; jd is the length of the moment lever arm, which is calculated to be $d_s - c_{simp}/3$ by assuming the linear distribution of flexural stress; c_{simp} is the depth of the neutral axis, for which $0.3d_s$ and $0.5d_s$ are adopted when $M_u/V_u > d_s$ and $M_u/V_u \le d_s$,[14] respectively; and V_u is the shear force corresponding to the given M_u at the section, which is the same with V_{tot} in Eq. (11). The shear demand to be resisted by the cracked tension zone can be simplified by assuming the shear crack angle as 45 degrees ($\pi/4$) in Eq. (9) as follows

$$v_{ci,req} = (\rho_{FRP}\Delta f_{sx} - \rho_{v,FRP}f_{v,FRP})\sin\theta\cos\theta$$
$$= (\rho_{FRP}f_{si} - 0.4f_{vu,FRP}\rho_{v,FRP})/2 \quad (17)$$

$$V_{ci,req} = v_{ci,req}b_w(d_s - c) \le V_u \quad (18)$$

Because the flexural crack width at the level of the longitudinal tension reinforcement (that is, at d_s) can be taken to be $w_f = \varepsilon_{si}s_{mx}$, the potential shear capacity of the cracked tension zone presented in Eq. (12) can be re-expressed by

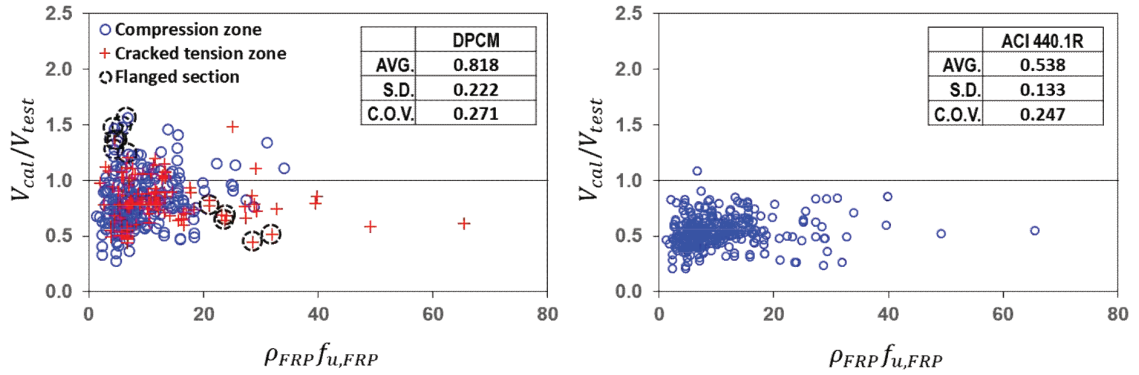

Fig. 9—Verification of detailed method for FRP-RC members with no stirrups. (Note: 1 MPa = 0.145 ksi.)

assuming the maximum size of aggregate to be 19 mm[14] as follows

$$v_{ci,cap} = \frac{0.18\lambda\sqrt{f_c'}}{0.31 + 0.686\eta w_f} = \frac{0.18\lambda\sqrt{f_c'}}{0.31 + 0.686\eta\varepsilon_{si}s_{mx}} \quad (19a)$$

$$V_{ci,cap} = v_{ci,cap}b_w(d_s - c) \quad (19b)$$

where ε_{si} can be taken as f_{si}/E_{FRP} from Eq. (16). Note that the shear strengths of FRP-RC members can be easily evaluated with no iterative calculation when design forces are provided because the stress in the flexural reinforcement (f_{si}) can be computed directly from the design bending moment by using Eq. (16).

Demand and capacity model for uncracked compression zone

As explained in the previous study,[14] the shear demand of the compression zone ($V_{cc,req}$) can be expressed as follows

$$V_{cc,req} = V_u - V_{ci,req} \geq 0 \quad (20)$$

The potential capacity of the intact compression zone ($V_{cc,cap}$) can be simplified from Eq. (14) and (15)[14] as follows

$$V_{cc,cap} = 0.47\lambda\sqrt{f_c'}b_w c_{simp} \quad (21)$$

The shear contribution of concrete (V_c) can be determined from the minimum of two intersecting points at $V_{ci,req} \geq V_{ci,cap}$ or $V_{cc,req} \geq V_{cc,cap}$. The shear strengths of FRP-RC members with no stirrups can then be determined as the minimum external shear force satisfying one of the following conditions

$$V_n = V_c = V_{ci,req} + V_{cc,req} \text{ at } V_{ci,req} \geq V_{ci,cap} \text{ or } V_{cc,req} \geq V_{cc,cap} \quad (22)$$

For FRP-RC members with FRP stirrups, the shear strength can be estimated by adding the shear contribution of FRP stirrups to Eq. (22), based on the simple summation method (SSM) presented in Lee et al.[12,13] as follows

$$V_n = V_c + V_{FRP} \text{ at } V_{ci,req} \geq V_{ci,cap} \text{ or } V_{cc,req} \geq V_{cc,cap} \quad (23)$$

As indicated in Eq. (23), for FRP-RC members reinforced in shear by using FRP stirrups, the contribution of FRP stirrups (V_{FRP}) calculated from Eq. (10) can be added to the shear contribution of concrete (V_c) to estimate the shear strength of the section (V_n).

VERIFICATION OF PROPOSED MODEL

A total of 437 shear test results on FRP-RC slender beams and slabs are mostly adopted from the existing shear database reported in Peng et al.,[4] to which 38 test results of FRP-RC beams with no stirrups were additionally collected from Michaluk et al.,[2] Jumaa and Yousif,[43] Nawy and Neuwerth,[5] and Ali et al.[6] by the authors. In the shear database of FRP-RC members, 341 test specimens were not reinforced in shear, and the other specimens were reinforced in shear using FRP stirrups. Note that detailed information on the shear database can be found in Appendixes B and C of Peng et al.[4] The types of FRPs used in the collected test specimens include basalt FRP (BFRP), carbon FRP (CFRP), and glass FRP (GFRP). A summary of the shear database is presented in Table 1. In the shear database, the shear span-depth ratio (a/d_s) ranges from approximately 2.3 to 9.6, where only the six specimens reported in Ali et al.[6] had a shear span-depth ratio a/d_s less than 2.5 ($a/d_s = 2.3$), and the effective depth (d_s) was distributed from 73.0 to 937.0 mm (2.87 to 36.89 in.). In addition, the concrete compressive strength (f_c') ranges from 13.0 to 102.0 MPa (1885 to 14,793 psi), and the longitudinal and transverse FRP reinforcement ratios (ρ_{FRP} and $\rho_{v,FRP}$) were distributed from 0.1 to 6.18% and from 0.12 to 2.26%, respectively. In addition, 22 test specimens with no stirrups were fabricated by using lightweight concrete (that is, $\lambda = 0.75$).

Figure 9 shows the strength ratios (V_{cal}/V_{test}) between the test results of FRP-RC beams with no stirrups and those estimated by the proposed model. The average and coefficient of variation (COV) of V_{cal}/V_{test} were estimated at 0.818 and 0.271, respectively, indicating a reasonable level of analytical accuracy compared to the ACI 440.1R-15 model,[1] which had average and COV V_{cal}/V_{test} values of 0.538 and 0.247, respectively. It is believed that the analytical accuracy of the proposed method can be improved further by addressing more detailed properties of the collected test specimens, including actual bond properties of FRP bars, and also by refining the crack spacing model as the key influential factors in estimating the local stress increases ($V_{cc,req}$) and

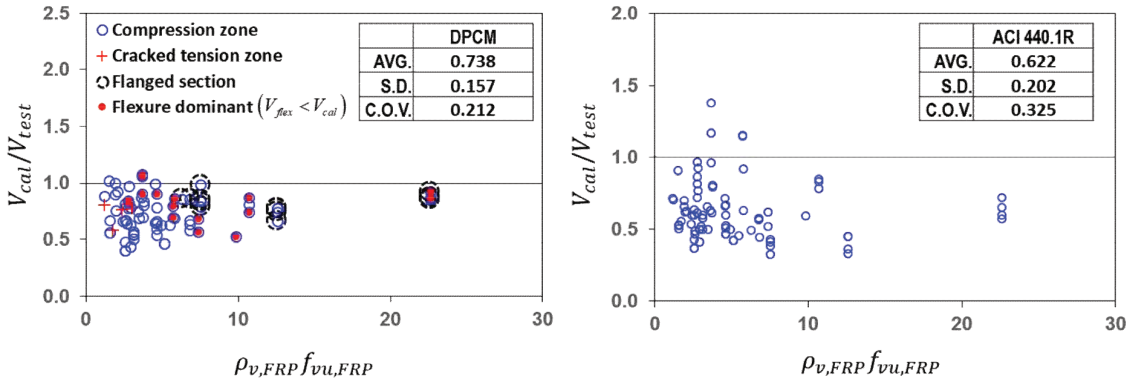

Fig. 10—Verification of detailed method for FRP-RC members with FRP stirrups. (Note: 1 MPa = 0.145 ksi.)

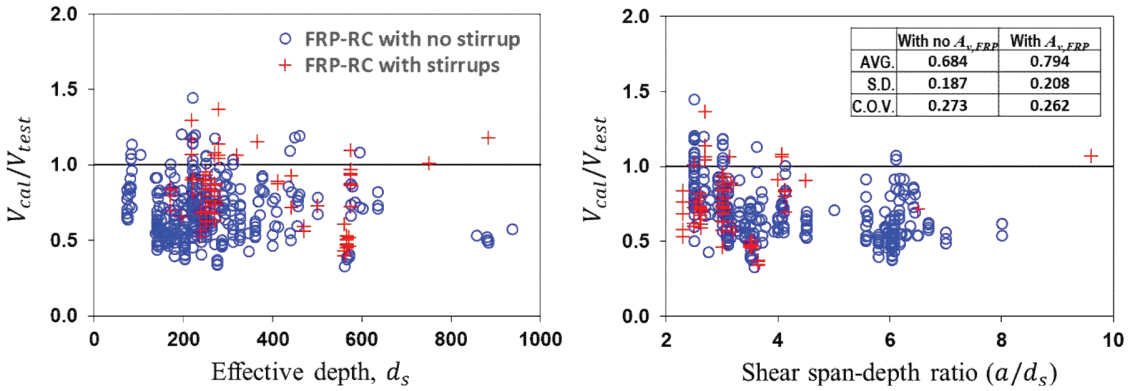

Fig. 11—Verification of simplified model. (Note: 1 mm = 0.0394 in.)

corresponding shear demands ($V_{ci,req}$ and $V_{cc,req}$), for which additional research is still required. It should be noted that the failure mode of the test specimens with no stirrups shows the clear tendency dominated by the cracked tension zone when $\rho_{FRP}f_{u,FRP}$ is greater than approximately 30 MPa (4351 psi). This is because the shear demand of the cracked tension zone obviously increases as the tension reinforcement ratio increases, according to Eq. (9), which indicates the shear strength of an FRP-RC member is not determined solely by the potential capacity but rather by the interaction between shear demand and potential capacity.

For the case of the FRP-RC members reinforced in shear by using FRP stirrups, as shown in Fig. 10, much enhanced analytical accuracy was obtained by the proposed method, while the ACI 440.1R-15 model showed much larger scatters in the data distribution of V_{cal}/V_{test} compared to those with no stirrups. Note that there was no specimen where the calculated shear strength of all the test results (V_{cal}) was not dominated by the theoretical flexural strength (V_{flex}) for the FPR-RC members with no stirrups. In contrast, for 18 test results out of a total of 84 specimens with FRP stirrups—expressed by using solid red circles in Fig. 10—their shear strengths calculated by using the proposed method (V_{cal}) were greater than their theoretical flexural strength (V_{flex}), for which a coexisting shear force at the flexural strength estimated from the ACI 440.1R-15 method was taken as the shear strength (that is, $V_{cal} \le V_{flex}$). This limit was also applied to estimate the shear strengths using ACI 440.1R-15. There is a strong trend in that the failure mode of the test specimens with FRP stirrups was mostly governed by the shear-resistance mechanism developed in the compression zone, and this can also be explained by the same logic as previously employed. Considering that the shear demand of the cracked tension zone decreases as the shear reinforcement ratio increases, it is evident that the shear demand subsequently and inevitably increases. Therefore, even with a large shear reinforcement ratio ($\rho_{v,FRP}f_{vu,FRP}$), the failure mode is much more likely to be dominated by the compression zone.

Figure 11 shows the results of the analysis of the simplified method. Note that no analysis result was dominated by the flexural strength. The analytical accuracy of the simplified method was decreased compared to that provided by the detailed method, but it still remains at an acceptable and reasonable level, with overall conservative estimations.

CONCLUSIONS

In this study, the dual-potential capacity model (DPCM) was formulated to be suitable for the analysis of the shear strength of fiber-reinforced polymer (FRP)-reinforced concrete (RC) members, and its simplified method was also presented. Verifications were made by using a total of 437 test specimens. On this basis, the following conclusions can be drawn:

1. In the proposed approach, the shear force demands in the tension and compression zones were mathematically derived, where the effects of the bond characteristics of FRP bars and the size effect were reflected in the analysis.

2. The effect of the low stiffness of FRP bars and the shear strengthening effect of FRP stirrups were reflected in the

shear demand curve and corresponding potential shear strength curve in both the cracked tension and compression zones. In addition, when FRP bars are ruptured, the shear demand curves are modified to consider the increasing shear demand in the compression zone.

3. The comparison of the analysis results to the test results showed that the proposed model could provide a reasonable level of accuracy in estimating the shear strengths of the FRP-RC beam members.

4. In addition, the simplified method was developed for better applicability of the DPCM, and its analytical accuracy was consistent in FRP-RC members with and without stirrups.

5. In addition, a significant shift in the shear failure mode of FRP-RC members with no stirrups was observed from the compression zone to the cracked tension zone as the FRP reinforcement ratios increased, and it appeared that the shear failure mode was mostly dominated by the compression zone when FRP stirrups were added.

6. It was confirmed that the proposed model could adequately reflect the effects of the main influential factors, such as member depths (that is, size effect), FRP reinforcement ratios, and shear span-depth ratio from the verification process.

AUTHOR BIOS

ACI member **Deuckhang Lee** *is an Associate Professor in the Department of Architectural Engineering at Chungbuk National University, Cheongju, Korea. He previously served as an Assistant Professor at Nazarbayev University, Kazakhstan, and a Postdoctoral Researcher at the University of Illinois Urbana-Champaign, Urbana, IL. He received his PhD from the University of Seoul, Seoul, Korea. He is a member of Joint ACI-ASCE Subcommittees 445-E, Shear & Torsion-Torsion; and 445-F, Shear and Torsion-Interface Shear. His research interests include performance-based seismic design of precast concrete structures, and shear and torsion in various structural concrete.*

Min-Kook Park *is a Research Professor in the Department of Architectural Engineering at the University of Seoul. He also serves in a research position at Delft University of Technology (TU Delft), Delft, the Netherlands. He received his PhD from the University of Seoul. His research interests include the shear design of reinforced, precast, and prestressed concrete members.*

ACKNOWLEDGMENTS

This work was supported by the National Research Foundation of Korea (NRF) grant funded by the Korean government (MSIT) (No. RS-2023-00209647). The second author also would like to acknowledge the support from the National Research Foundation of Korea (NRF) grant funded by the Korea government (MSIT) (No. NRF-2022R1C1C2012400).

NOTATION

A_{FRP} = area of FRP reinforcement in longitudinal direction
A_s = area of longitudinal reinforcement
$A_{v,FRP}$ = area of FRP reinforcement in transverse direction
a = shear span
$a_{g,max}$ = maximum aggregate size
b_w = web width of concrete section
C_c = compressive force in concrete
c = depth of neutral axis
c_{cv} = thickness of concrete cover
c_{simp} = simplified depth of neutral axis
d_b = diameter of FRP reinforcement
d_s = distance between extreme compression fiber and centroidal axis of longitudinal FRP reinforcement
E_c = elastic modulus of concrete
E_{FRP} = elastic modulus of FRP reinforcement
E_s = elastic modulus of steel reinforcement
e_c = elongation of concrete between cracks at reinforcement level
e_s = elongation of longitudinal FRP reinforcement
f_c' = compressive strength of concrete
f_r = modulus of rupture of concrete
f_s = stress in FRP longitudinal reinforcement
$f_{sx,max}$ = maximum stress in longitudinal tension reinforcement
$f_{sx,min}$ = minimum stress in longitudinal tension reinforcement between cracks
f_t = tensile strength of concrete
$f_{u,FRP}$ = tensile strength of FRP longitudinal reinforcement
$f_{v,FRP}$ = stress developed in FRP stirrup
$f_{vu,FRP}$ = tensile strength of FRP stirrup
f_{vy} = yield strength of shear reinforcement
f_y = yield strength of steel reinforcement
h = height of concrete section
jd = length of moment lever arm
M_u = bending moment
n_v = number of FRP stirrups passing through critical shear crack
S_{mx} = flexural crack spacing
$S_{m\theta}$ = shear crack spacing
s_v = spacing of FRP stirrup
s_x = slip between reinforcement and concrete at crack
T_s = forces in tensile reinforcement
t_f = thickness of flange
V_c = shear contribution of concrete
V_{cal} = analysis results estimated by proposed DPCM
$V_{cc,cap}$ = potential shear capacity of compression side
$V_{cc,req}$ = shear demand required in compression zone
$V_{ci,cap}$ = potential shear capacity of tension side
$V_{ci,req}$ = shear demand required in cracked tension zone
V_{FRP} = shear contribution of FRP stirrups
V_{flex} = theoretical flexural strength
V_n = nominal shear strength
V_{tot} = external shear force acting on FRP-RC section
V_u = factored shear force at section
w_f = flexural crack width at centroidal axis of FRP reinforcement
w_s = shear crack width
β = crack control factor
Δf_{sx} = local stress increase in longitudinal FRP reinforcement at crack surface
ε_{cu} = maximum strain at extreme concrete compression fiber
ε_r = flexural cracking strain of concrete
ε_s = strain of tensile reinforcement
ε_{si} = effective strain of tensile reinforcement for simplified method
ε_t = strain of extreme compression fiber of concrete
η = shear crack concentration factor
λ = lightweight concrete factor
$v_{ci,cap}$ = potential shear capacity of cracked tension zone
$v_{ci,req}$ = required shear stress in cracked tension zone
v_{test} = shear stress obtained from test
θ = inclination angle of shear crack
ρ_b = balanced FRP reinforcement ratio
ρ_{FRP} = longitudinal FRP reinforcement ratio
ρ_s = longitudinal reinforcement ratio
$\rho_{s,eff}$ = effective longitudinal reinforcement ratio
ρ_v = shear reinforcement ratio
$\rho_{v,FRP}$ = FRP shear reinforcement ratio
$\sigma_c(y)$ = normal compressive stress at location y from neutral axis
τ_{max} = maximum bond strength
τ_{min} = minimum bond strength
τ_x = average bond stress
ω_s = reinforcement index

REFERENCES

1. ACI Committee 440, "Guide for the Design and Construction of Structural Concrete Reinforced with Fiber-Reinforced Polymer (FRP) Bars (ACI 440.1R-15)," American Concrete Institute, Farmington Hills, MI, 2015, 88 pp.

2. Michaluk, C. R.; Rizkalla, S. H.; Tadros, G.; and Benmokrane, B., "Flexural Behavior of One-Way Concrete Slabs Reinforced with Fiber Reinforced Plastic Reinforcements," *ACI Structural Journal*, V. 95, No. 3, May-June 1998, pp. 353-364.

3. Benmokrane, B.; Tighiouart, B.; and Chaallal, O., "Bond Strength and Load Distribution of Composite GFRP Reinforcing Bars in Concrete," *ACI Materials Journal*, V. 93, No. 3, May-June 1996, pp. 246-252.

4. Peng, F.; Xue, W.; and Xue, W., "Database Evaluation of Shear Strength of Slender Fiber-Reinforced Polymer-Reinforced Concrete Members," *ACI Structural Journal*, V. 117, No. 3, May 2020, pp. 273-281.

5. Nawy, E. G., and Neuwerth, G. E., "Fiberglass Reinforced Concrete Slabs and Beams," *Journal of the Structural Division*, ASCE, V. 103, No. 2, Feb. 1977, pp. 421-440. doi: 10.1061/JSDEAG.0004559

6. Ali, I.; Thamrin, R.; Samad, A. A. A.; and Mohamad, N., "Diagonal Shear Cracks and Size Effect in Concrete Beams Reinforced with Glass Fiber Reinforced Polymer (GFRP) Bars," *Applied Mechanics and Materials*, V. 621, Aug. 2014, pp. 113-119. doi: 10.4028/www.scientific.net/AMM.621.113

7. Gao, D., and Zhang, C., "Shear Strength Calculating Model of FRP Bar Reinforced Concrete Beams without Stirrups," *Engineering Structures*, V. 221, Oct. 2020, Article No. 111025. doi: 10.1016/j.engstruct.2020.111025

8. Benmokrane, B.; Chaallal, O.; and Masmoudi, R., "Flexural Response of Concrete Beams Reinforced with FRP Reinforcing Bars," *ACI Structural Journal*, V. 93, No. 1, Jan.-Feb. 1996, pp. 46-55.

9. Tureyen, A. K., and Frosch, R. J., "Shear Tests of FRP-Reinforced Concrete Beams without Stirrups," *ACI Structural Journal*, V. 99, No. 4, July-Aug. 2002, pp. 427-434.

10. El Zareef, M. A.; Elbisy, M. S.; and Badawi, M., "Evaluation of Code Provisions Predicting the Concrete Shear Strength of FRP-Reinforced Members without Shear Reinforcement," *Composite Structures*, V. 275, Nov. 2021, Article No. 114430. doi: 10.1016/j.compstruct.2021.114430

11. Shehata, E.; Morphy, R.; and Rizkalla, S., "Fiber Reinforced Polymer Shear Reinforcement for Concrete Members: Behaviour and Design Guidelines," *Canadian Journal of Civil Engineering*, V. 27, No. 5, Oct. 2000, pp. 859-872. doi: 10.1139/l00-004

12. Lee, D.; Han, S.-J.; Ju, H.; and Kim, K. S., "Shear Strength of Prestressed Concrete Beams Considering Bond Mechanism in Reinforcement," *ACI Structural Journal*, V. 118, No. 3, May 2021, pp. 267-277.

13. Lee, D. H.; Han, S.-J.; and Kim, K. S., "Dual Potential Capacity Model for Reinforced Concrete Beams Subjected to Shear," *Structural Concrete*, V. 17, No. 3, Sept. 2016, pp. 443-456. doi: 10.1002/suco.201500165

14. Lee, D. H.; Han, S.-J.; Hwang, J.-H.; Ju, H.; and Kim, K. S., "Simplification and Verification of Dual Potential Capacity Model for Reinforced Concrete Beams Subjected to Shear," *Structural Concrete*, V. 18, No. 2, Apr. 2017, pp. 259-277. doi: 10.1002/suco.201600055

15. Lee, D. H.; Han, S.-J.; Kim, K. S.; and LaFave, J. M., "Shear Capacity of Steel Fiber-Reinforced Concrete Beams," *Structural Concrete*, V. 18, No. 2, Apr. 2017, pp. 278-291. doi: 10.1002/suco.201600104

16. Lee, D.; Han, S.-J.; Ju, H.; Zhang, D.; and Kim, K. S., "Shear Strength Model for Prestressed Concrete Beams with Steel Fibres Failed in Shear," *Magazine of Concrete Research*, V. 73, No. 14, July 2021, pp. 731-742. doi: 10.1680/jmacr.19.00391

17. Ju, H.; Lee, D.; Park, M.-K.; and Memon, S. A., "Punching Shear Strength Model for Reinforced Concrete Flat Plate Slab–Column Connection without Shear Reinforcement," *Journal of Structural Engineering*, ASCE, V. 147, No. 3, Mar. 2021, p. 04020358. doi: 10.1061/(ASCE)ST.1943-541X.0002939

18. Lee, D. H.; Kim, K. S.; Han, S.-J.; Zhang, D.; and Kim, J., "Dual Potential Capacity Model for Reinforced Concrete Short and Deep Beams Subjected to Shear," *Structural Concrete*, V. 19, No. 1, Feb. 2018, pp. 76-85. doi: 10.1002/suco.201700202

19. Lee, D. H.; Han, S.-J.; Kim, K. S.; and LaFave, J. M., "Shear Strength of Reinforced Concrete Beams Strengthened in Shear Using Externally-Bonded FRP Composites," *Composite Structures*, V. 173, Aug. 2017, pp. 177-187. doi: 10.1016/j.compstruct.2017.04.025

20. Lee, D.; Han, S.-J.; Joo, H.-E.; Kim, K. S.; Zhang, D.; and Kim, J., "Shear Crack Concentration in Reinforced Concrete Beams Subjected to Shear and Flexure," *Advances in Structural Engineering*, V. 23, No. 11, Aug. 2020, pp. 2305-2317. doi: 10.1177/1369433219895911

21. Lee, D.; Park, M.-K.; Ju, H.-E.; Han, S.-J.; and Kim, K. S., "Strengths of Thick Prestressed Precast Hollow-Core Slab Members Strengthened in Shear," *ACI Structural Journal*, V. 117, No. 2, Mar. 2020, pp. 129-140.

22. Ju, H., and Lee, D., "Nonlinear Analysis of Reinforced Concrete Members Subjected to Combined Torsion and Bending Moment," *ACI Structural Journal*, V. 118, No. 4, July 2021, pp. 55-70.

23. Reineck, K.-H.; Kuchma, D. A.; Kim, K. S.; and Marx, S., "Shear Database for Reinforced Concrete Members without Shear Reinforcement," *ACI Structural Journal*, V. 100, No. 2, Mar.-Apr. 2003, pp. 240-249.

24. Reineck, K.-H.; Bentz, E.; Fitik, B.; Kuchma, D. A.; and Bayrak, O., "ACI-DAfStb Databases for Shear Tests on Slender Reinforced Concrete Beams with Stirrups," *ACI Structural Journal*, V. 111, No. 5, Sept.-Oct. 2014, pp. 1147-1156. doi: 10.14359/51686819

25. Comité Euro-International du Béton (CEB), "CEB-FIP Model Code for Concrete Structures," International Federation for Structural Concrete, Lausanne, Switzerland, 1978.

26. Collins, M. P., and Mitchell, D., *Prestressed Concrete Structures*, Prentice-Hall, Hoboken, NJ, 1991, 766 pp.

27. Han, S.-J.; Lee, D. H.; Kim, K. S.; Seo, S.-Y.; Moon, J.; and Monteiro, P. J. M., "Degradation of Flexural Strength in Reinforced Concrete Members Caused by Steel Corrosion," *Construction and Building Materials*, V. 54, Mar. 2014, pp. 572-583. doi: 10.1016/j.conbuildmat.2013.12.101

28. El Maaddawy, T.; Soudki, K.; and Topper, T., "Analytical Model to Predict Nonlinear Flexural Behavior of Corroded Reinforced Concrete Beams," *ACI Structural Journal*, V. 102, No. 4, July-Aug. 2005, pp. 550-559.

29. Lee, D. H., and Kim, K. S., "Flexural Strength of Prestressed Concrete Members with Unbonded Tendons," *Structural Engineering and Mechanics*, V. 38, No. 5, June 2011, pp. 675-696. doi: 10.12989/sem.2011.38.5.675

30. Kim, K. S., and Lee, D. H., "Flexural Behavior Model for Post-Tensioned Concrete Members with Unbonded Tendons," *Computers and Concrete*, V. 10, No. 3, Sept. 2012, pp. 241-258. doi: 10.12989/cac.2012.10.3.241

31. Kim, K. S., and Lee, D. H., "Nonlinear Analysis Method for Continuous Post-Tensioned Concrete Members with Unbonded Tendons," *Engineering Structures*, V. 40, July 2012, pp. 487-500. doi: 10.1016/j.engstruct.2012.03.021

32. *fib*, "*fib* Model Code for Concrete Structures 2010," International Federation for Structural Concrete, Lausanne, Switzerland, 2013, 434 pp.

33. Jendele, L., and Cervenka, J., "Finite Element Modelling of Reinforcement with Bond," *Computers & Structures*, V. 84, No. 28, Nov. 2006, pp. 1780-1791. doi: 10.1016/j.compstruc.2006.04.010

34. Okelo, R., and Yuan, R. L., "Bond Strength of Fiber Reinforced Polymer Rebars in Normal Strength Concrete," *Journal of Composites for Construction*, ASCE, V. 9, No. 3, June 2005, pp. 203-213. doi: 10.1061/(ASCE)1090-0268(2005)9:3(203)

35. ACI Committee 318, "Building Code Requirements for Structural Concrete (ACI 318-19) and Commentary (ACI 318R-19) (Reapproved 2022)," American Concrete Institute, Farmington Hills, MI, 2019, 624 pp.

36. Vecchio, F. J., and Collins, M. P., "The Modified Compression-Field Theory for Reinforced Concrete Elements Subjected to Shear," *ACI Journal Proceedings*, V. 83, No. 2, Mar.-Apr. 1986, pp. 219-231.

37. Vecchio, F. J., "Disturbed Stress Field Model for Reinforced Concrete: Formulation," *Journal of Structural Engineering*, ASCE, V. 126, No. 9, Sept. 2000, pp. 1070-1077. doi: 10.1061/(ASCE)0733-9445(2000)126:9(1070)

38. Pérez Caldentey, A.; Corres Peiretti, H.; Peset Iribarren, J.; and Giraldo Soto, A., "Cracking of RC Members Revisited: Influence of Cover, $\phi/\rho_{s,ef}$ and Stirrup Spacing – An Experimental and Theoretical Study," *Structural Concrete*, V. 14, No. 1, Mar. 2013, pp. 69-78. doi: 10.1002/suco.201200016

39. Bentz, E. C.; Vecchio, F. J.; and Collins, M. P., "Simplified Modified Compression Field Theory for Calculating Shear Strength of Reinforced Concrete Elements," *ACI Structural Journal*, V. 103, No. 4, July-Aug. 2006, pp. 614-624.

40. Sherwood, E. G.; Bentz, E. C.; and Collins, M. P., "Effect of Aggregate Size on Beam-Shear Strength of Thick Slabs," *ACI Structural Journal*, V. 104, No. 2, Mar.-Apr. 2007, pp. 180-190.

41. Choi, K.-K.; Park, H.-G.; and Wight, J. K., "Unified Shear Strength Model for Reinforced Concrete Beams—Part I: Development," *ACI Structural Journal*, V. 104, No. 2, Mar.-Apr. 2007, pp. 142-152.

42. Kani, G. N. J., "The Riddle of Shear Failure and Its Solution," *ACI Journal Proceedings*, V. 61, No. 4, Apr. 1964, pp. 441-467.

43. Jumaa, G. B., and Yousif, A. R., "Size Effect in Shear Failure of High Strength Concrete Beams without Stirrup Reinforced with Basalt FRP Bars," *KSCE Journal of Civil Engineering*, V. 23, No. 4, Apr. 2019, pp. 1636-1650. doi: 10.1007/s12205-019-0121-3

CALL FOR ACTION

ACI Invites You To...

Share your expertise

Do you have EXPERTISE in any of these areas?

- BIM
- Chimneys
- Circular Concrete Structures Prestressed by Wrapping with Wire and Strand
- Circular Concrete Structures Prestressed with Circumferential Tendons
- Concrete Properties
- Demolition
- Deterioration of Concrete in Hydraulic Structures
- Electronic Data Exchange
- Insulating Concrete Forms, Design, and Construction
- Nuclear Reactors, Concrete Components
- Pedestal Water Towers
- Pipe, Cast-in-Place
- Strengthening of Concrete Members
- Sustainability

Then become a REVIEWER for the *ACI Structural Journal* or the *ACI Materials Journal*.

Become a Reviewer for the ACI Journals

How to become a Reviewer:

1. Go to: **http://mc.manuscriptcentral.com/aci**;
2. Click on "Create Account" in the upper right-hand corner; and
3. Enter your E-mail/Name, Address, User ID and Password, and Area(s) of Expertise.

Update your Manuscript Central user account information

Did you know that the database for MANUSCRIPT CENTRAL, our manuscript submission program, is separate from the ACI membership database?

How to update your user account:

1. Go to **http://mc.manuscriptcentral.com/aci**;
2. Log in with your current User ID & Password; and
3. Update your E-mail/Name, Address, User ID and Password, and Area(s) of Expertise.

QUESTIONS?

E-mail any questions to Journals.Manuscripts@concrete.org.

American Concrete Institute

Always advancing

ACI STRUCTURAL JOURNAL TECHNICAL PAPER

Title No. 122-S07

Two-Way Shear in Nonprestressed Slabs: Flexural Reinforcement Ratio Effects

by Madhura Sanjay Chavan, Mary Beth D. Hueste, and Aikaterini S. Genikomsou

*A detailed investigation of the ACI 445-*fib *punching shear database studied the effect of flexural reinforcement ratio on the punching shear strength of nonprestressed slabs. The ACI 318-19 expressions for the two-way shear strength of nonprestressed slabs do not directly include the flexural reinforcement ratio. The experimental data shows that this simplification can lead to unconservative predictions of shear strength for slabs with low flexural reinforcement ratios. ACI 318-19 introduced a minimum flexural reinforcement area requirement for two-way slabs to address this concern. Based on a review of the data, this study proposes modified expressions to directly incorporate the flexural reinforcement ratio* ρ *in the design two-way shear strength of nonprestressed slabs. This approach provides safer strength predictions for slabs with low reinforcement ratios, which can be critically important when evaluating existing structures. The proposed equations, in conjunction with the ACI 318-19 minimum flexural reinforcement requirement, can also promote safer designs for two-way slabs.*

Keywords: design provisions; flexural reinforcement ratio; nonprestressed slabs; punching shear strength; reinforced concrete; two-way shear.

INTRODUCTION

Slab-column connections in two-way slabs may be subjected to a combination of stresses from direct shear and unbalanced moment transfer that can cause two-way (punching) shear failures. Inclined cracks occur within the slab depth around the column or support perimeter and propagate through the thickness of the slab. Then, a major inclined crack can form, and when it reaches the compression zone, failure occurs. A trapezoidal-shaped failure cone occurs around the column, often referred to as a punching cone (Fig. 1), leading to loss of load-carrying capacity. Therefore, evaluation of punching shear failures is of critical importance in these slab systems because this brittle failure mode can lead to localized failures at the connections. In addition, without adequate structural integrity reinforcement, these localized failures can lead to progressive collapse of the structure.

Studies have shown that the flexural reinforcement ratio ρ influences the punching shear capacity of nonprestressed slabs; as ρ increases, the punching shear capacity also increases (Muttoni 2008; Widianto et al. 2009; Dam and Wight 2016; Hawkins and Ospina 2017; Dam et al. 2017). Some design codes (for example, Eurocode 2 [2004] and JSCE [2010]) therefore account for the influence of flexural reinforcement by incorporating this parameter in the respective design equations used to calculate the two-way shear strength of slabs. The ACI 318-19 (ACI Committee 318 2019) expressions for two-way shear strength do not directly include the flexural reinforcement ratio. The experimental data shows that this simplification can lead to unconservative predictions of two-way shear strength for slabs with low flexural reinforcement ratios. More recently, the ACI 318-19 provisions included a minimum flexural reinforcement area requirement to help address this issue.

Various analytical models for two-way nonprestressed reinforced concrete slabs have been proposed in the past to predict the punching shear strength of such systems more precisely. Alexander and Simmonds (1986) presented a method using a truss analogy to determine the capacity of slab-column connections and predict the failure mechanism. The truss model considers the role of bonded flexural reinforcement in resisting shear forces in the connection region. The proposed model consists of a three-dimensional truss where the top reinforcement acts as a tie element while the concrete acts as an inclined compression strut. The flow of forces within the connection region is described such that it is consistent with the cracking observed.

A more recent method, the critical shear crack theory (CSCT) proposed by Muttoni (2008), describes the influence of the rotation of the slab at failure on its punching shear strength. It states that the two-way shear strength of a slab is directly affected by the presence of a critical shear crack in the slab, which reduces the strength of the inclined compression strut. The presented method calculates the two-way shear strength of slabs and accounts for the influence of various key parameters, including the amount and the strength of flexural reinforcement and the size of the slab and column to name a few.

Park et al. (2011) developed a strength model to predict the punching shear strength of interior slab-column connections under direct shear. The model assumes that the compression zone of the slab-column connection is responsible for resisting the shear force acting on the connection. It defines the two-way shear strength of the connection as the interaction between compressive stress developed by the flexural moment and the shear stress. The punching shear strength depends on the compressive strength of concrete and the amount of flexural reinforcement.

Although the models summarized previously can predict the two-way shear strength of nonprestressed slabs with

ACI Structural Journal, V. 122, No. 1, January 2025.
MS No. S-2023-137.R2, doi: 10.14359/51742137, received June 12, 2024, and reviewed under Institute publication policies.

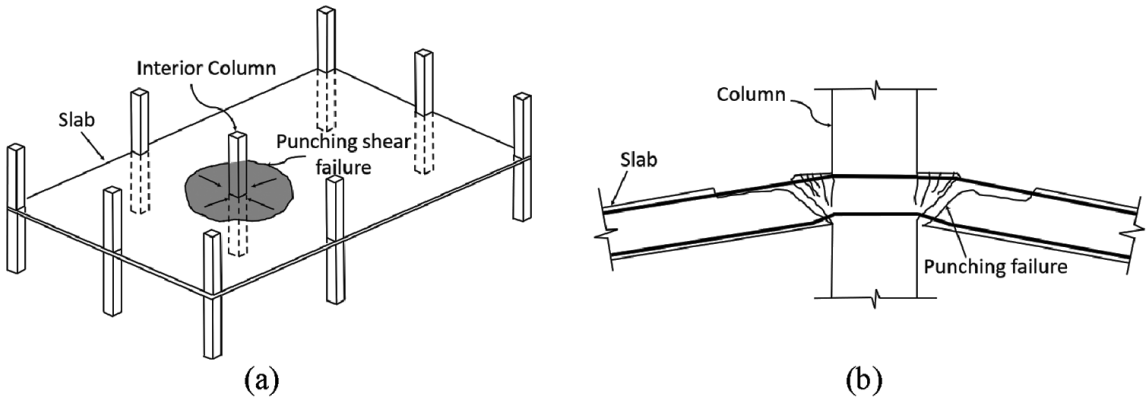

Fig. 1—Punching failure in flat slabs (adapted from Liberati et al. [2019] and ACI Committee 352 [2011]).

reasonable accuracy, their application for standard structural design can be complex and require significant computational effort. As such, this study proposes a modification to the ACI 318-19 two-way shear provisions to incorporate the effect of the flexural reinforcement ratio without compromising the inherent simplicity and ease of application of the design expressions.

This research reviewed the ACI 445-*fib* punching shear database (Ospina et al. 2012) to assess the influence of the flexural reinforcement ratio on the punching shear capacity of flat slabs, specifically for nonprestressed slabs without shear reinforcement subject to concentric punching shear without unbalanced moment transfer. Comparisons are provided between the two-way shear capacities determined by the provisions of ACI 318-19, Eurocode 2, and JSCE, and the experimental results for test slabs reported in the database. A modification to the ACI 318-19 provisions for two-way shear strength of nonprestressed slabs is proposed to incorporate a factor based on the flexural reinforcement ratio ρ into the design equations.

RESEARCH SIGNIFICANCE

This study provides a thorough review of the latest ACI 445-*fib* punching shear database for nonprestressed slabs. The analysis confirms the influence of the flexural reinforcement ratio ρ on two-way shear strength and the test data is evaluated relative to current code provisions. A modification to the ACI 318-19 two-way shear expressions is proposed to incorporate the influence of the flexural reinforcement ratio ρ. The suggested approach provides safer strength predictions for slabs with low flexural reinforcement ratios, which is especially critical when evaluating existing structures. The proposed equations can be used in conjunction with the ACI 318-19 minimum flexural reinforcement requirement to promote safer designs for two-way slabs.

TWO-WAY SHEAR STRENGTH PROVISIONS

Various approaches are used in codes to determine the two-way shear strength for nonprestressed slabs. The design provisions according to ACI 318-19, Eurocode 2, and JSCE are summarized in this section.

ACI 318-19

ACI 318-19, Section 22.6.5.2, states that for nonprestressed slabs without shear reinforcement, the nominal two-way concrete shear strength v_c shall be calculated in accordance with Table 22.6.5.2. Three expressions are provided, and v_c is taken as the minimum of the three calculated values, as follows

$$v_c = \min\begin{cases} 4\lambda_s\lambda\sqrt{f_c'(\text{psi})} \\ \left(2+\frac{4}{\beta}\right)\lambda_s\lambda\sqrt{f_c'(\text{psi})} \\ \left(2+\frac{\alpha_s d}{b_o}\right)\lambda_s\lambda\sqrt{f_c'(\text{psi})} \end{cases} \text{(in.-lb)}$$

or (1)

$$v_c = \min\begin{cases} 0.33\lambda_s\lambda\sqrt{f_c'(\text{MPa})} \\ 0.17\left(1+\frac{2}{\beta}\right)\lambda_s\lambda\sqrt{f_c'(\text{MPa})} \\ 0.083\left(2+\frac{\alpha_s d}{b_o}\right)\lambda_s\lambda\sqrt{f_c'(\text{MPa})} \end{cases} \text{(SI)}$$

where λ_s is the size effect modification factor given in ACI 318-19, Section 22.5.5.1.3, and provided in Eq. (2); λ is the modification factor for lightweight concrete given in ACI 318-19, Section 19.2.4.1, taken as 0.75 for lightweight concrete and 1.0 for normalweight concrete in this study; β is the ratio of the long to short dimensions of the column, concentrated load, or reaction area; α_s is a constant given in ACI 318-19, Section 22.6.5.3, and is taken as 40 for interior columns, 30 for edge columns, and 20 for corner columns; d is the effective slab depth, which is the distance from the extreme compression fiber to the centroid of the longitudinal tension reinforcement (in. [mm]), and is taken as the average depth in two directions for the reinforcement in a two-way slab; and b_o (in. [mm]) is the perimeter of the critical section located at a distance of $0.5d$ from the face of the column, concentrated load, or reaction area. For a square column, b_o is calculated assuming straight edges, while for a circular column, it is calculated assuming a square column of equivalent area. According to ACI 318-19, Section 22.6.3.1, the value of $\sqrt{f_c'}$ used in the calculation of v_c for nonprestressed slabs should not exceed 100 psi (8.3 MPa).

Table 1—Punching shear strength provisions in other design codes

Standard	Critical perimeter b_o	Two-way shear strength V_c	Size effect factor	Reinforcement ratio factor
Eurocode 2	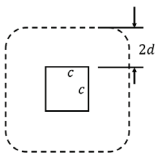 $b_o = 4(c + \pi d)$	$\frac{0.18}{\gamma_c}\sqrt[3]{100\rho f_{ck}}kb_od + 0.1f_{cp}b_od$ $\geq 0.035k^{3/2}\sqrt{f_{ck}}b_od + 0.1f_{cp}b_od$	$k = 1 + \sqrt{\frac{200}{d}} \leq 2.0$	$\sqrt[3]{100\rho}$ $\rho \leq 0.02$
JSCE	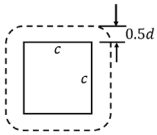 $b_o = 4c + \pi d$	$0.2\sqrt{f_c'}\beta_d\beta_p\beta_r b_o d/\gamma_b$	$\beta_r = 1 + \frac{1}{1 + 0.25u/d}$ $\beta_d = \sqrt[4]{1000/d} \leq 1.5$	$\beta_p = \sqrt[3]{100\rho}$ $\beta_\pi \leq 1.5$

Note: ρ is average flexural reinforcement ratio in two principal directions; γ_b and γ_c are member factor and partial factor for concrete and are taken as 1.0; b_o is critical section perimeter, mm; c is column dimension, mm; d is average effective depth, mm; f_c' is specified compressive strength of concrete, MPa; f_{ck} is characteristic concrete cylinder compressive strength, MPa; f_{cp} is average normal prestress, MPa; and u is perimeter dimension of column, mm. 1 mm = 0.039 in.; 1 MPa = 145 psi.

$$\lambda_s = \sqrt{\frac{2}{1 + \frac{d\,(\text{in.})}{10}}} \leq 1 \text{ (in.-lb)}$$

or (2)

$$\lambda_s = \sqrt{\frac{2}{1 + \frac{d\,(\text{mm})}{254}}} \leq 1 \text{ (SI)}$$

The basic equation for two-way shear strength of nonprestressed slabs in ACI 318-19 ($4\sqrt{f_c'}$) was first introduced in 1963 and was based on research by Moe (1961) and the recommendations of a report by Joint ACI-ASCE Committee 326 (1962). This equation provides a lower bound to the measured two-way shear strength of reported slab and footing tests available at the time and has essentially remained unchanged since its introduction. Most of the tests used to inform the development of this expression have a reinforcement ratio greater than 1.06% (Hawkins and Ospina 2017). The second expression was introduced in the 1977 edition of ACI 318 based on the work by Hawkins et al. (1971) and accounts for the effect of column rectangularity, while the third expression accounts for ratio of b_o/d and was added to ACI 318 in 1989 based on the research by Vanderbilt (1972). Both expressions are modifications of the basic expression (Alexander and Hawkins 2005). Finally, the size effect factor λ_s was added to the ACI 318 expressions in 2019 based on the work of Bažant et al. (2007) and Frosch et al. (2017).

In addition, a new provision in ACI 318-19 (Section 8.6.1.2) requires that a minimum amount of bonded flexural reinforcement $A_{s,min}$ be provided near the tension face of a nonprestressed two-way slab at the slab-column connections. The value of $A_{s,min}$ is calculated as

$$A_{s,min} = \frac{5\,v_{uv}\,b_{slab}\,b_o}{\phi\,\alpha_s f_y} \quad (3)$$

where v_{uv} is the factored shear stress on the slab critical section for two-way action, from the controlling load combination, without moment transfer (psi [MPa]); b_{slab} is the effective slab width calculated in accordance with Section 8.4.2.2.3 (in. [mm]); and f_y is the yield strength of the reinforcement bars (psi [MPa]). This equation was developed for interior columns where the factored shear force on the critical section for two-way shear is set equal to the shear force associated with local yielding at the column faces (Hawkins and Ospina 2017). At higher shear stresses, the possibility of flexure-driven punching failure in a nonprestressed slab increases if $A_{s,min}$ is not satisfied (ACI Committee 318 2019). It should also be noted that this expression uses the design shear demand v_{uv} rather than the reduced nominal two-way shear strength for design ϕv_c (where $\phi = 0.75$), which is either equal to or greater than the factored demand.

Eurocode 2 and JSCE

Both the European standard for design of concrete structures, Eurocode 2 (2004), and the Japanese standard specifications for concrete structures, JSCE (2010), directly account for the influence of bonded flexural reinforcement ratio on the punching shear strength of nonprestressed slabs.

Table 1 summarizes the expressions provided by each standard for calculating the two-way shear strength V_c of nonprestressed slabs with no shear reinforcement.

ANALYSIS OF ACI 445-*fib* DATABASE

The effect of the flexural reinforcement ratio ρ on the punching shear strength of nonprestressed slabs was studied by analyzing the ACI 445-*fib* punching shear database described by Ospina et al. (2012). The database contains 636 tests conducted on interior nonprestressed two-way slab-column connections under direct shear. No slab specimens included in the database contain any shear reinforcement.

Reduced database for evaluation

The original database was filtered based on the following criteria to select specimens to be used for this analysis. The criteria were selected to achieve a uniform data set

containing slab specimens with parameters that reasonably represent those found in full-scale structures. The specimens selected for further analysis have the following characteristics. The number of specimens removed when applying each parameter is noted as well.

1. Specimens have deformed steel reinforcement with a circular cross section (162 specimens removed).

2. Specimens have an effective depth d of at least 2 in. (51 mm) (124 specimens removed).

3. Specimens have a slab thickness between 3 and 14 in. (76 and 360 mm) (11 specimens removed).

4. Specimens have a column width to effective depth ratio c_1/d, where c_1 is the longer side of the column, between 0.5 and 6 (one specimen removed).

5. Specimens have a compressive strength of concrete at the time of slab testing $f_{c,Test}$ above 2000 psi (14 MPa) (seven specimens removed).

6. Specimens use normalweight concrete (four specimens removed).

7. Flexural reinforcement ratio ρ is between 0.2 and 3% (14 specimens removed).

8. The reported failure mode was one of three standard types: punching failure, flexural failure, or flexural-punching failure. Tests with the failure mode reported as ductile-punching, bond failure, and shear failure were excluded (18 specimens removed).

From the 636 test specimens in the database, 295 satisfied all eight criteria previously stated. From here on, these 295 specimens are referred to as the "database" that was used for further analysis. Of these 295 specimens, 16 specimens were reported as flexural failures. It is recognized that these specimens may not have achieved their full two-way shear strength; however, these data are considered to provide additional value and are included for completeness. A number of the subsequent plots distinguish the failure types for clarity.

Table A-1 in the Appendix* summarizes the database that was used in this study including the geometric and material parameters for the test slabs, and the failure load and failure mode as reported by researchers.

Summary of parameters

With respect to concrete compressive strength, different control specimens were used in the various experiments to determine the compressive strength of concrete used for the slab specimens. Therefore, the reported compressive strength values were converted to standard uniform strength values to facilitate the comparison of the various tests. In this study, all reported compressive strength values for different types of control specimens (cylinders, cubes, and so on), denoted as $f_{c,Test}$ in the original database, are converted to the strength f_{1c} of a slender prism of dimension 4.7 x 14.2 in. (120 x 360 mm) as follows

$$f_{1c} = (\text{Factor } f_{1c}) \times f_{c,Test} \quad (4)$$

*The Appendix is available at **www.concrete.org/publications** in PDF format, appended to the online version of the published paper. It is also available in hard copy from ACI headquarters for a fee equal to the cost of reproduction plus handling at the time of the request.

Table 2—Conversion factors for compressive strength of concrete (*fib* Bulletin 12 [2001] and ACI-*fib* 445 punching shear database)

Specimen shape	Dimensions, mm	Factor f_{1c}
Cylinder	75 x 150	0.90
Cylinder	100 x 200	0.92
Cylinder	100 x 300	1.00
Cylinder	150 x 300	0.95
Cylinder	160 x 320	1.00
Cube	100 x 100	0.71
Cube	150 x 150	0.79
Cube	200 x 200	0.83
Prism	120 x 360	1.00

Note: 1 mm = 0.039 in.

where Factor f_{1c} represents the applicable conversion factor for the slender prism taken from *fib* Bulletin 12 (2001) and summarized in Table 2. This approach is consistent with that used for the shear databank prepared by Reineck et al. (2003) for reinforced concrete beams without shear reinforcement. The reference concrete compressive strength f_{1c} thus obtained was used to calculate the nominal shear strength of the slab specimens in the database analysis.

The experimental data of the reduced set of 295 test specimens are summarized in Fig. 2 with respect to several parameters, as follows:

- Figures 2(a) and (b) show the distribution of the database in terms of slab thickness and effective depth. Most slabs (92%) have a slab thickness between 3 and 10 in. (76 and 250 mm). The database also contains a limited number of thicker slabs with a maximum thickness of 14 in. (360 mm).
- The distribution of the database with respect to flexural reinforcement ratio ρ is shown in Fig. 2(c). Nearly 80% (236 out of 295) of the slab specimens had a flexural reinforcement ratio between 0.5% and 2%.
- Figure 2(d) shows the distribution of the reference concrete compressive strength f_{1c} for the database. Of the 295 slab specimens, 208 had concrete compressive strength values in the range of 3000 to 6000 psi (21 to 40 MPa).
- The distribution of the yield strength of bonded flexural reinforcement in the test specimens in the database is shown in Fig. 2(e). Approximately 61% (179 out of 295) of the slabs had a flexural reinforcement with a yield strength range of 60 to 80 ksi (420 to 550 MPa) and approximately 16% (47 out of 295) have f_y between 80 and 100 ksi (550 and 690 MPa).
- Figure 2(f) shows the distribution of the database with respect to the column width to effective depth ratio c_1/d, where 246 slabs out of 295 have a c_1/d ratio ranging from 1 to 3.
- The distribution of critical perimeter to effective depth ratio b_o/d of the database is shown in Fig. 2(g), where the b_o/d varies widely (from 6 to 21).

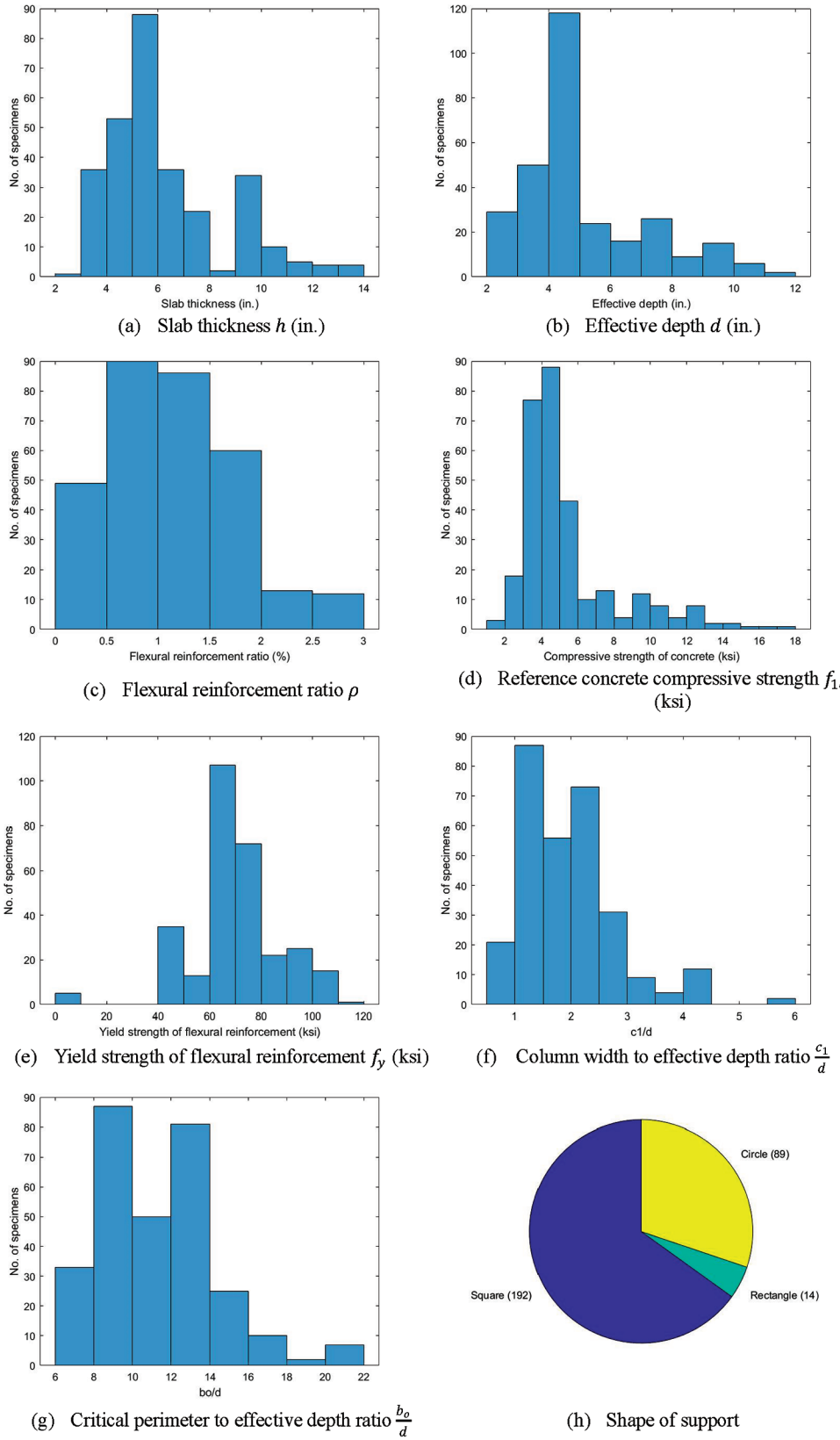

(a) Slab thickness h (in.)

(b) Effective depth d (in.)

(c) Flexural reinforcement ratio ρ

(d) Reference concrete compressive strength f_{1c} (ksi)

(e) Yield strength of flexural reinforcement f_y (ksi)

(f) Column width to effective depth ratio $\frac{c_1}{d}$

(g) Critical perimeter to effective depth ratio $\frac{b_o}{d}$

(h) Shape of support

Fig. 2—Distribution of parameters in database. (Note: 1 in. = 25.4 mm; 1 psi = 0.0069 MPa; 1 ksi = 7 MPa.)

- Figure 2(h) shows the distribution of specimens in the database with respect to the shape of support and the ratio of long-to-short dimension of the column section β. Of the 295 tests summarized in the database, 192 slab specimens have square supports and 89 have circular supports. Only 14 out of 295 specimens have rectangular supports such that β is greater than 1.0.

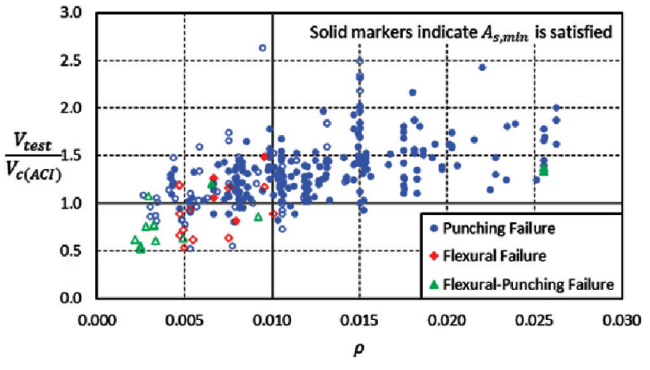

(a) $V_{c(ACI)}$ calculated using f_{1c}

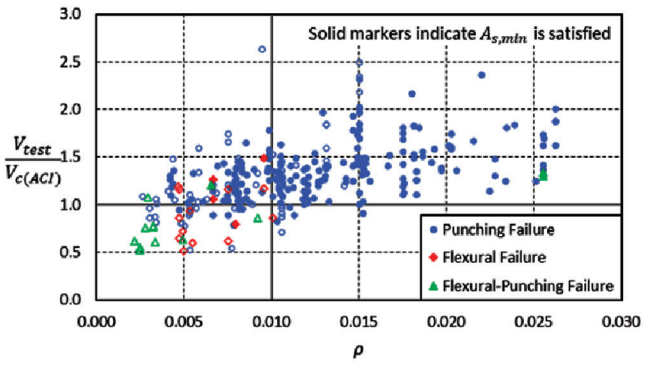

(b) $V_{c(ACI)}$ calculated using f_c'

Fig. 3—Relationship between $V_{test}/V_{c(ACI)}$ *and* ρ.

ANALYSIS OF NOMINAL SHEAR STRENGTH USING ACI 318-19

The two-way shear strength for each of the 295 concentrically loaded nonprestressed slab-column connection test specimens in the database were calculated using the limiting value of v_c (in psi units) from the ACI 318-19 provisions given in Eq. (1).

Figure 3 shows the relationship between the shear ratio $V_{test}/V_{c(ACI)}$ and the flexural reinforcement ratio ρ. V_{test} is the shear force at failure as reported by the researchers and $V_{c(ACI)}$ is the two-way shear strength (in force units) calculated using v_c (in stress units) from the ACI 318-19 provisions given in Eq. (1) multiplied by the critical shear perimeter area ($b_o d$). The two-way shear strength for all test specimens was determined using their respective reported material properties and specimen dimensions.

The reported failure mode is consistent with that observed and reported by the researchers for each study. As noted previously, specimens that failed in flexure may not have achieved their full two-way shear strength, but are included for completeness. The blue dots represent two-way slab specimens that failed due to punching shear, the red dots correspond to slab specimens that exhibited flexural failure, while the green dots refer to slab specimens that exhibited flexural-punching failure (yielding of the flexural reinforcement followed by punching shear failure).

The minimum area of bonded reinforcement $A_{s,min}$ required by ACI 318-19, Section 8.6.1.2, and shown in Eq. (3), was introduced in the 2019 Code. Therefore, slabs designed

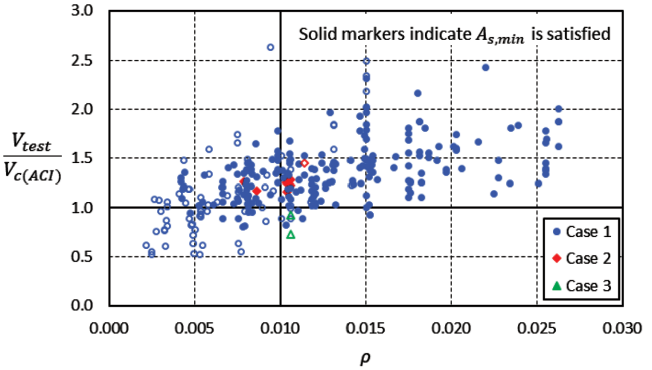

Fig. 4—Relationship between $V_{test}/V_{c(ACI)}$ *and* ρ *showing governing expression for* V_{ACI}.

using earlier editions of the Code may have lower areas of bonded reinforcement in the connection region. The open circles in Fig. 3 correspond to tests where $A_{s,min}$ was not provided. To compute the value of $A_{s,min}$ for each test specimen, the factored shear stress v_{uv} was taken as the maximum shear stress applied in the test. This approach is consistent with Section 8.6.1.2 of ACI 318-19, where $A_{s,min}$ is determined using the factored two-way shear demand v_{uv}, which may be lower than the nominal two-way shear strength v_c. Therefore, when v_{uv} is relatively low, the minimum required bonded flexural reinforcement ratio ρ within b_{slab} may be less than 1%, leading to a lightly reinforced slab-column connection. As the test data indicates, the use of ρ less than 0.010 within b_{slab} should be carefully considered.

The mean shear ratio is 1.32 with a coefficient of variation (CoV) of 0.33. Of the 295 test specimens shown in Fig. 3(a), 48 specimens (16.3%) have $V_{test}/V_{c(ACI)}$ less than 1.0. The overall trend clearly indicates that the ACI 318-19 provisions give more conservative shear strength values for slabs with a higher flexural reinforcement ratio ρ. However, the design shear values can be unconservative for slabs with lower reinforcement ratios, particularly below one percent. Note that a similar trend is observed in Fig. 3(b) when the concrete compressive strength f_c' for a 6 x 12 in. (150 x 300 mm) cylinder is used to calculate $V_{c(ACI)}$ as compared to using the compressive strength of a slender prism f_{1c}.

Figure 4 identifies which of the three expressions given in Eq. (1) governs for the test specimens. The first expression (Case 1) governs for almost 96% (282 out of 310) of the test specimens. The second expression that includes β (Case 2) governs for only 10 of the 14 specimens having rectangular supports and a β of 2.4 or greater. Finally, the third expression (Case 3) governs for only three slabs that have a ratio b_o/d greater than 20.

The shear strength corresponding to the formation of a yield line around the support is given as follows (Hawkins and Ospina 2017)

$$V_{flex} = 8\rho f_y d^2 \quad (5)$$

where f_y is the yield strength of the bonded flexural reinforcement. This expression is provided in a slightly different format in the commentary of ACI 318-19, Section R8.6.1.2, to support the derivation of $A_{s,min}$.

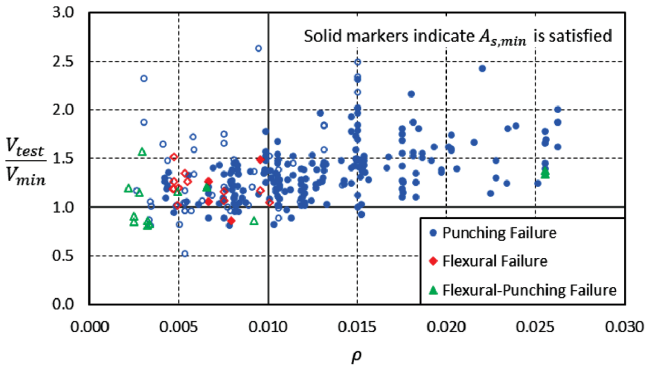

Fig. 5—Relationship between V_{test}/V_{min} *and* ρ.

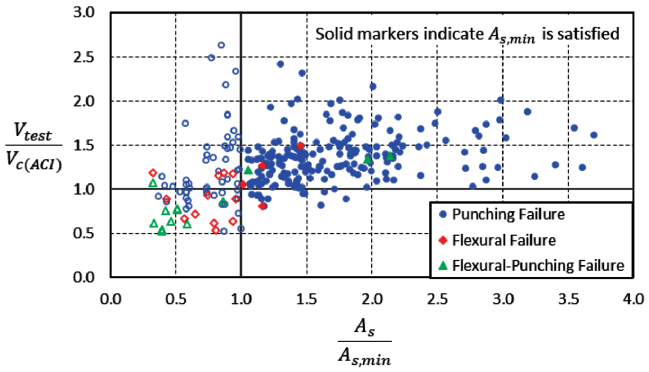

Fig. 6—Relationship between $V_{test}/V_{c(ACI)}$ *and* $A_s/A_{s,min}$.

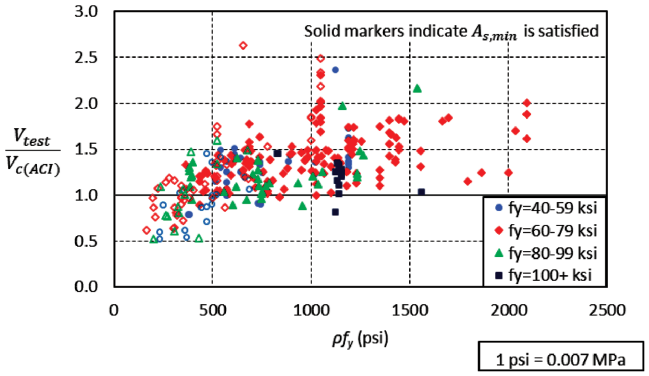

Fig. 7—Relationship between $V_{test}/V_{c(ACI)}$ *and* ρf_y *for ACI 318-19.*

Figure 5 depicts the relationship between the ratio V_{test}/V_{min} and ρ, where V_{min} is the minimum of the punching shear strength $V_{c(ACI)}$ calculated using Eq. (1) and the shear force at flexural failure V_{flex} calculated using Eq. (5). It can be observed that the number of points falling below the 1.0 is reduced significantly from 48 to 28 when the two-way shear strength of nonprestressed slabs is limited to the minimum of $V_{c(ACI)}$ and V_{flex}.

Figure 6 shows the relationship between $V_{test}/V_{c(ACI)}$ and $A_s/A_{s,min}$, where A_s is the area of the bonded flexural reinforcement provided within the width b_{slab} (defined in ACI 318-19, Section 8.4.2.2.3) of the test slab and $A_{s,min}$ is the minimum bonded flexural reinforcement required to be provided near the tension face of nonprestressed slabs as per Section 8.6.1.2 of ACI 318-19. It should be noted that ρ values provided in the database for the two-way slab specimens are

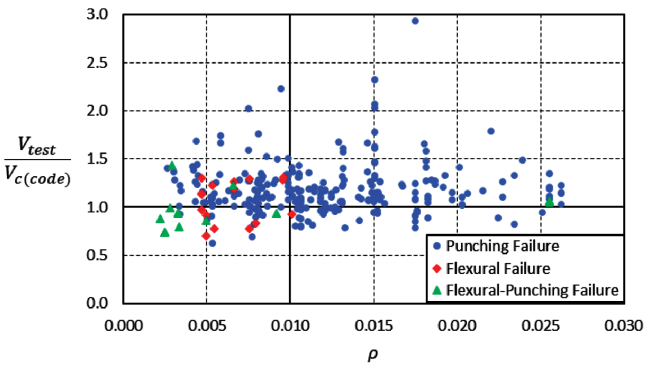

Fig. 8—Relationship between $V_{test}/V_{c(code)}$ *and* ρ *for Eurocode 2.*

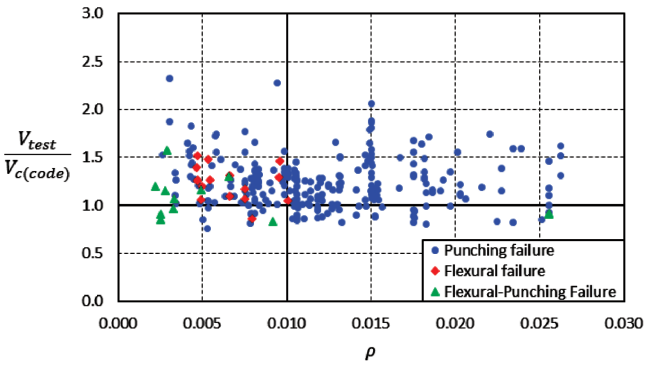

Fig. 9—Relationship between $V_{test}/V_{c(code)}$ *and* ρ *for JSCE.*

used to determine the respective values of A_s, and the specimens typically had a uniform distribution of reinforcement across the specimen width. It is observed that even for slabs where $A_{s,min}$ is provided within the effective width defined, the ACI 318-19 equations can give two-way shear strength values where $V_{test}/V_{c(ACI)}$ is less than 1.

Figure 7 shows the relationship between the shear ratio and ρf_y, which is the product of the bonded flexural reinforcement ratio ρ and the yield strength of the flexural reinforcement f_y, for the ACI 318-19 provisions. Out of 295 test specimens in the database, only 290 are plotted in Fig. 7 because the information of the reinforcement yield strength was not available for five of the slab specimens. It can be noted that the ACI 318-19 provisions for two-way shear strength of nonprestressed slabs give more conservative predictions as the product ρf_y increases. However, a large number of lightly reinforced slabs with lower values of ρf_y (less than 500) have shear ratios less than 1.0, thus indicating that the amount of bonded flexural reinforcement has a significant influence on the two-way shear strength of these slab-column connections.

ANALYSIS OF NOMINAL SHEAR STRENGTH USING SELECTED CODES

The specimen two-way shear strength values were also compared with the design punching shear capacities calculated using the equations of Eurocode 2 and JSCE given in Table 1. It should be noted that the values of all partial safety factors used in the equations for calculating the two-way shear strength are taken equal to unity for the present study. Figures 8 and 9 show the relationship between $V_{test}/$

Table 3—Different forms of k_ρ factor considered and corresponding analysis parameters

Considered k_ρ factor	$9\rho^{1/2}$	$4\rho^{1/3}$	$16\rho^{1/3*}$
Mean	1.43	1.52	1.53
Standard deviation	0.40	0.41	0.41
CoV	0.28	0.27	0.27
No. of points with shear ratio < 1.0	26/295	13/295	9/295

*When using this k_ρ factor, $\sqrt{f_c'}$ in the ACI 318-19 equation is replaced with $\sqrt[3]{f_c'}$ (psi units).

Note: 1 psi = 0.0069 MPa.

$V_{c(code)}$ and ρ, where $V_{c(code)}$ is the punching shear strength of nonprestressed slabs calculated using the provisions of Eurocode 2 or JSCE, as noted. The data shown uses the reference compressive strength of a slender prism f_{1c}. For both codes, the differences in the shear ratios are negligible when the concrete compressive strength f_c' for a 6 x 12 in. (150 x 300 mm) cylinder is used to calculate V_c. It should be noted that the expressions for calculating the punching shear capacity of nonprestressed two-way slabs provided in both codes incorporate the effect of bonded flexural reinforcement ρ, as shown in Table 1. The mean shear ratio $V_{test}/V_{c(code)}$ for Eurocode was 1.19 with a CoV of 0.27, while for JSCE the mean shear ratio was 1.21 with a CoV of 0.26. Of the 295 test specimens in the database, 67 slabs had a shear ratio less than 1.0 when using Eurocode 2, while 65 had a shear ratio less than 1.0 when using JSCE. The predictions of the selected design codes for slabs with lower flexural reinforcement ratios (less than 0.010) have fewer instances of overestimating the two-way shear strength as compared to the ACI 318-19 predictions. Also, there is a more uniform prediction of the shear strength by Eurocode 2 (2004) and JSCE (2010) as ρ varies. Thus, the possibility of directly incorporating the effect of the flexural reinforcement ratio into the design equations of ACI 318-19 was investigated, as discussed in the following section.

PROPOSED MODIFIED ACI 318 EQUATIONS AND DATABASE ANALYSIS

Proposed expressions

Regression analysis was conducted to study the relationship between the flexural reinforcement ratio and the punching shear strength of the slab specimens and to identify an appropriate factor, based on ρ, to reflect the reduced shear strength for low reinforcement ratios. Various forms of the two-way shear strength expressions were considered while seeking to maintain the overall simplicity of the current equation format for ease of implementation in design. The ACI 318-19 equations for two-way shear strength are maintained, while a new factor k_ρ is introduced to include the effect of ρ as follows

$$v_{c(prop)} = k_\rho v_{c(ACI)} \tag{6}$$

Three potential forms of the modification factor k_ρ were considered for application to the ACI 318-19 equations for the two-way concrete shear strength of nonprestressed slabs. These are summarized in Table 3. The coefficients applied to the bonded flexural reinforcement ratio ρ terms were selected based on the regression analysis results. The index powers for ρ were also selected based on the regression analyses, while also considering the values used in current codes to promote consistency and simplicity in the proposed expression. For example, ACI 318-19 uses $\rho^{1/3}$ for calculation of one-way concrete shear strength, JSCE uses $\rho^{1/2}$ for two-way concrete shear strength, and Eurocode 2 uses $\rho^{1/3}$ for two-way concrete shear strength. In the third option, the term $\rho^{1/3}$ is considered along with $\sqrt[3]{f_c'}$, which matches Eurocode 2.

Of the three equations, $k_\rho = 4\rho^{1/3}$ was selected because the resulting expressions provide a reasonable lower bound to the test data without further changes to the current ACI 318-19 equations. The proposed equations are also consistent with the one-way shear expressions introduced in ACI 318-19 for nonprestressed beams, where ρ is raised to the one-third power, while the concrete compressive strength is included as $\sqrt{f_c'}$.

The proposed modification to the ACI 318-19 equations provided in Eq. (1) is as follows

$$v_{c(prop)} = \min\begin{cases} 4\lambda_s\lambda k_\rho\sqrt{f_c'(\text{psi})} \\ \left(2+\dfrac{4}{\beta}\right)\lambda_s\lambda k_\rho\sqrt{f_c'(\text{psi})} \\ \left(2+\dfrac{\alpha_s d}{b_o}\right)\lambda_s\lambda k_\rho\sqrt{f_c'(\text{psi})} \end{cases} \text{(in.-lb)}$$

or (7)

$$v_{c(prop)} = \min\begin{cases} 0.33\lambda_s\lambda k_\rho\sqrt{f_c'(\text{MPa})} \\ 0.17\left(1+\dfrac{2}{\beta}\right)\lambda_s\lambda k_\rho\sqrt{f_c'(\text{MPa})} \\ 0.083\left(2+\dfrac{\alpha_s d}{b_o}\right)\lambda_s\lambda k_\rho\sqrt{f_c'(\text{MPa})} \end{cases} \text{(SI)}$$

where

$$0.5 \le k_\rho = 4\rho^{1/3} \le 1.0 \tag{8}$$

The maximum value of reinforcement ratio factor k_ρ is limited to 1.0 to avoid over estimating the two-way shear strength for higher ρ values and maintains an upper-bound v_c of $4\lambda_s\lambda\sqrt{f_c'(\text{psi})}$ [$0.33\lambda_s\lambda\sqrt{f_c'(\text{MPa})}$], consistent with ACI 318-19; while the minimum value of k_ρ of 0.5 provides a lower-bound v_c of $2\lambda_s\lambda\sqrt{f_c'(\text{psi})}$ [$0.165\lambda_s\lambda\sqrt{f_c'(\text{MPa})}$].

Note that the proposed modification to the ACI 318-19 equations is suggested to be used along with the provisions

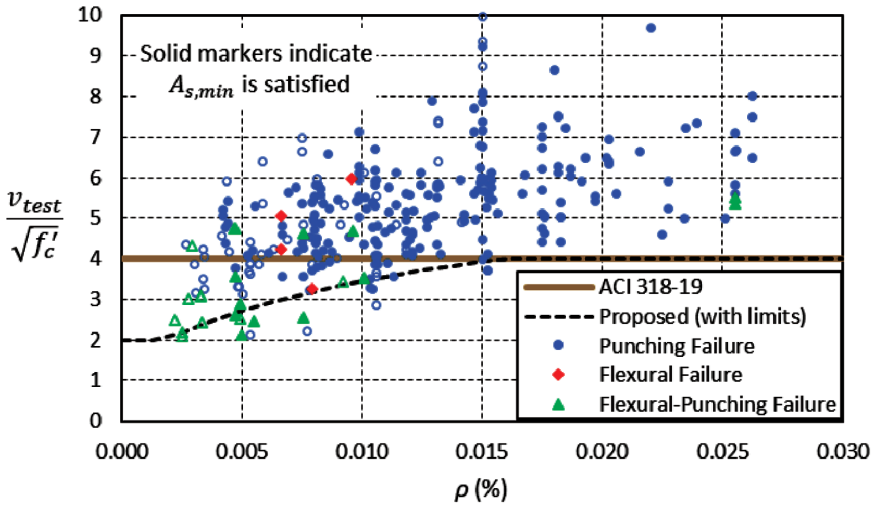

Fig. 10—Relationship between $v_{test}/\sqrt{f_c'}$ *and* ρ.

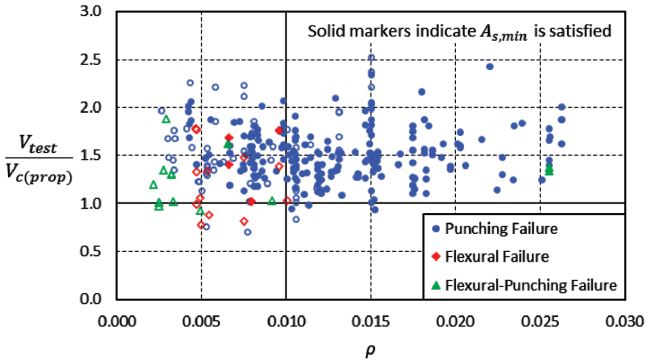

Fig. 11—Relationship between $V_{test}/V_{c(prop)}$ *and* ρ.

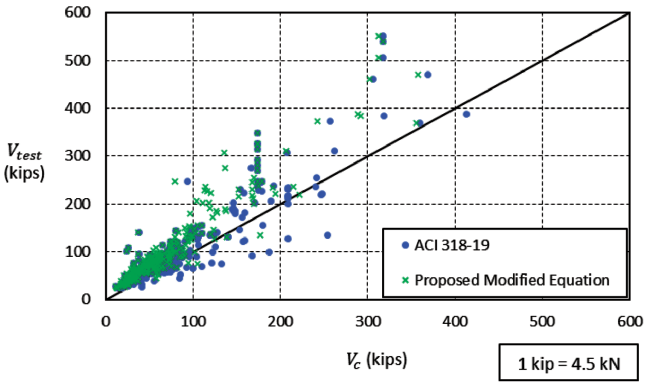

Fig. 12—Relationship between V_{test} *and* V_c *for ACI 318-19 and proposed equation.*

for minimum bonded flexural reinforcement per Section 8.6.1.2 of ACI 318-19 to provide a more comprehensive approach for design of nonprestressed slab-column connections without shear reinforcement. It is also important to emphasize that existing buildings constructed using earlier code provisions that did not require $A_{s,min}$ may have a low reinforcement ratio within the slab-column connection region. In this case, the proposed expressions provide a safer estimate of the two-way shear strength for evaluation of existing two-way slabs.

Figure 10 shows the relationship between $v_{test}/\sqrt{f_c'}$ and ρ for the ACI 318-19 provisions and for the proposed equation with the limits on k_ρ for 291 of 295 test slabs in the database. The four specimens not included in the figure have a value of $v_{test}/\sqrt{f_c'}$ greater than 10. It can be observed that the modified expressions for v_c given in Eq. (7), along with the limits on k_ρ, provide a lower bound for most of the data that fall below the horizontal line corresponding to $v_{test}/\sqrt{f_c'}$ equal to 4.0.

Shear ratio versus reinforcement ratio

The effect of bonded flexural reinforcement on shear strength ratio $V_{test}/V_{c(prop)}$, where $V_{c(prop)}$ is the two-way shear strength calculated using the proposed modified expressions given in Eq. (7) is shown in Fig. 11. It can be noted that the number of points falling below the line corresponding to a ratio of 1.0 significantly decreases from 48 to 13 as compared to the ratio when using the ACI 318-19 expressions shown in Fig. 3. When directly comparing the two-way shear strength expressions, the proposed expressions give safer predictions for nonprestressed slabs with low reinforcement ratios. The mean shear ratio for the proposed equations was found to be 1.52 with a CoV of 0.27.

Figure 12 shows the relationship between the maximum applied shear force and the two-way shear strength of the test slabs calculated using the ACI 318-19 provisions and the proposed modified equations for all 295 test slabs. It can be observed that the proposed equation provides safer estimates of the two-way shear strength for nonprestressed slabs.

Consideration of minimum area of flexural reinforcement

To avoid the possibility for a premature flexural-driven punching shear failure, $A_{s,min}$ was introduced in ACI 318-19 (refer to Eq. (3)) to provide sufficient bonded tension reinforcement in the region of the slab-column connection. The relationship between $V_{test}/V_{c(prop)}$ and $A_s/A_{s,min}$ is plotted in Figure 13. Note that to compute the values of $A_{s,min}$ for the test specimens, the maximum shear applied in the test was used to determine the factored shear stress. This figure shows that most points falling below the 1.0 line did not meet the minimum steel area requirements. Therefore, the

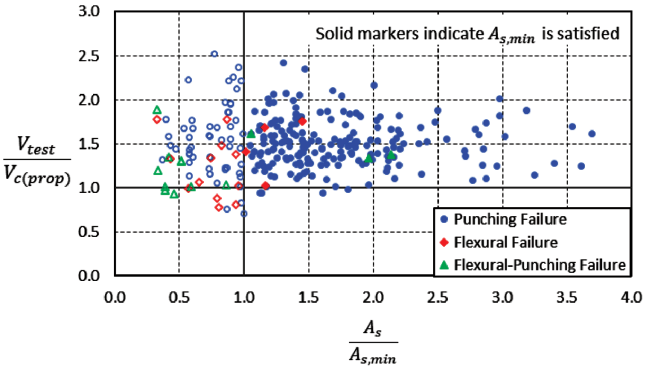

Fig. 13—Relationship between $V_{test}/V_{c(prop)}$ *and* $A_s/A_{s,min}$.

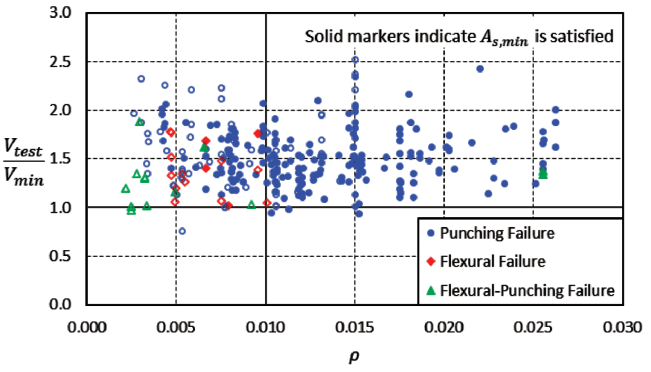

Fig. 14—Relationship between V_{test}/V_{min} *and* ρ.

combination of the proposed shear expressions, along with the provision for $A_{s,min}$, provides a more comprehensive approach for design of nonprestressed slab-column connections without shear reinforcement.

Figure 14 shows the relationship between V_{test}/V_{min}, where V_{min} is the minimum of $V_{c(prop)}$ and V_{flex}, and the flexural reinforcement ratio ρ. A reduced number of points (five total) fall below the 1.0 line when the two-way shear strength of nonprestressed slabs is limited to the minimum of $V_{c(prop)}$ and V_{flex}. This further confirms the benefit of using the proposed modified two-way shear strength expressions in combination with $A_{s,min}$.

When considering the application of the ACI 318-19 provisions, it is important to note that $A_{s,min}$ is determined using the value of the factored shear demand v_{uv}, which is often less than the design two-way shear strength. Therefore, the use of ρ less than 0.010 within b_{slab} should be closely evaluated. In addition, existing buildings constructed using earlier code provisions may have a low reinforcement ratio within the slab-column connection region. In this case, the proposed equations can provide a safer estimate of the two-way shear strength for evaluation of existing two-way slabs.

Influence of flexural reinforcement characteristics

Figure 15(a) shows the relationship between the shear ratio, V_{test}/V_c, and the yield strength of flexural reinforcement f_y. The blue dots indicate the shear ratio where V_c is calculated using the ACI 318-19 equations for two-way

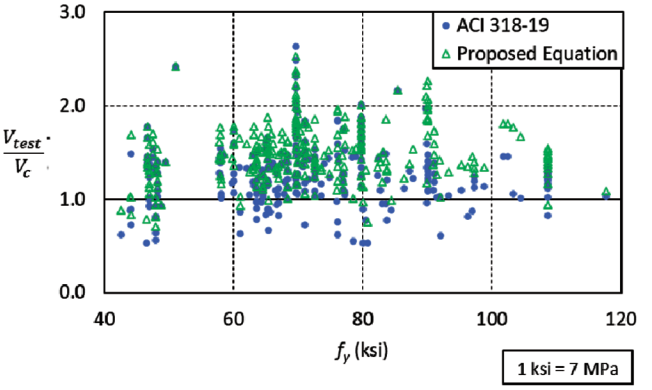

(a) $\frac{V_{test}}{V_c}$ versus f_y

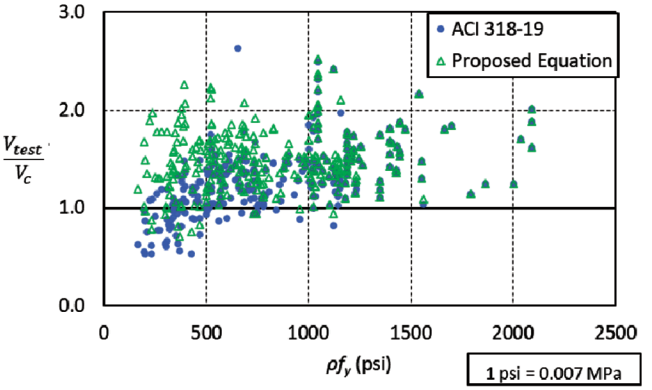

(b) $\frac{V_{test}}{V_c}$ versus ρf_y

Fig. 15—Relationship between V_{test}/V_c *and flexural reinforcement characteristics for ACI 318-19 and proposed expressions.*

shear, while the green dots indicate the shear ratio calculated using the proposed equations. The figure clearly shows that the number of points that fall below 1.0 reduced significantly when the punching shear strength was calculated using the proposed modified equations, particularly for values of f_y greater than 60 ksi (420 MPa). It can also be noted that the proposed equations provide a safer estimate of the two-way shear strength of nonprestressed slabs across a wide range of values of f_y for flexural reinforcement (60 to 120 ksi [414 to 827 MPa]). Figure 15(b) shows the relationship between the shear ratio and ρf_y for the ACI 318-19 provisions and the proposed modified equations. It can be noted that the level of conservatism in estimating the two-way shear strength increases as the product ρf_y increases. It can also be observed that a significant number of points that fall below the 1.0 line for the ACI 318-19 two-way shear strength (blue markers), especially with ρf_y less than 500 psi (3.4 MPa), are pushed above 1.0 when the proposed modified equations are used (green markers) (full-color PDF can be accessed at www.concrete.org). Thus, the proposed equations provide a safer estimate of the two-way shear strength of nonprestressed slabs as compared to the ACI 318-19 provisions.

Table 4—Statistical parameters for V_{test}/V_c for different codes and proposed equations

	All data (295 specimens)					Specimens with $\rho \le 0.01$ (124 specimens)				
Parameter	Eurocode 2	JSCE	ACI 318-19	ACI 318-19*	Proposed Eq.	Eurocode 2	JSCE	ACI 318-19	ACI 318-19*	Proposed Eq.
Mean	1.19	1.21	1.32	1.37	1.52	1.16	1.19	1.12	1.22	1.51
Standard deviation	0.32	0.32	0.44	0.33	0.41	0.25	0.26	0.30	0.20	0.35
CoV	0.27	0.26	0.33	0.24	0.27	0.22	0.22	0.27	0.16	0.23
No. of points < 1.0	67/295 (23%)	65/295 (22%)	48/295 (16%)	13/212 (6%)	13/295 (4%)	31/124 (25%)	25/124 (20%)	38/124 (31%)	7/62 (1%)	8/124 (6%)

*Experimental data excludes specimens that do not meet ACI 318-19 minimum bonded reinforcement area requirement for nonprestressed slabs ($A_{s,min}$).

Comparison of expressions for two-way shear strength

Table 4 provides an overall summary of the mean, standard deviation, and CoV for the shear ratio V_{test}/V_c for all the code and proposed expressions discussed previously. The table provides statistics when all 295 specimens are considered and when considering only the specimens with $\rho \le 0.01$ (124 specimens). The number of tests with a shear ratio less than 1.0 are also summarized in the last row of the table. The number of points falling below the 1.0 shear ratio line in Fig. 8 and 9 is greater for Eurocode 2 and JSCE; however the mean and CoV for these codes are lower.

In Table 4, an additional column is provided for each set of specimens, removing the specimens not satisfying the minimum bonded reinforcement area requirement for nonprestressed slabs ($A_{s,min}$) in ACI 318-19. This allows a review of the impact of this provision in ACI 318-19. It can be observed that, of the 212 specimens that satisfy the $A_{s,min}$ requirement, 13 specimens have a shear ratio less than 1.0. Of these 13 specimens, seven have a bonded flexural reinforcement ratio ρ less than 1%. When applying the proposed modified v_c expressions to the 212 specimens, it was observed that only four specimens had a shear ratio less than 1.0. Thus, the proposed expressions provide a lower bound value of v_c for most of the test data, avoiding overestimation of the two-way shear strength of nonprestressed slabs.

It can also be noted that the proposed modified expressions given in Eq. (7) provide more conservative results with less scatter as compared to the ACI 318-19 provisions. The proposed expressions lead to a significant reduction in the number of points with a shear ratio less than 1.0 relative to all codes considered. Therefore, there are fewer instances of overestimating the two-way shear strength when using the proposed expressions; and these occurrences reduce further when considering specimens with lower reinforcement ratios of $\rho \le 0.01$.

SUMMARY AND CONCLUSIONS

After a careful review of the two-way shear database and comparison of the shear ratios V_{test}/V_c for the ACI 318-19 provisions and the proposed modification factor for these expressions, the main conclusions of the paper can be summarized as follows.

1. The ACI 318-19 provisions give more conservative shear strength values for slabs with a higher flexural reinforcement ratio ρ. However, the design shear values can be unconservative for slabs with lower reinforcement ratios, particularly below 1%.

2. The aforementioned limitation was addressed in ACI 318-19 by requiring a minimum area of bonded flexural reinforcement in the support region ($A_{s,min}$). Other codes directly incorporate ρ in the expression for the two-way concrete shear strength v_c.

3. For the ACI 318-19 provisions, it is important to note that $A_{s,min}$ is determined using the value of the factored shear demand v_{uv}, which is often less than the design two-way shear strength. Therefore, the use of ρ less than 0.010 within b_{slab} should be carefully considered.

4. The proposed modification factor k_ρ for the v_c expressions in ACI 318-19, along with the limits on this factor, provide a lower bound value of v_c for most of the test data.

5. When directly comparing the two-way shear strength expressions, the proposed expressions for v_c give safer predictions for nonprestressed slabs with low reinforcement ratios. Therefore, the combination of the proposed shear expressions, along with the provision for $A_{s,min}$, provides a more comprehensive approach for design of nonprestressed slab-column connections without shear reinforcement.

6. Finally, it is noted that existing buildings constructed using earlier code provisions may have a low reinforcement ratio within the slab-column connection region. In this case, the proposed equations provide a safer estimate of the two-way shear strength for evaluation of existing two-way slabs.

AUTHOR BIOS

ACI member **Madhura Sanjay Chavan** *is a PhD Candidate in civil engineering at Texas A&M University, College Station, TX. She received her bachelor of engineering in civil engineering from the University of Pune, India, and her master of technology in structural engineering from Sardar Vallabhbhai National Institute of Technology, Surat, India. Her research interests include nonlinear finite element modeling and analysis of slab-column connections.*

Mary Beth D. Hueste, *FACI, is the Truman R. Jones, Jr. '43 Professor of Civil Engineering at Texas A&M University. She is a member of the ACI Technical Activities Committee; ACI Committees 318, Structural Concrete Building Code, and 374, Performance-Based Seismic Design of Concrete Buildings; and Joint ACI-ASCE Committee 352, Joints and Connections in Monolithic Concrete Structures. Her research interests include the behavior, analysis, and design of concrete structures.*

ACI member **Aikaterini S. Genikomsou** *is an Associate Professor of Civil Engineering at Queen's University, Kingston, ON, Canada. She is the Chair of Joint ACI-ASCE Committee 421, Design of Reinforced Concrete Slabs, and a member Joint ACI-ASCE Committee 447, Finite Element Analysis of Reinforced Concrete Structures, and Joint ACI-ASCE Subcommittee 445-C, Shear and Torsion-Punching Shear. Her research interests include*

the behavior, design, and analysis of reinforced concrete structures, and finite element modeling.

ACKNOWLEDGMENTS

The authors wish to express their gratitude and sincere appreciation to the members of ACI Subcommittee 318-E, Section and Member Strength, for their feedback and comments on this study, and Joint ACI-ASCE Subcommittee 445-C, Shear & Torsion-Punching Shear, for sharing the ACI 445-*fib* punching shear database. The authors would also like to thank P. Dominguez for his help in the analysis of the database during his graduate studies at Texas A&M University (TAMU). The support of the TAMU Zachry Department of Civil and Environmental Engineering during this study is greatly appreciated.

REFERENCES

ACI Committee 318, 2019, "Building Code Requirements for Structural Concrete (ACI 318-19) and Commentary (ACI 318R-19) (Reapproved 2022)," American Concrete Institute, Farmington Hills, MI, 624 pp.

Alexander, S. D. B., and Hawkins, N. M., 2005, "A Design Perspective on Punching Shear," *Punching Shear in Reinforced Concrete Slabs*, SP-232, American Concrete Institute, Farmington Hills, MI, pp. 97-108.

Alexander, S. D. B., and Simmonds, S. H., 1986, "Shear-Moment Transfer in Slab-Column Connections," *Structural Engineering Report No. 141*, 116 pp.

Bažant, Z. P.; Yu, Q.; Gerstle, W.; Hanson, J.; and Ju, J., 2007, "Justification of ACI 446 Code Provisions for Shear Design of Reinforced Concrete Beams," *ACI Structural Journal*, V. 104, No. 5, Sept.-Oct., pp. 601-610.

Dam, T. X., and Wight, J. K., 2016, "Flexurally-Triggered Punching Shear Failure of Reinforced Concrete Slab–Column Connections Reinforced with Headed Shear Studs Arranged in Orthogonal and Radial Layouts," *Engineering Structures*, V. 110, pp. 258-268. doi: 10.1016/j.engstruct.2015.11.050

Dam, T. X.; Wight, J. K.; and Parra-Montesinos, G. J., 2017, "Behavior of Monotonically Loaded Slab-Column Connections Reinforced with Shear Studs," *ACI Structural Journal*, V. 114, No. 1, Jan.-Feb., pp. 221-232.

EN 1992-1-1, 2004, "Eurocode 2: Design of Concrete Structures—Part 1: General Rules and Rules for Buildings," British Standards Institute, London, UK, 253 pp.

fib Bulletin 12, 2001, "Punching of Structural Concrete Slabs," Technical Report, Fédération internationale du béton, Lausanne, Switzerland, 307 pp.

Frosch, R. J.; Yu, Q.; Cusatis, G.; and Bažant, Z. P., 2017, "A Unified Approach to Shear Design," *Concrete International*, V. 39, No. 9, Sept., pp. 47-52.

Hawkins, N. M.; Fallsen, H. B.; and Hinojosa, R. C., 1971, "Influence of Column Rectangularity on the Behavior of Flat Plate Structures," *Cracking, Deflection and Ultimate Load of Concrete Slab Systems*, SP-30, American Concrete Institute, Farmington Hills, MI, pp. 127-146.

Hawkins, N. M., and Ospina, C. E., 2017, "Effect of Slab Flexural Reinforcement and Depth on Punching Strength," *Punching Shear in Structural Concrete Slabs: Honoring Neil M. Hawkins*, SP-315, American Concrete Institute, Farmington Hills, MI, pp. 117-140.

Joint ACI-ASCE Committee 326, 1962, "Shear and Diagonal Tension (ACI 326-62)," American Concrete Institute, Farmington Hills, MI.

Joint ACI-ASCE Committee 352, 2011, "Guide for Design of Slab-Column Connections in Monolithic Concrete Structures (ACI 352.1R-11)," American Concrete Institute, Farmington Hills, MI, 28 pp.

JSCE, 2010, "JSCE Guidelines for Concrete No. 15 – Standard Specifications for Concrete Structures – 2007 'Design," Japan Society of Civil Engineers, Tokyo, Japan.

Liberati, E. A. P.; Marques, M. G.; Leonel, E. D.; Almeida, L. C.; and Trautwein, L. M., 2019, "Failure Analysis of Punching in Reinforced Concrete Flat Slabs with Openings Adjacent to the Column," *Engineering Structures*, V. 182, pp. 331-343. doi: 10.1016/j.engstruct.2018.11.073

Moe, J., 1961, "Shearing Strength of Reinforced Concrete Slabs and Footings Under Concentrated Loads," *Development Department Bulletin No. D47*, Portland Cement Association, Skokie, IL, 130 pp.

Muttoni, A., 2008, "Punching Shear Strength of Reinforced Concrete Slabs Without Transverse Reinforcement," *ACI Structural Journal*, V. 105, No. 4, July-Aug., pp. 440-450.

Ospina, C. E.; Birkle, G.; and Widianto, 2012, "Databank of Concentric Punching Shear Tests of Two-way Concrete Slabs without Shear Reinforcement at Interior Supports," *2012 ASCE Structures Congress, Proceedings*, pp. 1814-1832.

Park, H. G.; Choi, K. K.; and Chung, L., 2011, "Strain-Based Strength Model for Direct Punching Shear of Interior Slab–Column Connections," *Engineering Structures*, V. 33, No. 3, pp. 1062-1073. doi: 10.1016/j.engstruct.2010.12.032

Reineck, K.-H.; Kuchma, D. A.; Kim, K. S.; and Marx, S., 2003, "Shear Database for Reinforced Concrete Members Without Shear Reinforcement," *ACI Structural Journal*, V. 100, No. 2, Mar.-Apr., pp. 240-249.

Vanderbilt, M. D., 1972, "Shear Strength of Continuous Plates," *Journal of the Structural Division*, V. 98, No. 5, pp. 961-973. doi: 10.1061/JSDEAG.0003248

Widianto; Bayrak, O.; and Jirsa, J. O., 2009, "Two-Way Shear Strength of Slab-Column Connections: Reexamination of ACI 318 Provisions," *ACI Structural Journal*, V. 106, No. 2, Mar.-Apr., pp. 160-170.

ACI STRUCTURAL JOURNAL TECHNICAL PAPER

Title No. 122-S08

Shear Strength of Steel Fiber-Reinforced Concrete Beams and One-Way Slabs

by Sergio M. Alcocer, Ghassan Almasabha, Julian Carrillo, Shih-Ho Chao, and Adam S. Lubell

Recent research data was evaluated with the aim of extending the applicability of using deformed steel fiber-reinforced concrete (SFRC) to enhance the shear strength of beams and one-way slabs. Experimental results were assessed for influences on the shear strength of SFRC members that do not contain stirrups of factors, including size effect, concrete density (normalweight and lightweight) and compressive strength, fiber-volume fraction (V_f), and the longitudinal steel reinforcement ratio. Estimates of steel stresses in longitudinal bars at the time of shear failure were carried out to identify differences in members with distinct longitudinal steel ratios and bar grades, consistent with the range of flexural design parameters in ACI 318-19. Results of these analyses and a reliability investigation of design equations applicable to members without fibers were used for proposing new provisions for the shear design of SFRC beams and one-way slabs based on the ACI 318-19 shear-strength model.

Keywords: beams; fiber-volume fraction; lightweight concrete (LWC); minimum shear reinforcement; normalweight concrete (NWC); one-way slabs; shear; size effect; steel fibers.

INTRODUCTION

Shear reinforcement in beams and one-way slabs typically consists of steel bars bent in the form of stirrups or hoops. In lieu of this reinforcement, the use of deformed steel fibers in the concrete is becoming more common due to enhanced member performance, similar as-built costs, and improved constructability due to reduced reinforcement congestion and simplified reinforcement details. When used in reinforced concrete (RC) beams and one-way slabs without transverse reinforcement, deformed steel fibers increase the shear strength by providing post-cracking diagonal tension resistance.

Steel fibers help restrain the propagation of cracks, reduce crack widths, and increase the deformation capacity of the concrete in tension and compression. Steel fibers act as stitches across cracks, thus reducing crack width and allowing transfer of load from one face of the crack to the other (Carrillo et al. 2021). Analysis of laboratory test data has demonstrated that shear resistance and ductility in RC members can be enhanced if specific steel-fiber characteristics and fiber dosages are satisfied (for example, Parra-Montesinos 2006; Naaman 2017).

Various analytical models to account for the shear-strength enhancement from fibers have been proposed by research groups. Published steel fiber-reinforced concrete (SFRC) shear-strength models have traditionally been semiempirical in nature, calibrated against limited data sets that did not contain results across the full range of typical design parameters that would be considered in design practice. Further, the reported member strengths were not always accompanied by detailed mechanical properties at the material scale.

Recent mechanical models for structural members, such as the 2010 *fib* Model Code (Fédération internationale du béton 2013), establishes SFRC beam shear strength through either an empirical approach or the modified compression field theory. The fiber contribution is factored in by considering the residual tensile strength of SFRC obtained from material laboratory testing.

The existing ACI 318 shear model was first incorporated in the 2008 edition and is based on a semiempirical approach (Parra-Montesinos 2006). Substituting minimum shear reinforcement with steel fibers is permitted for the shear design of slender beams—that is, with shear span-to-effective depth ratio $a/d \geq 2.5$. ACI 318-19 requires that a prescribed minimum quantity of deformed reinforcement as stirrups, $A_{v,min}$, be provided if $V_u > \phi\lambda 1.0\sqrt{f_c'}\, b_w d$ (psi) ($V_u > \phi\lambda 0.083\sqrt{f_c'}\, b_w d$ [MPa]) for beams or where $V_u > \phi V_c$ for slabs. As an exception, Table 9.6.3.1 permits this requirement to be waived for normalweight SFRC beams containing longitudinal flexure reinforcement, and where $h \leq 24$ in. (610 mm), $f_c' \leq 6000$ psi (42 MPa), and $V_u \leq \phi 2\sqrt{f_c'}\, b_w d$ (psi) ($V_u \leq \phi 0.17\sqrt{f_c'}\, b_w d$ [MPa]). In this case, the minimum value of fiber dosage required in Section 26.4.2.2(i) should be provided.

The ACI 318 shear model for calculating V_c underwent significant changes for the 2019 edition by implementing parameters related to the influence of member depth and the flexural reinforcement ratios (Kuchma et al. 2019). At the same time, a considerable increase in the available data for shear-critical SFRC members has occurred since the work by Parra-Montesinos (2006). This paper reports on an analytical study to expand the applicable range of the ACI 318 SFRC provisions for shear while maintaining a model format that does not require detailed mechanical models for the SFRC response in tension. Such a model would have applicability for both preliminary and detailed design, and could also be used for evaluation of SFRC structures where the concrete mixture design is unknown.

ACI Structural Journal, V. 122, No. 1, January 2025.

MS No. S-2023-198.R2, doi: 10.14359/51742138, received May 24, 2024, and reviewed under Institute publication policies.

SFRC IN ACI 318

SFRC provisions in ACI 318 were introduced in the 2008 edition and the technical requirements remain unchanged in ACI 318-19. Requirements are generally based on the study by Parra-Montesinos (2006), who summarized data from 147 laboratory tests of SFRC beams with hooked or crimped fibers failing in shear. All slender beams that contained $V_f \geq 0.75\%$ exhibited a shear stress at failure greater than $3.5\sqrt{f_c'}$ psi ($0.29\sqrt{f_c'}$ MPa). ACI 318-19 requires that SFRC conforms to ASTM A820/A820M (2016) and ASTM C1116/C116M (2015) and contains at least 100 lb of deformed steel fibers per yd^3 of concrete (equivalent to 60 kg/m^3). This steel-fiber dosage is equivalent to a fiber-volume fraction of 0.75%. ASTM A820/A820M (2016) is the standard specification for steel fibers for SFRC, whereas ASTM C1116/C116M (2015) is the standard specification for fiber-reinforced concrete (FRC). The compliance requirements for SFRC are based on minimum specified residual tensile stress values at midspan deflections of 1/300 and 1/150 of the clear span using four-point bending tests (4PBT) on small beams in accordance with ASTM C1609/C1609M (2019).

A review of current ACI provisions for shear strength of SFRC led to the identification of the following concerns:

(a) There is no direct consideration of the size effect in shear strength as the member depth h increases, nor of the influence of the longitudinal reinforcement ratio because the shear design equations for V_c in Section 22.5.5.1 are not explicitly required to be applied.

(b) It is not clear which equation(s) from Table 22.5.5 shall be used for determining V_c.

(c) It is unclear the design method to be used for SFRC when f_c' is between 6000 and 10,000 psi (42 and 69 MPa), and if the current restrictions on f_c' are applicable to both normalweight and lightweight concretes (LWCs).

(d) For one-way slabs, limits for the application of SFRC differ from those for beams.

(e) Because specifications of the design information and compliance requirements for SFRC that were firstly included in ACI 318-08 were purposely conservative because they were based on limited test data, it is advisable to study whether some of these specifications may be relaxed, such as reductions in the minimum fiber-volume fraction V_f.

Based on the concerns identified, the aim of this work was twofold: (a) to supplement the prescribed shear strength of SFRC of $\phi 2\sqrt{f_c'}$ psi ($\phi 0.17\sqrt{f_c'}$ MPa) by also allowing the design of SFRC beams and one-way slabs without stirrups exceeding a strength of ϕV_c, where V_c is determined using the ACI 318-19 shear strength model (Section 22.5.5.1); and (b) to extend the applicability of SFRC provisions to slender members with depths exceeding 24 in. (610 mm) and with compressive strengths higher than currently allowed.

RESEARCH SIGNIFICANCE

Designers of buildings are interested in extending the applicability of deformed SFRC in beams and one-way slabs. Recent experimental programs have provided new information on the shear strength of SFRC members. Analysis of a large database of tests allowed the assessment of size effect; concrete density (normalweight and lightweight); and its compressive strength, fiber-volume fraction, longitudinal steel reinforcement ratio, and steel reinforcement stresses on the shear strength of SFRC members. A reliability investigation was used to develop a new design method suitable for incorporation into the ACI 318 Code.

DATA SET OF SFRC BEAMS

The provisions in the 2008 ACI 318 Code were based on a data set consisting of 147 SFRC beams having an overall depth h not more than 24 in. (610 mm). However, recent experimental studies have provided information on shear strengths of SFRC beams with greater depths ranging from 36 to 60 in. (910 to 1500 mm) (Minelli et al. 2014; Shoaib et al. 2014; Zarrinpour and Chao 2017). To propose equation(s) appropriate for determining the contribution of concrete to shear strength, the size effect in SFRC beams is compared with that in concrete beams without stirrups. Further analysis is performed for beams with overall depths $h > 28$ in. (710 mm) to verify that the proposed equations provide a safe estimate of the shear strength of SFRC beams up to an effective depth of 36 in. (910 mm) (equivalent to an overall height of approximately 40 in. [1020 mm]). A detailed study of beams with low longitudinal steel reinforcement ratios is also discussed. A reliability investigation of the proposed design equations is described.

To assess the shear behavior of SFRC beams, a data set of 340 specimens that complied with features (i) to (x) was considered in the research reported herein:

(i) Specimens with deformed steel fibers conforming to ASTM A820.

(ii) Steel-fiber aspect ratio of at least 50 but not exceeding 100. Section 26.4.1.6.1.(a)(2) of ACI 318-19 requires steel fibers to comply with these limits on length-to-diameter ratio if steel-fiber reinforcement is used for shear resistance.

(iii) Nonprestressed rectangular cross sections.

(iv) Shear-dominated specimens. In all beams, no axial load was applied.

(v) Specimens did not contain stirrups.

(vi) Concrete with $f_c' \leq 10{,}000$ psi (69 MPa).

(vii) Normalweight and LWCs.

(viii) Four-point bending tests (4PBT), center- or three-point bending tests (3PBT), and tests under special conditions were included in the data set. Most tests (67%) were 4PBT while 3PBT accounted for 32% of the tests. In the remaining 1%, specimen restraints were different from those of roller-supported beams.

(ix) Slender beams with shear span-to-effective depth ratio $a/d \geq 2.5$.

(x) Specimens loaded monotonically under quasi-static conditions. The data set does not include specimens loaded cyclically or through impact loading.

Measured shear strengths, V_{test}, in the data set were obtained from the primary reference for each study. Other key parameters in the data set included the longitudinal steel reinforcement ratio ρ_w, shear span-depth ratio a/d, measured compressive strength of concrete f_{cm}, reported yield strength of longitudinal reinforcement f_y, steel fiber length-to-diameter ratio (fiber aspect ratio), and fiber-volume

fraction V_f. Source references used for developing the data set of shear-critical members may be found in Appendix A.* Appendix B includes the source references for an additional 57 tests of lightly reinforced beams that failed in flexure studied later in this paper. The data set with information on the 340 shear-controlled specimens is available in Appendix C. Data on the 57 lightly reinforced beams are included in Appendix D.

The distribution of the fiber length-to-diameter ratio (fiber aspect ratio) in the data set with 340 specimens is shown in Fig. 1(a). Most specimens had fiber aspect ratios between 50 and 70. The distribution of V_f of specimens in the data set is presented in Fig. 1(b). V_f varied between 0.5% (65 lb/yd^3 [39 kg/m^3]) and 3% (390 lb/yd^3 [231 kg/m^3]). The distribution of concrete compressive strength in the data set is shown in Fig. 1(c). From the graph, 35.3% of specimens had $f_c' > 6000$ psi (42 MPa). The distribution of specimen depth h in the data set (with 340 shear-critical beams) is presented in Fig. 1(d). Of the 340 beams, 314 beams had $h \le 24$ in. (610 mm). Further, of the 314 beams with $h \le 24$, 207 (66%) had concrete strengths $f_c' \le 6000$ psi (42 MPa), and 107 (34%) specimens had strengths 6000 psi (42 MPa) $< f_c' \le 10{,}000$ psi (69 MPa) (Fig. 1(e)). Moreover, of the 340 beams, 24 beams

*The Appendix is available at **www.concrete.org/publications** in PDF format, appended to the online version of the published paper. It is also available in hard copy from ACI headquarters for a fee equal to the cost of reproduction plus handling at the time of the request.

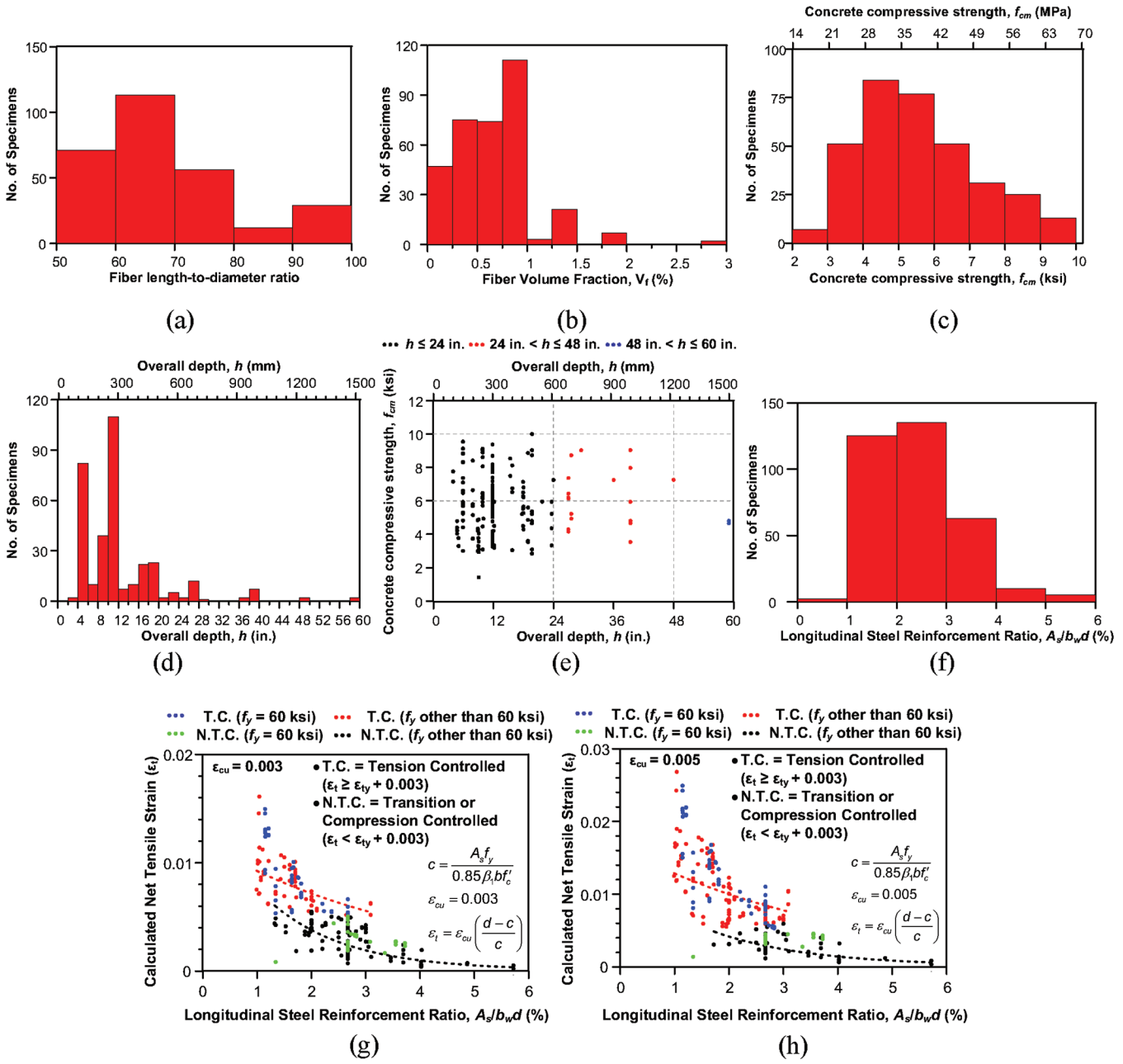

Fig. 1—Data set description; distribution of: (a) fiber length-to-diameter ratio; (b) steel fiber-volume ratio, V_f*; (c) measured concrete compressive strength* f_{cm}*; (d) beam overall depth* h*; (e) measured concrete compressive strength versus overall beam depth* h*; (f) longitudinal reinforcement ratio* ρ_w*; (g) net tensile strain assuming* $\varepsilon_{cu} = 0.003$*; and (h) net tensile strain assuming* $\varepsilon_{cu} = 0.005$*. (Note: 1 ksi = 6.895 MPa.)*

had depths 24 in. (610 mm) < $h \le$ 48 in. (1220 mm); from those, 11 had concrete strengths $f_c' \le$ 6000 psi (42 MPa), and 13 specimens had strengths 6000 psi (42 MPa) < $f_c' \le$ 10,000 psi (69 MPa) (Fig. 1(e)). The data set contains two beams with 48 in. (1220 mm) < $h \le$ 60 in. (1524 mm); both had concrete strengths $f_c' \le$ 6000 psi (42 MPa). The deepest shear-critical LWC beam tested had h = 28 in. (710 mm). The distribution of the longitudinal reinforcement ratio, $\rho_w = A_s/b_w d$, of specimens in the data set is shown in Fig. 1(f). The longitudinal reinforcement ratio varied between 1 and 6%, where 69% of specimens had ρ_w between 2 and 4% and 42% lesser than 2%. Further analysis of the data presented in Fig. 1(f) was conducted to differentiate between data that met the tension-controlled (TC) requirement as per the ACI 318 Code (that is, net tensile strain, ε_t, at strength ≥ net tensile yield strain of the longitudinal tension reinforcement, ε_{ty}, + 0.003) and those that did not (Fig. 1(g)). From the figure, it can be observed that there are 105 TC specimens and 137 transition or compression-controlled (NTC) specimens assuming a maximum concrete compressive strain, ε_{cu}, of 0.003, as specified by the ACI Code for plain concrete. Notably, in cases where the yield strength of reinforcing bars was not reported (98 specimens), an assumption was made that f_y equaled 60 ksi (420 MPa). However, large-scale beam testing has demonstrated that SFRC with a fiber-volume fraction of 0.75% exhibits a maximum concrete compressive strain, ε_{cu}, of approximately 0.007 (Karki 2011; Chao et al. 2023). Using a conservative estimate of ε_{cu} = 0.005, there are 167 TC specimens and 75 NTC specimens (Fig. 1(h)). It is noteworthy to mention that the minimum required longitudinal reinforcement area was computed and compared with the provided reinforcement area. It was found that all specimens had a longitudinal reinforcement area exceeding the ACI 318-19 minimum threshold.

ANALYSIS OF NOMINAL SHEAR STRENGTH OF SFRC USING DATA SET

Shear-strength model of ACI 318-19

The 2019 edition of the ACI 318 Code adopted a significantly different analytical model for the shear strength of nonprestressed members compared to earlier editions of the Code; a new set of equations to calculate V_c was included in 22.5.5. These equations for one-way shear strength consider the effects of member depth (the size effect), longitudinal tension reinforcement ratio, axial load ratio, and concrete strength (Kuchma et al. 2019). Equations (1), (2), (3), and (4) correspond to ACI 318-19 Eq. (22.5.5.1a), Eq. (22.5.5.1b), Eq. (22.5.5.1c), and Eq. (22.5.5.1.3), respectively. Either of Eq. (1) or Eq. (2) can be used to calculate concrete shear strength if the area of deformed reinforcing bars used as shear reinforcement, A_v, is larger than or equal to $A_{v,min}$. Otherwise, Eq. (3) and Eq. (4) must be used.

$$V_{c1} = \left[2\lambda\sqrt{f_c'} + \frac{N_u}{6A_g}\right] b_w d \quad (1)$$

[ACI 318-19 Eq. (22.5.5.1a)] (unit: psi)

$$V_{c1} = \left[0.17\lambda\sqrt{f_c'} + \frac{N_u}{6A_g}\right] b_w d \quad (1)$$

[ACI 318-19 Eq. (22.5.5.1a)] (unit: MPa)

$$V_{c2} = \left[8\lambda\left(\rho_w\right)^{1/3}\sqrt{f_c'} + \frac{N_u}{6A_g}\right] b_w d \quad (2)$$

[ACI 318-19 Eq. (22.5.5.1b)] (unit: psi)

$$V_{c2} = \left[0.66\lambda\left(\rho_w\right)^{1/3}\sqrt{f_c'} + \frac{N_u}{6A_g}\right] b_w d \quad (2)$$

[ACI 318-19 Eq. (22.5.5.1b)] (unit: MPa)

$$V_{c3} = \left[8\lambda_s\lambda\left(\rho_w\right)^{1/3}\sqrt{f_c'} + \frac{N_u}{6A_g}\right] b_w d \text{ if } A_v < A_{v,min} \quad (3)$$

[ACI 318-19 Eq. (22.5.5.1c)] (unit: psi)

$$V_{c3} = \left[0.66\lambda_s\lambda\left(\rho_w\right)^{1/3}\sqrt{f_c'} + \frac{N_u}{6A_g}\right] b_w d \text{ if } A_v < A_{v,min} \quad (3)$$

[ACI 318-19 Eq. (22.5.5.1c)] (unit: MPa)

$$\lambda_s = \sqrt{\frac{2}{1+\frac{d}{10}}} \le 1 \quad (4)$$

[ACI 318-19 Eq. (22.5.5.1.3)] (unit: in.)

$$\lambda_s = \sqrt{\frac{2}{1+\frac{d}{250}}} \le 1 \quad (4)$$

[ACI 318-19 Eq. (22.5.5.1.3)] (unit: mm)

where f_c' is specified compressive strength of concrete; λ is modification factor for LWC; N_u is factored axial force (positive for compression and negative for tension); A_g is gross area of concrete section; ρ_w is ratio $A_s/b_w d$; A_s is area of nonprestressed longitudinal tension reinforcement; and λ_s is the size effect factor. Based on the framework of the provisions for shear resistance of SFRC since their initial introduction in ACI 318-08, these new design criteria related to size effect and to reinforcement ratio are not explicitly applicable to the shear resistance of members reinforced with steel fibers.

Size effect

To assess the size effect in SFRC members, comparisons were made through the normalized shear stress at strength, $V_{test}/(\lambda\sqrt{f_{cm}}\, b_w d)$, where f_{cm} is the measured concrete compressive strength. The normalized shear stress at strength for different effective depths, d, is shown in Fig. 2(a). Different colors are used for distinct ranges of ρ_w (full-color PDF can be accessed at www.concrete.org). A modification factor λ = 1.0 was used for normalweight concrete (NWC), whereas λ = 0.75 was assumed for all LWC specimens. In the graph, green markers refer to LWC. The normalized

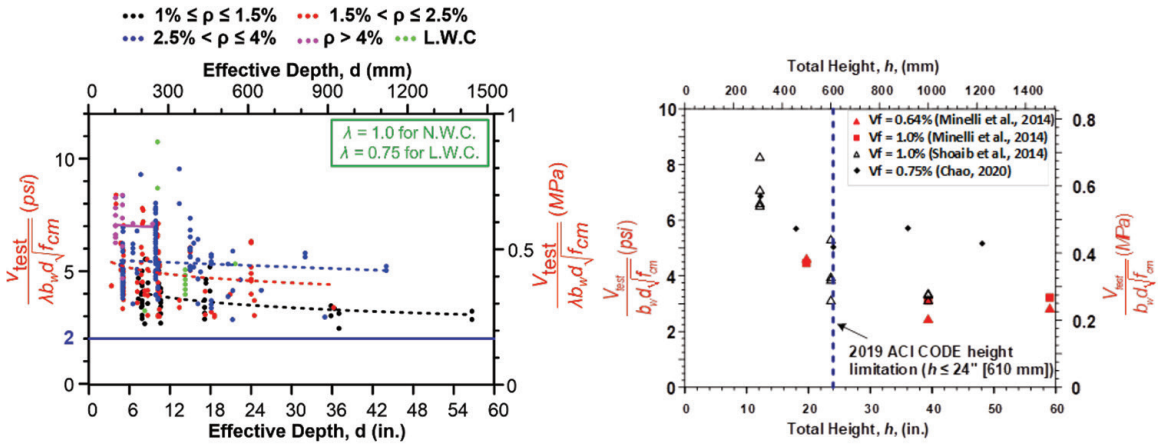

(a) (b)

Fig. 2—Normalized shear stress at failure as function of: (a) effective depth d *and for distinct* ρ_w *values; and (b) total height* h *for different steel fiber-volume fractions* V_f.

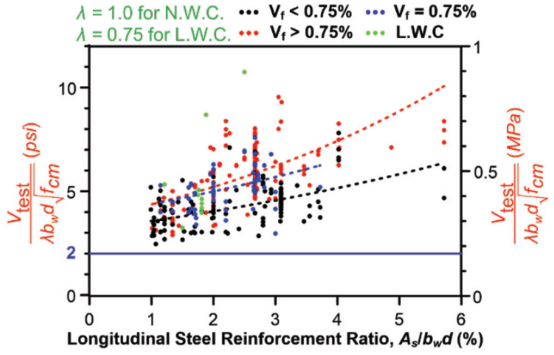

Fig. 3—Normalized shear stress at strength as function of ρ_w *and* V_f.

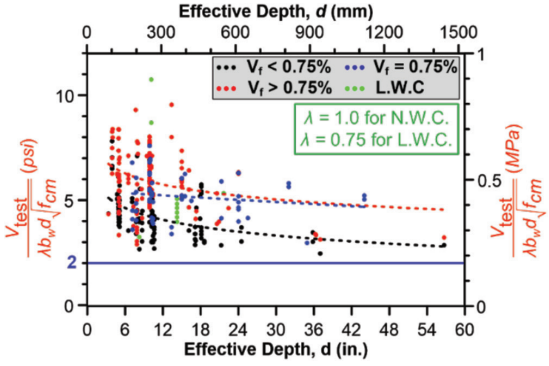

Fig. 4—Normalized shear stress for different values of V_f *for slender beams (*a/d ≥ *2.5).*

shear stress limit of $2\sqrt{f_{cm}}$ (psi) ($0.17\sqrt{f_{cm}}$ [MPa)]) is shown with a solid blue line. It is apparent from this graph that all 340 beams, regardless of d, reached shear strengths larger than $2\sqrt{f_{cm}}$ psi ($0.17\sqrt{f_{cm}}$ MPa). Strengths up to $5\lambda\sqrt{f_c'}b_w d$ psi ($0.42\lambda\sqrt{f_c'}b_w d$ MPa) were also observed. Even beams with d = 57 in. (h = 60 in.) (d = 1450 mm [h = 1524 mm]) exhibited normalized shear stresses greater than $2\sqrt{f_{cm}}$ psi ($0.17\sqrt{f_{cm}}$ MPa). It is also observed that there is a size effect in shear for SFRC beams; indeed, the normalized shear stress at failure decreased as d increased. For data with larger values of ρ_w, the size effect is less pronounced. In Fig. 2(b), the size effect in shear for SFRC beams can also be readily observed for three series of tests (Minelli et al. 2014; Shoaib et al. 2014; Chao 2020) aimed at assessing the size effect and tested with similar steel fiber-volume fractions.

Impact of longitudinal steel reinforcement ratio

The effect of longitudinal reinforcement ratio ρ_w on the normalized shear stress at failure is shown in Fig. 3. Different colors are used to identify distinct values of fiber-volume fraction V_f. Note that V_f = 0.75% is approximately equal to 100 lb/yd^3 (60 kg/m^3), which is the minimum dosage of fibers required in ACI 318-19 Section 26.4.2.2(i). SFRC beams with the minimum code-prescribed V_f are indicated with blue markers; LWC beams are indicated with green markers. From the graph, it is observed that normalized shear stress of beams tends to increase with ρ_w for all values of V_f. It is also apparent that the trend of increasing strength with ρ_w is very similar for V_f = 0.75% and V_f > 0.75%.

Influence of fiber-volume fraction

The influence of V_f on the shear strength is shown in Fig. 4. In general, higher normalized shear strengths are observed in beams with $d \le 24$ in. (610 mm) with $V_f \ge 0.75\%$ (blue and red markers) than in similar depth members with $V_f < 0.75\%$ (black markers). The data indicates that in beams with an overall depth greater than 36 in. (915 mm), a V_f less than 0.75% results in the lowest normalized shear stresses. Based on the data analyzed, it is apparent that V_f has less effect on shear strengths as member depth increased. Similar to Fig. 2, a size effect for SFRC beams is evident regardless of the value of V_f.

Assessment of stresses in reinforcing bars

An assessment of steel stresses in the longitudinal bars for the 340 shear-critical members was carried out. The objective was to verify that the data set was representative of possible longitudinal steel stresses corresponding to the permitted reinforcement grades under ACI 318-19. Steel stresses due to

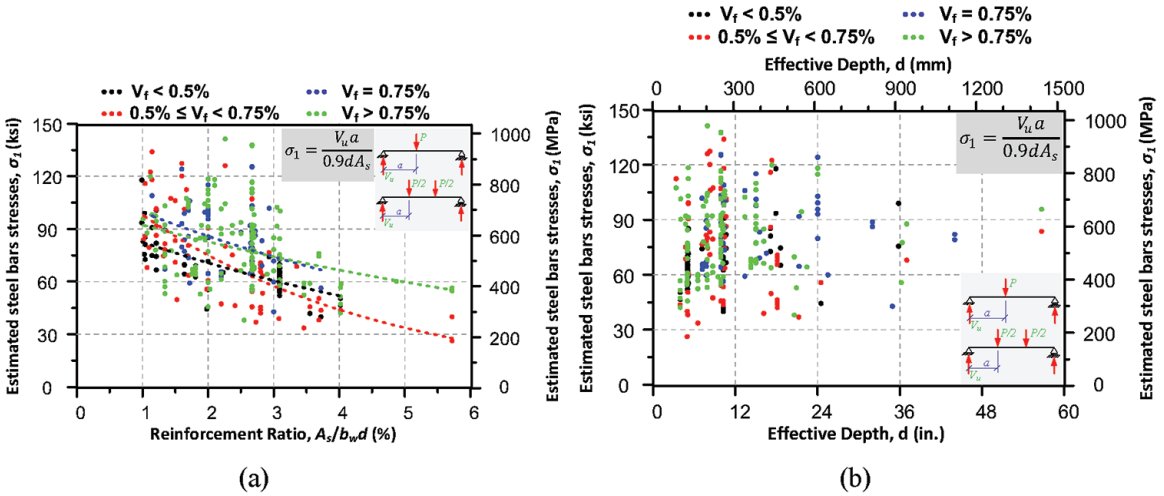

Fig. 5—Estimated stresses in longitudinal steel reinforcing bars for slender SFRC beams with different values of V_f*: (a) as function of* ρ_w*; and (b) as function of* d.

flexure were estimated at the location of maximum bending moment, at $x = a$ (Fig. 5) and using a simplified estimate of the internal lever arm of $0.9d$. Potential contribution of the fibers to flexural strength was ignored. Therefore, the stress in the steel reinforcing bars, σ_1, was estimated by Eq. (5)

$$\sigma_1 = \frac{V_{test}a}{0.9dA_s} \quad (5)$$

This simplified approach of estimating the reinforcing stress resulted in calculated stresses that were moderately higher than the actual bar stresses. Where the values exceeded approximately 90% of the reported yield stress of the bars, when available, other published test results for the specimens (for example, load deformation relationships, strain gauge data, and so on) were examined to confirm that the specimens represented shear-critical members rather than flexure-critical members.

Based on Fig. 5(a), it is observed that SFRC beams with lower ρ_w (approximately 1 to 1.5%) exhibited estimated bar stresses higher than those of beams having larger reinforcement ratios. Beams with higher ρ_w usually fail in shear before the flexural reinforcement stress approaches yielding and thus may be less appropriate for establishing simple design provisions for shear that are intended to apply to flexure-critical members. Moreover, use of higher steel-fiber dosages that impart increased shear strength may develop greater stresses in the steel bars of shear-critical members due to the higher imposed bending moment. For example, SFRC beams with $V_f > 0.75\%$ showed larger reinforcing bar stresses compared to similar beams with $V_f < 0.5\%$. Again, caution is needed when establishing simple design provisions for shear that are intended to apply to flexure-critical members which may limit the applicability to members with a minimum V_f, especially if V_f is not directly considered within the flexure- or shear-strength models.

Within the data set, the SFRC beams with smaller depths had higher estimated bar stresses compared to similar but deeper beams (Fig. 5(b)). This can be explained by the size effect in shear strength in SFRC beams discussed previously. Due to the size effect, deeper SFRC beams fail at lower normalized shear stresses, corresponding to lower imposed bending moments and lower estimate stresses in the flexural reinforcement. Within the data set, specimens with greater steel stresses typically had characteristics of $d < 24$ in. (610 mm) and $V_f \geq 0.5\%$. For shallower beams with $V_f < 0.5\%$ (black dots), lower tensile stresses in bars were estimated.

Yield strength of longitudinal steel reinforcement

The specified yield strength f_y was reported by authors for 242 slender SFRC beams out of the 340 specimens in the data set (71%). Out of the total number of specimens, 44 (18%) had Grade 40 (280 MPa) longitudinal reinforcement, 159 (66%) had Grade 60 (420 MPa), and 39 (16%) had Grade 80 (550 MPa). The data set did not include any beams with Grade 100 (690 MPa) reinforcement specified. As expected, the tested yield strength of the reinforcing bars (when reported) was higher than the specified strength according to the grade. Also refer to the discussion on estimated bar stresses earlier in the paper. Based on the bar strengths, it is proposed that the data set permits evaluation of SFRC shear design provisions for NWC applicable up to Grade 80 (550 MPa) reinforcement.

Out of the 340 shear-critical specimens, 10 were lightweight SFRC beams: four specimens had Grade 60 (420 MPa) reinforcement, whereas the specified yield strength was not reported by the authors for the remaining six specimens. With a much lower distribution in the data set, it is proposed that the data set is only applicable for development of LWC SFRC shear design provisions up to Grade 60 (420 MPa).

Assessment of ACI shear-strength model equations

As indicated previously, it is unclear in ACI 318-19 which equation(s) should be used to compute V_c for members constructed with SFRC. To identify appropriate equations in Section 22.5.5.1 for calculating V_c, the size effect in SFRC beams was compared with that in concrete beams without stirrups. The ratio of test-to-calculated shear strengths using Eq. (1) (Fig. 6(a)) and Eq. (2) (Fig. 6(b)) for SFRC

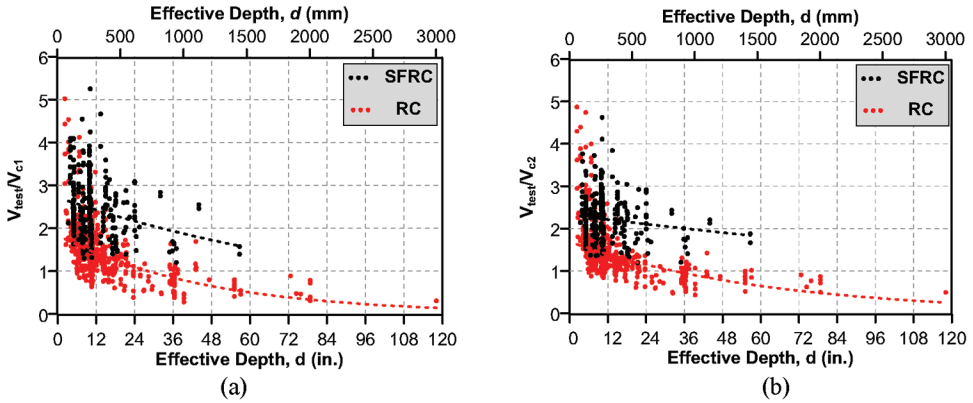

Fig. 6—Ratio of measured-to-calculated shear strengths versus beam depth for beams with a/d ≥ *2.5 and with different values of* V_f *and concrete beams without stirrups: (a)* V_{c1} *calculated using Eq. (1); and (b)* V_{c2} *determined using Eq. (2).*

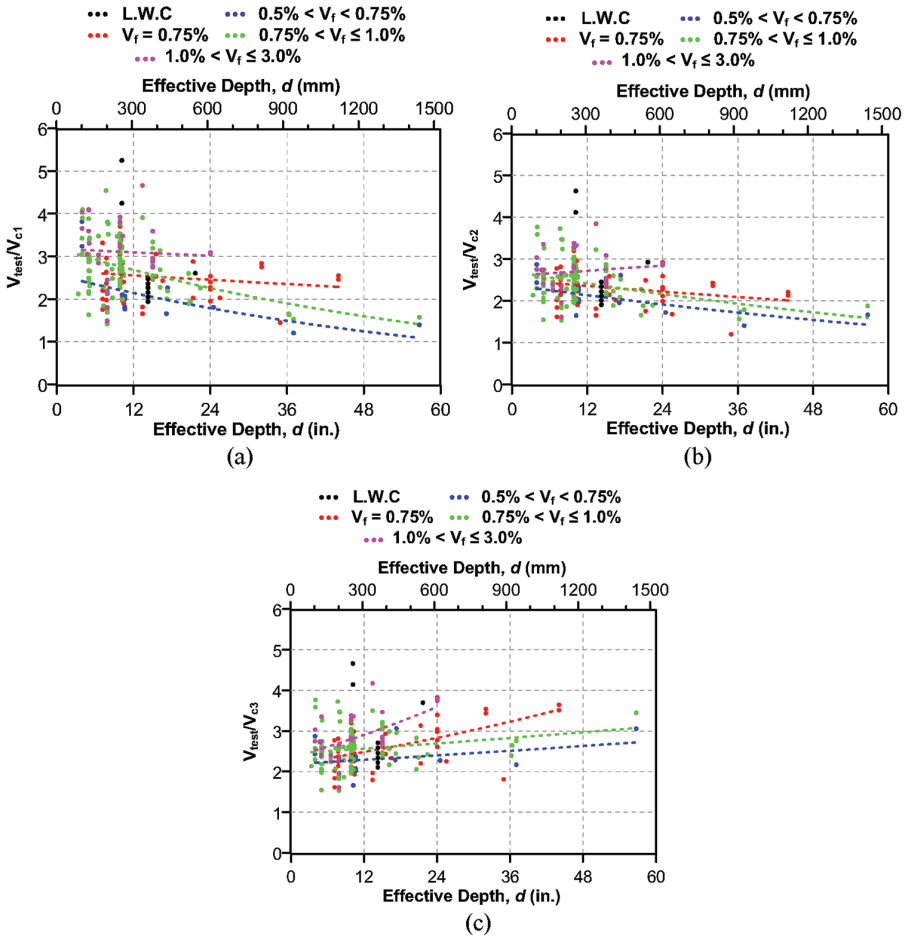

Fig. 7—Ratio of measured-to-calculated shear strengths versus beam depth for beams with a/d ≥ *2.5 and different values of* V_f *as function of* d*: (a)* V_{c1} *calculated using Eq. (1); (b)* V_{c2} *determined using Eq. (2); and (c)* V_{c3} *determined using Eq. (3).*

specimens (black markers) and beams without stirrups (red makers) is shown in Fig. 6. Data of concrete beams without stirrups were taken from Reineck et al. (2013). Note that the size effect in V_{c1} and V_{c2} (Eq. (1) and (2), respectively) is not considered in the calculation of V_c (that is, λ_s =1.0, where λ_s is the size effect factor). Therefore, the slope of the trend line when plotted against d can confirm the size effect. It is apparent from Fig. 6(a) that the size effect in shear is similar between SFRC and concrete beams without stirrups (that is, trend lines have similar slopes). It is also observed that the shear strength in SFRC specimens is, on average, approximately double that for beams without stirrups. In the case of V_{c2} (Eq. (2)) that considers ρ_w, a somewhat similar trend is observed for SFRC beams and RC specimens without stirrups. The quasi-horizontal trendline (less inclined than in Fig 6(a)) indicates that Eq. (2) is a more suitable expression for capturing the most significant variables that affect the concrete contribution to shear strength for SFRC beams, but that a size effect as a function of d is still present.

The ratio of measured strength, V_{test}, to nominal shear strength calculated with Eq. (1), (2), and (3), (V_{c1}, V_{c2}, and V_{c3}, respectively), are shown in Fig. 7 for various values of

V_f as a function of d. Values of V_f were divided in bins up to 3%. Different colors are used for distinctly different values of V_f. Black dots refer to LWC beams. V_{c3} from Eq. (3) explicitly takes into account the size effect through factor λ_s computed using Eq. (4). Note that the trendlines for V_{c3} increase moderately with depth d, suggesting there may be a slight overestimation of the impact on SFRC shear strength compared to members without fibers. However, it should be recognized that λ_s may also overestimate the size effect of very deep members without fibers. Additional laboratory data is needed in both cases to refine Eq. (4).

Figures 7(a) and (b) correspond to the nominal strength calculated using Eq. (1), V_{c1}, and Eq. (2), V_{c2}, using $N_u = 0$ (because specimens were not axially loaded) and the corresponding value for the λ factor, respectively. Figure 7(c) was developed for Eq. (3), V_{c3}, in which a size effect modification factor, λ_s, was implemented according to Eq. (4). It is apparent that the ratios of measured strength, V_{test}, to nominal shear strengths are larger than 1.0 for all nominal strength equations and for all values of V_f. These results indicate that using any of the equations from ACI 318-19 Table 22.5.5.1 provide safe estimates of shear strength. Figure 8 was developed in a manner similar to Fig. 7 but plotted as a function of ρ_w to understand trends with that parameter typical range of values for ρ_w used in design practice for slabs and beams (that is, 0.5 to 1.5%) is indicated with the shaded area.

As can be observed from Fig. 7 and 8, Eq. (1), (2), and (3) provide safe estimates of the shear strength of SFRC beams. In general, larger values of V_f result in a greater ratio of test-to-calculated strengths. Even though the compliance of one-third of the specimens in the data set with the ACI 318 residual strength requirement is unknown, because their SFRC was tested under EN 14651 (3PBT) (2005) or other methods different from ASTM C1609 (2019), the ratio of measured strength, V_{test}, to nominal shear strength (calculated with. Eq. (1), (2), (3), and (4)) was greater than 1.0.

Based on the data analysis, it is proposed that the strength V_c of SFRC slender beams will be at least that calculated using either Eq. (1) or Eq. (2). To further evaluate this finding, a reliability investigation was carried out. Results of this investigation are discussed later in the paper.

Beams with depths h > 28 in. (710 mm)

Current Code provisions limit the use of SFRC to an overall member depth of $h \leq 24$ in. (610 mm). This limitation was imposed considering the available information when the 2008 ACI 318 provisions were developed (Parra-Montesinos 2006). In view of the more recent information on beams with considerably greater depths, a special focus was made on these deeper members in this study. Fourteen NWC specimens having $h > 28$ in. (710 mm) are included in this subset of the data. The ratio of V_{test}/V_{c2} using Eq. (2) is plotted in Fig. 9. It is observed that Eq. (2) provides a safe

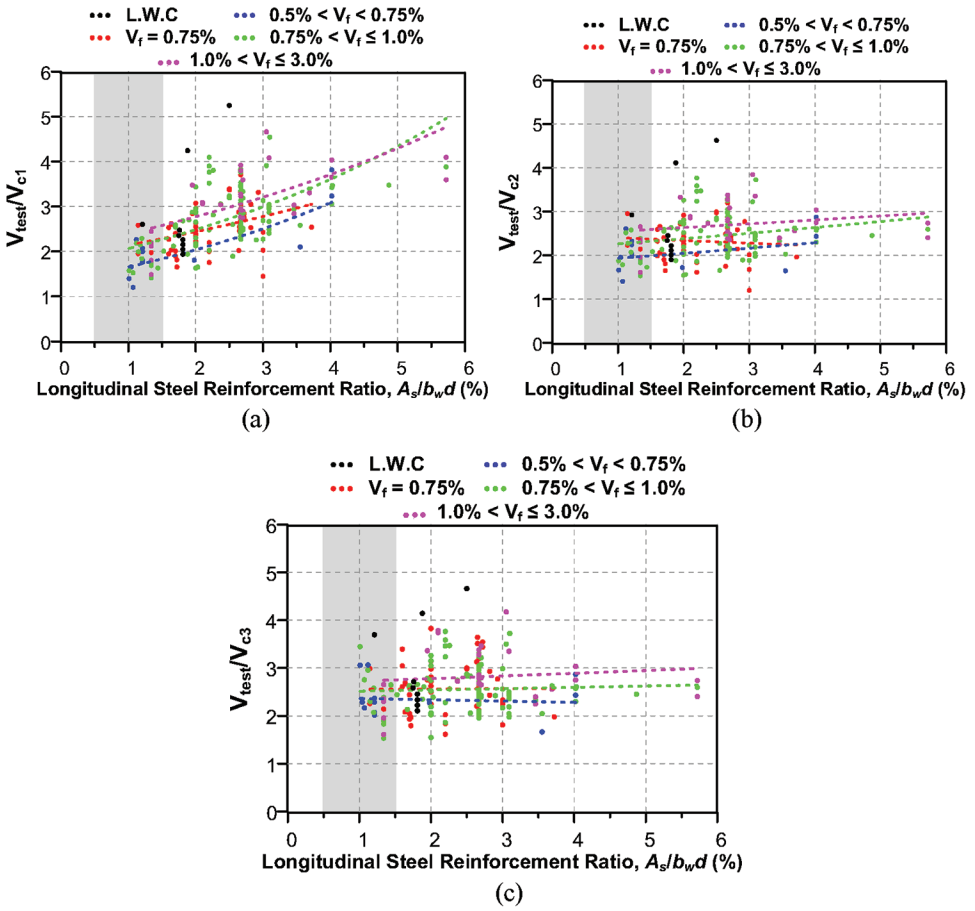

Fig. 8—Ratio of measured-to-calculated shear strengths versus beam depth for beams with a/d ≥ 2.5 and different values of V_f *as function of* ρ_w*: (a)* V_{c1} *calculated using Eq. (1); (b)* V_{c2} *determined using Eq. (2); and (c)* V_{c3} *determined using Eq. (3).*

estimate of the shear strength of SFRC beams up to an effective depth of 36 in. (915 mm) (equivalent to an overall depth of approximately 40 in. (1016 mm), assuming typical clear cover and multiple layers of reinforcement). When using V_{c2} that includes the effect of ρ_w, the minimum value of V_{test}/V_{c2} was greater than 1.2. Moreover, it is evident from Fig. 10 that all 14 specimens with overall depth $h > 28$ in. (710 mm) reached shear strengths larger than $2\sqrt{f_{cm}}$ psi ($0.17\sqrt{f_{cm}}$ MPa) (refer to the dashed line) for different combinations of h, ρ_w, and f_{cm}.

Effect of concrete compressive strength

Current shear design of SFRC beams in ACI 318-19 is applicable to beams with $f_c' \le 6000$ psi (42 MPa). Although higher compressive strengths are permitted for conventional concretes with no steel fiber reinforcement, SFRC-specific shear provisions cannot be used for those higher strengths according to ACI 318-19. To evaluate the adequacy of extending the use of SFRC shear provisions to concretes with compressive strengths up to 10,000 psi (69 MPa), the nominal shear strength using the ACI 318-19 shear-strength model was evaluated. The distribution of SFRC beams made with normalweight and LWCs in the data set is shown in Fig. 11. Due to the limited data available, the data set only comprises three LWC beams with concrete strengths that surpass the current limit of 6000 psi (42 MPa). Consequently, it is recommended to retain this limit of $f_c' \le 6000$ psi (42 MPa) for SFRC LWC beams and one-way slabs.

Figure 12 was developed to evaluate in more detail the influence of the measured concrete compressive strength f_{cm} on the shear strength of beams with different values of V_f. In the figure, the overall trendlines of the normalized value of V_{test}/V_{c1} and V_{test}/V_{c2} are not sensitive to the increase in concrete compressive strength from 6000 to 10,000 psi (42 to 69 MPa) (refer to the shaded area in gray), except for values of V_f larger than 1% (pink dots). This observation supports the proposal for raising the upper limit on applicability of the SFRC shear model to f_c' to 10,000 psi (69 MPa) for NWC.

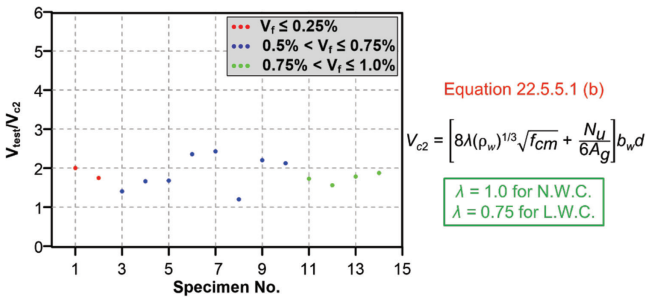

Fig. 9—Ratio of measured-to-calculated shear strengths using Eq. (2) for beams with overall depth h *> 28 in. (710 mm),* a/d *≥ 2.5, and with different values of* V_f.

Beams with $\rho_w \le 0.015$

Because beams and slabs in concrete buildings are typically designed with $\rho_w \le 1.5\%$, it was necessary to further assess the shear strength of SFRC specimens with $\rho_w \le 1.5\%$,

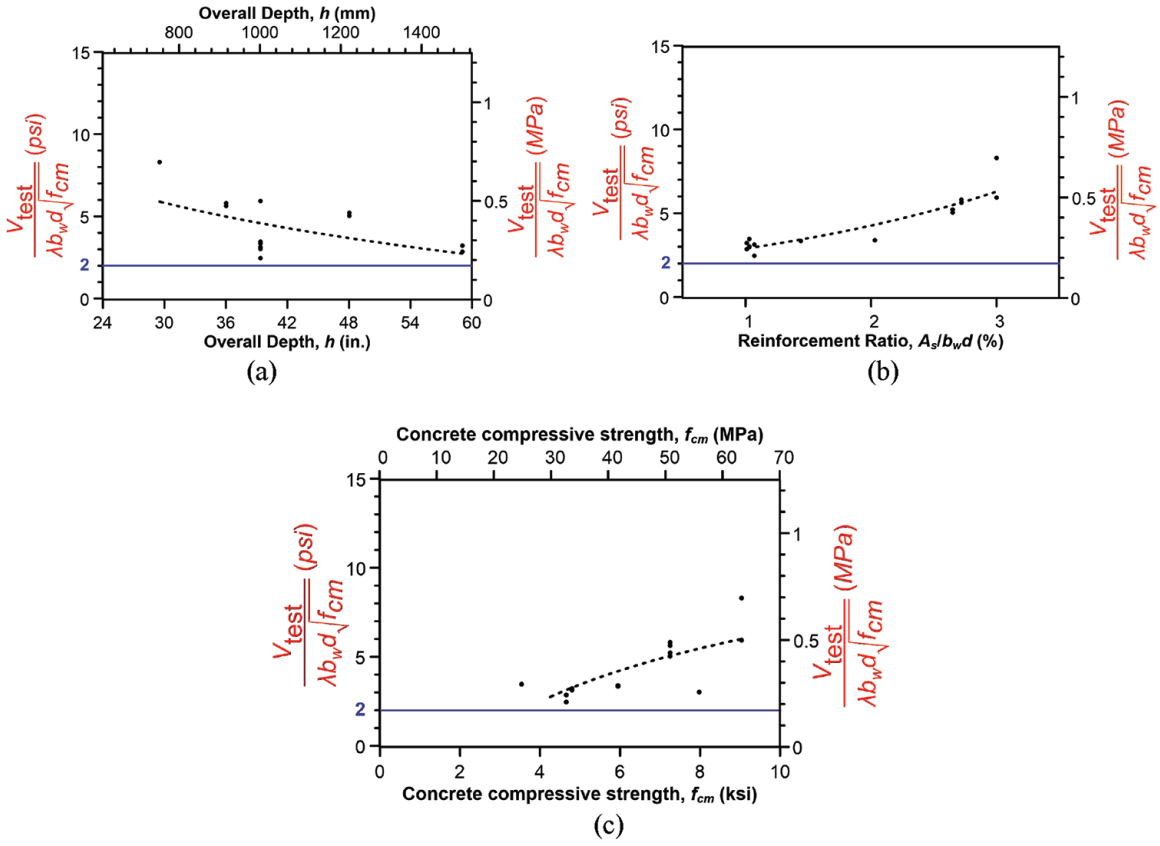

Fig. 10—Normalized shear stress for different values of: (a) overall depth h*; (b) steel reinforcement volume ratio* ρ_w*; and (c) measured concrete compressive strength* f_{cm}.

either failing in flexure or shear. The aim was to determine if there was any indication of SFRC specimens with $\rho_w \leq 1.5\%$, failing at shear stresses below $2\sqrt{f_{cm}}$ psi ($0.17\sqrt{f_{cm}}$ MPa). In the main data set, 48 specimens with $\rho_w \leq 1.5\%$ failed in shear. A separate data set of 57 lightly reinforced specimens used in this analysis was assembled that complied with all but one (type of failure) of the 10 features of the data set of SFRC beams section of this paper. These 57 beams failed in flexure, with data provided in Appendix D.

The normalized shear stress for lightly reinforced beams failing in shear or flexure and for different values of V_f is shown in Fig. 13. The ratio of $V_{test}/1.3V_{c2}$, where V_{c2} was calculated using Eq. (2), is presented in Fig. 14 and Fig. 15 for different longitudinal reinforcement ratios and effective beam depths, respectively. It should be noted that data in Fig. 14 and 15 are normalized using the factor 1.3 times V_{c2}, where the value 1.3 was determined through the reliability investigation presented in the following section of the paper. It is observed from these figures that the database contains one specimen with $V_f \leq 0.5\%$ that failed in flexure and that showed a V_{test}/V_{c2} ratio slightly less than 1.3. Note that $V_f \leq 0.5\%$ is less than the minimum fiber-volume content recommended through this study. For the 11 specimens with $\rho_w \leq 1.0\%$, either failing in shear or flexure, all had $V_{test}/V_{c2} > 1.3$.

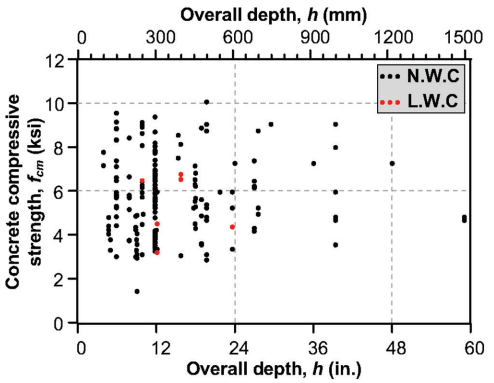

Fig. 11—Distribution of lightweight and NWCs versus beam depth h.

Reliability investigation of proposed design equations

As mentioned previously, based on the findings supported by Fig. 7 and 8, and acknowledging the existence of size effect in shear for SFRC beams (refer to Fig. 2 to 4), it is proposed to use the greater of V_{c1} (Eq. (1)) and "X*"* times V_{c2} (Eq. (2)) for the shear design of SFRC beams and one-way slabs. The value of "X*"* was determined as follows:

(i) Data was analyzed using V_{c2} (Eq. (2)) that assumes a size effect factor $\lambda_s = 1$.

(ii) Beams separated into the categories of $V_f \leq 0.75\%$ and $V_f > 0.75\%$ were first analyzed. The measured-to-calculated strength ratio for the data in each category was determined. The value of "X" was taken as the ratio corresponding to the 95th percentile (that is, 95% of observations have a strength ratio greater than "X").

(iii) A similar analysis to (ii) was completed for beams with $V_f \leq 0.50\%$ and $V_f > 0.50\%$ (note that $V_f = 0.50\%$ is equivalent to 65 lb/yd^3 [39 kg/m^3]).

From the analysis indicated in (ii), "X" was calculated as 1.4. The measured-to-calculated shear strengths for beams with $V_f \leq 0.75\%$ (red dots) and $V_f > 0.75\%$ (black dots) are shown in Fig. 16. The value of "X" is indicated with the blue

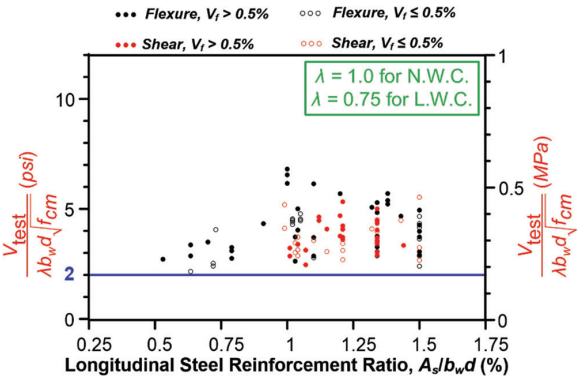

Fig. 13—Normalized shear stress for different values of V_f *versus longitudinal steel reinforcement ratio for beams failed in flexure or shear.*

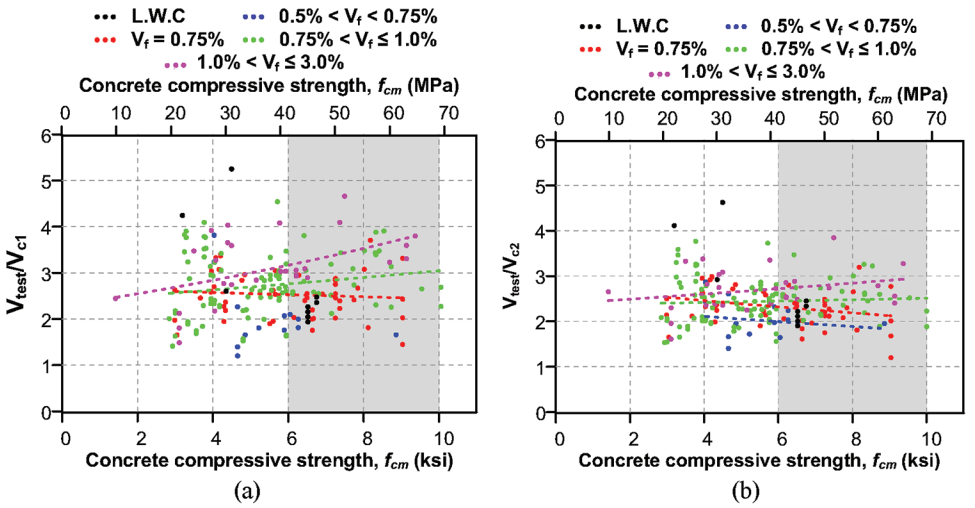

Fig. 12—Ratio of measured-to-calculated shear strengths versus concrete compressive strength for beams with a/d ≥ *2.5 and with different values of* V_f*: (a)* V_{c1} *calculated using Eq. (1); and (b)* V_{c2} *determined using Eq. (2).*

line. Only eight of the 195 specimens with $V_f \leq 0.75\%$ (red dots) and none of the 135 specimens with $V_f > 0.75\%$ fell below "X = 1.4".

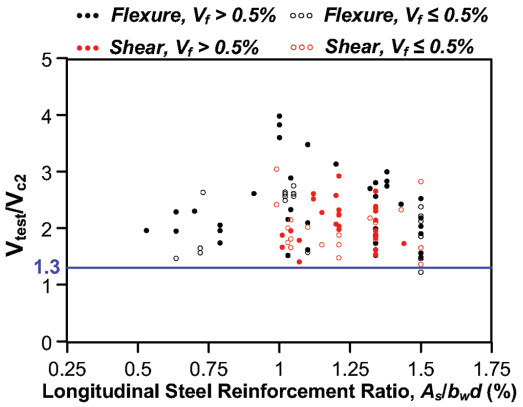

Fig. 14—Ratio of measured-to-calculated shear strengths versus longitudinal steel reinforcement ratio for beams failed in flexure or shear and calculated using Eq. (2).

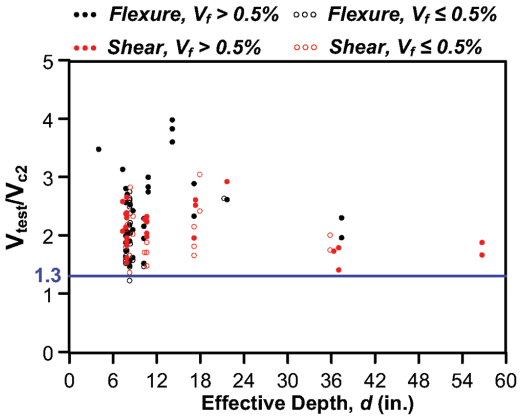

Fig. 15—Ratio of measured-to-calculated shear strengths versus effective beam depth for beams failed in flexure or shear and calculated using Eq. (2).

Figure 17 is equivalent to Fig. 16 but for beams with $V_f \leq 0.50\%$ and $V_f > 0.50\%$. The value of "X" was determined to be equal to 1.3. In this case, two of 340 specimens are below the "X = 1.3" line shown in blue. Of these two beams, one beam has $V_f \leq 0.50\%$, and the other has $V_f > 0.50\%$. From the data presented in Fig. 7, 8, 16, and 17, it is proposed that V_c can be taken as the greater of the shear strength from Eq. (1) and 1.3 times Eq. (2). This recommendation is made in combination with a proposed decrease in the minimum fiber dosage to 70 lb/yd^3 (42 kg/m^3) for NWC. This value corresponds to $V_f = 0.53\%$, which is slightly higher (and therefore more conservative) than the minimum fiber-volume fraction assessed in the data set—that is, $V_f = 0.5\%$. Due to limited test results of LWC specimens, the minimum deformed steel fiber dosage in ACI 318-19 equal to 100 lb/yd^3 (60 kg/m^3) is proposed to be maintained.

RECOMMENDED DESIGN PROVISIONS FOR SFRC

Based on the analysis of data set results, the following requirements are recommended for inclusion in the shear design provisions of ACI CODE-318 for SFRC beams and one-way slabs:

- $A_{v,min}$ is not required where $V_u \leq \phi V_c$ if constructed with SFRC:
  - For NWC with 6000 psi (42 MPa) $< f_c' \leq$ 10,000 psi (69 MPa) and Grade 60 (420 MPa) or Grade 80 (550 MPa) longitudinal reinforcement, $h \leq 40$ in. (1016 mm)
  - For LWC with $f_c' \leq 6000$ psi (42 MPa) and Grade 60 longitudinal reinforcement, $h \leq 24$ in. (610 mm)
- For nonprestressed beams and one-way slabs constructed with SFRC, V_c shall be taken as the greater of Eq. (1) (that is, ACI 318-19 Eq. (22.5.5.1a) and 1.3 times Eq. (2) (that is, ACI 318-19 Eq. (22.5.5.1b).
- SFRC used for shear resistance shall contain at least 70 lb of deformed steel fibers per yd^3 of concrete (42 kg/m^3) for NWC and 100 lb of deformed steel fibers per yd^3 of concrete for LWC (60 kg/m^3).

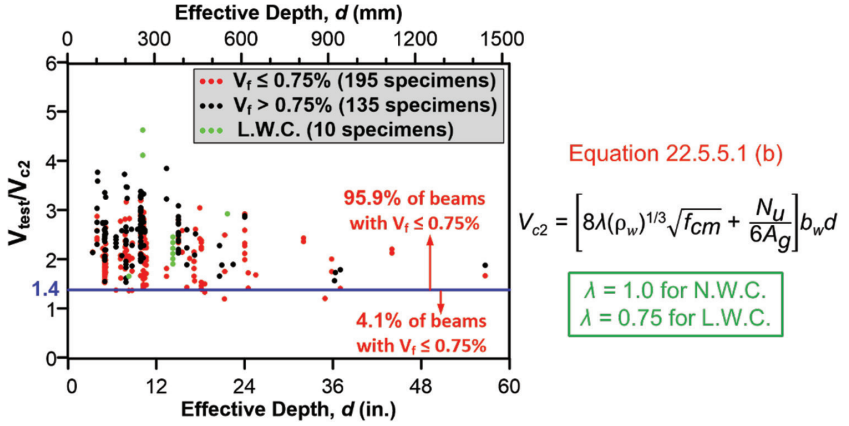

Fig. 16—Ratio of measured-to-calculated shear strengths using Eq. (2) versus effective beam depth for beams with a/d ≥ *2.5 and with* $V_f \leq 0.75\%$ *and* $V_f > 0.75\%$.

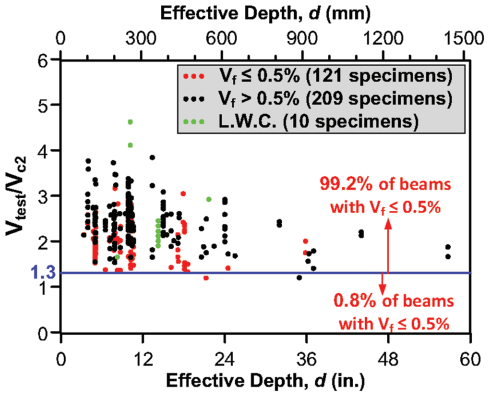

Fig. 17—Ratio of measured-to-calculated shear strengths using Eq. (2) versus effective beam depth for beams with a/d *≥ 2.5 and with* $V_f \le 0.50\%$ *and* $V_f > 0.50\%$.

CONCLUSIONS

The analysis of test results of shear-critical steel fiber-reinforced concrete (SFRC) members support the following conclusions:

1. Current beam overall depth limit $h \le 24$ in. (610 mm) in ACI 318-19 Section 9.6.3.1 can be safely extended to $h \le 40$ in. (1016 mm) for normalweight concrete (NWC) (refer to *Concern a*).

2. Taking into account the effects of lightweight concrete (LWC), size, and longitudinal reinforcement ratio (as described in *Concerns a* and *d*), it is safe to use the greater of Eq. (1) and 1.3 times Eq. (2) for calculating V_c in SFRC beams up to $5\lambda\sqrt{f_c'}b_w d$ psi ($0.42\lambda\sqrt{f_c'}b_w d$ MPa) (refer to Fig. 3 and 10). As a result, the current limit in Table 9.6.3.1 for $V_u \le \phi 2\sqrt{f_c'}b_w d$ psi ($V_u \le \phi 0.17\sqrt{f_c'}b_w d$ MPa) is no longer necessary. It should be noted that the Eq. (1) and (2) presented in this study correspond to Eq. (a) and (b) in Table 22.5.5.1 of ACI 318-19.

3. The limit of $f_c' \le 6000$ psi (42 MPa) can be extended to $f_c' \le 10{,}000$ psi (69 MPa) for NWC, which would align it with the limiting concrete strength for one-way shear strength in Section 22.5.3 of ACI 318-19 (refer to *Concerns a* and *c*).

4. The exception case in ACI 318-19 Table 9.6.3.1 could be extended to lightweight concrete (LWC) used in SFRC beams, but only for $f_c' \le 6000$ psi (42 MPa) (refer to *Concerns a* and *c*).

5. Due to limited data on deeper LWC specimens, it is proposed that the limit on overall depth of SFRC members where $A_{v,min}$ is not required be capped to 24 in. (610 mm) (refer to *Concern a*).

6. Because specifications of the design information and compliance requirements for SFRC that were first included in ACI 318-08 were purposely conservative, based on the analysis reported herein, the minimum fiber content can be reduced to 70 lb/yd^3 (42 kg/m^3) for NWC (*Concern e*).

7. The application of SFRC-specific shear provisions is restricted to NWC beams reinforced with Grade 60 (420 MPa) and Grade 80 (550 MPa) bars, as well as to LWC beams reinforced with Grade 60 (420 MPa) bars, owing to insufficient experimental data for Grade 100 (690 MPa) beam longitudinal reinforcement.

AUTHOR BIOS

Sergio M. Alcocer, *FACI, is a Professor in the Institute of Engineering at the National Autonomous University of Mexico (UNAM), Mexico City, Mexico, and part-time Professor in the Klesse College of Engineering and Integrated Design of The University of Texas at San Antonio, San Antonio, TX. He is Chair of Joint ACI-ASCE Committee 352, Joints and Connections in Monolithic Concrete Structures, and a member of ACI Committees 318, Structural Concrete Building Code, and 369, Seismic Repair and Rehabilitation, and past Chair of ACI Committee 374, Performance-Based Seismic Design of Concrete Buildings.*

ACI member **Ghassan Almasabha** *is an Assistant Professor at the Department of Civil Engineering, Faculty of Engineering, The Hashemite University, Zarqa, Jordan. He is a member of ACI Committee 374, Performance-Based Seismic Design of Concrete Buildings. He received his PhD in structural engineering from The University of Texas at Arlington, Arlington, TX, in 2019. His research interests include disaster-resilient structures, experimental testing of reinforced concrete (RC) elements, and analysis of engineered cementitious composites.*

ACI member **Julian Carrillo** *is a Professor in the Department of Civil Engineering at the Universidad Militar Nueva Granada, Bogotá, Colombia. He is a member of ACI Committees 133, Disaster Reconnaissance; 314, Simplified Design of Concrete Buildings; 369, Seismic Repair and Rehabilitation; 374, Performance-Based Seismic Design of Concrete Buildings; 440, Fiber-Reinforced Polymer Reinforcement; and 544, Fiber-Reinforced Concrete; and ACI Subcommittees 318-S, 318 Spanish Translation, and 445-B, Shear & Torsion-Seismic Shear. His research interests include the behavior and design of RC structures under seismic actions.*

ACI member **Shih-Ho Chao** *is an ACPA Tom Wheelan Professor and Distinguished Teaching Professor at the University of Texas at Arlington. He is a member of Joint ACI-ASCE Committee 423, Prestressed Concrete. He received the ACI Mete A. Sozen Award for Excellence in Structural Research and the ACI Chester Paul Siess Award for Excellence in Structural Research in 2021 and 2011, respectively. His research interests include prestressed concrete, seismic behavior of RC structures, and ultra-high-performance fiber-reinforced concrete (FRC).*

Adam S. Lubell, *FACI, is an Associate at Read Jones Christoffersen Ltd., Vancouver, BC, Canada, and an Adjunct Professor at the University of British Columbia, Vancouver, BC, Canada. He is Chair of Joint ACI-ASCE Committee 445, Shear and Torsion, and a member of ACI Subcommittee 318-E, Section and Member Strength. His research interests include the design and rehabilitation of reinforced and prestressed concrete structures, and the development of structural detailing guidelines to allow the use of high-performance materials.*

NOTATION

A_g	=	gross area of concrete section
A_s	=	area of nonprestressed longitudinal tension reinforcement
A_v	=	area of shear reinforcement
$A_{v,min}$	=	minimum area of shear reinforcement
a	=	shear span or distance measured from support to location of maximum moment
b_w	=	beam web width
c	=	neutral axis depth
d	=	effective depth
f_c'	=	specified compressive strength of concrete
f_{cm}	=	measured compressive strength of concrete
f_y	=	yield strength of longitudinal reinforcement steel
h	=	beam overall depth
N_u	=	factored axial force
V_c	=	nominal shear strength provided by concrete
V_{c1}	=	nominal shear strength provided by concrete using Eq. (1) (corresponding to ACI 318-19 Eq. (22.5.5.1a))
V_{c2}	=	nominal shear strength provided by concrete using Eq. (1) (corresponding to ACI 318-19 Eq. (22.5.5.1b))
V_{c3}	=	nominal shear strength provided by concrete using Eq. (1) (corresponding to ACI 318-19 Eq. (22.5.5.1c))
V_f	=	fiber-volume fraction
V_{test}	=	measured shear strength
V_u	=	factored shear force
β_1	=	factor relating depth of equivalent rectangular compressive stress block to depth of neutral axis
ε_{cu}	=	compressive strain in concrete at ultimate
ε_t	=	net tensile strain in extreme layer of longitudinal tensile reinforcement at ultimate (strength)

ε_{ty} = net tensile yield strain in extreme layer of longitudinal tensile reinforcement
ε_y = net tensile yield strain of the longitudinal tension reinforcement
ϕ = shear-strength reduction factor
λ = modification factor for LWC
λ_s = size effect factor
ρ_w = longitudinal steel reinforcement ratio
σ_1 = total stress in longitudinal steel reinforcement

REFERENCES

ACI Committee 318, 2008, "Building Code Requirements for Structural Concrete (ACI 318-08) and Commentary (ACI 318R-08)," American Concrete Institute, Farmington Hills, MI, 465 pp.

ACI Committee 318, 2019, "Building Code Requirements for Structural Concrete (ACI 318-19) and Commentary (ACI 318R-19)," American Concrete Institute, Farmington Hills, MI, 623 pp.

ASTM C1116/C1116M, 2015, "Standard Specification for Fiber-Reinforced Concrete," ASTM International, West Conshohocken, PA.

ASTM C1609/C1609M, 2019, "Standard Test Method for Flexural Performance of Fiber-Reinforced Concrete (Using Beam with Third-Point Loading)," ASTM International, West Conshohocken, PA.

ASTM A820/A820M, 2016, "Standard Specification for Steel Fibers for Fiber-Reinforced Concrete," ASTM International, West Conshohocken, PA.

Carrillo, J.; Vargas, J. D.; and Alcocer, S. M., 2021, "Model for Estimating the Flexural Performance of Concrete Reinforced with Hooked End Steel Fibers Using Three-Point Bending Tests," *Journal of the International Federation for Structural Concrete*, Mar., pp. 1-18.

Chao, S.-H., 2020, "Size Effect on Ultimate Shear Strength of SFRC Slender Beams," *ACI Structural Journal*, V. 117, No. 1, Jan., pp. 145-15.

Chao, S.-H.; Kaka, V.; and Shamshiri, M., 2023, "Structural Implications of the Synergistic Interactions between Steel Reinforcement and UHPC," Third International Interactive Symposium on UHPC, Wilmington, DE, June 4-7.

EN 14651, 2005, "Test Method for Metallic Fibered Concrete – Measuring the Flexural Tensile Strength (Limit of Proportionality (LOP), Residual)," European Committee for Standardization, CEN, Belgium, 19 pp.

Fédération internationale du béton, 2013, "*fib* Model Code for Concrete Structures 2010," *fib*, Lausanne, Switzerland, 434 pp.

Karki, N. B., 2011, "Flexural Behavior of Steel Fiber Reinforced Prestressed Concrete Beams and Double Punch Test For Fiber Reinforced Concrete," PhD dissertation, the University of Texas at Arlington, Arlington, TX, 422 pp.

Kuchma, D. A.; Wei, S.; Sanders, D. H.; Belarbi, A.; and Novak, L. C., 2019, "Development of the One-Way Shear Design Provisions of ACI 318-19 for Reinforced Concrete," *ACI Structural Journal*, V. 116, No. 4, July, pp. 285-295. doi: 10.14359/51716739

Minelli, F.; Conforti, A.; Cuenca, E.; and Plizzari, G., 2014, "Are Steel Fibres Able to Mitigate or Eliminate Size Effect in Shear?" *Materials and Structures*, V. 47, No. 3, pp. 459-473. doi: 10.1617/s11527-013-0072-y

Naaman, A., 2017, *Fiber Reinforced Cement and Concrete Composites*, Techno Press 3000, Ann Arbor, MI.

Parra-Montesinos, G. J., 2006, "Shear-Strength of Beams with Deformed Steel Fibers," *Concrete International*, V. 28, No. 11, Nov., pp. 57-66.

Reineck, K.-H.; Bentz, E. C.; Fitik, B.; Kuchma, D. A.; and Bayrak, O., 2013, "The ACI-DAFSTB Database of Shear Tests on Slender Reinforced Concrete Beams without Stirrups," *ACI Structural Journal*, V. 110, No. 5, Sept.-Oct., pp. 867-875.

Shoaib, A.; Lubell, A. S.; and Bindiganavile, V. S., 2014, "Size Effect in Shear for Steel Fiber-Reinforced Concrete Members without Stirrups," *ACI Structural Journal*, V. 111, No. 5, Sep., pp. 1081-1090. doi: 10.14359/51686813

Zarrinpour, M. R., and Chao, S.-H., 2017, "Shear Strength Enhancement Mechanisms of Steel Fiber-Reinforced Concrete Slender Beams," *ACI Structural Journal*, V. 114, No. 3, May, pp. 729-742. doi: 10.14359/51689449

ARE YOU A RESEARCHER?

SIGN UP FOR ORCID TODAY!

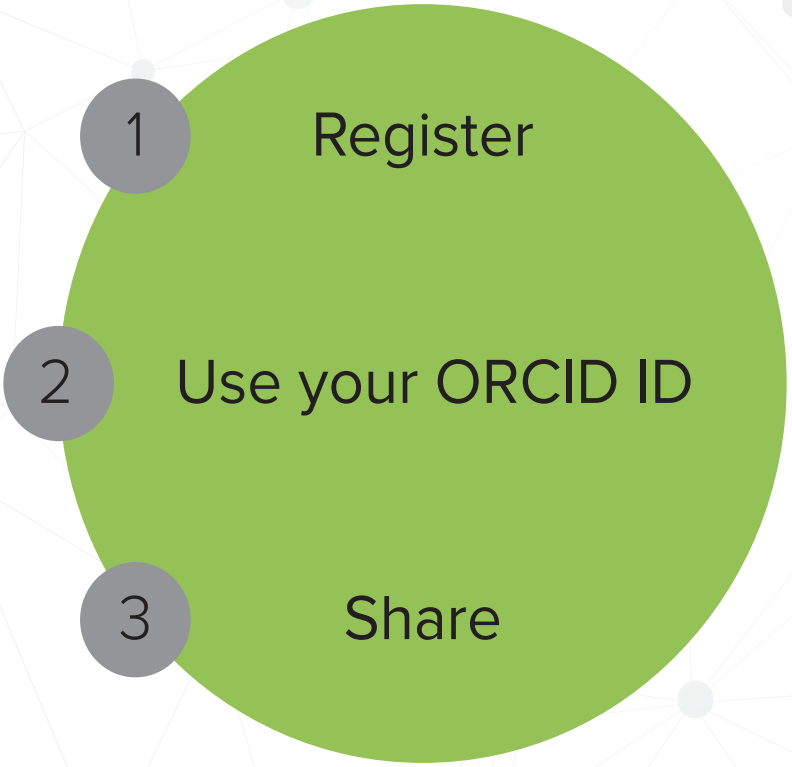

ORCID provides a digital identifier that distinguishes you from every other researcher and, through integration in key research workflows such as manuscript and grant submission, supports automated linkages between you and your professional activities, ensuring that your work is recognized.

ORCID services are FREE and it's as easy as **1-2-3**.

WWW.ORCID.ORG

ACI STRUCTURAL JOURNAL TECHNICAL PAPER

Title No. 122-S09

Cyclic Loading Test for Interior Precast Beam-Column Joints Using Slag-Based Concrete

by H.-S. Moon, H.-J. Hwang, C.-S. Kim, K.-W. Jo, J.-H. Jeong, C.-K. Park, and H.-G. Park

To reduce CO_2 emissions of concrete, a slag-based zero-cement concrete (ZC) of high strength (60 MPa [8.70 ksi]) was developed. In the present study, cyclic loading tests were conducted to investigate the seismic performance of full-scale interior precast beam-column joints using the new ZC. One monolithic portland cement-based normal concrete (NC) beam-column joint and two precast ZC beam-column joints were tested. The test parameters included concrete type, fabrication method, and beam bottom bar anchorage detail. The structural performance was evaluated, including the strength, deformation capacity, damage mode, and energy dissipation. The test results showed that the structural performance of the precast ZC beam-column joints could be equivalent, or superior, to that of the monolithic NC beam-column joint. Although the reinforcement details of the ZC joints do not satisfy the seismic design requirements of special moment frames in ACI 318-19, the seismic performance of the ZC joints satisfied the requirements of ACI 374.1-05 and AIJ 2002 Guidelines.

Keywords: beam-column joint; cyclic loading test; hook anchorage; precast concrete; seismic performance; slag-based concrete; zero-cement concrete (ZC).

INTRODUCTION

Zero-cement concrete (ZC) has been studied as an eco-friendly construction material that can reduce concrete-related CO_2 emissions by up to 80%.[1] ZC uses an activator (mostly sodium silicate [Na_2SiO_3] and sodium hydroxide [NaOH]) that directly reacts with industrial by-products, such as fly ash or slag cement, without the use of portland cement.[2-4] However, it has been known that ZC is sensitive to curing conditions[5-7] and has low workability[8] and low setting time.[9] Depending on the proportion of binders and activators and curing conditions, the material properties of ZC significantly vary: workability, setting time, early-age strength, 28-day strength, durability, and others.[10-12]

Several comprehensive studies have examined the material and structural performances of ZC. Li et al.[10] developed a ZC with binders of slag and fly ash, and the test results[13-17] revealed that ACI 318-19[18] was applicable to ZC members (beams under shear and flexure, development length of hooked and headed bars, beam-column joints, and shear transfer), though ZC members showed relatively brittle behavior and early cracking. Saranya et al.[11] developed a ZC with binders of slag cement and dolomite. The follow-up studies[19-23] on small-scale members reported that the behaviors of ZC members were similar to those of normal concrete (NC) members (beams under flexure, short columns under axial compression, and beam-column joints under monotonic and cyclic loadings). Khan et al.[12] developed a ZC with binders of fly ash and slag cement, and the test results[24-31] showed that the behaviors of ZC members were similar to those of NC members (beams under shear and slabs under punching shear), except for some members (beams under flexure and beam-column joints under cyclic loading).

Comparative studies on the seismic performance of ZC and NC beam-column joints have reported inconsistent results. Raj et al.[32] reported that the exterior joints of fly ash-based ZC (compressive strength f_c' = 34.0 MPa [4.93 ksi]) showed 47% greater ductility and less stiffness degradation than their NC counterparts. Datta and Premkumar[33] reported that the behaviors of exterior joints of ZC using fly ash and slag cement (f_c' = 40.2 MPa [5.83 ksi]) were similar to those of their NC counterparts. Saranya et al.[23] stated that the exterior joint of ZC using slag cement and dolomite (f_c' = 58.0 MPa [8.41 ksi]) showed 12% greater energy dissipation and 13% greater ductility than its NC counterpart. Ngo et al.[28] tested the exterior monolithic and precast joints of ZC using fly ash and slag cement (f_c' = 66.1 MPa [9.59 ksi]) and reported that the monolithic and precast ZC joints showed 23% and 48% less ductility than the monolithic and precast NC counterparts, respectively. Mao et al.[15] tested the interior and exterior joints of ZC using slag and fly ash (f_c' = 28.4 to 35.0 MPa [4.12 to 5.08 ksi]) and reported that the interior and exterior ZC joints designed by ACI 318-19[18] satisfied the requirements of ACI 374.1-05.[34] Mao et al.[16] reported that interior joints of ZC using slag and fly ash (f_c' = 24.7 to 58.4 MPa [3.58 to 8.47 ksi]) showed inferior structural performance (degree of cracking, stiffness, ductility, strength degradation, and energy dissipation capacity) to their NC counterparts. In calculating f_c' in the literature, the strength of cube specimens was multiplied by 0.8.

As such, extensive studies have been performed on ZC members. However, the existing studies have limitations in the verification of material and structural performance: most of the studies focused on a mixed binder of slag and fly ash, and 100% slag-based ZC was not studied. For activators, mixtures of Na_2SiO_3 and NaOH have been mainly used. In most studies, small-scale monolithic joint specimens were tested (joint width x depth x height ranged from 150 x 150 x 150 mm [5.91 x 5.91 x 5.91 in.] to 350 x 350 x 300 mm [13.8 x 13.8 x 11.8 in.]). However, as ZC is sensitive to

ACI Structural Journal, V. 122, No. 1, January 2025.
MS No. S-2023-261.R1, doi: 10.14359/51742139, received May 17, 2024, and reviewed under Institute publication policies.

Table 1—Mixture proportions of zero-cement concrete and normal concrete, kg/m³

Type	Cement	Slag cement	Activator		Water	Sand	Coarse aggregate	Dispersant
			CSA compound	NaOH				
NC	305	130	—	—	165	805	978	4
ZC	—	500	100	6	155	759	862	8.6

Note: CSA compound is calcium sulfoaluminate compound; NaOH is solid 100%; 1 kg/m³ = 0.062 lb/ft³.

curing conditions and has low workability, ZC is more applicable to precast concrete construction than cast-in-place concrete construction.

In the proposed research plan, a slag-based ZC was developed, having high strength (f_c' = 60 MPa [8.70 ksi]) and improved workability (slump > 210 mm [8.27 in.] and slump flow of 350 to 500 mm [13.8 to 19.7 in.]). A slag cement binder and a composite material activator of calcium sulfoaluminate (CSA) compound and solid sodium hydroxide (NaOH) were used. Tests of various structural members of ZC were planned to verify the application of the ZC to precast construction. In the present study, cyclic loading tests were conducted on full-scale interior beam-column joints. One monolithic NC beam-column joint and two precast ZC beam-column joints were tested. The test parameters included concrete type, fabrication method, and beam bottom bar anchorage detail. The seismic performance (the strength, deformation capacity, damage mode, and energy dissipation) of ZC beam-column joints was assessed by ACI 374.1-05.[34]

RESEARCH SIGNIFICANCE

For the application of ZC in practice, experimental studies on material and structural performances are necessary due to the lack of material information, insufficient structural member tests, and the absence of specific design codes. The present study aims to evaluate the applicability of current design codes and details to precast interior beam-column joints using a novel ZC. The present test results can be used as evidence to verify the seismic performance of precast ZC beam-column joints.

MATERIAL PROPERTIES

Table 1 shows the mixture proportions of the ZC and NC used in the present study. For NC, 70% cement + 30% slag cement were used for the binder. The development of ZC followed the typical concrete material development procedure, which involved performing trial-and-error mixing experiments. In the proposed ZC, instead of using portland cement, 100% slag cement (refer to Table 2) was used for the binder. Because slag cement does not react directly with water, an activator is needed to create an alkaline environment and initiate its reaction with water through the latent hydraulic reaction. After evaluating various candidate substances, a composition of CSA compound and NaOH was chosen for the activator. Through multiple mixing experiments, a ZC mixture with the desired performance was developed, and the productivity was evaluated through batch plant production.

The mixing process of ZC involves the following steps: 1) the coarse aggregates and sand are placed into a blender; 2) the mixture of slag cement and activator is added; and 3) the water and admixtures are added. The fresh ZC exhibits a slump over 210 mm (8.27 in.) and a slump flow of 350 to 500 mm (13.8 to 19.7 in.), which is maintained as 80% of the slump after 20 minutes. The slump level is proper for precast concrete production. The final setting time of fresh ZC ranges from 1 to 3 hours, and the temperature increases from 18 to 23°C (64.4 to 73.4°F) at casting up to 70°C (158°F) during hydration. The workability of the ZC was improved by using a dispersant and a relatively low curing temperature.

Table 2—Chemical composition of slag cement, %

Composition	SiO_2	CaO	Al_2O_3	MgO	Fe_2O_3	SO_3	K_2O
Slag cement	35.64	41.30	14.73	5.18	0.41	2.16	0.39

Eight ZC cylinders and four NC cylinders were prepared to investigate the material strength of beam-column joint specimens. The cylinders of Ø100 x 200 mm (Ø3.94 x 7.87 in.) were cured along with the joint specimens and were tested at 37 to 38 days (that is, at the test days of the joint specimens). After placing concrete, the joint specimens and cylinders were steam-cured following the temperature control of actual precast concrete production generally used in Korea (because the proposed ZC is sensitive to curing conditions, it is recommended to be cured with steam instead of being cured in the ambient conditions): 1) the specimens were initially cured at 20°C (68°F) for 2 to 3 hours; then the temperature was: 2) increased to 35°C (95°F) for 2 hours; 3) maintained at 35°C (95°F) for 8 hours in the case of ZC and 50 to 60°C (122 to 140°F) for 6 hours in the case of NC; and 4) lowered to 20°C (68°F) for 2 hours. After 2 days, the test specimens were cured at ambient conditions of –2.8 to 27.9°C (27.0 to 82.2°F) and 40.6 to 96.4% relative humidity (RH).

Figure 1 compares the stress-strain relationships of the ZC and NC cylinders. When the ZC cylinders were compared to the NC cylinders, the average compressive strength (f_c') was 0.4% lower, the average modulus of elasticity (E_c) was 4.0% lower, and the average strain at the peak strength (ε_{co}) was 11.0% greater. In detail, f_c' of ZC ranged from 56.0 to 68.0 MPa (8.12 to 9.86 ksi) (62.0 MPa [9.00 ksi] on average), and f_c' of NC ranged from 56.2 to 64.8 MPa (8.15 to 9.40 ksi) (62.3 MPa [9.04 ksi] on average). The modulus of elasticity (E_c) of ZC ranged from 29.3 to 38.5 GPa (4250 to 5584 ksi) (32.1 GPa [4656 ksi] on average), and E_c of NC ranged from 31.5 to 37.9 GPa (4569 to 5497 ksi) (33.3 GPa [4830 ksi] on average). The strain at the peak strength (ε_{co}) of ZC ranged from 0.00213 to 0.00287 (0.00248 on average), and ε_{co} of NC ranged from 0.00190 to 0.00246 (0.00222 on average).

TEST PLAN FOR BEAM-COLUMN JOINTS

Test specimens

Table 3 shows the test parameters of interior beam-column joint specimens, including concrete type (NC and ZC), fabrication method (monolithic and precast), and beam bottom bar anchorage detail (straight bars and 90-degree hooked bars). In the specimen names, the last letters denote the number and anchorage detail of beam bottom bars (2S is two straight bars, 2H is two hooked bars, and 3H is three hooked bars). Current design codes, including ACI 318-19[18] and KDS 14 20 80:2023,[35] require an emulative system of precast concrete: for earthquake design of precast concrete, the mechanical properties of precast concrete members should be equivalent to those of cast-in-place reinforced concrete (RC) members. For this reason, a monolithic joint specimen was used for NC, and the test results were compared with the test results of the ZC precast specimens.

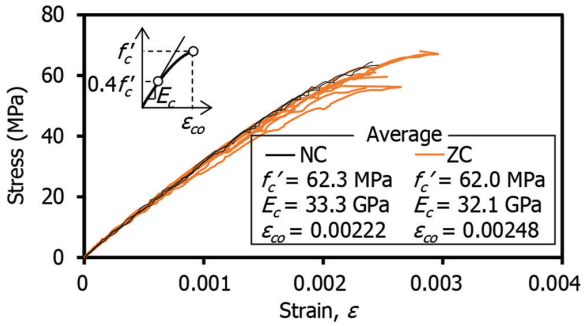

Fig. 1—Stress-strain relationships of ZC and NC cylinders.

Figure 2 shows the geometric configurations of the interior beam-column joint specimens. The width and depth of the column and beam sections were 500 x 650 mm (19.7 x 25.6 in.) and 350 x 500 mm (13.8 x 19.7 in.), respectively. The net height between the loading point and reaction point in the column was H = 2100 mm (82.7 in.). The net length between the roller supports in the beams was L = 4800 mm (189 in.).

The beam-column joint specimens were designed for intermediate moment frames according to ACI 318-19,[18] except for the connection details between precast members. In the columns, 12 D29 bars (that is, bar diameter d_b = 28.7 mm [1.13 in.], yield strength f_y = 625.1 MPa [90.7 ksi], and reinforcement ratio ρ = 3.08%) were used for longitudinal reinforcement. D13 bars (that is, d_b = 12.9 mm [0.51 in.] and f_y =

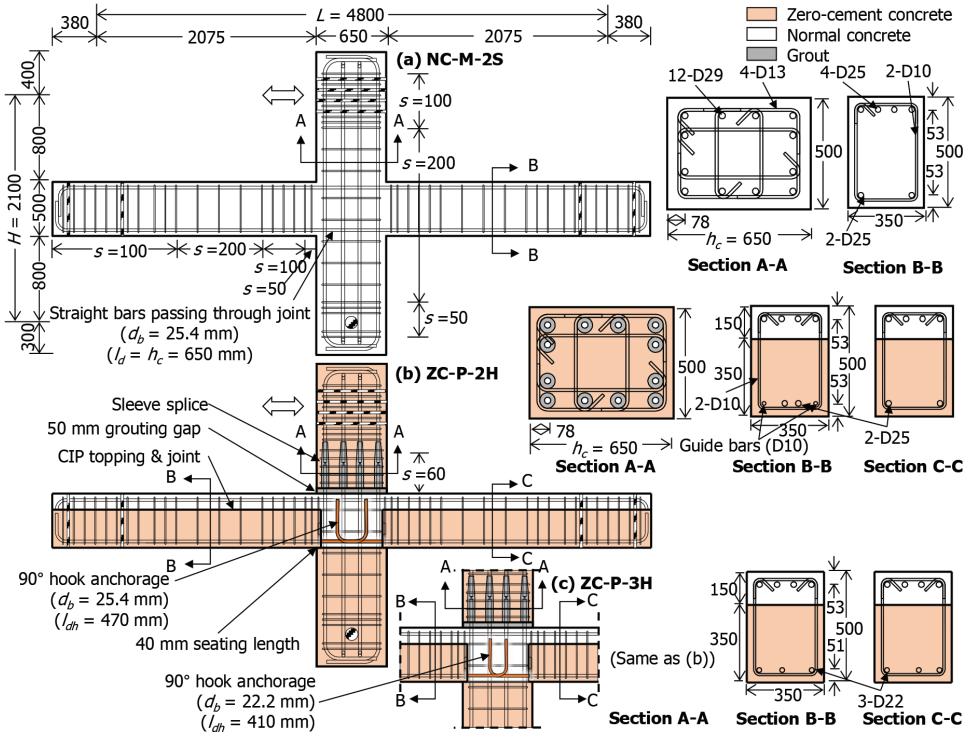

Fig. 2—Details of test specimens. (Note: Units in mm; 1 mm = 0.039 in.)

Table 3—Test parameters of beam-column joint specimens

Specimen	Concrete type f_c', MPa		Fabrication method	Beam bottom bar		
	Beam and column	Topping and joint		Reinforcing bar ρ (%)/f_y (MPa)	Anchorage detail	Development length, mm
NC-M-2S	NC (62.3)	NC (62.3)	Monolithic	2 D25 (0.65/658.0)	Straight	650
ZC-P-2H	ZC (61.2)	NC (52.6)	Precast	2 D25 (0.65/658.0)	90-degree hook	470
ZC-P-3H	ZC (62.8)	NC (48.5)	Precast	3 D22 (0.74/672.4)	90-degree hook	410

Note: NC is normal concrete; ZC is zero-cement concrete; f_c' is compressive strength; $\rho = A_s/bd$ is reinforcement ratio (A_s is cross-sectional area of longitudinal reinforcement, b is width, and d is effective depth); for D25, bar diameter d_b = 25.4 mm; for D22, d_b = 22.2 mm; f_y is yield strength of beam bottom bars; 1 MPa = 0.145 ksi; 1 mm = 0.0394 in.

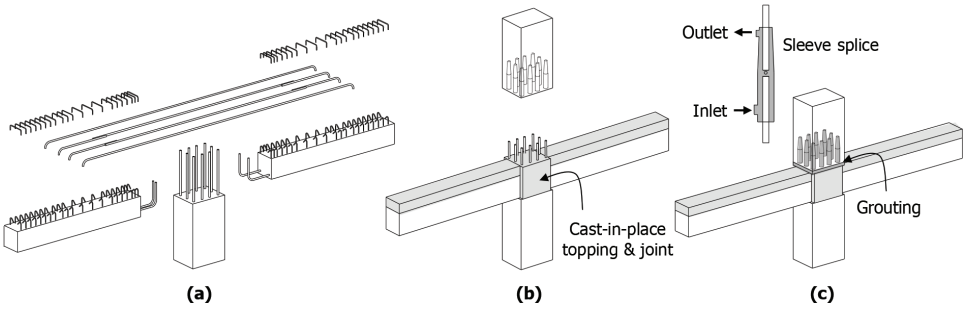

Fig. 3—Fabrication process of precast beam-column joint specimens.

552.8 MPa [80.2 ksi]) were used for hoops and crossties with 90- and 135-degree hooks at a spacing of 200 mm (7.87 in.) (≈0.5*d*, where *d* is effective depth). For the beam top bars, four D25 bars passed through the joint. D10 bars (that is, d_b = 9.5 mm [0.374 in.] and f_y = 555.8 MPa [80.6 ksi]) were used for U-stirrups with 135-degree hooks and crossties with 90-degree hooks at spacings of 100 to 200 mm (3.94 to 7.87 in.) (≈0.25 to 0.5*d*). For the beam bottom bars, details were different among the test specimens. The monolithic specimen (NC-M-2S) used two D25 bars (ρ = 0.65%), which were placed passing the joint (Fig. 2(a)). On the other hand, the precast joint specimens (ZC-P-2H and ZC-P-3H) used two D25 bars (ρ = 0.65%) and three D22 bars (ρ = 0.74%), respectively, which were anchored with a 90-degree hook in the joint panel zone (Fig. 2(b) and (c)).

Specimen NC-M-2S was a monolithic joint of NC. On the other hand, precast ZC specimens (ZC-P-2H and ZC-P-3H) were fabricated with precast ZC beams and columns by wet construction (Fig. 3): 1) both beams were seated on the edge of the lower column with a seating length of 40 mm (1.57 in.), and then straight beam top bars and stirrups were assembled (Fig. 3(a)); 2) NC was cast on the top of beams and at the beam-column joint (Fig. 3(b)); and 3) the upper column was connected by sleeve splices using high-strength non-shrink grout (f_c' = 94.3 to 94.6 MPa [13.7 ksi]) (Fig. 3(c)).

For the anchorage of beam bottom bars in monolithic beam-column joints, ACI 318-19[18] (for special moment frames) and ACI 352R-02[36] (for Type 2 connections [that is, intermediate/special moment frames]) specify the minimum value of the column-depth-to-reinforcing-bar-diameter ratio (h_c/d_b) as follows

$$\frac{h_c}{d_b} \geq 20 \text{ for } f_y \leq 420 \text{ MPa} \quad (1a)$$

$$\frac{h_c}{d_b} \geq 26 \text{ for } f_y \leq 550 \text{ MPa in ACI 318-19} \quad (1b)$$

$$\frac{h_c}{d_b} = 20\frac{f_y}{420} \geq 20 \text{ in ACI 352R-02} \quad (2)$$

ACI 318-19[18] (Eq. (1)) requires that the column-depth-to-reinforcing-bar-diameter ratio (h_c/d_b) be not less than 26 for $f_y \leq$ 550 MPa (79.8 ksi). In NC-M-2S, the h_c/d_b was 25.6, which is close to the requirement of ACI 318-19,[18] though the reinforcing bar grade (f_y = 658.0 MPa [95.4 ksi]) exceeded the yield strength limitation specified in the design Code. On the other hand, the h_c/d_b of NC-M-2S did not satisfy the requirement (=31.3) of ACI 352R-02[36] (Eq. (2)) for Type 2 connections. When a column depth is smaller than the requirement, the straight beam longitudinal reinforcement may slip within the joint under cyclic loading, which decreases the stiffness and energy dissipation capacity of the beam-column joint.

In the precast beam-column joints, the development lengths of the hooked bars (l_{dh}) were designed according to the requirement of intermediate/special moment frames in ACI 318-19[18] as follows

$$l_{dh} = \frac{f_y d_b}{5.4\sqrt{f_c'}} \quad (3)$$

In ZC-P-2H, two D25 bars with the development length of 470 mm (18.5 in.) were used (Fig. 2). In ZC-P-3H, three D22 bars with the development length of 410 mm (16.1 in.) were used; as smaller-diameter reinforcing bars were used, the development length was decreased.

Nominal strengths of test specimens

Table 3 presents the compressive strength of concrete used for the beam-column joint specimens. For the monolithic specimen, the compressive strength of NC was 62.3 MPa (9.04 ksi). For precast concrete specimens, the high-strength ZC was used at the beams and columns: f_c' = 61.2 and 62.8 MPa (8.88 and 9.11 ksi) for ZC-P-2H and ZC-P-3H, respectively. The compressive strength of the topping and joint concrete (that is, cast-in-place concrete) was 0.85 and 0.77 times the column concrete (that is, precast concrete) in ZC-P-2H and ZC-P-3H, respectively. The strengths of topping and joint concrete exceeded the minimum requirement of 0.70 in ACI 318-19.[18] For sleeve splices, high-strength non-shrink grout was used. The compressive strength of the grout in the 40 x 40 x 160 mm (1.57 x 1.57 x 6.30 in.) prism[37] was 94.3 and 94.6 MPa (13.7 ksi) for ZC-P-2H and ZC-P-3H, respectively.

Table 4 presents the nominal strengths of the beam-column joint specimens. The nominal strengths of the members were calculated using the actual material strengths measured from the material tests. Addressing the strong-column/weak-beam concept, the moment strength ratios of column to beam were $M_{nc}/M_{nb} \approx 2$. To prevent early joint shear failure, the nominal joint shear strengths (V_{jn}) were designed to exceed the joint shear demands (V_u) resulting from beam flexural yielding:

Table 4—Nominal strengths of beam-column joint specimens

Specimen	Strength	NC-M-2S	ZC-P-2H	ZC-P-3H
Column	Moment strength M_{nc}, kN·m	939	937	939
Beam	Positive moment strength M_{nb}^{+}, kN·m	288	286	330
	Negative moment strength M_{nb}^{-}, kN·m	552	551	552
	Nominal lateral strength P_n, kN	463	461	486
Joint	Nominal joint shear strength V_{jn}, kN	2715	2495	2396
	Joint shear demand V_u, kN	1551	1553	1621

Note: 1 kN = 0.225 kip; 1 kN·m = 0.735 kip·ft.

the joint shear strength-to-demand ratios were $V_{jn}/V_u \approx 2$. Appendix A* presents the calculation of nominal strengths.

Test setup

Figure 4 shows the test setup of the interior beam-column joint specimens under cyclic loading. Both beam ends were roller-supported, and the lower column was pin-supported at the bottom. Cyclic lateral loading was applied to the upper column using an actuator with a capacity of 2000 kN (449 kip) and a stroke of 508 mm (20 in.).

The loading plan followed ACI 374.1-05[34]: three load cycles were repeated at each loading step, and the lateral drift ratio increased in the order of 0.25, 0.35, 0.5, 0.75, 1.0, 1.5, 2.0, 2.75, 3.5, 4.5, 6.0, and 8.0% (Fig. 5). Axial load was not applied to the column, because an axial load less than the balanced point generally increases the joint shear strength.[34]

TEST RESULTS

Load-displacement relationship and deformation capacity

Figure 6 shows the lateral load (P)-drift ratio (δ) relationships of the beam-column joint specimens. The maximum loads (P_{max}) exceeded the nominal strengths based on the flexural yielding of beams (P_n). The hysteresis relationships of all the specimens were similar. The maximum loads occurred at approximately the same drift ratio in all the specimens: δ = ±2.75% in NC-M-2S and ZC-P-2H and δ = +2.75% and –3.5% in ZC-P-3H (refer to Table 5). Figure 6(d) compares envelope curves of the hysteresis relationships of all the specimens.

The yield drift ratio (δ_y) was defined based on the equivalent elastoplastic system with secant stiffness at 75% of P_{max} (Fig. 6(e)).[36,38] The ultimate drift ratio (δ_u) was defined as the post-peak point of 80% of P_{max}. The ductility was defined as the ratio of the ultimate drift ratio to yield drift ratio: $\mu = \delta_u/\delta_y$.

In Table 5, the average ductility (μ) of ZC-P-2H and ZC-P-3H was 52% and 32% greater than that of NC-M-2S,

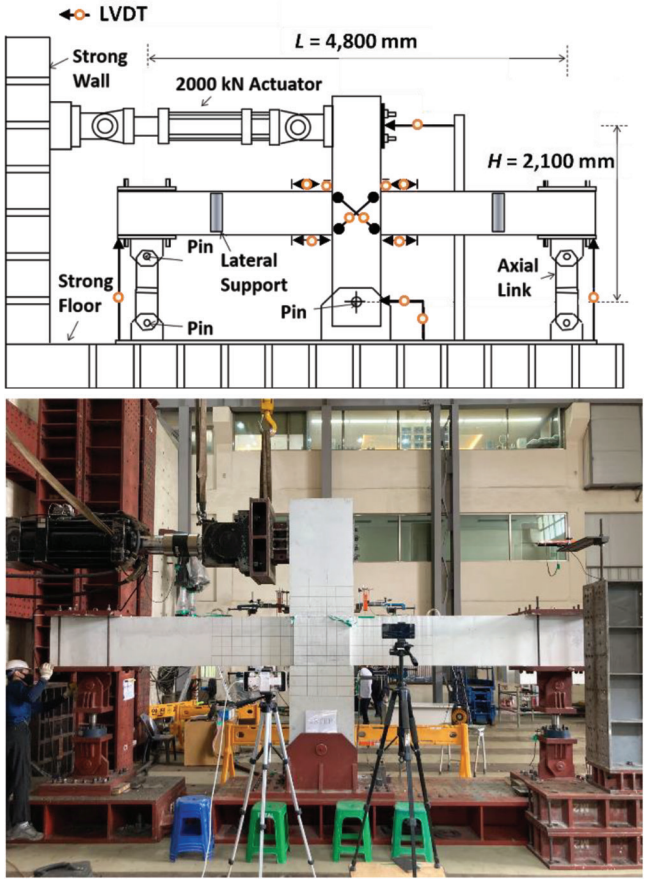

Fig. 4—Test setup for loading and measurement plan.

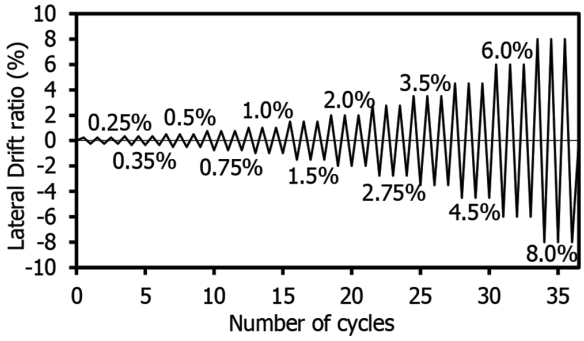

Fig. 5—Loading plan.

respectively. Further, NC-M-2S showed severe pinching behavior compared to ZC-P-2H and ZC-P-3H. The low ductility and energy dissipation of NC-M-2S are attributed to significant reinforcing bar bond-slip in the joint, which is caused by the straight beam bottom reinforcing bars. The average yield drift ratio (δ_y) of ZC-P-3H was 7% higher than ZC-P-2H due to the greater strength and higher beam bottom bar ratio. On the other hand, the ultimate drift ratio (δ_u) of ZC-P-3H was 7% less than that of ZC-P-2H.

Damage mode

Figure 7 shows damage modes at δ = 3.5% and at the end of the tests (δ = 8.0%). In all the specimens, the damage was concentrated at the beam-column interfaces: flexural yielding, formation of beam plastic hinge, and concrete spalling and crushing. In particular, the monolithic NC

*The Appendix is available at **www.concrete.org/publications** in PDF format, appended to the online version of the published paper. It is also available in hard copy from ACI headquarters for a fee equal to the cost of reproduction plus handling at the time of the request.

Table 5—Deformation capacities and energy dissipation ratios of specimens

Specimen	δ_y, %		δ at P_{max}, %		δ_u, %		$\mu = \delta_u/\delta_y$		κ at δ = 3.5%		
									Predicted*		
	Positive	Negative	Positive	Negative	Positive	Negative	Positive	Negative	Interior	Exterior	Tested
NC-M-2S	1.55	–1.59	2.67	–2.74	3.95	–4.45	2.55	2.79	0.296	—	0.189
ZC-P-2H	1.50	–1.54	2.70	–2.75	6.19	–6.14	4.11	4.00	0.276	0.258	0.306
ZC-P-3H	1.65	–1.61	2.72	–3.49	5.69	–5.80	3.45	3.59	0.267	0.206	0.282

*Predicted is predicted energy dissipation ratio through Eom et al.[43]

Note: δ_y is yield drift ratio; δ at P_{max} is drift ratio at maximum load; δ_u is ultimate drift ratio; $\mu = \delta_u/\delta_y$ is displacement ductility; κ is energy dissipation ratio at third cycle.

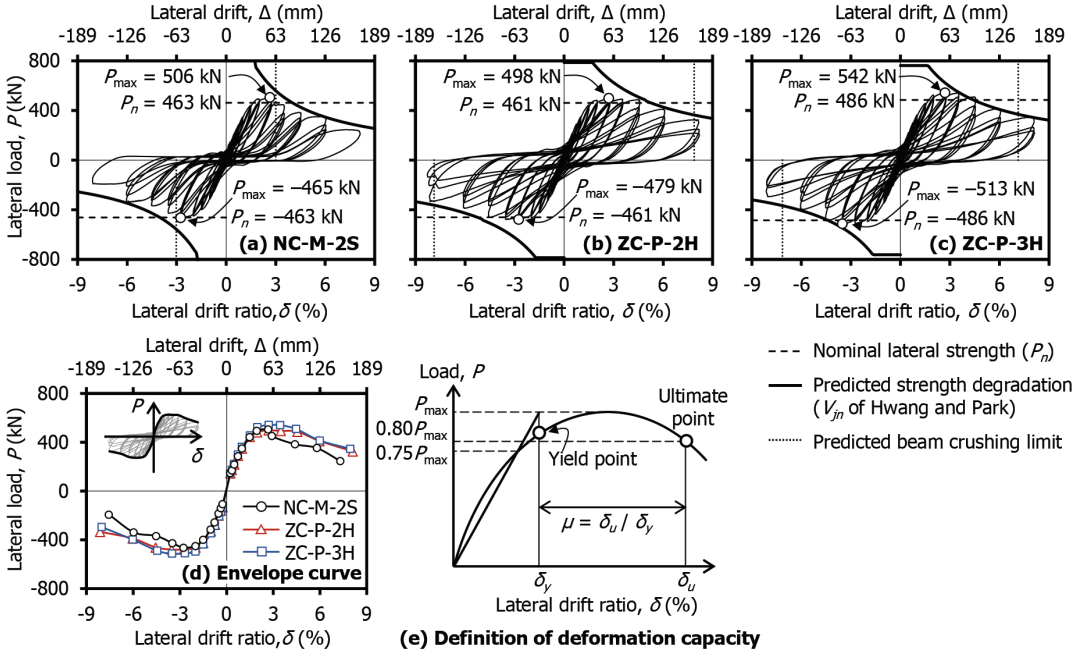

Fig. 6—Load-displacement relationships and envelope curves.

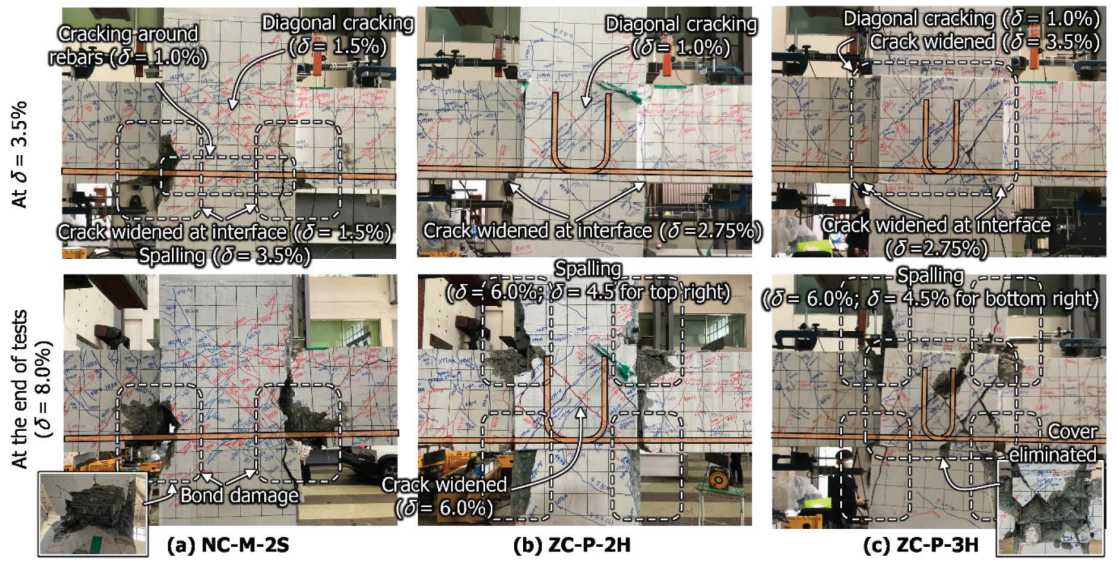

Fig. 7—Damage modes of beam-column joint specimens.

specimen (NC-M-2S) showed severe cracking at the beam-column interfaces (Fig. 7(a)), which resulted from insufficient development length and corresponding reinforcing bar bond-slip of the beam longitudinal bars. For this reason, significant strength degradation and pinching appeared in the hysteresis relationship (Fig. 6(a)). At δ = 1.5%, diagonal cracking occurred at the joint panel, and flexural cracks were widened at the bottom of the beam-column interfaces. At δ = 3.5%, due to severe bond-slip, the beam reinforcing bars were anchored to the opposite beams, which accelerated

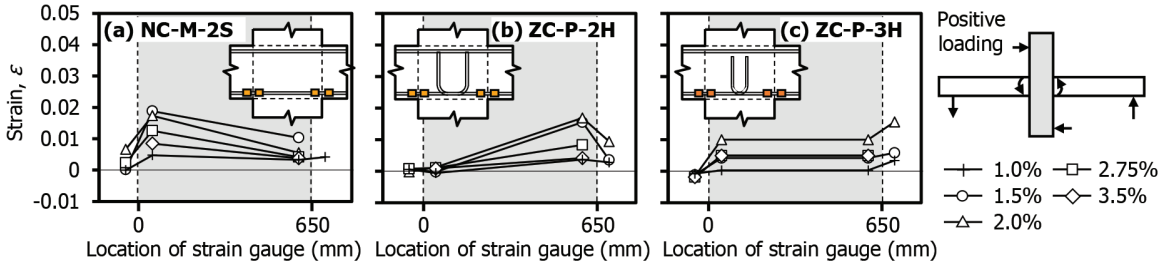

Fig. 8—Strain distribution of beam bottom bars under positive loading.

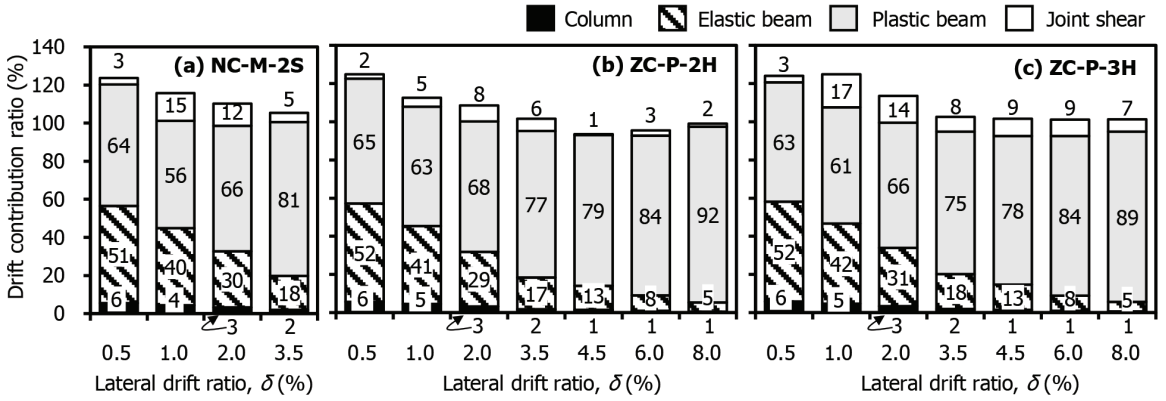

Fig. 9—Contributions of member deformations to overall lateral drift.

concrete damage and increased the bearing force on the concrete compressive zone.[39-41]

On the other hand, the precast ZC specimens (ZC-P-2H and ZC-P-3H) showed less damage at the beam-column interfaces (Fig. 7(b) and (c)). This is because reinforcing bar slip was relatively restrained by the use of a 90-degree hook anchorage. Thus, strength degradation after the maximum load was mitigated (Fig. 6(d)). At δ = 2.75%, flexural cracks were widened at the bottom of the beam-column interfaces. At δ = 4.5 to 6.0%, concrete crushing occurred at the interfaces of the precast beams and columns, mainly at the top of the beam-column interfaces due to the lower strength of the topping concrete. Although joint diagonal cracking occurred at δ = 1.0% in both the specimens, cracking became significant earlier in ZC-P-3H (at δ = 3.5% for ZC-P-3H and δ = 4.5 to 6.0% for ZC-P-2H).

Strain of beam bottom bars

Figure 8 shows the strain distribution of the beam bottom bars in the joint specimens at δ = 1.0 to 3.5%. The strain gauges were located at 30 mm (1.18 in.) outside and inside the beam-column interfaces. In NC-M-2S under positive loading (Fig. 8(a)), after δ = 1.5% (corresponding to the yield point), the reinforcing bar strains kept decreasing. On the other hand, in ZC-P-2H and ZC-P-3H, as the drift ratio increased, the reinforcing bar strains in tension increased until δ = 2.0% due to adequate bond strength (that is, hook anchorage) (Fig. 8(b) and (c)). In the strain distribution of the bottom tension reinforcing bar in ZC-P-2H (Fig. 8(b)), as the drift ratio increased further, the strain inside the joint (the second strain from the right) increased and was greater than the strain of the beam end (the first strain from the right). This result indicates that yield penetration occurred in the joint. On the other hand, in ZC-P-3H with smaller-diameter reinforcing bars (Fig. 8(c)), the strain inside the joint (the second strain from the right) was less than the strain of the beam end. This result indicates that the yield zone remained at the beam end. For this reason, in ZC-P-2H (Fig. 8(b)), as the drift ratio increased, the maximum strain occurred inside the joint. On the other hand, in ZC-P-3H with smaller-diameter reinforcing bars (Fig. 8(c)), the maximum strain occurred at the beam end.

Contributions to lateral drift

The lateral drift (Δ_{tot}) of a beam-column joint specimen is contributed to by the column deformation (Δ_c), beam elastic deformation (Δ_{be}), beam plastic deformation (Δ_{bp}), and joint shear deformation (Δ_j) (that is, $\Delta_{tot} = \Delta_c + \Delta_{be} + \Delta_{bp} + \Delta_j$).[42] The member deformations can be calculated by the lateral load or measurements of the linear variable displacement transducers (LVDTs), which are presented in Appendix B.

Figure 9 shows the contributions of the member deformations to the lateral drift ratio. The sum of the calculated contributions was approximately 100%, which indicates good agreement with the lateral drift ratios of the specimens. (The error in the calculation of lateral drift seems to be large at the small drift ratios. However, this is because the lateral deformation itself is small.) In all the specimens, the lateral drift was mainly contributed to by the beam deformation, including the elastic and plastic deformations. As the lateral drift ratio increased, the contribution of the beam plastic deformation to the lateral drift significantly increased. In ZC-P-3H, the contributions of member deformations were similar to those of NC-M-2S (not more than 6% difference) until the measurement of the beam flexural deformation in NC-M-2S was terminated at δ = 3.5% due to the severe

damage to the beams. On the other hand, ZC-P-2H showed a 1 to 12% lower contribution of joint shear deformation than that of ZC-P-2H.

Figure 10 shows the joint shear deformation at each drift ratio. Prior to δ = 2.0%, NC-M-2S and ZC-P-3H exhibited the largest joint shear deformation. In NC-M-2S, after δ = 2.0%, the joint shear deformation ceased to increase due to the lower strength and significant reinforcing bar bond-slip. On the other hand, in ZC-P-2H and ZC-P-3H, due to the 90-degree hooked bars anchored inside the joint, bond-slip was relatively less, and as the lateral deformation increased, the joint shear deformation increased. The joint shear deformation of ZC-P-2H with larger longitudinal bars was less than that of ZC-P-3H: 25 to 49% lower at δ = 3.5 to 8.0% (this will be discussed later).

Energy dissipation

Figures 11(a) to (c) show the energy dissipations per load cycle of the joint specimens. The energy dissipation was defined as the area enclosed by the hysteresis curve in each load cycle.

Until δ = 2.75%, corresponding to the maximum loads, all the specimens had similar energy dissipation capacity. ZC-P-2H and ZC-P-3H were nearly identical in energy dissipations. At δ = 2.75%, compared to the first load cycle, the energy dissipations at the second and third load cycles decreased to 81% and 72% in NC-M-2S, respectively, which was similar to the 84% and 77% in ZC-P-2H, and 85% and 75% in ZC-P-3H, respectively. However, after the maximum loads, the relative energy dissipations of the second and third load cycles of NC-M-2S became less than those of ZC-P-2H and ZC-P-3H. For example, at δ = 3.5%, compared to the first load cycle, the relative energy dissipations of the second and third load cycles decreased to 64% and 51% in NC-M-2S, respectively, which were more degraded than the 88% and 77% in ZC-P-2H and 85% and 75% in ZC-P-3H, respectively. Ultimately, the cumulative energy dissipation of NC-M-2S was 38% less than those of ZC-P-2H and ZC-P-3H. The lower energy dissipation of NC-M-2S is attributed to the bond-slip of the beam bottom reinforcing bars.

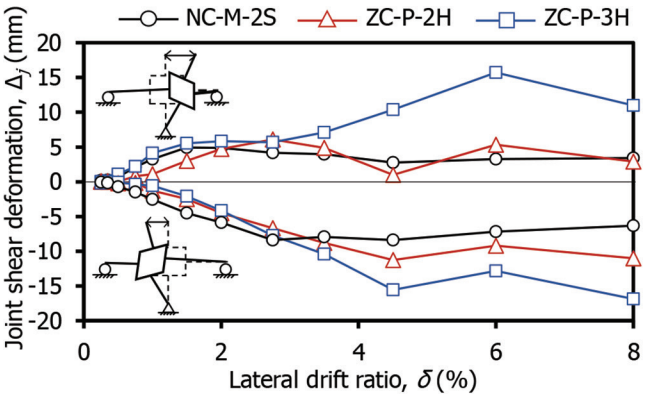

Fig. 10—Maximum joint shear deformation at each drift ratio.

PERFORMANCE EVALUATION

Effect of hook anchorage in joints

As mentioned in the test results, the hook anchorage of the beam bottom bars improved the structural performance of the beam-column joints. When comparing the monolithic specimen (NC-M-2S) and the precast specimens (ZC-P-2H and ZC-P-3H), the use of hook anchorage in the precast joints improved the cyclic behavior, bond performance of beam longitudinal bars, energy dissipation capacity, and deformation capacity.

Both ZC-P-2H and ZC-P-3H used hook anchorages in the joint, but the development lengths of hooked bars (l_{dh}) were different: l_{dh} = 470 mm (18.5 in.) for ZC-P-2H using D25 reinforcing bars, and l_{dh} = 410 mm (16.1 in.) for ZC-P-3H using D22 reinforcing bars. Although both the specimens satisfied the development length of the hook anchorage specified in ACI 318-19,[18] ZC-P-3H, using smaller-diameter reinforcing bars, showed less bond-slip and greater joint shear deformation (Fig. 9 and 10). This result indicates that the use of smaller-diameter reinforcing bars is effective in reducing bond-slip.

Nevertheless, the structural performances of ZC-P-2H and ZC-P-3H were similar in terms of the cyclic behavior, energy dissipation capacity, and deformation capacity. This is because both bond-slip and joint shear deformation do not contribute to energy dissipation. Thus, as the required development lengths of ACI 318-19[18] were satisfied, the properties of hook anchorage did not significantly affect the overall structural performance.

Evaluation of energy dissipation ratio

Figure 11(d) compares the energy dissipation ratios (κ) at each drift ratio of the specimens. The energy dissipation ratio was defined as the ratio of the actual energy dissipation (E_D) of the third load cycle to the idealized elastic-perfectly-plastic energy dissipation (E_{ep}): $\kappa = E_D/E_{ep}$. Note that the slope of the idealized elastic-perfectly-plastic curve was

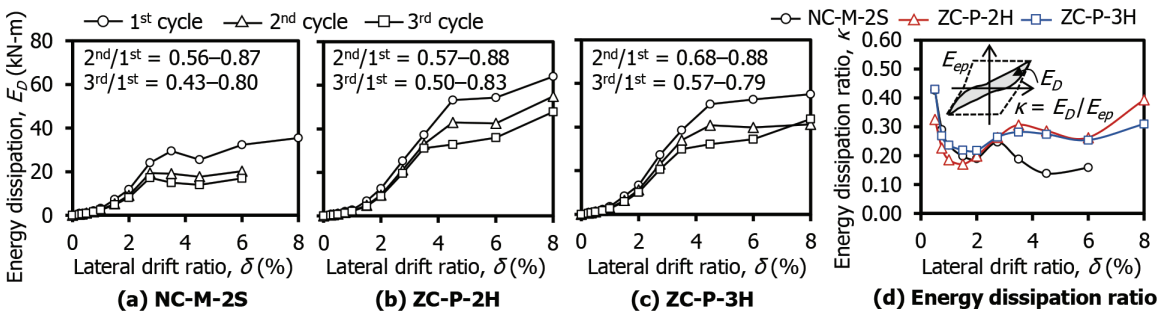

Fig. 11—Energy dissipation capacity.

Table 6—Seismic performance evaluation of ACI 374.1-05

Criterion		NC-M-2S		ZC-P-2H		ZC-P-3H	
		Positive	Negative	Positive	Negative	Positive	Negative
(a) Strong-column/weak-beam, kN	P_{max}	506	–465	498	–479	542	–513
	λP_n	1034	–1034	1032	–1032	1035	–1035
	Ratio	2.04	2.22	2.07	2.16	1.91	2.02
(b) Strength degradation, kN	$0.75P_{max}$	379	–349	374	–359	406	–385
	$P_{3.5\%}$	339	–324	459	–440	487	–463
	Ratio	0.894	0.928	1.23	1.23	1.20	1.20
(c) Energy dissipation ratio	$\kappa_{3.5\%}$	0.189		0.306		0.282	
(d) Stiffness degradation, kN/mm	$0.05K_i$	1.44	1.04	1.37	1.26	1.39	1.30
	$K_{3.5\%}$	0.82	0.44	4.78	4.23	4.28	3.38
	Ratio	0.57	0.42	3.48	3.35	3.07	2.61

Note: P_{max} is maximum load; λ is $\Sigma M_{nc}/\Sigma M_{nb}$ is overstrength factor (M_{nc} is nominal moment strength of column and M_{nb} is nominal moment strength of beam; P_n is nominal lateral load strength based on nominal moment strength of beam; $P_{3.5\%}$ is strength at third load cycle of $\delta = 3.5\%$; $\kappa_{3.5\%}$ is energy dissipation ratio at third load cycle of $\delta = 3.5\%$; K_i is initial stiffness; $K_{3.5\%}$ is secant stiffness at third load cycle of $\delta = 3.5\%$; 1 kN = 0.225 kip; 1 kN·m = 0.735 kip·ft; 1 kN/mm = 5.71 kip/in.

defined by the secant stiffness at the first load cycle (that is, the initial stiffness) of each drift ratio in each loading direction.

The energy dissipation ratios of the specimens were similar until $\delta = 2.75\%$ (maximum load point). After $\delta = 3.5\%$, the energy dissipation ratio of NC-M-2S began to decrease, whereas those of ZC-P-2H and ZC-P-3H remained relatively uniform.

Eom et al.[43] proposed the energy dissipation capacity of beam-column joints as a function of bar bond parameters on the basis of the existing test results of 69 interior and 63 exterior beam-column joints. The model was sophisticated by Hwang and Park[44,45] as follows

$$\kappa = 0.8\frac{h_c}{d_b}\frac{\sqrt{f_c'}}{f_y} + 0.05 \le 0.6 \text{ for interior joints} \quad (4a)$$

$$0.14 \le \kappa = 1.56\frac{l_{dh}}{d_b}\frac{\sqrt{f_c'}}{f_y} - 0.6 \le 0.5 \text{ for exterior joints} \quad (4b)$$

Table 5 compares the predictions with the test results of the energy dissipation ratio. At the third load cycle of $\delta = 3.5\%$, the prediction of Eq. (4a) overestimated the energy dissipation capacity of NC-M-2S (0.296 versus 0.189) due to reinforcing bar bond-slip, though at the earlier drift ratio of $\delta = 2.75\%$, the prediction was similar to the test result (0.248). On the other hand, the prediction of Eq. (4a) underestimated the energy dissipation ratios of ZC-P-2H and ZC-P-3H (0.276 versus 0.306 for ZC-P-2H and 0.267 versus 0.282 for ZC-P-3H). This is because Eq. (4a) was developed for monolithic interior joints with straight beam reinforcing bars. The prediction of Eq. (4b) (based on exterior joints with 90-degree hooked bars) underestimated the energy dissipation ratios more (0.258 versus 0.306 for ZC-P-2H and 0.206 versus 0.282 for ZC-P-3H).

Seismic performance evaluation of ACI 374.1-05

One of the main purposes of the present study is to investigate the seismic performance of the precast beam-column joints using the novel ZC. ACI 374.1-05[34] specifies acceptance criteria to evaluate the seismic performance of moment frames under high earthquake risk. The acceptance criteria (at the third load cycle of $\delta = 3.5\%$, except for (a)) are as follows: (a) the column should not yield at the maximum load (that is, $\lambda P_n/P_{max} > 1.0$); (b) the strength should be greater than 75% of the maximum load (that is, $P_{3.5\%}/0.75P_{max} > 1.0$); (c) the energy dissipation ratio should be greater than 1/8 (that is, $\kappa_{3.5\%} > 0.125$); and (d) the secant stiffness between $\delta = –0.35\%$ and +0.35% should not be less than 0.05 times the initial stiffness (that is, $K_{3.5\%}/0.05K_i > 1.0$). The notations are defined in the footnote of Table 6.

In Table 6, ZC-P-2H and ZC-P-3H satisfied all the acceptance criteria from (a) to (d). This result indicates that the precast ZC specimens (ZC-P-2H and ZC-P-3H) ensure the seismic performance of moment frames under high earthquake risk, though the ZC specimens were designed for intermediate moment frames. On the other hand, the monolithic NC specimen (NC-M-2S) with a small h_c/d_b did not satisfy criteria (b) and (d) (that is, ratio < 1.0) due to the significant pinching behavior caused by reinforcing bar bond-slip.

Seismic performance evaluation of AIJ 2002 Guidelines

To apply the current design code to the precast beam-column joints, the Architectural Institute of Japan (AIJ)[46] requires that the structural performance of precast members be equivalent to that of monolithic members designed by the current design code. The requirements are as follows: (a) and (b) the yield strength (P_y) and peak strength (P_{max}) of the precast member should exceed the strengths of the monolithic member, respectively; (c) the strength at the second load cycle (P_{2nd}) at $\delta = 2\%$ should exceed 80% of that of the first cycle (P_{1st}); (d) the discrepancy of the yield deformation (δ_y) between the precast and monolithic members should not be more than 20%; and (e) the energy dissipation ($E_{2\%}$)

Table 7—Seismic performance evaluation of AIJ 2002 Guidelines

Criterion		ZC-P-2H		ZC-P-3H	
		Positive	Negative	Positive	Negative
(a) Yield strength	P_y, kN	446	–429	476	–450
	Ratio	0.99	1.04	1.06	1.10
(b) Strength	P_{max}, kN	498	–479	542	–513
	Ratio	1.11	1.17	1.21	1.25
(c) Strength degradation	P_{1st}, kN	482	–464	524	–495
	P_{2nd}, kN	462	–451	505	–478
	P_{2nd}/P_{1st}	0.96	0.97	0.96	0.97
(d) Yield deformation	δ_y, %	1.50	–1.54	1.65	–1.61
	Ratio	0.97	0.96	1.06	1.01
(e) Energy dissipation	$E_{2\%}$, kN·m	9.60		11.2	
	Ratio	1.06		1.23	

Note: Ratio is ratio of corresponding specimen to NC-M-2S; P_y is yield strength; P_{max} is maximum load; P_{1st} is peak load at first cycle of $\delta = 2\%$; P_{2nd} is peak load at second load cycle of $\delta = 2\%$; δ_y is yield drift ratio; $E_{2\%}$ is energy dissipation at second load cycle of $\delta = 2\%$; 1 kN = 0.225 kip; 1 kN·m = 0.735 kip·ft.

of the precast member at the second load cycle of $\delta = 2\%$ should exceed 80% of that of the monolithic member.

In Table 7, the precast ZC specimens (ZC-P-2H and ZC-P-3H) satisfied the equivalence criteria to the monolithic NC specimen (NC-M-2S). In ZC-P-2H and ZC-P-3H, the yield strengths were 0.99 to 1.04 and 1.06 to 1.10, and the peak strengths were 1.11 to 1.17 and 1.21 to 1.25 times those of NC-M-2S, respectively, satisfying requirements (a) and (b). The strength degradation of ZC-P-2H and ZC-P-3H was 3 to 4% at $\delta = 2\%$, satisfying requirement (c) (that is, under 20%). The yield drift ratios of the ZC specimens were 0.96 to 0.97 and 1.01 to 1.06 times that of specimen NC-M-2S, respectively, satisfying requirement (d) (that is, over 0.80). The energy dissipations of ZC-P-2H and ZC-P-3H were 1.06 and 1.23 times those of NC-M-2S, respectively, satisfying requirement (e) (that is, over 0.80).

Evaluation of joint shear strength degradation

Hwang and Park[44,45] proposed a joint shear strength degradation model for interior and exterior RC beam-column joints. The proposed model can predict the shear strength (V_{jn}) of beam-column joints at the target drift ratio (δ_T), addressing the diagonal strut and truss mechanisms. Unlike conventional interior beam-column joints using straight bars, 90-degree hooked bars were used for the precast ZC joint specimens. Thus, a modification for the shear strength of interior joints with 90-degree hooked bars was proposed, considering the exterior beam-column joint model with 90-degree hooked bars. Appendix C presents detailed information on the shear strength model.

Figure 6 compares the load-displacement relationships of the beam-column joint specimens with the predicted strength degradation. Generally, the predicted strength degradation was similar to the envelope curves of the test results. In NC-M-2S, the proposed strength model predicted early beam crushing, which agreed with the actual failure mode (Fig. 7(a)). In ZC-P-2H and ZC-P-3H, the predictions agreed with the tested strengths, indicating that the proposed method is applicable to estimate the joint shear degradation of the precast ZC beam-column joints with 90-degree hook anchorage. Further study is required to confirm the application of the prediction models.

CONCLUSIONS

Cyclic loading tests were conducted to investigate the seismic performance of precast beam-column joints using a newly developed zero-cement concrete (ZC). Further, the applicability of the current design codes and prediction models to ZC joints was investigated. Three full-scale interior beam-column joint specimens (one monolithic normal concrete [NC] joint and two precast ZC joints) were tested. The test parameters included concrete type, fabrication method, and beam bottom bar anchorage detail. The structural performance was evaluated based on the strength, deformation capacity, damage mode, and energy dissipation. The major findings are summarized as follows:

1. The beam bottom bar anchorage detail of the joints mainly affected the damage modes and structural performance. The monolithic NC specimen, with continuous straight beam bottom bars, experienced severe reinforcing bar bond-slip after the maximum load. As a result, the NC specimen showed significant strength degradation and pinching in the load-displacement relationship. On the other hand, the precast ZC specimens, having 90-degree hook anchorage in the joint, exhibited typical joint diagonal cracking and joint shear deformation as the 90-degree hook anchorage mitigated bond-slip.

2. Thus, the precast ZC specimens showed equivalent or superior seismic performance to the monolithic NC specimen. The energy dissipation ratio of the precast ZC specimens was 82 to 87% greater and the displacement ductility was 32 to 52% greater than those of the monolithic NC specimen.

3. The major damage of the precast ZC specimens was joint shear strength degradation, which occurred in the joint panel zone of NC. Thus, ZC did not significantly affect the structural performance of the ZC joint specimens.

4. The tested strengths of the specimens agreed with the nominal strength of ACI 318-19 based on the beam yielding: $P_{max}/P_n = 1.00$ to 1.11. Although the design of ZC specimens was targeted for intermediate moment frames, the seismic performance of ZC specimens satisfied the requirements of ACI 374.1-05. The ZC specimens also satisfied the evaluation criteria of the AIJ 2002 Guidelines.

5. An existing model of joint shear strength degradation was modified to predict the joint shear strength of the precast ZC specimens with 90-degree hook anchorage. The predicted joint shear strength degradation agreed with the test results of the ZC specimens.

In the proposed precast concrete specimens, the joint was constructed with cast-in-place NC because ZC requires a high curing temperature, which is not applicable to cast-in-place concrete construction. As the present test results showed, the damage of the specimens occurred in the NC

joint rather than the ZC members. The structural performance of ZC beams and columns will be reported in the future.

AUTHOR BIOS

Han-Se Moon *is a PhD Candidate in the Department of Architecture and Architectural Engineering at Seoul National University, Seoul, South Korea, where he received his BE and MS in architectural engineering.*

ACI member **Hyeon-Jong Hwang** *is an Associate Professor in the College of Architecture at Konkuk University, Seoul, South Korea. He received his BE, MS, and PhD in architectural engineering from Seoul National University. He is a member of ACI Committee 369, Seismic Repair and Rehabilitation; ACI Subcommittee 318-L, International Liaison; and Joint ACI-ASCE Committees 352, Joints and Connections in Monolithic Concrete Structures, and 408, Bond and Development of Steel Reinforcement. His research interests include inelastic analysis and seismic design of reinforced concrete (RC) and composite structures.*

Chang-Soo Kim *is a Professor in the School of Architecture (Architectural Engineering Program) at Seoul National University of Science and Technology, Seoul, South Korea. He received his BS in architectural engineering from Pusan National University, Busan, South Korea, and his MS and PhD in structural engineering from Seoul National University. His research interests include structural design and performance evaluation of composite and precast concrete structures.*

Kwang-Won Jo *is a PhD Candidate in the Department of Architecture and Architectural Engineering at Seoul National University. He received his BE in architectural engineering from Chung-Ang University, Seoul, South Korea, and his MS from the Department of Architecture and Architectural Engineering at Seoul National University. His research interests include inelastic analysis and the seismic design of RC structures.*

Jae-Hong Jeong *is a Principal Researcher at the Institute of Construction Technology, Samsung C&T Corporation, South Korea. He received his BS and MS from Seoul National University in 1995 and 1997, respectively. His research interests include carbon-reducing concrete, eco-friendly cement, concrete pumpability, and fiber-reinforced concrete.*

Chan-Kyu Park *is a Master Researcher at the Institute of Construction Technology, Samsung C&T Corporation. He received his PhD from the Korea Advanced Institute of Science and Technology, Daejeon, South Korea, in 1997. His research interests include carbon-reducing concrete, concrete pumpability, and hydration control of mass concrete.*

Hong-Gun Park, *FACI, is a Professor in the Department of Architecture and Architectural Engineering at Seoul National University. He received his BE and MS in architectural engineering from Seoul National University and his PhD in civil engineering from The University of Texas at Austin, Austin, TX. His research interests include inelastic analysis and the seismic design of RC structures.*

ACKNOWLEDGMENTS

This research was supported by Samsung C&T Corporation and a grant (1615012983) from the Digital-Based Building Construction and Safety Supervision Technology Research Program funded by the Ministry of Land, Infrastructure and Transport of the Korean government. The authors are grateful to the authorities for their support.

NOTATION

d = effective depth from extreme compression fiber to centroid of longitudinal tension reinforcement, mm (in.)
d_b = diameter of reinforcing bar, mm (in.)
E_c = modulus of elasticity of concrete, MPa (ksi)
f_c' = compressive strength of concrete, MPa (ksi)
f_y = yield strength of reinforcing bar, MPa (ksi)
H = net height between loading point and reaction point in columns, mm (in.)
h_c = column depth, mm (in.)
L = net length between roller supports in beams, mm (in.)
l_{dh} = development length of reinforcing bar with standard hook, mm (in.)
M_{nb}^- = negative nominal moment strength of beam, kN·m (kip·ft)
M_{nb}^+ = positive nominal moment strength of beam, kN·m (kip·ft)
M_{nc} = nominal moment strength of column, kN·m (kip·ft)
P = lateral load, kN (kip)
P_{max} = maximum load or maximum lateral load strength, kN (kip)
P_n = nominal lateral load strength based on beam yielding, kN (kip)
s = spacing of transverse reinforcement, mm (in.)
V_{jn} = nominal shear strength of joint, kN (kip)
V_u = joint shear demand, kN (kip)
δ = lateral drift ratio, %
δ_T = target drift ratio, %
δ_u = ultimate drift ratio, %
δ_y = yield drift ratio, %
ε_{co} = strain of concrete at peak stress
κ = energy dissipation ratio
λ = overstrength factor = M_{nc}/M_{nb}
μ = displacement ductility
ρ = reinforcement ratio, %

REFERENCES

1. Korea Environmental Industry & Technology Institute, "Environmental Product Declaration Emission Factor (Korea LCI DB)," Seoul, South Korea, Aug. 2021, https://ecosq.or.kr/websquare.do#w2xPath=/ui/cer/ep/oa/EPOA310M04.xml.

2. Mo, K. H.; Alengaram, U. J.; and Jumaat, M. Z., "Structural Performance of Reinforced Geopolymer Concrete Members: A Review," *Construction and Building Materials*, V. 120, Sept. 2016, pp. 251-264. doi: 10.1016/j.conbuildmat.2016.05.088

3. Vashistha, P.; Park, S.; and Pyo, S., "A Review on Sustainable Fabrication of Futuristic Cementitious Binders Based on Application of Waste Concrete Powder, Steel Slags, and Coal Bottom Ash," *International Journal of Concrete Structures and Materials*, V. 16, No. 1, Dec. 2022, Article No. 51. doi: 10.1186/s40069-022-00541-9

4. Bakhoum, E. S., and Mater, Y. M., "Decision Analysis for the Influence of Incorporating Waste Materials on Green Concrete Properties," *International Journal of Concrete Structures and Materials*, V. 16, No. 1, Dec. 2022, Article No. 63. doi: 10.1186/s40069-022-00553-5

5. Yang, K.-H., and Song, J.-G., "The Properties and Applications of Alkali-Activated Concrete with No Cement," *Magazine of the Korea Concrete Institute*, V. 19, No. 2, Mar. 2007, pp. 42-48.

6. Amran, Y. H. M.; Alyousef, R.; Alabduljabbar, H.; and El-Zeadani, M., "Clean Production and Properties of Geopolymer Concrete; A Review," *Journal of Cleaner Production*, V. 251, Apr. 2020, Article No. 119679. doi: 10.1016/j.jclepro.2019.119679

7. Patil, A. A.; Chore, H. S.; and Dode, P. A., "Effect of Curing Condition on Strength of Geopolymer Concrete," *Advances in Concrete Construction*, V. 2, No. 1, Mar. 2014, pp. 29-37. doi: 10.12989/acc.2014.2.1.029

8. Olivia, M., and Nikraz, H., "Properties of Fly Ash Geopolymer Concrete Designed by Taguchi Method," *Materials & Design (1980-2015),* V. 36, Apr. 2012, pp. 191-198.

9. Topark-Ngarm, P.; Chindaprasirt, P.; and Sata, V., "Setting Time, Strength, and Bond of High-Calcium Fly Ash Geopolymer Concrete," *Journal of Materials in Civil Engineering*, ASCE, V. 27, No. 7, July 2015, p. 04014198. doi: 10.1061/(ASCE)MT.1943-5533.0001157

10. Li, N.; Shi, C.; Zhang, Z.; Zhu, D.; Hwang, H.-J.; Zhu, Y.; and Sun, T., "A Mixture Proportioning Method for the Development of Performance-Based Alkali-Activated Slag-Based Concrete," *Cement and Concrete Composites*, V. 93, Oct. 2018, pp. 163-174. doi: 10.1016/j.cemconcomp.2018.07.009

11. Saranya, P.; Nagarajan, P.; and Shashikala, A. P., "Development of Ground-Granulated Blast-Furnace Slag-Dolomite Geopolymer Concrete," *ACI Materials Journal*, V. 116, No. 6, Nov. 2019, pp. 235-243.

12. Khan, M. Z. N.; Shaikh, F. U. A.; Hao, Y.; and Hao, H., "Synthesis of High Strength Ambient Cured Geopolymer Composite by Using Low Calcium Fly Ash," *Construction and Building Materials*, V. 125, Oct. 2016, pp. 809-820. doi: 10.1016/j.conbuildmat.2016.08.097

13. Wu, C.; Hwang, H.-J.; Shi, C.; Li, N.; and Du, Y., "Shear Tests on Reinforced Slag-Based Geopolymer Concrete Beams with Transverse Reinforcement," *Engineering Structures*, V. 219, Sept. 2020, Article No. 110966. doi: 10.1016/j.engstruct.2020.110966

14. Du, Y.; Wang, J.; Shi, C.; Hwang, H.-J.; and Li, N., "Flexural Behavior of Alkali-Activated Slag-Based Concrete Beams," *Engineering Structures*, V. 229, Feb. 2021, Article No. 111644. doi: 10.1016/j.engstruct.2020.111644

15. Mao, Y.; Hwang, H.-J.; Du, Y.; Su, J.; Hu, X.; Liu, Y.; and Shi, C., "Bond and Anchorage Performance of Beam Flexural Bars in Beam-Column Joints Using Slag-Based Geopolymer Concrete and Their Effect on Seismic Performance," *Engineering Structures*, V. 273, Dec. 2022, Article No. 115062. doi: 10.1016/j.engstruct.2022.115062

16. Mao, Y.; Du, Y.; Hwang, H.-J.; Su, J.; Hu, X.; Liu, Y.; and Shi, C., "Seismic Performance of Interior Beam-Column Joints Using Reinforced

Slag-Based Geopolymer Concrete," *Earthquake Engineering & Structural Dynamics*, V. 52, No. 2, Feb. 2023, pp. 285-307.

17. Liu, Y.; Zhou, F.; Shen, Y.; Hwang, H.-J.; Du, Y.; Mao, Y.; and Shi, C., "Shear Transfer Strength of Alkali-Activated Slag-Based Concrete," *Journal of Building Engineering*, V. 70, July 2023, Article No. 106304. doi: 10.1016/j.jobe.2023.106304

18. ACI Committee 318, "Building Code Requirements for Structural Concrete (ACI 318-19) and Commentary (ACI 318R-19) (Reapproved 2022)," American Concrete Institute, Farmington Hills, MI, 2019, 624 pp.

19. Saranya, P.; Nagarajan, P.; and Shashikala, A. P., "Performance Evaluation of Geopolymer Concrete Beams under Monotonic Loading," *Structures*, V. 20, Aug. 2019, pp. 560-569. doi: 10.1016/j.istruc.2019.06.010

20. Saranya, P.; Nagarajan, P.; Shashikala, A. P.; and Salam, A. P., "Flexural Behaviour of GGBS-Dolomite Geopolymer Concrete Beams under Cyclic Loading," *Materials Science Forum*, V. 969, 2019, pp. 291-296. doi: 10.4028/www.scientific.net/MSF.969.291

21. Saranya, P.; Nagarajan, P.; and Shashikala, A. P., "Behaviour of GGBS-Dolomite Geopolymer Concrete Beam-Column Joints under Monotonic Loading," *Structures*, V. 25, June 2020, pp. 47-55. doi: 10.1016/j.istruc.2020.02.021

22. Saranya, P.; Nagarajan, P.; and Shashikala, A. P., "Behaviour of GGBS-Dolomite Geopolymer Concrete Short Column under Axial Loading," *Journal of Building Engineering*, V. 30, July 2020, Article No. 101232. doi: 10.1016/j.jobe.2020.101232

23. Saranya, P.; Nagarajan, P.; and Shashikala, A. P., "Seismic Performance of Geopolymer Concrete Beam-Column Joints under Reverse Cyclic Loading," *Innovative Infrastructure Solutions*, V. 6, No. 2, June 2021, Article No. 92.

24. Tran, T. T.; Pham, T. M.; and Hao, H., "Experimental and Analytical Investigation on Flexural Behaviour of Ambient Cured Geopolymer Concrete Beams Reinforced with Steel Fibers," *Engineering Structures*, V. 200, Dec. 2019, Article No. 109707. doi: 10.1016/j.engstruct.2019.109707

25. Tran, T. T.; Pham, T. M.; and Hao, H., "Effect of Hybrid Fibers on Shear Behaviour of Geopolymer Concrete Beams Reinforced by Basalt Fiber Reinforced Polymer (BFRP) Bars without Stirrups," *Composite Structures*, V. 243, July 2020, Article No. 112236. doi: 10.1016/j.compstruct.2020.112236

26. Huang, Z.; Chen, W.; Hao, H.; Chen, Z.; Pham, T. M.; Tran, T. T.; and Elchalakani, M., "Shear Behaviour of Ambient Cured Geopolymer Concrete Beams Reinforced with BFRP Bars under Static and Impact Loads," *Engineering Structures*, V. 231, Mar. 2021, Article No. 111730. doi: 10.1016/j.engstruct.2020.111730

27. Huang, J.-Q.; Kumar, S.; and Dai, J.-G., "Flexural Performance of Steel-Reinforced Geopolymer Concrete One-Way Slabs: Experimental and Numerical Investigations," *Construction and Building Materials*, V. 366, Feb. 2023, Article No. 130098. doi: 10.1016/j.conbuildmat.2022.130098

28. Ngo, T. T.; Tran, T. T.; Pham, T. M.; and Hao, H., "Performance of Geopolymer Concrete in Monolithic and Non-Corrosive Dry Joints Using CFRP Bolts under Cyclic Loading," *Composite Structures*, V. 258, Feb. 2021, Article No. 113394. doi: 10.1016/j.compstruct.2020.113394

29. Huang, Z.; Khan, M. Z. N.; Chen, W.; Hao, H.; Wu, Y.; Pham, T. M.; and Elchalakani, M., "Experimental and Numerical Study of the Performance of Geopolymer Concrete Columns Reinforced with BFRP Bars Subjected to Lateral Impact Loading," *Construction and Building Materials*, V. 357, Nov. 2022, Article No. 129362. doi: 10.1016/j.conbuildmat.2022.129362

30. Tran, T. T.; Pham, T. M.; Huang, Z.; Chen, W.; Ngo, T. T.; Hao, H.; and Elchalakani, M., "Effect of Fibre Reinforcements on Shear Capacity of Geopolymer Concrete Beams Subjected to Impact Load," *International Journal of Impact Engineering*, V. 159, Jan. 2022, Article No. 104056. doi: 10.1016/j.ijimpeng.2021.104056

31. Chen, C.; Zhang, X.; and Hao, H., "Investigation on the Impact Resistance of Reinforced Geopolymer Concrete Slab," *Journal of Cleaner Production*, V. 406, June 2023, Article No. 137144. doi: 10.1016/j.jclepro.2023.137144

32. Raj, S. D.; Ganesan, N.; Abraham, R.; and Raju, A., "Behavior of Geopolymer and Conventional Concrete Beam Column Joints under Reverse Cyclic Loading," *Advances in Concrete Construction*, V. 4, No. 3, Sept. 2016, pp. 161-172. doi: 10.12989/acc.2016.4.3.161

33. Datta, M., and Premkumar, G., "Comparative Study of Geopolymer Concrete with Steel Fibers in Beam Column Joint," *International Journal of Civil Engineering and Technology (IJCIET)*, V. 9, No. 4, Apr. 2018, pp. 234-247.

34. ACI Committee 374, "Acceptance Criteria for Moment Frames Based on Structural Testing and Commentary (ACI 374.1-05) (Reapproved 2019)," American Concrete Institute, Farmington Hills, MI, 2005, 9 pp.

35. KDS 14 20 80:2023, "Structural Concrete Design Code (Strength Design Method): Earthquake Design," Korea Construction Standards Center, Goyang, Gyeonggi, South Korea, 2023. (in Korean)

36. Joint ACI-ASCE Committee 352, "Recommendations for Design of Beam-Column Connections in Monolithic Reinforced Concrete Structures (ACI 352R-02) (Reapproved 2010)," American Concrete Institute, Farmington Hills, MI, 2002, 38 pp.

37. KS F 4044:2019, "Hydraulic-Cement Grout (Nonshrink)," Korean Industrial Standards, Chungcheongbuk-do, South Korea, 2019. (in Korean)

38. Park, R., "Evaluation of Ductility of Structures and Structural Assemblages from Laboratory Testing," *Bulletin of the New Zealand Society for Earthquake Engineering*, V. 22, No. 3, 1989, pp. 155-166. doi: 10.5459/bnzsee.22.3.155-166

39. Hwang, H.-J.; Park, H.-G.; Choi, W.-S.; Chung, L.; and Kim, J.-K., "Cyclic Loading Test for Beam-Column Connections with 600 MPa (87 ksi) Beam Flexural Reinforcing Bars," *ACI Structural Journal*, V. 111, No. 4, July-Aug. 2014, pp. 913-924. doi: 10.14359/51686920

40. Hwang, H.-J.; Eom, T.-S.; and Park, H.-G., "Bond-Slip Relationship of Beam Flexural Bars in Interior Beam-Column Joints," *ACI Structural Journal*, V. 112, No. 6, Nov.-Dec. 2015, pp. 827-837. doi: 10.14359/51687708

41. Hwang, H.-J.; Eom, T.-S.; and Park, H.-G., "Shear Strength Degradation Model for Performance-Based Design of Interior Beam-Column Joints," *ACI Structural Journal*, V. 114, No. 5, Sept.-Oct. 2017, pp. 1143-1154. doi: 10.14359/51700780

42. Park, H.-G.; Hwang, H.-J.; Lee, C.-H.; Park, C.-H.; and Lee, C.-N., "Cyclic Loading Test for Concrete-Filled U-Shaped Steel Beam–RC Column Connections," *Engineering Structures*, V. 36, Mar. 2012, pp. 325-336. doi: 10.1016/j.engstruct.2011.12.033

43. Eom, T.-S.; Hwang, H.-J.; and Park, H.-G., "Energy-Based Hysteresis Model for Reinforced Concrete Beam-Column Connections," *ACI Structural Journal*, V. 112, No. 2, Mar.-Apr. 2015, pp. 157-166.

44. Hwang, H.-J., and Park, H.-G., "Requirements of Shear Strength and Hoops for Performance-Based Design of Interior Beam-Column Joints," *ACI Structural Journal*, V. 116, No. 2, Mar. 2019, pp. 245-256. doi: 10.14359/51713290

45. Hwang, H.-J., and Park, H.-G., "Performance-Based Shear Design of Exterior Beam-Column Joints with Standard Hooked Bars," *ACI Structural Journal*, V. 117, No. 2, Mar. 2020, pp. 67-80.

46. AIJ, "Guidelines for the Design of Structural Precast Concrete Emulating Cast-in-Place Reinforced Concrete (AIJ Guidelines)," Architectural Institute of Japan, Tokyo, Japan, 2002, 261 pp.

ACI STRUCTURAL JOURNAL TECHNICAL PAPER

Title No. 122-S10

Cyclic Behavior of Steel-Jacket-Confined Ultra-High-Strength Concrete-Filled Steel Tubular Columns

by Hong-Song Hu, Li Xu, Hai-Jin Qiu, and Konstantinos Skalomenos

It has been experimentally proven that by using external confining steel jackets at high-stress locations of columns, cyclic behavior of steel or concrete columns can be improved. This study experimentally investigates the cyclic behavior of jacket-confined composite steel/concrete columns configured by square concrete-filled steel tubes (CFST) and ultra-high-strength (UHS) concrete (compressive strength nearly 125 MPa [18.1 ksi]). The CFST columns are locally confined by steel jackets at their base (that is, region of plastic hinge). Five novel steel-jacket-confined CFST (JC-CFST) columns are tested under combined constant axial and cyclic lateral loading and their responses are compared with those of three CFST counterparts. Test parameters include: (a) thickness of steel jacket; (b) profile of jacket section (square or rounded corners); (c) strength of steel tube (conventional and high-strength steel); and (d) axial load ratio, n. *Test results demonstrated that the confining stresses provided by the steel jacket started increasing after the concrete crashing. In JC-CFST specimens, the ultimate drift ratio,* θ_u, *improved almost proportionately to the jacket confinement index,* λ_m, *and significantly decreased as* n *increased. The use of high-strength steel for the steel tubes was also effective to increase* θ_u *by 20 to 25%. The cumulative energy dissipation of the JC-CFST columns was found to be much greater than that of the CFST counterparts due to the better deformation capacity of the former. The lateral displacement of the column caused by the base rotation was significant.*

Keywords: cyclic behavior; jacket-confined concrete-filled steel tube (CFST) column; steel jacket; ultra-high-strength (UHS) concrete.

INTRODUCTION

Concrete-filled steel tube (CFST) columns are widely used in tall building structures, especially at lower floors, due to their high strength-to-weight ratio and high axial stiffness (Skalomenos et al. 2015; Jin et al. 2019; Hu et al. 2024). Compared to all steel or concrete column sections, CFST columns can offer smaller dimensions and an enhanced seismic performance arising from the confined concrete and the restrained steel tube against inward local buckling (Goto et al. 2012; Xu et al. 2023). However, in very tall buildings where axial loads are extremely high, cross section dimensions increase significantly unless high-strength materials are used. In this context, the use of high-strength concrete is effective to reduce section dimensions but this solution alone is at the expense of column ductility, which limits the application of high-strength materials in CFST columns intended for earthquake-resistant structures.

A number of tests have been conducted on square CFST columns with concrete cylinder strength (f_c') exceeding 80 MPa (11.6 ksi) (Yu et al. 2008; Skalomenos et al. 2016; Xiong et al. 2017; Khan et al. 2017; Hu et al. 2023). In the works of Skalomenos et al. (2016) and Khan et al. (2017), a steel tube with a yield strength higher than 700 MPa (101.5 ksi) was also used. The deformation capacity of the CFST columns (ultimate drift ratio) improved with the strength and the amount of steel (steel content ratio) compared to columns with conventional-strength steel or a lower amount of steel. On the other hand, the increase in concrete strength led to opposite results. Hu et al. (2022) tested eight CFST columns configured with high-strength concrete (f_c' = 110 MPa [16.0 ksi]) under lateral cyclic loading. The experimental results showed that an increase in the axial compression ratio significantly reduced the deformation capacity of the column. When the axial load ratio was 0.5, the ultimate drift ratio was found to be nearly 2.0%, which may not be sufficient to satisfy the drift requirement of 3.0% under the maximum considered earthquake (Moehle 2014).

The use of thick steel tube sections can compensate for the negative impact of high-strength concrete on the seismic performance of CFST columns (Xiong et al. 2017) but drastically increase weight and cost due to the linear production of steel members. Increasing the thickness of the steel section only at the high-stress location of the column would be more efficient to maintain the small size of the section for the rest of the column. This can be achieved by adding an additional steel section only for the critical location of the column—for instance, a spiral reinforcement in the tube (Hu et al. 2020a; Teng et al. 2021; Ahmed et al. 2023), tie bars to connect the faces of the steel tube (Ho and Lai 2013; Yang et al. 2014; Ding et al. 2020), and external confining jackets (Choi and Xiao 2010; Cosgun et al. 2023; Xu et al. 2023). Regarding the latter solution, test results showed that confining steel jackets can enhance both the deformability and load-carrying capacity of the columns. In the same direction of confining jackets, fiber-reinforced polymer (FRP)-confined CFST columns have been extensively studied (Choi and Xiao 2010; Teng et al. 2013; Yu et al. 2016; Du et al. 2022). Test results showed that the FRP-based jackets are effective to some extent in improving the deformation capacity of the column but have a low effect in strengthening the load-carrying capacity.

Most studies have concentrated on the cyclic performance of CFST columns with normal-strength concrete or other performance aspects, such as post-fire behavior (Bengar and

ACI Structural Journal, V. 122, No. 1, January 2025.
MS No. S-2023-305.R2, doi: 10.14359/51743295, received June 12, 2024, and reviewed under Institute publication policies.

Shahmansouri 2021; Memarzadeh et al. 2022). Until now, there have been no studies on the cyclic behavior of jacket-confined square CFST columns made of high-strength concrete ($f_c' > 100$ MPa [14.5 ksi]). To fill this research gap, this study carries out an experimental investigation on a novel configuration of steel jacket-confined CFST (JC-CFST) columns made of square steel welded tube filled by ultra-high-strength (UHS) concrete with compressive strength of nearly 125 MPa (18.1 ksi) (Fig. 1). To avoid localized and high stress-concentration zones, a chamfered square steel tube is adopted as a confining jacket; the gap between the inner steel tube and the external jacket is filled with non-shrinkage mortar to transfer the confining force provided by the jacket; in addition, to ensure that the jacket does not carry the axial stresses, a layer of low-friction material is pasted on the outer wall of the square steel tube before the mortar is filled. The confining jacket applies only at the energy dissipative regions of the column (that is, possible locations of plastic hinge formation, such as the base of the column). The proposed jacket-confined CFST columns are intended to be used in moment-resisting frames. For moment-resisting frames, the confining jackets can be easily installed at the ends of a column (Mao and Xiao 2006; Yu et al. 2016; Zhang et al. 2021). It should be noted that the proposed jacket-confined CFST columns are not intended to be used in braced frames. In braced frames, the braces are designed to dissipate energy through yielding and the columns are designed to maintain elasticity during earthquake excitation. Thus, additional confinement of columns is not necessary. In the current study, the behavior of the proposed UHS JC-CFST column is assessed by discussing the damage progress during cyclic loading, the P-Δ effects arising from the secondary bending moment, the effectiveness of the confining stress provided by the steel-tube jacket, the bending moment and drift capacities, lateral displacement components along the column height caused by bending, shear and base rotation, and the energy dissipation capacity.

RESEARCH SIGNIFICANCE

Adding a steel jacket in the potential plastic hinge zone is a feasible method to improve the deformation capacity of CFST columns made of UHS concrete under lateral cyclic loading. The current study performed a cyclic lateral loading test on the JC-CFST columns and CFST counterparts. The damage evolution and lateral deformation behavior of JC-CFST columns were investigated. The influence of different parameters on the deformation capacity of columns was discussed. The test results provided some design recommendations for further practical application of this column type.

EXPERIMENTAL PROGRAM

Test specimens

This experimental program includes eight specimens: five JC-CFST and three reference CFST column specimens made of square steel tubes and UHS concrete infill. Figure 2 introduces the overall design of the JC-CFST specimens. Except the steel jacket, the design configurations of the

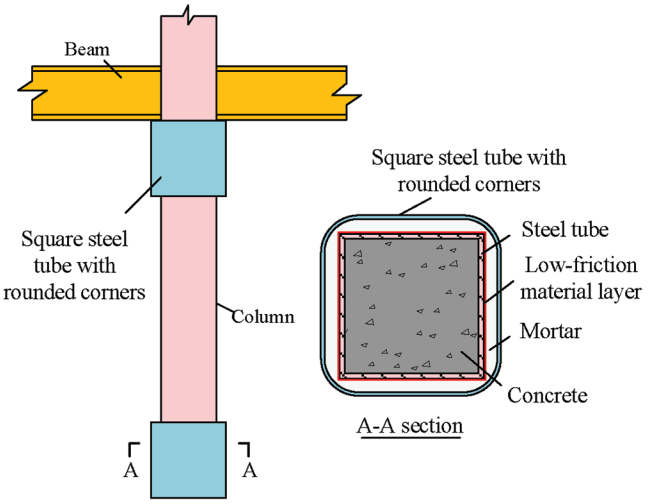

Fig. 1—Illustrative drawing of proposed JC-CFST columns.

reference CFST and the JC-CFST specimens are the same. The main steel tube of the column was made by welding four identical plates. Considering a typical value for width-to-thickness ratio for the steel tube as well as the loading capacity of the actuators used, the outer width (b) and nominal thickness of the steel tube were determined as 240 and 8 mm (9.45 and 0.31 in.), respectively. For JC-CFST columns, a steel jacket was fabricated at the base of the column. Two different tubular sections were prepared for the confining jackets: one typical square tube with sharp corners and one with rounded corners to assess the effect of stress concentration. Both steel jackets were fabricated by welding in the middle of each side of the tube two identical cold-formed C-shaped steel sections. The inner width, B, of the steel jacket was 290 mm (11.42 in.), and the radius, r, for the rounded jacket was 58 mm (2.28 in.). The height of the jacket, h_j, was equal to 300 mm (11.81 in.) (equivalent to 1.25b). A non-shrinkage mortar was used to fill in the gap for successful confinement. To eliminate the longitudinal stress transmitted from the CFST tube to the steel jacket as much as possible, a polytetrafluoroethylene (PTFE) layer of 0.1 mm (0.004 in.) thickness was used to wrap the CFST column before filling the mortar. In addition to the confining jacket section, some critical parameters were also selected as test variables, including the strength of the CFST tube, the thickness of the steel jacket, and the axial load ratio. Other parameters were determined based on common scenarios. Two steel grades were used for the fabrication of the CFST column—namely Q355 and Q550—which provide a nominal yield stress equal to 355 and 550 MPa (51.5 and 79.8 ksi), respectively. For the steel jackets with rounded corners, two thicknesses, t_{sj}, were adopted—a thickness of 2.63 and 5.62 mm (0.10 and 0.22 in.). The thickness of the jacket with sharp corners was 5.62 mm (0.22 in.). All jackets were made of Q355 grade steel.

In the jacket-confined part of the column, both the inner steel tube and the external jacket contribute confinement to the core concrete. However, the difference is that the external jacket is completely used to confine the concrete, while the inner steel tube mainly resists the longitudinal load, and the hoop confining stress is relatively small (Sakino et al. 2004).

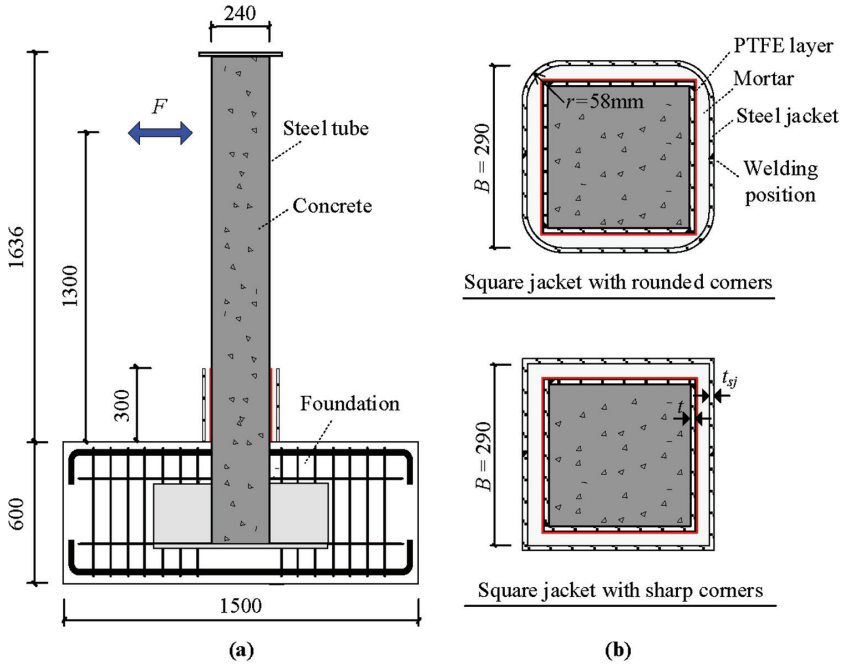

Fig. 2—Details of JC-CFST specimens: (a) side view of specimen; and (b) cross-section configurations of jacket-confined CFST column. (Note: Units in mm; 1 mm = 0.04 in.)

Therefore, it is necessary to adopt different indexes to indicate the two different confinements.

The steel tube's confining level can be reflected by the confinement coefficient (Hatzigeorgiou 2008), ξ_s

$$\xi_s = \frac{f_{yt}A_{st}}{f_c'A_c} \tag{1}$$

where f_{yt} denotes the yield strength of the steel tube plate; and A_{st} and A_c denote the cross-sectional areas of the steel tube and concrete, respectively.

The maximum average confining stress contributed by the jacket, p_m, can be computed according to the force equilibrium

$$p_m = \frac{2t_{sj}f_{yj}}{B} \tag{2}$$

where t_{sj} and f_{yj} are the thicknesses and the yield strength of the jacket, respectively. For a square section, only the four corners and the core region are effectively confined, as shown by the gray area in Fig. 3. It is assumed that the edge of the effectively confined region makes an angle of 45 degrees with the jacket side (Lam and Teng 2003); the ratio of the effectively confined area to the total area of the concrete can be explicitly calculated as

$$k_e = \frac{A_e}{A_c} = 1 - \frac{2(B-2r)^{0.5}(2b-4t-B-2r)^{1.5}}{3(b-2t)^2} \tag{3}$$

where A_e denotes the effective confined area of the concrete.

Accordingly, the maximum confinement level offered by the jacket can be computed by

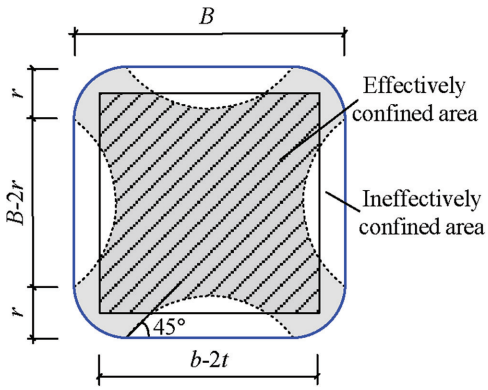

Fig. 3—Effective range of concrete confined by steel jacket.

$$\lambda_m = \frac{k_e p_m}{f_c'} \tag{4}$$

where λ_m is termed as jacket confinement index.

The axial load ratio, n, is computed by

$$n = \frac{P}{f_c'A_c + f_{yt}A_{st}} \tag{5}$$

where P represents the axial compressive load. Considering the axial compression level of the columns at the bottom floors of some typical super-high-rise buildings under rare earthquake excitation (Wang et al. 2023; Cheng et al. 2023), two levels of n values were used in this research program equal to 0.42 and 0.47. Table 1 lists the test specimens alongside with their material properties, dimensions, jacket characteristics, and axial load ratio. In the specimen label, the letters "N" and "H" denote the Q355 (normal) and Q550 (high-strength) steel tubes, respectively; the letters "RS" and "CS" indicate if the square jacket has rounded corners or not, respectively; the number following "RS" and "CS"

Table 1—Test matrix

Specimen label	f_{yt}, MPa (ksi)	t, mm (in.)	b/t	f_c', MPa (ksi)	Jacket type	t_{sj}, mm (in.)	ξ_s	λ_m	N, kN (kip)	n
CJ-N-0.42	397 (57.6)	7.75 (0.31)	31.0	124 (18.0)	—	—	0.46	0	3750 (844)	0.42
CJ-N-0.47	397 (57.6)	7.75 (0.31)	31.0	122 (17.7)	—	—	0.46	0	4200 (940)	0.47
CJ-N-CS3-0.42	397 (57.6)	7.75 (0.31)	31.0	125 (18.1)	Square jacket with rounded corners	2.63 (0.10)	0.46	0.05	3750 (844)	0.42
CJ-N-CS6-0.42	397 (57.6)	7.75 (0.31)	31.0	123 (17.8)	Square jacket with rounded corners	5.62 (0.22)	0.46	0.10	3750 (844)	0.42
CJ-N-CS6-0.47	397 (57.6)	7.75 (0.31)	31.0	122 (17.7)	Square jacket with rounded corners	5.62 (0.22)	0.46	0.10	4200 (940)	0.47
CJ-H-0.42	715 (103.7)	8.11 (0.32)	29.6	125 (18.1)	—	—	0.86	0	4900 (1103)	0.42
CJ-H-RS6-0.42	715 (103.7)	8.11 (0.32)	29.6	126 (18.3)	Square jacket with sharp corners	5.62 (0.22)	0.86	0.06	4900 (1103)	0.42
CJ-H-CS6-0.42	715 (103.7)	8.11 (0.32)	29.6	123 (17.8)	Square jacket with rounded corners	5.62 (0.22)	0.86	0.10	4900 (1103)	0.42

Table 2—Specific values for mechanical properties of steel

Type	Thickness, mm (in.)	Elastic modulus, MPa (ksi)	Yield strength, MPa (ksi)	Ultimate strength, MPa (ksi)	Elongation at fracture, %
Q355 plate (steel tube)	7.75 (0.31)	217,000 (31,472)	397 (57.6)	560 (81.2)	21.2
Q550 plate (steel tube)	8.11 (0.32)	228,000 (33,067)	715 (103.7)	774 (112.3)	19.9
Q355 plate-I (steel jacket)	2.63 (0.10)	210,000 (30,457)	363 (52.6)	516 (74.8)	27.5
Q355 plate-II (steel jacket)	5.62 (0.22)	200,000 (29,007)	338 (49.0)	506 (73.4)	25.2

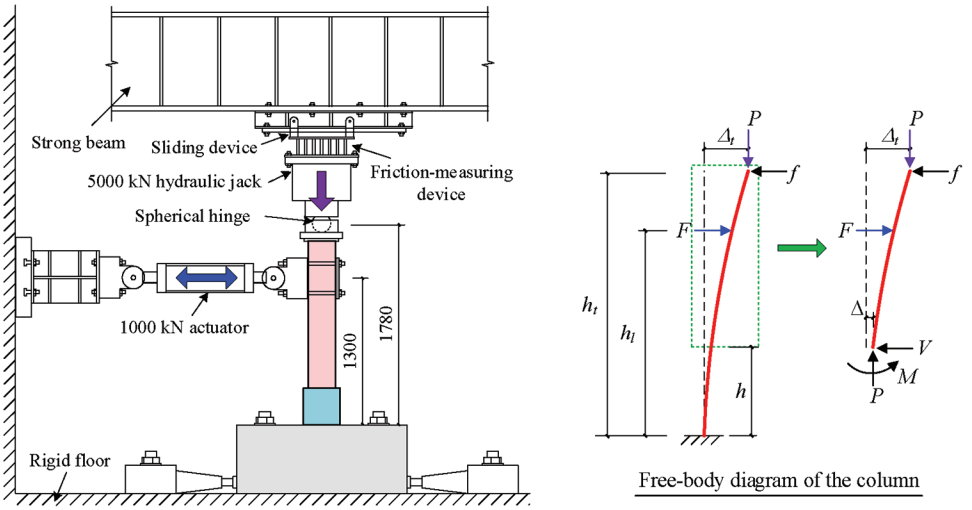

Fig. 4—Test setup. (Note: Units in mm; 1 mm = 0.04 in.; 1 kN = 0.225 kip.)

is the nominal thickness of the jacket; and the last value denotes the axial load ratio.

Material properties

The cylinder concrete compressive strength is presented in Table 1. Tensile coupon tests (three coupons for each steel grade) were carried out according to GB/T 228.1 to specify the stress-strain relationship of the steel materials. Specific values for the mechanical properties of steel are shown in Table 2.

Test setup and instrumentation

Figure 4 shows the test setup. The test column was fixed to the rigid floor by anchor rods. The axial load, P, was applied by a vertical hydraulic jack, and the lateral cyclic load, F, was applied by a horizontal actuator, which was 1300 mm (51.2 in.) from the column base (that is, h_l = 1300 mm [51.2 in.]). A sliding device and a friction-measuring device were arranged between the hydraulic jack and the strong beam. Although the sliding device surface was coated with a low-friction material, the friction force, f, may not be negligible due to the high axial load applied in the test (3750 ~ 4900 kN [844 ~ 1103 kip]). Therefore, a friction-measuring device (Liu et al. 2019) was positioned between the jack and the sliding device. The bottom of the vertical jack was provided with a spherical hinge, and the distance between the center of the spherical hinge and the bottom of the column is 1780 mm (70.1 in.) (that is, h_t = 1780 mm [70.1 in.]). As the bending moment at the spherical hinge can be approximated as 0, the bending moment at any column section (M) can be calculated according to the free-body equilibrium (refer to Fig. 4)

$$M = F \times (h_l - h) + P \times (\Delta_t - \Delta) - f \times (h_t - h) \quad (6)$$

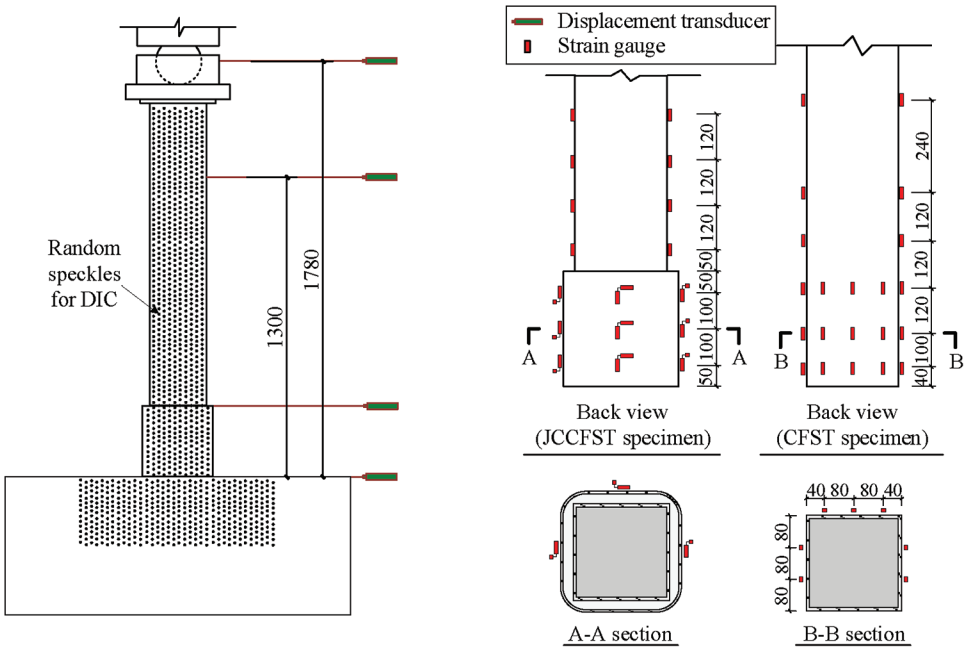

Fig. 5—Illustrative drawings of instrumentation layout. (Note: Units in mm; 1 mm = 0.04 in.)

where h denotes the height of the calculated section; and Δ_l and Δ denote the lateral displacements at the spherical hinge center and calculated section, respectively.

Figure 5 displays the layout of the measuring device. The lateral displacements at various critical locations, such as at the spherical hinge of the hydraulic jack, the loading point of the horizontal actuator, the top end of the jacket, and the top of the foundation were captured by displacement transducers. As shown in Fig. 5, longitudinal strain gauges were affixed to the steel tube within a height of approximately 3b. For the JC-CFST columns, transverse and longitudinal strain gauges were also affixed to the jacket. In addition to the displacement transducers and strain gauges, the digital image correlation (DIC) technique (Janeliukstis and Chen 2021) was applied to accurately measure the displacement flows of the front face (tube web) of the column.

Loading protocol

The axial load, P, was applied first and kept constant for the whole duration of loading, followed by a lateral cyclic load. The lateral drift ratio was applied in the order of 0.25, 0.5, 1.0, 1.5, 2.0, 2.5, 3.0, 3.5, and 4.0%. Three cycles were repeated for drift ratios lower than or equal to 1.5%, while for the remaining drift ratios two cycles were repeated. The rate of the lateral displacement was 0.1 mm/s (0.004 in./s) throughout the loading. The test was stopped when axial loading was not possible to remain constant or the lateral strength of the column decreased rapidly to zero.

TEST RESULTS AND DISCUSSION

Moment-drift ratio relationship and damage evolution

The test results in terms of bending moment at the base of the column, M_b, against the drift ratio, θ, for each test specimen were displayed in Fig. 6. M_b was calculated by employing Eq. (6) with $h = 0$, while θ was determined as follows

$$\theta = \frac{\Delta_l - \Delta_0}{h_l} \tag{7}$$

In Eq. (8), Δ_l and Δ_0 (very small) refers to the horizontal displacement at the lateral loading point (refer to Fig. 5) and the top of the foundation, respectively. Table 3 lists important damage states to describe the failure evolution of the test specimens. In Fig. 6, important damage states are also highlighted directly on the M_b-θ curves. Among these damage states: (a) yielding of the steel tube of unconfined CFST specimens and yielding of the jackets of JC-CFST specimens was determined through the longitudinal strain gauge measurements (in JC-CFST specimens, yielding of the inner CFST tube was not possible to be identified as strain gauges were only mounted in steel jackets); (b) the concrete crushing was determined by the sound; while (c) the damage states initiation (that is, the local buckling and the fracture of welds) at the steel jacket or tube were visually observed.

The failure evolution of the conventional CFST columns (that is, CJ-N-0.42, CJ-N-0.47, and CJ-H-0.42) was similar. The steel tubes of Specimens CJ-N-0.42 and CJ-N-0.47 yielded at a low drift ratio (less than 0.25%) due to the high axial load ratio applied. However, the steel tube of Specimen CJ-H-0.42 yielded at a higher drift ratio (approximately 1.0%) because higher-strength steel (Q550) was adopted for this specimen (Skalomenos et al. 2016). In all CFST specimens, concrete crushing initiated almost at the peak bending moment during the loading cycle of $\theta = 1.5\%$. If not at the same drift ratio, local buckling of the steel tube occurred immediately in a subsequent drift ratio. As the loading progressed, a circumferential bulge was observed around the base of the column, as shown in Fig. 7(a). In Specimens CJ-N-0.47 and CJ-H-0.42, the welds of the steel tube (Fig. 7(b)) fractured during the loading cycles of $\theta =$

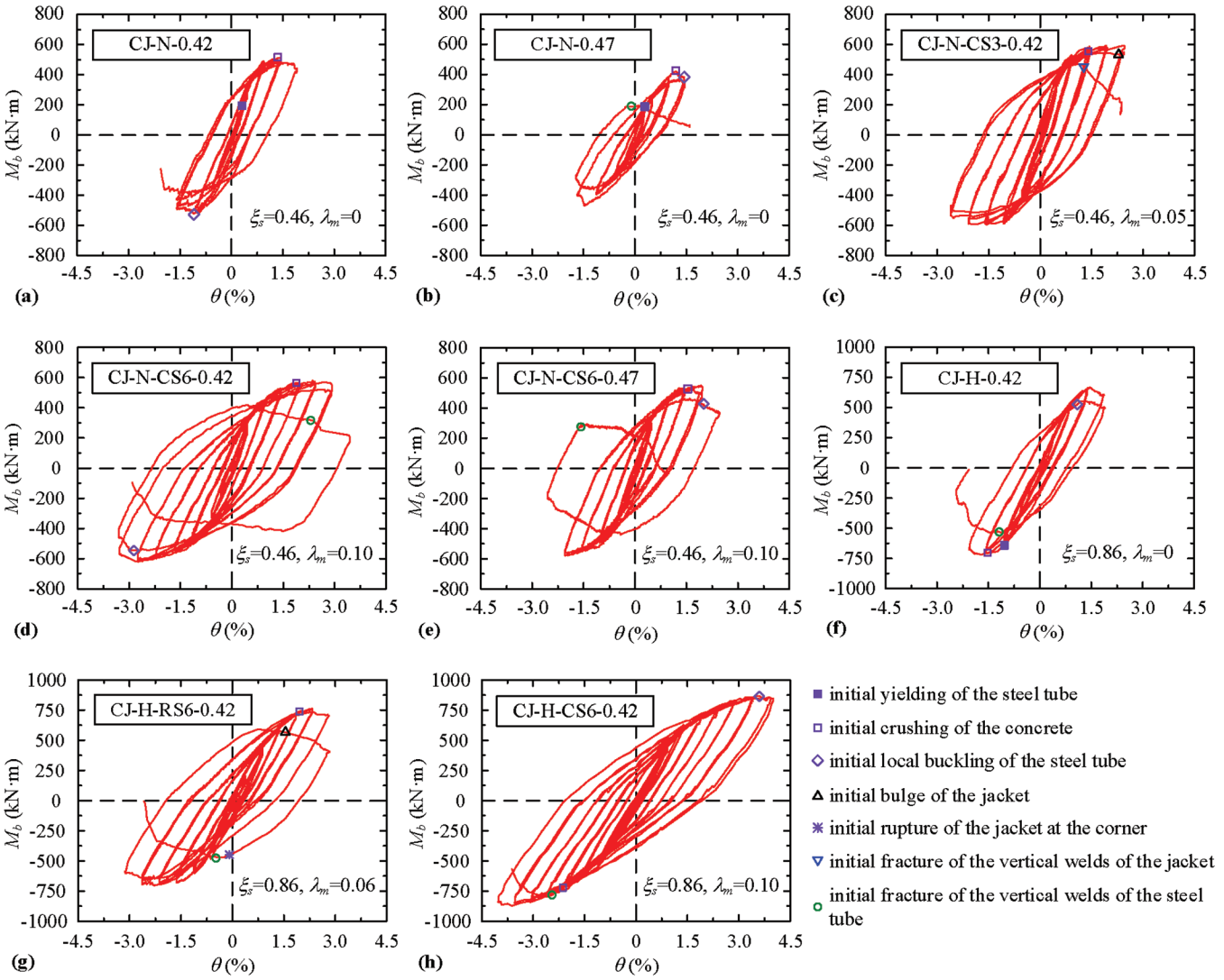

Fig. 6—M_b-θ hysteresis relationships: (a) CJ-N-0.42; (b) CJ-N-0.47; (c) CJ-N-CS3-0.42; (d) CJ-N-CS6-0.42; (e) CJ-N-CS6-0.47; (f) CJ-H-0.42; (g) CJ-H-RS6-0.42; and (h) CJ-H-CS6-0.42. (Note: 1 kN·m = 8.859 kip·in.)

Table 3—Important damage states of test specimens

Specimens	Initial yielding of steel tube	Initial crushing of concrete	Initial local buckling of steel tube	Initial bulge of jacket	Initial rupture of jacket at corner	Initial fracture of vertical welds of jacket	Initial fracture of vertical welds of steel tube
CJ-N-0.42	First cycle of θ = 0.25%	First cycle of θ = 1.5%	First cycle of θ = 1.5%	—	—	—	—
CJ-N-0.47	First cycle of θ = 0.25%	First cycle of θ = 1.5%	First cycle of θ = 1.5%	—	—	—	Second cycle of θ = 1.5%
CJ-N-CS3-0.42	—	First cycle of θ = 1.5%	—	Second cycle of θ = 2.5%	—	First cycle of θ = 3.0%	—
CJ-N-CS6-0.42	—	First cycle of θ = 2.0%	First cycle of θ = 3.0%	—	—	—	Second cycle of θ = 3.5%
CJ-N-CS6-0.47	—	First cycle of θ = 1.5%	First cycle of θ = 2.5%	—	—	—	First cycle of θ = 2.5%
CJ-H-0.42	First cycle of θ = 1.0%	First cycle of θ = 1.5%	First cycle of θ = 2.0%	—	—	—	Second cycle of θ = 2.0%
CJ-H-RS6-0.42	—	First cycle of θ = 1.5%	—	Second cycle of θ = 3.0%	Second cycle of θ = 3.0%	—	Second cycle of θ = 3.0%
CJ-H-CS6-0.42	—	First cycle of θ =2.0%	Second cycle of θ = 4.0%	—	—	—	Second cycle of θ = 4.0%

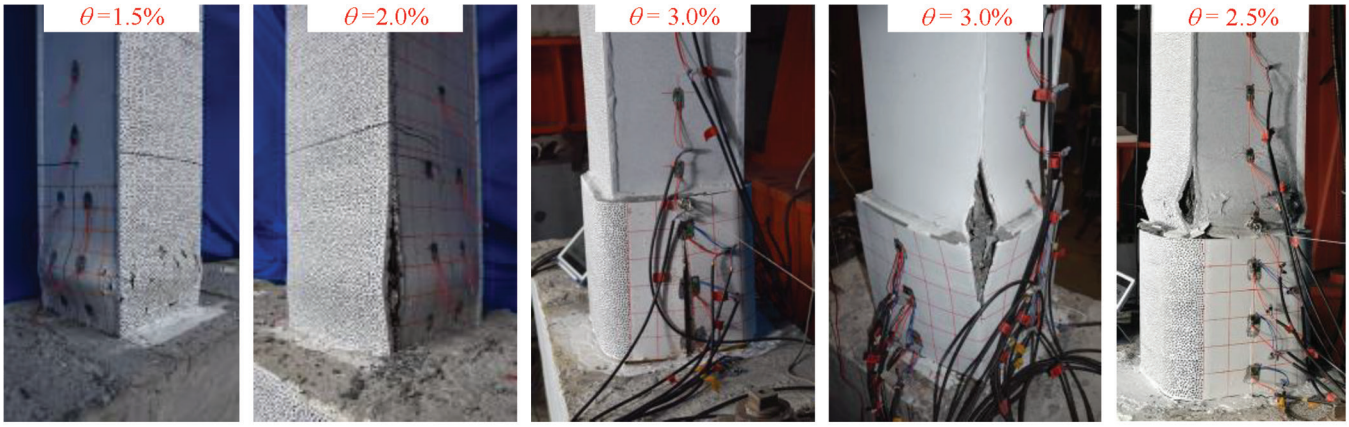

Fig. 7—Typical damage states during test process: (a) CJ-N-0.47; (b) CJ-H-0.42; (c) CJ-N-CS3-0.42; (d) CJ-H-RS6-0.42; and (e) CJ-N-CS6-0.47.

1.5% and 2.0%, respectively, indicating a better ductility for the high-strength steel CFST column (CJ-H-0.42).

The jacket confinement index of CJ-N-CS3-0.42 and CJ-H-RS6-0.42 was approximately equal to 0.05 in both specimens. Concrete crushing initiation in these two specimens occurred at the first loading cycle of θ = 1.5%. The jacket of Specimen CJ-N-CS3-0.42 with rounded corners experienced an outward circumferential bulge during the second loading cycle of θ = 2.5%, while the vertical welds of the jacket fractured during the first loading cycle of θ = 3.0% due to the severe crashing of concrete (Fig. 7(c)). At the time when the fracture occurred in the welding lines of the jacket, the transverse strain of the jacket section was measured merely 0.014. This indicates that the jacket is likely to have failed due to welding defects and not because of excessive yielding. The jacket of Specimen CJ-H-RS6-0.42 with the sharp corners experienced an initial circumferential bulge during the second loading cycle of θ = 3.0%, and subsequently, one jacket corner ruptured at the same loading cycle. Following the jacket rupture, vertical welds of the CFST steel tube fractured at the same corner (Fig. 7(d)), resulting in an immediate drop of axial load. The rupture at the corner of the square jacket was mainly caused by the very high-stress concentration in this region. Therefore, the square jacket with rounded corners is recommended.

The JC-CFST specimens with λ_m = 0.10 and jackets with rounded corners (that is, Specimens CJ-N-CS6-0.42, CJ-N-CS6-0.47, and CJ-H-CS6-0.42) exhibited a similar behavior among them. Concrete crushing in these specimens initiated during the loading cycles of θ = 1.5 or 2.0%. In Specimens CJ-N-CS6-0.42 (Q355) and CJ-H-CS6-0.42 (Q550), where n = 0.42, the steel tube above the jacket bulged during the loading cycles of θ = 3.0% and 4.0%, respectively. In Specimen CJ-N-CS6-0.47 (Q355), where n = 0.47, buckling occurred in the steel tube earlier during the first loading cycle of θ = 2.5%, followed by fracture in the vertical welding lines of the steel tube (Fig. 7(e)). Tube fracture led to an immediate drop in axial load.

Figure 8 shows the final failure mode as obtained from all test specimens. In CFST columns, local buckling of the steel tubes and concrete damage localized at a height of nearly 200 mm (7.87 in.) measured from the base of the column. In JC-CFST columns, local buckling of the CFST steel tubes happened within a region of 200 mm (7.87 in.) above the jacket, while the CFST steel tubes within the jacket-confined region did not experience buckling. Except Specimen CJ-N-CS3-0.42, where its jacket fractured prematurely, the length of the concrete damage zone of the other JC-CFST specimens was between 1.7b and 1.9b. These results imply that a confining jacket with appropriate thickness can more evenly distribute the plastic hinge region within a certain length of the column and not just relocate it outside the confined zone. This can reduce damage concentration and avoid sudden drops in the column's axial load-carrying capacity.

Second-order effects (P-Δ bending moment)

As demonstrated through Eq. (6), the bending moment at the base of the column is the result of three forces: lateral force F, axial force N, and friction force f. The bending moment caused by F is in the same direction as that caused by the axial force (that is, the P-Δ moment). On the contrary, the force f acts in the opposite direction. Figure 9 displays the hysteretic behavior of these three components of the bending moment. It can be found that the bending moment caused by friction remained almost constant during the tests and was approximately 8 to 13% of the corresponding peak total bending moment. The P-Δ moment increased approximately linearly to the drift ratio and led to a significant drop of the lateral resistance of the columns. At θ = 2.0%, the reduction of the bending moment resistance of Specimen CJ-N-0.42 was 12% with respect to the peak bending moment, whereas the lateral load resistance had reduced by 25% with respect to its peak value. Similarly, at θ = 3.0%, the bending moment resistance of Specimen CJ-N-CS6-0.42 decreased only by 5%, while the lateral load resistance decreased by 20%. The high P-Δ effects are attributed to the relatively large axial compression capacities of the columns arising from the use of UHS concretes. Therefore, the P-Δ effect should be fully considered when designing the structures using CFST or JC-CFST columns with UHS concretes, especially when a high axial load ratio is applied.

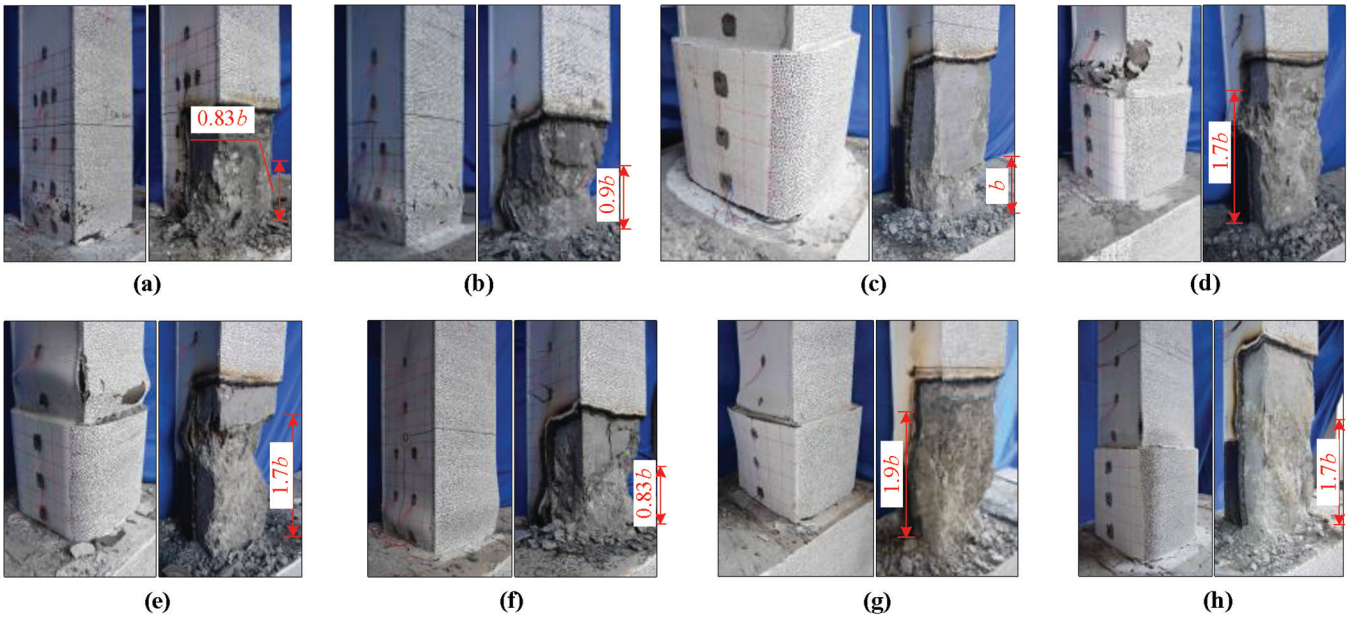

Fig. 8—Final failure modes: (a) CJ-N-0.42; (b) CJ-N-0.47; (c) CJ-N-CS3-0.42; (d) CJ-N-CS6-0.42; (e) CJ-N-CS6-0.47; (f) CJ-H-0.42; (g) CJ-H-RS6-0.42; and (h) CJ-H-CS6-0.42.

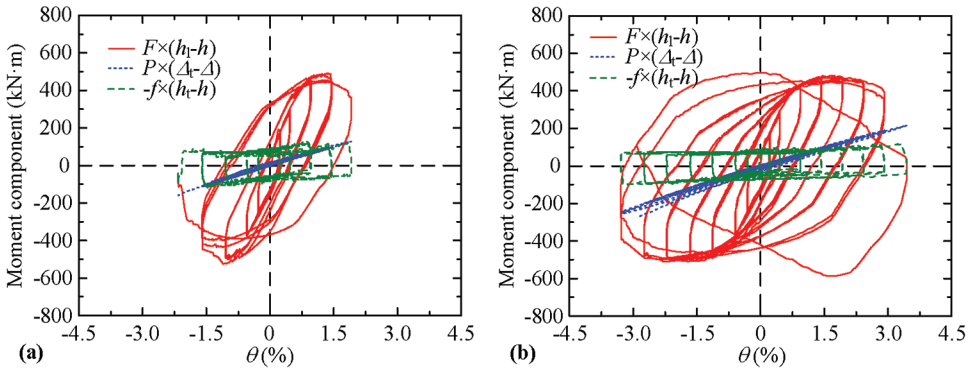

Fig. 9—Bending moment components versus drift ratio curves: (a) CJ-N-0.42; and (b) CJ-N-CS6-0.42. (Note: 1 kN·m = 8.859 kip·in.)

Effective confining stresses offered by steel jacket

In the fabrication of JC-CFST columns, a PTFE sheeting was used at the inner square tube to minimize the longitudinal stress transmitted to the jacket (refer to Fig. 2). The effectiveness of the PTFE layer in eliminating such axial stresses was validated by the obtained ratios of the measured longitudinal to transverse strains developed in the jackets during the tests. The values were approximately –0.3 and –0.5, respectively, before and after the yielding of steel. Therefore, the hoop stresses of the jacket section, σ_{sj}, can be determined based on measured transverse strains and the stress-strain relationship of the steel jacket. The effective confining stresses offered by the steel jacket, p_e, can then be determined by

$$p_e = \frac{2t_{sj}\sigma_{sj}}{B}k_e \quad (8)$$

Figure 10 represents the p_e-θ relationships for each JC-CFST specimen. Among the measured locations instrumented by strain gauges (refer to Fig. 5), the one that developed fastest was chosen to determine the hoop stress (σ_{sj}). It can be observed that p_e took very small values when θ < 1.5%, but when θ exceeded 1.5%, p_e increased quickly. This result is consistent with the phenomenon that concrete infill crushing occurred at θ = 1.5% for these specimens. For the specimens with an axial load ratio of 0.42, the jacket of specimens with λ_m = 0.1 (that is, CJ-N-CS6-0.42 and CJ-H-CS6-0.42) yielded at θ = 2.5%. The jacket with a smaller λ_m was more prone to yield, and those specimens with λ_m ≈ 0.05 (CJ-N-CS3-0.42 and CJ-H-RS6-0.42) yielded at θ = 2.0%. For the specimen with n = 0.47 (that is, CJ-N-CS6-0.47), the jacket yielded rapidly during the load cycle of θ = 1.5% due to the greater axial load ratio. Note that once the jacket has been yielded, the value of p_e stops increasing (just a small increase it may be observed). Figure 11 indicates the yielding initiation of the jacket with a green circle mark (full-color PDF can be accessed at www.concrete.org).

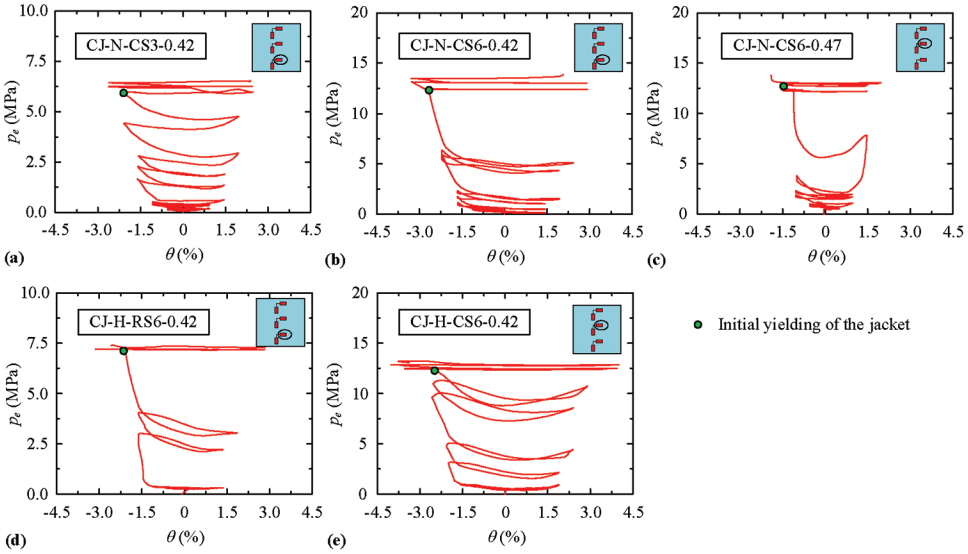

Fig. 10—Effective confining stress: (a) CJ-N-CS3-0.42; (b) CJ-N-CS6-0.42; (c) CJ-N-CS6-0.47; (d) CJ-H-RS6-0.42; and (e) CJ-H-CS6-0.42. (Note: 1 MPa = 0.145 ksi.)

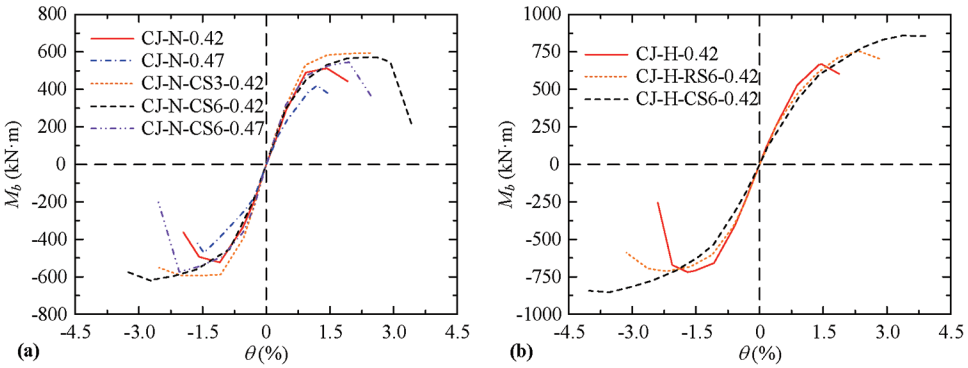

Fig. 11—Envelope curves: (a) specimens with conventional-strength steel tubes; and (b) specimens with high-strength steel tubes. (Note: 1 kN·m = 8.859 kip·in.)

Moment and deformation capacities

Figure 11 summarizes the envelope curves of M_b-θ relationships for all specimens. Table 4 shows the drift ratios at the key points (yield, peak, ultimate), the bending plastic moment capacity, and the ductility. The yield drift ratio, θ_y, is defined as 4/3 times the drift ratio corresponding to $0.75M_{bm}$ (M_{bm} represents the peak moment at the base of the column) (Park 1988). θ_m represents the drift ratio for the peak moment. The ultimate drift ratio, θ_u, denotes the drift ratio corresponding to $0.8M_{bm}$ (in the post-peak stage). In some specimens (that his, CJ-N-0.47, CJ-N-CS3-0.42, CJ-H-RS6-0.42, and CJ-H-CS6-0.42), sudden failure happened and there was no smooth capacity deterioration path in the envelope curve. For this situation, θ_u is considered as the drift ratio of the last loading cycle before terminating the experiment. The ductility coefficient $\mu = \theta_u/\theta_y$. As shown in Fig. 11 and Table 4, the average θ_y of the specimens with conventional-strength (Q355) steel was approximately 1.0%, which is a typical value for steel structures. The θ_y generally increased as the yield strength of the steel tube increased. Specimens made of high-strength (Q550) steel tubes reached a θ_y nearly to 1.6%. The confining jacket enhanced the bending moment capacity of the CFST columns. The M_{bm} of the JC-CFST specimens (except Specimen CJ-H-RC6-0.42, in which the jacket ruptured prematurely) was found to be 12 to 20% higher than that of their CFST counterparts.

The thickness of the confining jacket and its corners design (sharp or curved), the yield strength of the steel tube (f_{yt}), and the axial load ratio (n) clearly affected the ultimate drift ratios (θ_u) of the columns. Figure 12 shows the trendline between θ_u and λ_m for different values of f_{yt} and n. It can be seen that the value of θ_u increased almost proportionally with the λ_m, showing a greater impact in specimens made of high-strength steel (Q550). The use of higher-strength steel alone also found effective to increase θ_u. When the yield strength, f_{yt}, increased from 397 to 715 MPa (57.6 to 103.7 ksi), the value of θ_u increased by 20 to 25% in JC-CFST specimens. This increase is attributed to the fact that higher-strength steel tubes can provide higher confining forces, thereby improving the deformability of the concrete (Skalomenos et al. 2016; Hu et al. 2020b). The ratio n also had a significant effect on θ_u. When n increased from 0.42 to 0.47, θ_u decreased from 3.2 to 2.2% for the specimens with $\lambda_m = 0.1$ and $f_{yt} = 397$ MPa (57.6 ksi), which is nearly a 30% reduction. A higher axial load ratio leads to higher initial axial compressive stress to the column, making the

Table 4—Primary test results

Specimen label	Loading direction	θ_y, %	M_{bm}, kN·m (kip·in.)	θ_m, %	θ_u, %	m
CJ-N-0.42	+	0.92	512.2 (4538)	1.43	1.92	2.09
	–	–0.95	–523.3 (–4636)	–1.09	–1.79	1.88
CJ-N-0.47	+	1.01	420.1 (3722)	1.20	1.45	1.43
	–	–1.26	–471.2 (–4174)	–1.48	–1.68	1.33
CJ-N-CS3-0.42	+	0.99	581.2 (5149)	1.92	2.45	2.47
	–	–0.91	–593.3 (–5256)	–1.56	–2.53	2.78
CJ-N-CS6-0.42	+	1.16	572.2 (5069)	2.42	3.05	2.64
	–	–1.28	–621.1 (–5502)	–2.72	–3.27	2.56
CJ-N-CS6-0.47	+	1.00	546.4 (4841)	1.95	2.26	2.26
	–	–1.07	–573.2 (–5078)	–2.05	–2.20	2.07
CJ-H-0.42	+	1.12	668.2 (5920)	1.46	1.88	1.68
	–	–1.12	–719.1 (–6371)	–1.70	–2.14	1.91
CJ-H-RS6-0.42	+	1.63	766.3 (6789)	2.33	2.82	1.74
	–	–1.24	–728.4 (–6453)	–2.19	–3.14	2.52
CJ-H-CS6-0.42	+	2.22	859.4 (7613)	3.36	3.91	1.76
	–	–2.08	–852.4 (–7551)	–3.54	–4.02	1.93

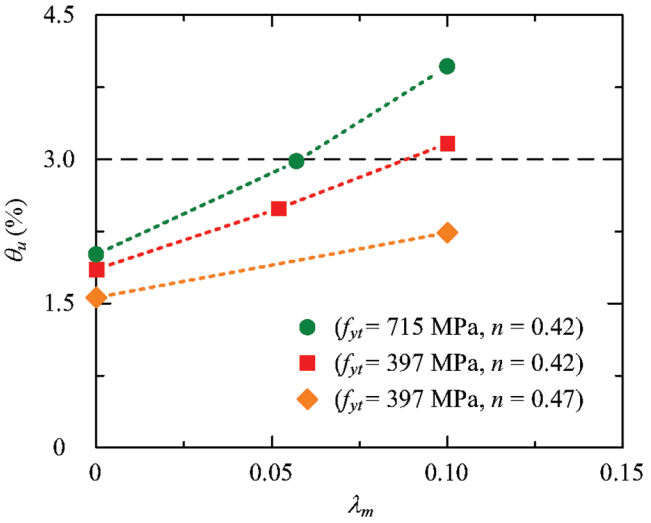

Fig. 12—Trendline between ultimate drift ratio θ_u *and jacket confinement index* λ_m.

concrete infill more prone to crush and the steel tube more prone to local buckling, thus directly reducing the deformation capacity of the columns. In conclusion, for $n = 0.42$, θ_u exceeded 3.0% in high-strength steel tube specimens with $\lambda_m \geq 0.06$ and in conventional-strength steel tube specimens with $\lambda_m = 0.1$. The drift ratio of 3.0% can be considered as a design threshold for special moment-resisting frames under maximum considered earthquakes (Moehle 2014).

Energy dissipation

The energy dissipation during the i-th loading cycle, $E_d(i)$, can be calculated by

$$E_d(i) = \int_{\text{cycle } i} F d\Delta_l - \int_{\text{cycle } i} f d\Delta_t + \int_{\text{cycle } i} P d\delta \qquad (9)$$

where δ is the axial shortening of the column. Figure 13 displays the energy dissipation per loading cycle, E_d, against θ. It was observed that the energy dissipation of the two loading cycles of the same drift ratio was almost same; therefore, only the first loading cycle was used to calculate the energy dissipation for each hysteresis loop shown in Fig. 13. Conventional-strength steel CFST specimens begun to dissipate energy for values of $\theta > 0.5\%$, while high-strength steel CFST specimens for values of $\theta > 1.0\%$ due to the greater elastic response of the material itself. Except the last drift level, all JC-CFST specimens provided the same E_d values with the corresponding conventional CFST specimens. Some specimens (that is, CJ-N-0.47, CJ-H-0.42, and CJ-H-RS6-0.42) exhibited greater energy dissipation at the last drift level of the loading history because axial shortening of these specimens increased suddenly during this level of θ. Thus, the part of the energy dissipation caused by the axial force (that is, the third term in the right-hand side of Eq. (9)) increased significantly. Moreover, because the JC-CFST specimens appear to have better deformation capacity than the corresponding conventional CFST specimens, the final cumulative energy dissipation of the former was approximately two to five times that of the latter. The E_d value of Specimen CJ-N-CS6-0.47 with $n = 0.47$ was slightly higher than that of Specimen CJ-N-CS6-0.42 with $n = 0.42$. High compressive loads induce compressive axial stresses that serve to clamp the cracks of concrete infill closed even at some large drift levels. As a result, flexural stiffness is more effective to resist loads in the reversed loading cycles, which inherently leads to a fatter hysteresis loop and greater energy dissipation capacity.

Lateral displacement analysis through DIC

During the cyclic loading, the lateral displacements along the height of columns are mainly attributed to three different

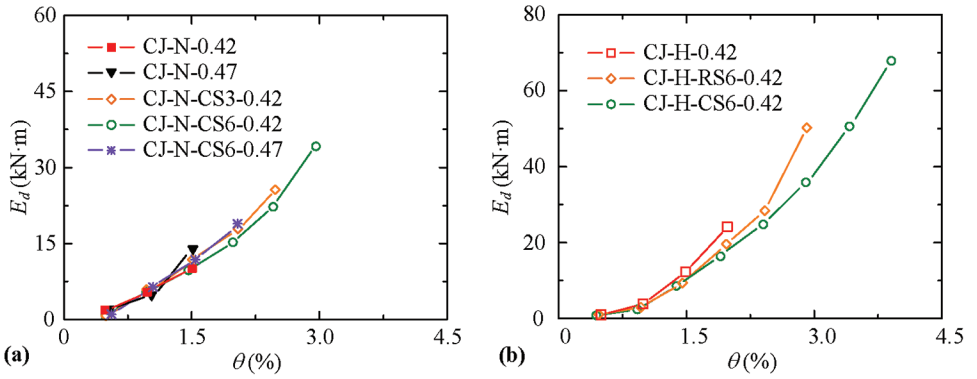

Fig. 13—Energy dissipation per load cycle: (a) specimens with conventional-strength steel tubes; and (b) specimens with high-strength steel tubes. (Note: 1 kN·m = 8.859 kip·in.)

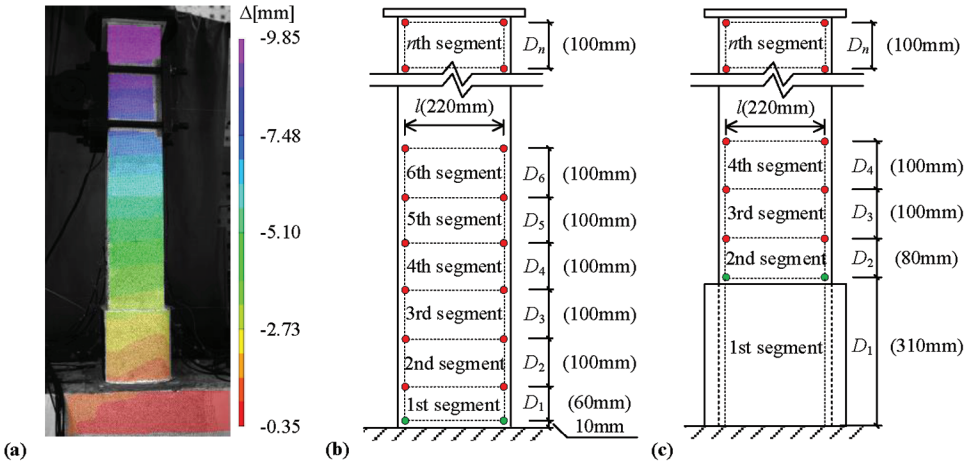

Fig. 14—Digital image correlation technique measurement: (a) lateral displacement profile; (b) partition of conventional CFST columns; and (c) partition of JC-CFST columns. (Note: 1 mm = 0.04 in.)

types of deformation. These are the flexural deformation, the shear deformation, and the deformation caused by the rotation of the column base. Because the DIC method can accurately measure the full-field displacement flows of the front face of the test specimen (Fig. 14(a)), it was possible herein to calculate the displacement caused by each of the components mentioned previously.

Each test column can be divided into multiple segments (Fig. 14(b) and (c)), and the mean curvature of the i-th segment, ϕ_i, can be calculated by

$$\phi_i = (\delta_{i,l} - \delta_{i,r})/(D_i l) \quad (10)$$

where $\delta_{i,l}$ and $\delta_{i,r}$ denote the variations of the left and right sides of the i-th segment, respectively; and D_i and l denote the height and width of the i-th segment, respectively. Note that the displacement measurements of the CFST segment in the jacket-confined region of a JC-CFST column cannot be captured because of the presence of the jacket.

Figure 15 displays the curvature distributions along the height of Specimens CJ-H-0.42 and CJ-H-CS6-0.42. It can be seen that the curvature increases locally at the base of the column for a zone of approximately 220 mm (8.66 in.) for the conventional Specimen CJ-H-0.42, while for the jacket-confined Specimen CJ-H-CS6-0.42, the curvature is developed more uniformly within a larger region of the column base (approximately 520 mm [20.5 in.]) experiencing large values only at the end of the test. In conventional CFST specimens, where the bending moment is linearly distributed along the column height, plastic deformations are concentrated mainly in the bottom part of the column, forming a severe plastic hinge zone. On the contrary, JC-CFST specimens exhibited an improved bending moment and deformation capacity within the confined region. As the bending moment increases, the unconfined part of the column may yield before the bottom confined region reaches its maximum bending moment capacity. Therefore, a better plastic engagement of the column in the total deformation can be seen in JC-CFST columns.

The lateral displacement caused by flexural deformation, Δ_{lf}, can be further calculated by

$$\Delta_{lf} = \sum_{i=1}^{n} \phi_i D_i s_i \quad (11)$$

where s_i denotes the distance from the lateral loading point to the center of the i-th segment; and n denotes the number of segments.

In conventional CFST specimens, the lateral displacement caused by the column base rotation, Δ_{lr}, can be computed by

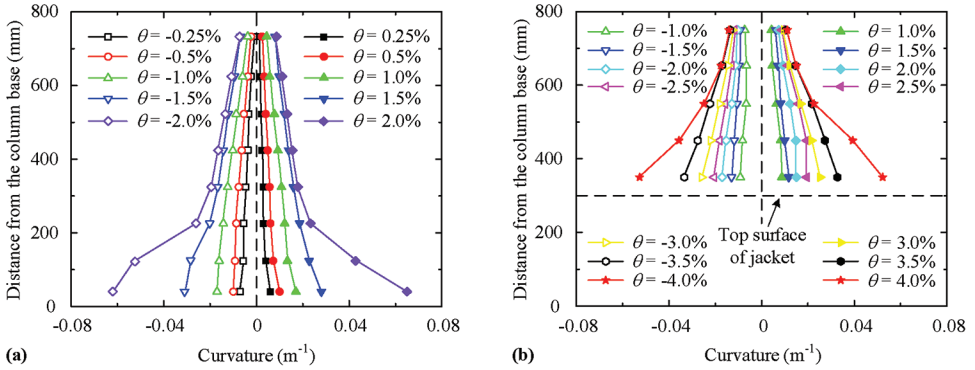

Fig. 15—Curvature distribution: (a) CJ-H-0.42; and (b) CJ-H-CS6-0.42. (Note: 1 mm = 0.04 in.)

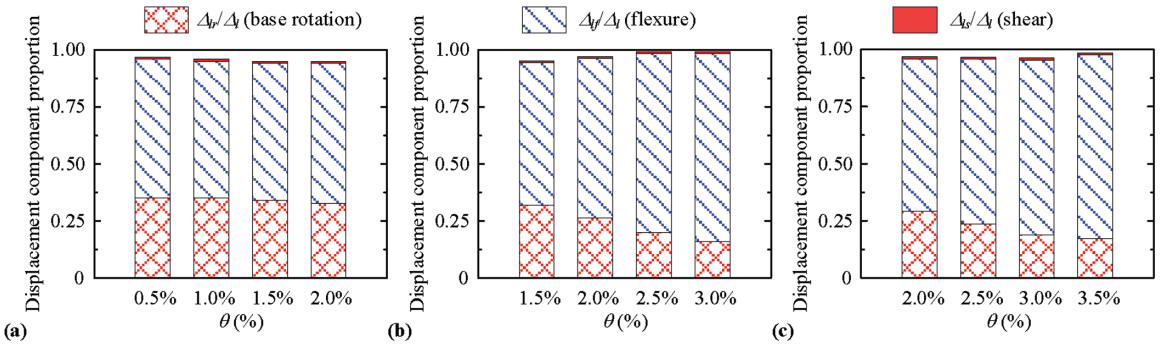

Fig. 16—Share of displacement components: (a) CJ-H-0.42; (b) CJ-N-CS6-0.42; and (c) CJ-H-CS6-0.42.

$$\Delta_{lr} = \theta_b h_l = \frac{(\delta_{b,l} - \delta_{b,r})}{l} h_l \quad (12)$$

where θ_b denotes the column base rotation; and $\delta_{b,l}$ and $\delta_{b,r}$ denote the longitudinal displacements at the left and right sides of the base section, respectively, measured at the locations marked with green specks (refer to Fig. 14(b)). Note that it is not possible to calculate the base rotation of the JC-CFST columns by taking the aforementioned approach because of the shielding of the jacket. However, the measured M_b-θ_b relationships of the conventional CFST columns imply that the value of θ_b was almost linearly associated with M_b, and the values of M_b/θ_b were nearly to 148,000 kN·m/rad (1,311,132 kip·in./rad). Due to the foundation configurations of all the specimens were the same, the rotation stiffness, κ, of the JC-CFST specimens can be approximated assumed to be 148,000 kN·m/rad (1,311,132 kip·in./rad). Accordingly, $\theta_b = M_b/\kappa$, then the mean curvature of the jacket-confined zone can be determined by

$$\phi_0 = \frac{(\delta_{0,l} - \delta_{0,r})/l - M_b/k}{D_1} \quad (13)$$

where $\delta_{0,l}$ and $\delta_{0,r}$ denote the longitudinal displacements measured at the two locations marked with green points (refer to Fig. 14(c)).

The lateral displacement caused by the shear deformations, Δ_{ls}, can be computed by

$$\Delta_{ls} = \sum_{i=1}^{n} \frac{d_i}{2l} (\delta_{i,d1} - \delta_{i,d2}) \quad (14)$$

where d_i denotes the i-th segment's diagonal length; and $\delta_{i,d1}$ and $\delta_{i,d2}$ denote the i-th segment's variations of two diagonal lengths.

Figure 16 shows for some representative specimens (CJ-H-0.42, CJ-N-CS6-0.42, CJ-H-CS6-0.42) the share of the three displacement components to the total lateral displacement at different drift levels. In can be observed that the sum of three deformation components was close to total lateral displacement, Δ_l, which confirmed the accuracy of the aforementioned method. The contribution of shear deformation of the column was negligible (<1.0%) because the nominal shear capacity of the CFST columns provided by the steel web plates (that is, $2f_{yt}bt/\sqrt{3}$) was approximately three times the corresponding peak lateral load. In addition to the flexural deformation of the column, the lateral displacement caused by the base rotation was also evident. This rotation was caused by the slip of the tensile steel tube from the anchorage zone and the deformations of the concrete surrounding the embedded part. The proportion of this rotation to the total lateral displacement (that is, Δ_{lr}/Δ_l) was ranged from 17 to 37%, and the ratio Δ_{lr}/Δ_l generally diminished with the drift level. This is attributed to the fact that the moment resistance of the test column increased slowly after yielding, leading to a slow increase in the base rotation. This fact indicates that the effect of the base rotation should be considered in the analysis of the structure with CFST or JC-CFST columns.

CONCLUSIONS

In the present study, the cyclic behavior of jacket-confined concrete-filled steel tube (JC-CFST) columns made of ultra-high-strength (UHS) concrete was experimentally

investigated. The parameters included the jacket thickness, the jacket section profile (square sections with sharp or rounded corners), the steel tube strength (conventional and high-strength steel), and the axial load ratio, n. The main findings are as follows:

1. In the JC-CFST column specimens with jacket height, $h_j = 1.25b$, and jacket confinement index $\lambda_m = 0.05$ to 0.1 (except for one specimen, where its jacket was prematurely fractured), the unconfined region yielded before the jacket-confined region reaches its maximum moment capacity, which resulted in a larger plastic damage zone. The length of the concrete damage region of the JC-CFST specimens ranged between $1.7b$ and $1.9b$ (only $0.83b$ for the conventional CFST column). This result implies that a confining jacket with appropriate thickness can more evenly distribute the plastic hinge region within a larger length of the column and not just relocating it outside the confined zone.

2. The ultimate drift ratio, θ_u, improved almost proportionately with λ_m. A steel jacket with $\lambda_m = 0.1$ was effective in increasing the θ_u of the specimens with $n = 0.42$ from 1.85% to 3.16%. The application of high-strength steel tubes also enhanced θ_u. When the yielding strength of the steel tube, $f_{yt,}$ raised from 397 to 715 MPa (57.6 to 103.7 ksi), θ_u enhanced from 3.16 to 3.97% in JC-CFST specimens with $\lambda_m = 0.1$ and $n = 0.42$. As it was expected, θ_u significantly decreases with n. When n increased from 0.42 to 0.47, θ_u decreased from 3.2 to 2.2% in JC-CFST specimens with $\lambda_m = 0.1$ and f_{yt} = 397 MPa (57.6 ksi), and decreased from 1.86 to 1.56% in CFST specimens with $f_{yt} = 397$ MPa (57.6 ksi).

3. The confining jacket can be easily installed at the ends of a column without affecting the joint connection; thus, the proposed jacket-confined CFST column is feasible to be used in moment-resisting frames. When $n = 0.42$ and $h_j = 1.25b$, to meet the drift demand (3.0%) of special moment-resisting frames, the value of λ_m should not be less than 0.1 for the JC-CFST columns with $f_{yt} = 397$ MPa (57.6 ksi) (conventional steel), and not less than 0.06 for the JC-CFST columns with $f_{yt} = 715$ MPa (103.7 ksi) (high-strength steel). A square steel jacket with rounded corners is recommended, as it is more effective in avoiding high stress concentration at the corners of the jacket.

4. P-Δ effects caused a notable decrease in the lateral load resistance. At $\theta = 2.0\%$, the degradation of the bending moment resistances of the CFST columns with $n = 0.42$ was within 12% with respect to the peak moments, whereas the lateral load resistance had reduced by approximately 25% with respect to their peak values. This reduction increases as the axial load ratio or the applied drift ratio increases. The energy dissipation per loading cycle of the JC-CFST columns was essentially the same as that of the CFST counterparts before the column failure. Nevertheless, the cumulative energy dissipation of the JC-CFST specimens was approximately two to five times that of the CFST counterparts due to the better deformability.

5. According to digital image correlation results, the contribution of shear deformation of the column was negligible (<1.0%). In addition to the flexural deformation of the column, the lateral displacement caused by the base rotation was also evident, its proportion to the total lateral displacement ranged from 17 to 37%.

AUTHOR BIOS

Hong-Song Hu *is a Professor in the College of Civil Engineering at Huaqiao University, Xiamen, China. He received his BS and PhD in civil engineering from Tsinghua University, Beijing, China. His research interests include steel-concrete composite structures and prefabricated structures.*

Li Xu *is a Lecturer in the College of Civil Engineering at Fujian University of Technology, Fuzhou, China. He received his BS and MS in hydraulic engineering from Fuzhou University, Fuzhou, China. He received his PhD in structural engineering from Huaqiao University, Xiamen, China. His research interests include steel and composite structures.*

Hai-Jin Qiu *is a Graduate Student in the College of Civil Engineering at Huaqiao University. He received his BS in civil engineering from Nanchang University, Nanchang, China. His research interests include experimental study of composite structures.*

Konstantinos Skalomenos *is an Assistant Professor in the School of Engineering at University of Birmingham, UK, and in the Department of Civil Engineering, University of West Attica, Athens, Greece. He has received his diploma in civil engineering and his MSc and PhD in structural and earthquake engineering from the University of Patras, Patras, Greece. His research interests include composite steel/concrete structures and high-performance materials.*

ACKNOWLEDGMENTS

This work was supported by the National Natural Science Foundation of China (52278183, 51878303), the Natural Science Foundation of Fujian Province (2023J02019, 2023J05190), the Construction Technology Project of Xiamen Construction Bureau (XJK2022-1-17), and the Key Laboratory for Structural Engineering and Disaster Prevention of Fujian Province (SEDPFJ-2022-02). The support is gratefully acknowledged by the cooresponding author L. Xu and co-authors.

REFERENCES

Ahmed, M.; Sheikh, M. N.; Hadi, M. N. S.; and Liang, Q. Q., 2023, "Nonlinear Analysis of Square Spiral-Confined Reinforced Concrete-Filled Steel Tubular Short Columns Incorporating Novel Confinement Model and Interaction Local Buckling," *Engineering Structures*, V. 274. doi: 10.1016/j.engstruct.2022.115168

Bengar, H. A., and Shahmansouri, A. A., 2021, "Post-Fire Behavior of Unconfined and Steel Tube Confined Rubberized Concrete under Axial Compression," *Structures*, V. 32, pp. 731-745. doi: 10.1016/j.istruc.2021.03.041

Cheng, Y.; Liu, J. P.; Shan, W. C.; and Li, J., 2023, "Seismic Performance of Inclined CFT Frame-Core Tube-Outrigger Truss Structure System," *Journal of Building Structures*, V. 44, No. 6, pp. 12-23. (in Chinese)

Choi, K. K., and Xiao, Y., 2010, "Analytical Model of Circular CFRP Confined Concrete-Filled Steel Tubular Columns under Axial Compression," *Journal of Composites for Construction*, ASCE, V. 14, No. 1, pp. 125-133. doi: 10.1061/(ASCE)CC.1943-5614.0000056

Cosgun, S. I.; Kaya, A.; and Gencturk, B., 2023, "Computational Modeling of the Axial Behavior of Corroded and Buckled Short Steel Piles Strengthened Using Concrete-Filled GFRP Jackets," *Engineering Failure Analysis*, V. 147. doi: 10.1016/j.engfailanal.2023.107147

Ding, F. X.; Pan, Z. C.; Lai, Z. C.; and Yu, Z. W., 2020, "Experimental Study on the Seismic Behavior of Tie Bar Stiffened Round-Ended Concrete-Filled Steel Tube Columns," *Journal of Bridge Engineering*, ASCE, V. 25, No. 10, p. 04020071.

Du, Y. S.; Gao, D. H.; Chen, Z. H.; Zheng, Z. H.; and Wang, X. D., 2022, "Behaviors of FRP Confined Rectangular Concrete-Filled Thin-Walled Steel Tubular Stub Columns Using High-Strength Materials under Axial Load," *Composite Structures*, V. 280. doi: 10.1016/j.compstruct.2021.114915

GB/T 228.1-2010, 2010, "Metallic Materials-Tensile Testing-Part 1: Method of Test at Room Temperature (GB/T 228.1)," Standard Press of China, Beijing, China.

Goto, Y.; Mizuno, K.; and Kumar, G. P., 2012, "Nonlinear Finite Element Analysis for Cyclic Behavior of Thin-Walled Stiffened Rectangular Steel Columns with In-Filled Concrete," *Journal of Structural Engineering*, ASCE, V. 138, No. 5, pp. 571-584. doi: 10.1061/(ASCE)ST.1943-541X.0000504

Hatzigeorgiou, G. D., 2008, "Numerical Model for the Behavior and Capacity of Circular CFT Columns, Part II: Verification and Extension,"

Engineering Structures, V. 30, No. 6, pp. 1579-1589. doi: 10.1016/j.engstruct.2007.11.002

Ho, J. C. M., and Lai, M. H., 2013, "Behaviour of Uni-Axially Loaded CFST Columns Confined by Tie Bars," *Journal of Constructional Steel Research*, V. 83, pp. 37-50. doi: 10.1016/j.jcsr.2012.12.014

Hu, H. S.; Chen, Z. X.; Wang, H. Z.; and Guo, Z. X., 2022, "Seismic Behavior of Square Spiral-Confined High-Strength Concrete-Filled Steel Tube Columns under High Axial Load Ratio," *Engineering Structures*, V. 252, p. 113600 doi: 10.1016/j.engstruct.2021.113600

Hu, H. S.; Deng, Y. P.; Zhang, H.; Zhang, Y. X.; and Sun, H. L., 2024, "Equivalent Stress-Strain Models of Components in High-Strength Concrete-Filled Circular Steel Tube Columns," *Journal of Constructional Steel Research*, V. 212. doi: 10.1016/j.jcsr.2023.108254

Hu, H. S.; Xu, L.; Guo, Z. X.; and Shahrooz, B. M., 2020a, "Behavior of Eccentrically Loaded Square Spiral-Confined High-Strength Concrete-Filled Steel Tube Columns," *Engineering Structures*, V. 216. doi: 10.1016/j.engstruct.2020.110743

Hu, H. S.; Wang, H. Z.; Guo, Z. X.; and Shahrooz, B. M., 2020b, "Axial Compressive Behavior of Square Spiral-Confined High-Strength Concrete-Filled Steel-Tube Columns," *Journal of Structural Engineering*, ASCE, V. 146, No. 7. doi: 10.1061/(ASCE)ST.1943-541X.0002702

Hu, H. S.; Yang, Z. J.; Xu, L.; Zhang, Y. X.; and Gao, Y. C., 2023, "Axial Compressive Behavior of Square Concrete-Filled Steel Tube Columns with High-Strength Steel Fiber-Reinforced Concrete," *Engineering Structures*, V. 285. doi: 10.1016/j.engstruct.2023.116047

Janeliukstis, R., and Chen, X., 2021, "Review of Digital Image Correlation Application to Large-Scale Composite Structure Testing," *Composite Structures*, V. 271. doi: 10.1016/j.compstruct.2021.114143

Jin, L.; Fan, L. L.; Li, P.; and Du, X. L., 2019, "Size Effect of Axial-Loaded Concrete-Filled Steel Tubular Columns with Different Confinement Coefficients," *Engineering Structures*, V. 198. doi: 10.1016/j.engstruct.2019.109503

Khan, M.; Uy, B.; Tao, Z.; and Mashiri, F., 2017, "Behaviour and Design of Short High-Strength Steel Welded Box and Concrete-Filled Tube (CFT) Sections," *Engineering Structures*, V. 147, pp. 458-472. doi: 10.1016/j.engstruct.2017.06.016

Lam, L., and Teng, J. G., 2003, "Design-Oriented Stress-Strain Model for FRP-Confined Concrete in the Rectangular Columns," *Journal of Reinforced Plastics and Composites*, V. 22, No. 13, pp. 1149-1186. doi: 10.1177/0731684403035429

Liu, L.; Pan, P.; Wang, H. S.; Feng, P.; and Zhao, M. H., 2019, "Development and Application of Friction Force Measurement Device for Compression-Shear Tests," *Journal of Building Structures*, V. 40, No. 6, pp. 133-139. (in Chinese)

Mao, X. Y., and Xiao, Y., 2006, "Seismic Behavior of Confined Square CFT Columns," *Engineering Structures*, V. 28, No. 10, pp. 1378-1386. doi: 10.1016/j.engstruct.2006.01.015

Memarzadeh, A.; Shahmansouri, A. A.; and Pologanathan, K., 2022, "A Novel Prediction Model for Post Fire Elastic Modulus of Circular Recycled Aggregate Concrete Filled Steel Tubular Stub Columns," *Steel and Composite Structures*, V. 44, No. 3, pp. 295-310.

Moehle, J., 2014, *Seismic Design of Reinforced Concrete Buildings*, McGraw-Hill Education, New York.

Park, R., 1988, "State-of-the-Art Report on Ductility Evaluation from Laboratory and Analytical Testing," *Proceedings of the Ninth World Conference on Earthquake Engineering*, Tokyo/Kyoto, Japan.

Sakino, K.; Nakahara, H.; Morino, S.; and Nishiyama, I., 2004, "Behavior of Centrally Loaded Concrete-Filled Steel-Tube Short Columns," *Journal of Structural Engineering*, ASCE, V. 130, No. 2, pp. 180-188. doi: 10.1061/(ASCE)0733-9445(2004)130:2(180)

Skalomenos, K. A.; Hatzigeorgiou, G. D.; and Beskos, D. E., 2015, "Seismic Behavior of Composite Steel/Concrete MRFs: Deformation Assessment and Behavior Factors," *Bulletin of Earthquake Engineering*, V. 13, No. 12, pp. 3871-3896. doi: 10.1007/s10518-015-9794-2

Skalomenos, K. A.; Hayashi, K.; Nishi, R.; Inamasu, H.; and Nakashima, M., 2016, "Experimental Behavior of Concrete-Filled Steel Tube Columns Using Ultrahigh-Strength Steel," *Journal of Structural Engineering*, ASCE, V. 142, No. 9, p. 04016057 doi: 10.1061/(ASCE)ST.1943-541X.0001513

Teng, J. G.; Hu, Y. M.; and Yu, T., 2013, "Stress-Strain Model for Concrete in FRP-Confined Steel Tubular Columns," *Engineering Structures*, V. 49, pp. 156-167. doi: 10.1016/j.engstruct.2012.11.001

Teng, J. G.; Wang, J. J.; Lin, G.; Zhang, J.; and Feng, P., 2021, "Compressive Behavior of Concrete-Filled Steel Tubular Columns with Internal High-Strength Steel Spiral Confinement," *Advances in Structural Engineering*, V. 24, No. 8, pp. 1687-1708. doi: 10.1177/1369433220981656

Wang, F. A.; Long, H. Y.; Gao, B. T.; Liu, C.; Cao, Y. F.; Yuan, M. L.; and Mu, W. Z., 2023, "Structural Design For Xi'an Andaz Hotel Project," *Journal of Building Structures*, V. 53, pp. 27-34. (in Chinese)

Xiong, M. X.; Xiong, D. X.; and Liew, J. Y. R., 2017, "Axial Performance Of Short Concrete Filled Steel Tube with High and Ultra-High-Strength Materials," *Engineering Structures*, V. 136, pp. 494-510. doi: 10.1016/j.engstruct.2017.01.037

Xu, L.; Hu, H. S.; Lan, Y. T.; Liu, R. Y.; and Xia, H. J., 2023a, "Numerical Study on the Behavior of Eccentrically Loaded Square Spiral-Confined High-Strength Concrete-Filled Steel Tube Columns," *Structures*, V. 55, pp. 2122-2123. doi: 10.1016/j.istruc.2023.07.030

Xu, L.; Hu, H. S.; Peng, B.; and Guo, Z. X., 2023b, "Seismic Performance of Composite Jacket-Confined Square High-Strength Concrete-Filled Steel Tube Columns," *Journal of Constructional Steel Research*, V. 211, p. 108128. doi: 10.1016/j.jcsr.2023.108128

Yang, Y.; Wang, Y.; and Fu, F., 2014, "Effect of Reinforcement Stiffeners on Square Concrete-Filled Steel Tubular Columns Subjected to Axial Compressive Load," *Thin-Walled Structures*, V. 82, pp. 132-144. doi: 10.1016/j.tws.2014.04.009

Yu, Q.; Tao, Z.; and Wu, Y. X., 2008, "Experimental Behavior of High-Performance Concrete-Filled Steel Tubular Columns," *Thin-Walled Structures*, V. 46, No. 4, pp. 362-370. doi: 10.1016/j.tws.2007.10.001

Yu, T.; Hu, Y. M.; and Teng, J. G., 2016, "Cyclic Lateral Response of FRP-Confined Circular Concrete-Filled Steel Tubular Columns," *Journal of Constructional Steel Research*, V. 124, pp. 12-22. doi: 10.1016/j.jcsr.2016.05.006

Zhang, S. M.; Li, X. Z.; Chen, X. T.; and Huang, Z. F., 2021, "Axial Compression Behavior of Square CFST Short Columns Reinforced by Circular Steel Tube," *Journal of Building Structures*, V. 42, pp. 170-179. (in Chinese)

ACI STRUCTURAL JOURNAL TECHNICAL PAPER

Title No. 122-S11

Implications of ACI CODE-440.11 Code Provisions on Design of Glass Fiber-Reinforced Polymer-Reinforced Concrete Footings

by Zahid Hussain and Antonio Nanni

The first edition of ACI CODE-440.11 was published in September 2022, where some code provisions were either based on limited research or only analytically developed. Therefore, some code provisions, notably shear and development length in footings, are difficult to implement. This study, through a design example, aims at a better understanding of the implications of code provisions in ACI CODE-440.11-22 and compares them with ones in CSA S806-12, thereby highlighting a need for reconsiderations. An example of the footing originally designed with steel reinforcement was taken from the ACI Reinforced Concrete Design Handbook *and redesigned with GFRP reinforcement as per ACI CODE-440.11-22 and CSA S806-12. A footing designed as per ACI CODE-440.11-22 requires a thicker concrete cross section to satisfy shear requirements; however, when designed as per CSA S806-12, the required thickness becomes closer to that of the steel-reinforced concrete (RC) footing. The development length required for a glass fiber-reinforced polymer-reinforced concrete (GFRP-RC) cross section designed as per ACI CODE-440.11-22 was 13% and 92% greater than that designed as per CSA S806-12 and ACI 318-19, respectively. Also, the reinforcement area required to meet detailing requirements is 170% higher than that for steel-RC cross section. Based on the outcomes of this study, there appears to be a need for reconsideration of some code provisions in ACI CODE-440.11-22 to make GFRP reinforcement a viable option for RC members.*

Keywords: building code; footing; glass fiber-reinforced polymer (GFRP) reinforcement; reinforced concrete; shear.

INTRODUCTION

ACI CODE-440.11-22[1] is a milestone for practitioners interested in the use of nonmetallic reinforcement for concrete structures, even though some provisions make the design difficult and the implementation challenging. For example, the current code requirements for shear in ACI CODE-440.11-22[1] were derived based on the neutral axis depth of the cracked cross section, differently from ACI 318-19.[2] The equations are further dependent on the axial stiffness of glass fiber-reinforced polymer (GFRP) reinforcement. Because GFRP reinforcement has lower stiffness than steel, the shear design of GFRP-reinforced concrete (RC) members requires deeper cross sections, making execution difficult, particularly for shallow foundations.

ACI CODE-440.11-22[1] conservatively ignores some of the beneficial effects on the shear capacity of GFRP-RC members, which are otherwise addressed in Canadian Standard Association (CSA) S806-12.[3] For example, in calculating one-way shear resistance provided by concrete, CSA S806-12[3] considers the arching effect. Also, one-way and two-way shear strength are both dependent on the longitudinal reinforcement ratio, whereas ACI CODE-440.11-22[1] uses the axial stiffness of GFRP reinforcement in calculating the neutral axis depth for a cross section.

It appears that implementation of shear and development length provisions in ACI CODE-440.11-22 would be difficult due to some assumptions made during their development. Therefore, this study was carried out to show the implications of code provisions in ACI CODE-440.11-22[1] on the design of GFRP-RC members (a square footing) by providing a comparison with CSA S806-12[3] and ACI 318-19,[2] highlighting the conservatism in ACI CODE-440.11-22[1] code provisions.

RESEARCH SIGNIFICANCE

The significance of this research lies in the critical examination and evaluation of certain provisions within ACI 440.11-22 pertaining to GFRP reinforcement. A substantial portion of these provisions has been formulated either through analytical methodologies or with reliance on limited research. The undue conservativeness of these provisions poses implementation challenges in the design process and complicates practical implementation of GFRP reinforcement as a suitable substitute for metallic reinforcement. Therefore, this study serves the imperative purpose of identifying and elucidating specific provisions that warrant reconsideration in light of recent advancements in research.

MATERIALS AND METHODS

The analysis and comparison of code provisions in ACI CODE-440.11-22,[1] CSA S806-12,[3] and ACI 318-19[2] was carried out using a footing example taken from the *ACI Reinforced Concrete Design Handbook, A Companion to ACI 318-19*.[4] The selected design example (originally for steel-RC) was redesigned using GFRP reinforcement as per provisions in ACI CODE-440.11-22[1] and CSA S806-12.[3] The footing supports the load from a square interior column, as shown in Fig. 1. The constituent materials selected for the footing design are shown in Table 1. The concrete strength, f_c', is 28 MPa while the GFRP reinforcement is compliant with the material specification ASTM D7957/D7957M.[5] The mechanical properties of GFRP bars affecting design include

ACI Structural Journal, V. 122, No. 1, January 2025.
MS No. S-2023-360.R1, doi: 10.14359/51742142, received June 15, 2024, and reviewed under Institute publication policies.

Table 1—Properties of GFRP reinforcement, concrete, and soil

Designation		Nominal diameter, mm	Nominal area, mm^2	Elastic modulus, MPa	Guaranteed tensile strength, MPa	Ultimate strain, %	Concrete strength, MPa	Concrete clear cover, mm	$q_{(D+L)}$, kN/m^2
GFRP reinforcement	ASTM D7957	28.6	645	44,816	565	1.2	—	—	—
	ASTM D8505			60,000	793	1.3	—	—	—
Concrete		—	—	24,870	—	0.0035 (CSA) 0.003 (ACI)	28.0	76.0	—
Soil bearing capacity		—	—	—	—	—	—	—	268

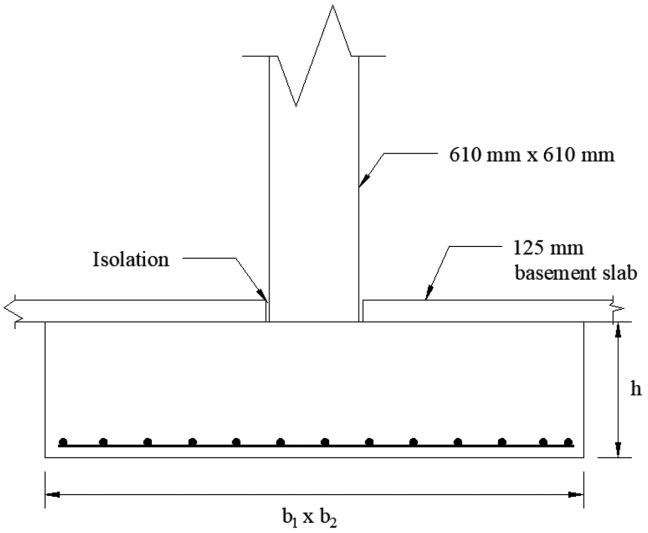

Fig. 1—Square footing with square column. (Reproduced from ACI Reinforced Concrete Design Handbook.*[4])*

guaranteed ultimate tensile strength (f_{fu}), corresponding ultimate strain (ε_{fu}), modulus of elasticity (E_f), and modular ratio (n_f). A value of 1.20 for the bond coefficient, k_b, was selected as per ACI CODE-440.11-22[1] and CSA S806-12[3] Sections 24.3.2.3 and 8.3.1.1, respectively. Similarly, a value of 0.85 was adopted for the environmental reduction factor, C_E, as indicated in ACI CODE-440.11-22,[1] Section 20.2.2.3. A concrete cover, c_c, of 76 mm is used as specified in ACI CODE-440.11-22[1] and CSA S806-12[3] in Sections 20.5.1.3.1 and 8.3, respectively. The admissible soil bearing capacity considered for the dead and live loads was 268 kN/m^2, as given in the *ACI Reinforced Concrete Design Handbook*.[4] Table 1 also presents the properties of new-generation GFRP bars with high elastic modulus and strength, which are currently not specified in ACI CODE-440.11-22.

The square footing carried an axial dead load equal to 2407 kN, plus a live load of 863 kN. These loads were combined as per ASCE 7-16[6] to compute the maximum factored demand. First, the square footing is designed as per ACI CODE-440.11-22[1] and CSA S806-12.[3] Later, a comparison based on the design of this footing following the provisions of three building codes (that is, ACI CODE-440.11-22,[1] CSA S806-12,[3] and ACI 318-19[2]) is presented. Also, a discussion about the development and implications of shear and development length equations in ACI CODE-440.11-22[1] is provided.

Table 2—Strength reduction factor Φ (ACI CODE-440.11-22, Section 21.2.1)

Action or structural element	Φ
Moment, axial force, or combined axial moment and axial force (Section 21.2.2)	0.55 to 0.65*
Shear	0.75

*Applicable to over-reinforced sections.

Code provisions

ACI CODE-440.11-22 code requirements—For applicable factored load combinations, design strength at all sections shall satisfy the requirements of ACI CODE-440.11-22,[1] Sections 7.5.1.1 and 8.5.1.1, as given here

$$\Phi S_n \geq U \tag{1}$$

where S_n is nominal moment, shear, axial or torsional strength; U is shear, moment, torsional moment, or axial force resulting from the factored loads; and Φ is strength reduction factor calculated as per ACI CODE-440.11-22,[1] as given in Table 2.

The maximum spacing of longitudinal GFRP reinforcement, s, is limited as specified by ACI CODE-440.11-22,[1] Sections 24.3.2a and 24.3.2b

$$s \leq \frac{0.81 E_f}{f_{fs} k_b} - 2.5 c_c \tag{2}$$

$$s \leq 0.66 \frac{E_f}{f_{fs} k_b} - 2.5 c_c \tag{3}$$

where f_{fs} is stress at service loads, MPa.

The development length of the longitudinal GFRP reinforcement is governed by Code Section 25.4.2.1, as the greater of Eq. (4), (5), and (6) given herein

$$l_d = \frac{d_b \left(\frac{f_{fr}}{0.083 \sqrt{f_c}} - 340 \right)}{13.6 + \frac{c_b}{d_b}} \omega \tag{4}$$

where f_{fr} *is* tensile stress in GFRP reinforcement required to develop the full nominal section capacity, MPa; c_b is lesser of: a) the distance from center of a bar to nearest concrete surface; and b) one-half the center-to-center spacing of bars

being developed, or one-half the center-to-center spacing of the bars, mm; d_b *is* nominal bar diameter, mm; and ω is bar location modification factor, taken equal to 1.5, if more than 300 mm of fresh concrete is placed below the horizontal reinforcement being developed and 1.0 for all other cases.

$$20d_b \tag{5}$$

$$300 \text{ mm} \tag{6}$$

The reinforcement area shall be provided as greater of area required by the ultimate factored moment demand and area necessary to ensure that the flexural strength exceeds the cracking strength, indicated in ACI CODE-440.11-22,[1] Sections 7.6.1.1 and 24.4.3.2, provided as Eq. (7) and (8)

$$A_{f_{min}-1} = \frac{2.1}{f_{fu}} A_g \tag{7}$$

$$A_{f_{min}-2} = \frac{20{,}000}{E_f} \tag{8}$$

where A_g is gross area of the cross section, mm^2.

Concrete cross-sectional dimensions shall be selected to avoid diagonal compression failure as in ACI CODE-440.11-22[1] section 22.5.1.2, provided as Eq. (9)

$$V_u \leq \Phi 0.2 f_c' bd \tag{9}$$

where V_u is factored shear force at a section, kN.

The nominal shear strength can be calculated as per ACI CODE-440.11-22,[1] Section 22.5.1.1, given as

$$V_n = V_c + V_f \tag{10}$$

where V_n is nominal shear strength, kN; V_c is nominal shear strength provided by the concrete, kN; and V_f *is* nominal shear strength provided by GFRP shear reinforcement, kN.

The one-way shear strength provided by concrete can be calculated as the greater of two expressions from ACI CODE-440.11-22[1], Sections 22.5.5.1a and 22.5.5.1b, as given herein

$$V_c = 0.42 \lambda_s k_{cr} \sqrt{f_c'}\, bd \tag{11}$$

$$V_c = 0.066 \lambda_s \sqrt{f_c'}\, bd \tag{12}$$

where k_{cr} is ratio of the depth of elastic cracked section neutral axis to the effective depth, given by the code commentary Section R22.5.5.1, as shown herein

$$k_{cr,rect} = \sqrt{2\rho_f n_f + (\rho_f n_f)^2} - \rho_f n_f \tag{13}$$

where $\rho_f = A_f / b_d$ is the reinforcement ratio; A_f is the area of GFRP longitudinal reinforcement, mm^2; and $n_f = E_f / E_c$ is the modular ratio.

$$n_f = \frac{E_f}{E_c} = \text{Modular Ratio}$$

where E_c is modulus of elasticity of concrete (MPa), calculated as given by the Code Sections 19.2.2.1a and 19.2.2.1(b), given as Eq. (14) and (15).

$$E_c = w_c^{1.5} 0.043 \sqrt{f_c'} \tag{14}$$

$$E_c = 4700 \sqrt{f_c'} \tag{15}$$

$\lambda_s = \sqrt{2/(1 + 0.004d)}$ is size effect factor, as given in ACI 440.11-22,[1] Section 22.5.5.1, Table 22.5.5.1.3, and should be less than or equal to 1.0.

Similarly, two-way shear strength is calculated as maximum strength calculated with Eq. (22.6.5.2a) and (22.6.5.2b), as given herein

$$v_c = 0.83 \lambda_s k_{cr} \sqrt{f_c'} \tag{16}$$

$$v_c = 0.13 \lambda_s \sqrt{f_c'} \tag{17}$$

where v_c is stress corresponding to nominal two-way shear strength of slab or footing, MPa.

CSA S806-12 code requirements—Chapter 8 of CSA S806-12[3] contains the provisions for the design of concrete members with FRP reinforcement. All the FRP-RC sections shall be designed so that the failure of the section is initiated by the crushing of concrete in the compression zone. However, if the factored resistance of a section is greater than 1.6 times the moment due to the factored loads, the concrete section can be designed so that failure is controlled by FRP rupture.

The Code Section 8.2.3 specifies that the minimum clear concrete cover in RC members shall be twice the diameter of a bar ($2d_b$) or 30 mm, whichever is greater. The ultimate strain in concrete at the extreme compression fiber shall be assumed to be equal to 0.0035 (that is, different from the ACI assumption of 0.003), and its tensile strength shall be neglected.

The Code Section 8.4.2 states that the minimum reinforcement of a flexural member shall be proportioned so that factored resisting moment (M_r) is at least 1.5 times greater than the cracking moment (that is, $M_r \geq 1.5M_{cr}$). Also, the minimum reinforcement area in slabs equal to $(400/E_f)A_g$ shall be provided in each of the two orthogonal directions. The reinforcement shall not be less than $0.0025A_g$ and shall be spaced no further than three times the slab thickness or 300 mm, whichever is less.

The provisions for one-way shear strength are given in Section 8.4.4, which states that the factored shear resistance of members with GFRP longitudinal reinforcement shall be determined as per Eq. (8) to (14) in CSA S806-12, provided as Eq. (18)

$$V_r = V_c + V_{sF} \tag{18}$$

where V_r is the factored shear resistance, kN; V_c is factored shear resistance provided by concrete, kN; and V_{sF} is factored shear resistance provided by FRP shear reinforcement, kN.

Factored shear resistance provided by concrete for members with effective depth greater than 300 mm, with no axial load may be calculated as per Section 8.4.4.5, provided as Eq. (19)

$$V_c = 0.05\lambda \emptyset_c k_m k_r (f_c')^{\frac{1}{3}} b_w d_v \quad (19)$$

where λ is the factor to account for concrete density; Φ_c is the strength reduction factor, taken equal to 0.65 as per Section 6.5.3.2; b_w is minimum effective web width, mm; d_v is effective shear depth, taken as the greater of $0.9d$ or $0.72h$, mm; and k_m is the coefficient accounting for the effect of moment at a section on shear strength, calculated as per Eq. (8) to (18) in the Code and provided in Eq. (20)

$$k_m = \sqrt{\frac{V_f d}{M_f}} \leq 1.0 \quad (20)$$

where V_f is the factored shear force, kN; d is distance from extreme compression fiber to the centroid of longitudinal bar, mm; M_f is factored moment, kN·m; and k_r is coefficient accounting for the effect of reinforcement rigidity on its shear strength, calculated as per Eq. (8) to (19) in CSA S806-12 and provided as Eq. (21)

$$k_r = 1 + (E_f \rho_{FW})^{1/3} \quad (21)$$

where ρ_{FW} is longitudinal FRP reinforcement ratio.

The concrete strength calculated in accordance with Section 8.4.4.5 in CSA S806-12[3] shall not be greater than Eq. (22) and less than Eq. (23) as stated in Section 8.4.4.5.

$$V_c \leq 0.22 \emptyset_c \sqrt{f_c'} b_w d_v \quad (22)$$

$$V_c \geq 0.11 \emptyset_c \sqrt{f_c' b_w d_v} \quad (23)$$

In determination of V_c, f_c' shall not be taken greater than 60 MPa.

Different from ACI CODE-440.11-22,[1] CSA S806-12[3] Section 8.4.4.6 states that sections within a distance of $2.5d$ from the face of the support where the support causes compression in the beam parallel to the direction of shear force at a section, V_c shall be calculated as the value determined according to Section 8.4.4.5 (Eq. (19)) multiplied by the factor k_a (that is, factor to account for the arching effect on shear strength) as per Section 8.4.4.6, provided in Eq. (24)

$$k_a = \frac{2.5}{\frac{M_f}{V_f d}} \geq 1.0 \quad (24)$$

The value of k_a shall not exceed 2.5.

CSA S806-12,[3] Section 8.4.4.7, addresses shear modification for members with size exceeding 300 mm and without minimum transverse shear reinforcement, the value of V_c calculated as per Section 8.4.4.5 (CSA S806-12[3]) shall be multiplied by the factor k_s (that is, factor to account for size effect) as given in Section 8.4.4.7 (CSA S806-12[3]) and provided in Eq. (25)

$$k_s = \frac{750}{450 + d} \leq 1.0 \quad (25)$$

Punching shear resistance can be calculated as per CSA S806-12,[3] Section 8.7.2, which states that factored shear due to punching shall not exceed the limits specified by Eq. (8-39), (8-40), and (8-41) of CSA S806-12,[3] provided as Eq. (26), (27), and (28)

$$v_r = \left(1 + \frac{2}{\beta_c}\right)\left[0.028\lambda \emptyset_c (E_f \rho_F f_c')^{\frac{1}{3}}\right] \quad (26)$$

where v_r is factored shear stress resistance, MPa; β_c is ratio of long side to short side of column; E_f is modulus of elasticity of FRP reinforcement, MPa; and ρ_f is reinforcement ratio.

$$v_r = \left[\left(\frac{\alpha_s d}{b_o}\right) + 0.19\right] 0.147\lambda \emptyset_c (E_f \rho_F f_c')^{\frac{1}{3}} \quad (27)$$

where $\alpha_s = 4$ for interior columns, 3 for edge columns, and 2 for corner columns.

$$v_r = 0.056\lambda \emptyset_c (E_f \rho_F f_c')^{\frac{1}{3}} \quad (28)$$

When calculating v_r using Eq. (26) to (28), the value of f_c' shall not be taken greater than 60 MPa. If the effective depth of the structural slab system exceeds 300 mm, the value of v_r obtained from Section 8.7.2[3] shall be multiplied by $(300/d)^{0.25}$ to include the effect of member size, as stated in CSA S806-12,[3] Section 8.7.4.

The development length of bars in tension shall be either determined directly from the tests or shall be taken as the greater of 300 mm he value obtained from Section 9.3,[3] as provided in Eq. (29)

$$l_d = 1.15 \frac{k_1 k_2 k_3 k_4 k_5}{d_{cs}} \frac{f_F}{\sqrt{f_c'}} A_b \quad (29)$$

where d_{cs} is the smaller of: a) the distance from closest concrete surface to the center of the bar being developed; and b) two-thirds of center-to-center spacing between bars being developed, mm; k_1 is bar location factor taken equal to 1.3 for horizontal reinforcement placed so that more than 300 mm of fresh concrete is cast in the member below the development length or splice and 1.0 for other cases; k_2 is concrete density factor is taken equal to 1.3, 1.2, and 1.0 for low-density, semi-low-density, and normalweight concrete; k_3 is bar size factor is taken equal to 0.8 for $A_b \leq 300$ mm^2 and 1.0 for $A_b \geq 300$ mm^2; k_4 is bar fiber factor is taken equal to 1.0 for GFRP and CFRP and 1.25 for AFRP; and k_5 is bar surface profile factor is taken equal to 1.0 for surface roughened or sand-coated surfaces, 1.05 for spiral pattern

surfaces, 1.0 for braided surfaces, 1.05 for ribbed surfaces, and 1.80 for indented surfaces.

DESIGN EXAMPLE

Design of GFRP-RC foundation as per ACI CODE-440.11-22

The bottom of the square footing is located 0.91 m below the basement slab (that is, original footing given in *ACI Reinforced Concrete Design Handbook*[4]). Therefore, it is considered a shallow foundation.[1] The square footing is redesigned with applicable Code provisions for one- and two-way slabs as stated in ACI CODE-440.11-22[1] Section 13.3. The minimum base area of the shallow foundation was selected to satisfy the code requirements in Section 13.3.1.1. It requires that the minimum base area of the foundation shall be proportioned not to exceed the permissible bearing pressure when subjected to forces and moments applied to the foundation. It was observed that with applicable load combinations and allowable soil capacity provided in the *ACI Reinforced Concrete Design Handbook*,[4] the minimum required base area of footing was 12.2 m^2. Therefore, it was decided to use a 3.6 x 3.6 m foundation that slightly exceeds the required dimensions. The dimensions of the footing and critical section for one- and two-way shear verification are shown in Fig. 2, where b_1 and b_2 are the length and width of footing ($b_1 = b_2$ for this case of square footing), and b_1' and b_2' are the critical perimeter dimensions for two-way shear ($b_1' = b_2'$ for this case of square column). Also shown are the critical sections for one-way shear (that is, at a distance d from the column face) and two-way shear (that is, at a distance $d/2$ from the column face), and c_1 and c_2 are column dimensions (that is, 610 x 610 mm, as provided in *ACI Reinforced Concrete Design Handbook*).[4]

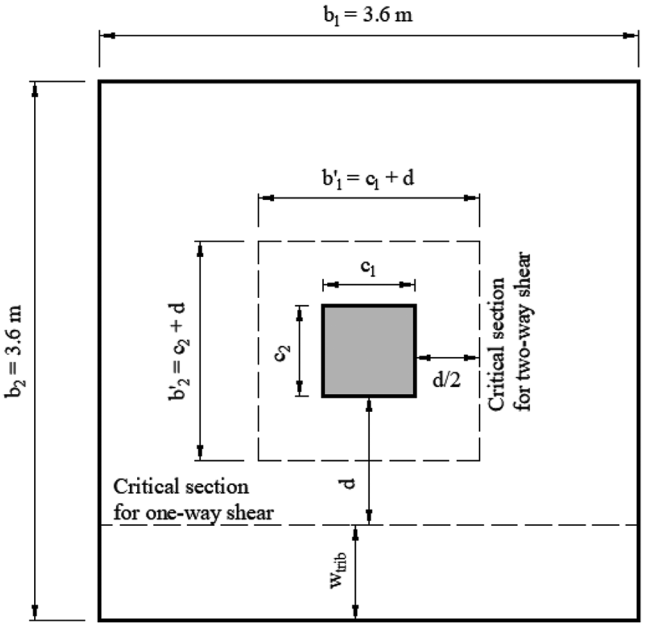

Fig. 2—Square footing, column dimensions, and critical sections for one-way and two-way shear.

The column does not impart a moment to the footing so that the soil pressure under the footing is uniform. ACI 440.11-22[1] Section 13.2.6.2 states that for one-way shallow foundations and two-way isolated footings, it is permissible to neglect the size effect factor specified in Sections 22.5 and 22.6 for one-way and two-way shear provisions, respectively. Consequently, the size effect factor was neglected in both calculations, and it was assumed that shear strength is only provided by concrete cross section.

The tributary area contributing to one-way shear and two-way shear were equal to 2.47 and 10.7 m^2, respectively. The k_{cr} value was first calculated using a reinforcement ratio (ρ_f) of 0.004 and a modular ratio (n_f) 1.8, resulting equal to 0.11. (Note: $\rho_f = 0.004$ was adopted to meet both strength and serviceability requirements.) However, Code Section R22.5.5.1 requires a lower bound of 0.16 on the value of k_{cr} (that is, $k_{cr} = 0.16$) in Eq. (22.5.5.1b); hence, this value was used to calculate shear strength.

Ignoring the size effect factor and using normalweight concrete, the GFRP-RC footing required a larger thickness for one-way shear than its steel-RC counterpart subjected to the same loads (that is, to 0.94 m, versus 0.91 m). Using $h = 0.94$ m, the one-way shear strength of GFRP-RC footing calculated as per ACI CODE-440.11-22[1] Sections 22.5.5.1a and 22.5.5.1b was equal to 815 kN, which exceeds the demand of 786 kN.

Using $h = 0.94$ m, the two-way shear strength was calculated as per Section 22.6, resulting equal to 2684 kN, which was less than demand of 3590 kN. Hence, the concrete cross section thickness was increased to 1.12 m to satisfy two-way shear requirements. As shown in Table 3, the two-way shear strength at a thickness equal to 1.12 m is 3488 kN, which is greater than the demand of 3413 kN. It should be noted that the two-way shear strength for the steel-RC is 5902 kN at a thickness equal to 0.91 m, as also shown in Table 3. This may be because shear strength in steel-RC cross section depends on effective cross section where a section between two cracks is considered. Hence, the entire section

Table 3—Design of steel-RC and GFRP-RC footing as per ACI 318-19[2] and ACI CODE-440.11-22[1]

Quantity		Steel-RC ACI 318-19						GFRP-RC ACI CODE-440.11-22					
		Demand			Capacity			Demand			Capacity		
		h, m	Moment, kN·m	Shear, kN	$\frac{A_{s\_req}}{A_{s\_pro}}$	Moment, kN·m	Shear, kN	h, m	Moment, kN·m	Shear, kN	$\frac{A_{f\_req}}{A_{f\_pro}}$	Moment, kN·m	Shear, kN
One-way shear		0.91	—	850	—	—	925	1.12	—	578	—	—	986
Two-way shear			—	3651		—	5902		—	3413		—	3488
Flexural strength	(ASTM D7957)		1356	—	0.85	2045	—		1356	—	0.83	4706	—
	(ASTM D8505)										0.84	4717	

contributes to the shear strength. However, in the case of GFRP-RC, only uncracked concrete above the neutral axis is considered effective in resisting the applied forces.

The critical section for the maximum moment was assumed at the face of the column as shown in Fig. 3. The tributary area contributing to the moment was equal to 5.4 m^2 and the ultimate moment calculated was equal to 1356 kN-m. The reinforcement area required to meet strength requirements was equal to 0.015 m^2. However, to meet serviceability requirements stated in ACI CODE-440.11-22,[1] Sections 24.3.2(a), 24.3.2(b), and 24.3.2.2, and temperature and shrinkage requirements stated in Section 7.6.1.1, the provided reinforcement area was increased to 0.018 m^2. In this footing design, M29 bars were placed at 127 mm center to center. The flexural capacity of GFRP-RC footing designed as per ACI CODE-440.11-22[1] was equal to 4706 kN·m. The reinforcement area for steel-RC footing was equal to 0.007 m^2, and its moment capacity was 2045 kN·m (refer to Table 3). A sketch of dimensions and reinforcement details of GFRP-RC footing designed as per ACI CODE-440.11-22[1] are provided in Fig. 4.

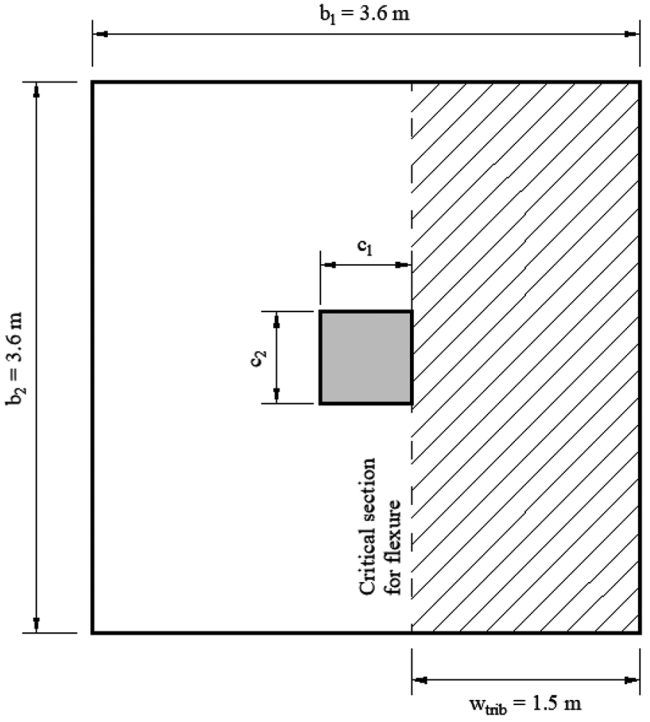

Fig. 3—Critical section for moment.

In the summer of 2023, ASTM published new specification ASTM D8505/D8505M, which defines the physio-mechanical properties of a new generation of GFRP bars.[7] These bars have higher elastic modulus and strength compared to ones specified in ASTM D7957/D7957M.[5,7] While ACI CODE-440.11-22 does not cover these bars, the footing was redesigned as per ASTM D8505/D8505M to investigate their influence on the design. The properties of new-generation bars are provided in Table 1.

The use of high-elastic-modulus and high-strength bars in the design of GFRP-RC footing resulted in the reduction of required reinforcement ratio. The shear strength equations in ACI CODE-440.11-22 depend on the axial stiffness of GFRP reinforcement, which is incorporated by factor k_{cr}, with lower bound of 0.16 on its value. Even though using new-generation bars resulted in reduction of required reinforcement ratio, the lower bound on the value of k_{cr} controlled the shear design. Therefore, the shear strength of the footing remained the same.

The impact of using new-generation bars, however, was evident in flexure design of the footing. Even though minimum reinforcement was still controlled by serviceability requirements, the GFRP bars were comparatively less stressed, which allowed an increase in the required center-to-center spacing. Hence, the footing designed with new-generation bars required 20 M29 GFRP bars compared to 28 M29 when using the old-generation bars specified in ASTM D7957.[5]

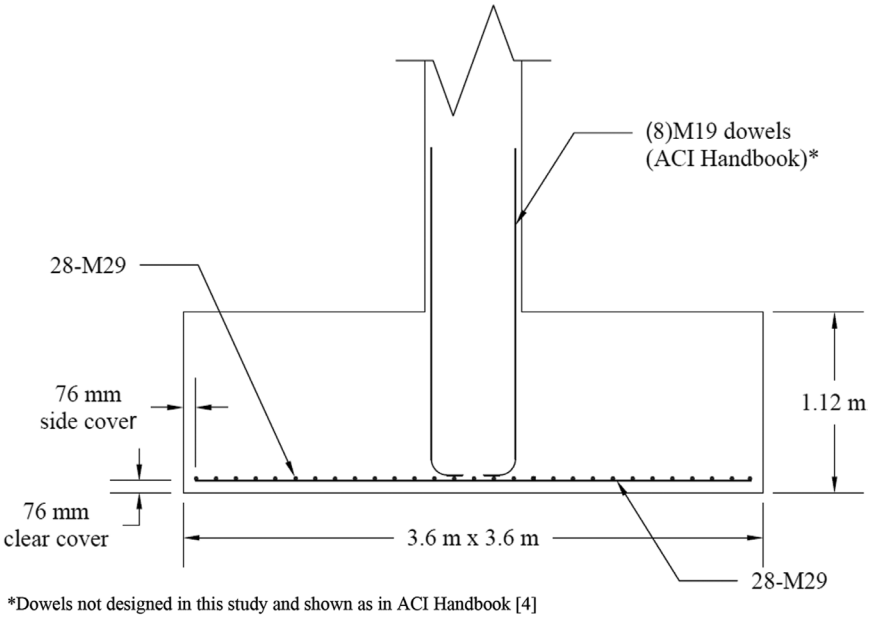

Fig. 4—GFRP-RC footing designed as per ACI 440.11 reinforcement detailing.

Table 4—Design of GFRP-RC footing as per ACI CODE-440.11-22[1] and CSA S806-12[3]

Quantity		GFRP-RC ACI CODE-440.11-22						GFRP-RC-CSA S806-12					
		Demand			Capacity			Demand			Capacity		
		h, m	Moment, kN·m	Shear, kN	$\frac{A_{f\_req}}{A_{f\_pro}}$	Moment, kN·m	Shear, kN	h, m	Moment, kN·m	Shear, kN	$\frac{A_{f\_req}}{A_{f\_pro}}$	Moment, kN·m	Shear, kN
One-way shear		1.12	—	578	—	—	986	1.02	—	670	—	—	1055
Two-way shear			—	3413		—	3488		—	3488		—	3522
Flexural strength	(ASTM D7957)		1356	—	0.83	4706	—		1356	—	0.16	8682	—
	(ASTM D8505)				0.83	4717					0.17	7093	

The GFRP-RC shallow foundation required a larger reinforcement area than steel-RC and higher values of thickness. The extra materials and excavation costs may impose limitations on its application.

Design of GFRP-RC footing as per CSA S806-12

In this section, the footing example taken from *ACI Reinforced Concrete Design Handbook*[4] was redesigned as per the guidelines of CSA S806-12.[3] GFRP reinforcement properties, admissible soil pressure, and concrete strength are the same as provided in Table 1.

The minimum base area of the footing remains the same as used previously (that is, 3.6 x 3.6 m). The initial concrete cross-section thickness adopted in the design as per CSA S806-12[3] was equal to the thickness of steel-RC footing (that is, 0.91 m), which later was increased to value shown in Table 4.

The one-way and two-way shear strength of the GFRP-RC footing was calculated as per CSA S806-12[3] Sections 8.4.4.5 and 8.7.2, respectively, using a concrete density factor (λ) equal to 1.0 corresponding to normalweight concrete. The coefficients k_m and k_r were calculated as per Section 8.4.4.5 equal to 0.70, and 8.37, respectively. The effective shear depth (d_v) was taken as the greater of the value 0.9d (where d is effective of cross section) and 0.72h, which was equal to 0.8 m. The size effect factor (k_s) for one-way shear was calculated as per Section 8.4.4.7, equal to 0.55 and arch effect equal to 1.1. The strength reduction factor used for shear design was equal to 0.65 as per CSA S806-12,[3] Section 6.5.3.2 (different from ACI CODE-440.11-22[1] where it is equal to 0.75). Using a footing thickness of 0.91 m, the one-way shear strength was calculated as per Section 8.4.4.5, Eq. (8-19), equal to 1072 kN, which was greater than the demand of 800 kN.

The two-way shear strength was calculated as per Section 8.7, Eq. (8-39), (8-40), and (8-41) (reproduced herein as Eq. (26), (27), and (28)). Given an interior square column (610 x 610 mm), the factor β_c was taken equal to 1.0 and a_s was taken equal to 4.0. The size effect factor for two-way shear (k_s) was calculated as per Section 8.7.4 equal to 0.78.

Using a footing thickness of 0.91 m, the two-way shear strength was calculated as per Section 8.7 equal to 3226 kN which was less than demand of 3612 kN. Hence, the thickness was increased to 1.02 m to satisfy two-way shear requirement resulting in a strength of 3522 kN which is greater than the demand of 3488 kN (refer to Table 4).The required thickness value (that is, 1.02 m) for two-way shear is 0.1 m (9%) less than that required for GFRP-RC footing designed as per ACI 440.11-22[1] (that is, 1.12 m).

When the footing thickness was increased to meet two-way shear requirements, the one-way shear capacity decreased to 1055 from 1072 kN due to size effect.

The critical section for a maximum moment is at the face of the column as shown in Fig. 3. The tributary area contributing to the moment was equal to 5.4 m^2 and the ultimate moment was equal to 1356 kN·m. The flexural reinforcement area used was greater of the value required to resist the ultimate moment and minimum reinforcement stipulated in CSA S806-12[3] Sections 8.4.2.1 and 8.4.2.3. It should be noted that the reinforcement area required for the ultimate moment was equal to 0.004 m^2. However, it was increased to 0.03 m^2 (6.5 times more than needed for moment) to meet the minimum reinforcement requirements, which required M29 bars placed at 76 mm center-to-center. The moment capacity of the footing becomes 8682 kN·m, which by far exceeds demand (refer to Table 4). A sketch with dimensions and reinforcement details of GFRP-RC footing designed as per CSA S806-12[3] is given in Fig. 5.

The ratio of reinforcement area required for ultimate moment to that of provided reinforcement area highlights the conservatism in code provisions for minimum reinforcement requirement. The minimum reinforcement requirements for slabs in CSA S806-12,[3] Section 8.4.2.3, that are also applicable to foundations may result in very large quantities of FRP flexural reinforcement. If the intention of this provision is to control shrinkage and temperature cracking, this reinforcement may not be effective in shallow foundations because bars are placed only at the footing bottom. Also, temperature variations and drying shrinkage may not be critical concerns in elements surrounded by soil.

Similar to ACI CODE-440.11, the footing was redesigned as per provisions of CSA S806-12 with new-generation bars as per specifications of ASTM D8505.[7] In CSA S806-12, both one-way and two-way shear provisions depend on elastic modulus and reinforcement ratio. However, the impact of using high-elastic-modulus bars was undermined by reduction in the required reinforcement ratio. Therefore, no positive impact was visible on the shear strength of the footing. On the other hand, the reinforcement area required for flexure design decreased when using high-elastic-modulus bars. For example, when the footing was designed with

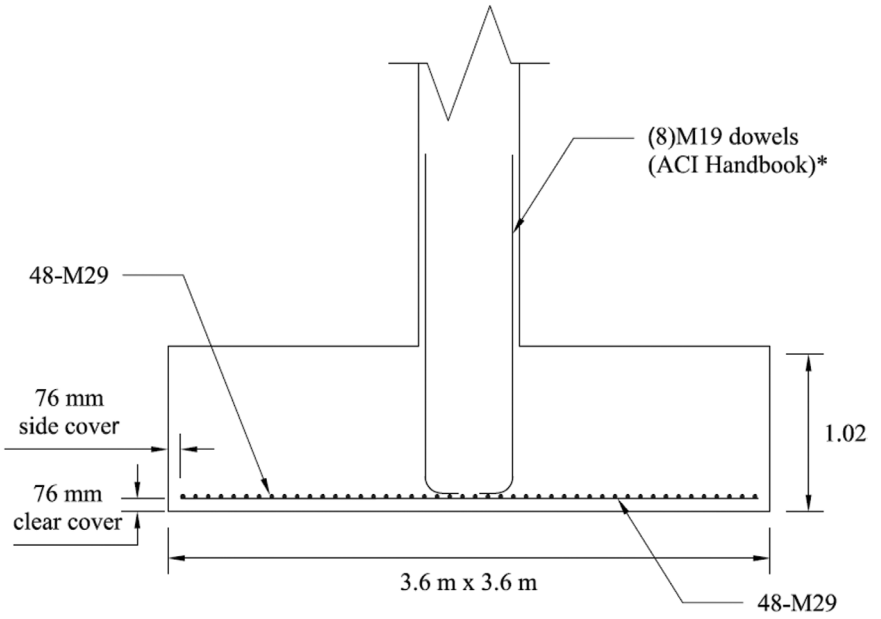

Fig. 5—GFRP-RC footing designed as per CSA S806-12 reinforcement detailing.

new-generation bars, the required number of bars decreased to 35 M29 bars against 48 M29 when using old-generation bars specified in ASTM D7957.

DETAILING OF GFRP REINFORCEMENT

The minimum length required for the anchorage of GFRP reinforcement was calculated as per ACI CODE-440.11-22,[1] Section 25.4.2.1 for M29 bars. The bar location modification factor (y) was taken equal to 1.0 for tension reinforcement placed at 76 mm from the base of the footing. The factor, c_b/d_b, was equal to 2.18. The development length calculated as per Section 25.4.2.1, Eq. (25.4.2.1a) (Eq. (4)), was equal to 1.38 m, which was greater than those calculated with Eq. (25.4.2.1b) (Eq. (5)) and (25.4.2.1c) (Eq. (6)). Therefore, the value (that is, 1.38 m) obtained from Eq. (25.4.2.1a) was adopted in the footing design as per ACI CODE-440.11-22[1] and must be provided in the footing to develop full capacity of the section at the point of maximum moment.

Similarly, the development length was calculated as per CSA S806-12,[3] Eq. (9.1). The modification factor for bar location, k_1, was taken equal to 1.0; concrete density factor, k_2, equal to 1.0; bar size factor, k_3, 1.0; bar fiber factor, k_4, 1.0; and surface profile factor, k_5, was taken equal to 1.0 for sand-coated bars. The development length calculated was equal to 1.23 m. The value obtained from equation 9.1 (that is, 1.23 m) was greater than the minimum required 0.30 m as per Section 9.3.1. Hence, 1.23 m was adopted for footing design as per CSA S806-12[3] and must be provided in the footing to develop full capacity of the section at the point of maximum moment.

ACI CODE-440.11-22[1] and CSA S806-12[3] incorporate stresses in the bar (f_{fr}) in development length equations. Because footings designed as per CSA S806-12[3] required a larger reinforcement area to satisfy minimum reinforcement requirements, the bars were less stressed, consequently requiring less development length than in the case of ACI CODE-440.11-22.[1] The development length required for GFRP-RC as per CSA S806-12[3] is 71% and ACI CODE-440.11-22[1] is 92% more than that required for steel-RC, which required 0.72 m.

The use of new-generation bars resulted in the reduction of the required reinforcement ratio. Therefore, reinforcing bars were placed at bigger spacing compared to old-generation low-elastic-modulus bars. These bars were more stressed compared to closely spaced bars, thereby, required longer development length values. The required development length increased to 2.16 and 1.64 m, respectively, for ACI 440.11-22 and CSA S806-12, respectively.

OBSERVATIONS

Tureyen and Frosch[8] proposed a physical model for calculating concrete contribution to the shear strength of GFRP-RC beams. The model considered cracked section, rather than a section between two cracks, as in the case of ACI 318-19 shear equations.[2] This model was later adopted by ACI CODE-440.11-22[1] with modifications proposed by Nanni et al.[9] for calculating one-way shear, as provided in Eq. (11) and (12) of this manuscript. The modifications proposed by Nanni et al.[9] intended to avoid penalizing lightly reinforced sections. The one-way shear equation in ACI CODE-440.11-22[1] rendered a test-to-predicted ratio equal to 2.59 for 20 GFRP-RC beams, highlighting the conservatism involved in the equations.[10]

Ospina[11] suggested an equation for two-way shear prediction of GFRP-RC slabs, equal to twice the value of one-way shear proposed by Tureyen and Frosch.[8] Realizing the fact that the suggested equation will penalize lightly reinforced slabs, Nanni et al.[9] proposed modifications to the equation proposed by Ospina.[11] Both equations proposed by Ospina[11] and Nanni et al.[9] became part of ACI CODE-440.11-22[1] code, given as Eq. (16) and (17) in this manuscript. The analysis of two-way shear equation in ACI CODE-440.11-22

Table 5—Design of GFRP-RC footing as per ACI CODE-440.11-22[1] at different soil bearing capacities

	Soil bearing capacity 268 kN/m^2							Soil bearing capacity 536 kN/m^2						
	Dimensions, m					Capacity		Dimensions, m					Capacity	
Quantity	h	b_1	b_2	Development length, m	$\frac{A_{f\_req}}{A_{f\_pro}}$	Moment, kN·m	Shear, kN	h	b_1	b_2	Development length, m	$\frac{A_{f\_req}}{A_{f\_pro}}$	Moment, kN·m	Shear, kN
One-way shear	1.12	3.6	3.6	1.38	—	—	986	0.97	2.5	2.5	1.34	—	—	585
Two-way shear						—	3488						—	2813
Flexural strength	—	—	—		0.83	4706	—	—	—	—		0.92	2330	—

rendered a test-to-predicted ratio equal to 1.8 against a database of 51 elevated GFRP-RC slabs.[12-20] Conservatism will further increase when this equation is applied to the foundations. Using shear equations developed for elevated GFRP-RC slabs to shallow foundations leads to implementation challenges for comparatively new technology in the construction industry. As observed in the current study, ACI CODE-440.11-22,[1] shear provisions required cross sections that are 100 and 210 mm bigger than those required by CSA S806-12 and ACI 318-19,[2] respectively. Also, it required reinforcement area that is 170% bigger than that of a cross section with steel-RC (0.019 m^2 versus 0.007 m^2). The bigger reinforcement areas in ACI CODE-440.11-22[1] intend to meet detailing requirements (that is, crack width and stress at service loads), which may not be critical concerns in the footings.

The development length equation in ACI CODE-440.11-22 results in very large values (that is, 92% more than steel-RC), and this, coupled with the challenge of adding a hook at the end of long longitudinal bars, makes design impractical and costly. In the current design example, the required dimensions are large enough to compensate the required development length. However, when the soil stiffness increases or the loads are smaller, the required footing dimensions decrease; thereby, it will be difficult to meet the required development length within the available dimensions. To illustrate this effect, the soil bearing capacity was made twice the value originally given in the *ACI Reinforced Concrete Design Handbook*,[4] (that is, from 268 to 536 kN/m^2). Consequently, the required footing dimensions decreased to 2.5 from 3.6 m as in the case of original footing, as shown in Table 5. Though the footing dimensions decreased but the stress in the bars did not change significantly as minimum reinforcement area required by ACI CODE-440.11-22[1] controls in both cases. Therefore, the required development length was equal to 1.32 m, slightly less than required originally. Adjusting a development length equal to 1.32 m within available dimensions will be difficult. The required development length and available dimensions in two cases discussed previously are provided in Table 5.

The current development length equation is based on the test data obtained more than two decades ago, with bars used in those tests that are no longer used in construction projects.[21] Therefore, it is necessary to reassess and update the development length equation based on recent literature which incorporates improvements in the material and surface properties,[22,23] thereby developing a more representative equation for calculating development length for GFRP-RC members.

CONCLUSIONS AND RECOMMENDATIONS

In this study, an example of square footing subject to axial load only was taken from *ACI Reinforced Concrete Design Handbook*[4] and redesigned with glass fiber-reinforced polymer (GFRP) reinforcement compliant with ASTM D7957 as per ACI CODE-440.11-22[1] and CSA S806-12[3] to show the implications of code provisions. The concrete strength f_c' was assumed to be 28 MPa, bond coefficient k_b = 1.20, and concrete cover was 76 mm in the design of GFRP-reinforced concrete (RC) for both codes.

Based on the outcomes of this design and detailing, the following conclusions were drawn:

- GFRP-RC footing designed as per ACI CODE-440.11-22 required more concrete cross-section thickness to satisfy shear requirements than steel-RC designed as per ACI 318-19. The thicker cross section may lead to implementation challenges, particularly on sites with water-table issues. Similarly, ACI CODE-440.11-22 required a higher longitudinal reinforcement area to satisfy detailing provisions.
- The GFRP-RC footing designed as per CSA S806-12 required a concrete cross-section thickness slightly more than that of steel-RC, but less than as per ACI 440.11-22. However, the longitudinal reinforcement area was much higher than in the other two cases.
- It was observed that ACI CODE-440.11-22 shear equations disregard arching effect in thicker members for one-way shear and adopts an empirical coefficient in two-way shear that seems conservative. Hence, the required thickness of a shallow foundation is bigger than that designed as per CSA S806-12.
- The equations for computing development length in GFRP are more demanding than in the case of steel (that is, 92% more than that of steel-RC). This is challenging when dealing with footings of relatively small dimensions.
- The use of new-generation high-elastic-modulus, high-strength bars did not affect the shear strength. However, a positive impact was noticed on the flexural capacity of GFRP-RC footings.

AUTHOR BIOS

Zahid Hussain *is a PhD Candidate in Civil and Architectural Engineering Department at the University of Miami, Coral Gables, FL. He received his BE and ME in civil engineering from Quaid-e-Awam University of Engineering, Science and Technology, Nawabshah, Sindh, Pakistan, and Universiti Tun Hussein Onn Malaysia, Batu Pahat, Johor, Malaysia, respectively. His research interests include sustainable materials, computational methods, and the design and behavior of fiber-reinforced polymer (FRP)-reinforced structures.*

Antonio Nanni, *FACI, is an Inaugural Senior Scholar, Professor, and Chair of the Civil and Architectural Engineering Department at the University of Miami. He is a member of ACI Committees 440, Fiber-Reinforced Polymer Reinforcement, and 549, Thin Reinforced Cementitious Products and Ferrocement.*

ACKNOWLEDGMENTS

The authors would like to thank the National Science Foundation (NSF) for their financial support of the lead author under Grant No. 1916342.

NOTATION

A_{fv}	=	area of shear reinforcement, mm^2
b	=	width of cross section, mm
c_b	=	lesser of: a) distance from center of bar to nearest concrete surface; or b) one-half center-to-center spacing of bars being developed, mm
c_c	=	concrete cover, mm
d	=	distance from extreme compression fiber to centroid of longitudinal tension reinforcement, mm
d_b	=	nominal diameter of bar, mm
d_v	=	effective shear depth, taken as greater of 0.9d or 0.72h, mm
E_c	=	modulus of elasticity of concrete, MPa
E_f	=	modulus of elasticity of GFRP reinforcement, MPa
f_c'	=	compressive strength of concrete at 28 days, MPa
f_{fr}	=	tensile stress in GFRP reinforcement required to develop full nominal section capacity, MPa
f_{fs}	=	stress at service loads, MPa
k_b	=	bond-dependent coefficient
k_{cr}	=	ratio of depth of elastic cracked section neutral axis to effective depth
k_m	=	coefficient considering effect of moment at section on shear strength
k_r	=	coefficient considering effect of reinforcement rigidity on its shear strength
M_f	=	factored moment, kN·m
M_u	=	ultimate factored moment at section, kN·m
n_f	=	modular ratio
P_u	=	ultimate factored load, kN
S_{max}	=	maximum allowed spacing, mm
S_n	=	nominal moment, shear, axial, or torsional strength
U	=	strength of member or cross section required to resist factored loads or related internal moments and forces
V_c	=	nominal shear strength provided by concrete, kN
V_f	=	nominal shear strength provided by GFRP shear reinforcement, kN
V_n	=	nominal shear strength, kN
V_r	=	factored shear resistance, kN
V_{sF}	=	factored shear resistance provided by FRP shear reinforcement, kN
V_u	=	factored shear force at section, kN
v_c	=	stress corresponding to two-way shear strength of slab or footing, MPa
v_r	=	factored shear stress resistance, MPa
w_c	=	density, unit weight of normal weight concrete, kg/m^3
β_c	=	ratio of long side to short side of column
ε_f	=	strain in GFRP flexural reinforcement
Φ	=	strength reduction factor
λ	=	factor to account for concrete density
λ_s	=	size effect factor
ρ_{FW}	=	longitudinal FRP reinforcement ratio
ω	=	bar location modification factor

REFERENCES

1. ACI Committee 440, "Building Code Requirements for Structural Concrete Reinforced with Glass Fiber-Reinforced Polymer (GFRP) Bars — Code and Commentary (ACI CODE-440.11-22)," American Concrete Institute, Farmington Hills, MI, 2023, 266 pp.

2. ACI Committee 318, "Building Code Requirements for Structural Concrete (ACI 318-19) and Commentary (ACI 318R-19) (Reapproved 2022)," American Concrete Institute, Farmington Hills, MI, 2019, 624 pp.

3. CSA S806-12, "Design and Construction of Building Structures with Fiber Reinforced Polymers (Reaffirmed in 2017 and 2021 without changes)," CSA Group, Toronto, ON, Canada, 2012, 208 pp.

4. American Concrete Institute, *ACI Reinforced Concrete Design Handbook: A Companion to ACI 318-19*, ACI MNL-17(21), H. R. Hamilton, ed., ACI, Farmington Hills, MI, 2019, pp. 1-568.

5. ASTM D7957/D7957M-22, "Standard Specifications for Solid Round Glass Fiber Reinforced Polymer Bars for Concrete Reinforcement," ASTM International, West Conshohocken, PA, 2022, 5 pp.

6. ASCE 7-16, "Minimum Design Loads and Associated Criteria for Buildings and other Structures," American Society of Civil Engineers, Reston, VA, 2016, 889 pp.

7. ASTM D8505/D8505M-23, "Standard Specifications for Solid Round Glass Fiber Reinforced Polymer Bars for Concrete Reinforcement," ASTM International, West Conshohocken, PA, 2023, 5 pp.

8. Tureyen, K. A., and Frosch, R. J., "Concrete Shear Strength: Another Perspective," *ACI Structural Journal*, V. 100, No. 5, Sept.-Oct. 2003, pp. 609-615.

9. Nanni, A.; De Luca, A.; Zadeh, H. J., *FRP Reinforced Concrete Structures – Theory, Design and Practice*, CRC Press, Boca Raton, FL, Apr. 3, 2014, 400 pp.

10. Halvonik, J.; Borzovic, V.; and Laniova, D., "Comparison of Shear Behavior of Concrete Beams Reinforced with GFRP Bars and Steel Bars," *Structures*, V. 43, 2022, pp. 657-668. doi: 10.1016/j.istruc.2022.06.065

11. Ospina, E. C., "Alternative for Concrete Punching Capacity Evaluation of Reinforced Concrete Two-way Slabs," *Concrete International*, V. 27, No. 9, Sept. 2005, pp. 53-57.

12. Ospina, C. E.; Alexander, D. B. S.; and Cheng, R. J. J., "Punching of Two-Way Concrete Slabs with Fiber-Reinforced Polymer Reinforcing Bars or Grids," *ACI Structural Journal*, V. 100, No. 5, Sept.-Oct. 2003, pp. 589-598.

13. El-Ghandour, A. W.; Pilakoutas, K.; and Waldron, P., "Punching Shear Behavior of Fiber-Reinforced Polymers Reinforced Concrete Flat Slabs: Experimental Study," *Journal of Composites for Construction*, ASCE, V. 7, No. 3, 2003, pp. 258-265. doi: 10.1061/(ASCE)1090-0268(2003)7:3(258)

14. Hassan, M.; Ahmed, E. A.; and Benmokrane, B., "Punching Shear Strength of Glass Fiber-Reinforced Polymer Reinforced Concrete Flat Slabs," *Canadian Journal of Civil Engineering*, V. 40, 2013, pp. 951-960. doi: 10.1139/cjce-2012-0177

15. Lee, H. J.; Yoon, Y. S.; Cook, D. W.; and Mitchell, D., "Improving Punching Shear Behavior of Glass Fiber Reinforced Polymer Reinforced Slabs," *ACI Structural Journal*, V. 106, No. 4, July-Aug. 2009, pp. 427-434.

16. El-Gamal, S.; El-Salakawy, E. F.; and Benmokrane, B., "Behavior of Concrete Slabs Reinforced with FRP Bars Under Concentrated Loads," *ACI Structural Journal*, V. 102, No. 5, Sept.-Oct. 2005, pp. 727-734.

17. Bouguerra, K.; Ahmed, E. A.; El-Gamal, S.; and Benmokrane, B., "Testing of Full Scale Concrete Bridge Deck Slabs Reinforced with Fiber-Reinforced Polymer (FRP) Bars," *Construction and Building Materials*, V. 25, No. 10, 2011, pp. 3956-3965. doi: 10.1016/j.conbuildmat.2011.04.028

18. Sarhan, I. A.; Mahmoud, A. S.; and Hussian, M. A., "Punching Shear Resistance of High Strength GFRP Reinforced Concrete Flat Slabs," *Iraqi Journal of Civil Engineering*, V. 11, No. 1, pp. 72-93.

19. Dulude, C., and Hassan, M., "Punching Shear Behavior of Flat Slabs Reinforced with Glass Fiber-Reinforced Polymer Bars," *ACI Structural Journal*, V. 110, No. 5, Sept.-Oct. 2013, pp. 723-725.

20. Kurtoğlu, A. E.; Bilgehan, M.; Gülşan, M. E.; and Çevik, A., "Experimental and Theoretical Investigation of the Punching Shear Strength of GFRP-Reinforced Two-Way Slabs," *Structural Engineering International*, V. 33, No. 3, 2023, pp. 379-388. doi: 10.1080/10168664.2022.2093689

21. Wambeke, B. W., and Shield, C. K., "Development Length of Glass Fiber Reinforced Polymer Bars in Concrete," *ACI Structural Journal*, V. 103, No. 1, Jan.-Feb. 2006, pp. 11-17.

22. Ortiz, J. D.; Hussain, Z.; Hosseini, S. A.; Benmokrane, B.; and Nanni, A., "Lap Splice Assessment of GFRP Rebars in Reinforced Concrete Beams under Flexure," *Construction and Building Materials*, V. 419, 2024, p. 135408. doi: 10.1016/j.conbuildmat.2024.135408

23. Ortiz, J. D.; Hussain, Z.; Hosseini, S. A.; Benmokrane, B.; and Nanni, A., "Assessment of the Flexural Bond Stresses of New Generation GFRP Bars," *Proceedings of the 16th International Symposium on Fiber-Reinforced Polymer (FRP) Reinforcement for Concrete Structures (FRPRCS-16)*, SP-360, A. M. Okeil, P. Sadeghian, J. J. Myers, and M. D. Lopez, eds., American Concrete Institute, Farmington Hills, MI, pp. 318-329.

ACI STRUCTURAL JOURNAL TECHNICAL PAPER

Title No. 122-S12

Design and Detailing Guidelines for Axially Loaded Ultra-High-Performance Concrete Columns

by Milana Cimesa and Mohamed A. Moustafa

With a well-thought-out packing theory for sand, fine aggregates, cement, a water-cement ratio lower than 0.2, and steel fibers, ultra-high-performance concrete (UHPC) achieves remarkable mechanical properties. Despite UHPC's superior mechanical properties compared to conventional concrete, its use remains limited, especially in structural applications, due to factors such as high cost, lack of design standards and guidelines, and inadequate correlation between material properties and structural behavior. By compiling and synthesizing the behavior of 70 structural- or full-scale axial UHPC columns, this research provides a new set of generalized design and detailing guidelines for axial UHPC columns. The study first uses the assembled database to assess and revisit the current ACI 318 axial strength design factors for applicability for UHPC. Next, the behavior trends are carefully analyzed to provide detailed recommendations for proper transverse reinforcement (ρ_t volume), spacing-to-longitudinal reinforcing bar diameter ratio (s/d_b, where s represents the centerline-to-centerline spacing between transverse reinforcement), and UHPC steel fiber ratio for best use of confinement.

Keywords: axial columns; circular columns; confinement effect; lateral reinforcement ratio (ρ_t); reinforcement configuration; spacing-to-longitudinal reinforcing bar diameter ratio (s/d_b); square and rectangular columns; strength reduction factor; structural-scale columns.

INTRODUCTION

Due to its superior properties, ultra-high-performance concrete (UHPC) provides qualities that might change concrete structures' design and construction paradigm once and for all. With the well-thought-out packing theory for blending sand, fine aggregates, and cement at a water-cement ratio lower than 0.2, and with the use of steel fibers, UHPC achieves remarkable mechanical properties that exceed 17.4 ksi (120 MPa) in compressive strength and 0.72 ksi (5 MPa) in tensile strength (Bajaber and Hakeem 2021; Graybeal et al. 2020). Besides approximately five times higher compressive and two times tensile strength when compared to normal-strength concrete (NSC), UHPC exhibits extraordinary enhancement in ductility, durability, toughness, resistance to spalling, and energy absorption capacity (Hung et al. 2021). It is noted that UHPC can be mixed without steel fibers. However, given the crucial role of steel fibers in bridging microcracks and preventing their further expansion, and, in turn, contributing to UHPC's remarkable behavior and significantly enhancing its ductility (Du et al. 2021; Hung et al. 2021), all literature and data used herein refer only to UHPC with steel fiber reinforcement.

Due to its outstanding properties, UHPC allows for reducing structural element sizes, decreasing overall structure weight and carbon footprint, requiring less maintenance, and having a longer service life (Bajaber and Hakeem 2021; Graybeal et al. 2020; Hung et al. 2021; Russell and Graybeal 2013). For instance, shorter spans in NSC bridges can be replaced with much longer ones of the same weight when using UHPC. Despite UHPC showcasing superior mechanical properties compared to NSC, its use remains limited, especially in structural applications, due to factors such as high cost, lack of design standards and guidelines, absence of appropriate large-scale manufacturing technology, lack of knowledge on the standard test methods and specifications for the UHPC material, and inadequate correlation between material properties and structural behavior (Bajaber and Hakeem 2021; Cimesa and Moustafa 2024; Graybeal et al. 2020; Hung et al. 2021; Russell and Graybeal 2013). In particular, while UHPC girders and flexural members are getting more attention in terms of larger applications, UHPC columns still fall behind and lack clear design and construction guidelines. Columns are vertical load-bearing elements crucial for stability and integrity, especially lower-floor columns in buildings and those of bridge piers, which carry significant loads within a structure and, therefore, are specific structural elements of concern.

Numerous research studies have been dedicated to examining UHPC compressive behavior at the material level, aiming to establish foundational insights that can extend to axial members such as columns. Some studies investigated confinement effects using 2 x 4 in. (5.1 x 10.2 cm) and 3 x 6 in. (7.6 x 15.2 cm) cylinders, while others explored the impact of incorporating nanofibers in confined 3 x 6 in. (7.6 x 15.2 cm) UHPC cylinders' compressive behavior (Naeimi and Moustafa 2021; Cimesa and Moustafa 2022). Additionally, other research efforts in this domain assessed the influence of curing methods; steel fiber distribution techniques and orientation; comparative behavior of cylinders and cubes; and the use of various microfiber types that are eco-friendly, sustainable; and more affordable (Bajaber and Hakeem 2021; Graybeal 2014; Graybeal et al. 2020; Haber et al. 2018; Kang et al. 2011; Kasaei and Esmaeili 2016; Kusumawardaningsih et al. 2015; Meng et al. 2018; Russell and Graybeal 2013; Teng et al. 2021). This is especially concerning because columns are vertical load-bearing elements crucial for the integrity and

ACI Structural Journal, V. 122, No. 1, January 2025.
MS No. S-2023-362.R1, doi: 10.14359/51742143, received June 15, 2024, and reviewed under Institute publication policies.

stability of structures, such as bridge piers and lower-floor columns in buildings, which carry significant loads and are critical structural components. A thorough understanding of the material paves the way for properly comprehending and devising the best structural applications that adequately use the material. Prototyping or structural-scale testing and demonstration becomes the next natural step to enabling a more precise assessment and avoiding any adverse scale effect if only small-scale and material characterization specimens are relied on to interpret and advance structural elements' behavior and design. As such, this study is concerned with UHPC research at the structural scale, focusing on axial columns.

Structural-scale research studies in the literature investigate the behavior of UHPC and high-strength concrete (HSC) short and long columns, most of which are summarized by Hosinieh et al. (2015) for both centric and eccentric axial loading. Such studies concerned with axial columns include the work by Aboukifa and Moustafa (2022a,b), Cimesa et al. (2023), Empelmann et al. (2008), Hung and Yen (2021), Shin et al. (2017, 2018), and Sugano et al. (2007). Other studies focused on columns in seismic force-resisting systems (SFRS), such as the work by Aboukifa et al. (2020), Aboukifa and Moustafa (2021), Wei et al. (2019), and Kadhim et al. (2022). Some of the parameters that have been taken into consideration in those studies are steel fiber ratio, lateral and longitudinal reinforcement ratio, column height, cross-sectional geometry, and incorporation of different nano and microfibers.

Moreover, the literature presents research on concrete composite compression elements (Chen et al. 2018; Hoang and Fehling 2017; Li et al. 2023; Mirza and Lacroix 2004). While concrete composite columns such as steel tubes filled with NSC and UHPC exhibit exceptional performance, their widespread adoption is hindered by the high costs associated with materials, construction, and substantial energy consumption when it comes to steel production (Empelmann et al. 2008). As an alternative, strategically designing and reinforcing UHPC is a viable approach to enhance the performance of reinforced concrete columns and provide a replacement for composite columns.

In several research studies, equations have been proposed to calculate crucial design values, including maximum failure load, optimum steel fiber content, reinforcement ratio, compressive ductility, and unconfined and confined strength values (Empelmann et al. 2008; Hung and Yen 2021; Shin et al. 2017, 2018; Sugano et al. 2007). However, there has been a notable absence of insights into two critical aspects of UHPC column design in the existing literature: 1) guidance on the transverse reinforcement detailing in terms of reinforcement ratio (ρ_t) limits and spacing-to-longitudinal reinforcing bar diameter ratio (s/d_b); and 2) a generalized axial design equation that can be applied exclusively to any type of UHPC mixtures. Therefore, this research effort addresses this long-standing gap by assembling and analyzing an exclusive database of 70 structural- or full-scale UHPC columns tested under axial compressive loading. The columns in the database include brand-new data from approximately 20 columns that the authors recently tested as part of an ACI-funded project (Cimesa et al. 2023). In addition, the database uses test results from the work of Aboukifa and Moustafa (2022a), Empelmann et al. (2008), Hosinieh et al. (2015), Hung and Yen (2021), Shin et al. (2017, 2018), and Sugano et al. (2007). The details of the database and a brief review of the aforementioned studies, whose results are included in the database, are included in the next section.

In general, one of the goals of this study is to determine appropriate limits for the lateral reinforcement ratio and confirm whether existing guidance on relevant limits, such as the spacing-to-longitudinal reinforcing bar diameter ratio, is appropriate for UHPC. This needs to be done while taking into consideration the high cost of UHPC material and the necessity that ultra-high-strength material dictates or calls for a higher reinforcement ratio to avoid inadequate confining strength provided by lateral reinforcing bar when larger spacing is used (Richart et al. 1929).

Therefore, this study uses large data sets in the light of two main design philosophies. The first advocates for a minimum lateral reinforcement ratio to prevent premature failure and reinforcing bar buckling, ensuring adequate concrete performance while making it economically available for wide applications and simpler for axial design calculations when only cylinder strength is used. The second philosophy suggests a more sophisticated approach that considers a range of reinforcement ratios that fully use all mechanical attributes of UHPC at its best by engaging confined structural behavior, but will require the correct future models to estimate the confined strength of UHPC.

In summary, using the two main design philosophies mentioned earlier, the main objectives of this research study are to: 1) establish a database of structural tests of axial UHPC columns; 2) develop a full understanding of the effect of transverse reinforcement detailing about axial column behavior for a wide range of designs and UHPC types as covered by the database, with a focus on ρ_t and s/d_b and possible confinement effects while also taking into consideration steel fiber contributions; and 3) use this database and enhanced understanding to revisit the current ACI 318 axial strength design and statistically deduce modification factors and design limits that are presented in the form of recommendations and guidelines. These objectives are valuable for incorporation into future UHPC design guidelines, codes, and standards, and will help further promote UHPC column applications and implementation.

RESEARCH SIGNIFICANCE

This research uses, for the first time, a comprehensive database of structural- and full-scale axial UHPC columns to inform axial design capacity and capture axial behavior trends that can be related to transverse reinforcement detailing. The major research outcomes include a proposed modification factor for the current ACI 318 axial design equation to be adopted for UHPC columns, as well as recommendations for the minimum transverse reinforcement ratio and when to consider confinement effects. The results of this study are expected to have a major impact on the practice of UHPC design, where the authors are currently working with ACI Subcommittee 239-C, Structural Design on UHPC, for the potential incorporation of the outcomes of this study into

the axial design section of the structural design guide that is currently being developed by the subcommittee.

ASSEMBLED DATABASE AND REVIEW OF INCORPORATED LITERATURE

This section provides a brief literature review of the relevant structural-scale axially loaded columns to introduce all the columns that have been incorporated into the database used in this study. The database is simplified and presented in Table 1. For some of the discussion points in this paper, the columns are separated into two groups, where one compiles and synthesizes square and rectangular columns (more appropriate for buildings), and the other focuses on circular columns (typically used in bridges). It is worth noting that the buckling of the columns used in this study is not concerning due to the columns' heights and testing boundary conditions, which led to slenderness ratio values lower than 22, and is permitted to be neglected per ACI 318.

Square and rectangular columns

Cimesa et al. (2023) investigated the structural behavior of 16 full-scale columns using three different types of UHPC mixtures, where four had rectangular cross sections of 10 x 16 in. (25.4 x 40.6 cm), and the other 12 had square cross sections of 12 x 12 in. (30.5 x 30.5 cm). Five square columns were made out of a commercially available UHPC mixture that uses white cement and features a white appearance when the concrete sets (the authors refer to it as Type A UHPC). Four rectangular and two square columns are designated as Type B UHPC and were made of a commercially available mixture that incorporates carbon nanofiber paste into its ingredients matrix to provide the confinement effect on the nano level, filling the nanopores and preventing their further propagation (Yoo et al. 2022). The last five square columns (Type C) were made of an economic or semi-proprietary mixture that uses locally sourced sand and cement to reduce the UHPC mixture's overall cost. All 16 columns incorporated 0.5 in. (1.27 cm) long steel fibers with a diameter of 0.008 in. (0.02 cm). One square column of each type (that is, Type A, B, and C) incorporated 1% of steel fibers, while the rest of the columns used 2% of steel fibers by volume. The height of all columns was 9 ft (2.7 m). The preliminary observations and conclusions drawn from this research study, based on 16 columns, are evaluated here using a larger data set of 70 columns. In particular, the following observation from previous work motivates this study and is further evaluated: the ACI 318-19 (ACI Committee 318 2019) transverse reinforcement spacing limit of s/d_b less or equal to 6, which is appropriate for NSC special moment-resisting frame columns, is also appropriate for UHPC columns. Violating this limit might or might not lead to premature longitudinal bar buckling; therefore, more data from the literature are used herein to revisit this conclusion. The transverse reinforcement should also laterally constrain longitudinal bars more than 6 in. (15.2 cm) away from the closest constrained reinforcing bar. In the authors' previous work, they also showed that a high transverse reinforcement ratio, such as 3.8%, can lead to more congestion and prevent proper steel fiber dispersion or proper flowability of the concrete, so where to define the sweet spot where UHPC benefits from confinement but without too much congestion is one of the investigation points in this study.

Aboukifa and Moustafa (2022a) tested five 11 ft (3.4 m) tall UHPC square columns with cross-sectional dimensions of 11 x 11 in. (27.9 x 27.9 cm) under axial compressive loading. The variables in this study were longitudinal reinforcing bar sizes, transverse reinforcement, and steel fiber ratios of 1% and 2%. Aboukifa and Moustafa (2022a) concluded that UHPC columns have a sudden failure caused by longitudinal bar buckling, followed by the transverse bar rapture and cover concrete spalling, similar to the observation made in the recent work by the authors (Cimesa et al. 2023). Decreasing the confinement ratio by 50% led to the reduction of the axial strength, peak, and ultimate strain capacities. However, columns including only 1% of steel fiber had the same axial capacity as columns with 2%, along with a 16% drop in the peak and ultimate strain capacity. Furthermore, steel fibers postponed the yielding of the longitudinal reinforcement and delayed the inclusion of the transverse reinforcement confinement effect. Using the actual cylinder's strength value and yielding of the longitudinal reinforcing bars, the ACI 318-19 equation for estimating the axial capacity of the columns was shown to overestimate the actual axial capacity of the UHPC columns determined from the test, while using the nominal values will lead to at least a factor of safety of 2. In their study, Aboukifa and Moustafa (2022a) proposed using a strength reduction or correction factor—referred to as α throughout this paper, as explained later—of 0.75 for UHPC, as opposed to 0.85 for NSC, which is, again, another key objective of this study to verify such a value using larger data sets.

Another research study on UHPC columns was done by Empelmann et al. (2008). The authors tested six square UHPC 23.6 in. (60 cm) tall columns with cross-sectional dimensions of 7.9 x 7.9 in. (20 x 20 cm), two NSC, and two HSC columns using different lateral reinforcement configurations. They concluded that the basic design assumptions for NSC and HSC apply to the UHPC columns, with the need for adjusting the safety parameters. Also, this research study proposed equations for steel fiber volume and the required ratio of lateral reinforcement.

A summary table of short and slender columns loaded under centric and eccentric loading found in the literature until 10 years ago can be found in a research study by Hosinieh et al. (2015). Besides a thorough literature review, the authors examined the structural behavior of six 39.4 in. (100 cm) tall square columns with cross-sectional dimensions of 9.8 x 9.8 in. (25 x 25 cm) under axial compression. They concluded that close spacing and configuration of the lateral reinforcement have a significant role in enhancing the axial strength and toughness of the columns, while the inclusion of steel fibers promotes the confinement effect, leading to the greater ductility of UHPC columns. Moreover, for a given spacing, the configuration does not enhance strength as much as it affects the toughness of the columns. One of the conclusions of this study is that confinement models suitable for HSC do not precisely describe UHPC confinement behavior due to the exclusion of the steel fiber effect.

Table 1—Design and reinforcement details of all UHPC columns in assembled database

Column ID and reference study		Reinforcement confinement	A_{gross}, cm^2	*SF*, %	Longitudinal reinforcement			Transverse reinforcement				
					Size	ρ_l, %	f_y, MPa	Size	*s*, cm	ρ_t, %	f_y, MPa	s/d_b
Cimesa et al. (2023)	1	A	1006	2	8 No. 5	1.59	490	No. 3	7.6	1.40	503	4.8
	2	A	979	1	8 No. 5	1.63	490	No. 3		1.40	503	4.8
	3	A	934	2	8 No. 5	1.71	490	No. 4		2.54	483	4.8
	4	A	907	2	8 No. 5	1.76	490	No. 4	15.2	1.27	483	9.6
	5	A	928	2	8 No. 5	1.72	490	No. 3		0.70	503	9.6
	6	E	1101	2	8 No. 5	1.41	483	No. 3	12.7	0.82	503	10.0
	7	J	1054	2	12 No. 4	1.47	483	No. 3	6.4	3.80	503	5.0
	8	E	1088	2	12 No. 4	1.42	483	No. 3	6.4	1.64	503	5.0
	9	N	1083	2	12 No. 4	1.43	483	No. 3	6.4	1.95	503	5.0
	10	A	957	2	8 No. 5	1.67	490	No. 3	7.6	1.40	503	4.8
	11	A	922	1	8 No. 5	1.74	490	No. 3	7.6	1.40	503	4.8
	12	A	990	2	8 No. 5	1.62	490	No. 3	7.6	1.40	503	4.8
	13	B	948	2	12 No. 4	1.63	483	No. 3	7.6	1.40	503	6.0
	14	C	981	2	12 No. 4	1.58	483	No. 3	7.6	2.84	503	6.0
	15	C	1019	1	12 No. 4	1.52	483	No. 3	7.6	2.84	503	6.0
	16	B	965	2	12 No. 4	1.61	483	No. 3	7.6	1.40	503	6.0
Aboukifa and Moustafa (2022a)	17	A	781	2	8 No. 5	2.05	459	No. 3	7.6	1.54	482	4.8
	18	A		2	8 No. 5	2.05	459		15.2	0.77		4.8
	19	A		2	8 No. 5	1.32	461		7.6	1.54		4.0
	20	A		2	8 No. 5	2.91	447		7.6	1.54		6.0
	21	A		1	8 No. 5	2.05	459		7.6	1.54		4.8
Empelmann et al. (2008)	22	D	400	1.25	4 Ø28	6.16	700	Ø8	8.4	1.34	560	3.0
	23	F		1.25	8 Ø28	12.31	700		8.4	2.38		3.0
	24	D		1.25	4 Ø14	1.54	500		8.4	1.34		6.0
	25	D		1.25	4 Ø28	6.16	700		6.1	1.99		2.1
	26	D		1.25	4 Ø28	6.16	700		4.1	2.99		1.5
	27	D		0	4 Ø28	6.16	560		4.1	2.99		1.5
	28	D		2.13	4 Ø28	6.16	700		6.1	1.99		2.1
	29	D		1.25	4 Ø26.5	5.52	870		6.1	1.99		2.3
Hosinieh et al. (2015)	30	I	625	2.5	8 15M	2.56	455	10M	4.1	6.52	453	2.5
	31	I		2.5	8 15M				6.1	4.35		3.8
	32	I		2.5	8 15M				7.9	3.26		5.0
	33	I		2.5	8 15M				11.9	2.17		7.5
	34	K		2.5	12 15M	3.84			6.1	5.80		3.8
	35	K		2.5	12 15M				11.9	2.90		7.5
Hung and Yen (2021)	36	G	1225	0	8 D25	3.3	509	D13	8.9	3.13	453	3.5
	37	G		0						3.13		
	38	H		0.75						3.13		
	39	H		1.5						3.13		
	40	A		0.75						2.09		
	41	A		1.5						2.09		

Table 1 (cont.)—Design and reinforcement details of all UHPC columns in assembled database

Column ID and reference study		Reinforcement confinement	A_{gross}, cm^2	*SF*, %	Longitudinal reinforcement			Transverse reinforcement				
					Size	ρ_l, %	f_y, MPa	Size	*s*, cm	ρ_t, %	f_y, MPa	s/d_b
Hung and Yen (2021)	42	G	1225	0.75	8 D25	3.3	509	D13	18.0	1.56	453	7.1
	43	G		1.5						1.56		
	44	H		0.75						1.56		
	45	H		1.5						1.56		
	46	A		0.75						1.04		
	47	A		1.5						1.04		
Shin et al. (2017)	48	A	484	1.5	8 D16	3.28	575	D10	4.1	3.75	565	2.5
	49	F		1.5					5.3	4.75		3.4
	50	F		1.5					4.1	6.41		2.5
	51	F		1.5				D13	4.3	10.59		2.7
	52	A		1.5				D10	16.5	0.91		10.4
	53	A		1.5					4.8	3.13		3.0
	54	F		1.5					7.9	3.20		5.0
	55	F		1.5					6.4	4.00		4.0
	56	F		1.5					4.8	5.34		3.0
Sugano et al. (2007)	57	K	400	2	12 D10	2.15	685		3.6	7.18	700	5.8
	58	K		2					4.6	5.59		
	59	K		2					3.6	7.18		
	60	K		2					4.6	5.59		
Cimesa et al. (2023)	61	M	1297	2	10 No. 6	2.19	480	No. 3	7.6	1.01	492	4.0
	62	M		2					3.8	2.02		2.0
	63	L		2					7.6	1.01		4.0
	64	L		2					3.8	2.02		2.0
Shin et al. (2018)	65	M	625	1.5	8 D16	3.28	575	D10	3.6	3.77	565	2.2
	66			1.5				D10	4.3	3.14	565	2.6
	67			1.5				D13	4.3	5.46	554	2.7
	68			1.5				D10	3.0	4.40	565	1.9
	69		1225	1.5	8 D22	3.41	490	D13	3.8	4.45	554	1.7
	70			1.5				D13	4.6	3.75	554	2.0

Note: 1 cm^2 = 0.155 in.^{2}; 1 MPa = 0.145 ksi; 1 ksi = 6.89 MPa.

Furthermore, this research study proposed an unconfined UHPC model, which agrees with the experimental data presented in their study.

Variables such as steel fiber content, lateral reinforcement ratio, inclusion of coarse aggregate configuration, and inclusion of coarse aggregates were taken into consideration in a research study by Hung and Yen (2021). They tested 12 UHPC columns that were 35.4 in. (90 cm) tall with cross-sectional dimensions of 13.8 x 13.8 in. (35 x 35 cm). A 135- and 90-degree hooked-end effect were also investigated. The conclusions drawn from this research study were that transverse reinforcement and steel fiber content had negligible influence on the initial stiffness of the UHPC columns, while the inclusion of the coarse aggregates enhanced secant stiffness by approximately 100%. While coarse aggregates had a significant influence on the stiffness, they had almost no influence on the peak strength. High transverse reinforcement ratio and inclusion of coarse aggregates did not prevent early spalling of the cover concrete in non-fiber UHPC columns, while steel fiber-reinforced UHPC columns significantly improved the peak strength and restrained concrete spalling and crack propagation to macrocracks. Similar to the conclusion made by Aboukifa and Moustafa (2022a), Cimesa et al. (2023), and Hosinieh et al. (2015), the axial load dropped significantly right after the columns reached their maximum capacity. Furthermore, Hung and Yen (2021) concluded that ACI 318-19 significantly overestimates maximum compressive strength, while the ACI ITG-4.3R equation underestimates the maximum strength by 10% on average. They also proposed an analytical model for the post-peak compressive strength of UHPC columns accounting for steel fiber content and reinforcement detailing.

In a research study by Shin et al. (2017), nine 35.4 in. (90 cm) tall UHPC columns were designed according to the

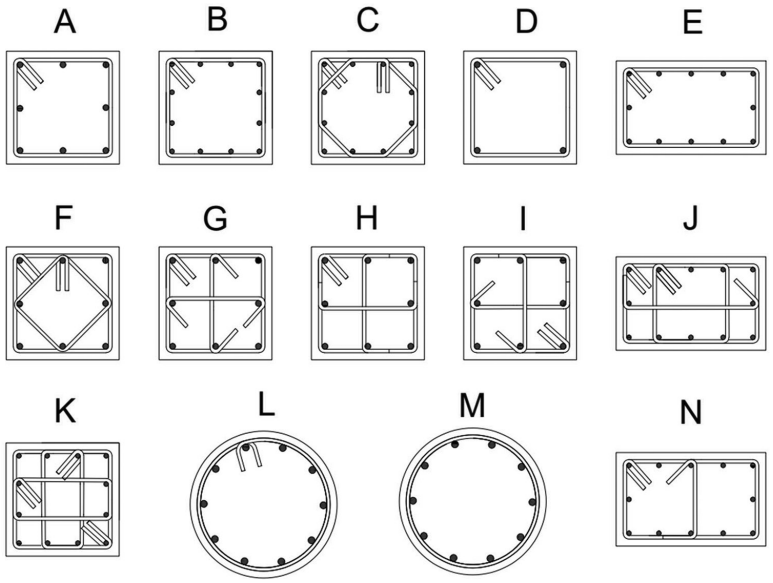

Fig. 1—Configuration of longitudinal and transverse reinforcement of 70 columns in assembled database.

CSA A23.3-14 (2014) and ACI 318-14 (ACI Committee 318 2014) provisions, with cross-sectional dimensions of 8.7 x 8.7 in. (22 x 22 cm), and tested under axial compressive loading. The analysis of the testing included the effect of the transverse reinforcement configuration (only hoops versus hoops with the diamond-shaped hoops) and different volumetric ratios of two different types of UHPC mixtures with strengths of 21.8 and 26.1 ksi (150 and 180 MPa) using hybrid steel fibers composed of 1% of longer 0.8 in. (1.95 cm) fibers and 0.5% of shorter 0.6 in. (1.6 cm) steel fibers. The authors concluded that the inclusion of 1.5% steel fibers prevented premature cover concrete spalling, leading to a proposed strength reduction factor of 0.85, the same as for the NSC. Furthermore, the beneficial effect of steel fibers can partially substitute traditional confining reinforcement at any transverse reinforcement ratio. The authors also concluded that the transverse reinforcement ratio has the most significant effect on the post-peak behavior when compared to its configuration. The quantification of the ductility using the toughness index (T.I.) was proposed, along with the axial load-strain behavior, taking into consideration the benefits of steel fibers on postponing concrete spalling, resulting in increased ductility and toughness.

Sugano et al. (2007) investigated the behavior of nine 23.2 in. (59 cm) tall UHPC columns with a cross-sectional area of 7.9 x 7.9 in. (20 x 20 cm) confined by high- and ultra-high-strength lateral reinforcement with a yield strength of 101.5 and 203 ksi (700 and 1400 MPa), respectively. The authors concluded that the strength of the confined core increases with the increase in the amount of lateral reinforcement. They proposed empirical equations for the compressive ductility and the ratio of the strength of core concrete and standard cylinder strength. However, it is noted that the present study considers only columns reinforced by 101.5 ksi (700 MPa) lateral reinforcement because the ultra-high lateral reinforcement confinement effect is not common and is beyond the scope of this paper.

The key attributes of the reviewed columns are summarized in Table 1, which, in turn, refers to the illustrations in Fig. 1 for all longitudinal and transverse reinforcement configurations of square, rectangular, and circular columns used in this study. As such, Table 1 presents the following data: reinforcement configuration, gross area (A_{gross}), steel fiber volumetric ratio (*SF*), longitudinal reinforcement size, area ratio, and nominal and actual yielding (size, ρ_l,f_y actual, and f_y nominal), transverse reinforcement size, spacing, volumetric ratio, nominal and actual yielding, and the spacing-to-longitudinal reinforcing bar diameter ratio (size, ρ_t,f_y actual, f_y nominal, and s/d_b). Also, the readers are referred to the ACI project final report by Cimesa et al. (2023) for more detailed information in terms of axial strain and load capacities and strain in longitudinal and transverse reinforcement of the columns from the University of Nevada, Reno used in this study.

Circular columns

Cimesa et al. (2023) constructed four 9 ft (2.74 m) tall circular columns at a precast construction yard in California to demonstrate a more economical and seamless production process of large-scale mixing using construction-scale equipment, such as pan and truck mixers with a capacity of 5 and 8.5 yd^3 (3.8 and 6.5 m^3), respectively. All of the columns included 2% steel fibers by volume and semi-proprietary mixtures similar to the authors' previous work on square Type C columns discussed earlier. Two out of the four circular columns were spirally confined with the spacing of 1.5 and 3 in. (3.8 and 7.6 cm), while the other two were confined with individual hoops also spaced at 1.5 and 3 in. (3.8 and 7.6 cm). The authors concluded that the two closely spaced columns with hoops and spirals had almost the same axial capacity, while the ductility of the spirally reinforced columns was 26% higher than the circular hoop-confined column. In a non-seismic region, columns with closely spaced hoops would be preferable to the closely spaced spirals due to the ease of construction. Similar to

the research study by Aboukifa and Moustafa (2022a), this study also proposed a strength reduction factor of 0.75 when nominal properties are incorporated into the equation of the axial capacity.

One year after publishing their work on 35.4 in. (90 cm) tall square columns, Shin et al. (2018) constructed and tested another four small-scale (diameter of 9.8 in. [25 cm]) and two structural-scale (diameter of 13.4 in. [340 mm]) UHPC circular columns spirally confined. As in their work reviewed previously, 1.5% hybrid fibers were used for all six circular columns, using two different concrete types with different strengths. The investigation of the structural behavior under axial compressive loading was made based on the effect of spiral ratio, two UHPCs with different strengths, and the presence of hybrid steel fibers. Both CSA A23.3-14 and ACI 318-14 provisions were evaluated against the structural behavior of six circular columns. It was concluded that circular columns had superior behavior compared to the square columns confined by hoops tested and evaluated in their previous study (Shin et al. 2017), but the shape of the columns does not have any effect on the cover spalling. Also, they reconfirmed that more transverse reinforcement is needed for the UHPC columns than for NSC due to the reduced performance of transverse reinforcement in confining ultra-high-strength concrete, the same as the old classical statement by Richart et al. (1929). Furthermore, the authors concluded that the amount of transverse reinforcement has a more profound effect on post-peak response than the closely spaced spirals. When the actual performance of the columns is compared to the design requirements found in CSA A23.3-14 and ACI 318-14 provisions, it was concluded that both of the provisions have a conservative approach to the detailing of the circular columns. The authors proposed the design recommendation for spiral reinforcement, taking into consideration the ductility requirement for the moderate seismic region using the confinement effectiveness coefficient K_e.

The circular columns included in the database are also conveniently illustrated in Fig. 1, and their design attributes are summarized in Table 1. Overall, this section, while introducing the selected database columns, also shows that not all individual studies provide similar conclusions or design recommendations. Hence, a comprehensive study such as the one in hand, which collects all this data and analyzes it together while eying generalization and normalized trends and incorporating data from new and emerging UHPC types, is timely and could be of great interest to the UHPC code-developing communities as they lay the foundation for future UHPC structures.

DESIGN OF AXIAL UHPC COLUMNS: NEW DEVELOPMENTS AND DISCUSSION OF SAFETY MARGINS

This section is concerned with the first objective of the study, which is revisiting the ACI 318 procedure for axial column strength capacity. An overview of the design equations is presented first, followed by the discussion of the α and margins of safety data for a subset of the database—that is, not all 70 columns are considered here because some columns were very short and over-confined because of the test setup and boundary conditions. Such columns are more appropriate for investigating reinforcement trends but not design capacity generalization. As shown later in this section, the ACI 318 cylinder strength correction or reduction factor, referred to as α or the α factor from this point onwards, is estimated using two different approaches.

Overview of ACI axial design equations

The current ACI 318-19 provisions for the axial design strength of NSC columns define different levels or values of the axial strength for design calculations: nominal axial strength with no eccentricity effect (P_o), nominal axial strength (P_n), and maximum nominal axial strength ($P_{n,max}$) where the nominal axial strength is multiplied by 0.85 for spirals and 0.80 for rectilinear hoops or circular hoops to account for accidental eccentricity effects or construction errors. It is noted in ACI 318-19 that nominal axial strength (P_n) should not exceed maximum nominal axial strength ($P_{n,max}$). In addition to the eccentricity adjustment, there is the main reduction factor, popularly known as the Ø factor, which is taken as 0.65 for columns with rectilinear or circular hoops and 0.75 for columns with spiral reinforcement. As such, the design strength is notated as $ØP_{n,max}$. For convenience and completeness, Eq. (1) through (3) provide the ACI procedure for estimating P_n, $P_{n,max}$, and $ØP_{n,max}$, respectively. The equations use values of gross area (A_{gross}), cylinder strength (f_c'), area of longitudinal steel (A_{st}), and yielding of longitudinal reinforcing bar that is limited to 80 ksi (550 MPa)

$$P_o = \alpha f_c'(A_{gross} - A_{st}) + f_y A_{st} \quad (1)$$

where α is the cylinder strength reduction or correction factor and is 0.85 for NSC

$$P_{n,max} = 0.80P_o \text{ (rectilinear and circular hoops)}$$
$$P_{n,max} = 0.85P_o \quad (2)$$

$$ØP_{n,max} = 0.65P_{n,max} \text{ (rectilinear and circular hoops)}$$
$$ØP_{n,max} = 0.65P_{n,max} \text{ (spirals)} \quad (3)$$

Previous research, as shown in the previous section, renders such equations as not necessarily appropriate for UHPC columns, especially for the α factor, which is carefully revisited next.

Revisited strength reduction factor α for UHPC columns

Two approaches are considered to back-calculate the α factor using the selected columns' test results from the database. The first approach is to use the maximum load capacity of the column that was obtained experimentally from the tests along with actual material properties, which can return α values suitable for actual capacity estimation if needed for research purposes. The second approach is the practical one that back-calculates α using actual load capacity obtained from tests as reference capacity, but combines it with the nominal/specified characteristics of both UHPC and steel, which is what is typically used for design. Table 2 shows

Table 2—Calculations of α factor and margins of safety based on α = 0.75 in ACI design equation as applied to subset of column database found in literature

Reference study and column ID		A_{gross}, cm^2	A_{steel}, cm^2	f_y actual, MPa	f_c' test day, MPa	f_y nominal, MPa	f_c' nominal, MPa	P_{max}, kN	α_{actual}	α_{design}	P_o, kN	$P_{max}/\varnothing P_{n,max}$
Cimesa et al. (2023)	1	979	16	490	161	414	138	8954	0.64	0.77	10,618	1.97
	2	934	16	490	163	414	138	10,627	0.53	0.62	10,160	1.62
	3	907	16	490	163	414	138	9364	0.66	0.79	9880	2.01
	4	928	16	490	163	414	138	8469	0.59	0.71	10,097	1.82
	5	1101	15	483	170	414	152	7989	0.52	0.62	12,984	1.61
	6	1054	15	483	170	414	152	11,134	0.39	0.45	12,451	1.18
	7	1088	15	483	170	414	152	9724	0.59	0.67	12,846	1.72
	8	1083	15	483	170	414	152	12,322	0.49	0.56	12,789	1.46
	9	957	16	490	170	414	152	11,516	0.64	0.72	11,370	1.85
	10	922	16	490	119	414	152	7219	0.67	0.76	10,965	1.95
	11	990	16	490	150	414	138	9501	0.60	0.48	10,734	1.27
	12	948	15	483	150	414	138	7224	0.60	0.66	10,289	1.70
	13	981	15	483	150	414	138	10,302	0.46	0.51	10,631	1.35
	14	1019	15	483	150	414	138	9319	0.66	0.73	11,018	1.86
	15	965	15	483	150	414	138	7753	0.57	0.63	10,458	1.63
	16	781	16	459	177	414	165	11,410	0.49	0.54	10,151	1.43
Aboukifa and Moustafa (2022a)	17	781	16	459	201	414	165	11,312	0.79	0.85	10,151	2.16
	18	781	16	461	191	414	165	11,645	0.69	0.84	10,151	2.14
	19	781	16	447	192	414	165	11,886	0.75	0.87	10,151	2.21
	20	781	16	459	178	414	165	11,201	0.76	0.89	10,151	2.25
	21	400	25	700	155	700	155	6517	0.77	0.83	6090	2.12
Empelmann et al. (2008)	22	400	49	700	155	700	155	7357	0.82	0.82	7526	2.06
	23	400	6	500	155	500	155	5614	0.72	0.72	4884	1.88
	24	400	25	700	155	700	155	6058	0.87	0.87	6090	2.21
	25	400	25	700	155	700	155	6223	0.74	0.74	6090	1.91
	26	400	25	700	160	700	160	7224	0.77	0.77	6228	1.97
	28	400	22	870	155	870	155	5778	0.92	0.92	6312	2.23
	29	1225	41	509	118	420	116	11,752	0.66	0.66	12,015	1.76
Hung and Yen (2021)	38	1225	41	509	123	420	116	13,118	0.69	0.73	12,015	1.88
	39	1225	41	509	115	420	116	10,369	0.76	0.83	12,015	2.10
	40	1225	41	509	122	420	116	10,640	0.61	0.63	12,015	1.66
	41	1225	41	509	113	420	116	12,010	0.59	0.65	12,015	1.70
	42	1225	41	509	115	420	116	11,828	0.74	0.75	12,015	1.92
	43	1225	41	509	108	420	116	10,111	0.72	0.74	12,015	1.89
	44	1225	41	509	112	420	116	9826	0.63	0.61	12,015	1.62
	45	1225	41	509	119	420	116	11,499	0.58	0.59	12,015	1.57
	46	1225	41	509	118	420	116	11,427	0.67	0.71	12,015	1.84
	47	1297	28	443	141	414	138	14,937	0.67	0.71	14,292	1.83
Cimesa et al. (2023)	61	1297	28	443	141	414	138	15,386	0.76	0.79	14,292	1.64
	62	1297	28	443	141	414	138	13,563	0.79	0.81	14,292	1.69
	63	1297	28	443	141	414	138	15,386	0.69	0.71	14,292	1.82
	64	625	16	575	181	500	180	8496	0.79	0.81	9021	2.07

Table 2 (cont.)—Calculations of α factor and margins of safety based on α = 0.75 in ACI design equation as applied to subset of column database found in literature

Reference study and column ID		A_{gross}, cm^2	A_{steel}, cm^2	f_y actual, MPa	f_c' test day, MPa	f_y nominal, MPa	f_c' nominal, MPa	P_{max}, kN	α_{actual}	α_{design}	P_o, kN	$P_{max}/ØP_{n,max}$
Shin et al. (2018)	65	625	16	575	163	500	150	7793	0.69	0.70	7651	1.48
	66	625	16	575	181	500	180	8750	0.69	0.77	9021	1.60
	67	625	16	575	163	500	150	7962	0.71	0.73	7651	1.52
	68	1225	31	490	181	431	180	16,414	0.71	0.78	17,455	1.63
	69	1225	31	490	163	431	150	14,986	0.69	0.70	14,768	1.48
	70	979	16	490	161	414	138	8954	0.69	0.76	10,618	1.59
								Mean	0.67	0.72	—	1.79
								Median	0.69	0.73	—	1.82

Note: 1 MPa = 0.145 ksi; 1 kN = 0.225 kip.

the calculated α factor values when both approaches are employed for a subset of 48 columns out of the 70 in the full database. Only 48 columns were used in the α calculations here, and margins of safety in the next section, for the reasons explained before.

The α strength reduction factor is used in a nominal axial strength calculation to account for any uncertainty in loading, material properties, construction practices, and so on. For NSC, the practice is to use an α value of 0.85, which means that 85% of cylinder strength should be accounted for when calculating the axial strength of the axial structural element. However, UHPC material properties are significantly different than NSC, mostly due to the inclusion of steel fibers and the exclusion of coarse aggregates. Therefore, future guidelines, standards, and codes must consider a UHPC-sensible α strength reduction factor value, which can use empirical methods as presented herein. Table 2 shows the back-calculation of the two strength reduction factor values based on the implementation of the actual or nominal values into the equation for P_o. The value of α actual was back-calculated using the maximum load capacity of the column, along with the actual material properties based on cylinders tested on the same day as columns and steel stress values extracted from actual reinforcing bar coupons stress-strain using the average measured strains in longitudinal bars at failure. The α design was back-calculated based on the maximum load capacity of the column and the nominal values of longitudinal yield strength (that is, 60 ksi [414 MPa] for Grade 60) and typical UHPC 28-day strength as proposed by UHPC vendors (which ranges from 20 to 22 ksi [137.9 to 151.7 MPa] for most of the currently available UHPC mixtures in the market).

As shown in Table 2, the mean and median values of the strength reduction factor α calculated for all 48 columns based on the actual material properties are 0.67 and 0.69, respectively. This value is on average obtained from all square, rectangular, and circular columns. Such a range of α values is not really of any benefit to the design process, especially as it assumes that the actual steel or concrete stress at failure is uniform across the entire column or structural member, which is not true. As such, this value is reported here only for academic purposes and future references if needed.

For design purposes, the mean and median values for α based on the nominal material properties are shown in Table 2 to be 0.72 and 0.73, respectively. These averages are estimated from 48 values based on the selected 48 columns, so for completeness, a histogram of the distribution of all 48 back-calculated α design values is provided in Fig. 2. The histogram shows the larger common number of repetitions for α based on the specific data ranges is 0.75. In light of this analysis, and for the sake of a well-rounded number that also agrees with previous research, this research recommends employing a strength reduction factor (α factor) of 0.75 for UHPC in axial design equations. The lower value, 0.75, as opposed to the standard 0.85 for NSC, could be attributed to the relative effect of steel fibers, which is more pronounced in cylinders than when combined with traditional lateral reinforcement in the structural elements, leading to a larger variation in the strength between cylinders and columns than in NSC with no steel fibers effects.

Margins of safety using proposed design equation

After confirming the α factor of 0.75 for UHPC, the ACI equations were adopted for the 48 columns used before to calculate design capacities, as shown also in Table 2. The table presents calculations of the values for $ØP_{n,max}$ when the proposed α factor is 0.75, and nominal properties of UHPC and steel (also listed in the table) are taken into consideration. To access each column's margin of safety, the maximum axial load of the column obtained from the tests is divided by the design value calculated using Eq. (3) to obtain the ratio $P_{max}/ØP_{n,max}$. As can be noticed from Table 2, the mean and median estimates for such margin of safety for UHPC columns are 1.79 and 1.82, respectively. Similar to what is presented for the α factor, a histogram of the distribution of the 48 margin of safety values is plotted and presented in Fig. 3, showing 1.93 as the value at the interface of the two most obtained value ranges. In general, it is beneficial to get a sense of the margin of safety in UHPC-designed columns, and an average margin of safety of 1.8 or 1.9 seems reasonable. However, such a margin of safety is highly dependent on all the layers of safety embedded in the design equations, such as the accidental eccentricity and ϕ factors. As such, the calculated values in Table 2 are presented to the community to call for future research to assess whether it is reasonable to

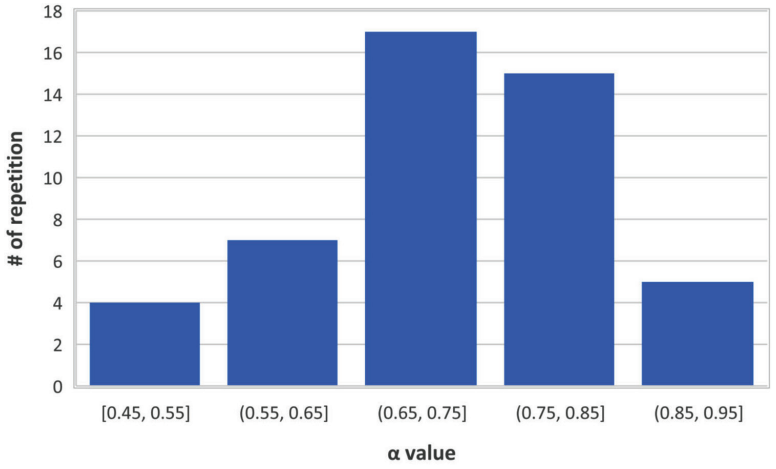

Fig. 2—Histogram for distribution of α *factor values when calculated using nominal design values.*

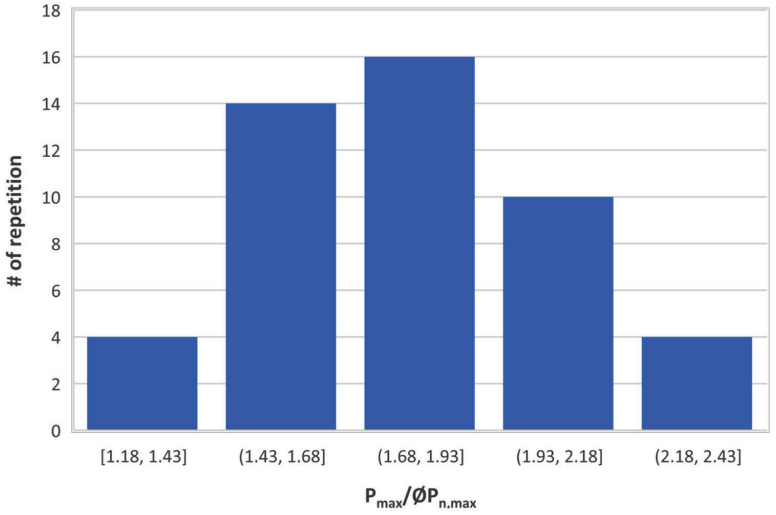

Fig. 3—Histogram for distribution of margin of safety in axial load capacity based on ACI axial design capacity estimation using α *factor of 0.75.*

continue to use current ACI 318 factors of safety for UHPC or whether dedicated factors are needed for UHPC for better balance between design economy and use of the material.

EFFECT OF TRANSVERSE REINFORCEMENT ON AXIAL CAPACITY

This section is mainly concerned with the effect of the volumetric lateral reinforcement ratio (ρ_t volume) and the transverse reinforcement spacing-to-longitudinal reinforcing bar diameter ratio (s/d_b) on the axial load capacity. The discussion is divided based on the cross-sectional shape, where square and rectangular-shaped columns are analyzed separately from the circular columns.

Effect of volumetric lateral reinforcement ratio

In this study, only the volumetric reinforcement ratio was considered due to the more precise and straightforward estimation when compared to the area ratio when additional octagonal or diamond shapes are considered for transverse reinforcement (for example, configurations C and F in Fig. 1). Equation (4) illustrates how the calculation of the volumetric reinforcement ratio is done, where *b* and *d* values are taken as the dimension from the outside to the outside of the lateral reinforcement, perpendicular to each other; *Perimeter* represents the lateral reinforcement perimeter; A_{steel} is the area of the steel bar; and *s* is a longitudinal spacing of the lateral reinforcement measured from the center-to-center of the bars, as presented in Fig. 4. The schematic illustration of the dimensions shown in Fig. 4 is also applicable for the calculation of the area or volumetric reinforcement ratio for the circular hoops and spirals due to the same philosophy. In the case of the addition of the rectangular hoop, such as in configurations J and K in Fig. 1, and octagonal and diamond-shaped lateral reinforcement, represented as configurations C and F, *b* and *d* would be the dimensions of the two perpendicular dimensions of rectangular, octagonal, and diamond-shaped hoops. In the case of the circular columns, the area and volumetric calculations are the same and are calculated according to Eq. (5), where *D* represents the diameter of the spiral or rectangular hoop, and *s* is the spacing in between.

In this study, all the reinforcement ratios reported in the respective source studies of the literature used in the database were recalculated again for all 70 columns using Eq. (4) and (5) to ensure consistent calculations across all the presented

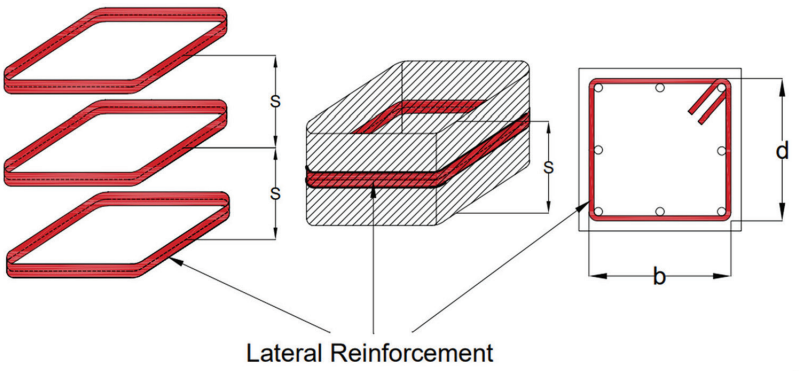

Fig. 4—Illustration of center-to-center spacing of rectilinear hoops, which is also applicable to circular columns and spiral pitch.

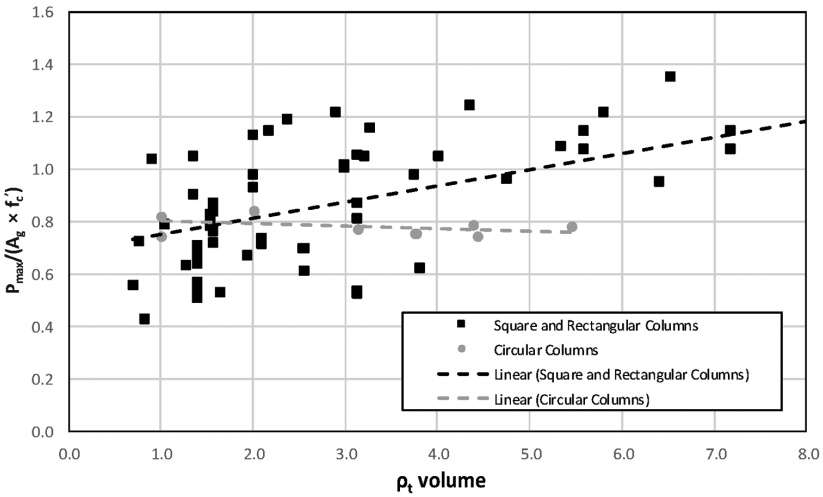

Fig. 5—Correlation between lateral reinforcement ratio (ρ_t volume) and normalized axial strength for square and rectangular columns set and circular columns set.

data and trends. The summary of the volumetric transverse reinforcement ratio is presented in Table 1.

$$\rho_{t\text{-square and rectangular}} = \frac{Perimeter\ A_{st}}{sbd} \quad (4)$$

$$\rho_{t\text{-circular}} = \frac{4A_{st}}{sD} \quad (5)$$

To explore the effect of the amount of the transverse reinforcement, as represented by ρ_t, a correlation with a normalized axial load capacity is sought. The lateral reinforcement ratios, calculated using Eq. (4) and (5), are plotted on the x-axis of the graph shown in Fig. 5. The y-axis represents the normalized axial capacity of all 70 columns, calculated by dividing the maximum axial load of a given column by the product of its cross-sectional gross area and the cylinder strength on the day of column testing. A linear regression trendline is fitted to the data and shown in the figure to help capture and explain new behavior trends. For square and rectangular columns, Fig. 5 suggests the general trend that as the reinforcement ratio increases, the axial capacity also increases. However, this trend is very general and does not necessarily help provide any specific detailing or reinforcement limit guidance. Accordingly, the data are investigated in different ways that split the data pairs into regions set by some reinforcement limit, as shown in Fig. 6 and 7.

Figure 6 aims to find whether there is a cutoff limit for ρ_t at which the behavior significantly changes. Several trial values ranging from ρ_t = 1 to 3% were used to split the data into groups of less than or greater than a defined limit, and at approximately ρ_t = 2%, an interesting change in the trendline slopes before and after this value is observed. For demonstration purposes, Fig. 6 shows this split and the two-grouping approach for four different ρ_t limits of 1.6%, 1.8%, 2.0%, and 2.2%. Notably, 2% serves as a crucial transition point between the empirical data sets, distinguishing lower reinforcement ratios below 2% from those exceeding 2%. This differentiation is vital, as for generalized design guidance, this limit can signify the limit between an unacceptable and the minimum acceptable reinforcement ratio and can render the 2% as the minimum recommended ρ_t for the design of UHPC columns.

Building off the 2% limit, the experimental data are used to further categorize columns into four distinct regions, as shown in Fig. 7, where each region offers new and practical insights for future UHPC column design. The first region spans from ρ_t = 0 to 2%. This range is chosen to be deemed unacceptable for UHPC column design due to the high variation and predominantly lower values of the column capacity, as indicated by the steep trendline, which renders a poor underuse of the UHPC mechanical capabilities.

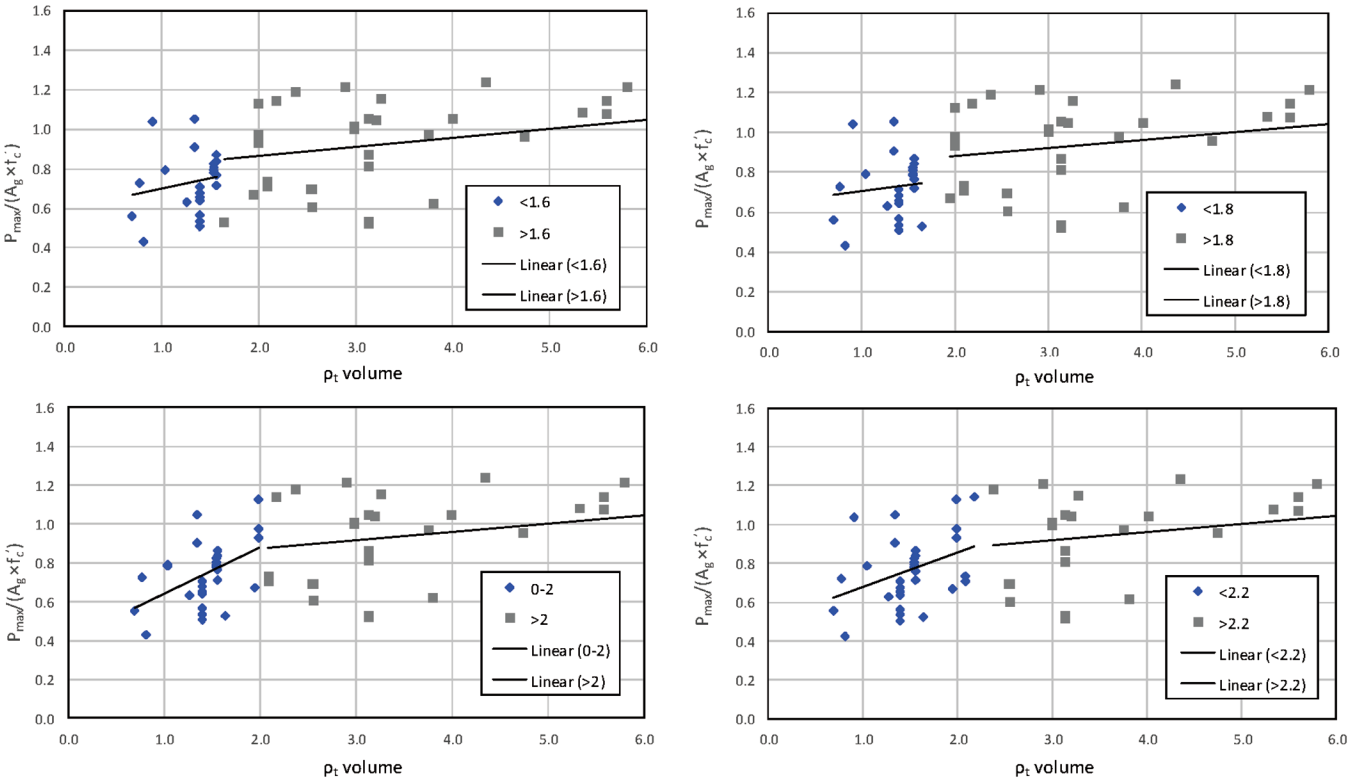

Fig. 6—Correlation between lateral reinforcement ratio when data trends are split at ρ_t values of 1.6, 1.8, 2, and 2.2% and normalized axial strength.

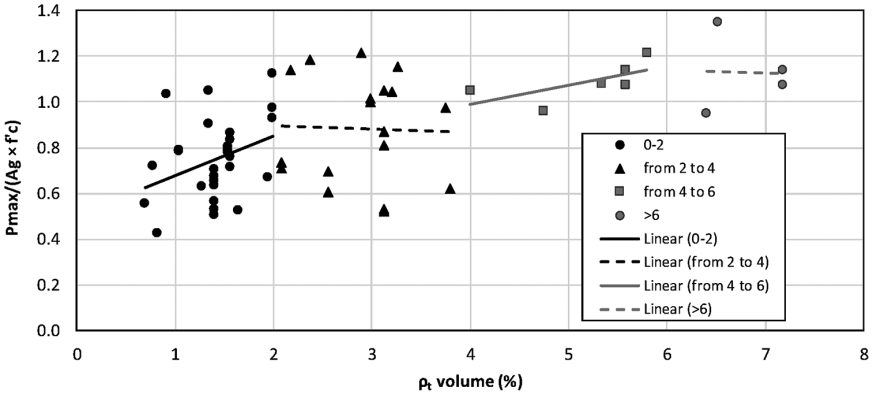

Fig. 7—Correlation between lateral reinforcement ratio and normalized axial strength when data are divided over four regions based on ρ_t values noted in legend.

The second region, from 2 to 4% of lateral reinforcement, represented with an almost flat trendline, represents the region that is acceptable for the design of the column, where just the nominal or specified cylinder strength can be considered the same as the confined core strength. In other words, there is no need to calculate a confined UHPC compressive strength value, as ρ_t of 2 to 4% is just sufficient confinement for UHPC compressive strength to be adequately used but not enhanced. In the case of the first design philosophy that was described in an earlier section, which emphasizes the economic side of using UHPC, the second region using ρ_t of 2 to 4% should be considered when reinforcement material and labor costs can be slightly saved to reduce overall cost and, with that, extract moderate behavior from moderately confined UHPC columns.

The third region, from 4 to 6%, is a region appropriate for the second design philosophy, with an emphasis on extracting the most out of confined UHPC columns. The ascended trendline shows the positive change using a higher reinforcement ratio and the capacity of the column when compared to the second region. As previously mentioned, the strength of UHPC calls for a higher reinforcement ratio than NSC if the same confinement effectiveness is desired, based on classical as well as new research (Richart et al. 1929; Shin et al. 2017, 2018). This region should be the main focus of column design, for example, in high-seismic regions, to secure ductile column behavior and use the significant strength of the confined UHPC. An important characteristic of this region of the behavior is that if ρ_t of 4 to 6% is used, the confined core strength value should be taken into consideration, replacing the unconfined cylinder

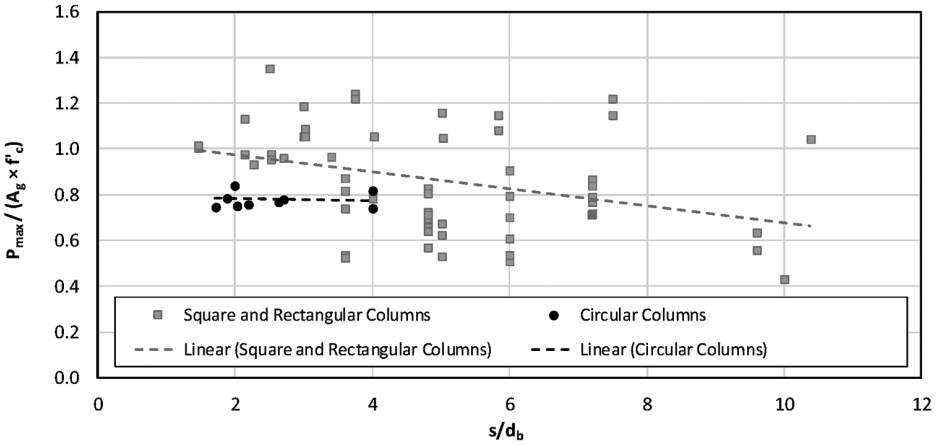

Fig. 8—Correlation between s/d_b *and normalized axial strength for square and rectangular columns set and circular columns set.*

strength value in the axial design equations with a proper value. UHPC confinement models are beyond the scope of this work; however, future research is highly recommended to develop generalized and UHPC sensible confinement models to use when higher confinement reinforcement is considered in design.

Finally, the fourth region, which is limited to 8% for a better-contained view of the data, and starts at the minimal reinforcement ratio of 6%, shows that there are no additional benefits for the extra reinforcement beyond 6%, and as such, it is discouraged to target this behavior region for the design of UHPC columns. This is again because the flat trendline emphasizes that an unnecessary high reinforcement ratio would not enhance the axial load capacity of the columns.

All the previous discussions are relevant to square and rectangular columns because, as seen from the first collective behavior trends plots in Fig. 5, circular columns are less sensitive to lateral reinforcement detailing than square and rectangular columns. This implies that the confined core strength does not have to be taken into consideration, and a proposed minimum lateral reinforcement ratio can be used. The trendline is almost flat, implying that with the increase in the volumetric reinforcement ratio, there is no increase in the load capacity. Furthermore, for the points of the lower reinforcement ratio, it can be assumed that circular columns are using the full potential of the steel fibers and their interaction with lateral reinforcement, keeping the load capacity at the same level as the columns with the higher lateral ratio. However, it is worth noting that these conclusions were drawn based only on two research studies of 10 circular columns total, where eight had spiral lateral reinforcement, and two had circular hoops. Therefore, more experimental data sets are needed to support the conclusions of this recommendation for circular columns or spiral reinforcement.

Effect of spacing-to-longitudinal reinforcing bar diameter ratio (s/d_b)

Similar to the correlations established before between normalized axial capacity and transverse reinforcement ratio, Fig. 8 depicts the same but for the correlation of the s/d_b used in the columns. As can be noticed, the empirical trendline descends from the left to the right, which means that the capacity declines with the increase in the spacing, or using smaller-diameter longitudinal bars when keeping the spacing constant. ACI 318-19 proposes the mentioned ratio to be less than or equal to 6 for NSC in seismic columns. However, from Fig. 8, it can be noted that even when this ratio exceeds the value of 6, the load capacity does not significantly decline until s/d_b exceeds 8 or so. Therefore, the spacing and longitudinal bar diameter ratio limit can be relaxed to 8 instead of 6, according to the very approximate empirical trends of the square and rectangular columns data set. On the other hand, the scattered data points show the highest load capacity can be achieved when this ratio is between 2 and 4, as can be seen in Fig. 8, but this can be unpractical for UHPC columns with the desired uniform steel fiber dispersion.

Similar to the correlation presented in Fig. 5, the correlation in Fig. 8 for the circular columns has almost the same trend. The trendline is flat, implying that a change in the ratio of spacing and longitudinal reinforcement ratio going from 2 to 4 almost does not have an impact on the load capacity. Therefore, circular columns are less sensitive to the detailing of the transverse reinforcement when compared to square and rectangular columns, which is a similar conclusion to one already made for the lateral reinforcement ratio. However, more empirical data sets are needed to support this conclusion.

CONFINEMENT ANALYSIS FOR CONFINEMENT PURPOSES

In this section, all 70 columns' data are used again, in light of some of the uncovered trends the previous section plotted, to take a deeper look at confinement considerations in terms of the correlation between the axial load and confining stress, the range of ρ_t that should require additional confinement calculations, and the interplay between the confinement contribution of the steel fibers and traditional transverse reinforcement.

Correlation between confining stress and normalized axial capacity

The correlation between the confining stress, as estimated in the transverse reinforcement, and the normalized axial load capacity is calculated for all 70 columns combined and presented in Fig. 9. The confining stress of the lateral reinforcement with a nominal yield strength of 60 to 80 ksi (415 to 550 MPa) is calculated as a product of the minimum lateral

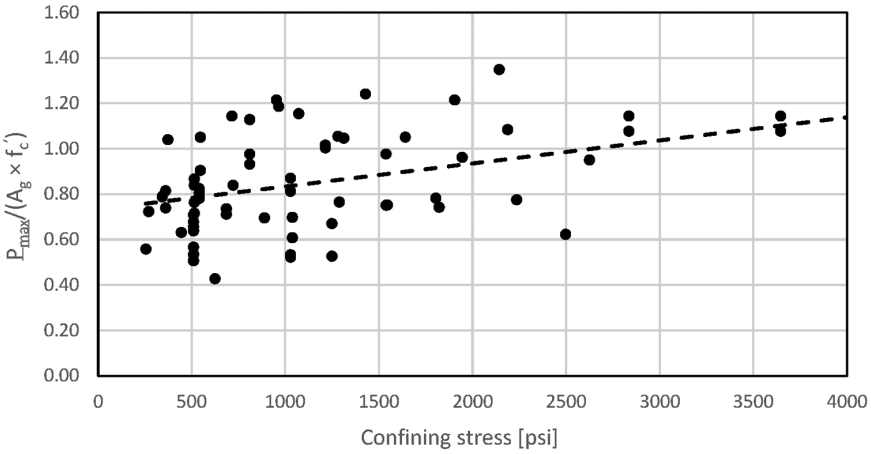

Fig. 9—Correlation between confining stress provided by lateral reinforcement and normalized load capacity for all 70 columns' data combined.

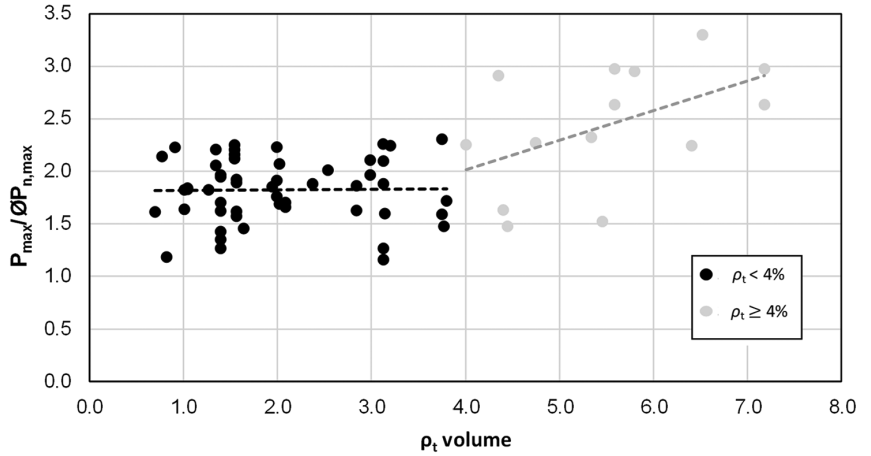

Fig. 10—Correlation between lateral transverse reinforcement ratio and respective margin of safety in axial load capacity estimation when data are split over two regions: less than or greater than ρ_t of 4%.

volumetric reinforcement ratio of one of the two directions of square and rectangular columns multiplied by the actual lateral reinforcement yield strength and is taken as the x-axis values for Fig. 9. The figure shows again the general trend that more confining stress can increase the UHPC columns' axial capacity, and this time, the data from circular, square, and rectangular columns, as well as columns with high-strength steel confinement, are all blended in this trend. The figure suggests that the actual confining stress for the majority of the data points is only a fraction of the overall UHPC compressive strength, which explains why not too much confinement effect can be manifested for the regular 2 to 4% reinforcement ratio, as explained earlier.

In another attempt to identify when, or for what range of ρ_t, the confinement effects need to be accounted for in terms of calculated confined UHPC strength, Fig. 10 shows a different way of correlation between the ρ_t lateral reinforcement ratio and the estimated margin of safety for each column ($P_{max}/ØP_{n,max}$). The data are split at ρ_t = 4%, which is the minimum value at which confinement needs to be accounted for, to see whether there is any interesting change in the trendline. If the margin of safety is considered for the correlation, unlike the normalized load capacity, a certain level or account of safety, as embedded in the ACI equations, should be prevalent in the trendline independent of ρ_t values. This is exactly what can be seen for $\rho_t < 4\%$, where almost the average 1.8 margin of safety is represented by the trendline. However, for $\rho_t \geq 4\%$, the trendline rises, which suggests that the design capacity (that is, $ØP_{n,max}$ in the dominator of the margin of safety ratio) is underestimated. For the trendline to stay almost constant, the $ØP_{n,max}$ should return higher values if higher UHPC compressive strength is used, and this is yet more evidence of when the confined UHPC strength needs to be considered—that is, for $\rho_t > 4\%$.

Steel fiber effect

The same data as before in Fig. 5 or 9 are plotted again in Fig. 11 but with a different subgrouping for the data. The goal here is to understand the interplay between the confinement contribution of the steel fibers and traditional transverse reinforcement. As such, the correlation between the lateral reinforcement ratio and normalized axial load capacity is sought for two groups. The first group includes the data from all columns with a 2% or more steel fiber ratio, while the second group is for the columns with a steel fiber ratio of less than 2%. The trendlines of the two data groups

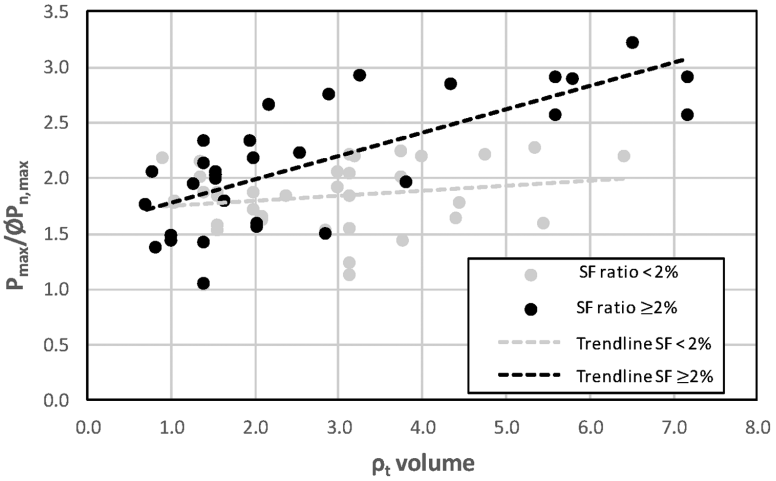

Fig. 11—Correlation between lateral transverse reinforcement ratio and respective margin of safety in axial load capacity estimation when data are split based on steel fiber percentage.

still show the same trend now, which is increased load capacity for higher transverse reinforcement ratio. However, what is new here is that each of the two trendlines has a very different slope, including a much steeper slope for columns with a 2% or more steel fiber ratio compared to the other group with a lower steel fiber ratio. This means that when sufficient steel fibers are provided (that is, at least 2%), the UHPC columns will benefit more and better from the transverse reinforcement and confinement effects. This observation, based on the empirical trends here, confirms the benefits of steel fibers in UHPC, where a higher percentage of the steel fibers assists in confining the concrete by bridging the microcracks and preventing their further propagation of the cover and core concrete. Furthermore, this bridging effect postpones the spalling of the cover concrete and final failure, leading to improved structural behavior. Naeimi and Moustafa (2021) concluded that on the material level, there is no need for more than 4% inclusion of the steel fibers due to the significant increase in the cost of the material for almost no change in the mechanical properties of the UHPC cylinders.

RECOMMENDATIONS AND CONCLUDING REMARKS

This research study provides new ways of looking at an exclusive database of 70 structural ultra-high-performance concrete (UHPC) column tests that was assembled to develop generalized design and detailing guidelines for axial UHPC columns. The following recommendations and concluding remarks are made based on the empirical data analysis and trends presented in this paper:

- The strength reduction factor (α) for applying the ACI 318 axial strength design equation is revisited, and a value of 0.75 is proposed to use for UHPC columns as opposed to the 0.85 value that is appropriate only for normal-strength concrete (NSC).
- The average margin of safety for axial UHPC columns stands at 1.8 to 1.9. This seems to be reasonable for structural design and confirms that the current ACI 318 factors of safety embedded in the design equations are appropriate to use for UHPC. However, future research is invited to look into dedicated factors of safety for UHPC if a better balance between design economy and use of the material is desired.
- A minimum volumetric transverse reinforcement ratio (ρ_t) of 2% is recommended for axial UHPC columns, and up to ρ_t of 4%, the unconfined nominal UHPC compressive strength as obtained from cylinders can be used in the design equations. Only when a higher transverse reinforcement ratio of 4 to 6% is used should the confined UHPC strength be estimated and used in the axial design equation. Moreover, no more than ρ_t of 6% should be used in UHPC columns as no additional benefits on axial load capacity or performance are gained.
- Circular columns are less sensitive to lateral reinforcement detailing than square and rectangular columns. This implies that the confined core strength does not have to be taken into consideration, and a proposed minimum lateral reinforcement ratio can be used (from 2 to 4%) for circular columns.
- The spacing-to-longitudinal reinforcing bar diameter ratio (s/d_b) should not exceed 8, which is slightly relaxed relative to the limiting value of 6 required for ductile NSC columns.
- With the increase in the steel fiber content, UHPC benefits more from traditional transverse reinforcement confinement. As such, UHPC mixtures should not use less than 2% of steel fiber by volume when used in structural axial columns.

AUTHOR BIOS

Milana Cimesa *is a Bridge Engineer at TYLin and recent PhD graduate of the Department of Civil and Environmental Engineering at the University of Nevada, Reno, Reno, NV. She received her Bachelor of Science in Civil Engineering in 2020 and her PhD from the University of Nevada, Reno. Her research interests include ultra-high-performance concrete (UHPC) and its compressive and confinement behavior for bridges and building columns.*

Mohamed A. Moustafa *is an Associate Professor in the Department of Civil and Urban Engineering at New York University Abu Dhabi, Abu Dhabi, UAE, and an Adjunct Professor at the University of Nevada, Reno. He received his MS and PhD in civil and environmental engineering from the University of California (UC), Berkeley, Berkeley, CA, in 2010 and 2014, respectively, as well as a certificate in engineering and business for sustainability from UC Berkeley in 2014.*

NOTATION

A_{gross} = gross cross-sectional area of column
A_{st} = longitudinal reinforcement area
d_b = diameter of reinforcing bar
f_c' = cylinder compressive strength
f_y = steel yield strength
P_n = nominal axial strength
$P_{n,max}$ = maximum nominal axial strength
P_o = nominal axial strength with no eccentricity effect
s = centerline spacing between transverse reinforcement
α = strength reduction or correction factor
ρ_l = longitudinal reinforcement ratio
ρ_t = volumetric transverse reinforcement ratio

REFERENCES

Aboukifa, M., and Moustafa, M. A., 2021, "Experimental Seismic Behavior of Ultra-High Performance Concrete Columns with High Strength Steel Reinforcement," *Engineering Structures*, V. 232, Article No. 111885. doi: 10.1016/j.engstruct.2021.111885

Aboukifa, M., and Moustafa, M. A., 2022a, "Reinforcement Detailing Effects on Axial Behavior of Full-Scale UHPC Columns," *Journal of Building Engineering*, V. 49, Article No. 104064. doi: 10.1016/j.jobe.2022.104064

Aboukifa, M., and Moustafa, M. A., 2022b, "Structural and Buckling Behavior of Full-Scale Slender UHPC Columns," *Engineering Structures*, V. 255, Article No. 113928. doi: 10.1016/j.engstruct.2022.113928

Aboukifa, M.; Moustafa, M. A.; and Itani, A., 2020, "Comparative Structural Response of UHPC and Normal Strength Concrete Columns under Combined Axial and Lateral Cyclic Loading," *Structural Performance of Concrete Columns Incorporating Advanced Materials and Structural Systems*, SP-341, M. A. ElGawady, ed., American Concrete Institute, Farmington Hills, MI, pp. 71-96.

ACI Committee 318, 2014, "Building Code Requirements for Structural Concrete (ACI 318-14) and Commentary (ACI 318R-14)," American Concrete Institute, Farmington Hills, MI, 520 pp.

ACI Committee 318, 2019, "Building Code Requirements for Structural Concrete (ACI 318-19) and Commentary (ACI 318R-19) (Reapproved 2022)," American Concrete Institute, Farmington Hills, MI, 624 pp.

Bajaber, M. A., and Hakeem, I. Y., 2021, "UHPC Evolution, Development, and Utilization in Construction: A Review," *Journal of Materials Research and Technology*, V. 10, pp. 1058-1074. doi: 10.1016/j.jmrt.2020.12.051

Chen, S.; Zhang, R.; Jia, L.-J.; Wang, J.-Y.; and Gu, P., 2018, "Structural Behavior of UHPC Filled Steel Tube Columns under Axial Loading," *Thin-Walled Structures*, V. 130, pp. 550-563. doi: 10.1016/j.tws.2018.06.016

Cimesa, M., and Moustafa, M. A., 2022, "Experimental Characterization and Analytical Assessment of Compressive Behavior of Carbon Nanofibers Enhanced UHPC," *Case Studies in Construction Materials*, V. 17, Article No. e01487. doi: 10.1016/j.cscm.2022.e01487

Cimesa, M., and Moustafa, M. A., 2024, "UHPC Modulus of Elasticity: Assessment and New Developments Using Companion Materials and Structural Data," *Engineering Structures*, V. 310, Article No. 118146. doi: 10.1016/j.engstruct.2024.118146

Cimesa, M.; Romero, A. J.; and Moustafa, M. A., 2023, "Axial Behavior and Transverse Reinforcement Requirements of UHPC Columns with Emerging Mixtures: Assessment of Existing ACI Provisions and New Developments," Final Report submitted to ACI Foundation Concrete Research Council, University of Nevada, Reno, Reno, NV, 73 pp.

CSA A23.3-14, 2014, "Design of Concrete Structures," CSA Group, Toronto, ON, Canada, 297 pp.

Du, J.; Meng, W.; Khayat, K. H.; Bao, Y.; Guo, P.; Lyu, Z.; Abu-Obeidah, A.; Nassif, H.; and Wang, H., 2021, "New Development of Ultra-High-Performance Concrete (UHPC)," *Composites Part B: Engineering*, V. 224, Article No. 109220. doi: 10.1016/j.compositesb.2021.109220

Empelmann, M.; Teutsch, M.; and Steven, G., 2008, "Expanding the Application Range of RC-Columns by the Use of UHPC," *Tailor Made Concrete Structures: New Solutions for Our Society*, J. C. Walraven and D. Stoelhorst, eds., CRC Press, London, UK, pp. 461-468.

Graybeal, B., 2014, "Design and Construction of Field-Cast UHPC Connections," Report No. FHWA-HRT-14-084, Federal Highway Administration, Washington, DC, 36 pp.

Graybeal, B.; Brühwiler, E.; Kim, B.-S.; Toutlemonde, F.; Voo, Y. L.; and Zaghi, A., 2020, "International Perspective on UHPC in Bridge Engineering," *Journal of Bridge Engineering*, ASCE, V. 25, No. 11, p. 04020094. doi: 10.1061/(ASCE)BE.1943-5592.0001630

Haber, Z. B.; De la Varga, I.; Graybeal, B. A.; Nakashoji, B.; and El-Helou, R., 2018, "Properties and Behavior of UHPC-Class Materials," Report No. FHWA-HRT-18-036, Office of Infrastructure Research and Development, Federal Highway Administration, McLean, VA, 170 pp.

Hoang, A. L., and Fehling, E., 2017, "A Review and Analysis of Circular UHPC Filled Steel Tube Columns under Axial Loading," *Structural Engineering and Mechanics*, V. 62, No. 4, pp. 417-430. doi: 10.12989/sem.2017.62.4.417

Hosinieh, M. M.; Aoude, H.; Cook, W. D.; and Mitchell, D., 2015, "Behavior of Ultra-High Performance Fiber Reinforced Concrete Columns under Pure Axial Loading," *Engineering Structures*, V. 99, pp. 388-401. doi: 10.1016/j.engstruct.2015.05.009

Hung, C.-C., and Yen, C.-H., 2021, "Compressive Behavior and Strength Model of Reinforced UHPC Short Columns," *Journal of Building Engineering*, V. 35, Article No. 102103. doi: 10.1016/j.jobe.2020.102103

Hung, C.-C.; El-Tawil, S.; and Chao, S.-H., 2021, "A Review of Developments and Challenges for UHPC in Structural Engineering: Behavior, Analysis, and Design," *Journal of Structural Engineering*, ASCE, V. 147, No. 9, p. 03121001. doi: 10.1061/(ASCE)ST.1943-541X.0003073

Kadhim, M. M. A.; Semendary, A. A.; Hammed, M.; and Cunningham, L. S., 2022, "Numerical Investigation of Hybrid UHPC Columns Subject to Lateral Impact," *Journal of Building Engineering*, V. 47, Article No. 103914. doi: 10.1016/j.jobe.2021.103914

Kang, S. T.; Lee, B. Y.; Kim, J.-K.; and Kim, Y. Y., 2011, "The Effect of Fibre Distribution Characteristics on the Flexural Strength of Steel Fibre-Reinforced Ultra High Strength Concrete," *Construction and Building Materials*, V. 25, No. 5, pp. 2450-2457. doi: 10.1016/j.conbuildmat.2010.11.057

Kasaei, J., and Esmaeili, J., 2016, "Effect of Different Curing Regimes on Strength and Transport Properties of UHPC Containing Recycled Steel Tire Wires as Micro Steel Fibers," *Proceedings of the First International Interactive Symposium on Ultra-High Performance Concrete*, Des Moines, IA, 8 pp.

Kusumawardaningsih, Y.; Fehling, E.; and Ismail, M., 2015, "UHPC Compressive Strength Test Specimens: Cylinder or Cube?" *Procedia Engineering*, V. 125, pp. 1076-1080. doi: 10.1016/j.proeng.2015.11.165

Li, P.; Xu, L.; Abbas, M. A. A. M.; and Ren, Z., 2023, "Material Synergy and Parameter Optimization of Axially-Loaded Circular UHPC-Filled Steel Tubes," *Journal of Constructional Steel Research*, V. 202, Article No. 107772. doi: 10.1016/j.jcsr.2022.107772

Meng, W.; Khayat, K. H.; and Bao, Y., 2018, "Flexural Behaviors of Fiber-Reinforced Polymer Fabric Reinforced Ultra-High-Performance Concrete Panels," *Cement and Concrete Composites*, V. 93, pp. 43-53. doi: 10.1016/j.cemconcomp.2018.06.012

Mirza, S. A., and Lacroix, E. A., 2004, "Comparative Strength Analyses of Concrete-Encased Steel Composite Columns," *Journal of Structural Engineering*, ASCE, V. 130, No. 12, pp. 1941-1953. doi: 10.1061/(ASCE)0733-9445(2004)130:12(1941)

Naeimi, N., and Moustafa, M. A., 2021, "Compressive Behavior and Stress–Strain Relationships of Confined and Unconfined UHPC," *Construction and Building Materials*, V. 272, Article No. 121844. doi: 10.1016/j.conbuildmat.2020.121844

Richart, F. E.; Brandtzæg, A.; and Brown, R. L., 1929, "The Failure of Plain and Spirally Reinforced Concrete in Compression," Bulletin No. 190, University of Illinois Engineering Experiment Station, Urbana, IL, 82 pp.

Russell, H. G., and Graybeal, B. A., 2013, "Ultra-High Performance Concrete: A State-of-the-Art Report for the Bridge Community," Report No. FHWA-HRT-13-060, Office of Infrastructure Research and Development, Federal Highway Administration, McLean, VA, 176 pp.

Shin, H.-O.; Min, K.-H.; and Mitchell, D., 2017, "Confinement of Ultra-High-Performance Fiber Reinforced Concrete Columns," *Composite Structures*, V. 176, pp. 124-142. doi: 10.1016/j.compstruct.2017.05.022

Shin, H.-O.; Min, K.-H.; and Mitchell, D., 2018, "Uniaxial Behavior of Circular Ultra-High-Performance Fiber-Reinforced Concrete Columns Confined by Spiral Reinforcement," *Construction and Building Materials*, V. 168, pp. 379-393. doi: 10.1016/j.conbuildmat.2018.02.073

Sugano, S.; Kimura, H.; and Shirai, K., 2007, "Study of New RC Structures Using Ultra-High-Strength Fiber-Reinforced Concrete (UFC)," *Journal of Advanced Concrete Technology*, V. 5, No. 2, pp. 133-147. doi: 10.3151/jact.5.133

Teng, L.; Huang, H.; Du, J.; and Khayat, K. H., 2021, "Prediction of Fiber Orientation and Flexural Performance of UHPC Based on Suspending Mortar Rheology and Casting Method," *Cement and Concrete Composites*, V. 122, Article No. 104142. doi: 10.1016/j.cemconcomp.2021.104142

Wei, J.; Li, J.; and Wu, C., 2019, "An Experimental and Numerical Study of Reinforced Conventional Concrete and Ultra-High Performance Concrete Columns under Lateral Impact Loads," *Engineering Structures*, V. 201, Article No. 109822. doi: 10.1016/j.engstruct.2019.109822

Yoo, D.-Y.; Oh, T.; and Banthia, N., 2022, "Nanomaterials in Ultra-High-Performance Concrete (UHPC) – A Review," *Cement and Concrete Composites*, V. 134, Article No. 104730. doi: 10.1016/j.cemconcomp.2022.104730

ACI STRUCTURAL JOURNAL TECHNICAL PAPER

Title No. 122-S13

Bond Strength between High-Performance Concrete and 7 mm Non-Pretensioned Plain Steel Wire

by Andrzej Seruga and Marcin Dyba

This paper examines the bond behavior between non-pretensioned plain steel wire and high-performance concrete (HPC). It investigates the effects of embedment length and concrete compressive strength on bond performance for the production of railway sleepers. To determine the performance, pullout concrete specimens reinforced with 7 mm diameter plain steel wire were cast and tested under a uniaxial load. The main test parameters include the embedment length: 40, 80, 120, 240, 330, and 460 mm; and concrete compressive strength: 40, 60, 72, and 88 MPa. The modified pullout test method developed at Cracow University of Technology was used in the experimental investigation.

The study unequivocally demonstrates that the maximum bond stress between HPC and a non-pretensioned plain steel wire with a diameter of 7 mm decreases as the embedment length increases, irrespective of the concrete's compressive strength. Furthermore, it was observed that the average bond stress increases with an increase in the concrete's compressive strength with time. After conducting tests on HPC specimens with compressive strengths ranging from 60 to 88 MPa and embedment lengths ranging from 40 to 120 mm, it was determined that the resulting maximum adhesion bond stress was 2.22 MPa. This was 52% higher than the bond stress found in test pieces made of concrete with f_{cm} = *40 MPa. Additionally, the average residual bond stress was found to be twice that of concrete with a compressive strength of 40 MPa. These findings demonstrate a clear advantage of using HPC in terms of bond stress.*

Keywords: bond behavior; bond stress-slip relationship; high-performance concrete (HPC); plain steel wire; pullout test.

INTRODUCTION

As the railway industry strives for greater efficiency, the use of prestressed concrete sleepers is becoming more widespread in Europe, particularly in Poland. However, many of these concrete ties are cracking long before their intended life spans have been met. In some cases, cracking has been primarily linked to the bond performance of the wires or strands used to reinforce the concrete sleepers.

Prestressing force from the tensioned tendon must be fully introduced into the concrete before the rail load is applied at the rail seat. The rail seat is located approximately 0.5 m from the end of the sleepers (it depends on the design solution). The length required to transfer the prestressing force into the precast concrete element must be less than 0.5 m. If this does not occur, the prestressed concrete railroad sleepers will not have the full design capacity at the time of load application and may also be in danger of cracking.

In the United States, the production of prestressed concrete railroad ties commonly uses low-relaxation steel wires with a diameter of 5.32 mm. However, some manufacturers opt for 9.52 mm diameter low-relaxation steel strands due to cost considerations. It is worth noting that these smaller-diameter strands can also be indented, similar to the 5.32 mm diameter wires.[1]

Since 1995, plain steel low-relaxation wires with a diameter of 7 mm, indented steel low-relaxation wires with a diameter of 7.5 mm, and low-relaxation steel strands with a diameter of 12.9 mm have been used in Poland for the production of prestressed concrete sleepers. An appropriate anchoring system must always be used to ensure the shortest possible prestressing force transmission length that meets the design requirements. For steel wires, buttonhead anchorage should be used. Regardless of the anchorage system, it is essential to ensure proper interaction between the prestressing tendon and the concrete over the entire length of the element to ensure optimum performance of the sleeper under fatigue loading.

BACKGROUND

In the first period of development of prestressed concrete technology, it was thought that, with wire diameters of less than 6 mm and stresses in prestressing steel of 1400 MPa, the use of additional anchorages would be unnecessary. The necessary transfer length was given as 20 wire diameters. This was due to two reasons: 1) the decrease in the wire cross-sectional area-to-circumference ratio with small wire diameters; and 2) the belief that when tension is released, the wires at the ends increase their diameter according to the Poisson's ratio and become wedged in the concrete.

The mechanisms by which forces are transferred between the reinforcement and the surrounding concrete are different for plain and ribbed bars, as well as for strands and prestressing wires. Plain bars and wires must rely on the transfer of forces by adhesion between the concrete and the reinforcement prior to bar slip and by the wedging action of small particles that break away from the concrete surface after slip, also known as sliding friction.[2] The bond of initially prestressed wires is further enhanced by the Hoyer effect.[3-5] As a standard, ACI 318-63[6] was the last to include provisions for the bond of plain bars.

Tests were conducted at the Swiss Federal Laboratories for Materials Science and Technology (Empa) in

ACI Structural Journal, V. 122, No. 1, January 2025.
MS No. S-2023-368.R2, doi: 10.14359/51742145, received May 24, 2024, and reviewed under Institute publication policies.

Switzerland[7] to evaluate the bond between concrete and tendons in pretensioned concrete elements. The test elements were made of high-performance concrete (HPC) with a compressive strength of over 50 MPa and included either smooth or indented wires. The study suggests that tendon slip is influenced by various factors, such as wire diameter, surface nature, and introduced stress. The slip can vary from 0.1 mm to several millimeters, and the length of transmission increases over time due to concrete creep. Nevertheless, this phenomenon stabilizes after 12 months, and the transfer length increases by 1.5 to 2.5 times. It has been observed that the stress exerted on the radial direction at the end of the prestressed concrete element is approximately 80 MPa. The bond stress was found to increase with increasing compressive strength of the concrete, the age of the concrete, increasing stress in the wire, decreasing wire diameter, and the roughness of the steel surface.[8] Furthermore, it has been shown that for dynamic loads, the bond stress is 50 to 80% of the bond stress value for static loads. The sudden release of tension (by cutting or flame cutting) was not acceptable. It was also found that for pretensioned concrete elements with a concrete compressive strength of approximately 45 MPa at the time of release, wire stresses of approximately 1200 MPa, at distances equal to 0.25, 0.50, 0.75, and 1.0 transfer lengths, convey 35 to 45%, 75 to 80%, 90 to 95%, and 100% of the wire stress value, respectively. Table 1 presents the average bond stress (f_b) and transmission length (l_t) values obtained from experimental tests conducted with a pretension of 1200 MPa and a concrete compressive strength of 45 MPa. For initial stress in a wire of 1500 MPa, Roš[7] states for a diameter of ϕ = 1.5 mm, transfer length l_t = 100 to 150 mm; for ϕ = 2 mm, l_t = 200 to 250 mm; and for ϕ = 3 mm, l_t = 350 to 400 mm. The table shows the transmission length values determined experimentally for wires of different diameters. Based on the results of component deformation measurements (indirect transmission length measurement), the average bond stresses for the individual wires were determined. These stresses take into account the Hoyer effect. The results obtained clearly show lower bond stresses for wires with larger diameters. For the wire with the largest diameter of 5 mm, the bond stress was 1 MPa. These results provide a solid foundation for testing 7 mm wires embedded in high-strength concrete elements.

Marshall[9] carried out experimental tests in England on beams with a cross section of 100 x 100 mm and lengths ranging from 100 to 1800 mm. The test elements were made of concrete using aluminous cement with a compressive strength of 80 MPa when tension was released. The prestress was 1100 to 1500 MPa before the tension was released. The stress in the concrete as a result of prestressing was 20 MPa. The transfer length found for 5 mm diameter wire was (125 to 150)ϕ, while for 2 mm diameter wire, it was approximately (60 to 90)ϕ. Based on the measured strains, the bond stress was calculated, which was in the range of 0.7 to 4.9 MPa.

Arnold[1] evaluated the bond performance of 13 different steel wires and strands for prefabricated prestressed concrete railroad sleepers. Further, Momeni[10] conducted and developed similar research. The wires were denoted as "WA" through "WM" and included plain, spiral, chevron, diamond, two-dot, and four-dot indentation types.[11] WA wire was used as a baseline for comparison of wire bond performance. Six ASTM A1081/A1081M-12[12] pullout tests were conducted on each of these wire types, and the obtained pullout values were recorded and averaged. The results are summarized by Gamble.[13] It should be noted that the listed average pullout values were recorded for a wire slip of 2.54 mm, and a special mortar mixture was used to manufacture the test elements. The calculated average maximum bond stress for the plain (smooth) wire was 0.85 MPa at a slip of s = 3.30 mm, with an adhesion stress of 0.75 MPa. During the experimental tests, it was observed that the average compressive strength of the mortar was $f_{c,avecube(mortar)}$ = 31.54 MPa.

Table 1—Average values of bond stress and transmission length for pretension of 1200 MPa and concrete of 45 MPa

Wire type	ϕ, mm	f_b, MPa	l_t, mm	Diameter multiplication factor
Plain round wire	1.5	3.25	140	90 to 95
Plain round wire	2	1.75	340	170
Plain round wire	3	1.25	720	240
Plain round wire	5	1	1500	300

Note: 1 mm = 0.0394 in.; 1 MPa = 0.145 ksi.

To investigate the bond behavior of indented wires in pretensioning, Geßner and Henne[14] realized the experimental investigations on indented wires with very low indentation depths: wires of 7.5, 9.5, and 10.5 mm diameter with indentation depths of 0.15, 0.10, and 0.09 mm, accordingly. Some tests were done with plain wires (7 and 8 mm diameter). Two concrete compositions were used for the tests with concrete compressive strength at a release of 25 and 50 MPa. The edge length of the square specimens was 150 mm. The embedment length was determined to be l_{emb} = 1.5ϕ. The results of the pullout tests demonstrated the fundamental differences between the bond behavior of plain wires, indented wires, and strands. Savic et al.[15] realized the research focused on bond performance between steel and concrete in prestressed concrete ties using different types of steel wire and consistent concrete mixture (f_{ci} = 31.03 and 41.37 MPa). The wire types included plain, spiral, and wire with chevron-shaped indents. All wires used in these tests were Ø5.32 mm diameter. Plain wire indicated very good performance with the largest value of transfer length.

The distribution of bond stress-slip relation (relationship) for plain wire obtained in experimental studies does not correspond to the real conditions encountered at the time of tensioning force release. The maximum bond stress is close to the adhesive stress.

In evaluating the results obtained, it should be emphasized that they only allow the determination of the suitability of a particular type of wire for the production of prestressed concrete elements. Bond stress-slip relationships can be considered representative of the exploitation condition (pullout method), which is information for the manufacturer. Designers of prestressed concrete elements—for example, prestressed concrete railroad sleepers—want to know the

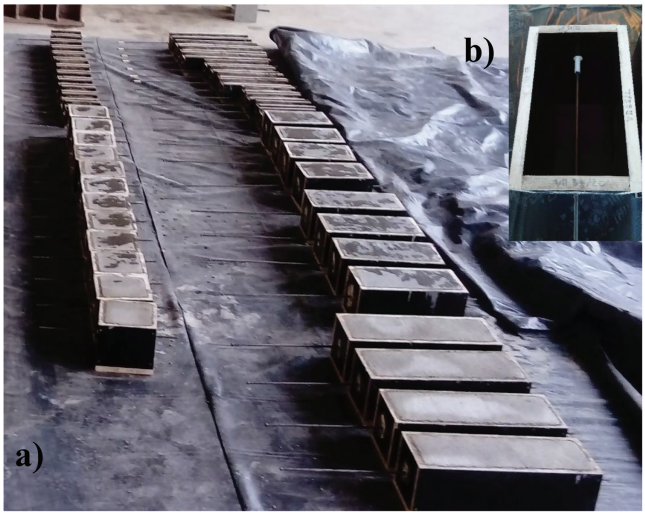

Fig. 1—Concrete specimens for bond stress testing: (a) after 24 hours of casting; and (b) mold with 7 mm wire before casting.

real value of the bond stress of concrete to the prestressing tendon at the time of tensioning force release with a concrete compressive strength of 50 MPa. This is the information needed to determine the transmission length, a value that can be determined experimentally during the production of the precast element.

In *fib* Model Codes 1990 and 2010,[16,17] a calculation model was proposed for conventional concrete and plain steel prestressing wires in the form of Eq. (1)

$$f_{b,max} = f_{b,res} = 0.1\sqrt{f_{ck}} \quad (1)$$

for $s = s_1 = s_2 > s_3 = 0.01$ mm, which is assumed for conventional concrete.

RESEARCH SIGNIFICANCE

Plain steel wires are widely adopted in the production of HPC railroad ties due to their many nonobvious advantages. However, it should be noted that there is a significant lack of research into the performance of the bond. In addition, there are no standard guidelines for the design of anchorage, transfer, and development length in HPC. The design is carried out by analogy to conventional concrete. Therefore, to establish design guidelines, it would be prudent and important to thoroughly investigate the bond between this wire and HPC.

The purpose of the research undertaken was to determine the bond stress of HPC to a non-pretensioned steel wire of 7 mm diameter. Furthermore, a very important cognitive element was determining the adhesive bond and the mechanism of bond failure to the steel wire depending on the embedment length and the cross section of the tested element. These tests can also be used to predict the transfer length.

EXPERIMENTAL INVESTIGATION

Test specimen fabrication

To take into account the influence of the thickness of the concrete cover on the value of the actual bond stress of HPC to a 7 mm diameter plain steel prestressing wire, molds with two cross sections of 160 x 160 mm and 80 x 80 mm were made. The 160 x 160 mm section size is comparable to the cross section of the Polish railway sleeper in its central region. In real production, the concrete cover for prestressing wire is 40 mm.[18] Therefore, it was decided to produce molds with a second cross section of 80 x 80 mm. The total number of test specimens was 96. Due to the use of identical wires from two different manufacturers, concreting was carried out in two identical series. Figure 1(a) shows the concreted specimens in one series. Each series consisted of 24 specimens of 160 x 160 mm cross section and 24 of 80 x 80 mm. Four specimens with a section of 160 x 160 mm and another four with a section of 80 x 80 mm were made for each active embedment length: 40, 80, 120, 240, 330, and 460 mm. The specimens were tested at one of four design terms: after 1, 3, 7, and 28 days of concrete maturation. The specimens with active embedment lengths of 40, 80, and 120 mm were 160 mm in length. For active adhesion lengths of 240, 330, and 460 mm, the lengths of the specimens were 280, 370, and 500 mm, respectively. The lengths of the 7 mm diameter wires were cut so that 100 and 240 mm free ends protruded from the test element. All test elements were concreted with the wires horizontally located in individual wooden molds (Fig. 1). Inside the mold, a rigid polyvinyl chloride (PVC) tube of 140, 100, and 60 mm in length was embedded on each wire from the longer protruding end to exclude adhesion of the concrete to the wire. The free spaces between the wire and the ends of the casing were sealed with silicone to prevent cement slurry from entering the PVC tube. Figures 2(a) and (b) show the 160 x 160 mm and 80 x 80 mm cross section test specimens. The geometric dimensions of the individual test elements are presented in Table 2.

The concrete mixture with the appropriate composition (Table 3) was placed in the molds and then compacted mechanically using a 30 mm diameter poker vibrator. All test elements, including the standard samples taken to determine the mechanical properties of the concrete, were covered with three layers of polyethylene sheeting after finishing the top surface. All test elements were unmolded after 22 hours of concrete curing and were then prepared for experimental testing. After cleaning the protruding wires, two aluminum angles were glued onto the front surface of the concrete specimens from the free end of the wire (length of 100 mm), allowing the extensometers to be connected. The tests were carried out in a materials testing machine according to the modified pullout test method developed at Cracow University of Technology.[19,20] The first tests were carried out after 24 hours of concrete curing. The test elements to be tested after 3, 7, and 28 days of concrete curing were covered with three layers of polyethylene sheeting. The aim of the tests was to determine the relationship between the pullout force and the slip of the non-pretensioned wire from the moment of loss of adhesion to the slip value $s = 10$ mm. The method of embedding the specimen in the testing machine is shown

in Fig. 3, while the connection of the extensometers to the specimen at the free end of the wire is illustrated in Fig. 4. The setup scheme is presented in Fig. 2. The force from the steering mechanism lifts the frame structure, which transfers the load onto the concrete specimen through pressure on the bottom surface. Chucking the reinforcement in the gripping jaws of the testing machine resulted in the slip of the wire toward the concrete. The load was controlled by displacement with a loading rate of 0.01 mm/s. The force value was continuously recorded digitally.

Plain prestressing wires with a diameter of 7 mm and strength of 1670 MPa, supplied by two manufacturers, were used for the experimental tests. As a result of laboratory tests carried out in the materials testing machine at the Institute of Building Materials and Structures at Cracow University of Technology, the basic mechanical properties of the wires were determined. The mechanical properties of steel wires are presented in Table 4.

Table 2—Specimens dimensions and quantity

Specimen cross section	Total length l_{tot}, mm	Embedment length l_{emb}, mm	Number of pieces n
160 x 160 mm	500	460	8
	370	330	8
	280	240	8
	160	120	8
	160	80	8
	160	40	8
80 x 80 mm	500	460	8
	370	330	8
	280	240	8
	160	120	8
	160	80	8
	160	40	8

Note: 1 mm = 0.0394 in.

Experimental results

The values of the pullout forces of a wire from the concrete element with cross-sectional areas of 160 x 160 mm and 80 x 80 mm, following a non-pretensioned plain steel prestressing wire with different active embedment lengths, were used to calculate bond stress-slip relationship at certain ages of concrete. Then, the age of the concrete was replaced by the average concrete compressive strength as determined experimentally at the time of the experimental tests after 1, 3, 7, and 28 days of concrete maturation (40, 60, 72, and 88 MPa, respectively). The mechanical properties of concrete at any stage of the tests are listed in Table 5. Pullout tests were conducted until a wire slip of s = 10 mm was achieved. The adhesive strength and force values for the following slips (s) were selected from the full electronic test record for each test specimen: 0.01, 0.0254, 0.1, 0.254, 1, 2.54, 4, 6, 8, and

Table 3—Mixture design for HPC (per 1 m³)

Components	Quantities, kg
Rapid-hardening portland cement CEM I 42.5R	476
River sand, 0 to 2 mm	665
Basalt aggregate, 2 to 8 mm	650
Basalt aggregate, 8 to 16 mm	580
Silica fume, 5%	24
Water	156
High-range water-reducing admixture	5.2
w/b	0.31

Note: w/b is water-binder ratio; 1 m³ = 1.31 yd³; 1 kg = 2.20 lb; 1 mm = 0.0394 in.

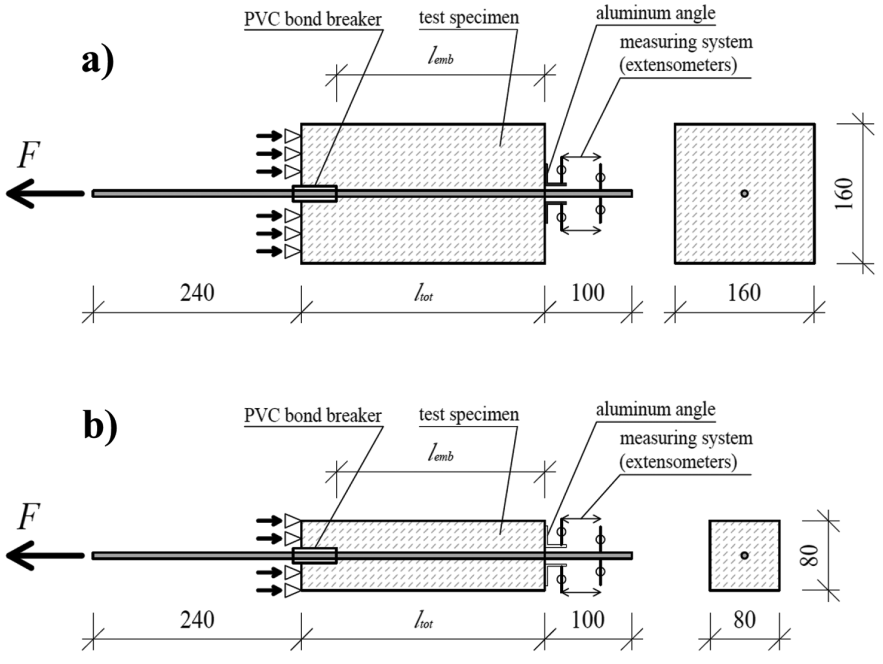

Fig. 2—Test setup with specimens of cross sections of: (a) 160 x 160 mm; and (b) 80 x 80 mm.

Fig. 3—General view of concrete specimen during testing.

Fig. 4—Extensometer mounted at free end of plain steel prestressing wire of 7 mm during testing.

Table 4—Mechanical properties of steel wires for tests

	First manufacturer	Second manufacturer
Wire diameter	ϕ = 7 mm	ϕ = 7 mm
Cross-sectional area	A_p = 38.48 mm^2	A_p = 38.48 mm^2
Breaking force	F_k = 65.35 kN	F_k = 64.98 kN
Tensile strength	f_p = 1698.3 MPa	f_p = 1687.8 MPa
Conventional yield strength	$f_{p0,2}$ = 1540.0 MPa	$f_{p0,2}$ = 1530.3 MPa
Modulus of elasticity	E_p = 206,160 MPa	E_p = 206,450 MPa
Average elongation at maximum force	A_{gt} = 4.10%	A_{gt} = 4.06%

Note: 1 mm^2 = 0.00155 in.^{2}; 1 MPa = 0.145 ksi; 1 kN = 0.225 kip; 1 mm = 0.0394 in.

Table 5—Mechanical properties of HPC

Concrete age	$f_{c,cyl}$, MPa (ϕ150 x 300 mm)	$f_{c,cube}$, MPa (150 x 150 x 150 mm)	$f_{ct,dir}$, MPa (ϕ150 x 300 mm)	E_c, MPa (ϕ150 x 300 mm)
24 hours	39.50	47.54	—	35,300
2 days	53.47	64.08	3.10	39,360
3 days	59.83	72.29	3.39	42,270
7 days	71.53	80.82	4.05	46,000
28 days	88.39	93.13	4.83	49,660
90 days	93.19	100.19	6.14	53,100

Note: 1 mm = 0.0394 in; 1 MPa = 0.145 ksi; 1 mm = 0.0394 in.

10 mm. The average maximum forces and the corresponding average wire slip values were also recorded.

Figures 5(a) to (d) show the distributions of the average pullout force-slip relationship as a function of embedment length, determined on specimens with a cross section of 160 x 160 mm for concrete compressive strengths of 40, 60, 72, and 88 MPa, respectively. Analogous distributions of the F_{ave}-s relationship obtained for specimens with a cross section of 80 x 80 mm are shown in Fig. 6(a) to (d).

The bond stress of the HPC to a 7 mm diameter non-pretensioned plain steel prestressing wire was calculated according to Eq. (2)

$$f_b = \frac{F}{C \cdot l_{emb}} \tag{2}$$

where f_b is the bond stress; F is the pullout force; $C = \pi \cdot \phi$ is the circumference of a wire; and l_{emb} is the embedment length of a wire.

The average values of the bond stress of the HPC to a non-pretensioned plain steel prestressing wire with a diameter of 7 mm, obtained on test elements with cross sections of 160 x 160 mm and 80 x 80 mm with different active embedment lengths, are summarized in Tables 6 to 8. The tables also show the average maximum bond stresses. The distributions of the average bond stress-slip relationship for HPC specimens with cross sections of 160 x 160 mm and 80 x 80 mm and the non-pretensioned plain steel wire of 7 mm diameter are shown in Fig. 7.

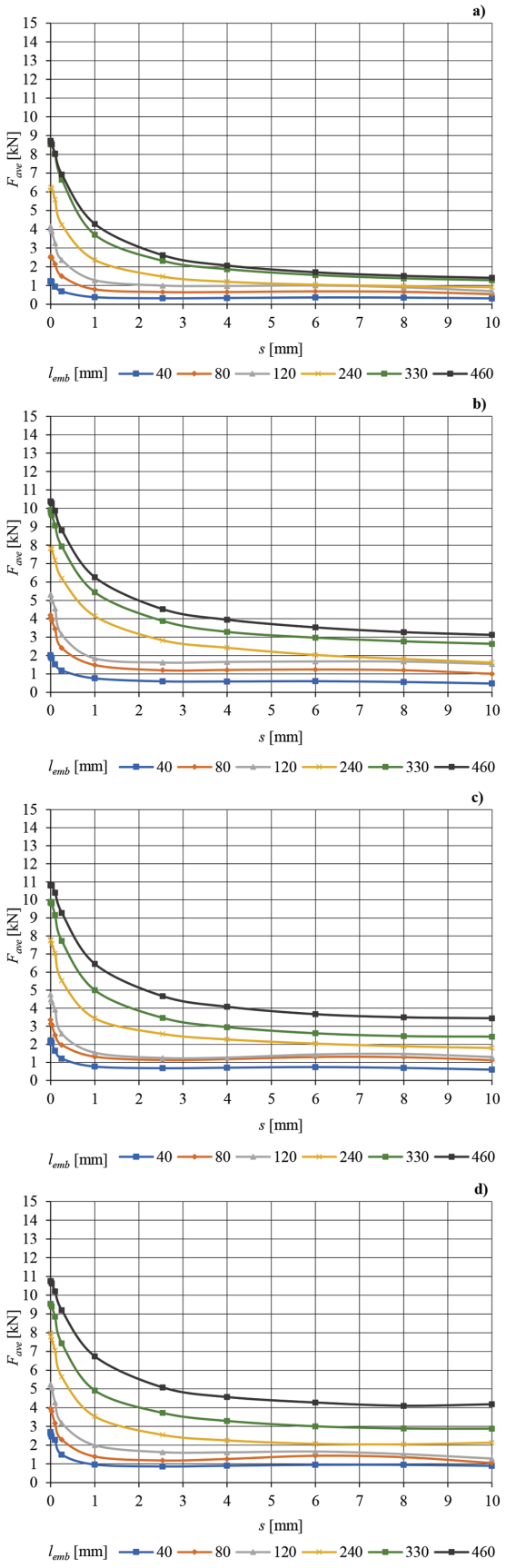

Fig. 5—Average pullout force-slip relationship for HPC specimen with cross section of 160 x 160 mm and non-pretensioned plain steel wire of 7 mm diameter for f_{cm} *= (a) 40 MPa; (b) 60 MPa; (c) 72 MPa; and (d) 88 MPa.*

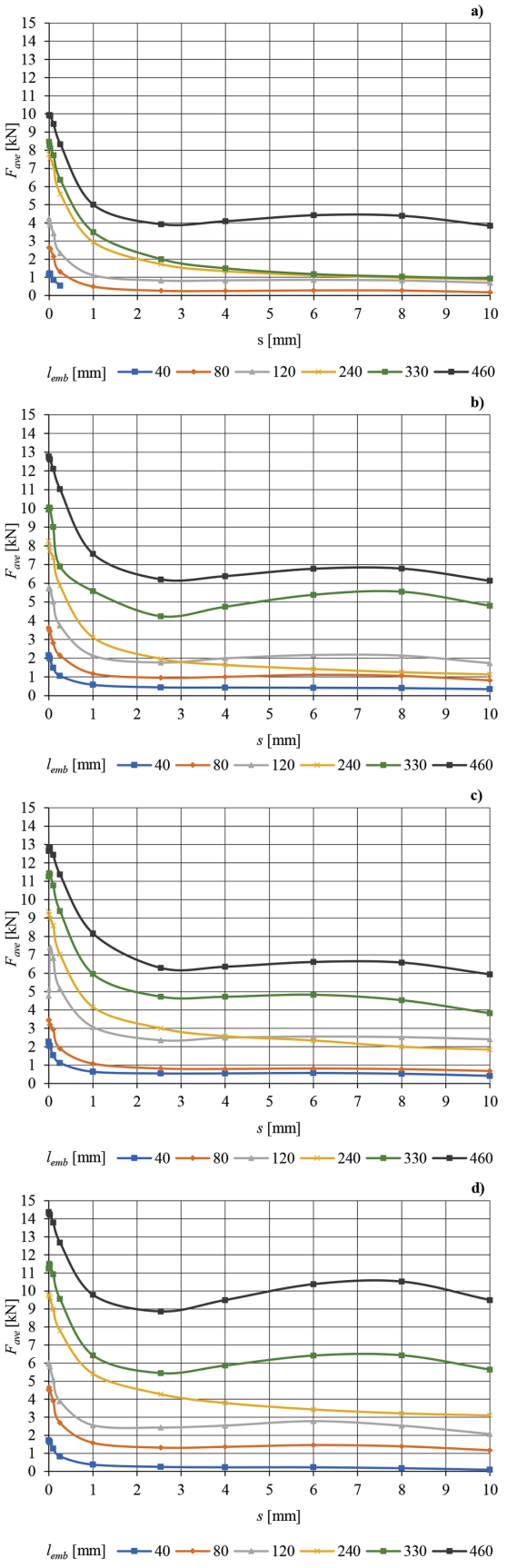

Fig. 6—Average pullout force-slip relationship for HPC specimen with cross section of 80 x 80 mm and non-pretensioned plain steel wire of 7 mm diameter for f_{cm} *= (a) 40 MPa; (b) 60 MPa; (c) 72 MPa; and (d) 88 MPa.*

Table 6—Bond stress average values of HPC specimens to non-pretensioned 7 mm diameter steel wire with l_{emb} = 40 to 460 mm: specimen cross sections of 160 x 160 mm and 80 x 80 mm

	f_{cm} = 40 MPa		f_{cm} = 60 MPa		f_{cm} = 72 MPa		f_{cm} = 88 MPa	
s, mm	$f_{b,ave}$, MPa	CoV, %	$f_{b,ave}$, MPa	CoV, %	$f_{b,ave}$, MPa	CoV, %	$f_{b,ave}$, MPa	CoV, %
Adhesion	1.30	8.7	1.79	6.5	1.75	6.6	1.90	16.1
0.01	1.30	7.6	1.76	6.5	1.73	9.0	1.89	16.7
0.0254	1.27	7.5	1.71	6.9	1.76	12.5	1.84	16.9
0.1	1.11	8.5	1.50	6.5	1.56	15.4	1.64	20.0
0.254	0.83	11.0	1.17	9.7	1.21	16.5	1.27	21.4
1	0.45	15.0	0.73	13.5	0.76	19.4	0.82	27.3
2.54	0.32	24.8	0.57	16.1	0.59	22.3	0.68	35.8
4	0.29	29.0	0.56	22.4	0.58	27.2	0.68	41.1
6	0.29	31.5	0.57	26.8	0.59	30.4	0.71	44.8
8	0.27	31.6	0.55	28.8	0.57	30.0	0.68	47.0
10	0.24	33.2	0.48	26.0	0.51	28.7	0.60	47.3
$f_{b,max\ ave}$	1.32	7.6	1.79	6.7	1.85	11.7	1.91	16.8
$f_{b,ave}$ (s = 1 to 10)	0.31	27.5	0.57	22.3	0.60	26.3	0.69	40.5
$f_{b,ave}$ (s = 2.54 to 10)	0.28	30.0	0.54	24.0	0.57	27.7	0.67	43.2

Note: CoV is coefficient of variation; 1 mm = 0.0394 in.; 1 MPa = 0.145 ksi.

Table 7—Bond stress average values of HPC specimens to non-pretensioned 7 mm diameter steel wire with l_{emb} = 40 to 120 mm: specimen cross sections of 160 x 160 mm and 80 x 80 mm

	f_{cm} = 40 MPa		f_{cm} = 60 MPa		f_{cm} = 72 MPa		f_{cm} = 88 MPa	
s, mm	$f_{b,ave}$, MPa	CoV, %	$f_{b,ave}$, MPa	CoV, %	$f_{b,ave}$, MPa	CoV, %	$f_{b,ave}$, MPa	CoV, %
Adhesion	1.46	3.6	2.23	6.8	2.09	1.8	2.35	16.8
0.01	1.46	1.0	2.18	7.1	2.05	6.7	2.33	17.0
0.0254	1.42	1.0	2.10	7.8	2.13	13.3	2.24	17.0
0.1	1.17	3.1	1.77	7.4	1.80	17.9	1.93	22.4
0.254	0.79	9.0	1.29	9.6	1.29	18.0	1.36	21.9
1	0.42	22.0	0.76	15.2	0.79	24.5	0.82	29.6
2.54	0.32	37.1	0.62	14.3	0.64	26.8	0.70	37.9
4	0.33	37.6	0.64	16.2	0.66	30.3	0.72	40.5
6	0.35	35.0	0.66	16.8	0.70	29.8	0.78	41.4
8	0.33	32.9	0.64	16.6	0.68	30.1	0.73	44.9
10	0.28	36.3	0.54	14.9	0.60	33.6	0.61	52.3
$f_{b,max\ ave}$	1.49	1.5	2.23	6.9	2.28	11.7	2.36	17.5
$f_{b,ave}$ (s = 1 to 10)	0.34	33.5	0.64	15.7	0.68	29.2	0.73	41.1
$f_{b,ave}$ (s = 2.54 to 10)	0.32	35.8	0.62	15.8	0.66	30.1	0.71	43.4

Note: CoV is coefficient of variation; 1 mm = 0.0394 in.; 1 MPa = 0.145 ksi.

EXPERIMENTAL RESULTS AND DISCUSSION

The distributions of the pullout force-slip relationship obtained on test elements with a cross section of 160 x 160 mm were denser (Fig. 5) than 80 x 80 mm specimens (Fig 6). The F_{ave}-s relationship profile of the 160 x 160 mm test elements was more compact and regular, regardless of the compressive strength of the concrete. These elements are stiffer. When the maximum force value was reached at a wire, the descending curve had a concave shape over the slip length up to 2.54 mm. Over the remaining distance—that is, from s = 2.54 mm to s = 10 mm—the dependency curve was linear, with a slight downward trend. In the case of test elements with a cross section of 80 x 80 mm, the F_{ave}-s dependence curves were not dense; this is particularly true for test elements with embedment lengths of 330 and 460 mm. For these elements, the F_{ave}-s relationship profiles diverged significantly from the others. This phenomenon may be attributed to the greater slenderness of these elements relative to the other specimens. The profiles of the bond stress-slip curves were similar. Once adhesion was overcome, the bond stress decreased with increasing slip to a value of approximately 2.54 mm, followed by

Table 8—Average values of maximum bond stress of HPC specimens to non-pretensioned 7 mm diameter plain steel wire: specimen cross sections of 160 x 160 mm and 80 x 80 mm

l_{emb}, mm	f_{cm} = 40 MPa	f_{cm} = 60 MPa	f_{cm} = 72 MPa	f_{cm} = 88 MPa	*
40	1.39	2.37	2.56	2.50	2.20
80	1.48	2.23	1.94	2.45	2.02
120	1.59	2.10	2.33	2.13	2.04
240	1.33	1.53	1.62	1.69	1.54
330	1.18	1.38	1.47	1.45	1.37
460	0.92	1.14	1.17	1.24	1.12
†	1.31	1.79	1.85	1.91	—
‡	1.49	2.23	2.28	2.36	—

*Average values of maximum bond stress for all f_{cm}.

†Average values of maximum bond stress for all embedment lengths.

‡Average values of maximum bond stress for l_{emb} = 40 to 120 mm.

Note: 1 mm = 0.0394 in.; 1 MPa = 0.145 ksi.

some stabilization, with a slight decrease to a slip value of 10 mm. The most significant differences occurred in the area of maximum bond stress values. It appeared that the maximum bond stress results were significantly lower for test specimens with embedment lengths of 240, 330, and 460 mm. These stresses were lower as the embedment length increased (Table 8).

The average bond stresses of HPC to a 7 mm diameter non-pretensioned plain steel wire, calculated considering all embedment lengths, are given in Table 6. Analogous stresses calculated for test elements with embedment lengths of 40, 80, and 120 mm are summarized in Table 7. The literature review is clear: concrete elements reinforced with wires have more reliable bond stress values when the embedment length is short.[1,4,7,13-15] This is because the bond stresses are more evenly distributed over the shorter active length. Therefore, the authors decided to analyze the data set with a 40 to 120 mm embedment length. Both tables give the average values of the maximum bond stresses depending on the concrete compressive strength. In addition, both tables show the calculated average values of the residual bond stress in the wire slip range of 1 to 10 mm and 2.54 to 10 mm. The distributions of the bond stress-slip relationship for all embedment lengths are shown in Fig. 8, and for embedment lengths of 40, 80, and 120 mm in Fig. 9. In both cases analyzed, the bond stress distribution determined for test elements with a concrete compressive strength of 40 MPa was well below the concentrated bond stress distributions calculated for test elements made of concrete with compressive strengths of 60, 72, and 88 MPa.

Considering the embedment lengths of 40, 80, and 120 mm, the average residual bond stress for concrete elements with compressive strengths of 60, 72, and 88 MPa was 0.66 MPa (for s = 2.54 ÷ 10 mm) and was twice that of concrete with a compressive strength of 40 MPa (Table 6). In contrast, the average adhesion stress determined on test elements from HPC with compressive strengths of 60, 72, and 88 MPa was 2.22 MPa, 52% greater than the adhesion for specimens from concrete with a compressive strength of 40 MPa ($f_{b,a}$ = 1.46 MPa).

From the data in Tables 6 and 7, it was determined that the maximum bond stress was almost equal to the adhesion. To be precise, in the tests, it occurred at an average wire slip value of s = 0.0097 mm. The average value of the maximum bond stress determined for elements with embedment lengths of 40, 80, and 120 mm from concrete with compressive strengths of 60, 72, and 88 MPa was 2.29 MPa, 53% higher than the corresponding stress for concrete with a compressive strength of 40 MPa.

The average values of the maximum bond stress of the HPC to a 7 mm diameter non-pretensioned plain steel wire are summarized in Table 8. Also included are the average values of the maximum bond stress calculated considering all the embedment lengths analyzed, as well as for the embedment lengths of 40, 80, and 120 mm. The distributions of the average values of the maximum bond stress of HPC to a non-pretensioned plain steel wire of 7 mm diameter are illustrated in Fig. 10. It can clearly be seen that the maximum bond stress decreased with increasing embedment length, regardless of the concrete compressive strength.

The distributions of the average values of the maximum bond stress of HPC to a 7 mm diameter non-pretensioned plain steel wire, as a function of the concrete's compressive strength, are shown in Fig. 11. It can be seen that the average maximum bond stress increased as the concrete's compressive strength increased from 40 to 72 MPa. The curves tended to be flat after the concrete compressive strength was 72 MPa or higher. A more significant increase in maximum bond stress occurred for test elements with a short embedment length. The distributions of the average maximum bond stress considering all the embedment lengths analyzed, as well as for embedment lengths of 40, 80, and 120 mm, depending on the compressive strength of the concrete, are illustrated in Fig. 12.

None of the concrete specimens tested were cracked. The maximum stress in the steel prestressing wire was 373.7 MPa, which is only 0.22f_p, and the corresponding bond stress was 1.42 MPa (l_{emb} = 460 mm).

Taking into account the results of the bond stress-slip relationship determined for all test elements with both 160 x 160 mm and 80 x 80 mm cross sections, the relative

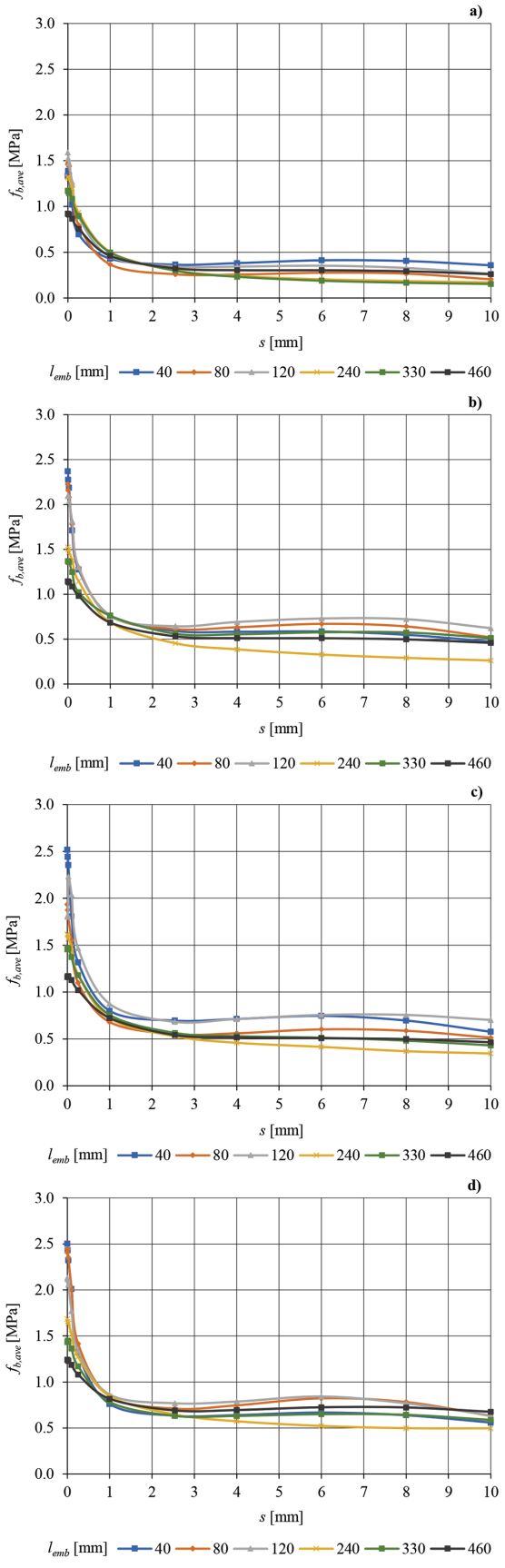

Fig. 7—Average bond stress-slip relationship for HPC specimen with cross sections of 160 x 160 mm and 80 x 80 mm and non-pretensioned plain steel wire of 7 mm diameter for f_{cm} *= (a) 40 MPa; (b) 60 MPa; (c) 72 MPa; and (d) 88 MPa.*

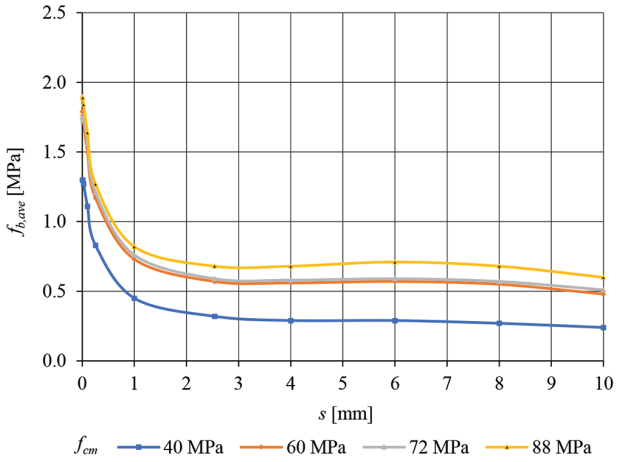

Fig. 8—Average values of bond stress-slip relationship for HPC to non-pretensioned plain steel wire of 7 mm diameter for all tested specimens. Specimen cross sections of 160 x 160 mm and 80 x 80 mm.

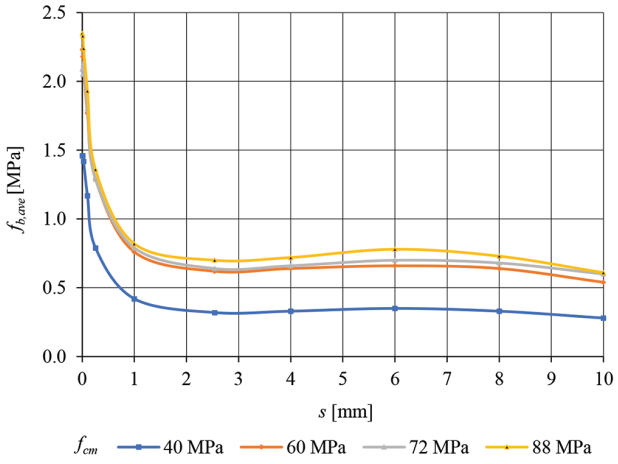

Fig. 9—Average values of bond stress-slip relationship for HPC to non-pretensioned plain steel wire of 7 mm diameter for specimens with l_{emb} *= 40 to 120 mm. Specimen cross sections of 160 x 160 mm and 80 x 80 mm.*

dependence of the average bond stress on the concrete compressive strength and on the square root of the concrete compressive strength was analyzed. The effects of the compressive strength of the HPC and the square root of the compressive strength of the HPC on the bond stress-slip relationship, considering all embedment lengths, are analyzed in Table 9. Analogous data for test elements with embedment lengths of 40, 80, and 120 mm are listed in Table 10. In both cases, a better fit of the mean values was obtained for the relationship $f_{b,ave}/\sqrt{f_{cm}}$ in the slip range up to $s = 0.254$ mm, and $f_{b,ave}/f_{cm}$ when the slip was in the range of 0.254 to 10 mm. The distributions of the relationships $f_{b,ave}/f_{cm}$ and $f_{b,ave}/\sqrt{f_{cm}}$ for $l_{emb} = 40$ to 120 mm are shown in Fig. 13 and 14, respectively.

Taking the experimental results obtained for specimens with embedment lengths of 40, 80, and 120 mm as reliable, the following relationships were proposed to determine the bond stress of HPC to a 7 mm diameter non-pretensioned plain steel wire.

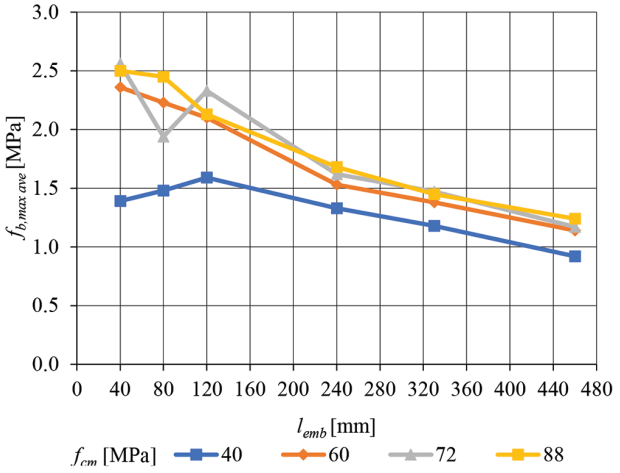

Fig. 10—Average values of maximum bond stress of HPC specimen to non-pretensioned 7 mm plain steel wire in relation to embedment length. Specimen cross sections of 160 x 160 mm and 80 x 80 mm.

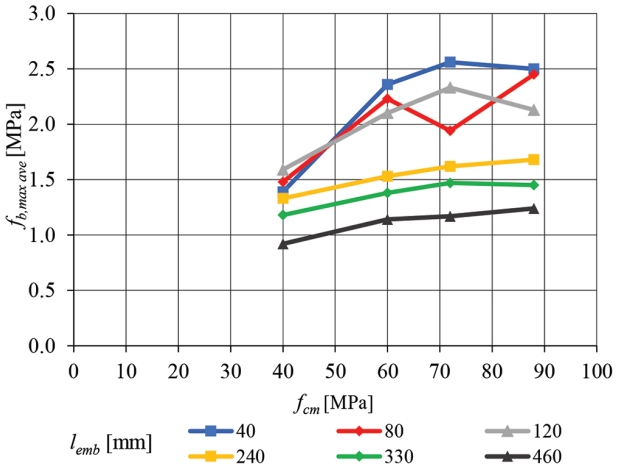

Fig. 11—Average values of maximum bond stress of HPC specimen to non-pretensioned 7 mm plain steel wire in relation to concrete compressive strength. Specimen cross sections of 160 x 160 mm and 80 x 80 mm.

Adhesion:

$$f_{b,a} = 0.254\sqrt{f_{cm}} \tag{3}$$

Residual bond stress:

$$f_{b,res} = 0.071\sqrt{f_{cm}} \tag{4}$$

Maximum bond stress:

$$f_{b,max} = 0.261\sqrt{f_{cm}} \text{ for } s_{max} = 0.01 \text{ mm} \tag{5}$$

Based on the results obtained from the presented experimental studies, a computational model capturing the bond stress-slip relationship for HPC and a 7 mm diameter non-pretensioned plain steel prestressing wire is presented in this paper

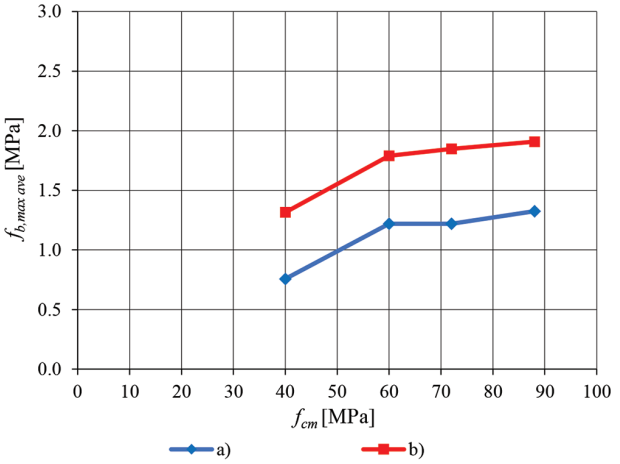

Fig. 12—Maximum bond stress average values of HPC to non-pretensioned 7 mm plain steel wire: (a) all embedment lengths; and (b) l_{emb} = 40 to 120 mm.

$$f_b = f_{b,max} - (f_{b,max} - f_{b,res}) \cdot \left[1 - \left(\frac{s_r - s}{s_r}\right)^5\right]$$
$$\text{for } s_0 = s_{max} = 0 < s < s_r = 25.4 \text{ mm}$$

$$f_b = f_{b,res} \text{ for } s \geq s_r = 25.4 \text{ mm} \tag{6}$$

assumed for

$$f_{b,a} = f_{b,max} = 0.25\sqrt{f_{cm}} \text{ for } l_{emb} = 40, 80, \text{ and } 120 \text{ mm}$$

$$f_{b,a} = f_{b,max} = 0.21\sqrt{f_{cm}}$$
$$\text{for } l_{emb} = 40, 80, 120, 240, 330, \text{ and } 460 \text{ mm}$$

$$f_{b,res} = 0.07\sqrt{f_{cm}} \tag{7}$$

where $f_{b,a}$ is the adhesive bond; $f_{b,max}$ is the maximum bond stress; $f_{b,res}$ is the residual bond stress; f_{cm} is the average concrete compressive strength; s_{max} is the slip at $f_{b,max}$; and s_r is the slip at $f_{b,res}$.

The starting point for the consideration of the bond model was the model developed by Melo et al.[21] and *fib* Model Code 2010.[17] However, the assumptions made by Melo et al. involved a complex calculation of the function coefficients, which made their model impractical. The *fib* Model Code model is simple but does not refer to the real phenomenon (it gives a constant value of the concrete bond).

Figure 15 displays the outcome of the fitting process for the concrete-wire bond stress-slip relationship, using the average concrete strength (f_{cm} = 65 MPa) obtained from the tests conducted on all the tested elements. Figure 16 shows the function fit for the test elements, considering embedment lengths ranging from 40 to 120 mm. A better fit of the proposed bond-slip model was obtained for the results obtained for test elements with embedment lengths of 40 to 120 mm for stresses in the development range and residual stresses.

Table 9—Influence of HPC compressive strength and square root of HPC compressive strength on relative bond stress-slip relationship for 7 mm plain steel wire (all embedment lengths): specimen cross sections of 160 x 160 mm and 80 x 80 mm

	$f_{b,ave}/f_{cm}$						$f_{b,ave}/\sqrt{f_{cm}}$					
	f_{cm}, MPa						f_{cm}, MPa					
s, mm	40	60	72	88	Average	CoV, %	40	60	72	88	Average	CoV, %
Adhesion	0.033	0.030	0.024	0.022	0.027	18.45	0.206	0.231	0.206	0.203	0.211	6.27
0.01	0.033	0.029	0.024	0.021	0.027	18.62	0.206	0.227	0.204	0.201	0.210	5.68
0.0254	0.032	0.029	0.024	0.021	0.026	17.90	0.201	0.221	0.207	0.196	0.206	5.19
0.1	0.028	0.025	0.022	0.019	0.023	17.03	0.176	0.194	0.184	0.175	0.182	4.84
0.254	0.021	0.020	0.017	0.014	0.018	15.79	0.131	0.151	0.143	0.135	0.140	6.21
1	0.011	0.012	0.011	0.009	0.011	11.09	0.071	0.094	0.090	0.087	0.086	11.73
2.54	0.008	0.010	0.008	0.008	0.008	9.42	0.051	0.074	0.070	0.072	0.067	16.19
4	0.007	0.009	0.008	0.008	0.008	11.02	0.046	0.072	0.068	0.072	0.065	19.68
6	0.007	0.010	0.008	0.008	0.008	11.28	0.046	0.074	0.070	0.076	0.066	20.83
8	0.007	0.009	0.008	0.008	0.008	12.58	0.043	0.071	0.067	0.072	0.063	22.02
10	0.006	0.008	0.007	0.007	0.007	11.81	0.038	0.062	0.060	0.064	0.056	21.67
$f_{b,max\ ave}$	0.033	0.030	0.026	0.022	0.028	17.84	0.209	0.231	0.218	0.204	0.215	5.60
$f_{b,ave}$ (s = 1 to 10)	0.008	0.010	0.008	0.008	0.008	9.63	0.049	0.074	0.071	0.074	0.067	17.80
$f_{b,ave}$ (s = 2.54 to 10)	0.007	0.009	0.008	0.008	0.008	10.62	0.044	0.070	0.067	0.071	0.063	20.12

Note: 1 mm = 0.0394 in.; 1 MPa = 0.145 ksi.

Table 10—Influence of HPC compressive strength and square root of HPC compressive strength on relative bond stress-slip relationship for 7 mm plain steel wire (embedment lengths l_{emb} = 40 to 120 mm): specimen cross sections of 160 x 160 mm and 80 x 80 mm

	$f_{b,ave}/f_{cm}$						$f_{b,ave}/\sqrt{f_{cm}}$					
	f_{cm}, MPa						f_{cm}, MPa					
s, mm	40	60	72	88	Average	CoV, %	40	60	72	88	Average	CoV, %
Adhesion	0.037	0.037	0.029	0.027	0.032	16.29	0.231	0.288	0.246	0.251	0.254	9.53
0.01	0.037	0.036	0.028	0.026	0.032	16.36	0.231	0.281	0.242	0.248	0.251	8.70
0.0254	0.036	0.035	0.030	0.025	0.031	15.22	0.225	0.271	0.251	0.239	0.246	8.01
0.1	0.029	0.030	0.025	0.022	0.026	13.76	0.185	0.229	0.212	0.206	0.208	8.66
0.254	0.020	0.022	0.018	0.015	0.019	13.87	0.125	0.167	0.152	0.145	0.147	11.77
1	0.011	0.013	0.011	0.009	0.011	12.78	0.066	0.098	0.093	0.087	0.086	16.16
2.54	0.008	0.010	0.009	0.008	0.009	12.65	0.051	0.080	0.075	0.075	0.070	18.91
4	0.008	0.011	0.009	0.008	0.009	12.77	0.052	0.083	0.078	0.077	0.072	18.91
6	0.009	0.011	0.010	0.009	0.010	10.84	0.055	0.085	0.082	0.083	0.077	18.53
8	0.008	0.011	0.009	0.008	0.009	12.48	0.052	0.083	0.080	0.078	0.073	19.33
10	0.007	0.009	0.008	0.007	0.008	13.04	0.044	0.070	0.071	0.065	0.062	19.79
$f_{b,max\ ave}$	0.037	0.037	0.032	0.027	0.033	15.07	0.236	0.288	0.269	0.252	0.261	8.62
$f_{b,ave}$ (s = 1 to 10)	0.009	0.011	0.009	0.008	0.009	11.73	0.054	0.083	0.080	0.078	0.074	18.16
$f_{b,ave}$ (s = 2.54 to 10)	0.008	0.010	0.009	0.008	0.009	12.37	0.051	0.080	0.078	0.076	0.071	19.34

Note: 1 mm = 0.0394 in.; 1 MPa = 0.145 ksi.

CONCLUSIONS

Based on the obtained results from the experimental investigations, the following conclusions were drawn with respect to the bond behavior of the non-pretensioned plain steel wire of 7 mm diameter in high-performance concrete (HPC):

- The modified pullout test method developed at Cracow University of Technology can be used to test the adhesive bond of concrete to 7 mm steel prestressing wire.
- Experimental tests of the bond of test elements made of HPC to non-pretensioned plain steel prestressing wire with a diameter of 7 mm showed that the maximum

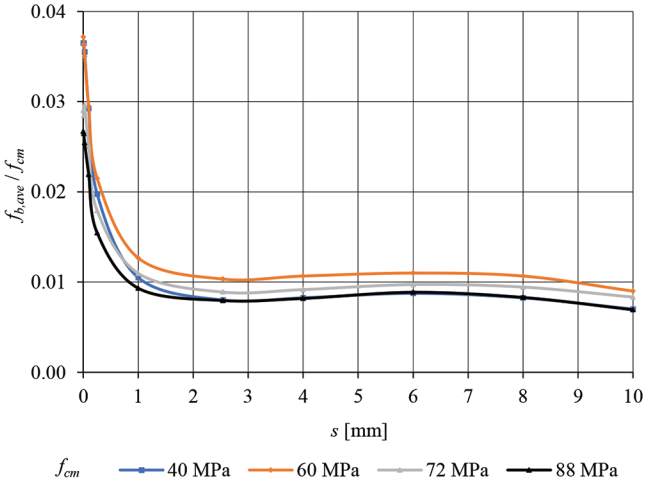

Fig. 13—Influence of HPC compressive strength on relative bond stress-slip relationship in pullout tests on specimens with embedment lengths of 40 to 120 mm and 7 mm non-pretensioned plain steel wire. Specimen cross sections of 160 x 160 mm and 80 x 80 mm.

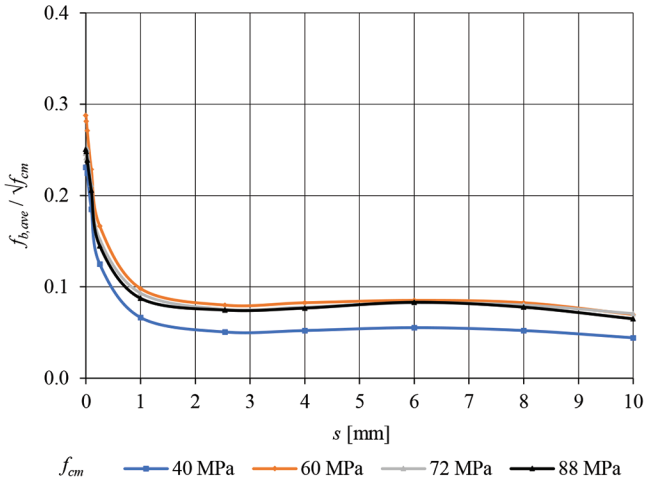

Fig. 14—Influence of square root of HPC compressive strength on relative bond stress-slip relationship in pullout tests on specimens with embedment lengths of 40 to 120 mm and 7 mm non-pretensioned plain steel wire. Specimen cross sections of 160 x 160 mm and 80 x 80 mm.

bond stress is equal to the adhesive bond. This phenomenon was confirmed against HPC with compressive strengths in the range of 40 to 88 MPa.

- In laboratory tests, specimens with a cross section of 80 x 80 mm ($c \geq 5\phi$) and above can be used to determine the bond stress, according to the developed method. An embedment length in the range of 40 to 120 mm is recommended.
- Experimental tests were carried out on test elements with different embedment lengths ranging from 40 to 460 mm. It was shown that the maximum bond stress of HPC to a non-pretensioned plain steel wire with a diameter of 7 mm decreased with increasing embedment length, irrespective of the concrete's compressive strength. Significantly higher values of bond stress were obtained for embedment lengths of 40, 80, and 120 mm.

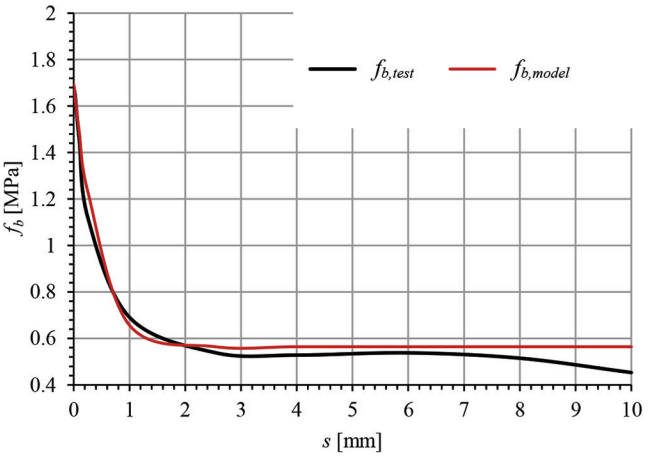

Fig. 15—Test results versus model of HPC bond-slip relationship to 7 mm diameter non-pretensioned steel prestressing wire (specimen cross sections of 160 x 160 mm and 80 x 80 mm and active embedment lengths of 40, 80, 120, 240, 330, and 460 mm).

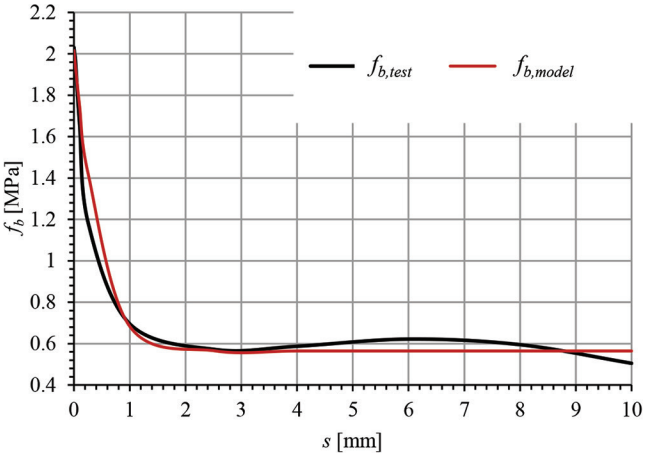

Fig. 16—Test results versus model of HPC bond-slip relationship to 7 mm diameter non-pretensioned steel prestressing wire (specimen cross sections of 160 x 160 mm and 80 x 80 mm and active embedment lengths of 40, 80, and 120 mm).

- It was also shown that the average bond stress of HPC to a non-pretensioned plain steel wire of 7 mm diameter increased with increasing concrete compressive strength. A significantly higher maximum bond stress was obtained for test elements made of concrete with a compressive strength between 60 and 88 MPa. This fact is important in view of the fact that, during the production of railway prestressed concrete sleepers, the release of tension occurs at a concrete compressive strength of at least 60 MPa.
- The average adhesion (maximum) bond stress determined on specimens made of HPC with a compressive strength in the range of 60 to 88 MPa and an embedment length in the range of 40 to 120 mm was 2.22 MPa, 52% higher than the similarly determined bond stress ($f_{b,a}$ = 1.46 MPa) on test pieces made of concrete with f_{cm} = 40 MPa.

- The average residual bond stress determined by analogy was 0.66 MPa (for $s = 2.54 \div 10$ mm) and is twice that of concrete with a compressive strength of 40 MPa.
- In *fib* Model Code 1990[16] and *fib* Model Code 2010,[17] a calculation model was proposed for conventional concrete and plain steel prestressing wire in the form of Eq. (1), from which it is shown that the maximum bond stress is equal to the residual stress. In the case of HPC, it is shown that the profile of the bond stress-slip relationship of the wire was a descending concave curve at $0 \le s \le 2.54$ mm. For slip intervals between 2.54 and 10 mm, the f_b-s relationship curve was a stabilized, slightly descending line.
- The analysis carried out showed that irrespective of the adhesion length, in the range of 40 to 460 mm, a better match of the average bond stress values was obtained for the relationship $f_{b,ave}/\sqrt{f_{cm}}$.
- Based on the results obtained from the experimental tests, a calculation model (Eq. (6)) was proposed for elements made of HPC and non-pretensioned plain steel wire with a diameter of 7 mm.
- Further experimental testing is required on test elements reinforced with plain 7 mm diameter pretensioned steel wire. The anticipated increase in bond stress of 20% as a result of the Hoyer effect will not result in a significant reduction in transmission length to achieve values below 0.5 m. Hence, it is necessary to use mechanical anchorage of plain prestressing wires in prestressed concrete sleepers.

AUTHOR BIOS

Andrzej Seruga *is a Professor at Cracow University of Technology, Kraków, Poland, where he received his MS, PhD, and DSc in civil engineering. His research interests include the watertightness of reinforced and prestressed concrete tanks, applications of high-performance concrete to prestressed elements, strengthening of existing structures, rigid concrete pavements, shotcrete technology, and sulfur concrete.*

Marcin Dyba *is an Associate Professor at Cracow University of Technology, where he received his BS, MS, and PhD in civil engineering. He also received his MS in applied computer science from the AGH University of Krakow, Kraków, Poland. His research interests include technology and design of precast, prestressed concrete structures and applications of high-performance concrete to prestressed elements.*

ACKNOWLEDGMENTS

This research was sponsored by the Faculty of Civil Engineering of Cracow University of Technology, Kraków, Poland.

NOTATION

A_{gt} = average elongation at maximum force
A_p = cross-sectional area (of wire)
C = circumference of wire
E_c = modulus of elasticity of concrete
E_p = modulus of elasticity of steel wire
F = force (pullout)
F_{ave} = average pullout force
F_k = breaking force (of steel wire)
f_b = bond stress
$f_{b,a}$ = adhesive bond
$f_{b,ave}$ = average bond stress
$f_{b,max}$ = maximum bond stress
$f_{b,res}$ = residual bond stress
$f_{c,avecube(mortar)}$ = average compressive strength of standard mortar
$f_{c,cube}$ = concrete compressive strength on cubic 15 x 15 x 15 cm samples
$f_{c,cyl}$ = concrete compressive strength on cylindrical ϕ15 x 30 cm samples
f_{ck} = characteristic concrete compressive strength
f_{cm} = average concrete compressive strength
$f_{ct,dir}$ = direct concrete tensile strength
f_p = tensile strength of steel
$f_{p0,2}$ = conventional yield strength
l_{emb} = embedment length
l_t = transmission length
l_{tot} = total length (of specimen)
n = number of pieces
s, s_1, s_2, s_3 = slip
s_{max} = slip at $f_{b,max}$
s_r = slip at $f_{b,res}$
ϕ = diameter of wire

REFERENCES

1. Arnold, M. L., "Un-Tensioned Pullout Tests to Predict the Bond Quality of Different Prestressing Reinforcements Used in Concrete Railroad Ties," master's thesis, Kansas State University, Manhattan KS, 2013, 415 pp.

2. Abrams, D. A., "Tests of Bond between Concrete and Steel," Bulletin No. 71, Engineering Experiment Station, University of Illinois Urbana-Champaign, Urbana, IL, Dec. 1913, 246 pp.

3. *fib*, "Bond of Reinforcement in Concrete. State-of-Art Report," *fib* Bulletin No. 10, International Federation for Structural Concrete, Lausanne, Switzerland, 2000, 434 pp.

4. den Uijl, J. A., "Comparative Study of Bond Properties of Different Types of Indented Wire," Stevin Report 5.85-10, Faculty of Civil Engineering, Delft University of Technology, Delft, the Netherlands, June 1985.

5. Dyba, M., and Derkowski, W., "Bond Stresses between Concrete and Prestressing in Pre-Tensioned Elements – State of the Art," *Cement Wapno Beton*, V. 23, No. 5, 2018, pp. 358-368.

6. ACI Committee 318, "Building Code Requirements for Reinforced Concrete (ACI 318-63)," American Concrete Institute, Farmington Hills, MI, 1963, 144 pp.

7. Roš, M. R., "Vorgespannter Beton," Swiss Federal Laboratories for Materials Science and Technology (EMPA) Report. No 155, 1946, Dübendorf, Zürich, Switzerland.

8. Olszak, W.; Kaufman, S.; Eimer, C.; and Bychawski, Z., "Teoria Konstrukcji Sprężonych (Theory of Prestressed Structures)," V. 1 and 2, PWN, Warsaw, Poland, 1961, 1258 pp. (in Polish)

9. Marshall, G., "End Anchorage and Bond Stress in Prestressed Concrete," *Magazine of Concrete Research*, V. 1, No. 3, Dec. 1949, pp. 123-127. doi: 10.1680/macr.1949.1.3.123

10. Momeni, A. F., "Effect of Concrete Properties and Prestressing Steel Indentation Type on the Development Length and Flexural Capacity of Pretensioned Concrete Members," PhD thesis, Kansas State University, Manhattan KS, 2016, 443 pp.

11. ASTM A881/A881M-10, "Standard Specification for Steel Wire, Indented, Low-Relaxation for Prestressed Concrete Railroad Ties," ASTM International, West Conshohocken, PA, 2010, 4 pp.

12. ASTM A1081/A1081M-12, "Standard Test Method for Evaluating Bond of Seven-Wire Steel Prestressing Strand," ASTM International, West Conshohocken, PA, 2012, 5 pp.

13. Gamble, W. L., "Discussion of 'Prediction Model for Development Length of Indented Prestressing Wires' by A. F. Momeni, R. J. Peterman, and B. T. Beck," *ACI Structural Journal*, V. 116, No. 1, Jan. 2019, pp. 278-279.

14. Geßner, S., and Henne, M., "Bond Behavior of Indented Wires in Pretensioning," *Proceedings*, 2016 PCI Convention and National Bridge Conference, Nashville, TN, Mar. 2016, 21 pp.

15. Savic, A.; Beck, B. T.; Shafiei Dastgerdi, A.; Peterman, R. J.; Riding, K.; and Robertson, A. A., "The Effect of Wire Type on Cracking Propensity in Prestressed Concrete Prisms," *Proceedings*, ASME/IEEE Joint Rail Conference, Snowbird, UT, Apr. 2019, 9 pp.

16. *fib*, "CEB-FIP Model Code 1990," International Federation for Structural Concrete, Lausanne, Switzerland, 1993, 460 pp.

17. *fib*, "*fib* Model Code 2010 – Final Draft: Volume 1," *fib* Bulletin No. 65, International Federation for Structural Concrete, Lausanne, Switzerland, 2012, pp. 247-256.

18. EN 13230-1:2016, "Railway Applications - Track - Concrete Sleepers and Bearers - Part 1: General Requirements," European Committee for Standardization, Brussels, Belgium, 2016, 42 pp.

19. Dyba, M., "Influence of Technological Parameters on Concrete-Steel Bond Between High Performance Concrete and Prestressing Strands," PhD thesis, Cracow University of Technology, Kraków, Poland, 2014, 340 pp.

aci Foundation

Building the Future

We're Building the Future

OUR MISSION

We make strategic investments in ideas, research, and people to create the future of the concrete industry.

Through its councils and programs, the ACI Foundation helps to keep the concrete industry at the forefront of advances in material composition, design, and construction.

OUR FOCUS

- Identifying technologies and innovations which provide needed solutions for the concrete industry
- Seeking concrete research projects that further the knowledge and sustainability of concrete materials, construction, and structures
- Supporting our future concrete innovators and leaders by administering fellowships and scholarships
- Helping honorably discharged veterans with our Veterans Rebate for ACI Certification program

www.acifoundation.org

ACI STRUCTURAL JOURNAL TECHNICAL PAPER

Title No. 122-S14

Curved Strut-and-Tie Recognition in Reinforced Concrete Elliptical Deep Beams

by Khattab Saleem Abdul-Razzaq, Baidaa N. Hasan, and Asala A. Dawood

Elliptical deep beams have a peculiarity: the compression paths (struts) are neither straight nor symmetrical within the same span. The asymmetrical horizontal curvature in one span leads to the formation of asymmetrical torsional moments. The strut-and-tie method (STM), approved by ACI 318-19 and most international codes, does not take into consideration the curvature of the strut and the consequent bending and torsional moments. Therefore, eight deep elliptical specimens were cast and reinforced with variable amounts of web and flexural reinforcement to study the role and importance of each one experimentally and theoretically from the STM point of view. Only the stress paths were cast and reinforced in two other specimens to study the STM in detail and to present alternative specimens to the reference ones with less weight and cost, in addition to providing openings for services. The STM has proven its effectiveness with asymmetrical, horizontally curved deep beams due to its ease and the high safety it provides. STM development has also been presented here by adding the effect of the horizontal curvature.

Keywords: elliptical ring deep beams; flexural reinforcement; proposed mathematical model; reinforced concrete; strut-and-tie method (STM); web reinforcement.

INTRODUCTION

In line with changing aesthetic preferences and a penchant for modernity, the presence of curves has emerged prominently in architecture, with the work of architect Zaha Hadid being one such example.[1] Therefore, engineers have recently grown interested in the analysis and design of structures with curvature, with elliptical deep beams serving as a case in point.[2-4] In such structures, the presence of curvature causes the supports not to lie on a straight line, and thus, torsional moments are generated.[5,6] The presence of torsional moments increases the complexity of the shear and flexural stresses already present in the deep beams.[7-9] While the form of each individual stress resultant and the related deformation are quite well known, this is not the case under combined stress resultants. As a result, it is no longer possible, nor justifiable, to obtain fundamental input parameters for an inelastic analysis. Because torsional moment is proportional to the integral of the flexural moment, maximal torsional moments would occur when flexural moments are zero in a curved beam exposed to gravity load. As a result, the regions of maximal flexural moment will often have small torsional moments.[10]

On the other hand, deep reinforced concrete beams have much greater shear strength than is expected using conventional analysis methods for shallow beams. This is due to their special ability to internally redistribute stresses before failure so that the resistance mechanisms are quite different from the shallow beams.[11,12] If the centered load is separated by a distance of twice the height of the beam and/or the clear span is equal to or less than four times the height, then the beam is classified as deep.[13] The strut-and-tie method (STM) is a design technique for reinforced and prestressed concrete that breaks down complex stress states in a structure into a group of straightforward stress paths. Truss members loaded with uniaxial stress parallel to the stress path's axis are the outcome of the stress paths. That is to say, the stresses are transmitted directly from the loading to the supporting points through the compression members (struts). In turn, the tensile members (ties) meet at the connecting points (nodes). When used for deep members or parts of deep members where the plane sections do not stay plane following the application of load, the STM proves to be a highly effective design technique. Flexural deformations do not account for the majority of the behavior of such elements (corbels, deep beams, dapped-end beams, or post-tensioned anchorage zones). The incapacity of using kinematic compatibility, thus, sometimes leads to difficulties in assessing these kinds of elements. The STM ignores kinematic restrictions. During the analysis step, both the overall equilibrium and the nodes' equilibrium are taken into account. To ascertain the yield conditions for struts, ties, and nodes, empirical observations of those elements are used to identify the constitutive relationships. As a result, the STM complies with the lower-bound theorem of plasticity, which merely demands the satisfaction of equilibrium and yield criteria. According to the lower-bound theorem of plasticity, a load will not cause the body to collapse if it is of a magnitude that allows for the maintenance of both internal and external equilibrium, as well as the determination of a stress distribution matching stresses within the yield surface.[14]

Similar to shallow members, deep beams are susceptible to shear, bending, and torsion. A reinforced concrete member's elastic torsional behavior up until the emergence of its first cracks is comparable to the reaction of a plain concrete member. For a member with longitudinal bars and stirrups, the torque moment upon cracking is roughly equivalent to the ultimate torque moment of the same concrete part. Even in the case of plain concrete, the conventional

ACI Structural Journal, V. 122, No. 1, January 2025.
MS No. S-2023-370.R2, doi: 10.14359/51742152, received May 23, 2024, and reviewed under Institute publication policies.

Saint-Venant solution to the torsion issue of those members fails to anticipate the final torsional strength, even if it accurately captures the elastic behavior.[15-18]

The authors' earlier research, in which the STM stress paths were reinforced, was expanded upon in the current study to examine the effectiveness of the STM in the analysis of simply supported deep beams,[19] continuous deep beams,[20] deep pile caps,[21] and concrete corbels.[22]

Abdul-Razzaq et al.[23] investigated the role of flexural and web reinforcing steel in six concrete ring deep beams, varying the steel reinforcement ratio. The authors concluded that the vertical web reinforcing steel plays a greater role in load capacity (94%) than the horizontal web reinforcement (36%) and that the combined contribution of both is more than that of the flexural one by approximately 42%. In addition to considering the significance of torsional moments, the authors also provided a mathematical model for the development of the STM, which allowed them to consider the role of web reinforcement in greater depth. Results from this proposed model were more in line with the experimental (11%) than with the theoretical estimation of the STM of ACI 318-19 (29%). By converting the curved struts into actual members, Abdul-Razzaq et al.[24] investigated the inclined direct stress paths of the struts in ring deep beams. Two of the specimens were in the shape of a frame that derived its cross-sectional dimensions from the STM in ACI 318-19, while the other three were conventional rings. According to the results, the suggested reinforcement increased service openings by approximately 24% while reducing weight and primary cost by roughly 18% and 13%, respectively.

Analyzing circular deep beams is easier than analyzing noncircular ones, such as elliptical deep beams. The reason is that circular beams have a constant radius of curvature, while elliptical beams have a radius that changes with their length. The degree to which the elastic instability behavior of these curved structural members is known will determine how these members are analyzed and designed; thus, the member's torsional and flexural stiffness will determine the behavior. Curved beams and girders loaded into or out of the plane become unstable when they deform laterally and torsionally out of the plane. When analyzing a curved structural member, it is necessary to assess four types of distortion deformations: bending moment, shearing force, Saint-Venant torsion, and warping torsion. The axial and shear contributions are often disregarded when analyzing the four distortion deformations.[25]

In the current research, the paths of the struts were embodied realistically so that their role became clear. They were also reinforced to become independent columns in terms of function. For elliptical deep beams, the curvature of the struts causes bending moments, which causes the beam to behave like a beam-column. Conversely, when failure approaches, the torsional forces brought on by the beam's horizontal curvature result in lateral displacement, inclined cracks, and the separation of the concrete cover.

RESEARCH SIGNIFICANCE

Because the elliptical beams are deep here, the formation of struts connected to the ties in the nodes is inevitable. The presence of asymmetry in the elliptical deep beams with varying horizontal curvature resulted in the formation of asymmetrically curved struts in a single span. The STM of ACI 318-19 does not account for the asymmetrically curved struts. Therefore, deep elliptical beams were studied herein under different reinforcement configurations to actually study the STM and suggest alternatives that save weight and cost in addition to the necessary openings for services. In addition, the stress paths were cast alone with minimum reinforcement. Finally, a mathematical model was proposed to modify the STM by incorporating the effects of these asymmetrically curved struts.

EXPERIMENTAL INVESTIGATION

Designation of test specimens

In the current experimental program, 10 specimens of reinforced concrete elliptical ring deep beams were cast and tested, as shown in Table 1 and Fig. 1. The following example is given for the designation method: elliptical ring deep beam specimen E.12.4.4 included 12 mm (0.57 in.) diameter bars for top and bottom flexural reinforcement, 4 mm (0.16 in.) diameter bars for vertical web reinforcement, and 4 mm (0.16 in.) bars for horizontal web reinforcement. To be more precise, the designation method may be summed up as follows: Elliptical.flexural reinforcement. vertical reinforcement.horizontal reinforcement.

From center to center, each elliptical ring beam measured 1500 mm (59.06 in.) in major diameter, 950 mm (37.4 in.) in minor diameter, 100 mm (3.94 in.) in section width, and 350 mm (13.78 in.) in section height. Four supports were set evenly apart to carry the elliptical ring. A central single load was applied to each midspan with a shear span-effective depth ratio (a/d) of 1.48.

Details of test specimens

The elliptical deep beam specimens were reinforced in a variety of ways, including a conventionally reinforced reference specimen (E.12.4.4) with equal amounts of flexural reinforcement at the top and bottom of 2Ø12 mm (two No. 4 [0.57 in.]), as shown in Fig. 2 and 3. The web reinforcement was vertical and horizontal bars of Ø4@66 mm (No. 1 @ 2.6 in.); ρ_v and ρ_h = 0.38%. In the second (E.12.4.0) and third (E.12.0.4) specimens, horizontal and vertical web reinforcement were omitted, respectively, while in the fourth specimen (E.12.0.0), both web reinforcements were completely omitted. In the fifth specimen (E.12.8.8), vertical and horizontal web reinforcements were increased in diameter to be Ø8@66 mm (No. 3 @ 2.6 in.); ρ_v and ρ_h = 1.5%. In the sixth (E.8.4.4) and seventh (E.0.4.4) specimens, the bottom and top flexural reinforcements were decreased from 2Ø12 mm (two No. 4 [0.57 in.]) to 2Ø8 mm (two No. 3 [0.31 in.]) and completely omitted, respectively. In the eighth specimen (E.0.0.0), all reinforcements were omitted. Regarding the ninth and tenth specimens, only the strut-and-tie paths were cast in them, once without reinforcing the struts (EFOT) and once with reinforcing the struts (EFSTM). In both

Table 1—Reinforcement description of tested specimens

Specimen No.	Specimen designation	f_c', MPa, cylinders	Top and bottom flexural reinforcement	Web reinforcement	Sketch
1	E.12.4.4	23.7	2Ø12 mm for both top and bottom ties	Vertical: Ø4 mm@66 mm center-to-center Horizontal: Ø4 mm@66 mm center-to-center	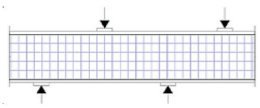
2	E.12.4.0	23		Vertical: Ø4 mm@66 mm center-to-center Horizontal: zero	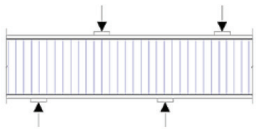
3	E.12.0.4	22.75		Vertical: zero Horizontal: Ø4 mm@66 mm center-to-center	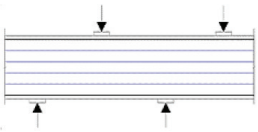
4	E.12.0.0	21.99		Vertical: zero Horizontal: zero	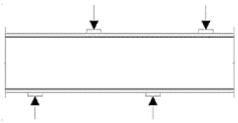
5	E.12.8.8	21.55		Vertical: Ø8 mm@66 mm center-to-center Horizontal: Ø8 mm@66 mm center-to-center	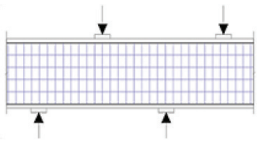
6	E.8.4.4	21.6	2Ø8 mm for both top and bottom ties	Vertical: Ø4 mm@66 mm center-to-center Horizontal: Ø4 mm@66 mm center-to-center	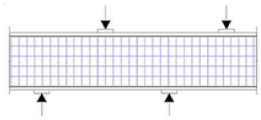
7	E.0.4.4	22.1	Zero		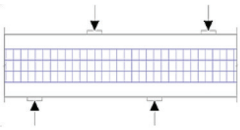
8	E.0.0.0	21.75	Zero	Vertical: zero Horizontal: zero	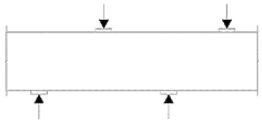
9	EFOT	21.2	2Ø12 mm for both top and bottom ties. Each strut: Zero	Top and bottom tie: Ø4 mm@100 mm center-to-center Struts: zero	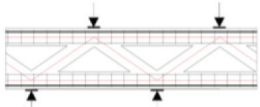
10	EFSTM	20.8	2Ø12 mm for both top and bottom ties. Each strut: 4Ø6 mm	Top and bottom tie: Ø4 mm @100 mm center-to-center Struts: Ø4 mm @96 mm center-to-center	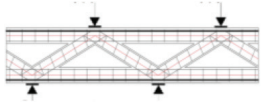

specimens, the cross section of the struts and ties was square, with dimensions of 100 x 100 mm (3.94 x 3.94 in.), based on the strut dimensions taken from the STM of ACI 318-19. In both specimens, the ties were reinforced by two 12 mm diameter steel bars (No. 4 [0.57 in.]) as flexural reinforcement, in addition to 4 mm (0.16 in.) diameter steel bars at 100 mm (No. 1 @ 3.94 in.) center-to-center as stirrups. ACI 318-19, Section 10.6.1.1, minimum longitudinal reinforcement for columns (ρ_{min} = 1%), which consists of four 6 mm (0.24 in.) diameter steel bars (No. 2), and stirrups measuring 4 mm (0.16 in.) diameter @ 96 mm (No. 1 @ 3.78 in.), were used as reinforcement for the struts in the EFSTM specimen.

Materials

The concrete was made using regular portland cement, locally accessible river sand, and coarse aggregate. The coarse aggregate's largest size allowed was 10 mm (0.39 in.). The used cement to fine aggregate to coarse aggregate ratio was 1:1.85:1.94, with a water-cement ratio (w/c) of 0.62. Six standard 150 x 300 mm (5.91 x 11.82 in.) cylinders and three 100 x 100 x 500 mm (3.94 x 3.94 x 19.69 in.) prisms were also formed during the casting of an elliptical ring beam specimen to measure the concrete's compressive, splitting, and modulus of rupture strengths. Here, 4 mm (No. 1 [0.16 in.]), 6 mm (No. 2 [0.24 in.]), 8 mm (No. 3 [0.31 in.]),

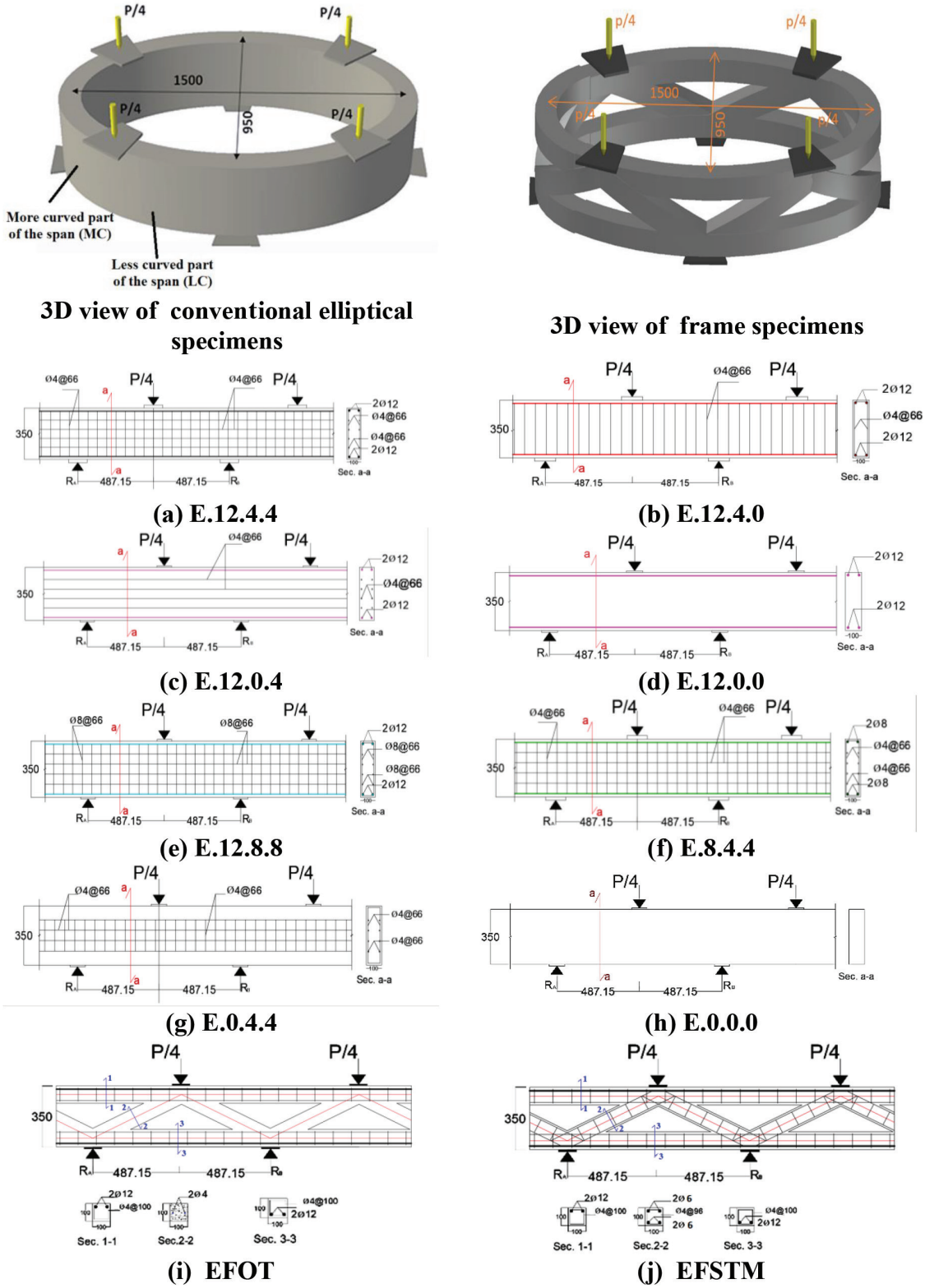

Fig. 1—Geometry and reinforcement details of elliptical specimens. (Note: All dimensions are in mm; 1 mm = 0.039 in.)

and 12 mm (No. 4 [0.47 in.]) diameter reinforcing deformed steel bars were used (Table 2). Prior to testing, all specimens were cured for 28 days.

Test setup

By adjusting the load point placements, the specimens were prepared for testing. The center of the span was fixed locations for the linear voltage displacement transducers (LVDTs). To prevent the impact of load concentration on the concrete, bearing plates with the dimensions 20 x 100 x 100 mm (0.79 x 3.94 x 3.94 in.), thickness x width x length, were employed at the loading and supporting locations. To get rid of any imperfections in the concrete surface, neoprene rubber pads were inserted between the bearing plate and the

Table 2—Steel reinforcement properties

Nominal diameter, mm	Actual diameter, mm	Yield stress, MPa	Ultimate stress, MPa	E_s, GPa	Yield strain ε_{yield}	Location of used bars
12	12	575.9	680	200	0.288%	Flexural reinforcement
8	8	517.7	656.2	200	0.259%	Flexural, vertical, and horizontal web reinforcement
6	5.9	432	520	200	0.216%	Longitudinal reinforcement for struts
4	4.8	550	740	200	0.275%	Vertical and horizontal web reinforcement

Note: Tests were carried out at the Structural Laboratory of the College of Engineering at the University of Diyala.

Fig. 2—Steel reinforcement for all specimens.

a- Steel mold for reference specimen. **b- Steel mold for frame specimen.**

Fig. 3—Casting concrete in steel molds.

test specimen, as shown in Fig. 4. Using a loading rate of 2 kN/s, the specimens were tested by being subjected to monotonic-static loading increments until failure. The test was finished when the overall load on the specimen began to decline.

Instrumentation

To monitor the strain values of the important zones, electrical strain gauges of 25 and 6 mm (0.98 and 0.24 in.) lengths were mounted to the concrete surface and reinforcing bars, respectively. The concrete strain was measured perpendicular to the struts, in addition to measuring the strains of the steel reinforcement parallel to the struts, the web steel bars, and the main reinforcing steel.

EXPERIMENTAL RESULTS AND DISCUSSION

The flexural crack load, diagonal crack load for both parts of the span (more curved [MC] and less curved [LC]), failure load, midspan deflection, and strain were studied, as shown in Table 3. Figure 5 shows the modes and locations of failure of specimens through which behavior can be ascertained. To organize the presentation of the results, the specimens were divided into three discussion groups. Accordingly, the first group is the web reinforcement role group, the second group

is the flexural reinforcement role group, and the third group is the compressive struts' role group.

Web reinforcement role (Group 1)

Group 1: Cracking pattern and failure mode—In E.12.4.4, in the outer face of the more-curved span part (MC), the first diagonal cracks appeared at 25% of the experimental failure load (P). That percentage became 16%P, 24%P, and 73%P in the cases of E.12.4.0, E.12.0.4, and E.12.0.0, respectively. As for the less-curved span part (LC), the cracks appeared at 47%P in E.12.4.4 and approximately 45%P, 64%P, and 81%P in E.12.4.0, E.12.0.4, and E.12.0.0, respectively. That is, the MC causes cracks to appear early, while they are delayed in the LC. That happens because the torsional stresses are greater in the MC than in the LC, so the total shear stresses in the MC are greater, especially in the outer face (Fig. 6).

The cracks resulting from torsional moments are distinguished from the strut of STM cracks by being at an angle of 45 degrees. Those torsional cracks do not connect directly to the loading and supporting points but rather meet with their counterparts in the adjacent spans to form the shape of a bowl. As a result, spalling and concrete cover separation occurred in the case of the reinforced web, while the splitting failure accompanied by the displacement of one of the crack sides toward the outer face occurred in the case of E.12.0.0. As for the flexural cracks, they appeared first in the inner face under the loading points and above the supporting points in a vertical manner. As the path from the loading to the supporting points was somewhat more direct in the inner face than in the outer face, flexural cracks appeared in the inner face earlier. Finally, specimens E.12.4.4 and E.12.4.0 failed in the MC part of the span. This makes sense because the MC is the more critical part of the span. In E.12.0.4 and E.12.0.0, failure occurred in the struts of the LC span part. Although the LC span part is less critical, the failure here occurred as a result of the effect of the strut horizontal component, which was supposed to be resisted by the omitted vertical web reinforcement. Therefore, it can be concluded that the role of web reinforcement is important, as it overshadows the curvature difference between the MC and LC.

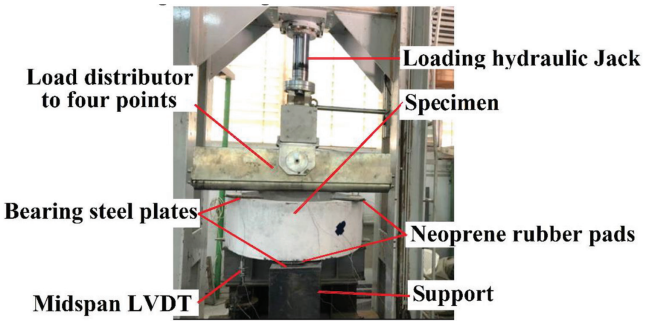

Fig. 4—Test setup.

Compared with E.12.4.4, load capacity decreased in E.12.4.0, E.12.0.4, and E.12.0.0 by approximately 24%, 38%, and 64%, respectively. That is, vertical web reinforcement affected the load capacity more than horizontal web reinforcement. The strut-and-tie angle being 32.5 degrees made the strut horizontal component larger than the vertical component, which made the vertical web reinforcement more important in resisting than the horizontal one.

In a related context, in E.12.8.8, the diagonal cracks appeared in the MC and LC span parts by approximately 17%P and 47%P, respectively. When the diameter of the web reinforcing steel was increased, the width of the cracks decreased without developing, so the failure mode changed from strut to node, with a slight increase in load capacity of

Table 3—Test results of specimens

No.	Beam designation	Δ, mm	$\Delta_{cr\text{-}flex}$, mm	$\Delta_{cr\text{-}diag}$, mm	$P_{cr\text{-}flex}/P$, %	LC $P_{cr\text{-}diag}/P$, %	MC $P_{cr\text{-}diag}/P$, %	P/P_{STM}	P, kN	$P_{cr\text{-}flex}$, kN	LC $P_{cr\text{-}diag}$, kN	MC $P_{cr\text{-}diag}$, kN	P_{STM}, kN	Failure mode
1	E.12.4.4	9.63	3.89	2.12	45.7	46.8	24.47	1.82	940	430	440	230	517	C (MC)
2	E.12.4.0	15.7	5.49	2.64	44.8	44.8	16.1	1.42	715	320	320	115	502	D (MC)
3	E.12.0.4	3.21	1.72	0.73	51.5	63.5	24	1.18	583	300	370	140	496	C (LC)
4	E.12.0.0	6.42	5.83	3.22	96.2	80.5	72.9	1.34	343	330	276	250	256	D (LC)
5	E.12.8.8	9.81	3.29	0.92	47	47	16.67	2.17	1020	480	480	170	470	N
6	E.8.4.4	6.81	2.01	1.94	37.9	35.5	33.13	1.81	845	320	300	280	468	C (MC)
7	E.0.4.4	7.75	3.66	4.32	33	68	41.24	—	485	160	330	200	—	F
8	E.0.0.0	5.5	4.87	—	90	—	—	—	174	155	—	—	—	F
9	EFOT	6.8	3.07	1.82	55	50	30	1.62	400	220	200	120	247	C (LC)
10	EFSTM	16.24	3.74	2.06	46.5	42	31	0.99	452	210	190	140	454	N

Note: C is compressive strut failure; F is flexural tie failure; D is diagonal splitting failure; N is nodal failure; P_{STM} is theoretical load according to ACI 318-19 STM; $P_{cr\text{-}diag}$ is first diagonal cracking load; $P_{cr\text{-}flex}$ is first flexural cracking load; P is experimental failure load; $\Delta_{cr\text{-}diag}$ is midspan deflection at first diagonal crack; $\Delta_{cr\text{-}flex}$ is midspan deflection at first flexural crack; Δ is midspan deflection at experimental failure load; MC is more curved part of span; LC is less curved part of span; 1 kN = 0.225 kip.

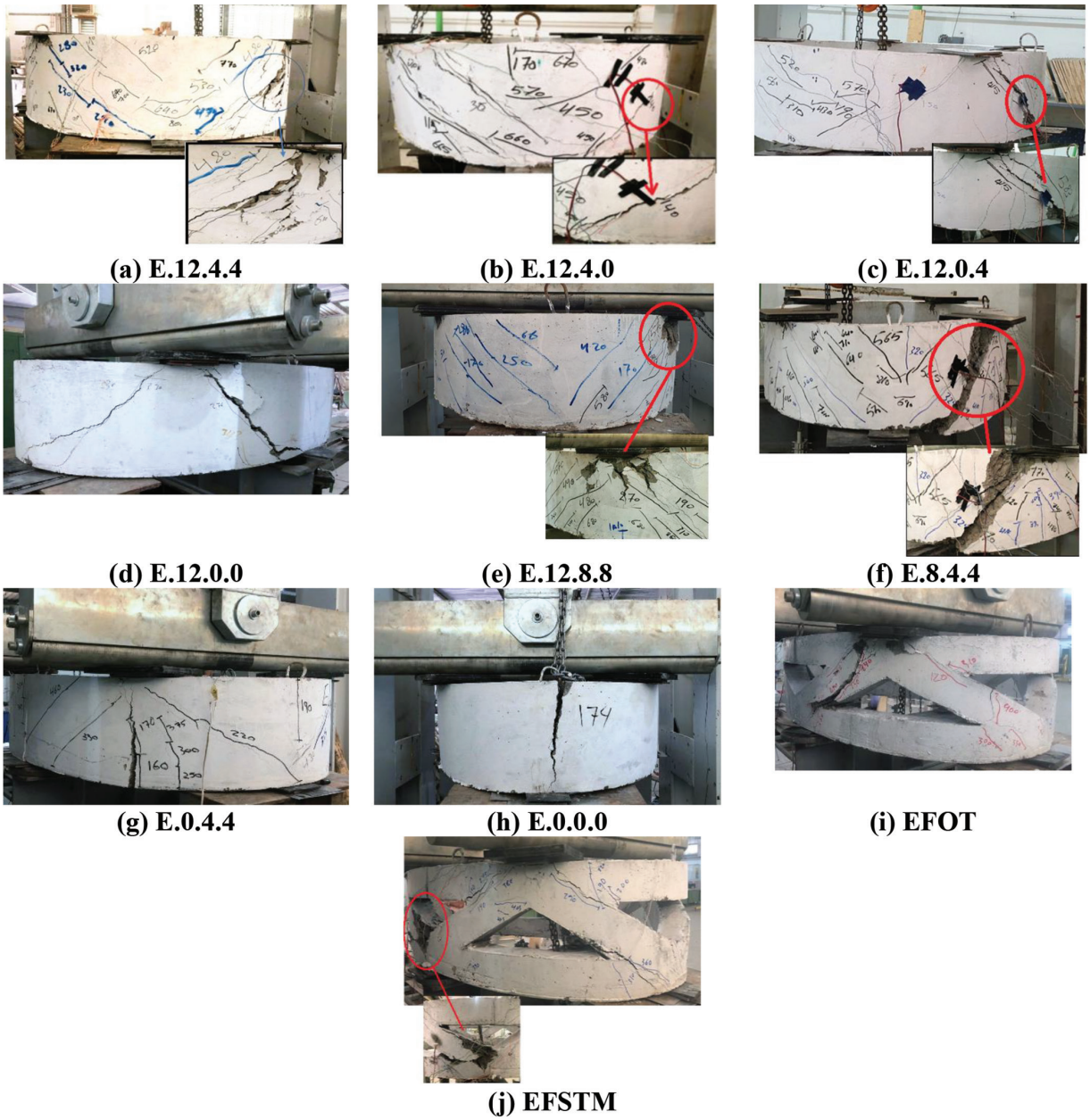

Fig. 5—Cracking pattern of test specimens at failure.

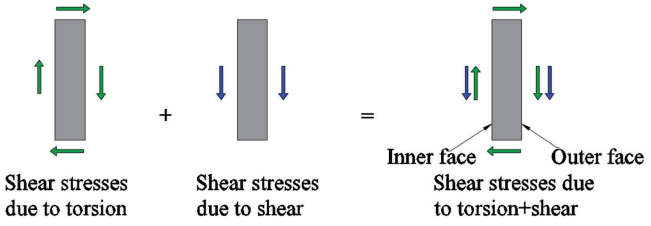

Fig. 6—Shear stresses due to shear and torsion in elliptical deep beams.

9%. Increasing the amount of reinforcing steel did not significantly delay the appearance of cracks because the concrete reached its maximum tensile strength in both cases, after which the stresses were transferred to the steel. Therefore, it can be said that using the ACI 318-19 minimum amount of reinforcing steel is sufficient because it provides the reasonable cost and load capacity and it avoids the less-preferred concrete brittle failure compared to ductile steel failure.

In specimen E.0.0.0, flexural cracks appeared first. Although flexural cracks are not usually considered dominant in deep beams, the absence of reinforcement makes them dominant, causing failure. This explains the huge decrease in the load capacity of E.0.0.0 of 81% compared to E.12.4.4. This took place because E.0.0.0 relied on the tensile strength of its concrete only, which is completely neglected by ACI 318-19. However, if only web reinforcement is maintained, as in specimen E.0.4.4, the failure of the flexure will be in the middle of the specimen span, accompanied by a decrease in load capacity of 48% compared to E.12.4.4. Here, it is possible to assert the contribution of web reinforcement in flexural strength.

Group 1: Load-deflection response—By means of the load-deflection response (Fig. 7), changing the reinforcement affects behavior, ductility, and stiffness. In E.12.4.0, the deflection increased, and stiffness decreased. This means that the horizontal web reinforcement resists the deflection more than the vertical web reinforcement. This behavior occurs because the web horizontal reinforcement, in combination with the flexural reinforcement, provides resistance to bending moments, in addition to resistance to torsional moments. In E.12.0.0, a decrease in stiffness took place after the appearance of cracks. In general, linear behavior dominated from the beginning of loading until shortly before failure, after which a bowing occurred, resulting from the transfer of stresses from the concrete to the reinforcing steel. This indicates that shear behavior is the dominant behavior.

Group 1: Strain variation—Concrete strain gauges were fixed in the MC and LC parts of the specimen span. Higher strain values occurred in the MC part of the span under consideration, meaning that the stresses were higher here (Fig. 8). Strain gauges also helped to identify more about the mode of failure based on whether the reinforcement reached yielding or not (Fig. 9). The sudden changes in the strain values recorded in the reinforcing steel clearly indicated the formation of cracks because the steel began to resist the stresses on its own. In specimens E.12.4.4 and E.12.4.0, only the web reinforcing steel reached the yield, while the flexural steel did not. This also indicates that the failure occurred in the struts of both specimens. In specimen E.12.0.4, both the web and the flexural reinforcement did not reach the yield, as the cracks formed a lesser angle with the horizon (approximately 28 to 30 degrees) due to the absence of vertical web reinforcement. The web and the flexural reinforcement did not reach the yield in specimen E.12.8.8—that is, the cracks did not develop much, so nodal failure took place.

Group 1: Estimation of STM—The STM of ACI 318-19 was not sensitive to the change in the reinforcing steel because it deals with reinforcing steel through the strut coefficient (β_s) only. The value of β_s was constant at 0.75 in the presence of minimum reinforcing steel, with a ratio of 0.25%, while in the case of less reinforcing steel, the value of β_s was 0.4, so the STM theoretical load capacity decreased significantly. The STM maintained its reservation despite changing the web reinforcing steel. In the reference specimen E.12.4.4, the STM theoretical load capacity became less than the experimental capacity by 45% (Fig. 10). In E.12.4.0, E.12.0.4 and E.12.0.0, the STM theoretical load capacity became less than the experimental by 30%, 15%, and 25%, respectively. Compared to

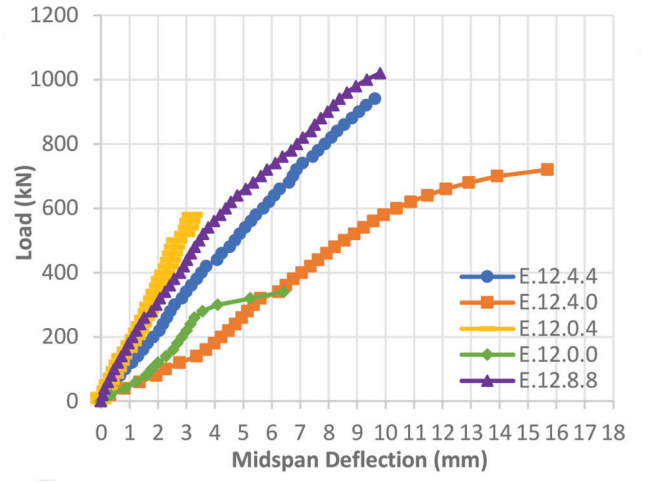

Fig. 7—Load-deflection response under effect of web reinforcement.

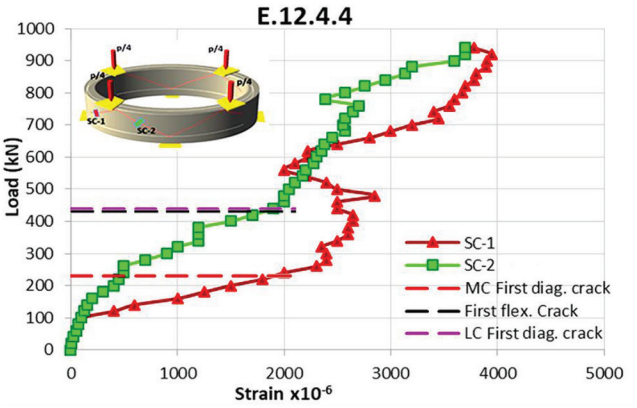

Fig. 8—Load versus average concrete strain in specimen E.12.4.4. (Note: 1 kN = 0.225 kip.)

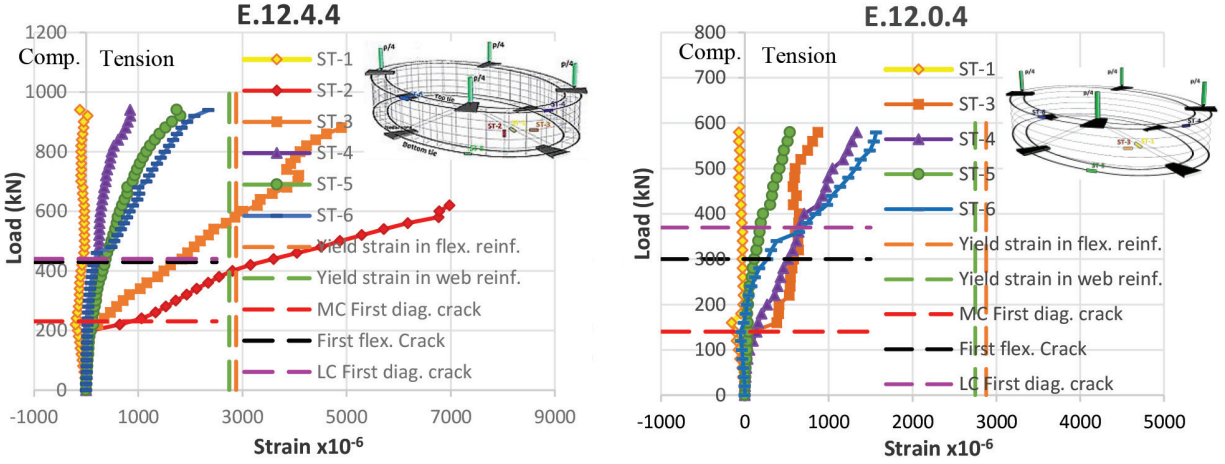

Fig. 9—Load versus steel strain values for specimens E.12.4.4 and E.12.0.4. (Note: 1 kN = 0.225 kip.)

Fig. 10—Comparison between P_{STM} *and* P *under effect of web reinforcement.*

E.12.4.4, when increasing the web reinforcing steel by 300% (E.12.8.8), the STM theoretical load capacity became less than the experimental by 54%. The STM assumes that the horizontal components of the struts are mainly resisted by the tie (flexural reinforcement). Nonetheless, because the tie here was continuous (tie of an elliptical ring beam), and also due to the contribution of the horizontal web reinforcement, a difference between the theoretical and experimental load capacities occurred.

Flexural steel reinforcement role (Group 2)

Group 2: Cracking pattern and failure mode—In E.8.4.4, initial diagonal cracks appeared in the MC span part at 33%*P* and in the LC span part at 36%*P*, while the first flexural cracking load was lower compared to E.12.4.4 by approximately 26%. This indicates the importance of flexural steel reinforcement in reducing the cracking load. By increasing the load upon testing, the behavior of E.8.4.4 did not differ significantly from E.12.4.4, as the failure mode remained at the struts in the MC part of the span, with a decrease in the load capacity of 10%. Flexural cracks appeared first in the inner face and then in the outer face because the reduction of reinforcement increased the effect of curvature. In E.0.4.4, the flexural cracking load decreased by approximately 63% compared to E.12.4.4. After, the diagonal cracks appeared in the MC span part at 41%*P* and the LC span part at 68%*P*. By the end of loading, flexural cracks developed significantly, causing failure in the lower tie, with a load capacity of approximately 48% lower compared to E.12.4.4. It has been seen that horizontal web reinforcement meaningfully contributed to the load capacity. More specifically, when both the web and the flexural steel reinforcements were omitted in E.0.0.0, compared with E.0.4.4, the load capacity decreased by 64%, with the failure mode changing to more brittle.

Group 2: Load-deflection response—It must be pointed out here that reducing the amount of flexural reinforcing steel in E.8.4.4 caused a change in load-deflection response from linear to nonlinear due to being more ductile, as shown in Fig. 11. The reduction in the flexural reinforcing steel (E.8.4.4) did not cause a decrease in stiffness compared with E.12.4.4 because the flexural reinforcement in both cases was sufficient enough not to cause tie failure, but with

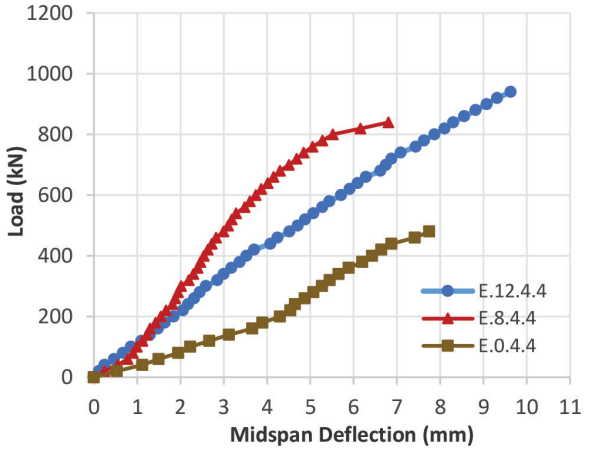

Fig. 11—Load-deflection response under effect of flexural reinforcement.

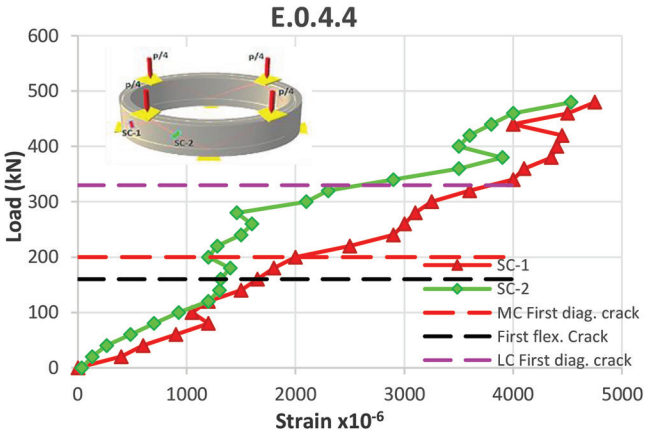

Fig. 12—Load versus average concrete strain for specimen E.0.4.4. (Note: 1 kN = 0.225 kip.)

somewhat less brittleness. The complete omission of flexural reinforcement in specimen E.0.4.4 caused a decrease in stiffness due to the lack of sufficient reinforcing steel to resist the bending and torsional moments.

Group 2: Strain variation—Concrete strain gauges were set in the specimen span's MC and LC parts. The MC part of the span under investigation had greater values, indicating that its stresses were larger (Fig. 12). Despite the fact that the flexural steel reinforcement reached the yield when its amount was reduced in E.8.4.4, the strut also failed due to the assistance provided by the horizontal web reinforcement to the flexural reinforcement. At the same time, the vertical web reinforcement reached the yield, and the horizontal web reinforcement approached the yield due to the development of strut cracks (Fig. 13). When omitting the flexural reinforcement in E.0.4.4, the strain values in the vertical web reinforcement did not increase much because the flexural cracks were parallel to the vertical web reinforcement strain gauges. As for the strain values of the horizontal web reinforcement, they approached yielding because the horizontal web reinforcement contributed to resisting the flexural cracks perpendicular to this reinforcement. In general, the flexural reinforcement did not frequently reach yield due to the nature of the deep beam's elliptical annular shape—that is, the spans were connected to each other. In addition, the

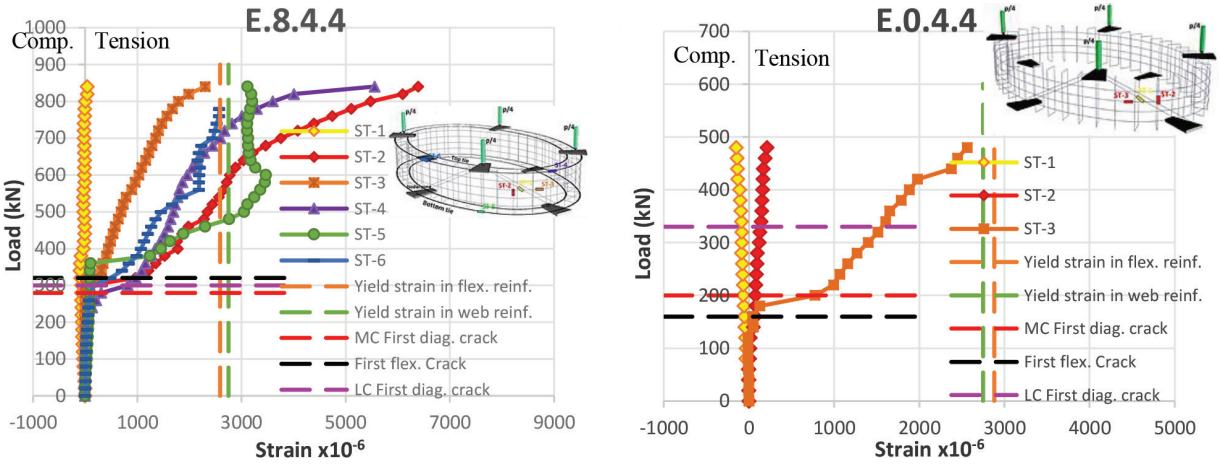

Fig. 13—Load versus steel strain values for specimens E.8.4.4 and E.0.4.4. (Note: 1 kN = 0.225 kip.)

positive and negative bending moments were generally few in the deep beams because the tie tensile forces decreased as the length of the shear span decreased. This makes sense because, in deep beams, the strut vertical component is mainly resisted by the concrete compressive strength, while the strut horizontal component is mainly resisted by the tie reinforcing steel, in addition to the contribution of horizontal web reinforcement. The non-yield of the flexural reinforcement (E.12.4.4) indicates that its role was small, but this did not diminish its importance because its omission in E.0.4.4 caused a more brittle failure, with a very low capacity of 48%. By comparing the load capacity between E.12.0.0 and E.0.4.4, it was found that web reinforcement is more influential than flexural reinforcement. That is true because horizontal web reinforcement is able to resist flexural stresses as well, while flexural reinforcement resists shear by dowel action only. That is why the loss of both flexural and web reinforcement in specimen E.0.0.0 gave the least load capacity and the most brittle failure than if one of them was omitted.

Group 2: Estimation of STM—Regarding E.8.4.4, the theoretical load capacity of the STM in ACI 318-19 was 45% less than the experimental load capacity (Fig. 14). On the other hand, the theoretical failure using the STM occurred in the tie (close to strut failure), while the laboratory specimen failed in the strut region. This supports the fact that tie reinforcement has a minor role in elliptical deep beams compared to other steel reinforcements. Additionally, the STM does not accurately describe this role here because it does not take into account the effect of span continuity. On the other hand, in E.0.4.4, the STM cannot give theoretical load capacity because it neglects the tensile strength of concrete and does not take into account the effect of elliptical ring beam continuity. Therefore, there was no tie in E.0.4.4—that is, the STM truss was not formed at all, while in the laboratory, E.0.4.4 resisted the applied loads by dint of the horizontal web steel without neglecting the low tensile resistance of the concrete.

Role of compressive struts (Group 3)

Group 3: Cracking pattern and failure mode—STM struts were represented by casting alone to see how ACI 318-19

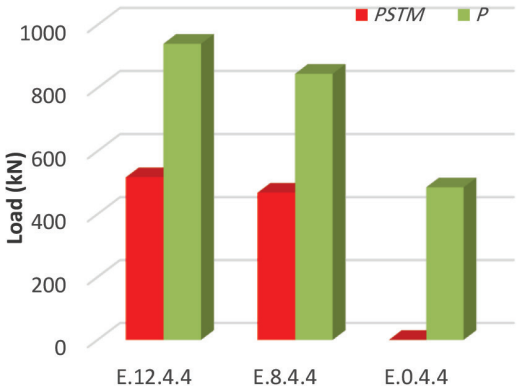

Fig. 14—Comparison between P_{STM} *and* P *under effect of flexural reinforcement.*

visualized the stresses flowing through them. Casting only the stress paths of the ACI 318-19 STM led to the formation of frame specimens. These struts were reinforced as compression members (EFSTM), while others were not reinforced (EFOT). By testing the EFOT specimen, the first strut diagonal cracks appeared in the MC span part at 31%*P*. After, the cracks appeared in the LC span part at 50%*P*, while tie flexural cracks appeared at 55%*P*. The perpendicular cracks on the outer faces of the struts were caused by the generated bending moments in the strut due to its curvature. They were similar to the bending moments generated in curved or straight columns under an eccentric axial load. The load capacity of the EFOT specimen was 57% less than E.12.4.4, while it was 17% more than E.12.0.0. In the EFOT, the bottle-shaped strut was not formed due to the limited strut width (prismatic strut), while in E.12.0.0, the bottle-shaped strut was formed, so perpendicular tensile stresses appeared on its struts, leading to splitting failure. In the EFSTM, cracks appeared in the MC span part at 31%*P* and in the LC span part at 42%*P*, while tie flexural cracks appeared at 47%*P*. The stress redistribution occurred because the struts were reinforced. By increasing the loading, at the supporting zone, nodal failure took place with a 52% lower load capacity than E.12.4.4. The load capacity did not increase much in the EFSTM compared to the EFOT, as the increase reached only 13%. The small difference in the load capacity of the EFSTM compared to the EFOT can be attributed to

the fact that the strength of the strut depends mainly on the compressive strength of the concrete, while the reinforcing steel added to the strut is the ACI 318-19 requirement for minimum reinforcement. It should be noted that a lateral displacement in the failed reinforced strut was seen with a concrete cover separation. This is due to torsional moments, although there were relatively few. In general, the LC span part had a greater load capacity than the MC because it had fewer bending and torsional moments due to being less curved. However, in the case of sufficient reinforcement provisions, failure occurred in the MC span part, meaning that the reinforcement strengthened the LC more than the MC. In the case of the LC, as a result of its straighter length, its axial force had a greater role than the bending and torsional moments. Therefore, splitting occurred in the LC when there was little or no reinforcement (E.12.0.4, E.12.0.0, EFOT, and EFSTM), while when it was sufficiently reinforced (E.12.4.4, E.12.4.0, and E.8.4.4), concrete confinement occurred, which made it stronger, meaning that the failure was transmitted to the MC span part.

Group 3: Load-deflection response—Compared to E.12.4.4, the stiffness was less in the EFOT and EFSTM. The EFSTM specimen showed more ductile behavior than the EFOT (Fig. 15). At the beginning of the loading, the load-deflection response was linear, which indicated the dominance of shear, but shortly before the failure, the response became nonlinear, accompanied by a small increase in deflection. In the EFOT, this deflection increase can be attributed mainly to the contribution of tie flexural steel reinforcement. In the EFSTM, the increases in deflection occurred more due to the stress redistribution and the increased ductility provided by the strut reinforcing steel. It should be observed here that the EFSTM had a higher deflection because the presence of the strut reinforcement made its joints rigid, meaning that they suffered more rotation, which generated a higher deflection in the middle of its tie.

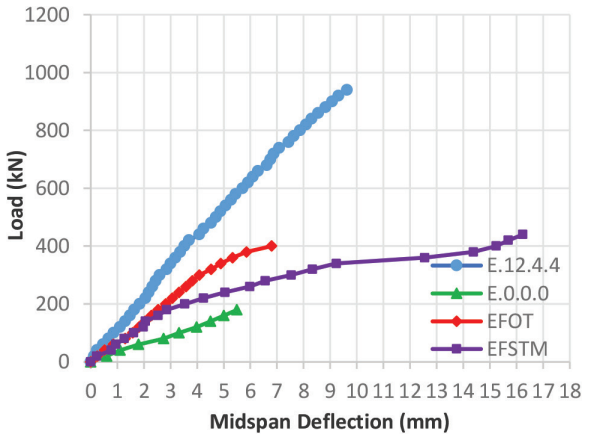

Fig. 15—Load-deflection response under effect of strut reinforcement.

Group 3: Strain variation—In both frame specimens, the strut-and-tie reinforcing steel did not reach the yield, meaning that failure occurred in the concrete of the struts and nodes (Fig. 16). On the other hand, the tie steel strain values in the EFSTM were approximately 200% more than that in the EFOT. Through the strain gauges fixed to the main longitudinal steel of the struts, the contribution of both the reinforcing steel and the concrete can be ascertained and compared with the contribution values according to ACI 318-19. Note that the bottom and top members in Table 4 are denoted by the symbols B and T, respectively. The contribution of reinforcing steel was 8% in the MC span part and 7% in the LC span part. These contribution values are considered low compared to ACI 318-19 estimates, which amounted to 37%. This is due to the fact that the ACI Code imposes the yield of the steel reinforcement. In the laboratory, the main strut reinforcing steel did not reach yield, as cracks appeared at both ends of the strut. Compared with the EFOT, there were fewer mid-strut cracks in the EFSTM due to stirrup confinement.

Group 3: Estimation of STM—In the laboratory, the difference in load capacity between the two frame specimens was 13%, which indicates the important role of the strut concrete in front of its reinforcement. The load capacity of the EFOT specimen maintained its superiority over the STM theoretical load capacity by approximately 38%, while the load capacity of the EFSTM specimen was almost equal to the STM theoretical load capacity (Fig. 17).

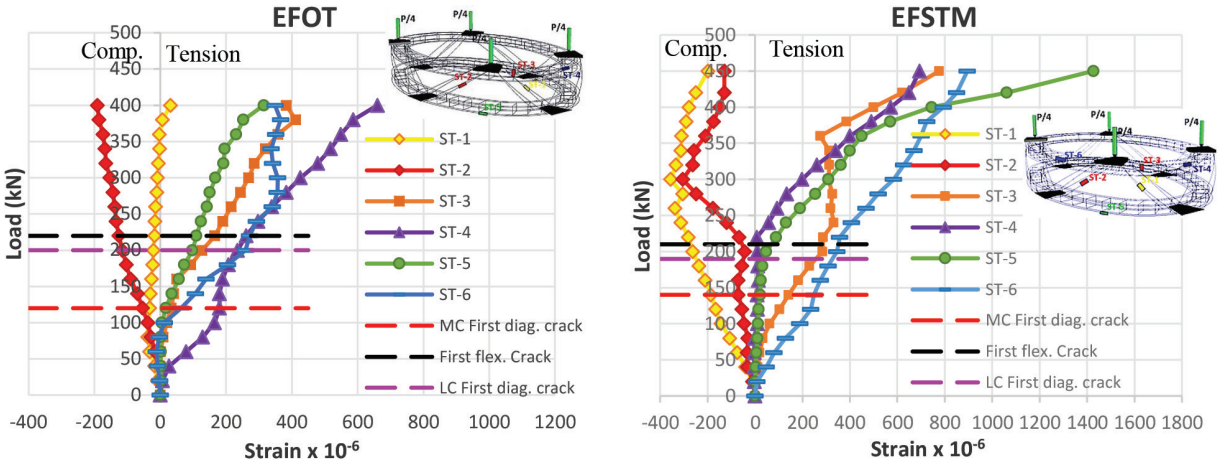

Fig. 16—Load versus steel strain values for EFOT and EFSTM specimens. (Note: 1 kN = 0.225 kip.)

Table 4—Reinforcement contribution of struts and ties strength depending on ACI 318-19 in EFSTM specimen

Specimen	STM truss member	Experimental			ACI 318-19 equations			$N_{s\text{-}exp}/N_{s\text{-}code}$	$N_{c\text{-}exp}/N_{c\text{-}code}$	Notes
		$N_{s\text{-}exp}$, kN	$N_{c\text{-}exp}$, kN	$N_{s\text{-}exp}/N_{c\text{-}exp}$	$N_{s\text{-}code}$, kN	$N_{c\text{-}code}$, kN	$N_{s\text{-}code}/N_{c\text{-}code}$			
EFSTM	MC Strut	8.05	97.2	0.08	48.9	132.6	0.37	0.16	0.73	—
	LC Strut	6.90	98.3	0.07	48.9	132.6	0.37	0.14	0.74	—
	MC T. Tie	31.40	—	—	130	—	—	0.24	—	ACI Code neglects concrete tensile force in tie (N_c)
	B. Tie	64.55	—	—	130	—	—	0.50	—	
	LC T. Tie	40.50	—	—	130	—	—	0.31	—	

Note: 1 kN = 0.225 kip.

Table 5—Comparison in terms of weight, cost, and service openings

Specimen	% Decrease in:						% gain in service openings
	Weight			Cost			
	Concrete	Reinforcement	Total Weight	Concrete	Reinforcement	Total Cost	
E.12.4.4	—	—	—	—	—	—	—
EFSTM	22.9	4.95	21.48	21.9	4.95	1.47	20.86

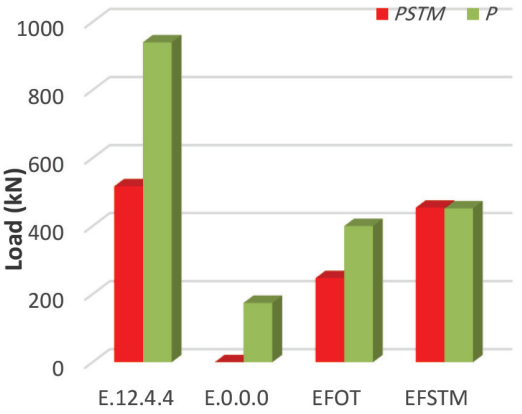

Fig. 17—Comparison between P_{STM} *and* P *under effect of strut reinforcement.*

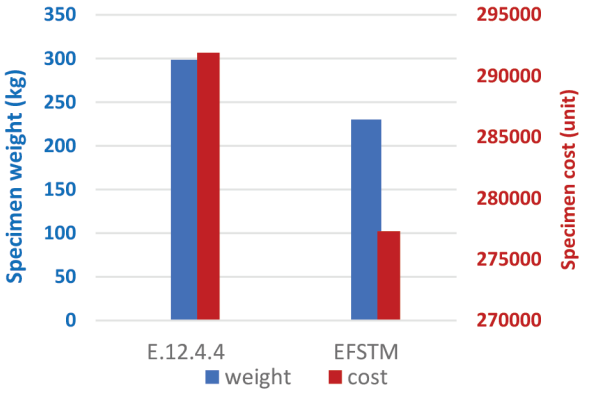

Fig. 18—Comparison in terms of weight and cost.

Comparisons in terms of cost, weight, and service openings

The EFSTM specimen can be presented here as an alternative to the traditional elliptical deep beam, as it can save weight and cost and provide openings for services, in addition to a distinctive architectural shape. The decrease in weight was 21%, the opening providing for the services passage was 21%, and the decrease in the cost was 1.5%. The 1.5% reduction in cost is calculated symbolically here because the real cost reduction will be reflected in large facilities as a result of light weight and availability of service openings, as shown in Table 5 and Fig. 18.

MODIFYING STM BY ADDING MOMENTS

This section addresses, in closed form, the topic of lateral stability against the buckling of horizontally curved beams without a constant radius of curvature. The underlying premise of this theoretical analysis is that the cross section in the strained state maintains its original shape, and second-order terms can be ignored because, in the buckling condition, the angular and lateral displacements are extremely tiny relative to the initial radius of curvature. Theoretical STM calculations of ACI 318-19 do not account for the bending moments generated by the strut curvature. Consequently, these bending moments were added to the STM by treating the strut here as a curved column, changing the STM to the non-straight strut-and-tie method (nSTM). Because the shape of the curvature in the current study is elliptical (Fig. 19), the value of the initial displacement (e_i) varies in each shear span, as well as the direct distance in a straight line between the load and the support (L). Therefore, both were compared theoretically with the traditional STM in addition to laboratory tests. The paths of the struts are drawn, in addition to their sectional dimensions, by finding the dimensions of the node and then the dimensions of the struts

$$w_t = 2(h - d) \quad (1)$$

$$w_c = 0.8w_t \quad (2)$$

$$\text{Lever arm: } jd = h - 0.5w_t - 0.5w_c - w_t \quad (3)$$

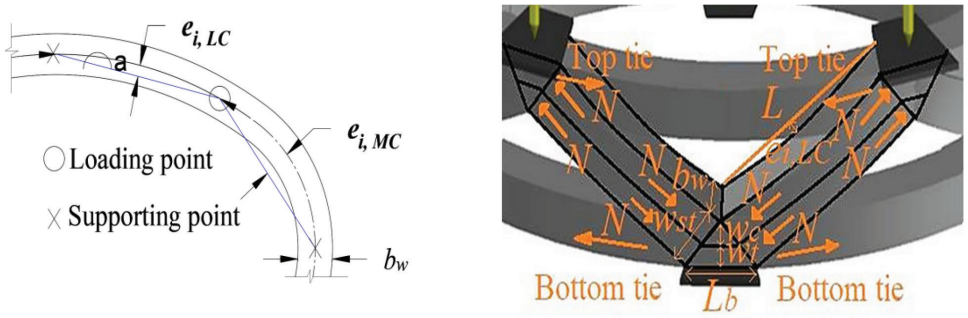

Fig. 19—Eccentricities of nSTM due to elliptical curvature.

$$\text{Strut-and-tie angle: } \theta = \tan^{-1}\left(\frac{jd}{a}\right) \tag{4}$$

$$w_{st} = \left(\left(\frac{0.5L_b w_c}{w_c + w_t}\right)\sin\theta + w_c\cos\theta\right) + \left(\left(0.5L_b - \frac{0.5L_b w_c}{w_c + w_t}\right)\sin\theta + w_t\cos\theta\right) \tag{5}$$

The applied load produces an axial force in the struts resulting from the direct transfer of loads. In addition, it produces bending moments resulting from curvature that reduce load capacity.

$$\text{Combined stresses: } \sigma = \frac{N}{A} \pm \frac{MC}{I} \tag{6}$$

Using Eq. (6) to calculate strut stresses:

$$0.85\beta_s f_c' = \frac{N}{w_{st} \times b_w} \pm \frac{N \times e \times \frac{b_w}{2}}{\frac{w_{st} \times b_w^3}{12}} \tag{7}$$

$$\text{The Euler equation: } N_E = \frac{E_c I \pi}{L^2} \tag{8}$$

Additional strut midheight out of straightness due to N:

$$e = \frac{\frac{N}{N_E}}{1 - \frac{N}{N_E}} \times e_i \tag{9}$$

where e_i is the initial strut midheight out of straightness: $e_{i\text{-}MC}$ for the more-curved span part; and $e_{i\text{-}LC}$ for the less-curved span part.

Substituting Eq. (9) in Eq. (7):

$$0.85\beta_s f_c' = \frac{N}{w_{st} \times b_w} \pm \frac{6Ne_i \frac{N/N_E}{1 - N/N_E}}{w_{st} \times b_w^2} \tag{10}$$

$$\text{Then } N = \frac{0.85\beta_s f_c' w_{st} b_w^2}{b_w \pm 6e_i \frac{N}{N_E - N}} \tag{11}$$

It is feasible to incorporate the influence of curvature along the strut while solving Eq. (11) for N. The value of N is extracted once for the MC and once for the LC, and then the least value is chosen. Next, the nSTM's overall theoretical load capacity: P_{nSTM} = number of struts × $N\sin\theta = 8N\sin\theta$

Check tie strength:

P_{nSTM} = number of struts × $A_s f_y \tan\theta = 8A_s f_y \tan\theta$

Next, check each node face; load capacity is determined by taking the minimum value of the strut, tie, and node strength.

Validation of proposed nSTM

The experimental failure loads and the findings of the nSTM in the MC and LC are compared in Table 6. It was discovered that ACI 318-19's STM is safe and suitably conservative. Moreover, adding the influence of strut bending moments does not boost its conservativeness. In more detail, compared to laboratory tests, the conservativeness of the STM was 0 to 54%, while the conservativeness of the proposed nSTM was 14 to 60%. Figure 20 illustrates the nSTM's effectiveness. All that is certain is that there was an overstated rise in the STM's conservatism. As a result, it is advised to employ the STM in this case as it is simple and safe and does not require any adjustments to the deeply curved horizontal beams. It is necessary to point out an important thing: using the STM without including the effect of curvature led to the load capacity of the EFSTM being equal to its laboratory load capacity. Nonetheless, after adding the effect of curvature, the nSTM theoretical load capacity became less than the laboratory load capacity by 14%, and this supports the idea that adding the effect of curvature to the STM makes it safer.

CONCLUSIONS

Ten laboratory specimens were cast and reinforced to study strut curvature in detail, with a proposal to extend the strut-and-tie method (STM) to be more realistic when dealing with such curved deep members. The most important conclusions reached in the current study can be summarized in the following points:

1. Although the STM does not take into account the curvature in the inclined struts of elliptical beams, it remains a conservative and safe method that engineers can use easily. In addition, a proposed mathematical model has been presented here to develop the STM by adding the role of bending moments. Based on the current study's limited number of specimens, the proposed model (the non-straight

Table 6—nSTM validation

No.	Specimen designations	P, kN	% change in P	ACI 318-19 P_{STM}, kN	P_{nSTM} MC, kN	P_{nSTM} LC, kN	P/P_{STM}	P/P_{nSTM} MC	P/P_{nSTM} LC
1	E.12.4.4	940	—	517	441	480	1.82	2.13	1.96
2	E.12.4.0	715	–24	502	429	467	1.42	1.67	1.53
3	E.12.0.4	583	–38	496	424	462	1.18	1.38	1.26
4	E.12.0.0	343	–64	256	234	246	1.34	1.47	1.39
5	E.12.8.8	1020	+9	470	403	438	2.17	2.53	2.33
6	E.8.4.4	845	–10	468	468	468	1.81	1.81	1.81
7	E.0.4.4	485	–48	—	—	—	—	—	—
8	E.0.0.0	174	–81	—	—	—	—	—	—
9	EFOT	400	–57	247	226	237	1.62	1.77	1.69
10	EFSTM	452	–52	454	390	423	0.99	1.16	1.07

Note: 1 kN = 0.225 kip.

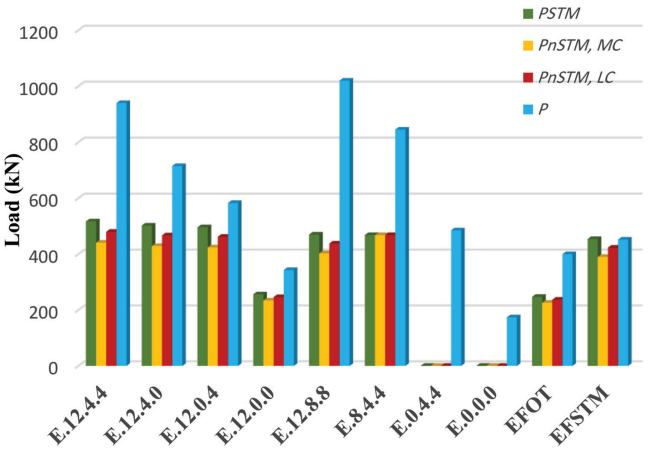

Fig. 20—Comparisons between P_{nSTM}, P_{STM}, *and* P. *(Note: 1 kN = 0.225 kip.)*

strut-and-tie method [nSTM]) also showed conservative results (9 to 15% less than the traditional STM of ACI 318-19), but it represents the reality of the combined stresses in a more realistic way.

2. Only STM stress paths were cast and reinforced with the minimum reinforcement of ACI 318-19. Accordingly, a specimen was obtained that was approximately 21% and 1.5% less in weight and cost, respectively, in addition to providing service openings of 21%. The proposed specimen was 52% lower in terms of experimental load capacity than the conventional reference specimen, but it remained equal to the theoretical calculations of the STM, which makes it a convincing alternative to the reference beam.

3. One of the main tasks of vertical web reinforcement is to resist the horizontal component of the strut. Therefore, its complete absence led to a 38% decrease in load capacity, in addition to the transfer of failure location from the more curved (MC) part of the beam span to the less curved (LC) part. The absence of horizontal web reinforcement, which resists the vertical component of the strut, also led to a 24% decrease in load capacity—that is, lower percentages because the strut-and-tie angle was less than 45 degrees.

4. The presence of flexural steel reinforcement was necessary because it is one of the members of the STM truss, which is formed in the elliptical deep beams during loading. That is, the absence of the flexural steel led to a rapid failure, not to mention the inability to perform theoretical calculations for the STM. On the other hand, the minimum reinforcement ratio recommended by ACI 318-19 was sufficient in terms of load capacity and cost. Therefore, the reduction in load capacity reached 10%, accompanied by no change in the failure mode.

AUTHOR BIOS

Khattab Saleem Abdul-Razzaq *is a Professor in the Department of Civil Engineering at the University of Diyala, Baqubah, Diyala, Iraq. He received his BSc and MSc from the University of Baghdad, Baghdad, Iraq, in 1997 and 1999, respectively. He received his PhD from Moscow State University of Civil Engineering, Moscow, Russia, in 2005. His research interests include reinforced concrete members.*

Baidaa N. Hasan *is a PhD Candidate in the Department of Civil Engineering at the University of Baghdad, where she received her BSc and MSc in 2019 and 2022, respectively. Her research interests include strut-and-tie modeling of reinforced concrete deep members.*

Asala A. Dawood *an Instructor in the Department of Civil Engineering at the University of Diyala, where she received her BSc and MSc in 2016 and 2020, respectively. She received her PhD Candidate from the Department of Civil Engineering at the University of Technology in 2024. Her research interests include reinforced deep concrete members.*

ACKNOWLEDGMENTS

The authors of the current research work are grateful to the laboratory staff at the Department of Civil Engineering/College of Engineering at the University of Diyala for their appreciated moral support.

REFERENCES

1. Jodidio, P., *Zaha Hadid: Complete Works 1979–Today*, Taschen, Cologne, Germany, 2022, 672 pp.

2. Mansur, M. A., and Rangan, B. V., "Study of Design Methods for Reinforced Concrete Curved Beams," *ACI Journal Proceedings*, V. 78, No. 3, May-June 1981, pp. 226-231.

3. Hsu, T. T. C., "Torsion of Structural Concrete—Behavior of Reinforced Concrete Rectangular Members," *Torsion of Structural Concrete*, SP-18, American Concrete Institute, Farmington Hills, MI, 1968, pp. 261-306.

4. Hsu, T. T. C.; Inan, M.; and Fonticiella, L., "Behavior of Reinforced Concrete Horizontally Curved Beams," *ACI Journal Proceedings*, V. 75, No. 4, Apr. 1978, pp. 112-123.

5. Badawy, H. E. I.; McMullen, A. E.; and Jordaan, I. J., "Experimental Investigation of the Collapse of Reinforced Concrete Curved Beams," *Magazine of Concrete Research*, V. 29, No. 99, June 1977, pp. 59-69. doi: 10.1680/macr.1977.29.99.59

6. Tamura, T., and Murata, H., "Experimental Study on the Ultimate Strength of R/C Curved Beam," *Proceedings of 7th International*

Conference on Fracture Mechanics of Concrete and Concrete Structures (FraMCoS-7), B. H. Oh, ed., Jeju, South Korea, May 2010, pp. 1783-1788.

7. Hassan, B. N.; Talal, A. H.; Khaleel, W. H.; Abdul-Razzaq, K. S.; and Dawood, A. A., "Parametric Study on Elliptical T-Section Deep Beams," *AIP Conference Proceedings*, V. 2787, No. 1, July 2023, Paper No. 080025.

8. Abdul-Razzaq, K. S.; Jalil, A. M.; and Dawood, A. A., "Ring Deep Beam – A Parametric Study," *AIP Conference Proceedings*, V. 2213, No. 1, Mar. 2020, Article No. 020128. doi: 10.1063/5.0000056

9. Talal, A. A.; Khaleel, W. H.; Hassan, B. N.; Abdul-Razzaq, K. S.; and Dawood, A. A., "A Finite Element Parametric Study of Reinforced Concrete Horizontally Circular Deep Beams," *E3S Web of Conferences*, V. 318, 2021, Article No. 03013.

10. Campbell, T. I.; Lee, E. Y. K.; and Chan, K. S., "Strength of Continuous Horizontally Curved Post-Tensioned Beams," *PCI Journal*, V. 25, No. 4, July-Aug. 1980, pp. 118-145. doi: 10.15554/pcij.07011980.118.145

11. Schlaich, J.; Schäfer, K.; and Jennewein, M., "Toward a Consistent Design of Structural Concrete," *PCI Journal*, V. 32, No. 3, May-June 1987, pp. 74-150. doi: 10.15554/pcij.05011987.74.150

12. Schlaich, J., and Schäfer, K., "Design and Detailing of Structural Concrete Using Strut-and-Tie Models," *The Structural Engineer*, V. 69, No. 6, Mar. 1991, pp. 113-125.

13. ACI Committee 318, "Building Code Requirements for Structural Concrete (ACI 318-19) and Commentary (ACI 318R-19) (Reapproved 2022)," American Concrete Institute, Farmington Hills, MI, 2019, 624 pp.

14. Nielsen, M. P., *Limit Analysis and Concrete Plasticity*, second edition, CRC Press, Boca Raton, FL, 1999, 936 pp.

15. Hsu, T. T. C., and Mo, Y. L., "Softening of Concrete in Torsional Members—Theory and Tests," *ACI Journal Proceedings*, V. 82, No. 3, May-June 1985, pp. 290-303.

16. Hsu, T. T. C., "Toward a Unified Nomenclature for Reinforced-Concrete Theory," *Journal of Structural Engineering*, ASCE, V. 122, No. 3, Mar. 1996, pp. 275-283.

17. Mansur, M. A.; Nagataki, S.; Lee, S. H.; and Oosumimoto, Y., "Torsional Response of Reinforced Fibrous Concrete Beams," *ACI Structural Journal*, V. 86, No. 1, Jan.-Feb. 1989, pp. 36-44.

18. Akhtaruzzaman, A. A., and Hasnat, A., "Torsion in Concrete Deep Beams with an Opening," *ACI Structural Journal*, V. 86, No. 1, Jan.-Feb. 1989, pp. 20-25.

19. Abdul-Razzaq, K. S., and Jebur, S. F., "Suggesting Alternatives for Reinforced Concrete Deep Beams by Reinforcing Struts and Ties," *MATEC Web of Conferences*, V. 120, 2017, Article No. 01004.

20. Abdul-Razzaq, K. S.; Jalil, A. M.; and Dawood, A. A., "Reinforcing Struts and Ties in Concrete Continuous Deep Beams," *Engineering Structures*, V. 240, Aug. 2021, Article No. 112339. doi: 10.1016/j.engstruct.2021.112339

21. Abdul-Razzaq, K. S., and Farhood, M. A., "Design-Oriented Testing and Modeling of Reinforced Concrete Pile Caps," *KSCE Journal of Civil Engineering*, V. 23, No. 8, Aug. 2019, pp. 3509-3524. doi: 10.1007/s12205-019-1650-5

22. Abdul-Razzaq, K. S., and Dawood, A. A., "Reinforcing Struts and Ties in Concrete Corbels," *ACI Structural Journal*, V. 118, No. 4, July 2021, pp. 153-162.

23. Abdul-Razzaq, K. S.; Talal, A. A.; and Dawood, A. A., "Role of Reinforcement in Concrete Ring Deep Beams," *ACI Structural Journal*, V. 120, No. 2, Mar. 2023, pp. 129-141.

24. Abdul-Razzaq, K. S.; Khaleel, W. H.; and Dawood, A. A., "Struts and Ties Realization in Reinforced Concrete Ring Deep Beams," *ACI Structural Journal*, V. 120, No. 4, July 2023, pp. 151-164.

25. Kang, Y. J., and Yoo, C. H., "Thin-Walled Curved Beams. I: Formulation of Nonlinear Equations," *Journal of Engineering Mechanics*, ASCE, V. 120, No. 10, Oct. 1994, pp. 2702-2101. doi: 10.1061/(ASCE)0733-9399(1994)120:10(2072)

ACI Honors and Awards Program Nominations

The American Concrete Institute is seeking your nominations for our Honors and Awards Program. Nominations are now being accepted for ACI's Honorary Member as well as for ACI's personal awards for individual or organizational merit, the ACI Young Member Award for Professional Achievement, the ACI Education Award, the ACI Certification Award, the ACI Concrete Sustainability Award, and more.

ACI selects the winners of its annual awards through an open nomination process.

You can participate in the Honors and Awards Program by nominating worthy candidates for award consideration.

Nomination forms can be found on the ACI website, www.concrete.org.

American Concrete Institute
+1.248.848.3188 • www.concrete.org

ACI STRUCTURAL JOURNAL TECHNICAL PAPER

Title No. 122-S15

Immediate Deflection of Cracked Prestressed Concrete Beams Based on Integration of Curvature

by Wassim Nasreddine, Adi Obeidah, Peter H. Bischoff, and Hani Nassif

Prediction of immediate deflection is evaluated for cracked prestressed concrete members using integration of curvature. Integration accounts for changes in member stiffness and strand eccentricity along the member length when applicable. Several approaches are considered, including a bilinear moment-deformation response and those using an effective moment of inertia based either on an effective prestress moment defined by an effective eccentricity of the prestress force or an offset in the cracked response with tension stiffening. Comparison is also made with deflection computed directly, assuming a uniform member stiffness based on the effective moment of inertia at the critical section where the moment is greatest. Results are evaluated using an extensive database for beams either fully or partially prestressed. The beams are simply supported under two-point loading and have a straight tendon profile with constant eccentricity. Integration of curvature is observed to improve prediction of immediate deflection in general and depends not only on the approach used but on several factors that include the cracking moment, elastic modulus of concrete, and the effect of approximating uncracked section properties with gross section properties.

Keywords: cracked; deflection; effective moment of inertia; integration; partially prestressed; prestressed concrete.

INTRODUCTION

Deflection of reinforced and prestressed concrete flexural members that are cracked under service load is often computed using an effective moment of inertia I_e assumed constant over the length of the member. The value for I_e is typically based on the critical section where the moment is greatest and is sometimes assumed to account for changes in stiffness along the member length (Branson 1965; Bischoff and Gross 2011). Some have argued that the use of a uniform value for I_e might not be suitable for complex loading and boundary conditions, as it does not always correctly account for the stiffer uncracked regions of the member (Ghali 1993; Razaqpur et al. 2000). Moreover, using a constant value of I_e may not be applicable for prestressed members with variable eccentricity of the prestressing tendons (Bischoff 2019). In some cases, integration of curvature might be more appropriate for computing deflection.

This paper evaluates immediate deflections computed for a cracked prestressed concrete beam using integration of curvature. Results are compared to a more direct method using a uniform value for I_e assumed to be representative of the member stiffness. Test results from a compiled database are used for comparison and validation purposes. Approaches assessed include a modified expression of Branson's I_e response shifted up to an effective prestress moment defined by an effective eccentricity of the prestress force (Tadros et al. 1985), expressions for I_e proposed by Bischoff et al. (2018) and Bischoff (2022) that also incorporate a shift in the I_e response (resulting from a shift in the cracked section response), and a simple bilinear moment-deformation response (PCI 2017; Bischoff 2019). This follows on from the work of Nasreddine et al. (2023) investigating several approaches for computing immediate deflection of cracked prestressed concrete members without integration, including ACI 318 (ACI Committee 318 2019).

RESEARCH SIGNIFICANCE

Estimating deflection and camber is an important part of the design process for prestressed concrete flexural members. This paper investigates the prediction of immediate deflection for cracked prestressed concrete based on the integration of curvature along the member span. Comparison is also made with deflection calculated directly assuming a uniform member stiffness based on the value of I_e at the critical section where the moment is greatest and stiffness lowest. Approaches proposed by Tadros et al. (1985), Bischoff et al. (2018), and Bischoff (2022), and an approach based on an assumed bilinear moment-curvature response are assessed for integration of curvature compared to computing deflection directly. Results are evaluated using a large database of test values (for 180 fully and partially prestressed beams) compiled by Nasreddine et al. (2023) and provide the reader with the level of accuracy and precision expected for each approach considered.

IMMEDIATE DEFLECTION

Reinforced concrete

Branson's (1965) approach for computing the immediate deflection of reinforced (nonprestressed) concrete with an equivalent moment of inertia I_e

$$I_e = \left(\frac{M_{cr}}{M_a}\right)^3 I_g + \left[1 - \left(\frac{M_{cr}}{M_a}\right)^3\right] I_{cr} \leq I_g \tag{1a}$$

was introduced into ACI 318 in the 1971 edition (ACI Committee 318 1971). Equation (1a) provides a gradual transition between the upper and lower bounds of I_g and

ACI Structural Journal, V. 122, No. 1, January 2025.

MS No. S-2023-373.R1, doi: 10.14359/51742153, received May 15, 2024, and reviewed under Institute publication policies.

I_{cr} as a function of M_{cr}/M_a when the member is cracked. The M_{cr}/M_a term raised to the power of three is assumed to provide an average effective moment of inertia over the length of the member. Increasing the power of the M_{cr}/M term to four in Eq. (1b) gives the effective moment of inertia at an individual section and is used when integrating curvature to obtain deflection (Branson 1965).

$$I_e = \left(\frac{M_{cr}}{M}\right)^4 I_g + \left[1 - \left(\frac{M_{cr}}{M}\right)^4\right] I_{cr} \le I_g \quad (1b)$$

M_a in Eq. (1a) is taken as the service load moment at the critical section (where the moment is greatest), while M in Eq. (1b) equals the moment at each section along the member span. M_{cr} is the cracking moment. The moment of inertia of the gross (uncracked) section I_g is an approximation for the uncracked transformed moment of inertia I_{tr}. I_{cr} is the moment of inertia of the cracked transformed section without prestressing.

Branson's equations for I_e give too stiff a response for flexural members with $I_{cr} < I_g/3$, such as slabs, slender tilt-up walls, and members reinforced with fiber-reinforced polymer (FRP) bars (Bischoff and Scanlon 2007). ACI 318-19 subsequently adopted a new expression for I_e, where

$$I_e = \frac{I_{cr}}{1 - \left(\frac{2/3\ M_{cr}}{M_a}\right)^2 \left(1 - \frac{I_{cr}}{I_g}\right)} \quad (2)$$

for $M_a > 2/3\ M_{cr}$, while $I_e = I_g$ for $M_a \le 2/3\ M_{cr}$. The reduced cracking moment of 2/3 M_{cr} accounts for early-age loading and tensile stresses that develop in the concrete from restraint to shrinkage by the internal steel reinforcement (Scanlon and Bischoff 2008). Equation (2) gives a sectional value for I_e and is consequently expected to overpredict deflection when used as an average (uniform) value for the member based on the critical section where the moment is greatest and the stiffness lowest. This approach has been shown to give reasonable estimates of deflection within 10% or so for moderately reinforced members (Bischoff and Gross 2011).

Prestressed concrete

The uncracked moment of inertia is used to compute the deflection of prestressed concrete flexural members that are not cracked under service load (Class U). For members that are cracked (Class T and Class C), immediate deflection has typically been computed using either an effective moment of inertia or a bilinear moment-deflection response (ACI 318 2019; PCI 2017).

Branson's Eq. (1a) continues to be used by ACI 318-19 for computing the immediate deflection of a cracked prestressed concrete member, but with an increased cracking moment $M_{cr} = (f_r + f_{pe})I_g/y_t$ to account for the effective prestress force. While not stated explicitly, the secant value of the I_e response is inferred to begin at zero external moment and provides a net deflection value Δ_{net} (relative to the camber from prestress) corresponding to the service load moment M_a as shown in Fig. 1. Nasreddine et al. (2023) observed that deflection is underestimated by 2% on average with this

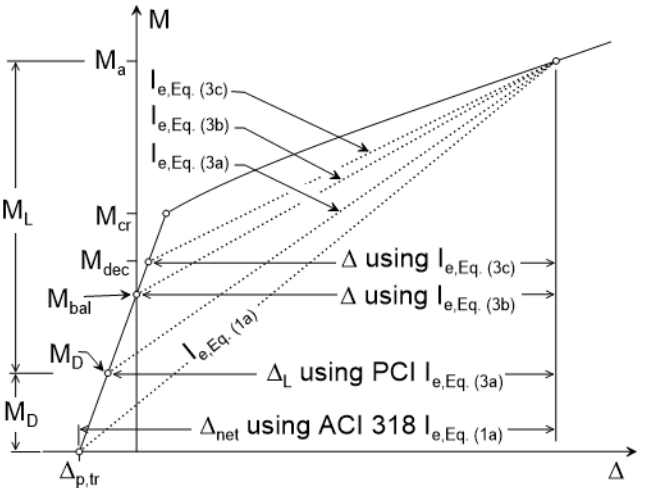

Fig. 1—Approaches for computing deflection based on modifications to Branson's approach.

approach but is underestimated by 13% on average when using I_{tr} instead of I_g in the expression for I_e. While Eq. (1a) appears to provide a reasonable estimate of deflection overall, the deflection was underestimated by 12% on average for the fully prestressed beams and overestimated by 11% on average for the partially prestressed beams defined as having nonprestressed reinforcement (Nasreddine et al. 2023).

Others such as Branson and Kripanarayanan (1971), Branson (1977), ACI Committee 435 (2000), and PCI (2017) assume the ACI 318 I_e response provides a secant value of I_e for live load deflection Δ_L of a cracked prestressed member. In this case, the I_e response originates at the prestress plus dead load deflection point corresponding to the dead load moment M_D shown in Fig. 1, where

$$I_e = \left(\frac{M_{cr} - M_D}{M_a - M_D}\right)^3 I_g + \left[1 - \left(\frac{M_{cr} - M_D}{M_a - M_D}\right)^3\right] I_{cr} \le I_g \quad (3a)$$

Deflection computed with Eq. (3a) for I_e gives the deflection for live load only. PCI (2017) uses Branson's Eq. (1a) but with an expression for M_{cr}/M_a (defined in terms of the rupture modulus f_r plus the stress in concrete from live load and for total stress at the precompressed tensile face) that is equivalent to the $(M_{cr} - M_D)/(M_a - M_D)$ ratio in Eq. (3a). This approach appeared in the first edition of the PCI Design Handbook (PCI 1971). Details are provided in Appendix A based on work from Branson and Kripanarayanan (1971). The approach assuming bilinear behavior (using a bilinear load-deflection response) has been in ACI 318 from 1971 onwards and appeared in the second edition of the PCI Design Handbook (PCI 1978).

Shaikh and Branson (1970) justified using the secant value of I_e adopted by PCI (1971) for computing deflection from the superimposed live load, based on a series of tests for prestressed and partially prestressed beams that showed predicted deflections within ±19% of measured values. The applied test loads were taken as the live load and computed deflection of the beams was relative to the position of the beam before application of the test loads (Shaikh 1967). The midspan moment M_D from the self-weight of these beams

was not more than 5 to 8% of the service load moment M_a used to calculate deflections. Consequently, any differences between the computed values of net deflection Δ_{net} using the ACI 318 approach (starting at zero load) and the PCI approach (with the live load deflection added onto the dead load deflection value) were not more than a few percent for most of the beams tested. Hence, little difference is expected between these two approaches unless additional dead load is added onto the beam.

Other work by Branson and Trost (1982a,b) shifts the I_{cr} response up to the balanced moment M_{bal} to give a secant value of I_e that originates at M_{bal} as shown in Fig. 1. This was thought to be equivalent to the zero-deflection point assumed for the case of a nonprestressed member, when

$$I_e = \left(\frac{M_{cr} - M_{bal}}{M_a - M_{bal}}\right)^3 I_g + \left[1 - \left(\frac{M_{cr} - M_{bal}}{M_a - M_{bal}}\right)^3\right] I_{cr} \le I_g \quad (3b)$$

Chen (1973) proposed using a secant value of I_e relative to the decompression moment M_{dec} corresponding to zero stress at the precompressed face of the critical section (Branson 1977) as this was thought to better reflect the degree of cracking in the member. In this case, the deflection value corresponding to M_{dec} needs to be included with the value computed using I_e from Eq. (3c) to obtain the total deflection (Fig. 1).

$$I_e = \left(\frac{M_{cr} - M_{dec}}{M_a - M_{dec}}\right)^3 I_g + \left[1 - \left(\frac{M_{cr} - M_{dec}}{M_a - M_{dec}}\right)^3\right] I_{cr} \le I_g \quad (3c)$$

Nasreddine et al. (2023) evaluated the accuracy of computing deflection directly using these proposed modifications to Branson's (1965) original expression for I_e, where the value of net deflection Δ_{net} increases as the secant value of the I_e response (dependent on the shifted moment) is shifted upwards from zero moment to M_{dec}. Differences between these approaches decrease for partially prestressed concrete as the amount of nonprestressed reinforcement increases. Other approaches were also considered. Equation (3c), along with the PCI bilinear load-deflection response (PCI 2017) and Bischoff's proposed approaches (Bischoff et al. 2018; Bischoff 2022), provided the most reasonable estimates of deflection, which were mostly overestimated by a moderate amount of not more than 10 to 15% depending on the approach.

DEFORMATION MODELS FOR ASSESSMENT

An approach proposed by Tadros et al. (1985), Bischoff's approaches (Bischoff et al. 2018; Bischoff 2022), and the PCI-based bilinear approach are evaluated in this paper for computing deflection by integration of curvature. Results from these approaches are compared with the more direct method of assuming a uniform value of I_e based on the stiffness at the critical section (at midspan for a simply supported member). The moment-curvature response for each approach considered is illustrated in Fig. 2. Tables 1(a) and 1(b) provide a summary of the deflection prediction approaches evaluated for computing curvature and deflection of a cracked prestressed concrete member.

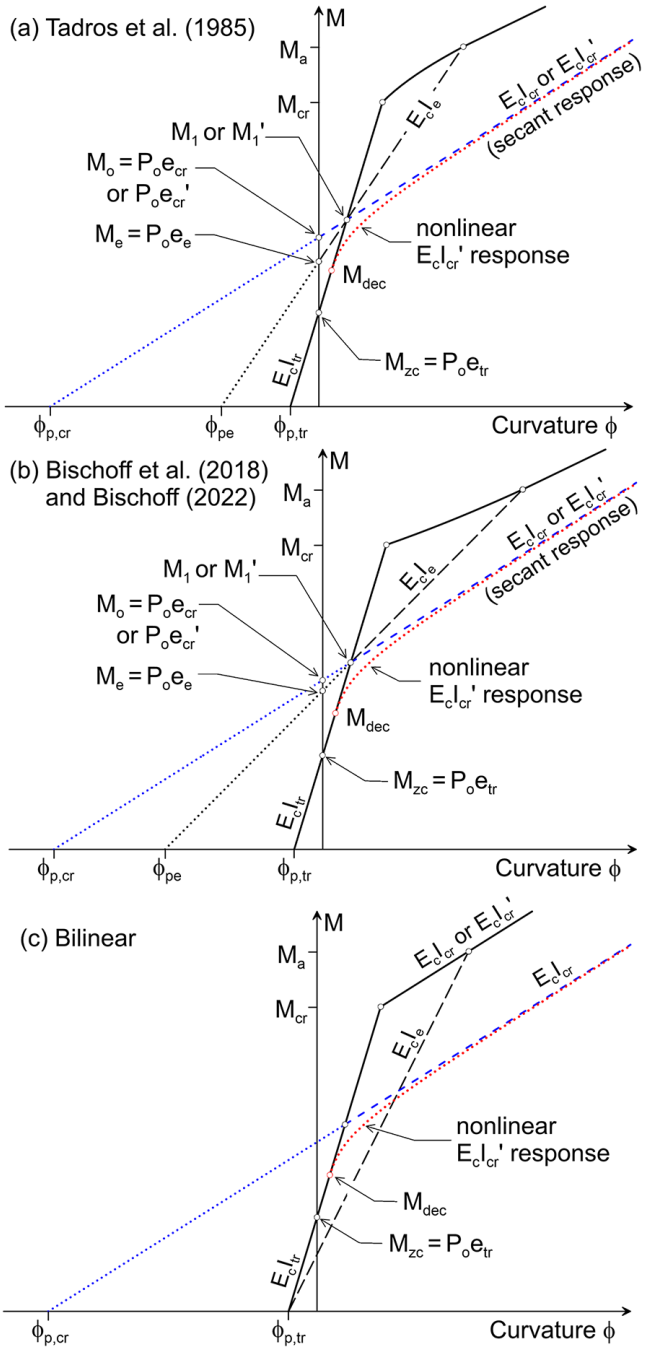

Fig. 2—Deformation models used in assessment.

Prestressed behavior and cracked section properties

The moment to cause cracking increases for a prestressed concrete flexural member, and the uncracked response begins with an initial camber (upwards deflection) arising from the eccentric prestress force. The cracked section response $E_c I_{cr}'$ is nonlinear (as labeled and shown by the dotted line in Fig. 2), and the cracked secant response is offset from the uncracked response because of the axial prestress force. The moment of inertia I_{cr}' of a partially cracked section is equal to the moment of inertia I_{tr} of the uncracked section at the decompression moment M_{dec}, after which I_{cr}' decreases with increasing moment (for $M > M_{dec}$) until it converges to the moment of inertia I_{cr} for a fully cracked section equivalent

Table 1(a)—Summary of deflection prediction approaches assessed

Approach	Integration method	Direct method
Effective eccentricity (Tadros et al. 1985)	$I_e = R^4 I_{tr} + [1 - R^4] I_{cr}'$ $\bar{y}_e = R^4 \bar{y}_{tr} + [1 - R^4]\, \bar{y}_{cr}'$ $e_e = R^4 e_{tr} + [1 - R^4] e_{cr}'$ with $R = (M_{cr} - M_{dec})/(M - M_{dec}) \le 1$	$I_e = R^3 I_{tr} + [1 - R^3] I_{cr}'$ $\bar{y}_e = R^3 \bar{y}_{tr} + [1 - R^3]\, \bar{y}_{cr}'$ $e_e = R^3 e_{tr} + [1 - R^3] e_{cr}'$ with $R = (M_{cr} - M_{dec})/(M_a - M_{dec}) \le 1$
	$\phi = -P_o e_e/(E_c I_e) + M/(E_c I_e)$	$\Delta = -k_p\,[P_o e_e/(E_c I_e)]\, L^2 + k_{M,sw}\,[M_{sw}/(E_c I_e)]\, L^2 + k_{M,F}\,[M_F/(E_c I_e)]\, L^2$
Bischoff et al. (2018)	$I_e = I_{cr}/[1 - ((M_{cr} - M_1)/(M - M_1))^2\,(1 - I_{cr}/I_{tr})]$ when $M_1 \le M_{cr}$ and $I_e = I_{cr}'/[1 - ((M_{cr} - M_1')/(M - M_1'))^2\,(1 - I_{cr}'/I_{tr})]$ when $M_1 > M_{cr}$ and $M_1' \le M_{cr}$	$I_e = I_{cr}/[1 - ((M_{cr} - M_1)/(M_a - M_1))^2\,(1 - I_{cr}/I_{tr})]$ when $M_1 \le M_{cr}$ and $I_e = I_{cr}'/[1 - ((M_{cr} - M_1')/(M_a - M_1'))^2\,(1 - I_{cr}'/I_{tr})]$ when $M_1 > M_{cr}$ and $M_1' \le M_{cr}$
	$\phi = (M_{shift} - P_o e_{tr})/(E_c I_{tr}) + (M - M_{shift})/(E_c I_e)$ $M_{shift} = M_1$ for $M_1 \le M_{cr}$ $M_{shift} = M_1'$ for $M_1 > M_{cr}$ and $M_1' \le M_{cr}$	$\Delta = -k_p\,[P_o e_{tr}/(E_c I_{tr})]\, L^2 + k_{M,sw}\,[M_{sw}/(E_c I_{tr})]\, L^2 + k_{M,F}\,[(M_{shift} - M_{sw})/(E_c I_{tr})] L^2 + k_{M,F}\,[(M_a - M_{shift})/(E_c I_e)] L^2$ $M_{shift} = M_1$ for $M_1 \le M_{cr}$ $M_{shift} = M_1'$ for $M_1 > M_{cr}$ and $M_1' \le M_{cr}$
Bischoff (2022)	$I_e = I_{cr}/[1 - \beta_{ts}\,((M_{cr} - M_1)/(M - M_1))\,(1 - I_{cr}/I_{tr})]$ with $\beta_{ts} = (M_{cr} - M_{dec})/(M - M_{dec})$	$I_e = I_{cr}/[1 - \beta_{ts}\,((M_{cr} - M_1)/(M_a - M_1))(1 - I_{cr}/I_{tr})]$ with $\beta_{ts} = (M_{cr} - M_{dec})/(M_a - M_{dec})$
	$\phi = (M_1 - P_o e_{tr})/(E_c I_{tr}) + (M - M_1)/(E_c I_e)$	$\Delta = -k_p\,[P_o e_{tr}/(E_c I_{tr})] L^2 + k_{M,sw}\,[M_{sw}/(E_c I_{tr})]\, L^2 + k_{M,F}\,[(M_1 - M_{sw})/(E_c I_{tr})] L^2 + k_{M,F}\,[(M_a - M_1)/(E_c I_e)] L^2$
Bilinear	$I_e = I_{cr}/[1 - (M_{cr}/M)^1(1 - I_{cr}/I_{tr})]$	$I_e = I_{cr}/[1 - \gamma\,(M_{cr}/M_a)^1(1 - I_{cr}/I_{tr})]$ $\gamma = 1$ for bilinear moment-deflection response or $\gamma = (1 + \alpha) - \alpha(M_{cr}/M_a)^2$ for integrated response with $\alpha = 1.33(a/L)^2/[1 - 1.33(a/L)^2]$ for two-point loading
	$\phi = -P_o e_{tr}/(E_c I_{tr}) + M_{cr}/(E_c I_{tr}) + (M - M_{cr})/(E_c I_{cr})$ or $\phi = -P_o e_{tr}/(E_c I_{tr}) + M/(E_c I_e)$	$\Delta = -k_p\,[P_o e_{tr}/(E_c I_{tr})] L^2 + k_{M,sw}[M_{sw}/(E_c I_e)] L^2 + k_{M,F}\,[(M_a - M_{sw})/(E_c I_e)] L^2$

Table 1(b)—Notes and supplementary equations for deflection approaches from Table 1(a)

For Tadros et al. (1985): I_{cr}', $\bar{y}_{cr}'$, and e_{cr}' can be replaced with I_{cr}, $\bar{y}_{cr}$, and e_{cr}
M refers to section moment and M_a refers to moment at the critical section (midspan)
$M_a = M_{sw} + M_F$, $M_{sw} = w_{sw}L^2/8$, and $M_F = Fa/2$ for two concentrated loads of magnitude $F/2$ each
$k_p = 1/8$, $k_{M,sw} = 5/48$, and $k_{M,F} = [3 - 4(a/L)^2]/24$ for two-point loading
$M_1 = [P_o e_{cr} - P_o e_{tr}(I_{cr}/I_{tr})]/(1 - I_{cr}/I_{tr})$ and $M_1' = [P_o e_{cr}' - P_o e_{tr}(I_{cr}'/I_{tr})]/(1 - I_{cr}'/I_{tr})$
$M_{cr} = (f_r + f_{pe})\,(I_{tr}/y_{t,tr})$ with $f_{pe} = P_e/A_{tr,np} + [(P_e e_{tr,np}) y_{t,np}]/I_{tr,np}$ and $P_e = f_{se} A_{ps}$
For partially prestressed members, M_{cr} is replaced with $M_{cr}' = [(2/3) + (1/3)(\rho_p/(\rho_p + \rho_s))] M_{cr}$ and M_{dec} is replaced with $M_{dec}' = [(2/3) + (1/3)(\rho_p/(\rho_p + \rho_s))] M_{dec}$
$P_o = f_{dc} A_{ps}$ with $f_{dc} = f_{se} + n_p f_{c,p}$ and $f_{c,p} = P_e/A_{tr,np} + [P_e(e_{tr,np})^2]/I_{tr,np}$
$e_{tr} = d_p - \bar{y}_{tr}$, $e_{tr,np} = d_p - \bar{y}_{tr,np}$, $e_{cr} = d_p - \bar{y}_{cr}$, $e_{cr}' = d_p - \bar{y}_{cr}'$
$A_{tr,np} = A_c \approx A_g$ for fully prestressed section (with no nonprestressed reinforcement)
$I_{tr,np} = I_c \approx I_g$ for fully prestressed section (with no nonprestressed reinforcement)

to a member with no prestress. Hence, $I_{cr} \le I_{cr}' \le I_{tr}$. While it is often assumed the cracked $E_c I_{cr}$ response lies below the cracking moment as shown in Fig. 2, the $E_c I_{cr}$ response can also lie above the cracking moment (depending on the amount of prestress) and computation of I_e is problematic when this happens (Bischoff et al. 2018).

Locating the neutral axis of a partially cracked section is iterative in nature because of the axial prestress force, and I_{cr}' is computed relative to the centroidal axis, which is not coincident with the neutral axis. For this reason, it is often convenient to approximate I_{cr}' with I_{cr} as the neutral axis for a fully cracked section coincides with the centroidal axis, and calculation of I_{cr} (together with the neutral axis location) is straightforward and less work.

The shift in the centroid location after cracking increases the eccentricity of the prestressing force. Ignoring this change in eccentricity (corresponding to the observed shift in both the $E_c I_{cr}$ and $E_c I_e$ secant responses shown in Fig. 2(a) and (b)) can lead to an overestimation of deflection (Tadros et al. 1985). Care also needs to be taken when defining the prestress force and whether this should be taken as the effective prestress force P_e, or the fictitious decompression force P_o defined by Nilson (1976). For more details, refer to Bischoff et al. (2018) and Bischoff (2022).

Effective eccentricity (of prestressing force) approach

Curvature response—Tadros et al. (1985) adapted Branson's original approach for computing the moment-curvature response using an expression for I_e given by

$$I_e = R^4 I_{tr} + [1 - R^4] I_{cr}' \le I_{tr} \tag{4a}$$

where $R = (M_{cr} - M_{dec})/(M - M_{dec})$ for $M > M_{cr}$, and $R = 1$ for $M \le M_{cr}$. The moment of inertia of the uncracked transformed section I_{tr} is often approximated with the gross moment of inertia I_g, while the moment of inertia I_{cr}' of the partially cracked transformed section can be approximated with the moment of inertia I_{cr} of a fully cracked transformed section (assuming a prestress force of zero) as shown in Fig. 2(a).

Figure 2(a) shows how the E_cI_e response is shifted up to an effective prestress moment $M_e = P_oe_e$ corresponding to zero curvature, where M_e is a product of the prestress force $P_o = f_{dc}A_{ps}$ (called the decompression force) and the effective eccentricity $e_e = d_p - \bar{y}_e$ of the prestress force relative to the effective centroid $\bar{y}_e$ of the partially cracked section. Sometimes, P_o is approximated with the effective prestress force P_e. The effective centroid depth is defined as

$$\bar{y}_e = R^4\bar{y}_{tr} + [1 - R^4]\,\bar{y}_{cr}' \le \bar{y}_{tr} \tag{4b}$$

where $\bar{y}_{tr}$ is the centroid location of the uncracked transformed section (approximated with the centroid location $\bar{y}_g$ of the uncracked gross section when I_g is used instead of I_{tr}), and $\bar{y}_{cr}'$ is the centroid location of the partially cracked section (approximated with the centroid location $\bar{y}_{cr}$ of the fully cracked section when I_{cr} is used instead of I_{cr}'). Equation (4b) leads to an effective eccentricity expressed as

$$e_e = R^4e_{tr} + [1 - R^4]e_{cr}' \ge e_{tr} \tag{4c}$$

where the eccentricity of the prestress force for the uncracked section $e_{tr} = d_p - \bar{y}_{tr}$ is replaced with $e_g = d_p - \bar{y}_g$ when I_g is used instead of I_{tr} and the eccentricity of the partially cracked section $e_{cr}' = d_p - \bar{y}_{cr}'$ is replaced with $e_{cr} = d_p - \bar{y}_{cr}$ when I_{cr} is used instead of I_{cr}'.

With this approach, the curvature ϕ of a cracked member is computed as

$$\begin{aligned}\phi &= \frac{M - P_oe_e}{E_cI_e} = -\frac{P_oe_e}{E_cI_e} + \frac{M}{E_cI_e} \\ &= -\phi_{pe} + \frac{M}{E_cI_e} \ge \frac{M - P_oe_{tr}}{E_cI_{tr}}\end{aligned} \tag{4d}$$

Equation (4d) suggests that the curvature after cracking can be expressed as a curvature arising from external load ($M/(E_cI_e)$) minus an effective curvature from the prestressing force ($\phi_{pe} = P_oe_e/(E_cI_e)$). Deflection is then computed by integrating curvature along the member length.

Central to this approach is the premise that the eccentricity of the prestressing force increases after cracking from e_{tr} to an effective value e_e. While not obvious, the shifted E_cI_e response also passes through an offset moment M_1' or M_1 corresponding to the intersection point of the uncracked E_cI_{tr} section response and a shifted E_cI_{cr}' or E_cI_{cr} cracked section response as shown in Fig. 2(a). The cracked moment of inertia I_{cr}' of the partially cracked transformed section and corresponding eccentricity e_{cr}' of the prestress force can be approximated with I_{cr} and e_{cr}, respectively, with reasonable accuracy so long as $M_1 \le M_{cr}$. Once $M_1 > M_{cr}$, I_{cr}' and e_{cr}' need to be used instead of I_{cr} and e_{cr} as the curvature can be underestimated with this approximation.

Direct deflection response—The effective moment of inertia based on the moment M_a at the critical section is used to compute deflection directly with an approach somewhat comparable to that developed by Abdelrahman and Rizkalla (1999) for FRP prestressed concrete.

$$I_e = R^3I_{tr} + [1 - R^3]I_{cr}' \le I_{tr} \tag{5a}$$

$$\bar{y}_e = R^3\bar{y}_{tr} + [1 - R^3]\bar{y}_{cr}' \le \bar{y}_{tr} \tag{5b}$$

$$e_e = R^3e_{tr} + [1 - R^3]e_{cr}' \ge e_{tr} \tag{5c}$$

for $R = (M_{cr} - M_{dec})/(M_a - M_{dec})$, which is now raised to the power of 3, and $e_e = d_p - \bar{y}_e$ after cracking. Both I_e and e_e are computed for the critical section. Deflection is computed as

$$\Delta = -k_p\left[\frac{P_oe_e}{E_cI_e}\right]L^2 + k_M\left[\frac{M_a}{E_cI_e}\right]L^2 \ge \left[\frac{k_MM_a - k_pP_oe_{tr}}{E_cI_{tr}}\right]L^2 \tag{5d}$$

For a simply supported beam of span L, $k_M = 5/48$ for a uniformly distributed load such as the member self-weight w_{sw} (defined as $k_{M,sw}$ in this paper), $k_M = [3 - 4(a/L)^2]/24$ for symmetric two-point loading with a shear span a for each concentrated load (defined as $k_{M,F}$), and $k_p = 1/8$ for straight prestressing tendons with constant eccentricity. For a member with two-point loading in addition to the member's self-weight

$$\Delta = -k_p\left[\frac{P_oe_e}{E_cI_e}\right]L^2 + k_{M,sw}\left[\frac{M_{sw}}{E_cI_e}\right]L^2 + k_{M,F}\left[\frac{M_F}{E_cI_e}\right]L^2 \tag{5e}$$

where $M_a = M_{sw} + M_F$, $M_{sw} = w_{sw}L^2/8$, and $M_F = Fa/2$ for two concentrated loads of equal magnitude $F/2$. Also, $\Delta \ge (k_{M,sw}M_{sw} + k_{M,F}M_F - k_pP_oe_{tr})L^2/(E_cI_{tr})$.

Naaman (1982) also uses Eq. (5a) for I_e but does not account for the jump in eccentricity of the prestress force after cracking, using $e_{tr} = d_p - \bar{y}_{tr}$ instead of e_e. Deflection after cracking is accordingly computed as $\Delta = -k_p[P_oe_{tr}/(E_cI_e)]L^2 + k_M[M_a/(E_cI_e)]L^2$ (compare this with Eq. (5d)) such that the effective secant member response runs through the balanced moment $M_{bal} = (k_p/k_M)P_oe_{tr}$ corresponding to zero deflection for the uncracked member. The effective prestress force P_e is also used instead of P_o. The result is greater deflection.

Bischoff's modified approaches

Curvature response—Bischoff's (2005, 2020) expression for I_e developed for reinforced concrete is adapted for cracked prestressed concrete by shifting the cracked E_cI_{cr} response upwards and forcing the effective E_cI_e response through the offset moment M_1 corresponding to the intersection point of the uncracked E_cI_{tr} response and shifted E_cI_{cr} response as shown in Fig. 2(b) (Bischoff et al. 2018). E_cI_{cr} is an approximation for E_cI_{cr}'. Using this approach

$$I_e = \frac{I_{cr}}{1 - \left(\frac{M_{cr} - M_1}{M - M_1}\right)^2\left(1 - \frac{I_{cr}}{I_{tr}}\right)} \tag{6a}$$

for $M > M_{cr}$, as long as $M_1 \le M_{cr}$. The offset moment $M_1 = [P_oe_{cr} - P_oe_{tr}(I_{cr}/I_{tr})]/[1 - (I_{cr}/I_{tr})]$ can also be used to define an effective prestress moment P_oe_e as seen from Fig. 2(b), giving an effective eccentricity $e_e = \xi e_{tr} + [1 - \xi]e_{cr}$ with $\xi = (I_e/I_{cr} - 1)/(I_{tr}/I_{cr} - 1)$. For a member where the E_cI_{cr} response lies above the cracking moment ($M_1 > M_{cr}$)

$$I_e = \frac{I_{cr}'}{1 - \left(\frac{M_{cr} - M_1'}{M - M_1'}\right)^2 \left(1 - \frac{I_{cr}'}{I_{tr}}\right)} \quad (6b)$$

for $M > M_{cr}$ and $M_1' \le M_{cr}$. The offset moment $M_1' = [P_o e_{cr}' - P_o e_{tr}(I_{cr}'/I_{tr})]/[1 - (I_{cr}'/I_{tr})]$ corresponds to the intersection point of the $E_c I_{tr}$ response and partially cracked $E_c I_{cr}'$ response. Recall that I_{cr}' requires locating the neutral axis depth, which depends on the prestress force and magnitude of the service load moment. I_{cr}' is computed relative to the centroid. The offset moment M_1' also defines an effective prestress moment $P_o e_e$ with $e_e = \xi e_{tr} + [1 - \xi] e_{cr}'$ and $\xi = (I_e/I_{cr}' - 1)/(I_{tr}/I_{cr}' - 1)$.

Shrinkage is accounted for through the use of the effective stress f_{se} in the prestressed reinforcement (after allowance for all prestress losses) to give a lower value for the effective prestress force P_e. A drop in the prestress force decreases the computed value of the cracking moment M_{cr} and reduces the shift in the uncracked and cracked member responses. Both outcomes increase deflection. For partially prestressed concrete with nonprestressed reinforcement, the cracking moment M_{cr} decreases further and is replaced with $M_{cr}' = [(2/3) + (1/3)(\rho_p/[\rho_p + \rho_s])]M_{cr}$ to account for tensile stresses that develop in the concrete from restraint to shrinkage by the nonprestressed reinforcement (Nasreddine et al. 2023). The decompression moment is also replaced with $M_{dec}' = [(2/3) + (1/3)(\rho_p/[\rho_p + \rho_s])]M_{dec}$.

The secant value of $E_c I_e$ is offset by either M_1 or M_1', giving a computed curvature of

$$\phi = \frac{M_{shift} - P_o e_{tr}}{E_c I_{tr}} + \frac{M - M_{shift}}{E_c I_e} \ge \frac{M - P_o e_{tr}}{E_c I_{tr}} \quad (7)$$

with the offset or shifted moment M_{shift} equal to either M_1 or M_1' as explained previously. The initial uncracked curvature from the prestressing force $\phi_{p,tr} = P_o e_{tr}/(E_c I_{tr})$ is also equal to $P_e e_{tr,np}/(E_c I_{tr,np})$, where $I_{tr,np}$ is the moment of inertia of the uncracked section with only the nonprestressed steel transformed and $e_{tr,np}$ is the eccentricity of the prestressing steel to the corresponding centroid of this uncracked transformed section. Deflection is computed by the integration of curvature.

Bischoff (2022) introduced a tension-stiffening factor $\beta_{ts} = (M_{cr} - M_{dec})/(M - M_{dec})$ into the expression for I_e to avoid having to use section properties related to a partially cracked section when $M_1 > M_{cr}$. I_e is expressed as

$$I_e = \frac{I_{cr}}{1 - \beta_{ts}\left(\frac{M_{cr} - M_1}{M - M_1}\right)\left(1 - \frac{I_{cr}}{I_{tr}}\right)} \quad (8)$$

where M_{cr} and M_{dec} are replaced by M_{cr}' and M_{dec}' for partially prestressed concrete. Equation (8) gives a value for I_e that varies between I_{tr} and I_{cr} when $M_1 \le M_{cr}$ as expected. However, the values of I_e vary between $-\infty$ and $+\infty$ when $M_1 > M_{cr}$ and $M_{cr} < M < M_1$. Once $M > M_1$, I_e varies between 0 and I_{cr}. The effective prestress moment $P_o e_e$ and corresponding effective eccentricity e_e are defined by M_1 as described earlier. The computed curvature is taken as

$$\phi = \frac{M_1 - P_o e_{tr}}{E_c I_{tr}} + \frac{M - M_1}{E_c I_e} \ge \frac{M - P_o e_{tr}}{E_c I_{tr}} \quad (9)$$

and deflection is computed by the integration of curvature.

Direct deflection response—Deflection is computed directly using the effective moment of inertia based on the moment M_a at the critical section (at midspan for a simply supported beam) for I_e defined by Eq. (6a) and (6b) or Eq. (8), but with M_a substituted for M in these equations (and for β_{ts}). $M_{shift} = M_1$ or M_1' for Eq. (6a) or (6b) and $M_{shift} = M_1$ for Eq. (8). Deflection is given by

$$\Delta = -k_p\left[\frac{P_o e_{tr}}{E_c I_{tr}}\right]L^2 + k_M\left[\frac{M_{shift}}{E_c I_{tr}}\right]L^2 + k_M\left[\frac{M_a - M_{shift}}{E_c I_e}\right]L^2 \ge \left[\frac{k_M M_a - k_p P_o e_{tr}}{E_c I_{tr}}\right]L^2 \quad (10a)$$

for one loading type. For a member with two-point loading in addition to the member's self-weight

$$\Delta = -k_p\left[\frac{P_o e_{tr}}{E_c I_{tr}}\right]L^2 + k_{M,sw}\left[\frac{M_{sw}}{E_c I_{tr}}\right]L^2 + k_{M,F}\left[\frac{M_{shift} - M_{sw}}{E_c I_{tr}}\right]L^2 + k_{M,F}\left[\frac{M_a - M_{shift}}{E_c I_e}\right]L^2 \quad (10b)$$

where $M_a = M_{sw} + M_F$. The camber $\Delta_{p,tr}$ from the prestress force defined by the first set of terms in Eq. (10a) or (10b) is equivalent to using $-k_p[P_e e_{tr,np}/(E_c I_{tr,np})]L^2$.

Bilinear approach

Curvature response—An assumed bilinear moment-curvature response for prestressed concrete is shown in Fig. 2(c), where the uncracked $E_c I_{tr}$ response is followed up to cracking and additional deformation after cracking either follows the $E_c I_{cr}'$ or $E_c I_{cr}$ response. The moment of inertia I_{cr}' of the partially cracked transformed section varies with the magnitude of the moment, while I_{cr} for a fully cracked section does not depend on the moment and is more practical in this instance. This approach forms the basis of the PCI (2017) bilinear moment-deflection response for computing deflection and was used by Pirayeh Gar et al. (2018) for computing deflection of FRP prestressed concrete members based on an assumed bilinear moment-curvature response. Earlier work by Bischoff et al. (2018) demonstrates the cracked section response does not typically originate at the cracking moment as assumed with this approach and can lie either below or above the cracking moment depending on the amount of prestressing.

Using a bilinear moment-curvature response to compute curvature after cracking gives

$$\phi = \frac{-P_o e_{tr}}{E_c I_{tr}} + \frac{M_{cr}}{E_c I_{tr}} + \frac{M - M_{cr}}{E_c I_{cr}} \quad (11a)$$

Once again, the initial curvature $\phi_{p,tr} = P_o e_{tr}/(E_c I_{tr})$ is the same as $P_e e_{tr,np}/(E_c I_{tr,np})$. Alternatively, curvature can be computed with an effective moment of inertia using

$$\phi = \frac{-P_o e_{tr}}{E_c I_{tr}} + \frac{M}{E_c I_e} \quad (11b)$$

as shown in Fig. 2(c) for an effective moment of inertia I_e, defined as

$$I_e = \frac{I_{cr}}{1 - \left(\frac{M_{cr}}{M}\right)^1 \left(1 - \frac{I_{cr}}{I_{tr}}\right)} \quad (12a)$$

Equation (12a) is similar to Bischoff's (2005) I_e expression for reinforced (nonprestressed) concrete but with the M_{cr}/M term raised to the power of one for a bilinear response instead of two (Alameh and Harajli 1989; Bischoff 2008, 2019). Deflection is computed by integrating curvature.

Pirayeh Gar et al. (2018) integrated curvature algebraically for an assumed bilinear moment-curvature response. Using I_e defined by Eq. (12a) for the section response gives an I_e expression for the member identified by Bischoff (2019) as

$$I_e = \frac{I_{cr}}{1 - \gamma\left(\frac{M_{cr}}{M_a}\right)^1 \left(1 - \frac{I_{cr}}{I_{tr}}\right)} \quad (12b)$$

Bischoff and Gross (2011) used a similar approach for FRP-reinforced (nonprestressed) concrete. Equation (12b) includes an integration factor γ to account for changes in stiffness along the member span and is used to compute deflection directly in lieu of integrating curvature. The moment M_a corresponding to the moment at the critical section is used instead of the section moment M. The factor $\gamma = (1 + \alpha) - \alpha\,(M_{cr}/M_a)^2$, with $\alpha = 1.33(a/L)^2/[1 - 1.33(a/L)^2]$ for a simply supported member under symmetric two-point loading with a shear span a for each concentrated load. For a simply supported member with a uniformly distributed load, γ is approximated using $a/L = 0.375$ to give $\alpha = 0.23$. The accuracy of this method obviously depends on the initial assumption of using a bilinear moment-curvature response.

Direct deflection response—Deflection is computed directly by either assuming a bilinear moment-deflection response or using an effective moment of inertia defined by Eq. (12b) based on the moment M_a at the critical section (taken at midspan for a simply supported beam). For a bilinear moment-deflection response

$$\Delta = -k_p\left[\frac{P_o e_{tr}}{E_c I_{tr}}\right]L^2 + k_M\left[\frac{M_{cr}}{E_c I_{tr}}\right]L^2 + k_M\left[\frac{(M_a - M_{cr})}{E_c I_{cr}}\right]L^2 \quad (13a)$$

while deflection computed with I_e defined by Eq. (12b) gives

$$\Delta = -k_p\left[\frac{P_o e_{tr}}{E_c I_{tr}}\right]L^2 + k_M\left[\frac{M_a}{E_c I_e}\right]L^2 \quad (13b)$$

Using Eq. (13b) with $\gamma = 1$ for I_e in Eq. (12b) gives the same deflection value computed with Eq. (13a), while using a value of γ corresponding to the type of member load and support conditions accounts for integration to give a stiffer response with less deflection.

For a member with two-point loading in addition to the member's self-weight

$$\Delta = -k_p\left[\frac{P_o e_{tr}}{E_c I_{tr}}\right]L^2 + k_{M,sw}\left[\frac{M_{sw}}{E_c I_e}\right]L^2 + k_{M,F}\left[\frac{(M_a - M_{sw})}{E_c I_e}\right]L^2 \quad (13c)$$

where $M_a = M_{sw} + M_F$. Using γ corresponding to a member with two-point loading is approximate in this case as part of the load comes from the member self-weight which is uniformly distributed.

DEFLECTION COMPARISON

The accuracy of deflection prediction models is evaluated by comparing the calculated values of deflection to experimental values from the literature. At any given load, the experimental deflection Δ_{exp} is obtained as follows

$$\Delta_{exp} = -\Delta_{camber} + \Delta_{sw} + \Delta_{meas} \quad (14)$$

where Δ_{meas} is the deflection (usually at midspan) measured from the loads applied during testing. The deflection due to member self-weight is $\Delta_{sw} = k_{M,sw}[M_{sw}/(E_c I_{tr})]L^2$, and the estimated camber is $\Delta_{camber} = k_p\,[P_e e_{tr,np}/(E_c I_{tr,np})]L^2$, where k_p corresponds to the tendon profile (equal to 1/8 for a straight tendon with constant eccentricity). Parabolic tendon profiles are not considered in this study.

Calculated values of deflection Δ_{calc} are determined by either integrating curvature or using the more direct method assuming a uniform value of I_e for member stiffness (Table 1(a)). Integrating curvature accounts for the change in stiffness along the member span by considering the variation of moment and change in eccentricity of the prestressing tendon when applicable. Calculation of deflection using a uniform member stiffness based on the moment at the critical section can overestimate deflection in many cases unless account is taken of the stiffer regions of the member.

DATABASE DESCRIPTION

A database assembled by Nasreddine et al. (2023) comprised of 180 beams prestressed with bonded steel tendons (with or without nonprestressed reinforcement) is used to validate the deflection approaches considered. The beams from this database are simply supported and prestressed with straight tendons having constant eccentricity. All beams were loaded under two-point loading. Up to three points are taken from the load-deflection response of each beam, located between cracking of the member and yielding of the reinforcement or tendons. The points are roughly equidistant and correspond to moments of approximately 1.2, 1.4, and 1.6M_{cr}.

RESULTS AND DISCUSSION

Calculated values of deflection Δ_{calc} using integration of curvature are compared with experimental values Δ_{exp} in Fig. 3 for the approaches considered and show a considerable scatter of results reflected by a coefficient of variation (COV) between 30 to 35%. Plots show lines for perfect prediction and ±30% deviation. Statistical values of the deflection prediction ratio $\Delta_{calc}/\Delta_{exp}$ are summarized in Table 2 for the mean and COV, plus the percentage of results with $\Delta_{calc} < \Delta_{exp}$ (unconservative) and within ±30% of Δ_{exp}. Results are

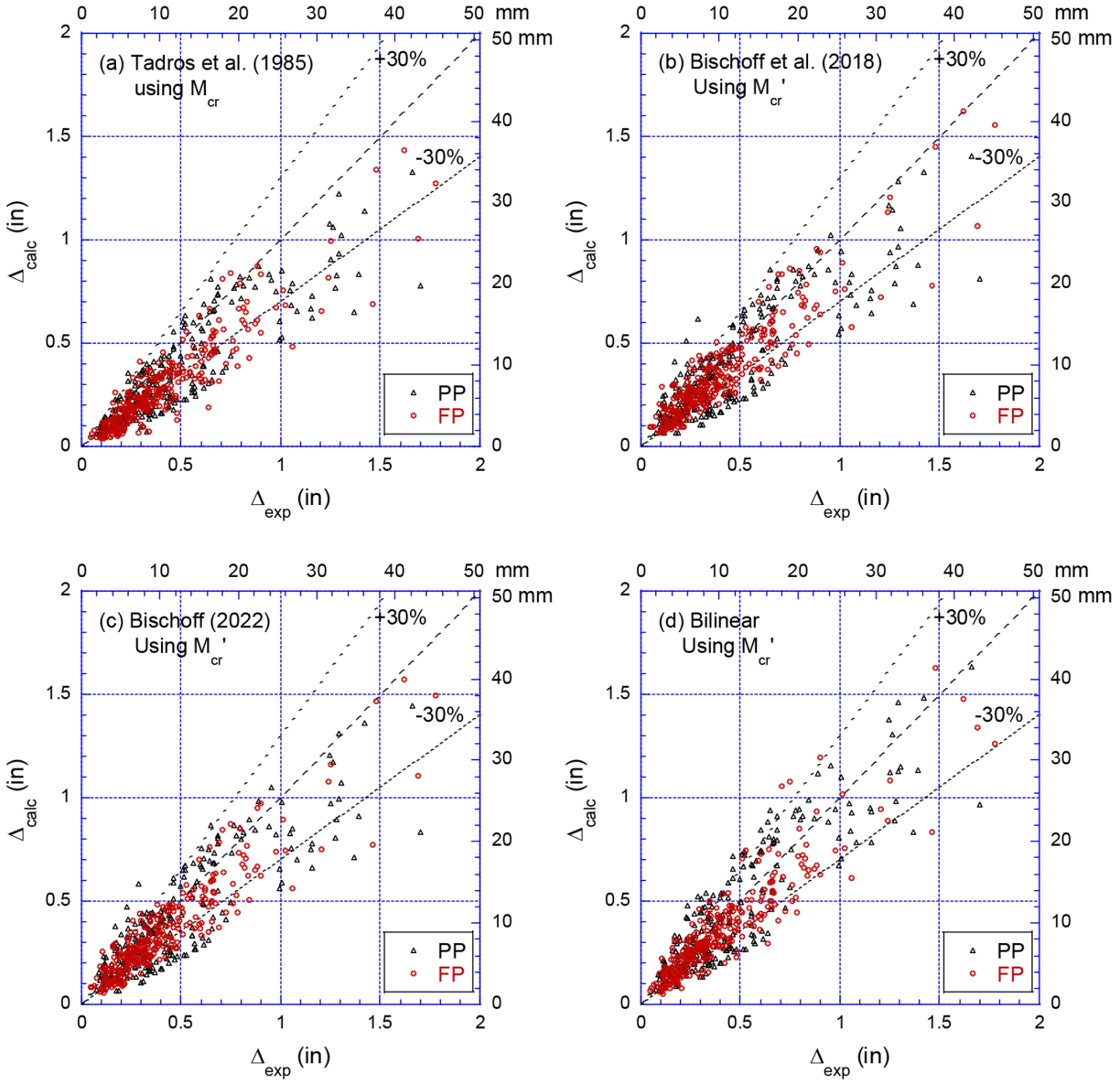

Fig. 3—Calculated deflections using integration of curvature versus experimental deflections.

presented for the entire database and for the fully prestressed (FP) and partially prestressed (PP) beams separately.

Deflection is calculated using the ACI 318 equations for $f_r = 7.5\sqrt{f_c'}$ in psi ($0.62\sqrt{f_c'}$ in MPa) and $E_c = w_c^{1.5}33\sqrt{f_c'}$ in psi ($w_c^{1.5}0.0423\sqrt{f_c'}$ in MPa) for $f_c' \le 8000$ psi (55 MPa). For higher strength concrete with $f_c' > 8000$ psi (55 MPa), $E_c = (40{,}000\sqrt{f_c'} + 1{,}000{,}000)(w_c/145)^{1.5}$ in psi or $(3300\sqrt{f_c'} + 6900)(w_c/2300)^{1.5}$ in MPa. The transformed moment of inertia I_{tr} for the uncracked section is used instead of I_g for all calculations, and computed results are presented for the full cracking moment except for Bischoff's two approaches and the PCI bilinear approach which also include the effect of using a reduced cracking moment M_{cr}' to account for shrinkage restraint from the nonprestressed steel in the partially prestressed members.

Effect of integrating curvature

The effect of deflection calculation using integration of curvature compared to the direct calculation method is summarized in Table 2. In all cases, the integration of curvature underestimates deflection on average for the database of beams from this study.

The approach by Tadros et al. (1985) was evaluated using both I_{cr}' and I_{cr} in the expression for I_e (Eq. (4a) and (5a)). Using I_{cr} instead of I_{cr}' decreases the computed value of deflection by approximately 5%. Deflection is underestimated on average by 40% or more using the direct method and by 25 to 30% when integrating curvature. Integrating curvature increases the computed value of deflection compared to the direct method, which is contrary to expected. This occurs when deflection is separated into an upwards component from the effective prestress subtracted from a downwards component caused by load, and because of differences in the I_e equation for the two methods (compare Eq. (4a) for integration with Eq. (5a) for direct computation of deflection).

The average deflection ratio $\Delta_{calc}/\Delta_{exp}$ is much better for the three other approaches considered. Deflection (for the full cracking moment) is underestimated by 10 to 12% on average when integrating curvature. Integrating curvature

Table 2—Statistical parameters for ratio of calculated to experimental deflections ($\Delta_{calc}/\Delta_{exp}$)

Approach (full database)	Approach details	Deflection method	Mean ($\Delta_{calc}/\Delta_{exp}$)			FP+PP			FP	PP
			FP+PP	FP	PP	COV, %	%<1	% within ±30%	COV, %	COV, %
Tadros et al. (1985)	I_{tr} and I_{cr}'	Direct	0.60	0.54	0.69	35	94	28	31	34
		Integration	0.75	0.72	0.78	31	85	53	29	32
	I_{tr} and I_{cr}	Direct	0.57	0.50	0.66	37	96	23	32	34
		Integration	0.71	0.67	0.76	32	88	47	31	32
Bischoff et al. (2018)	I_{tr} and I_{cr} or I_{cr}'	Direct	1.07 (1.10)	1.13	1.00 (1.07)	36 (37)	45 (43)	66 (66)	34	38 (42)
		Integration	0.90 (0.94)	0.93	0.87 (0.94)	34 (35)	66 (63)	67 (66)	32	36 (40)
Bischoff (2022)	I_{tr} and I_{cr}	Direct	1.04 (1.09)	1.10	0.97 (1.08)	34 (35)	49 (44)	67 (66)	31	36 (40)
		Integration	0.88 (0.92)	0.91	0.84 (0.95)	32 (34)	71 (66)	66 (65)	30	35 (38)
Bilinear	I_{tr} and I_{cr}	Direct	1.04 (1.14)	1.13	0.93 (1.16)	32 (32)	48 (41)	66 (62)	29	35 (36)
		Integration	0.88 (0.97)	0.93	0.81 (1.02)	31 (32)	71 (61)	66 (67)	28	34 (34)
Bilinear (using I_e with γ)	I_{tr} and I_{cr}	Direct	0.88 (0.97)	0.93	0.81 (1.03)	31 (32)	71 (61)	66 (68)	28	34 (35)

Note: 104 FP beams and 76 PP beams; values in brackets are for Δ_{calc} using reduced cracking moment M_{cr}' and reduced decompression moment M_{dec}' for PP beams.

decreases the average deflection ratio from 1.07 (using the direct method) to 0.90 with Bischoff et al. (2018), and from 1.04 to 0.88 using either Bischoff (2022) or the bilinear approach. Using the direct calculation method with the bilinear approach but incorporating an appropriate integration factor γ into I_e correctly accounts for the integration of curvature, as demonstrated by the results in Table 2.

Effect of cracking moment

Bischoff's two approaches and the bilinear approach give a greater deflection prediction ratio for the FP beams compared to the PP beams when using the full cracking moment M_{cr} as observed from Table 2. This necessitates the use of a reduced cracking moment M_{cr}' to account for shrinkage restraint stresses that develop in the concrete from the nonprestressed reinforcement in a PP beam (Nasreddine et al. 2023). Computed deflections of the PP beams increase with the reduced cracking moment M_{cr}' to give a value somewhat comparable to the FP beams in most cases. The COV is greater for the PP beams (approximately 35%) than the FP beams (approximately 30%) and increases when using M_{cr}'.

Overall, when using M_{cr}', deflection computed by integrating curvature is underestimated on average by 6 to 8% using either of Bischoff's two approaches and by 3% when using the bilinear approach. In comparison, deflection computed with the direct method overestimates deflection by approximately 10% using either of Bischoff's two approaches and by 14% with the bilinear approach.

Effect of concrete elastic modulus

A total of 77 (56 FP and 21 PP) out of the 180 beams from the database reported a measured value of the modulus of elasticity of concrete. The beams from this reduced database were used to study the effect of estimating deflection with a computed value of the concrete modulus $E_{c,calc}$ compared to the measured value $E_{c,meas}$. The average ratio of calculated-to-measured modulus of elasticity ($E_{c,calc}/E_{c,meas}$) is 1.14 for these beams. Results of the comparison are shown in Table 3 for deflection computed using integration of curvature.

Deflection computed with $E_{c,calc}$ is obviously underestimated when compared to values computed with $E_{c,meas}$ when $E_{c,calc} > E_{c,meas}$. Likewise, deflection is overestimated in those cases where $E_{c,calc} < E_{c,meas}$. Average deflection prediction ratios are between 7 and 8% less when using the calculated value of E_c compared to using the measured value. There is little difference in the COV with either $E_{c,calc}$ or $E_{c,meas}$. Results using the measured value of E_c give an overall average deflection ratio close to one for either of Bischoff's approaches (using both M_{cr} and M_{cr}') and for the bilinear approach (for M_{cr} only). The elastic modulus was also back-calculated from the uncracked slope of the measured load-deflection response (defined as $E_{c,test}$). The value of $E_{c,test}$ was 3% higher than $E_{c,meas}$ on average, with little difference in the mean value of the deflection prediction ratio for deflection computed with either $E_{c,meas}$ or $E_{c,test}$.

Effect of I_g versus I_{tr}

Prediction of deflection has been assessed with I_e based on the moment of inertia I_{tr} of the uncracked transformed section in all deflection calculations (Tables 2 and 3). Table 4 summarizes the effect of approximating I_{tr} with the gross moment of inertia I_g. When integrating curvature to obtain deflection, using I_g increases the computed value of deflection by approximately 4 to 6% on average, except for the bilinear approach, where deflection is increased by approximately 10%. Deflection is underpredicted by 22% on average using Tadros et al. (1985), 6 to 7% using Bischoff's two approaches with M_{cr}, and 2% for the bilinear approach with M_{cr}. For calculations using the reduced cracking moment M_{cr}', deflection is underpredicted by 4% and overpredicted by 6% on average when using either of Bischoff's approaches or the bilinear approach, respectively.

Table 3—Effect of E_c on deflection prediction ratio $\Delta_{calc}/\Delta_{exp}$ using integration

Approach (reduced database)	Approach details	Mean $\Delta_{calc}/\Delta_{exp}$ for FP+PP			COV, %	
		$E_{c,meas}$	$E_{c,calc}$	% change	$E_{c,meas}$	$E_{c,calc}$
Tadros et al. (1985)	I_{tr} and I_{cr}'	0.85	0.78	–8.2%	25	31
Bischoff et al. (2018)	I_{tr} and I_{cr} or I_{cr}'	1.00 (1.02)	0.93 (0.94)	–7.0% (–7.8%)	24 (24)	24 (25)
Bischoff (2022)	I_{tr} and I_{cr}	0.98 (1.01)	0.91 (0.94)	–7.1% (–6.9%)	23 (23)	23 (25)
Bilinear	I_{tr} and I_{cr}	0.99 (1.06)	0.92 (0.99)	–7.1% (–6.6%)	23 (24)	22 (27)

Note: 56 FP beams and 21 PP beams; values in brackets are for Δ_{calc} using M_{cr}' and M_{dec}' for PP beams.

Table 4—Effect of I_g on deflection prediction ratio $\Delta_{calc}/\Delta_{exp}$

Approach (full database)	Approach details	Deflection method	Mean $\Delta_{calc}/\Delta_{exp}$			COV, %	%<1	% within ±30%
			FP+PP	FP	PP			
Tadros et al. (1985)	I_g and I_{cr}'	Direct	0.62	0.55	0.71	36	93	31
		Integration	0.78	0.76	0.81	32	81	59
Bischoff et al. (2018)	I_g and I_{cr} or I_{cr}'	Direct	1.11 (1.13)	1.16	1.04 (1.09)	36 (37)	41 (39)	64 (63)
		Integration	0.94 (0.96)	0.96	0.92 (0.97)	34 (36)	61 (59)	66 (66)
Bischoff (2022)	I_g and I_{cr}	Direct	1.10 (1.13)	1.15	1.03 (1.11)	34 (36)	41 (39)	64 (63)
		Integration	0.93 (0.96)	0.95	0.90 (0.98)	32 (34)	63 (59)	68 (67)
Bilinear	I_g and I_{cr}	Direct	1.16 (1.25)	1.24	1.04 (1.25)	32 (32)	36 (29)	61 (56)
		Integration	0.98 (1.06)	1.03	0.91 (1.12)	31 (32)	58 (49)	66 (67)

Note: Values in brackets are for Δ_{calc} using M_{cr}' and M_{dec}' for PP beams.

Evaluation using net deflection

Values of deflection without the camber from prestressing give the net deflection Δ_{net}, which equals the deflection from member self-weight plus the applied test load. Table B1 in Appendix B summarizes the comparison of calculated deflections with experimental values based on the net deflection. Mean values of the deflection prediction ratio for net deflection are typically not more than 2 to 4% different from the evaluation for deflection including the camber (except for the approach by Tadros et al. (1985), where the difference is closer to 10% or more). There is also little difference between comparisons using the net deflection and the measured deflection from the test load only as the deflection from the member self-weight is low.

CONCLUSIONS

The following conclusions are focused mostly on the calculation of deflection by integration of curvature compared to direct calculation using the four approaches summarized in Table 1(a). Conclusions related to the calculation of deflection using the direct method for other approaches can be found in Nasreddine et al. (2023).

- Compared to the direct method, integrating curvature decreases the computed value of deflection by approximately 15% on average for the approaches considered, except for the approach by Tadros et al. (1985) where the deflection increases by 25%. When integrating curvature to obtain deflection, Tadros et al. (1985) underestimates deflection (based on the mean value of the deflection prediction ratio) by 25%, while Bischoff's two approaches and the bilinear approach underestimate deflection by 10 to 12%. Deflection calculations are based on the full cracking moment and use I_{tr} in calculations for the cracking moment and effective moment of inertia I_e.
- Using a reduced cracking moment to account for shrinkage restraint from the nonprestressed reinforcement provides computed values of deflection for the partially prestressed (PP) beams somewhat comparable to the fully prestressed (FP) beams, improving prediction of deflection by 5 to 10% depending on the approach. On average, Bischoff's two approaches underestimate deflection by 6 to 8% and the bilinear approach underestimates deflection by 3% when computing deflection by integrating curvature and using M_{cr}'. In contrast, Bischoff's approaches overestimate deflection by 9 to 10% and the bilinear approach overestimates deflection by 14% when using the direct method for computing deflection.
- Using the calculated modulus of elasticity of concrete decreases computed values of deflection by approximately 8% compared to using the measured values of E_c for the beams from the reduced database (for 77 out of the 280 beams reporting measured values of E_c). This occurs because $E_{c,calc} > E_{c,meas}$. When computing deflection by integrating curvature in combination with using a reduced cracking moment and the measured elastic modulus of concrete, Bischoff's two approaches overestimate deflection by 2% on average, and the bilinear approach overestimates deflection by 6%. The approach by Tadros et al. (1985) underestimates deflection by 15% but without using a reduced cracking moment.
- Approximating I_{tr} with the gross moment of inertia I_g in deflection calculations (used to determine M_{cr} and I_e) increases computed values of deflection by between 3 to 10% depending on the approach. Bischoff's approaches

underestimate deflection by approximately 4% on average while the bilinear approach overestimates deflection by 6% when integrating curvature using a reduced cracking moment and the ACI equations for f_r and E_c.

- Using the direct method for computing deflection with an expression for I_e that includes an appropriate integration factor to account for the integration of curvature is shown to work well for the bilinear approach.
- Bischoff's two approaches (Bischoff et al. 2018; Bischoff 2022) yield reasonable estimates of deflection when integrating curvature based on an effective moment of inertia computed with a reduced cracking moment for the PP beams. The bilinear approach also provides reasonable estimates of deflection but is more sensitive to parameters that include using a reduced cracking moment M_{cr}' and approximating I_{tr} with I_g.

Results from this evaluation provide the reader with the level of accuracy and precision that can be expected for each approach considered. Results have been validated using an extensive database of 180 beams obtained from 23 independent studies. The approaches proposed by Bischoff (2022) and the bilinear approach show the most reasonable promise for further development. Previous work by Nasreddine et al. (2023) and this paper are expected to provide a basis for developing a simplified design approach to compute the immediate deflection of a cracked prestressed concrete flexural member. Time-dependent deflections under sustained load have so far not been considered (aside from the use of the effective stress f_{se} for the prestressing steel) but can be incorporated into a design approach using an effective elastic modulus of the concrete to account for creep effects.

AUTHOR BIOS

ACI member **Wassim Nasreddine** *is a Research Associate at Rutgers University, New Brunswick, NJ. He is a member of ACI Committee 435, Deflection of Concrete Building Structures. His research interests include prestressed concrete member behavior, innovative concrete materials, and strengthening and retrofitting of concrete structures.*

ACI member **Adi Obeidah** *is a former Research Associate at Rutgers University. He received his BS and MS from the American University of Sharjah, Sharjah, UAE, and his PhD from Rutgers University. His research interests include prestressed fiber-reinforced concrete and ultra-high-performance concrete (UHPC) behavior with non-metallic reinforcement, strengthening, and retrofitting of concrete elements.*

Peter H. Bischoff, *FACI, is an Honorary Research Professor in the Civil Engineering Department at the University of New Brunswick, Fredericton, NB, Canada. He is a member of ACI Committees 224, Cracking; 435, Deflection of Concrete Building Structures; 440, Fiber-Reinforced Polymer Reinforcement; and 440C, FRP Reinforced Concrete Building Code. He received the ACI Design Award in 2014. His research interests include the serviceability behavior of concrete structures.*

Hani Nassif, *FACI, is Professor of structural engineering at Rutgers University. He is a member of ACI Committees 209, Creep and Shrinkage in Concrete; and 435, Deflection of Concrete Building Structures; and Joint ACI-ASCE Committee 343, Concrete Bridge Design. His research interests include structural concrete and the use of advanced cementitious and composite materials.*

ACKNOWLEDGMENTS

Partial support received from C2SMART (Connected Cities for Smart Mobility toward Accessible and Resilient Transportation) and the New Jersey Department of Transportation through the Bridge Resource Program (BRP) is gratefully appreciated. The organizations cited are not responsible for the accuracy of facts nor the views expressed by the authors.

NOTATION

A_c = concrete cross-sectional area, not including area of reinforcement ($\cong A_g$)
A_g = gross area of concrete section
A_{ps} = area of prestressed longitudinal tension reinforcement
A_s = area of nonprestressed longitudinal tension reinforcement
A_s' = area of nonprestressed longitudinal compression reinforcement
$A_{tr,np}$ = area of uncracked transformed section without A_{ps} (including nonprestressed reinforcement A_s and A_s' only if present)
a = shear span for symmetric two-point loading
b = width of compression face of member
c_{cr} = distance from compression face to neutral axis of a fully cracked cross section ($\equiv \bar{y}_{cr}$)
d_p = effective depth of prestressed reinforcement
d_s = effective depth of nonprestressed tension reinforcement
E_c = elastic modulus of concrete
$E_{c,calc}$ = calculated elastic modulus of concrete
$E_{c,meas}$ = measured elastic modulus of concrete
$E_{c,test}$ = elastic modulus of concrete back-calculated from uncracked test response
E_p = elastic modulus of prestressed reinforcement
e_{cr} = eccentricity of prestressed reinforcement relative to centroid of fully cracked section ($= d_p - \bar{y}_{cr}$ with $\bar{y}_{cr} = c_{cr}$)
e_{cr}' = eccentricity of prestressed reinforcement relative to centroid of partially cracked section ($= d_p - \bar{y}_{cr}'$)
e_e = effective eccentricity of prestressed reinforcement ($= d_p - \bar{y}_e$)
e_g = eccentricity of prestressed reinforcement relative to centroid of gross concrete section ($= d_p - \bar{y}_g$)
e_{tr} = eccentricity of prestressed reinforcement relative to centroid of uncracked transformed section including A_{ps} plus A_s and A_s' if present ($= d_p - \bar{y}_{tr}$). Replaced with e_g when I_g used instead of I_{tr}.
$e_{tr,np}$ = eccentricity of prestressed reinforcement relative to centroid of uncracked transformed section with only the nonprestressed reinforcement (A_s and A_s') transformed when present ($= d_p - \bar{y}_{tr,np}$)
F = total applied force on test beam (from two concentrated loads for two-point loading)
f_c' = compressive strength of concrete
$f_{c,p}$ = stress in concrete at prestressing level from the eccentric prestress force
f_D = concrete stress at tensile face from dead load assuming section is uncracked ($= M_D y_t / I_g$)
f_{dc} = decompression stress (stress in prestressed reinforcement corresponding to zero stress in concrete at prestress level)
f_e = $f_{tot} - f_r$
f_L = concrete stress at tensile face from live load assuming section is uncracked ($= M_L y_t / I_g$)
f_{pe} = compressive stress in concrete from effective prestress force at precompressed tensile face
f_r = modulus of rupture of concrete
f_{se} = effective stress in prestressed reinforcement after allowance for all prestress losses
f_{tot} = total concrete stress at tensile face from eccentric prestressing force plus dead load and live load assuming section is uncracked ($= -f_{pe} + f_D + f_L$)
h = overall height of member
I_c = moment of inertia of (uncracked) concrete section ($\cong I_g$)
I_{cr} = moment of inertia of fully cracked transformed section (equivalent to cracked section where reinforcement is not prestressed)
I_{cr}' = moment of inertia of partially cracked transformed section
I_e = effective moment of inertia
I_g = moment of inertia of gross (uncracked) section
I_{tr} = moment of inertia of uncracked transformed section (including A_{ps} plus A_s and A_s' if present)
$I_{tr,np}$ = moment of inertia of uncracked transformed section with only nonprestressed reinforcement (A_s and A_s') transformed (in other words, without A_{ps})
k_M = deflection coefficient for external loading
$k_{M,F}$ = deflection coefficient for member with two-point loading
$k_{M,sw}$ = deflection coefficient for distributed load from member self-weight
k_p = deflection coefficient for prestressing force
L = member span
M = external moment applied to member, section moment
M_a = service load moment at critical section

M_{bal} = balanced moment corresponding to zero deflection
M_{cr} = moment applied to nonprestressed or prestressed section that results in flexural cracking
M_{cr}' = reduced cracking moment (to account for shrinkage restraint stresses from nonprestressed reinforcement)
M_D = dead load moment
M_{dec} = decompression moment corresponding to zero stress at tension face of prestressed member
M_{dec}' = reduced decompression moment
M_e = effective prestress moment ($= P_o e_e$)
M_F = moment from applied concentrated loads
M_L = live load moment
$(M_L)_{cr}$ = $M_{cr} - M_D$
M_o = product of P_o and e_{cr} or P_o and e_{cr}'
M_{shift} = offset moment to account for shift in I_{cr} response or I_{cr}' response ($=M_1$ or M_1')
M_{sw} = moment at critical section (usually midspan) from member self-weight
M_{zc} = zero curvature moment (corresponding to product of P_o and e_{tr})
M_1 = intercept of shifted $E_c I_{cr}$ response with uncracked $E_c I_{tr}$ response
M_1' = intercept of shifted $E_c I_{cr}'$ response with uncracked $E_c I_{tr}$ response
n_p = ratio of E_p to E_c
P_e = effective prestress force
P_o = fictitious decompression force
R = interpolation coefficient
w_c = unit weight of concrete
w_{sw} = distributed dead load from member self-weight
$\bar{y}_{cr}$ = centroid location relative to compression face of fully cracked transformed section
$\bar{y}_{cr}'$ = centroid location relative to compression face of partially cracked transformed section
$\bar{y}_e$ = effective centroid depth
$\bar{y}_g$ = centroid location relative to compression face of gross (uncracked) section
y_t = distance from centroid of uncracked section to tension face
$y_{t,np}$ = distance from centroid to tension face of uncracked transformed section without A_{ps} but including A_s and A_s', if present ($= h - \bar{y}_{tr,np}$)
$y_{t,tr}$ = distance from centroid to tension face of uncracked transformed section with A_{ps} and including A_s plus A_s' if present ($= h - \bar{y}_{tr}$)
$\bar{y}_{tr}$ = centroid location relative to compression face of the uncracked transformed section (including A_{ps} and A_s plus A_s', if present)
$\bar{y}_{tr,np}$ = centroid location relative to compression face of the uncracked transformed section without A_{ps} (including A_s and A_s', if present)
α = integration factor coefficient
β_{ts} = tension-stiffening factor
Δ = deflection
Δ_{calc} = calculated or predicted member deflection
$\Delta_{calc}/\Delta_{exp}$ = deflection prediction ratio
Δ_{camber} = deflection from prestressing only
Δ_{exp} = experimental deflection (including deflection from camber, member self-weight, and applied test force)
Δ_L = deflection from live load
Δ_{meas} = measured deflection (at midspan) from applied test force(s)
Δ_{net} = net deflection
$\Delta_{p,tr}$ = deflection (camber) from eccentric prestressing of uncracked member
Δ_{sw} = deflection from member self-weight
ϕ = curvature
$\phi_{p,cr}$ = curvature of cracked section from prestressing force
$\phi_{p,tr}$ = initial uncracked curvature from the prestressing force
ϕ_{pe} = effective curvature from prestressing force
γ = integration factor
ρ_p = ratio of A_{ps} to bd_p
ρ_s = ratio of A_s to bd_s
ξ = interpolation coefficient

REFERENCES

Abdelrahman, A. A., and Rizkalla, S. H., 1999, "Deflection Control of Concrete Beams Pretensioned by CFRP Reinforcements," *Journal of Composites for Construction*, ASCE, V. 3, No. 2, May, pp. 55-62. doi: 10.1061/(ASCE)1090-0268(1999)3:2(55)

ACI Committee 318, 1971, "Building Code Requirements for Reinforced Concrete (ACI 318-71)," American Concrete Institute, Farmington Hills, MI, 78 pp.

ACI Committee 318, 2019, "Building Code Requirements for Structural Concrete (ACI 318-19) and Commentary (ACI 318-19R) (Reapproved 2022)," American Concrete Institute, Farmington Hills, MI, 624 pp.

ACI Committee 435, 2000, "Control of Deflection in Concrete Structures (ACI 435R-95) (Reapproved 2000)," American Concrete Institute, Farmington Hills, MI, 77 pp.

Alameh, A. S., and Harajli, M. H., 1989, "Deflection of Progressively Cracking Partially Prestressed Concrete Flexural Members," *PCI Journal*, V. 34, No. 3, May-June, pp. 94-128. doi: 10.15554/pcij.05011989.94.128

Bischoff, P. H., 2005, "Reevaluation of Deflection Prediction for Concrete Beams Reinforced with Steel and Fiber Reinforced Polymer Bars," *Journal of Structural Engineering*, ASCE, V. 131, No. 5, May, pp. 752-767. doi: 10.1061/(ASCE)0733-9445(2005)131:5(752)

Bischoff, P. H., 2008, "Discussion of "Tension Stiffening in Lightly Reinforced Concrete Slabs" by R. I. Gilbert," *Journal of Structural Engineering*, ASCE, V. 134, No. 7, July, pp. 1259-1260. doi: 10.1061/(ASCE)0733-9445(2008)134:7(1259)

Bischoff, P. H., 2019, "Discussion of "Deflection of FRP Prestressed Concrete Beams" by S. Pirayeh Gar, J. B. Mander, and S. Hurlebaus," *Journal of Composites for Construction*, ASCE, V. 23, No. 2, Apr., p. 07019001. doi: 10.1061/(ASCE)CC.1943-5614.0000934

Bischoff, P. H., 2020, "Comparison of Existing Approaches for Computing Deflection of Reinforced Concrete," *ACI Structural Journal*, V. 117, No. 1, Jan., pp. 231-240. doi: 10.14359/51718072

Bischoff, P. H., 2022, "Deformation Model for Reinforced and Cracked Prestressed Concrete," *ACI Structural Journal*, V. 119, No. 1, Jan., pp. 243-254. doi: 10.14359/51733138

Bischoff, P. H., and Gross, S. P., 2011, "Equivalent Moment of Inertia Based on Integration of Curvature," *Journal of Composites for Construction*, ASCE, V. 15, No. 3, June, pp. 263-273. doi: 10.1061/(ASCE)CC.1943-5614.0000164

Bischoff, P. H.; Naito, C. J.; and Ingaglio, J. P., 2018, "Immediate Deflection of Partially Prestressed Concrete Flexural Members," *ACI Structural Journal*, V. 115, No. 6, Nov., pp. 1683-1693. doi: 10.14359/51702381

Bischoff, P. H., and Scanlon, A., 2007, "Effective Moment of Inertia for Calculating Deflections of Concrete Members Containing Steel Reinforcement and Fiber-Reinforced Polymer Reinforcement," *ACI Structural Journal*, V. 104, No. 1, Jan.-Feb., pp. 68-75. doi: 10.14359/18434

Branson, D. E., 1965, "Instantaneous and Time-Dependent Deflections of Simple and Continuous Reinforced Concrete Beams," *HPR Report* No. 7, Part 1, Alabama Highway Department, Bureau of Public Roads, Montgomery, AL, 78 pp.

Branson, D. E., 1977, *Deformation of Concrete Structures*, McGraw-Hill, New York, NY, 546 pp.

Branson, D. E., and Kripanarayanan, K. M., 1971, "Loss of Prestress, Camber and Deflection of Non-Composite and Composite Prestressed Concrete Structures," *PCI Journal*, V. 16, No. 5, Sept.-Oct., pp. 22-52. doi: 10.15554/pcij.09011971.22.52

Branson, D. E., and Trost, H., 1982a, "Unified Procedures for Predicting the Deflection and Centroidal Axis Location of Partially Cracked Non-Prestressed and Prestressed Concrete Members," *ACI Journal Proceedings*, V. 79, No. 2, Mar.-Apr., pp. 119-130. doi: 10.14359/10887

Branson, D. E., and Trost, H., 1982b, "Application of the I-Effective Method in Calculating Deflections of Partially Prestressed Members," *PCI Journal*, V. 27, No. 5, Sept.-Oct., pp. 62-77. doi: 10.15554/pcij.09011982.62.77

Chen, C. I., 1973, "Integrated Procedures for Predicting the Initial and Time-Dependent Deformation of "Reinforced" Concrete Structures," PhD thesis, University of Iowa, Iowa City, IA.

Ghali, A., 1993, "Deflection of Reinforced Concrete Members: A Critical Review," *ACI Structural Journal*, V. 90, No. 4, July-Aug., pp. 364-373. doi: 10.14359/9648

Naaman, A. E., 1982, *Prestressed Concrete Analysis and Design: Fundamentals*, McGraw-Hill Book Company, New York, NY, 670 pp.

Nasreddine, W.; Obeidah, A.; Bischoff, P. H.; and Nassif, H., 2023, "Assessment of Deflection Prediction Models for Cracked Prestressed Concrete Beams," *ACI Structural Journal*, V. 120, No. 6, Nov., pp. 167-179. doi: 10.14359/51739094

Nilson, A. H., 1976, "Flexural Stresses After Cracking in Partially Prestressed Beams," *PCI Journal*, V. 21, No. 4, July-Aug., pp. 72-81. doi: 10.15554/pcij.07011976.72.81

PCI, 1971, *PCI Design Handbook: Precast and Prestressed Concrete*, first edition, Precast/Prestressed Concrete Institute, Chicago, IL.

PCI, 1978, *PCI Design Handbook: Precast and Prestressed Concrete*, second edition, Precast/Prestressed Concrete Institute, Chicago, IL.

PCI, 2017, *PCI Design Handbook: Precast and Prestressed Concrete (MNL-120-17)*, eighth edition, Precast/Prestressed Concrete Institute, Chicago, IL.

Pirayeh Gar, S.; Mander, J. B.; and Hurlebaus, S., 2018, "Deflection of FRP Prestressed Concrete Beams," *Journal of Composites for Construction*, ASCE, V. 22, No. 2, April, p. 04017049. doi: 10.1061/(ASCE)CC.1943-5614.0000832

Razaqpur, A. G.; Svecova, D.; and Cheung, M. S., 2000, "Rational Method for Calculating Deflection of Fiber-Reinforced Polymer Reinforced Beams," *ACI Structural Journal*, V. 97, No. 1, Jan.-Feb., pp. 175-183. doi: 10.14359/847

Scanlon, A., and Bischoff, P. H., 2008, "Shrinkage Restraint and Loading History Effects on Deflections of Flexural Members," *ACI Structural Journal*, V. 105, No. 4, July-Aug., pp. 498-506. doi: 10.14359/19864

Shaikh, A. F., 1967, "Use of Non-Tensioned Steel in Prestressed Concrete Beams," PhD thesis, University of Iowa, Iowa City, IA.

Shaikh, A. F., and Branson, D. E., 1970, "Non-Tensioned Steel in Prestressed Concrete Beams," *PCI Journal*, V. 15, No. 1, Feb., pp. 14-36. doi: 10.15554/pcij.02011970.14.36

Tadros, M. K.; Ghali, A.; and Meyer, A. W., 1985, "Prestressed Loss and Deflection of Precast Concrete Members," *PCI Journal*, V. 30, No. 1, Jan.-Feb., pp. 114-141. doi: 10.15554/pcij.01011985.114.141

APPENDIX A—PCI EFFECTIVE MOMENT OF INERTIA

PCI (2017) computes the deflection Δ_L from the live load using an effective moment of inertia I_e based on work by Branson and Kripanarayanan (1971) as shown in Fig. A1, where

$$\Delta_L = k_M\left[\frac{M_L}{E_c I_e}\right]L^2 \tag{A1}$$

$$I_e = \left(\frac{(M_L)_{cr}}{M_L}\right)^3 I_g + \left[1-\left(\frac{(M_L)_{cr}}{M_L}\right)^3\right]I_{cr} \tag{A2}$$

$$(M_L)_{cr} = M_{cr} - M_D \tag{A3}$$

with $M_{cr} = (f_r + f_{pe})(I_g/y_t)$ and $M_D = f_D(I_g/y_t)$ where f_D is the stress at the tensile face from the dead load moment assuming the section is uncracked. Knowing that $f_{tot} = -f_{pe} + f_D + f_L$, or in a rearranged form $f_D = f_{tot} + f_{pe} - f_L$, leads to

$$(M_L)_{cr} = \left[(f_r + f_{pe}) - f_D\right]\left(\frac{I_g}{y_t}\right) = \left[f_L - (f_{tot} - f_r)\right]\left(\frac{I_g}{y_t}\right) \tag{A4}$$

Finally, using $M_L = f_L(I_g/y_t)$ gives

$$\frac{(M_L)_{cr}}{M_L} = \frac{\left[f_L - (f_{tot} - f_r)\right]\left(\frac{I_g}{y_t}\right)}{f_L\left(\frac{I_g}{y_t}\right)} = \frac{\left[f_L - (f_{tot} - f_r)\right]}{f_L} = 1 - \frac{(f_{tot} - f_r)}{f_L} \tag{A5}$$

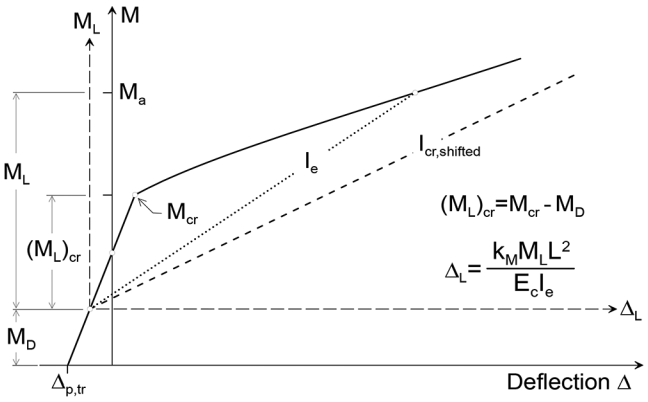

Fig. A1—PCI effective moment of inertia approach for computing live load deflection.

as defined in PCI (2017) for the M_{cr}/M_a term in Bransons's Eq. (1a). Alternatively, substituting Eq. (A3) into Eq. (A2) with $M_L = M_a - M_D$ gives Eq. (A6) which is identical to Eq. (3a).

$$I_e = \left(\frac{M_{cr} - M_D}{M_a - M_D}\right)^3 I_g + \left[1-\left(\frac{M_{cr} - M_D}{M_a - M_D}\right)^3\right]I_{cr} \tag{A6}$$

PCI (1971) originally set $f_e = f_{tot} - f_r$ to give $(M_L)_{cr}/M_L = 1 - f_e/f_L$ and provided a graphical solution for I_e/I_g in terms of f_e/f_L and I_{cr}/I_g. The total tensile stress in concrete f_{tot} from the prestress and loads was often set to a stress limit of $12\sqrt{f_c'}$ in psi ($1.0\sqrt{f_c'}$ in MPa).

APPENDIX B—EVALUATION BASED ON NET DEFLECTION

Table B1 provides an alternative evaluation comparing calculated to experimental deflections based on the net deflection value (deflection from member self-weight plus deflection from the applied test load). Comparison with Table 2 shows a small difference in many cases (except for the approach by Tadros et al. [1985], where the difference is greater).

Table B1—Evaluation for ratio of calculated to experimental deflections based on net deflection

Approach (full database)	Approach details	Deflection method	Mean $\Delta_{calc}/\Delta_{exp}$			FP+PP			FP	PP
			FP+PP	FP	PP	COV, %	%<1	% within ±30%	COV, %	COV, %
Tadros et al. (1985)	I_{tr} and I_{cr}'	Direct	0.67	0.61	0.75	27	94	39	25	24
		Integration	0.79	0.76	0.83	24	85	65	24	24
	I_{tr} and I_{cr}	Direct	0.64	0.58	0.73	28	96	34	26	24
		Integration	0.76	0.72	0.81	25	88	60	25	24
Bischoff et al. (2018)	I_{tr} and I_{cr} or I_{cr}'	Direct	1.06 (1.08)	1.10	1.00 (1.06)	29 (31)	45 (43)	77 (75)	28	30 (34)
		Integration	0.92 (0.95)	0.94	0.89 (0.96)	27 (29)	66 (63)	75 (75)	26	27 (32)
Bischoff (2022)	I_{tr} and I_{cr}	Direct	1.03 (1.07)	1.08	0.98 (1.06)	28 (29)	49 (44)	77 (76)	26	28 (32)
		Integration	0.90 (0.94)	0.92	0.87 (0.96)	25 (27)	71 (66)	75 (76)	24	26 (30)
Bilinear	I_{tr} and I_{cr}	Direct	1.03 (1.11)	1.10	0.94 (1.12)	26 (26)	48 (41)	76 (72)	24	26 (28)
		Integration	0.90 (0.97)	0.94	0.84 (1.01)	24 (25)	71 (61)	76 (78)	23	25 (27)
Bilinear (using I_e with γ)	I_{tr} and I_{cr}	Direct	0.90 (0.97)	0.94	0.85 (1.02)	24 (25)	71 (61)	77 (79)	23	26 (27)

Note: Values in brackets are for Δ_{calc} using M_{cr}' and M_{dec}' for PP beams.

ACI STRUCTURAL JOURNAL TECHNICAL PAPER

Title No. 122-S16

Shear Strength Database for Nonprestressed High-Strength High-Performance Fiber-Reinforced Cementitious Composites and Ultra-High-Performance Concrete Beams without Stirrups

by Manuel Bermudez and Chung-Chan Hung

Numerous shear tests on high-strength high-performance fiber-reinforced cementitious composites (HS-HPFRCCs) and ultra-high-performance concrete (UHPC) over the last three decades have enriched the understanding of their shear strength. This study integrates these experiments, which focused on specific shear strength parameters, into a comprehensive analysis. The Initial Collection Database, containing 247 shear tests, was developed for this purpose. From this, the Evaluation Shear Database was derived using specific filtering criteria, resulting in 118 beams pertinent to HS-HPFRCC and UHPC materials. These databases are accessible to the engineering community to advance the evaluation and development of shear strength formulations in structural design codes. This study concludes with an analysis of a subset of the Evaluation Shear Database, consisting of beams with reported uniaxial tensile strength. This analysis demonstrates the Evaluation Shear Database's applicability and highlights limitations in existing design equations. Notably, their reliance on a single predictor variable constrained predictive power.

Keywords: beam shear; high-performance fiber-reinforced cementitious composites (HPFRCC); shear database; shear strength; ultra-high-performance concrete (UHPC).

INTRODUCTION

Nearly four decades after the seminal 1962 Joint ACI-ASCE Committee 326[1] report, which delineated the primary shear-resisting mechanisms, Joint ACI-ASCE Committee 445[2] developed a comprehensive database of shear tests on nonprestressed reinforced concrete (RC) beams without stirrups. The most recent version of this RC database[2] includes a collection of 1365 beams. Its Evaluation Shear Databank (ESDB), featuring 784 slender beams, played a pivotal role in calibrating the latest shear design provisions of ACI 318-19.[3] Databases of this caliber are indispensable in fostering confidence in the development of design equations and enabling researchers to understand the current state of the art.

Ultra-high-performance concrete (UHPC),[4-6] also known as ultra-high-performance fiber-reinforced concrete (UHPFRC), is an emerging material in the construction industry. UHPC is distinguished by its extreme durability and ultra-high compressive strength, achieved through a low water-binder ratio (w/b), high content of cementitious materials, finely ground admixtures, and optimized gradation of granular materials. UHPC can be recognized as a specialized category within high-strength, high-performance fiber-reinforced cementitious composites (HS-HPFRCC).[7-9] These composites exhibit pseudo-tensile elastic-plastic behavior and a multiple cracking response, as noted by ACI Committee 239[10] and Naaman.[7] Over the past three decades, extensive shear test campaigns on both HS-HPFRCC and UHPC have generated a significant body of data, which can facilitate the development of robust, data-driven methodologies. A well-structured database employing a systematic approach to data collection is essential for the development of shear provisions applicable to HS-HPFRCC and UHPC beams. However, creating a database for shear tests on HS-HPFRCC and UHPC beams presents challenges similar to those encountered by Joint ACI-ASCE Committee 445.[2]

A primary challenge is the quantification of material properties, such as compressive strength, which often requires conversion factors due to varying measurement methods (cylinders versus cubes) across different studies. Additionally, accurately categorizing shear failure requires verifying the beam's flexural capacity to ensure that its peak strength is predominantly controlled by shear. For HS-HPFRCC and UHPC beams, the material's tensile strength is typically determined through uniaxial or indirect tensile tests. However, the absence of a standardized method for quantifying tensile strength, coupled with its frequent omission in shear test reports, poses a significant challenge. Another complexity arises from the detailed mixture compositions of HS-HPFRCC and UHPC, including the maximum aggregate size and fiber reinforcement, which are often not documented in many shear test reports. This lack of information necessitates an extensive review of the literature, including cross-referencing multiple studies, to compile comprehensive data.

The development of shear design equations for HS-HPFRCC and UHPC beams requires accurate and reliable data to evaluate their predictive performance effectively. This study aimed to create a repository that allows researchers to store and share their shear test results with the engineering

ACI Structural Journal, V. 122, No. 1, January 2025.
MS No. S-2024-023.R1, doi: 10.14359/51743296, received June 3, 2024, and reviewed under Institute publication policies.

community. To achieve this, an Initial Collection Database was established, systematically compiling all available data from shear tests on nonprestressed HS-HPFRCC and UHPC beams. Additionally, an Evaluation Shear Database was developed, incorporating specific filtering criteria tailored to HS-HPFRCC and UHPC beams. This database is intended to support the development of shear equations through data-driven approaches. The study also demonstrated the use of the Evaluation Shear Database in assessing the predictive performance of existing design equations, using the equations from the Swiss Society of Engineers and Architects (SIA)[11] and Federal Highway Administration (FHWA)[12] as examples.

RESEARCH SIGNIFICANCE

Establishing a comprehensive database of experimental data from shear tests on nonprestressed HS-HPFRCC and UHPC beams is a crucial step toward developing shear design provisions. The Initial Collection Database acts as a foundational resource, showcasing the current state of the art in these advanced fiber-reinforced concrete (FRC) beams. Additionally, the Evaluation Shear Database provides a reliable collection of beams that adhere to specific filtering criteria designed for HS-HPFRCC and UHPC materials. Accurately quantifying the shear strength of these beams lays the groundwork for advancing research into more complex scenarios, including those involving stirrup reinforcement and prestressing.

INITIAL COLLECTION DATABASE

The criteria for integrating beams into the Initial Collection Database must consider the developmental history of HS-HPFRCC and UHPC. Naaman and Reinhardt[4] highlighted the challenge of establishing fixed criteria to define FRCC as high-performance materials. They proposed distinguishing HPFRCC from other concrete types based on the presence of tensile strain-hardening behavior and multiple cracking. Meanwhile, defining "ultra-high performance" remains a complex issue, as emphasized by Naaman and Reinhardt[4] and Naaman and Wille.[13] Given that UHPC has been progressively evolving since the 1990s, many researchers during that period and in subsequent decades did not explicitly categorize their materials as HS-HPFRCC or UHPC. In response, this study collected all available experimental results published after 1990 that corresponded with the developmental trajectory of HS-HPFRCC or UHPC. These results were then subjected to appropriate control criteria for filtering. Within the Initial Collection Database, researchers used various labels for their materials, including UHPFRC, UHS-FR-CC, HSFRC, HPFRCC, HPC, SFRC-UHPC, SFR-UHPC, and UHPC.

The selection of beams for the Initial Collection Database was based on several key criteria. Regarding material properties, Naaman[14] highlighted the ongoing debate among researchers regarding the compressive strength threshold for defining UHPC. This debate, persisting for over a decade, is evident in the varying definitions provided by ACI Committee 239,[10] ASTM C1856/C1856M-17,[15] AFNOR Group,[16] SIA,[11] FHWA,[12] and others.[17] The lack of a standardized definition is further complicated by the emergence of nonproprietary UHPC mixtures. Some of these mixtures do not meet the compressive strength thresholds of 120 MPa (17.5 ksi) (ASTM C1856/C1856M[15]) or 150 MPa (22 ksi) (ACI Committee 239[10]) but were still classified as UHPC. Notably, the FHWA guidelines[18] for the design and detailing of noncontact lap-splice connections apply to UHPC with a minimum compressive strength of 97 MPa (14 ksi). Consequently, broadening the compressive strength limit range to include beams that meet other filtering criteria was a logical step. In the Initial Collection Database, beams were required to have a compressive strength greater than 80 MPa (11.6 ksi). Additionally, the absence of standardized testing methods has resulted in a variety of testing protocols and specimen sizes, complicating the comparison of reported UHPC compressive strength values. The difference in compressive strength measurements, with some researchers using cylinders and others using cubes, highlights the size effect on concrete's strength. To address these variations, the database adopts the conversion factors for compressive strength recommended by Graybeal and Davis.[19]

Establishing the Initial Collection Database presented another challenge: the majority of studies did not report the cracking and post-cracking strengths of the materials under tension. Consequently, it was not feasible to use tensile strain-hardening behavior as a strict criterion for filtering the initial data. Additionally, while HS-HPFRCC and UHPC typically employ a minimum fiber volume fraction of 0.5 to 0.75% to achieve crack control and tensile strain hardening, this threshold was lowered to 0.1% in the database's establishment. This adjustment served two purposes: 1) to reflect the focus of the original studies on the impact of fiber amount on shear strength; and 2) to broaden the database for future applications. Regarding the structural behavior filtering criteria, the original studies needed to clearly indicate that shear was the primary failure mode of the tested beams.

Appendix A2* lists 42 references that satisfied the established selection criteria, contributing to the Initial Collection Database. This database comprises 247 nonprestressed HS-HPFRCC and UHPC beams without stirrups, as detailed in Appendix A3. It encompasses a wide range of data, including material strengths, cross-sectional geometry, loading and support configurations, details of longitudinal and fiber reinforcement, and measurements of cracking and peak loads. The notation of the collected data parameters is presented in Appendix A1. Table 1 provides a comprehensive breakdown of the beams' characteristics in the Initial Collection Database. All beams had a cylindrical compressive strength exceeding 80 MPa (11.6 ksi), with only 16% surpassing 150 MPa (22 ksi). The material's uniaxial tensile strength (f_t) was reported for only 31% of the beams, among which just 23% met the 5.2 MPa (0.75 ksi) threshold required by the Precast/Prestressed Concrete Institute (PCI)[17] and AASHTO[20] for UHPC classification. The

*The Appendixes are available at **www.concrete.org/publications** in PDF format, appended to the online version of the published paper. They are also available in hard copy from ACI headquarters for a fee equal to the cost of reproduction plus handling at the time of the request.

Table 1—Selection criteria for Initial Collection Database of nonprestressed HS-HPFRCC and UHPC beams subjected to shear tests

Criteria	Individual criterion	No. of tests that fulfilled criterion	No. of tests that did not fulfill criterion
1	$f_{c,cylinder}' \geq 80$ MPa (11.6 ksi)	247	0
1.1	120 MPa (17.5 ksi) $\leq f_{c,cylinder}' \leq$ 150 MPa (22 ksi)	102	145
1.2	$f_{c,cylinder}' >$ 150 MPa (22 ksi)	39	208
2	f_t provided	76	171
2.1	$f_t \geq 5.2$ MPa (0.75 ksi)	50	26
3	d_a provided	200	47
3.1	$d_a \leq 5$ mm (0.25 in.)	122	78
4	$b_w = b \geq 30$ mm (1.2 in.)	247	0
4.1	$b_w = b \geq 50$ mm (2 in.)	228	19
5	$h > 70$ mm (2.75 in.)	247	0
6	$a/d \geq 2.5$	131	116
7	$a/d < 2.5$	116	131
8	$\rho = (A_s/bd) > 1.5\%$	208	39
9	$\rho_w = (A_s/b_w d) > 1.5\%$	231	16

maximum aggregate size (d_a) was documented for 81% of the beams; within this subset, 49% had an aggregate size of 5 mm (0.25 in.) or smaller, aligning with ASTM C1856/C1856M[15] specifications for UHPC.

Table 2 showcases the range of parameters within the database, illustrating its comprehensiveness across a wide spectrum of essential parameters. The variation in the maximum aggregate size (d_a), ranging from 0.2 to 22 mm (0.0079 to 0.866 in.), reflects past studies that explored the impact of aggregate size on the performance of HS-HPFRCC and UHPC materials. The beams in the database were reinforced with various types of fibers, leading to a broad range in the fiber length-to-diameter ratio (L_f/D_f). Specifically, 58% of the beams used straight steel fibers, 27% employed hooked-end steel fibers, 1% used double hooked-end steel fibers, 2% incorporated polyvinyl alcohol (PVA) fibers, 1% featured polypropylene fibers, and 2% were reinforced with basalt fibers. The remaining 9% of the beams used hybrid fibers. These hybrids comprised combinations including two hooked-end steel fibers of different dimensions, two straight steel fibers of varying dimensions, straight steel fibers combined with hooked-end steel fibers, two hooked-end steel fibers mixed with PVA, and a blend of hooked-end steel fibers with polypropylene fibers.

In terms of beam designs, 92% of the beams in the database had a minimum width of at least 50 mm (2 in.), aligning with the standard in the RC database.[2] However, for this study, the minimum width requirement was reduced to 30 mm (1.2 in.) to accommodate the optimized cross sections made possible by the ultra-high mechanical properties of HS-HPFRCC and UHPC. All beams exceeded a height of 70 mm (2.75 in.). Additionally, 53% of the beams were classified as slender, with a shear span-effective depth ratio (a/d) of at least 2.5, while the remainder were considered deep or non-slender. The beams predominantly had three cross-sectional shapes: 72% were rectangular, 19% were I-shaped, and 9% were T-shaped. Regarding load configurations, 75% of the beams were tested under four-point bending, and the remaining 25% underwent three-point bending. The longitudinal reinforcement ratios typically ranged between 1.5 and 8%, indicative of designs intended for shear-controlled failure.

Table 2—Ranges of parameters of beams in databases

Parameters	Initial Collection Database		Evaluation Shear Database	
	Minimum	Maximum	Minimum	Maximum
$f_{c,cylinder}'$, MPa	80	215	80	208
f_t, MPa	1.6	18.7	1.6	11.2
d_a, mm	0.2	22	0.2	22
L_f/D_f	13	667	38	211
V_f, %	0.1	3	0.4	3
F (fiber factor)	0.003	1.26	0.09	1.26
b_w, mm	30	310	30	300
b, mm	100	600	100	500
a, mm	150	2769	215	2760
d, mm	54	923	124	920
a/d	0.9	8	1	4.5
h, mm	76	1000	150	1000
ρ, %	0.7	8.2	0.7	8.2
ρ_w, %	0.9	22	1.9	22
v_{cr}, MPa	0.4	18	0.8	18
v_u, MPa	1.7	43	2.3	25

Note: 1 MPa = 0.145 ksi; 1 mm = 0.0394 in.

The failure modes of the beams, as labeled by the original authors, included terms such as "Shear," "Shear-Flexure," "Tensile Failure in the Web," "Tension Failure," "Diagonal Tension," "True Shear (splitting)," "Shear Compression," "DT+ST (Diagonal Tension + Shear Tension)," "ST+SC (Shear Tension + Shear Compression)," "Diagonal Tension Mode," and "DT + CC (Diagonal Tension + Concrete Compression)." Despite the variety of labels, all these terms indicate shear failure. The extensive range of parameters within the database accounts for the notable variability observed in both shear cracking strength (v_{cr}) and peak shear strength (v_u). Notably, v_{cr} was not reported for 48% of the beams. The Initial Collection Database can be accessed at https://fearless-uhpcandhshpfrc.wordpress.com/download/ using the password: 1beam#DATABASE.

EVALUATION SHEAR DATABASE

Building upon the foundational work of the Initial Collection Database, a critical step was taken to refine and specifically include beams whose peak strength was predominantly governed by shear damage in the Evaluation Shear Database. It is essential to acknowledge that not all

beams initially classified under shear failure by their original authors may genuinely exhibit such a failure mode, a complexity previously noted by Joint ACI-ASCE Committee 445.[2] For example, from a total of 1365 nonprestressed RC beams without stirrups in the RC database, Joint ACI-ASCE Committee 445[2] selected a filtered subset of 1060 beams. These beams were identified as having their peak strength predominantly governed by shear damage. This subset was instrumental in the development of the shear provisions[21] of ACI 318-19.[3]

In this study, a three-step filtering process was used to establish the Evaluation Shear Database, focusing on HS-HPFRCC and UHPC beams that exhibited shear-controlled peak strength. Beams whose peak strength was not exclusively governed by shear, such as those experiencing flexure-shear, flexure, or anchorage failure, were excluded from the subset. This exclusion is crucial to ensure the accuracy of the evaluation of shear strength equations and to avoid any misleading interpretations.

Step 1: Strength-based filter

For inclusion in the Evaluation Shear Database, beams must exhibit an actual strength lower than the demand at flexural capacity. Peng et al.[22] developed a method for evaluating the flexural strength of UHPC beams, which accounts for the contributions of tensile strength to the overall flexural capacity. However, in the Initial Collection Database, uniaxial tensile strength (measured from dog bones or prisms) or indirect tensile strength (derived from inverse analysis on bending tests) was reported for only 31% and 7% of the beams, respectively. This underreporting of tensile strength in HS-HPFRCC and UHPC materials used in the beams presents a challenge in using this parameter to estimate flexural capacity. To address this issue, three conservative strength models were applied in the first step to estimate the flexural capacity of the beams in the Initial Collection Database.

The first strength model is from ACI 318-19[3] for conventional RC beams, which neglects the contributions of fibers and compressive reinforcing bars to flexural strength. The model is as follows

$$M_{n,\text{ACI318}} = A_s f_y \left(d - \frac{a_c}{2}\right) \tag{1}$$

where $M_{n,\text{ACI318}}$ is the flexural capacity calculated based on ACI 318-19[3]; A_s is the area of tensile reinforcing bars; f_y is the nominal yield strength of longitudinal reinforcing bars; and a_c is the depth of the stress block. It should be noted that detailed information about the compressive steel reinforcing bars was not consistently documented in several studies included in the Initial Collection Database. Furthermore, it is crucial to recognize that simplifying the parabolic stress distribution into an equivalent rectangular stress block may not accurately capture the magnitude and location of the compression resultant in HS-HPFRCC and UHPC beams. In these high-strength materials, the stress distribution is likely to be narrower and more peaked compared to conventional concrete. Consequently, employing a rectangular stress block approximation was deemed a conservative approach in this context.

The second flexural strength model was from Joint ACI-ASCE Committee 445[2] for establishing the RC database,[2] as follows

$$\mu_{\mu,\text{RC DATABASE}} = \frac{M_{n,\text{RC DATABASE}}}{bd^2 f_c'} = \omega_l \zeta \tag{2}$$

where ω_l is the mechanical reinforcement ratio, defined as $\rho f_y / f_c'$; and ζ is a coefficient representing the ratio of z/d, where z is the internal lever arm, defined as $d - 0.5x$. Here, x denotes the height of the uniform stress block in the compression zone and is calculated as $\omega_l d/\kappa_c$. The coefficient κ_c, used for the compression stress block, is defined as $1 - f_c'/250$. This equation calculates the flexural strength in a dimensionless format, as described by the CEB-FIP Model Code 1990.[23] Similar to Eq. (1), Eq. (2) also neglects the contributions of fibers and compressive steel reinforcing bars to the flexural strength of beams.

The third flexural strength model, originally developed for high-strength steel FRC beams, is expressed as follows[24]

$$M_{n,\text{FRC Eq.}} = \frac{1}{2}\rho f_y b d^2 (2 - \eta) + 0.83 F b d^2 (0.75 - \eta)(2.15 + \eta) \tag{3}$$

In this equation, $\eta = (\rho f_y + 2.32F)/(0.85 f_c' + 3.08F)$, where F is the fiber factor, defined as $(L_f/D_f)(V_f d_f)$. This model expands on the one introduced by ACI Committee 544[25] for conventional FRC beams. However, it is considered conservative when applied to HS-HPFRCC and UHPC beams, as it does not fully account for the tensile strain-hardening and high ductility characteristics inherent to these materials.

In the assessment of flexural strength, the cylindrical compressive strength f_c' was used. Additionally, the nominal yield strength f_y was applied instead of the actual strength of the reinforcing bars, adding a reasonably conservative bias to the assessment. After calculating the flexural strengths using Eq. (1) and (3), the corresponding shear demands—that is, $V_{mn,\text{ACI318}}$ and $V_{mn,\text{FRC Eq.}}$—were determined based on force equilibrium, considering the specific bending test setup. For the evaluation using Eq. (2), the calculated flexural capacity $\mu_{\mu,\text{RC DATABASE}}$ was compared to $\mu_{\mu,Test}$, which is the actual peak load from the experimental test normalized by $bd^2 f_c'$.

Figures 1 and 2 illustrate the distribution of the calculated strength ratios against the longitudinal reinforcement ratio for all beams, with the evaluation results summarized in Table 3. A total of 141 (57%) and 154 (62%) beams satisfied the strength-based filter, with $V_{u,Test}/V_{mn,\text{ACI318}} < 1$ and $V_{u,Test}/V_{mn,\text{FRC Eq.}} < 1$, respectively. Meanwhile, 114 beams (46%) had a $\mu_{\mu,Test}/\mu_{\mu,\text{RC DATABASE}}$ ratio of less than 1. However, considering the conservativeness of Eq. (2), Joint ACI-ASCE Committee 445[2] suggests a threshold of 1.1, and 147 beams (59%) met this criterion. Notably, the evaluation using Eq. (3) resulted in a higher filtering rate compared to the other strength models due to its consideration of fiber reinforcement. Based on the strength-based filter in Step 1,

out of the 247 beams analyzed, 135 consistently exhibited a strength ratio of less than 1 for Eq. (1) and (3) and 1.1 for Eq. (2) (as shown in Fig. 1).

Step 2: Damage-pattern filter

The conservative nature of the strength-based criteria used in Step 1 may result in a significantly reduced database, limiting the available shear strength data for HS-HPFRCC and UHPC beams. Specifically, the inclusion of fiber reinforcement in HS-HPFRCC and UHPC beams can increase flexural strength by 10% to 25%[22,26] due to enhanced tensile strength, confinement, and ductility. To include more qualified data in the Evaluation Shear Database, Step 2 involved a detailed analysis of crack patterns in beams with a strength-based filter ratio between 1 and 1.3. Given that Eq. (1) identified the highest number of beams within this threshold, it was used as the benchmark among the three strength models. This approach led to the selection of 67 beams (27%) for a thorough examination of their damage patterns to confirm shear-controlled peak strength.

Figure 3 presents four beams[27-30] as examples to demonstrate the detection methodology used in Step 2. The images, as reported by the original authors, were modified by adding red rectangles to highlight the flexural cracks. While these beams exhibited significantly localized shear cracks, they also showed a dense array of vertical cracks in the flexural tension region along the shear span. These flexural cracks, which initiated before the localization of shear cracks, compromised the shear-resisting mechanism of the beam, thereby adversely affecting the beams' peak strength. As a result, these beams were excluded from the Evaluation Shear Database.

The data cleansing procedure implemented in Steps 1 and 2 revealed that, out of the 247 beams in the Initial Collection Database, 141 beams had clear evidence of peak strength being solely controlled by shear damage.

Step 3: Data-integrity filter

During the development of the Evaluation Shear Database for HS-HPFRCC and UHPC beams, it was observed that a subset of beams, despite passing the strength-based and damage-pattern filters, had issues that compromised the accurate assessment of their shear capacity. These issues included insufficient design details, ambiguous failure patterns, or nonstandard test procedures. As indicated in

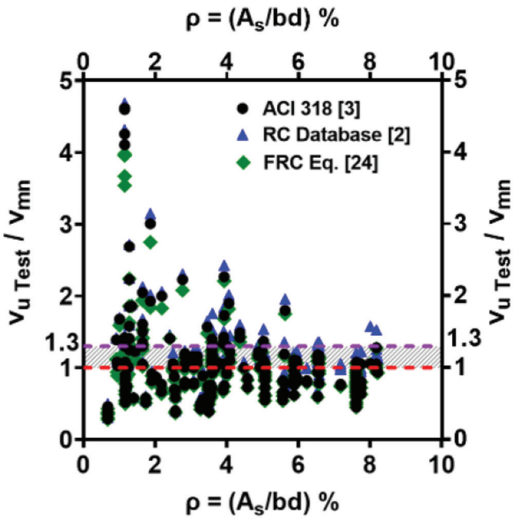

Fig. 1—Comparative analysis of experimental peak load versus nominal flexural capacity.

Table 3—Filtering criteria for Evaluation Shear Database of nonprestressed HS-HPFRCC and UHPC beams

Data filters (DF)		Criteria	Fulfilled	Unfulfilled
Materials	1	$f_{c,cylinder}' \geq 80$ MPa (11.6 ksi)	247	0
	2	$\sigma_p > \sigma_c$	247	0
Dimensions	3	$b_w = b \geq 30$ mm (1.2 in.)	247	0
	4	$h > 70$ mm (2.75 in.)	247	0
Damage patterns	5	$V_{u,Test}/V_{mn,ACI318} < 1.0$	141	106
	5.1	$V_{u,Test}/V_{mn,RC\ DATABASE} < 1.0$	114	133
	5.1.1	$V_{u,Test}/V_{mn,RC\ DATABASE} < 1.1$	147	100
	5.2	$V_{u,Test}/V_{mn,FRC\ Eq.} < 1.0$	154	93
	6	Shear-controlled peak strength	141	106

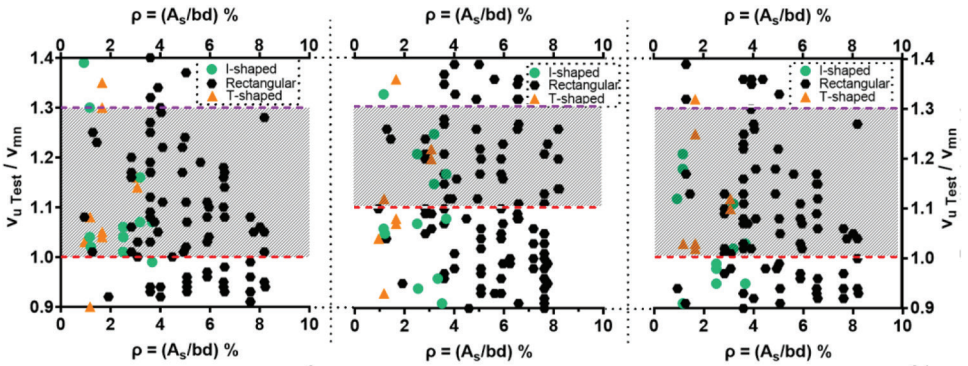

a. Eq. (1) from ACI 318[3] b. Eq. (2) from Joint ACI-ASCE Committee 445[2] c. Eq. (3) for FRC[24]

Fig. 2—Graphical representation with truncated y-axis to emphasize regions indicative of potential flexure-shear or flexural failures.

Table 4, 16 of these beams lacked documentation on fiber properties and volume fraction (V_f). The failure pattern of five beams was characterized by significant bond-slip of the longitudinal reinforcing bars, along with localized shear cracks. Additionally, two beams underwent two-stage tests involving flexure followed by shear. These beams have been cataloged in a separate tab within the Microsoft Excel spreadsheet. The data-integrity screening process ultimately led to the exclusion of 23 beams from the Evaluation Shear Database, bringing the total number of beams in the final data set to 118.

Overview of Evaluation Shear Database

The Evaluation Shear Database, a comprehensive Excel document compiling data points specific to the shear strength of HS-HPFRCC and UHPC beams, is accessible at https://fearless-uhpcandhshpfrc.wordpress.com/download/ (refer to Appendix A4). Table 2 and Fig. 4 summarize the range of key design parameters for the test beams included in the database. Despite the application of selective filtering, the range of distribution for these design parameters has only been slightly reduced compared to the Initial Collection Database, thus maintaining the database's comprehensiveness in terms of material properties, beam dimensions, a/d, longitudinal reinforcement ratio, and shear strength.

The beams in the Evaluation Shear Database predominantly feature the following cross-sectional shapes: 69% rectangular, 28% I-shaped, and 3% T-shaped. Regarding the a/d, 44 beams (37%) had a ratio below 2.5, while 74 beams (63%) had a ratio of 2.5 or higher. The load configurations were more commonly four-point bending (65%) as opposed to three-point bending (35%). The mean material property values in the database featured f_c' = 129 MPa (18,710 psi),

Table 4—Subsequent application of filtering criteria to assess data adequacy for evaluating shear equations

Data filters (DF)		Criteria	Remaining of 141	Difference
Data adequacy	7.1	Missing fiber properties and content	125	16
	7.2	Missing reinforcing bar anchorage detailing	120	5
	7.3	Missing key experimental data	118	2
Summary		**End of filtering process**	**118**	**23**

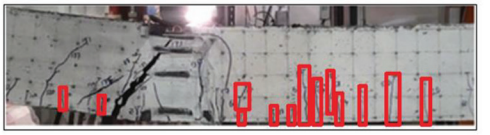

a. U-B6 from Kodur et al.[27] ($V_{u,test}$ / $V_{mn,\ ACI318}$=1.01)

b. B2 from Ridha et al.[28] ($V_{u,test}$ / $V_{mn,\ ACI318}$=1.03)

c. BS1.5-2.0 from Jabbar et al.[29] ($V_{u,test}$ / $V_{mn,\ ACI318}$=1.08)

d. H32 from Shoaib[30] ($V_{u,test}$ / $V_{mn,\ ACI318}$=1.29)

Fig. 3—Damage-pattern analysis in beams with strength ratios between 1 and 1.3.

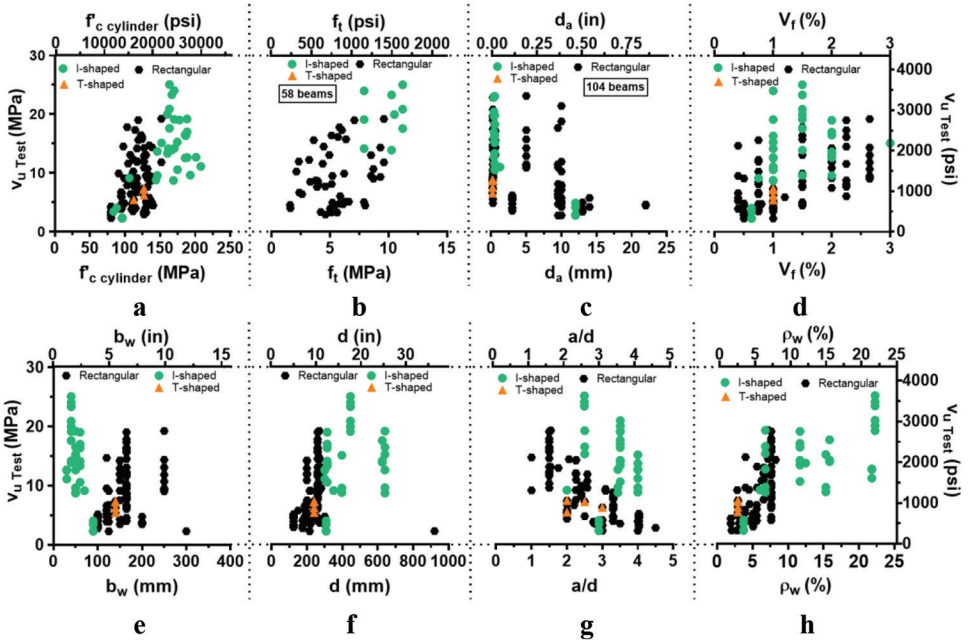

Fig. 4—Distribution of beam shear strengths against different parameters in Evaluation Shear Database (118 beams).

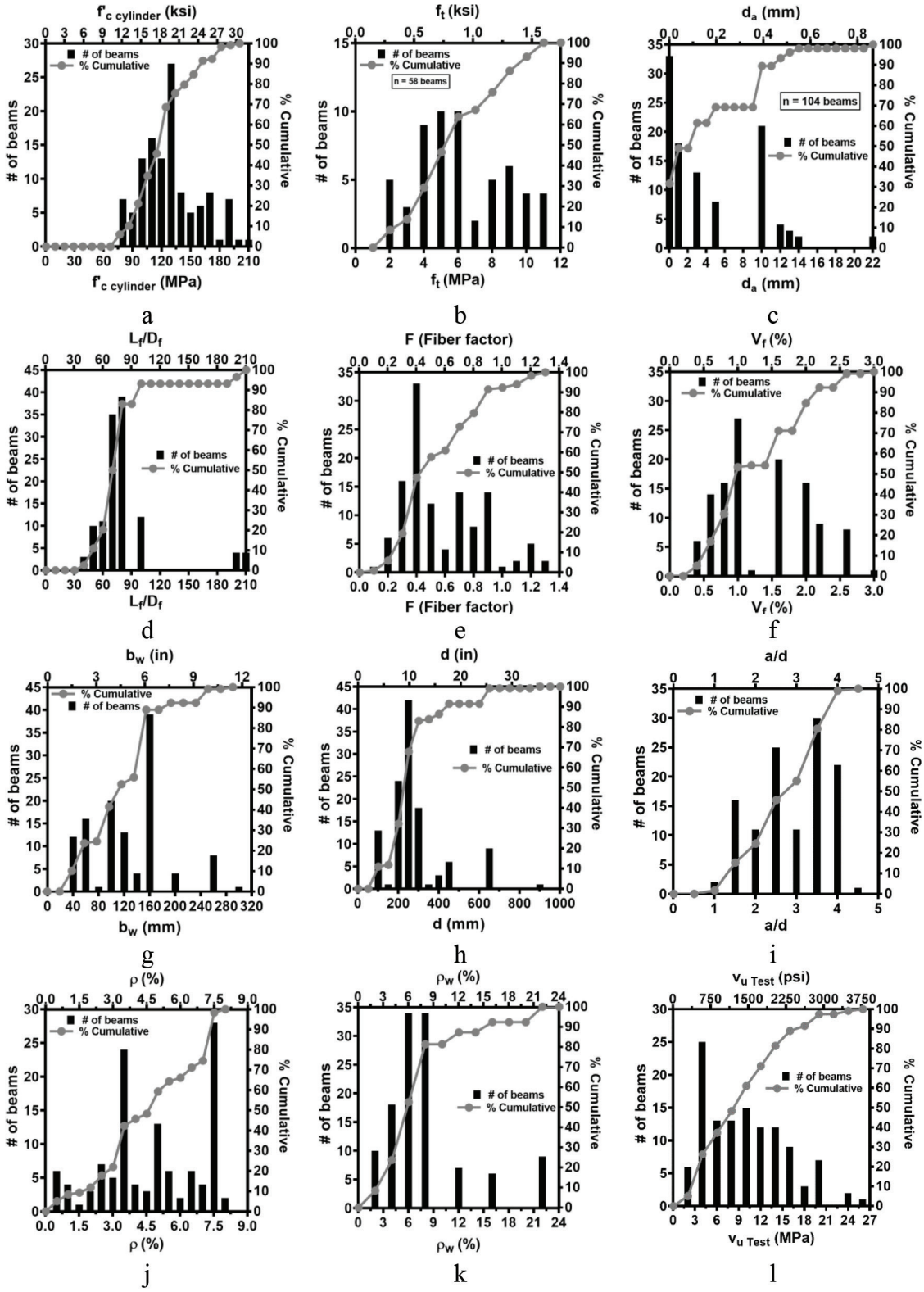

Fig. 5—Frequency histograms with cumulative distribution function (CDF) curves of parameters in Evaluation Shear Database (118 beams).

f_t = 6.1 MPa (885 psi), d_a = 4.4 mm (0.17 in.), and V_f = 1.3%. The average values for geometry and reinforcement were b_w = 126 mm (4.96 in.), d = 287 mm (11.3 in.), a/d = 2.85, and ρ_w = 7.85%. Notably, the mean shear cracking strength of 65 beams (55% of the total) was 4.8 MPa (696 psi), with the overall mean peak shear strength of all beams being more than double at 9.8 MPa (1421 psi). Figure 5 illustrates the distribution of these relevant parameters in the Evaluation Shear Database.

A sensitivity analysis conducted by Bermudez and Hung[31] examined the parameters that had a significant impact on the shear strength of HS-HPFRCC and UHPC beams. This

analysis highlighted the profound influence of key parameters, including compressive strength (f_c'), shear span-effective depth ratio (a/d), longitudinal reinforcement ratio (ρ_w), fiber contribution to shear strength (v_b), shape factor (b/b_w), and the size effect factor as per ACI 318-19[3] (λ_s). Consequently, Bermudez and Hung[31] developed a shear predictive equation for nonprestressed HS-HPFRCC and UHPC beams incorporating these critical parameters. The high predictive accuracy of this equation demonstrates the database's utility and affirms the significance of the identified parameters.

EVALUATION OF SHEAR STRENGTH EQUATIONS

The establishment of the shear strength database for HS-HPFRCC and UHPC was intended to offer insights that will guide future revisions and improvements in structural design protocols. It aimed to highlight areas of alignment as well as potential gaps. This objective was demonstrated in the study by evaluating the predictive capacity of shear strength equations for UHPC beams without stirrups, as outlined in SIA[11] and FHWA,[12] presented in Eq. (4) and (5), respectively

$$v_{UHPC} = 0.9(0.93 f_{Utud} \cdot \cot\theta) \text{ in MPa} \quad (4)$$

$$v_{UHPC} = 0.9(\gamma f_{t,loc} \cdot \cot\theta) \text{ in MPa} \quad (5)$$

Both equations estimate shear strength by relying on the shear crack angle and uniaxial tensile strength of UHPC (denoted as f_{Utud} in Eq. (4) and $f_{t,loc}$ in Eq. (5)). In the evaluation, the uniaxial tensile strength (f_t) reported in the Evaluation Shear Database was denoted as f_{Utud} in Eq. (4) and $f_{t,loc}$ in Eq. (5). In Eq. (5), a reduction coefficient $\gamma = 0.85$ is employed to account for the variability in UHPC's tensile strength, influenced by the orientation and placement of fibers. The shear-resisting area in these equations is based on the Modified Compression Field Theory[32] (MCFT) and AASHTO[20] approaches, represented as $b_w z$, where z is estimated to be $0.9d$. However, in the Evaluation Shear Database, the shear strength is calculated using the shear-resisting area $b_w d$. To facilitate an accurate comparison, a factor of 0.9 was incorporated into the equations. Additionally, the angle θ, representing the shear crack angle between the principal compression stress and the beam axis, was determined based on the actual shear crack angles observed in experimental tests for this study. These experimental angles sometimes deviated from the established limits of each equation: a minimum of 30 degrees for Eq. (4), and a range of 25 to 45 degrees for Eq. (5). When experimental angles exceeded these limits, the respective limit was applied.

To evaluate Eq. (4) and (5), a subset of beams was selected based on their compliance with the specifications of each equation. Specifically, the selected beams were required to have a compressive strength exceeding 120 MPa (17.5 ksi), a tensile strength of at least 7.7 MPa (1.12 ksi) for Eq. (4) and 5.2 MPa (0.75 ksi) for Eq. (5), and an a/d of 2.5 or greater. Of the 58 beams (49% of the total) that reported f_t, 16 met the criteria for Eq. (4) and 23 for Eq. (5). The calculation results are summarized in Table 5, and detailed calculations can be found at https://fearless-uhpcandhshpfrc.wordpress.com/download/.

The statistical analysis of Eq. (4) and (5) yielded mean values of 1.18 and 1.00 for the experimental shear test versus predicted shear strength, with standard deviations of 0.54 and 0.61 and average absolute errors of 44% and 65%, respectively. Figure 6(a) illustrates the relationship between the experimental shear strength and the predictions of each equation. The nearly horizontal trend lines for Eq. (4) and (5) indicate limited predictive capability. Figure 6(b) presents a statistical summary of the shear strength predictions for both equations. In this figure, the whiskers on the box plots represent the data's range, the centerline indicates the median, and the cross sign denotes the mean. The predictions of Eq. (4) appeared symmetrically distributed, as evidenced by the mean's proximity to the median and the equal length of the whiskers. In contrast, Eq. (5), despite a reasonable mean of 1.00, exhibited a median closer to 0.7, indicating a lower central tendency. This was accompanied by a wide interquartile range and an extended upper whisker, suggesting a greater likelihood of overestimation.

The influence of material properties, including f_c', f_t, and V_f, on the shear strength predictions of the equations is depicted in Fig. 7(a) to (c). For both equations, an increase in f_c' led to a more pronounced underestimation of shear strength, with the $v_{u,Test}/v_{u,Prediction}$ ratio reaching up to 2.5. The impact of varying f_t on prediction accuracy was not distinctly evident, suggesting that both equations adequately accounted for the influence of f_t on shear strength. Similarly, the effect of V_f on the accuracy of both equations was not significant when V_f ranged between 1 and 2%. However, when V_f exceeded this range, both equations tended to overestimate shear strength, as indicated by the analysis of the limited experimental database.

The analysis results showed that design parameters of beams including d, a/d, and ρ_w significantly influenced the accuracy of shear strength predictions for both equations, as illustrated in Fig. 7(d) to (f). As d increased from 150 to 500 mm (6 to 20 in.), the predictions of both equations consistently shifted from overestimation to underestimation, with the $v_{u,Test}/v_{u,Prediction}$ reaching as high as 2.5. However, when d further increased to 625 mm (25 in.), the $v_{u,Test}/v_{u,Prediction}$ moderately decreased to between 0.8 and 1.7. An increase in the a/d from 2.5 to 4.0 consistently reduced the $v_{u,Test}/v_{u,Prediction}$ for both equations, shifting the predictions from underestimation (up to a ratio of 2.5) to overestimation (down to a ratio of 0.3). Additionally, the tension reinforcing bar ratio ρ_w significantly influenced the accuracy of both equations. When ρ_w was less than 7.5%, both equations tended to overestimate shear strength. However, they showed a considerable tendency to underestimate shear strength in nonrectangular beams, namely I-shaped beams.

Overall, both equations demonstrated similar trends in their predictions under the influence of various key design parameters. Notably, their performance is limited in accurately accounting for the impact of different shear-transfer mechanisms and dowel action, which are influenced by the values of a/d and ρ_w, respectively. These results highlight the need for future studies to develop shear strength equations

Table 5—Summary table comparing shear predictions of Eq. (4) and (5)

Reference	Beam	f_t, MPa	θ (Eq. (4))	θ (Eq. (5))	$v_{u,\text{Eq. (4)}}$, MPa	$v_{u,\text{Eq. (5)}}$, MPa	$v_{u,Test}$, MPa	$v_{u,Test}/v_{u,\text{Eq. (4)}}$	$v_{u,Test}/v_{u,\text{Eq. (5)}}$
Hong et al.[33]	1-S25	10.3	40	40	10.2	9.4	23.3	2.3	2.5
	1-S35	10.5	30*	25*	15.2	17.2	20.0	1.3	1.2
	1-S35-B	10.3	30*	25*	14.9	16.8	13.9	0.9	0.8
	2-S25	11.2	30	30	16.3	14.9	25.1	1.5	1.7
	2-S35	11.2	30	30	16.3	14.9	20.9	1.3	1.4
	2-S35-B	11.2	34	34	13.9	12.7	17.6	1.3	1.4
	3-S25	7.9	31	31	11.0	10.1	24.0	2.2	2.4
	3-S35	7.9	30*	28	11.5	11.4	19.1	1.7	1.7
	3-S35-B	7.9	36	36	9.1	8.3	14.2	1.6	1.7
Yavaş et al.[34]	S6(0.5)	5.6	—	25	—	9.2	3.3	—	0.4
	S6(1.0)	5.8	—	25*	—	9.5	4.8	—	0.5
	S6(1.5)	8.0	30*	27	11.6	12.0	4.5	0.4	0.4
	S13(0.5)	5.4	—	25	—	8.9	4.5	—	0.5
	S13(1.0)	6.6	—	25*	—	10.8	5.1	—	0.5
	H30(1.0)	5.2	—	25*	—	8.5	5.0	—	0.6
	H60(1.5)	6.1	—	30	—	8.1	4.7	—	0.6
	DH60(1.0)	6.3	—	25*	—	10.3	5.1	—	0.5
	DH60(1.5)	7.9	30	30	11.5	10.5	5.0	0.4	0.5
Yang et al.[35]	NUHPCB2	9.6	30*	29	13.9	13.2	11.8	0.8	0.9
	NUHPCB4	9.3	30*	28	13.5	13.4	9.3	0.7	0.7
	NUHPCB5	8.7	30*	25*	12.6	14.3	10.7	0.8	0.7
	NUHPCB6	8.7	30*	25*	12.6	14.3	9.0	0.7	0.6
	NUHPCB8	8.5	36	36	9.8	8.9	9.5	1.0	1.1

*Shear crack angles have been modified to fit within the equation's range limits.

Note: — is not included in the evaluation because it did not comply with any of the standard specifications.

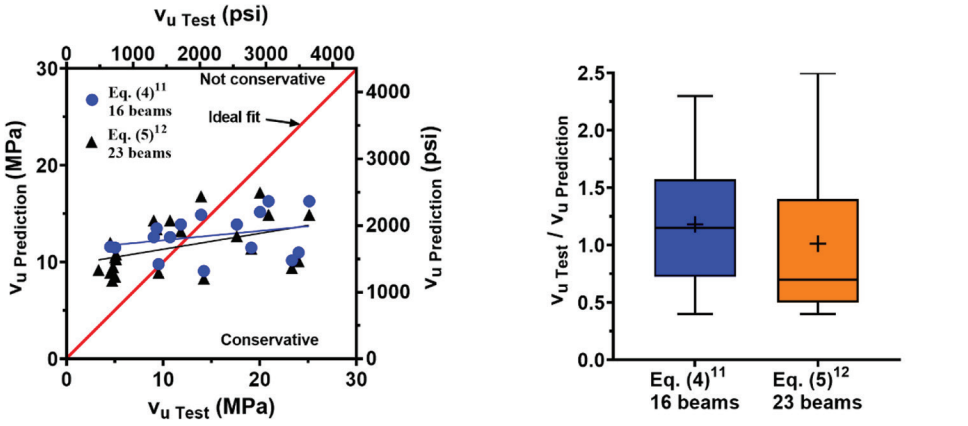

(a) Experimental test vs predicted (b) Box plot graph of design standards

Fig. 6—Evaluation of shear predictions of design standards on f_t *data set.*

for UHPC beams that more accurately consider the effects of key design parameters, including material strength, fiber volume fraction, beam depth, shear span-depth ratio, longitudinal reinforcement ratio, and cross-sectional shape. Furthermore, the current shear database for HS-HPFRCC and UHPC beams should be expanded as more high-quality shear test results become available.

SUMMARY AND CONCLUSIONS

To facilitate the development of shear design provisions for nonprestressed high-strength high-performance fiber-reinforced cementitious composites (HS-HPFRCC) and ultra-high-performance concrete (UHPC) beams, two comprehensive databases compiling experimental data from existing shear tests were established. The Initial Collection

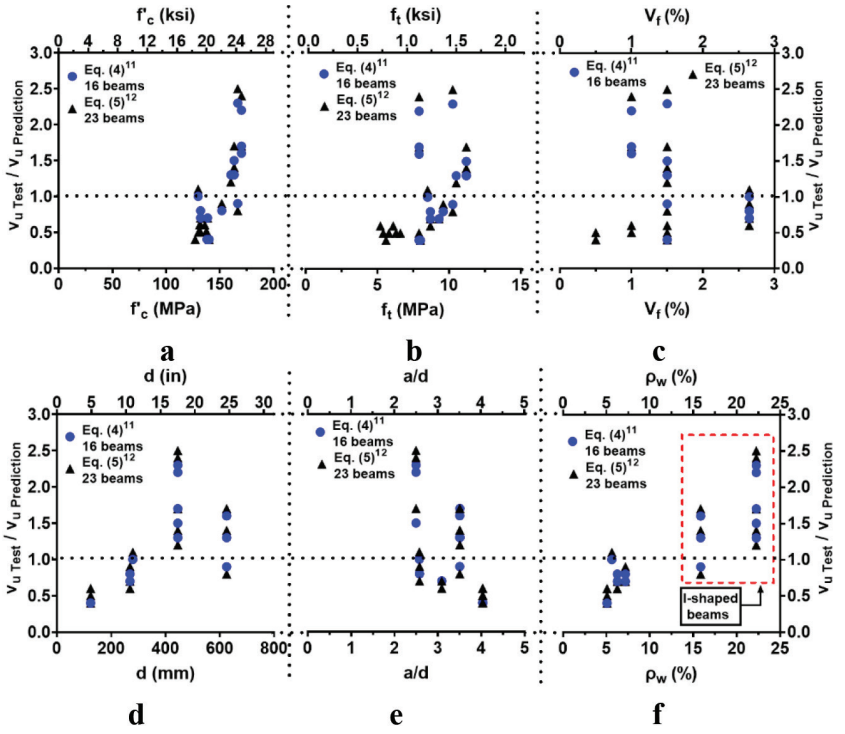

Fig. 7—Influences of different design parameters on shear prediction accuracy of design equations.

Database encompasses an extensive range of shear test data from 247 beams, covering a broad spectrum of parameters, including material strength, fiber reinforcement, loading configurations, dimensions, designs, and cross-sectional shapes. This database serves as a foundational resource, showcasing the current state of the art in these advanced fiber-reinforced concrete beams.

Subsequently, a rigorous filtering process involving strength-based, damage-pattern, and data-integrity filters was employed. This process identified HS-HPFRCC and UHPC beams with shear-controlled peak strength while excluding those with mixed-mode failure, incomplete experimental information, or ambiguous test results. This meticulous data cleansing led to the creation of the Evaluation Shear Database, comprising 118 beams. This validated subset of the Initial Collection Database is instrumental in assessing shear strength equations and developing new data-driven models.

The applicability of the Evaluation Shear Database was demonstrated by evaluating the performance of shear strength equations for UHPC beams from SIA[11] and FHWA.[12] The analysis, conducted on a subset that aligned with the specifications of each equation, revealed that both equations adequately accounted for the influence of UHPC's tensile strength on beam shear strength. The SIA[11] and FHWA[12] equations yielded mean values of 1.18 and 1.00 for the experimental test result versus predicted shear strength, with standard deviations of 0.54 and 0.61, respectively. However, their performance is limited in accurately accounting for different shear-transfer mechanisms and dowel action. The results also underscore the need for future studies to develop shear strength equations for UHPC beams that more accurately consider key design parameters, including material strength, fiber volume fraction, beam depth, shear span-effective depth ratio, longitudinal reinforcement ratio, and cross-sectional shape.

The comprehensive data from the Initial Collection and Evaluation Shear Databases have been systematically compiled in Excel spreadsheets, which are openly accessible for potential applications. These databases are poised for expansion as more high-quality shear test results become available, further enriching the resource.

AUTHOR BIOS

ACI member **Manuel Bermudez** *is a PhD Candidate in civil engineering at National Cheng Kung University, Tainan City, Taiwan. He is a member of ACI Committee 239, Ultra-High-Performance Concrete, and Joint ACI-ASCE Committee 445, Shear and Torsion.*

ACI member **Chung-Chan Hung** *is a Professor of civil engineering at National Cheng Kung University and a Research Fellow at the National Center for Research on Earthquake Engineering in Taiwan. He received his MS in mechanical engineering and PhD in civil engineering from the University of Michigan, Ann Arbor, MI, in 2010. His research interests include high-strength reinforced concrete structures, high-performance fiber-reinforced cementitious materials and structures, and structural retrofitting.*

ACKNOWLEDGMENTS

Funding from the National Science and Technology Council, Taiwan (Grant No. 109-2636-E-006-015), partially supported this research. For inquiries, C.-C. Hung, the second author, is the corresponding author. The views expressed are those of the authors and do not reflect the official policy or position of the National Science and Technology Council.

REFERENCES

1. Joint ACI-ASCE Committee 326, "Shear and Diagonal Tension," *ACI Journal Proceedings*, V. 59, No. 1-3, Jan.-Mar. 1962, 131 pp.

2. Reineck, K.-H.; Bentz, E. C.; Fitik, B.; Kuchma, D. A.; and Bayrak, O., "ACI-DAfStb Database of Shear Tests on Slender Reinforced Concrete Beams without Stirrups," *ACI Structural Journal*, V. 110, No. 5, Sept.-Oct. 2013, pp. 867-876.

3. ACI Committee 318, "Building Code Requirements for Structural Concrete (ACI 318-19) and Commentary (ACI 318R-19) (Reapproved 2022)," American Concrete Institute, Farmington Hills, MI, 2019, 624 pp.

4. Naaman, A. E., and Reinhardt, H. W., "Characterization of High Performance Fiber Reinforced Cement Composites—HPFRCC," *High Performance Fiber Reinforced Cement Composites 2 (HPFRCC 2): Proceedings of the Second International RILEM Workshop*, A. E. Naaman and H. W. Reinhardt, eds., Ann Arbor, MI, 1996, pp. 1-24.

5. Graybeal, B. A., "Material Property Characterization of Ultra-High Performance Concrete," Report No. FHWA-HRT-06-103, Federal Highway Administration, McLean, VA, 2006, 188 pp.

6. Hung, C.-C.; El-Tawil, S.; and Chao, S.-H., "A Review of Developments and Challenges for UHPC in Structural Engineering: Behavior, Analysis, and Design," *Journal of Structural Engineering*, ASCE, V. 147, No. 9, Sept. 2021, p. 03121001. doi: 10.1061/(ASCE)ST.1943-541X.0003073

7. Naaman, A. E., *Fiber Reinforced Cement and Concrete Composites*, Techno Press 3000, Sarasota, FL, 2017, 765 pp.

8. Lequesne, R. D.; Parra-Montesinos, G. J.; and Wight, J. K., "Seismic Behavior and Detailing of High-Performance Fiber-Reinforced Concrete Coupling Beams and Coupled Wall Systems," *Journal of Structural Engineering*, ASCE, V. 139, No. 8, Aug. 2013, pp. 1362-1370. doi: 10.1061/(ASCE)ST.1943-541X.0000687

9. Athanasopoulou, A., and Parra-Montesinos, G., "Experimental Study on the Seismic Behavior of High-Performance Fiber-Reinforced Concrete Low-Rise Walls," *ACI Structural Journal*, V. 110, No. 5, Sept.-Oct. 2013, pp. 767-778.

10. ACI Committee 239, "Ultra-High-Performance Concrete: An Emerging Technology Report (ACI 239R-18)," American Concrete Institute, Farmington Hills, MI, 2018, 21 pp.

11. SIA, "Technical Leaflet SIA 2052: UHPFRC—Materials, Design and Construction," Swiss Society of Engineers and Architects, Zurich, Switzerland, 2016.

12. Graybeal, B. A., and El-Helou, R., "Structural Design with Ultra-High Performance Concrete," Report No. FHWA-HRT-23-077, Federal Highway Administration, McLean, VA, 2023, 294 pp.

13. Naaman, A. E., and Wille, K., "The Path to Ultra-High Performance Fiber Reinforced Concrete (UHP-FRC): Five Decades of Progress," *Ultra-High Performance Concrete and Nanotechnology in Construction: Proceedings of Hipermat 2012 - 3rd International Symposium on UHPC and Nanotechnology for High Performance Construction Materials*, M. Schmidt, E. Fehling, C. Glotzbach, S. Fröhlich, and S. Piotrowski, eds., Kassel, Germany, 2012, pp. 3-15.

14. Naaman, A. E., "Half a Century of Progress Leading To Ultra-High Performance Fiber Reinforced Concrete: Part 1 - Overall Review," *Proceedings of the 2nd International RILEM Conference on Strain Hardening Cementitious Composites (SHCC2-Rio)*, R. D. Toledo Filho, F. A. Silva, E. A. B. Koenders, and E. M. R. Fairbairn, eds., Rio de Janeiro, Brazil, 2011, pp. 17-26.

15. ASTM C1856/C1856M-17, "Standard Practice for Fabricating and Testing Specimens of Ultra-High Performance Concrete," ASTM International, West Conshohocken, PA, 2017, 4 pp.

16. NF P 18-710, "National Addition to Eurocode 2 — Design of Concrete Structures: Specific Rules for Ultra-High Performance Fibre-Reinforced Concretes (UHPFRC)," Association Française de Normalisation (AFNOR Group), Saint-Denis, France, 2016, 136 pp.

17. Tadros, M. K.; Abo El-Khier, M.; Gee, D.; Kurt, A.; Lucier, G.; and Wagner, E., "Implementation of Ultra-High Performance Concrete in Long-Span Precast Pretensioned Elements for Concrete Buildings and Bridges: Phase II Report," e.construct, Omaha, NE, and Precast/Prestressed Concrete Institute, Chicago, IL, 2021, 753 pp.

18. Haber, Z. B., and Graybeal, B. A., "Lap-Spliced Rebar Connections with UHPC Closures," *Journal of Bridge Engineering*, ASCE, V. 23, No. 6, June 2018, p. 04018028. doi: 10.1061/(ASCE)BE.1943-5592.0001239

19. Graybeal, B., and Davis, M., "Cylinder or Cube: Strength Testing of 80 to 200 MPa (11.6 to 29 ksi) Ultra-High-Performance Fiber-Reinforced Concrete," *ACI Materials Journal*, V. 105, No. 6, Nov.-Dec. 2008, pp. 603-609.

20. AASHTO, "Guide Specifications for Structural Design with Ultra-High Performance Concrete," first edition, American Association of State Highway and Transportation Officials, Washington, DC, 2024, 97 pp.

21. Kuchma, D. A.; Wei, S.; Sanders, D. H.; Belarbi, A.; and Novak, L. C., "Development of the One-Way Shear Design Provisions of ACI 318-19 for Reinforced Concrete," *ACI Structural Journal*, V. 116, No. 4, July 2019, pp. 285-295. doi: 10.14359/51716739

22. Peng, F.; Yi, W.; and Fang, Z., "Design Approach for Flexural Strength of Reinforced Ultra-High-Performance Concrete Members Considering Size Effect," *ACI Structural Journal*, V. 119, No. 1, Jan. 2022, pp. 281-294.

23. *fib*, "CEB-FIP Model Code 1990," International Federation for Structural Concrete, Lausanne, Switzerland, 1993, 460 pp.

24. Imam, M.; Vandewalle, L.; Mortelmans, F.; and Van Gemert, D., "Shear Domain of Fibre-Reinforced High-Strength Concrete Beams," *Engineering Structures*, V. 19, No. 9, Sept. 1997, pp. 738-747. doi: 10.1016/S0141-0296(96)00150-2

25. ACI Committee 544, "Design Considerations for Steel Fiber Reinforced Concrete (ACI 544.4R-88) (Reapproved 2009)," American Concrete Institute, Farmington Hills, MI, 1988, 18 pp.

26. Kodsy, A., and Morcous, G., "Flexural Strength Prediction Models of Non-prestressed Ultra-High Performance Concrete (UHPC) Components," *Structures*, V. 34, Dec. 2021, pp. 4532-4547. doi: 10.1016/j.istruc.2021.10.047

27. Kodur, V.; Solhmirzaei, R.; Agrawal, A.; Aziz, E. M.; and Soroushian, P., "Analysis of Flexural and Shear Resistance of Ultra High Performance Fiber Reinforced Concrete Beams without Stirrups," *Engineering Structures*, V. 174, Nov. 2018, pp. 873-884. doi: 10.1016/j.engstruct.2018.08.010

28. Ridha, M. M. S.; Sarsam, K. F.; and Al-Shaarbaf, I. A. S., "Experimental Study and Shear Strength Prediction for Reactive Powder Concrete Beams," *Case Studies in Construction Materials*, V. 8, June 2018, pp. 434-446.

29. Jabbar, A. M.; Mohammed, D. H.; and Hamood, M. J., "Using Fibers instead of Stirrups for Shear in Ultra-High Performance Concrete T-beams," *Australian Journal of Structural Engineering*, V. 24, No. 1, 2023, pp. 36-49. doi: 10.1080/13287982.2022.2088654

30. Shoaib, A., "Shear in Steel Fiber Reinforced Concrete Members without Stirrups," PhD thesis, University of Alberta, Edmonton, AB, Canada, 2012, 394 pp.

31. Bermudez, M., and Hung, C.-C., "Shear Strength Equation and Database for High-Strength High-Performance Fiber-Reinforced Concrete and Ultra-High-Performance Concrete Beams without Stirrups," *ACI Structural Journal*, V. 121, No. 4, July 2024, pp. 185-195.

32. Vecchio, F. J., and Collins, M. P., "The Modified Compression-Field Theory for Reinforced Concrete Elements Subjected to Shear," *ACI Journal Proceedings*, V. 83, No. 2, Mar.-Apr. 1986, pp. 219-231.

33. Hong, S.-G.; Hong, N.; and Lee, J.-h., "Shear Strength of UHPFRC Beams Without Stirrups: Fracture Mechanics Approach," *High Tech Concrete: Where Technology and Engineering Meet – Proceedings of the 2017* fib *Symposium, held in Maastricht, The Netherlands, June 12-14, 2017*, D. A. Hordijk and M. Luković, eds., Springer, Cham, Switzerland, 2018, pp. 447-55.

34. Yavaş, A.; Hasgul, U.; Turker, K.; and Birol, T., "Effective Fiber Type Investigation on the Shear Behavior of Ultrahigh-Performance Fiber-Reinforced Concrete Beams," *Advances in Structural Engineering*, V. 22, No. 7, May 2019, pp. 1591-1605. doi: 10.1177/1369433218820788

35. Yang, J.; Doh, J.-H.; Yan, K.; and Zhang, X., "Experimental Investigation and Prediction of Shear Capacity for UHPC Beams," *Case Studies in Construction Materials*, V. 16, June 2022, Article No. e01097. doi: 10.1016/j.cscm.2022.e01097

NEW Symposium Publications from ACI

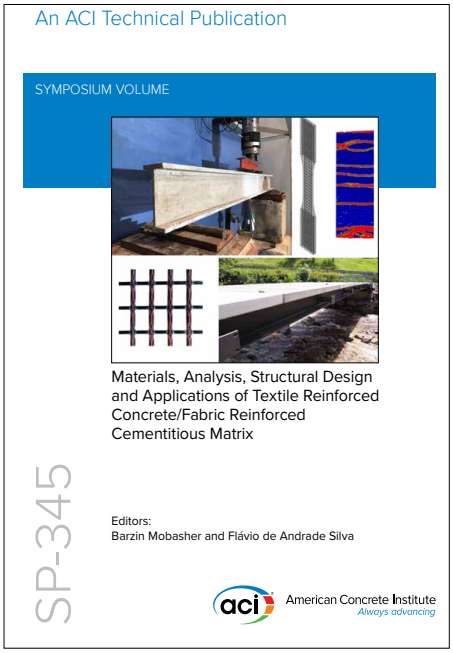

SP-345: Materials, Analysis, Structural Design and Applications of Textile Reinforced Concrete/Fabric Reinforced Cementitious Matrix

Several state-of-the-art sessions on textile-reinforced concrete/fabric-reinforced cementitious matrix (TRC/FRCM) were organized by ACI Committee 549 in collaboration with RILEM TC MCC during the ACI Fall 2019 Convention in Cincinnati, OH, and the ACI Virtual Technical Presentations in June 2020. The forum provided a unique opportunity to collect information and present knowledge in the field of TRC and FRCM as sustainable construction materials.

Available in PDF format: $69.50
(FREE to ACI members)

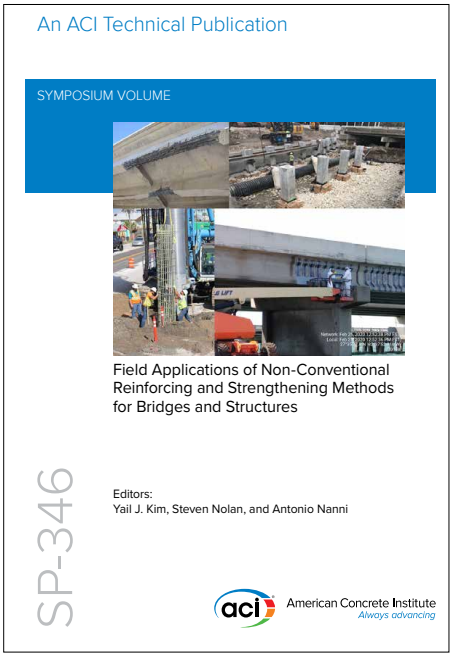

SP-346: Field Applications of Non-Conventional Reinforcing and Strengthening Methods for Bridges and Structures

A sustainable built environment requires a comprehensive process from material selection through to reliable management. Although traditional materials and methods still dominate the design and construction of our civil infrastructure, nonconventional reinforcing and strengthening methods for concrete bridges and structures can address the functional and economic challenges facing modern society.

Available in PDF format: $69.50
(FREE to ACI members)

American Concrete Institute
+1.248.848.3700 • www.concrete.org

ACI STRUCTURAL JOURNAL TECHNICAL PAPER

Title No. 122-S17

Performance of Mechanical Couplers of High-Strength Reinforcing Bars under Inelastic Strain Demands

by L. K. Sharma, W. Abdullah, S. Niroula, N. Budhathoki, and W. M. Ghannoum

ACI 318 permits the use of mechanical couplers for Grade 60 (420 MPa) bars in hinge regions, but not for higher-grade bars. This restriction was introduced due to limited testing of mechanical couplers under inelastic strain demands and is hindering the use of higher-grade bars in seismic regions. Eleven mechanical couplers splicing Grade 80 (550 MPa) bars through varying connection details were tested in a uniaxial testing machine to evaluate their performance compared to bare bars under reversed cyclic inelastic strain demands, akin to those experienced in hinge regions of special seismic systems. The low-cycle fatigue life of coupled subassemblies is compared to those of the bare bars tested under the same loading protocol. Results indicate that some coupled bars can have equivalent fatigue life to the bare bars, while others can have substantially reduced fatigue life. A qualification test is proposed to qualify mechanical splices for use in seismic hinge regions of special concrete systems.

Keywords: couplers; fatigue test; Grade 80 (550 MPa); inelastic cyclic tests; mechanical splices.

INTRODUCTION

There is a growing demand for higher-strength steel reinforcing bars in seismic and non-seismic applications owing to the need to reduce bar congestion, lower material quantities, and reduce economic and environmental impacts of concrete construction. The issue of reinforcement congestion becomes especially problematic in situations requiring ductile seismic detailing. Lap splices of reinforcing bars can also cause over-reinforcement, which might lead to non-ductile behavior in the spliced area due to stress concentration at the lap ends, unintentionally affecting the structure's deformation capacity.[1,2] In addition, lap splices are not permitted within hinge regions of special frame and wall systems, which would lead to impractically long dowel bars, especially for concrete walls. Mechanical couplers can be used to alleviate lap splice congestion and, if permitted in hinge regions, can facilitate construction considerably by shortening dowel bars past sections of maximum moment demand.

The latest revision to ACI 318[3] represents a notable shift toward adopting higher-grade reinforcing bars in building construction, specifically Grades 80 and 100 (550 and 690 MPa). Furthermore, while the use of mechanical splices for Grade 60 (420 MPa) bars in areas prone to inelastic strain during seismic events has been standard practice, the 2019 update of ACI 318 limits the use of mechanical splices with Grade 80 or 100 (550 or 690 MPa) bars in hinge regions, citing a lack of research on their effectiveness at these higher grades. During earthquakes, longitudinal bars located in hinge regions undergo large inelastic strain reversals, causing low-cycle fatigue damage and possibly fracture in reinforcing bars.[4-8] Low-cycle fatigue refers to premature material failure due to a relatively small number of load or deformation cycles, typically involving large strains beyond the elastic limit.[4,5,9-15]

There have been limited simulated seismic tests on concrete members with mechanical couplers and Grade 60 (420 MPa) bars in hinge regions[16-19]; no such tests have been published for couplers in the U.S. market with higher-grade bars. In addition, results from the limited concrete component tests with mechanical couplers in hinge regions cannot be generalized across the entire body of couplers in the U.S. market, given the wide variety of available mechanical coupler types. As a result, there is uncertainty regarding the performance of mechanical couplers in hinge regions across all bar grades, and particularly for higher reinforcing bar grades. To address such uncertainty, more simulated seismic tests are needed on concrete members with couplers in hinge regions. However, given the large diversity of mechanical couplers in the U.S. market, it may not be practical to test them all in concrete members. Alternatively, a relatively simple and inexpensive qualification test could be used to evaluate the performance of mechanical couplers under the reversed tension/compression inelastic strain cyclic loading experienced by bars and couplers in hinge regions. Such tests that subject mechanical couplers to reversed cyclic strain demands, however, are not currently available.

The work presented herein was conducted with two primary objectives: 1) to evaluate the low-cycle fatigue performance of commonly used mechanical couplers in the United States; and 2) to develop a new testing methodology that is specifically designed to subject mechanical couplers to reversed inelastic strain demands typical of hinge regions, and that could be used to prequalify coupler devices for use in hinge regions of concrete members.

The low-cycle fatigue behavior of No. 8 (25 mm) Grade 80 (550 MPa) high-strength steel (HSS) bars coupled with different mechanical couplers available in the U.S. market is investigated experimentally. HSS bars produced using the two main manufacturing techniques in the United States are considered—namely, microalloying (MA) and

ACI Structural Journal, V. 122, No. 1, January 2025.
MS No. S-2024-115.R2, doi: 10.14359/51743341, received September 22, 2024, and reviewed under Institute publication policies.

quenching and self-tempering (QST). In total, 11 coupler types were tested. The couplers originated from four manufacturers in the United States and covered a range of properties, including threaded and grouted mechanisms and coupler lengths ranging from approximately 3 to 14 in. (75 to 355 mm). Coupled bar subassemblies were cycled in a uniaxial testing machine to strain amplitudes of 2.5% until fracture from low-cycle fatigue. The low-cycle fatigue life of coupled subassemblies are compared to those of the bare bars tested under the same loading protocol. Findings offer insights into the low-cycle fatigue behavior of couplers using various connection details and provide necessary data for setting parameters for qualification testing of couplers for use in hinge regions, where relatively large inelastic strain demands are expected.

RESEARCH SIGNIFICANCE

The research presented addresses a critical gap in the current state of practice in qualifying mechanical couplers for seismic applications. This study introduces a novel qualification testing protocol designed to evaluate the performance of mechanical couplers subjected to reversed inelastic strain demands, representative of those found in seismic hinge regions. Through experimental testing of 11 different mechanical coupler types from various manufacturers, the research identifies differences sometimes exceeding an order of magnitude tenfold or more in the low-cycle fatigue endurance of coupler subassemblies and provides valuable insights into the inelastic performance of mechanical couplers compared to bare bars. The findings offer a simple and practical solution to the challenge of qualifying mechanical couplers for use in hinge regions of seismic structural systems.

BACKGROUND

Restrictions on the placement of mechanical splices in critical regions where yielding is likely to occur are in place in several design codes.[3,20-22] ACI 318-19[3] classifies mechanical splices into Type 1, which must develop 125% the yield strength of the bar, and Type 2, which must develop the full tensile strength of the bar. The Code prohibits Type 1 mechanical splices for all reinforcement grades and Type 2 splices for Grades 80 and 100 (550 and 690 MPa) bars in hinge regions of seismic systems. Except for Type 2 mechanical couplers for Grade 60 (420 MPa) bars, couplers are not permitted within yield zones. Similarly, Caltrans[21] and AASHTO[22] do not allow mechanical splices in hinge regions for any bar grade. In addition, the latter bridge codes restrict mechanical couplers for higher-grade bars (above Grade 60 [420 MPa]) in any location of a bridge. Limitations stem from concerns about the ability of existing mechanical couplers to develop the tensile strength of higher-grade bars, while concerns that strain demands and low-cycle fatigue under inelastic cycling can result in premature failure of mechanical splices have hindered their use in hinge regions.

Studies using high-strength reinforcing bars[7,9,10,13,23,24] have shown that strain demands on longitudinal bars in hinge regions vary primarily based on section dimensions, drift demands, axial load level, and the tensile-to-yield strength ratio (T/Y) of the bars, which in turn varies with bar grade. Such studies have demonstrated that strain demands in hinge regions can, in effect, reach the uniform strain capacity[25,26] (the strain measured at peak bar stress) of reinforcing bars. In addition, higher-grade bars tend to have lower T/Y, which results in more limited plasticity spread in hinge regions and consequently larger strain demands compared with levels experienced by lower-grade bars.[9,23,24] Therefore, couplers of HSS bars in hinge regions not only need to resist larger stresses but can also experience larger strain demands at any given lateral drift of a structure.

Limited experimental studies have been conducted on mechanical couplers with Grade 60 (420 MPa) bars within hinge regions, with no such testing found on Grade 80 or 100 (550 or 690 MPa) bars.[16,18,19,27-29] Available test data suggest a general decline in performance when mechanical splices are placed in hinge regions.[30] Specifically, the use of couplers with Grade 60 (420 MPa) bars in hinges has been shown to reduce the drift capacity of coupled members compared to control specimens without couplers. Instances of premature bar fracture in coupled bars have been documented. However, tests involving short and compact couplers, as well as tests where couplers were placed in a footing adjacent to the hinge region, have indicated the possibility of performance comparable to that of connections without splices.[18,27,28,30]

Several competing acceptance criteria are available in the United States and internationally for mechanical couplers.[3,21,31,32] Couplers are required to meet prequalification criteria to allow their use in various applications. All available criteria require mechanical splices to achieve a minimum tensile stress based on the specified yield or tensile strength of reinforcing bars. Some have additional compression stress criteria. Most also have slip criteria that are verified using differing loading protocols, stress levels, and measurement methods. Caltrans California Test (CT) 670[21] has the strictest strain criterion, requiring the development of the bar necking or a strain in the spliced bars nearing the specified uniform elongation of the bars based on ASTM A706/A706M-22a.[25] None, however, have criteria for qualifying mechanical splices for hinge region applications based on reversed inelastic strain demands. AC133[31] has a criterion for special Type 2 couplers that requires cyclic excursions to limited inelastic strains. However, the loading protocol restricts strain demands to five times the yield strain and requires the application of cycles that do not reverse inelastic strains, a behavior that is not representative of reversing strains observed in hinge regions.[7,9,13,23,24] Finally, current mechanical splice acceptance criteria in the United States were created with Grade 60 (420 MPa) bars in mind and may not scale adequately for higher-grade bars.

With the recent allowance of higher-grade bars in design codes, the exploration of mechanical splicing for Grade 80 (550 MPa) bars is becoming increasingly vital. The convenience of splicing within hinge regions, along with the necessity for longer development lengths for these higher-grade bars, emphasizes the need for mechanical splices for higher-grade bars. This necessitates the development of prequalification criteria aimed at ensuring the mechanical splices can

Table 1—Types of mechanical couplers used in study and their coupling mechanisms

Manufacturer	Coupler name	Description
M1	Cold-Swaged Coupler (Swaged)	Swaged bars, taper-threaded device, butt splice
M1	Standard Threaded Coupler-1 (Threaded-1)	Threaded bars, butt splice
M2	Taper-Threaded Coupler-1 (Taper Threaded-1)	Taper-threaded bars
M3	Upset Head Butt-Splice Coupler (End Grip)	Mechanical butt splice with upset heads
M3	Friction-Forged Taper-Threaded Coupler-2 (Friction Welded-2)	Friction-forged bars, taper-threaded device, butt splice
M3	Standard Threaded Coupler -2 (Threaded-2)	Threaded bar, butt splice
M4	Friction-Forged Taper-Threaded Coupler-1 (Friction Welded-1)	Friction-forged bars, taper-threaded device
M4	Taper-Threaded Coupler-2 (Taper Threaded-2)	Taper-threaded bars
M4	Grouted/Threaded Coupler-1 (Grouted/Threaded-1)	Grouted connection at one end and taper-threaded bar at the other
M5	Grouted Splice Coupler (Grouted-1)	Grouted splice coupler
M5	Slim Grouted Splice Coupler (Grouted-2)	Slim grouted splice coupler

achieve the desired behaviors, particularly ductile behavior, and inelastic cyclic fatigue endurance in hinge regions of special seismic systems.

EXPERIMENTAL PROGRAM

A primary objective of the experimental program is to study the behavior of mechanical splices consisting of Grade 80 (550 MPa) HSS bars coupled with a variety of mechanical couplers available in the U.S. market. Test data for the study are also used to define qualification test procedures for qualifying mechanical splices for use in the hinge regions of special seismic systems. To achieve the objectives, in-air tests of mechanical splices were conducted in a uniaxial testing machine by applying fully reversed inelastic strain demands on splice subassemblies until bar fracture. Tests were akin to those conducted by Sokoli et al.,[9] Slavin and Ghannoum,[33] and Ghannoum and Slavin[34] on bare bars of various steel grades. In addition, tension tests were also conducted on coupled bar specimens to determine the tensile strength of the splices.

Test parameters

Eleven distinct types of couplers, employing different coupling mechanisms as detailed in Table 1, were used to join Grade 80 (550 MPa) reinforcing bars conforming to the ASTM A706/A706M standard, including supplement S1, Additional Requirements for Bars Used in Earthquake Resistant Structures.[25] The high-strength bars were manufactured using the two predominant methods used in the United States for that grade—namely, MA and QST.[33,34] To minimize variability in the properties of the bars, all bar samples used in all mechanical splice specimens were sourced from a single MA and a single QST production batch. Furthermore, to minimize the possibility of installation errors, only factory-installed mechanical splices were used. The scope of bar sizes was limited to No. 8 (25 mm) bars, with a diameter of 1 in. (25.4 mm).

Clear bar gripping span

The clear bar gripping span is defined as the distance from the end of the coupler to the edge of the machine grips for coupled specimens. For bare-bar specimens, the specified gripping span was half the clear distance between grips. Different gripping spans ranging from 1.5 to three times the nominal diameter of the bar (d_b) were investigated. In each test, the gripping spans at both ends of a coupled specimen were maintained identical. As expected, a decrease in the bar gripping span resulted in less-pronounced bar buckling under compression loading, as shown in Fig. 1. On the other hand, for the shorter clear span of $1.5d_b$, the exposed bars are within the theoretical disturbed stress region adjacent to the grips and the couplers, generally taken as $2d_b$ from a disturbance.[21] At the end, the shorter clear gripping span of $1.5d_b$ was selected to minimize buckling of bare-bar and coupled specimens and avoid the need for lateral bracing. Avoiding bracing makes the test simpler to conduct and therefore more attractive as a qualification test for couplers in seismic applications.

The shorter gripping span of $1.5d_b$ limited buckling for all but one coupler type, coupler Grouted-1. For that coupler, grout spalling during testing at the coupler ends increased the gripping span and resulted in excessive buckling. Inelastic cyclic results for that specimen are not reported for this reason.

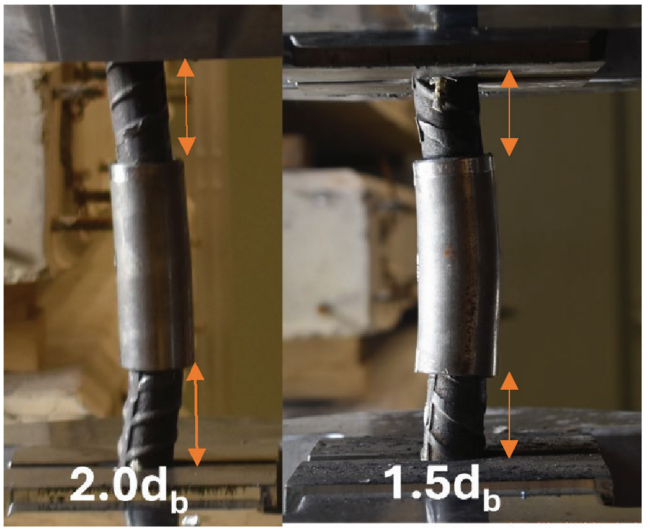

Fig. 1—Photograph showing lateral buckling for clear spans 2.0d_b and 1.5d_b with Taper Threaded-2 coupler.

Loading protocols

Monotonic tension tests—Mechanical properties of bare bars were obtained from monotonic tension tests according to ASTM A370-22[35] and ASTM E8/E8M-22.[26] Coupled specimens were tested following the monotonic tension test procedure outlined in CT 670.[21]

Inelastic reversed cyclic tests—A reversed cyclic loading protocol, oscillating between +2% strain (tension) and –0.5% strain (compression), was implemented for coupled and bare-bar specimens to simulate the representative strain conditions encountered by longitudinal bars in flexural members undergoing significant inelastic deformations.[4,13] Inelastic cyclic tests were carried out under strain control by applying a cyclic strain protocol with a sinusoidal shape with respect to time. Cyclic testing was conducted at a rate of 0.012 Hz. Cyclic tests on both bare and coupled bar specimens commenced with an initial tension loading to achieve the desired longitudinal strain amplitude, followed by a transition to the designated longitudinal compression strain. This process was repeated, cycling between tension and compression strain values, until the specimens failed due to fracture. Specimens sustaining fracture near the machine grips were discarded. The number of half-cycles fracture was recorded for all tests. In general, a minimum of three specimens were tested for each set of test parameters.

Test procedure

Monotonic and inelastic cyclic tests were conducted using a universal testing machine equipped with grips measuring 4.75 in. (120 mm) in length to ensure rotational fixity at the specimen ends, as shown in Fig. 2 and 3. To reduce the risk of fractures due to stress concentrations at grip edges, specimens were swaged with aluminum tubing following the recommendation of Ghannoum and Slavin.[34]

Data acquisition

The load applied to specimens was recorded by the testing machine load cell. High-contrast black and white paper targets were glued along specimen length after mill scale was removed. Surface targets were tracked on specimens using a monochrome camera with a resolution of 4872 x 3248 pixels and a minimum frame rate of three frames per second. Target locations and numbering are illustrated in Fig. 2 for monotonic tests and Fig. 3 for inelastic cyclic tests. Additional details regarding the operational principles of the digital image correlation (DIC) system used in the study are available in the cited references.[9,34,36,37] For monotonic tension tests of bare bars and coupled subassemblies, the strain over an 8 in. (200 mm) gauge length of bare bar was recorded as the bar strain. For inelastic cyclic tests, the average strain between targets labeled as [0, 2] and [6, 8] was calculated in real time and provided to the uniaxial machine controller to conduct testing under strain control. The controller was programmed to cycle between values of 2.5% and –0.5% for that average measured strain, ensuring accurate strain-controlled testing.

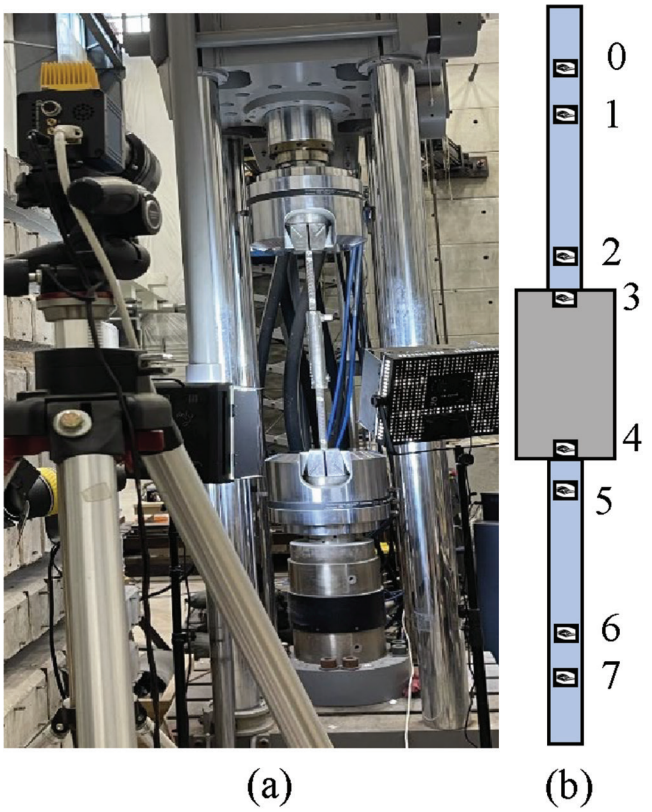

Fig. 2—(a) Mechanical splice specimen installed in universal testing machine; and (b) typical monitored surface targets and their numbering along coupled specimens during monotonic tension tests.

Measured quantities

Several metrics were used to compare the performance of the coupled bar subassemblies with bare bars. Mechanical properties of coupled subassemblies obtained from monotonic tension tests include tensile strength, elastic modulus, uniform strain, and fracture strain, with strain measured along the clear bare-bar portions of the coupled subassemblies. To assess cyclic fatigue behavior, the number of half-cycles to fracture was used as the primary metric for evaluating low-cycle fatigue life, while fracture patterns

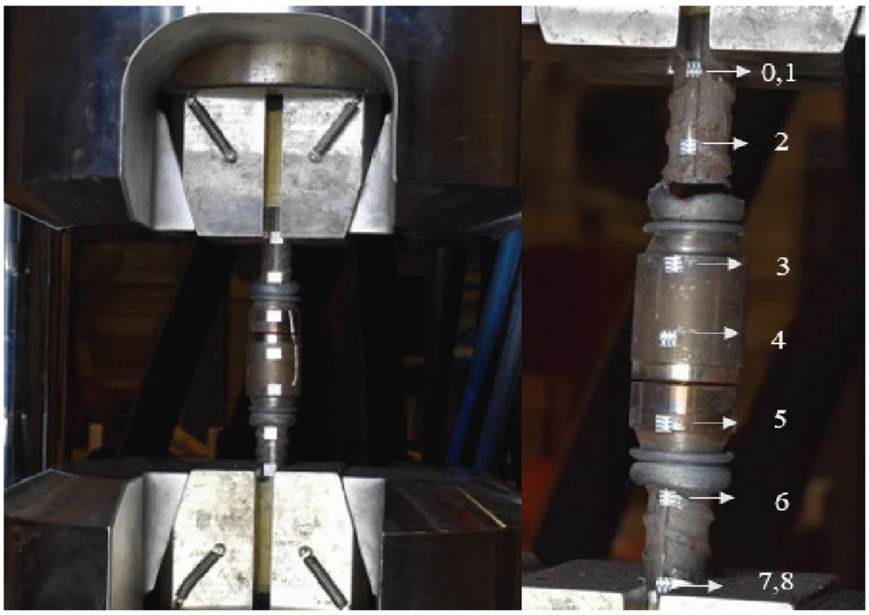

Fig. 3—(a) Specimen with 1.5d_b gripping span; and (b) typical monitored surface targets and their numbering along coupled specimens during inelastic cyclic tests.

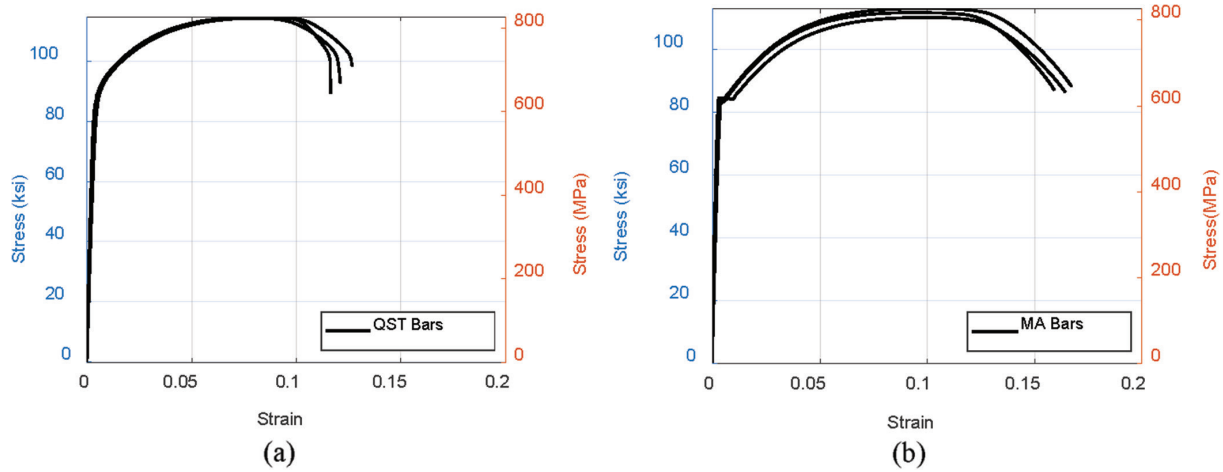

Fig. 4—Stress-strain relationships for No. 8 (25 mm) bars from monotonic tension tests: (a) QST bars; and (b) MA bars.

were also examined. Deformations across the couplers (between targets [2 to 6], as shown in Fig. 3) were measured to compare deformation behavior across couplers with that of bare bars of equivalent length. This metric provides insight into slip behavior at the interface between couplers and the bars they connect.

TEST RESULTS

Bare-bar specimens

Monotonic tension tests—For each of the two types of bars (MA and QST), a minimum of three samples underwent monotonic tension testing. Stress-strain plots for each are shown in Fig. 4. The ensuing mechanical properties of each bar type are averaged across all samples and summarized in Table 2. These same two batches of bars were used for all coupled specimens as well.

As can be seen in Table 2, bars tested satisfied ASTM A706/A706M[25] regarding yield strength, tensile strength, and the ratio of actual tensile to yield strength for Grade 80 (550 MPa) reinforcement. Minor differences were observed in the *T*/*Y* and elongations between MA bars and QST bars, with MA bars showing slightly higher values, as was also observed by Ghannoum and Slavin.[34] The modulus of elasticity for both types of bars was lower than the specified modulus of elasticity for reinforcing bars (29,000 ksi [200,000 MPa]), indicating that the bars may have been run lighter than specified. Additionally, both bar types met the 7% uniform strain requirement of ASTM A706/A706M for No. 8 (25 mm) Grade 80 (550 MPa) bars. As previously indicated, the reinforcing bars used in this study were sourced from one MA and one QST batch. This was done to minimize bar variability and consequently obtain a more direct comparison of the performance of mechanical couplers.

Table 2—Summary of monotonic tension test results on bars (average across three specimens per bar type)

Manufacturing process	Bar size	Yield strength, ksi (MPa) [COV]*	Tensile strength, ksi (MPa) [COV]	Tensile/yield strength ratio [COV]	Elastic modulus, ksi (MPa) [COV]	Uniform strain, % [COV]	Fracture strain, % [COV]
QST	No. 8 (25 mm)	88.4 (613.9) [1.18%]	114.7 (790.3) [0.31%]	1.29 [0.77%]	25,300 (174,317) [5.57%]	8.0 [3.19%]	12.1 [4.13%]
MA	No. 8 (25 mm)	83.9 (578.1) [0.91%]	111.6 (768.9) [1.29%]	1.34 [1.48%]	26,700 (183,963) [8.06%]	9.72 [2.14%]	16.4 [2.47%]

*COV is coefficient of variation.

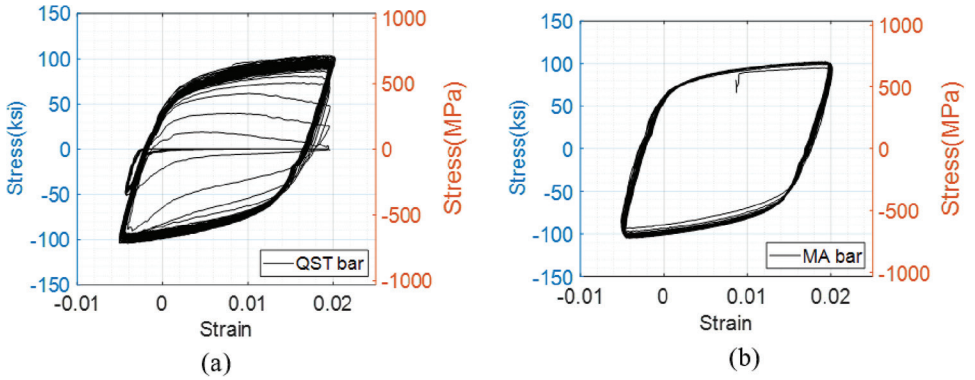

Fig. 5—Typical stress-strain relationships from inelastic tests for 1.5d_b gripping span: (a) QST bar; and (b) MA bar.

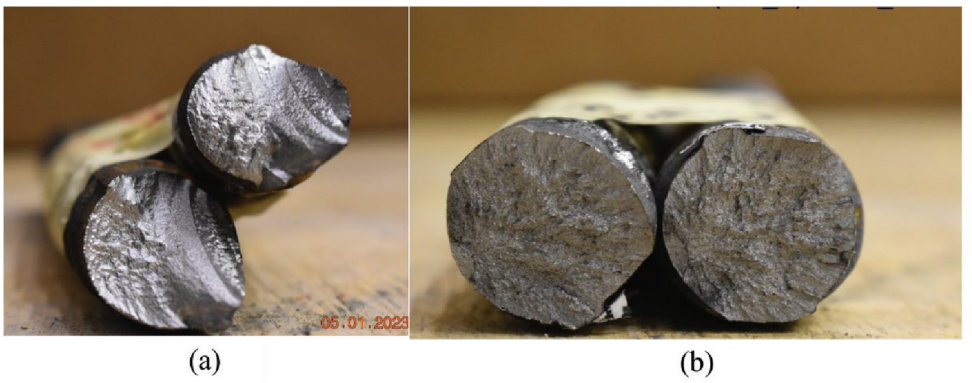

Fig. 6—Typical fracture planes for bars: (a) QST bars; and (b) MA bars.

Inelastic cyclic tests—Typical stress-strain plots for each bar type during inelastic cyclic testing are depicted in Fig. 5. A notable observation is the strength degradation exhibited by the QST bars before fracture, as demonstrated in Fig. 5(a). This degradation becomes more pronounced with an increasing number of cycles before the bars ultimately fracture. In contrast, MA bars display minimal strength degradation before experiencing sudden fracture due to low-cycle fatigue. These findings are consistent with previous studies' observations about inelastic cyclic tests of reinforcing bars.[9,34,38] Furthermore, this pattern of strength degradation during cyclic loading was also observed in coupled specimens, as presented in subsequent sections.

As previously observed by Sokoli et al.,[9] Slavin and Ghannoum,[33] Ghannoum and Slavin,[34] and Gonzalez,[38] the initiation point of the primary fatigue crack was identified at the base of the transverse bar deformations in most cases. Two distinct patterns of fracture propagation were observed. For QST bars, the pattern of fracture propagation followed the base of the transverse deformation, continuing along this path until the bar fractured. The fracture planes of QST bars indicate a more ductile fracture mechanism, as illustrated in Fig. 6(a), which is also corroborated by the gradual strength loss observed during cycling that is generated by a gradual crack propagation. By contrast, for MA bars, the primary fatigue crack tended to propagate horizontally across the barrel of the bar, while the sudden loss of strength and the smoother failure planes (Fig. 6(b)) indicate a more brittle fracture behavior.

On average, MA bars sustained 174 half-cycles before fracture, whereas QST bars showed modestly higher resistance, enduring 207 half-cycles. Therefore, despite differences in the fracture behavior and fracture planes of the two types of bars, they both sustained comparable numbers of half-cycles to fracture. The fatigue life of the MA and QST bars selected for this study were around the 50th percentile of the low-cycle fatigue performance of bars in the United States, as presented in Ghannoum and Slavin.[34] Because fracture under inelastic cycling of tested mechanical splices always occurred in the bars and not in the couplers, as

Table 3—Monotonic tension test results for mechanical splices on QST bars

Bar type	Coupler manufacturer	Coupler	Ultimate stress, ksi (MPa)	Uniform strain, %	Fracture strain, %	Fracture region
QST/ Grade 80	M1	Threaded-1	107.6 (741.4)	3.24	NA	Coupler-bar interface
			107.9 (743.4)	3.32	NA	Inside coupler
		Swaged	114.6 (789.6)	9.19	13.54	Between targets 1 and 2
			114.3 (787.5)	6.90	12.79	Between 5 and 6
	M2	Taper Threaded-1	107.6 (741.4)	2.79	NA	Coupler-bar interface
			112.3 (773.7)	4.93	NA	Inside coupler
	M3	Threaded-2	107.7 (742.1)	3.70	NA	Coupler-bar interface
			108.1 (744.8)	3.48	NA	Coupler-bar interface
		Friction Welded-2	114.1 (786.1)	8.44	15.08	Between targets 1 and 2
			113.9 (784.8)	7.82	13.40	Between targets 1 and 2
		End Grip	114 (785.5)	9.84	13.91	Between targets 1 and 2
			113.7 (783.4)	9.27	13.64	Between targets 5 and 6
	M4	Taper Threaded-2	114.5 (788.9)	8.79	12.97	Between targets 5 and 6
			114.3 (787.5)	8.91	12.65	Between targets 1 and 2
		Grouted/Threaded	114.1 (786.1)	8.91	12.51	Between targets 1 and 2
			114.5 (788.9)	8.73	NA	Outside gauge length
		Friction Welded-1	114.4 (788.2)	9.36	11.72	Between targets 5 and 6
			114.3 (787.5)	10.51	12.63	Between targets 5 and 6
	M5	Grouted-2	114.3 (787.5)	8.85	13.35	Between targets 5 and 6
			114.4 (788.2)	7.56	12.75	Between targets 1 and 2
		Grouted-1	113.8 (784.1)	6.76	10.39	Between targets 5 and 6
			114.5 (788.9)	7.80	15.99	Between targets 5 and 6

demonstrated subsequently, the fatigue performance of the mechanical splices is likely correlated with that of the bare bars. As such, because the selected bars represent the median fatigue performance of bars in the United States, the fatigue performance of the mechanical splice specimens presented in this study is expected to represent the median response for the mechanical splices across various batches of Grade 80 bars.

Coupled bar specimens

Monotonic tension tests—In the monotonic tension tests conducted on coupled specimens, stress levels exceeding 100 ksi (690 MPa) were achieved for all tests, as shown in Tables 3 and 4. All couplers were therefore found to comply with both Type 1 and Type 2 coupler requirements of ACI 318-19, which require samples to achieve 125% of the specified yield strength or 100% of the specified tensile strength of the bar for Type 1 and Type 2, respectively. The tensile stress levels attained were within 94% of the tensile strengths measured for the bare bars, as presented in Tables 2 and 3.

Uniform strains were taken as the smallest of the strains measured over an 8 in. (200 mm) gauge length between targets 1 and 5 and targets 2 and 6 at peak stress. Fracture strains were taken as the largest strain recorded prior to fracture between targets 1 and 5 and targets 2 and 6. If the fracture occurred outside of those targets, fracture strain was not reported in Tables 3 and 4. While the stress capacities for all couplers were comparable, stark differences are observed in their uniform strain capacities. Some splices satisfied the ASTM A706/A706M requirement of 7% minimum uniform strain for bare bars, while others sustained much lower strains.

Inelastic reversed cyclic tests

Deformation across couplers—Deformation along the coupled specimens (Δ_{total}) was monitored between targets 2 and 6 to assess the slip behavior of each type of coupler, as shown in Fig. 3(b). Coupler deformation was further segmented as follows: slip between coupler and top bar (Δ_{ct}) measured between targets 2 and 3, slip between coupler and bottom bar (Δ_{cb}) measured between targets 5 and 6, and deformation of the coupler body itself (Δ_c) measured between targets 3 and 5.

Sample deformation plots are presented in Fig. 7 and 8 for End Grip and Taper Threaded-2 couplers to illustrate the range of observed behaviors. The End Grip coupler exhibited markedly higher deformations than all tested couplers, while the Taper Threaded-2 coupler exhibited the least.

In general, observed coupler deformation behavior could be classified as comprising limited slip and body deformation or comprising significant slip and/or body deformation (Table 5). For all couplers, body deformation (Δ_c) was relatively small compared with the slip deformations (Table 5).

Table 4—Mechanical tension test results for mechanical splices on MA bars

Bar type	Coupler manufacturer	Coupler	Ultimate stress, ksi (MPa)	Uniform strain, %	Fracture strain, %	Fracture region
MA/Grade 80	M1	Threaded-1	107.4 (739.7)	4.60	5.82	Coupler-bar interface
			109.2 (752.6)	5.62	6.35	Coupler-bar interface
		Swaged	111.9 (770.6)	10.22	17.41	Between targets 1 and 2
			109 (750.9)	6.06	20.59	Between targets 5 and 6
	M2	Taper Threaded-1	109.2 (752.7)	6.90	NA	Inside coupler
			110.9 (763.8)	4.13	NA	Outside gauge length
	M3	Threaded-2	109.6 (755)	5.69	NA	Outside gauge length
			107.8 (742.9)	5.29	NA	Outside gauge length
		Friction welded-2	112.2 (773.3)	8.00	14.15	Between targets 5 and 6
			111.7 (769.3)	4.41	16.33	Between targets 1 and 2
		End grip	112 (771.7)	7.80	15.75	Between targets 5 and 6
			110.6 (762)	7.43	14.48	Between targets 1 and 2
	M4	Taper threaded-2	109.9 (756.9)	11.99	17.33	Between targets 1 and 2
			111.2 (766.4)	10.64	16.03	Between targets 1 and 2
		Grouted/Threaded	110.7 (762.6)	6.87	17.19	Between targets 1 and 2
			111.9 (771.3)	8.87	18.19	Between targets 5 and 6
		Friction welded-1	112.8 (777.3)	8.51	15.85	Between targets 5 and 6
			114.8 (791.2)	11.50	16.32	Between targets 1 and 2
	M5	Grouted-2	111.8 (770)	9.41	14.05	Between targets 1 and 2
			110.4 (760.8)	7.45	17.65	Between targets 1 and 2
		Grouted-1	113.9 (784.6)	11.87	NA	Outside gauge length
			110.1 (758.9)	6.91	18.82	Between targets 1 and 2

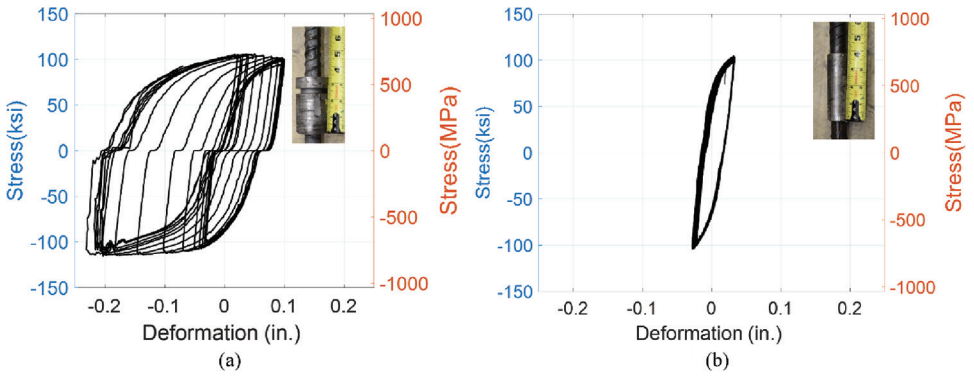

Fig. 7—Typical deformation behaviors along couplers (targets 2 to 6, Δ_{total}) for: (a) End Grip; and (b) Taper Threaded-2 on MA bars. (Note: 1 in. = 25.4 mm.)

As can be seen in Table 5, the slip behavior at the top and bottom junctions varied substantially for most specimens, emphasizing that slip is generally more prominent at one end of a coupler than the other. Furthermore, the relatively high variability in deformations between samples of the same splice type points to the complex interplay of factors influencing the inelastic cyclic performance of coupled specimens. Tighter quality control in the installation procedures could potentially help reduce the observed variability and lead to more consistent behavior.

Fatigue performance

Figure 9 illustrates the total number of half-cycles to fracture for specimens subjected to the (+2%, –0.5%) strain protocol, with a specified clear gripping span of $1.5d_b$. Table 6 presents the number of half-cycles to fracture as well as the number of half-cycles until the peak strength dropped to 80% of the peak. This second metric was introduced because some of the QST specimens exhibited a gradual drop in strength, with many cycles occurring at relatively low strength. Figure 10 illustrates the total number of half-cycles to 80% of the peak stress. As can be seen in Fig. 9, Fig. 10, and Table 6, the fatigue life of tested mechanical

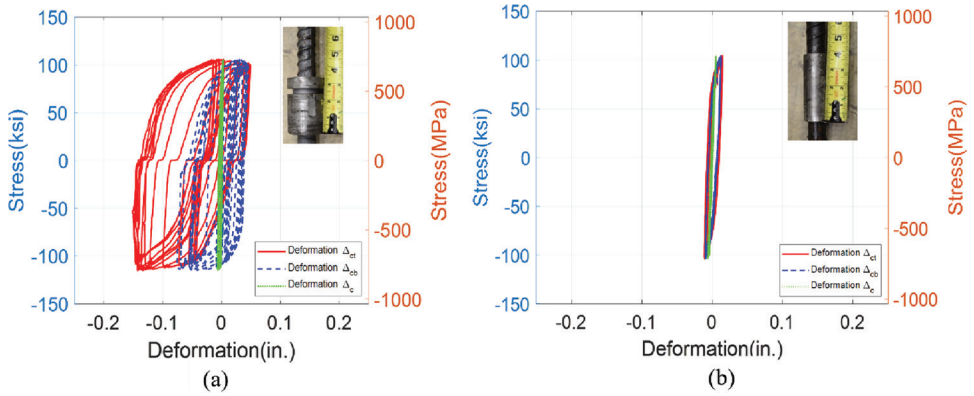

Fig. 8—Typical deformation behavior of mechanical splices, with deformations across top, bottom, and coupler body highlighted: Δ_{ct}, Δ_{cb}, and Δ_c, respectively: (a) end grip; and (b) taper threaded-2. (Note: 1 in. = 25.4 mm.)

Table 5—Deformation along mechanical splice specimens

Bar type	Coupler	Δ_{ct}, in. (mm)	Δ_{cb}, in. (mm)	Δ_c, in. (mm)	Δ_{total}, in. (mm)
MA bars	Threaded-1	0.040 (1.008)	0.042 (1.067)	0.008 (0.195)	0.084 (2.142)
	Swaged	0.065 (1.659)	0.030 (0.762)	0.028 (0.703)	0.107 (2.709)
	Taper threaded-1	0.032 (0.819)	0.028 (0.718)	0.009 (0.222)	0.065 (1.664)
	Threaded-2	0.042 (1.067)	0.039 (0.991)	0.007 (0.178)	0.084 (2.142)
	Friction welded-2	0.013 (0.330)	0.018 (0.449)	0.009 (0.229)	0.033 (0.821)
	End grip	0.0682 (1.732)	0.053 (1.338)	0.005 (0.132)	0.107 (2.725)
	Taper threaded-2	0.017 (0.432)	0.016 (0.394)	0.007 (0.178)	0.031 (0.781)
	Grouted/Threaded	0.065 (1.643)	0.165 (4.199)	0.014 (0.356)	0.227 (5.757)
	Friction welded-1	0.010 (0.262)	0.013 (0.339)	0.010 (0.254)	0.028 (0.711)
	Grouted-2	0.086 (2.193)	0.089 (2.252)	0.018 (0.457)	0.186 (4.733)
QST bars	Threaded-1	0.063 (1.592)	0.454 (11.532)	0.007 (0.195)	0.513 (13.030)
	Swaged	0.172 (4.377)	0.029 (0.745)	0.018 (0.457)	0.207 (5.275)
	Taper threaded-1	0.050 (1.278)	0.034 (0.864)	0.007 (0.178)	0.085 (2.167)
	Threaded-2	0.060 (1.516)	0.056 (1.422)	0.006 (0.161)	0.118 (2.980)
	Friction welded-2	0.014 (0.362)	0.017 (0.438)	0.009 (0.229)	0.035 (0.883)
	End grip	0.752 (19.11)	0.052 (1.321)	0.004 (0.112)	0.778 (19.761)
	Taper threaded-2	0.015 (0.389)	0.218 (5.546)	0.007 (0.186)	0.136 (3.463)
	Grouted/Thread	0.0425 (1.079)	0.0496 (1.257)	0.011 (0.292)	0.096 (2.451)
	Friction welded-1	0.0135 (0.343)	0.0562 (1.422)	0.009 (0.241)	0.068 (1.752)
	Grouted-2	0.112 (2.853)	0.1691 (4.301)	0.076 (1.938)	0.237 (6.028)

splices varied substantially, with some showing equivalent performance to the bare bars and others showing substantially lower fatigue performance—as low as 10% of bare-bar fatigue life. In general, for each device type, the fatigue performance was comparable for MA and QST bars, with splices of QST bars tending to have modestly larger fatigue life, similar to the QST bare bars exhibiting modestly superior fatigue life to that of the MA bare bars. For End Grip and Taper Threaded-2, however, specimens with QST bars exhibited substantially higher fatigue performance than those with MA bars. No physical interpretation could be found to explain this discrepancy.

A correlation was identified between the uniform strain sustained by mechanical splice specimens during tension testing and the numbers of half-cycles to fracture, as presented in Fig. 11. The correlation coefficient between the uniform strain and half-cycles to fracture is 0.66. This value indicates a positive correlation, suggesting that as the uniform strain sustained in tension testing increases, the mean half-cycles to fracture tend to increase as well. The *p*-value associated with this correlation is 0.027, which indicates that the correlation is statistically significant, whereby there is a less than 3% probability that the observed correlation is due to chance. This indicates that similar mechanisms may be at play in limiting both ductility and fatigue properties of mechanical splices.

Fracture surfaces and locations

As illustrated in Fig. 12, fractures due to low-cycle fatigue occurred in several locations: between the coupler and the

Table 6—Mean half-cycles to fracture or to 80% of peak stress

Product	Failure criteria	Mean half-cycles to fracture [% bare bar]		Number of samples tested (N)		COV, %	
		QST	MA	QST	MA	QST	MA
Bare Bar	Fracture	206.7 [100%]	173.6 [100%]	3	3	14.49	5.47
	80% of peak stress	172.3 [100%]	173.6 [100%]			11.15	5.47
Threaded-1	Fracture	50.4 [24%]	46.5 [27%]	3	3	18.91	44.22
	80% of peak stress	50.0 [29.0%]	46.5 [27%]			18.97	44.22
Swaged	Fracture	216.8 [105%]	183 [105%]	3	3	17.15	20.22
	80% of peak stress	210.2 [121.9%]	184 [105%]			20.28	20.22
Taper Threaded-1	Fracture	25.37 [12%]	36.9 [21%]	3	4	28.56	117.75
	80% of peak stress	24.2 [14.04%]	36.9 [21%]			25.84	117.75
Threaded-2	Fracture	20.2 [10%]	23.4 [13%]	3	3	45.72	48.1
	80% of peak stress	20.51 [11.7%]	23.4 [13%]			46.36	48.1
Friction Welded-2	Fracture	59.95 [29%]	76.1 [44%]	4	5	24.71	1.54
	80% of peak stress	59.95 [29%]	76.1 [44%]			24.71	1.54
End Grip	Fracture	264.9 [128%]	124.9 [72%]	5	5	83.17	64.19
	80% of peak stress	165.4 [95.6%]	124.9 [72%]			60.72	64.19
Taper Threaded-2	Fracture	176.1 [85%]	76.1 [44%]	4	5	51.18	47.25
	80% of peak stress	156.7 [90.9%]	76.1 [44%]			44.01	47.25
Grouted/Threaded	Fracture	127.1 [61%]	84.9 [49%]	3	4	85.6	84.29
	80% of peak stress	105.7 [61.3%]	84.9 [49%]			69.37	84.29
Friction Welded-1	Fracture	84.95 [41%]	63.9 [37%]	4	3	64.56	47.53
	80% of peak stress	82.5 [47.9%]	63.9 [37%]			63.97	47.53
Grouted-2	Fracture	161.4 [78%]	115.5 [67%]	2	2	19.4	75.88
	80% of peak stress	140.2 [81.4%]	115.5 [67%]			27.41	75.88

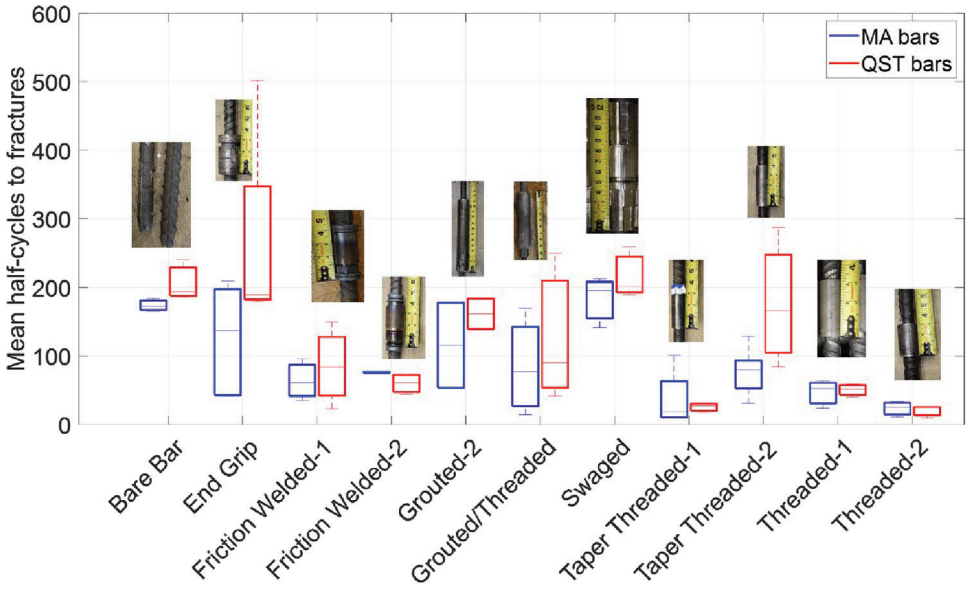

*Fig. 9—Mean half-cycles to fracture for all mechanical splices subjected to the (+2%, –0.5%) strain protocol, with clear gripping span of 1.5*d_b.

testing machine grips, at the junction between the coupler and the bar, within the coupler itself, and inside the grout. Additionally, instances of pullout from the grout were observed. No instances of coupler fracture were observed. Most bar fractures occurred near the coupler-bar interface. This may be due to stress concentrations within this area, likely the result of abrupt changes in the cross-sectional area

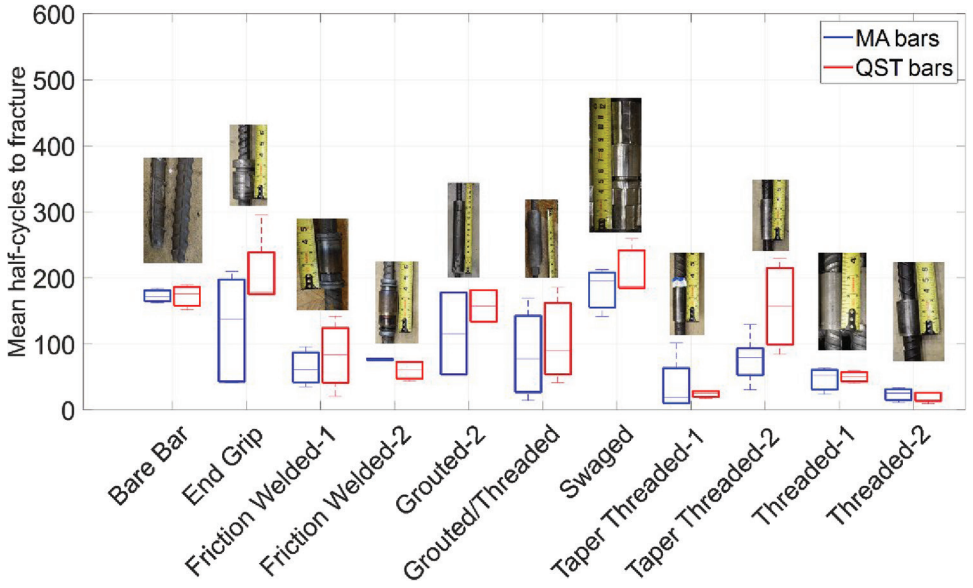

*Fig. 10—Mean half-cycles to 80% of peak stress for all mechanical splices subjected to (+2%, –0.5%) strain protocol, with clear gripping span of 1.5*d_b.

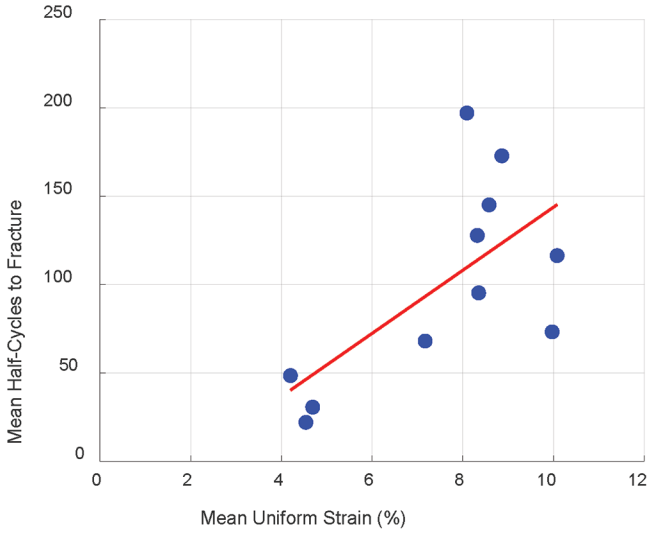

Fig. 11—Mean half-cycles to fracture versus mean uniform strain sustained in tension testing. Data points represent mean values for samples of same coupler type and steel production. Linear regression fit shown to illustrate correlation.

of the reinforcing bar and possible disruptions in the bar surface during the installation process.

DISCUSSION

Tension performance

All mechanical splices were able to develop a tensile stress in the bars of at least 100 ksi (690 MPa) and within 94% of the bare-bar measured tensile stresses. The 100 ksi (690 MPa) threshold corresponds to the Types 1 and 2 coupler strength criteria in ACI 318-19, which are 1.25 times the specified yield strength and the specified minimum tensile strength for the bars, in accordance with ASTM A706/A706M. On the other hand, the tensile strains developed by the mechanical splices varied considerably, with some developing the specified minimum tensile strain of the bars in ASTM A706/A706M and others only developing substantially lower strains.

Low-cycle fatigue performance

The experimental results revealed wide variability in the low-cycle fatigue performance of coupled bars compared to bare bars. Some mechanical splices were only able to sustain a fraction of the cycles to fracture of the bars they connected, with some only having 10% of the bare-bar performance. On the other hand, some mechanical splices demonstrated superior fatigue life, closely approximating or even exceeding the performance of bare bars in terms of the number of half-cycles to fracture. This suggests that with the appropriate selection and qualification of mechanical splices, coupled bars can achieve a fatigue life comparable to that of bare bars, supporting their potential use in hinge regions of seismic applications. A positive correlation was identified between the uniform strain sustained by mechanical splice specimens during tension testing and the numbers of half-cycles to fracture. This indicates that similar mechanisms may be at play in limiting both ductility and fatigue properties of mechanical splices. Additional testing is needed to extend findings to other coupler types and steel grades.

The investigation into fracture locations indicated a common occurrence of fractures near the coupler-bar interface, pointing to this as a critical area of stress concentration.

Inelastic deformations across couplers

Inelastic deformation across the couplers varied significantly among the specimens tested, with some showing negligible slip and coupler body deformations and others showing substantial slip levels. Findings therefore emphasize the importance of considering coupler deformation characteristics in the design and selection process to ensure that mechanical splices can accommodate expected strain

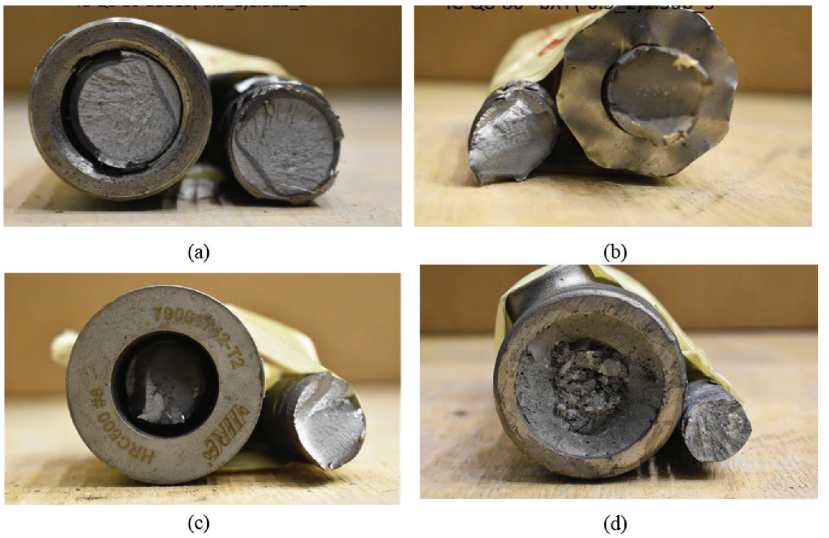

Fig. 12—Failure locations for coupled specimens: (a) bar fracture at coupler junction; (b) bar fracture between coupler and grip; (c) bar fracture inside coupler; and (d) bar fracture inside grout.

demands without compromising overall structural stiffness and ductility.

Recommendations for qualification testing

Based on the observed variability in tension strain and inelastic cyclic fatigue performance of mechanical splices, inelastic cyclic and tension qualification tests are recommended for mechanical splices to be used in seismic hinge regions. A tension test that monitors the tensile strains developed in bars adjacent to couplers is recommended. An acceptance criterion on the developed strain that is on the order of the specified uniform strain of the bars being connected is found to be attainable and is advised. An inelastic reversed cyclic strain protocol is recommended for qualification to simulate strain demands on bars in hinge regions. To limit buckling of specimens during testing, a relatively short clear gripping span of 1.5 times the bar diameter is recommended. Such a short span limits the need for lateral bracing of specimens during testing, which would add complexity to the qualification test. A strain amplitude of 2.5% was found to work well in testing while being representative of strain demands in longitudinal bars of special seismic members. The required number of half-cycles to fracture for the qualification test could be set close to that of the bars being spliced because some couplers were able to achieve that performance. However, a lower number of half-cycles to fracture could be justified based on acceptable performance in concrete members subjected to simulated seismic loading.

CONCLUSIONS

The study sheds light on the potential for mechanical splices to be used in seismic applications with higher-grade bars, provided they undergo representative qualification testing. Eleven types of mechanical couplers were tested in monotonic tension and under reversed cyclic strain demands. Key observations from testing include:

1. All mechanical splices were able to develop the tensile strength requirements of $1.25f_y$ (yield strength) or f_u (tensile strength) of ACI 318-19 for Types 1 and 2 mechanical splices.

2. Under tension loading, some mechanical splices fractured after the bars they connected exceeded the minimum uniform strain requirement of ASTM A706/A706M, while others could only achieve a fraction of that strain.

3. The aforementioned findings indicate that a strength criterion for mechanical splices cannot guarantee ductility. Consequently, for couplers at locations where yielding of bars is expected, a strain criterion would be more appropriate. For hinge regions, targeting the bar's specified minimum uniform strain for mechanical splices is advised and supported by the fact that several devices were able to achieve that strain under tension loading.

4. Experimental results revealed a wide variability in the low-cycle fatigue performance of coupled bars compared to bare bars. Some mechanical splices were only able to sustain a fraction of the cycles to fracture of the bars they connected, while others matched or even exceeded the fatigue life of the bare bars.

5. The observation that some mechanical couplers had relatively low fatigue life supports concerns about the potential for poor performance of couplers in hinge regions, not only for Grade 80 (550 MPa) bars but also for other grades. This study only tested 11 types of couplers; additional testing of different coupler types may uncover additional high and low performers among the body of mechanical couplers in the U.S. market.

6. Study results therefore indicate that the Type 1 and Type 2 strength-based criteria for mechanical splices of ACI 318-19 are inadequate for identifying devices that can be used in hinge regions of seismically loaded members or on bars designed to sustain straining beyond yield, such as structural integrity and continuity bars in concrete construction.

7. A qualification testing protocol subjecting mechanical splice specimens to reversed cyclic inelastic strain is proposed to qualify coupling devices for use in hinge regions of concrete members subjected to seismic loading.

Study results therefore demonstrate that mechanical splices can, with proper selection and qualification, match the performance of bare bars in terms of low-cycle fatigue life and withstand significant deformation demands. However, the critical importance of addressing the vulnerability of the coupler-bar interface to stress concentrations and fracture highlights the need for ongoing research and development in mechanical splice technology to ensure these systems continue to reliably perform under seismic loading conditions. The study included testing mechanical splices only on No. 8 (25 mm) Grade 80 (550 MPa) bars. Additional testing should be conducted to extend findings across bar sizes and bar grades, as well as across a wider sample of mechanical coupler devices.

AUTHOR BIOS

Latip Kumar Sharma *is a PhD Student at The University of Texas at San Antonio, San Antonio, TX. He received his BS in civil engineering and MS in structural engineering from Tribhuvan University, Kirtipur, Nepal. His research interests include the behavior of high-strength reinforcing bars in seismic applications.*

Wrya Abdullah *is Associate Professor in the Department Civil of Engineering, College of Engineering, the University of Sulaimani, Sulaimani, Kurdistan Region, Iraq. He received his BS from the University of Sulaimani; his MS from the University of Sheffield, Sheffield, UK; and his PhD from the University of Sulaimani. He also completed a postdoctorate at The University of Texas at San Antonio. His research interests include seismic analysis and retrofitting of reinforced concrete structures.*

Sudhir Niroula *is a PhD Student at The University of Texas at San Antonio. He received his BS in civil engineering and MS in structural engineering from Tribhuvan University.*

Narayan Budhathoki *is an MS Student at The University of Texas at San Antonio. He received his BS in civil engineering from Tribhuvan University.*

ACI member **Wassim M. Ghannoum** *is a Professor at the The University of Texas at San Antonio. He is a member of the ACI Technical Activities Committee; and ACI Committees 318, Structural Concrete Building Code; and 369S, Seismic Evaluation and Retrofit Code. His research interests include the behavior of reinforced concrete structures at high-damage states, the use of novel materials in concrete construction, and the life-span extension of concrete structures.*

ACKNOWLEDGMENTS

The generous financial support of the Charles Pankow Foundation, the Concrete Reinforcing Steel Institute (CRSI), the ACI Foundation, and CRSI members CMC, Nucor, and mechanical splice manufacturers is gratefully acknowledged. Material donations from CRSI and its members are also gratefully acknowledged.

REFERENCES

1. Villalobos, E.; Escolano-Margarit, D.; Ramírez-Márquez, A. L.; and Pujol, S., "Seismic Response of Reinforced Concrete Walls with Lap Splices," *Bulletin of Earthquake Engineering*, V. 15, No. 5, 2017, pp. 2079-2100. doi: 10.1007/s10518-016-0051-0

2. Almeida, J. P.; Prodan, O.; Tarquini, D.; and Beyer, K., "Influence of Lap Splices on the Deformation Capacity of RC Walls. I: Database Assembly, Recent Experimental Data, and Findings for Model Development," *Journal of Structural Engineering*, ASCE, V. 143, No. 12, 2017, p. 04017156. doi: 10.1061/(ASCE)ST.1943-541X.0001853

3. ACI Committee 318, "Building Code Requirements for Structural Concrete (ACI 318-19) and Commentary (ACI 318R-19) (Reapproved 2022)," American Concrete Institute, Farmington Hills, MI, 2019, 624 pp.

4. Sokoli, D., and Ghannoum, W. M., "High-Strength Reinforcement in Columns under High Shear Stresses," *ACI Structural Journal*, V. 113, No. 3, May-June 2016, pp. 605-614. doi: 10.14359/51688203

5. To, D. V.; Sokoli, D.; Ghannoum, W. M.; and Moehle, J. P., "Seismic Performance of Tall Moment Frames with High-Strength Reinforcement," *ACI Structural Journal*, V. 118, No. 1, Jan. 2021, pp. 113-124.

6. Rautenberg, J. M.; Pujol, S.; Tavallali, H.; and Lepage, A., "Reconsidering the Use of High-Strength Reinforcement in Concrete Columns," *Engineering Structures*, V. 37, 2012, pp. 135-142. doi: 10.1016/j.engstruct.2011.12.036

7. Huq, M. S.; Weber-Kamin, A. S.; Ameen, S.; Lequesne, R. D.; and Lepage, A., "High-Strength Steel Bars in Reinforced Concrete Walls: Influence of Steel Mechanical Properties on Deformation Capacity," Charles Pankow Foundation, Haymarket, VA, 2017, 318 pp.

8. Barcley, L., and Kowalsky, M., "Seismic Performance of Circular Concrete Columns Reinforced with High-Strength Steel," *Journal of Structural Engineering*, ASCE, V. 146, No. 2, 2020, p. 04019198. doi: 10.1061/(ASCE)ST.1943-541X.0002452

9. Sokoli, D.; Hogsett, G.; Limantono, A.; Suselo, A.; Al-Tarafany, D.; and Ghannoum, W. M., "Acceptable Elongations and Low-Cycle Fatigue Performance for High-Strength Reinforcing Bars," Charles Pankow Foundation, Haymarket, VA, 2019, 213 pp.

10. ASTM A706/A706M-16, "Standard Specification for Deformed and Plain Low-Alloy Steel Bars for Concrete Reinforcement," ASTM International, West Conshohocken, PA, 2016, 7 pp.

11. Brown, J., and Kunnath, S. K., "Low-Cycle Fatigue Failure of Reinforcing Steel Bars," *ACI Materials Journal*, V. 101, No. 6, Nov.-Dec. 2004, pp. 457-466.

12. Mander, J. B.; Panthaki, F. D.; and Kasalanati, A., "Low-Cycle Fatigue Behavior of Reinforcing Steel," *Journal of Materials in Civil Engineering*, ASCE, V. 6, No. 4, 1994, pp. 453-468. doi: 10.1061/(ASCE)0899-1561(1994)6:4(453)

13. Sokoli, D.; Limantono, A.; and Ghannoum, W. M., "Special Moment Frames with High-Strength Reinforcement—Part 2: Columns," *ACI Structural Journal*, V. 117, No. 2, Mar. 2020, pp. 253-265.

14. Zhong, K.; Ghannoum, W. M.; and Deierlein, G. G., "Influence of High-Strength Reinforcing Bars on Seismic Safety of Concrete Frames," *ACI Structural Journal*, V. 118, No. 5, Sept. 2021, pp. 299-311.

15. To, D. V., and Moehle, J. P., "Special Moment Frames with High-Strength Reinforcement—Part 1: Beams," *ACI Structural Journal*, V. 117, No. 2, Mar. 2020, pp. 239-252.

16. Brueggen, B.; Waugh, J.; Aaleti, S.; Johnson, B.; French, C.; Sritharan, S.; and Nakaki, S. D., "Tests of Structural Walls to Determine Deformation Contributions of Interest for Performance-Based Design," *Structural Engineering Research Frontiers: Proceedings of the Research Frontiers Sessions of Structures Congress 2007*, J. W. Wallace, ed., Long Beach, CA, 2007, pp. 1-16.

17. Haber, Z. B.; Saiidi, M. S.; and Sanders, D. H., "Seismic Performance of Precast Columns with Mechanically Spliced Column-Footing Connection," *ACI Structural Journal*, V. 111, No. 3, May-June 2014, pp. 639-650. doi: 10.14359/51686624

18. Haber, Z. B., "Precast Column-Footing Connections for Accelerated Bridge Construction in Seismic Zones," PhD dissertation, University of Nevada, Reno, Reno, NV, 2013, 612 pp.

19. Haber, Z. B.; Saiidi, M. S.; and Sanders, D. H., "Behavior and Simplified Modeling of Mechanical Reinforcing Bar Splices," *ACI Structural Journal*, V. 112, No. 2, Mar.-Apr. 2015, pp. 179-188. doi: 10.14359/51687455

20. NZS 3101.1:2006, "Concrete Structures Standard - Part 1: The Design of Concrete Structures," Standards New Zealand, Wellington, New Zealand, 2006.

21. California Test 670, "Method of Tests for Mechanical and Welded Reinforcing Steel Splices," California Department of Transportation (Caltrans), Sacramento, CA, 2013, 13 pp.

22. AASHTO, "AASHTO Guide Specifications for LRFD Seismic Bridge Design," second edition, American Association of State Highway and Transportation Officials, Washington, DC, 2011.

23. Sokoli, D.; Limantono, A.; and Ghannoum, W. M., "Plasticity Spread in Columns Reinforced with High Strength Steel," *Proceedings of the 16th World Conference on Earthquake Engineering (16WCEE 2017)*, Santiago, Chile, 2017, Paper No. 234, 11 pp.

24. Sokoli, D.; Limantono, A. A.; Hogsett, G.; Al-Teraffy, D.; To, D. V.; Moehle, J. P.; and Ghannoum, W. M., "Critical Strain Demands for Performance Evaluation of High-Strength Reinforcing Bars," *Proceedings of the Eleventh U.S. National Conference on Earthquake Engineering (11NCEE)*, Los Angeles, CA, 2018, pp. 1-7.

25. ASTM A706/A706M-22a, "Standard Specification for Deformed and Plain Low-Alloy Steel Bars for Concrete Reinforcement," ASTM International, West Conshohocken, PA, 2022, 9 pp.

26. ASTM E8/E8M-22, "Standard Test Methods for Tension Testing of Metallic Materials," ASTM International, West Conshohocken, PA, 2022, 31 pp.

27. Ameli, M. J.; Brown, D. N.; Parks, J. E.; and Pantelides, C. P., "Seismic Column-to-Footing Connections Using Grouted Splice Sleeves,"

ACI Structural Journal, V. 113, No. 5, Sept.-Oct. 2016, pp. 1021-1030. doi: 10.14359/51688755

28. Bompa, D. V., and Elghazouli, A. Y., "Inelastic Cyclic Behaviour of RC Members Incorporating Threaded Reinforcement Couplers," *Engineering Structures*, V. 180, 2019, pp. 468-483. doi: 10.1016/j.engstruct.2018.11.053

29. Dahal, P. K., and Tazarv, M., "Mechanical Bar Splices for Incorporation in Plastic Hinge Regions of RC Members," *Construction and Building Materials*, V. 258, 2020, Article No. 120308 doi: 10.1016/j.conbuildmat.2020.120308

30. Tazarv, M., and Saiidi, M. S., "Seismic Design of Bridge Columns Incorporating Mechanical Bar Splices in Plastic Hinge Regions," *Engineering Structures*, V. 124, 2016, pp. 507-520. doi: 10.1016/j.engstruct.2016.06.041

31. AC133, "Acceptance Criteria for Mechanical Connector Systems for Steel Reinforcing Bars," ICC Evaluation Service, Brea, CA, 2010.

32. ISO 15835-1:2018, "Steels for the Reinforcement of Concrete—Reinforcement Couplers for Mechanical Splices of Bars–Part 1: Requirements," International Organization for Standardization, Geneva, Switzerland, 2018, 9 pp.

33. Slavin, C. M., and Ghannoum, W. M., "Defining Structurally Acceptable Properties of High-Strength Steel Bars through Material and Column Testing - Part 1: Material Testing Report," Charles Pankow Foundation, Haymarket, VA, 2015, 135 pp.

34. Ghannoum, W. M., and Slavin, C. M., "Low-Cycle Fatigue Performance of High-Strength Steel Reinforcing Bars," *ACI Materials Journal*, V. 113, No. 6, Nov.-Dec. 2016, pp. 803-814. doi: 10.14359/51689116

35. ASTM A370-22, "Standard Test Methods and Definitions for Mechanical Testing of Steel Products," ASTM International, West Conshohocken, PA, 2022, 51 pp.

36. Rajaei, S.; Hogsett, G.; Chapagain, B.; Banjade, S.; and Ghannoum, W., "Vision-Based Large-Field Measurements of Bridge Deformations," *Journal of Bridge Engineering*, ASCE, V. 28, No. 11, 2023, p. 04023075. doi: 10.1061/JBENF2.BEENG-5973

37. Sokoli, D.; Shekarchi, W.; Buenrostro, E.; and Ghannoum, W. M., "Advancing Behavioral Understanding and Damage Evaluation of Concrete Members Using High-Resolution Digital Image Correlation Data," *Earthquakes and Structures*, V. 7, No. 5, 2014, pp. 609-626. doi: 10.12989/eas.2014.7.5.609

38. Gonzalez, J., "Improving Fatigue Life Properties of Steel Reinforcing Bars," master's thesis, The University of Texas at San Antonio, San Antonio, TX, 2022, 144 pp.

NEW Symposium Publications from ACI

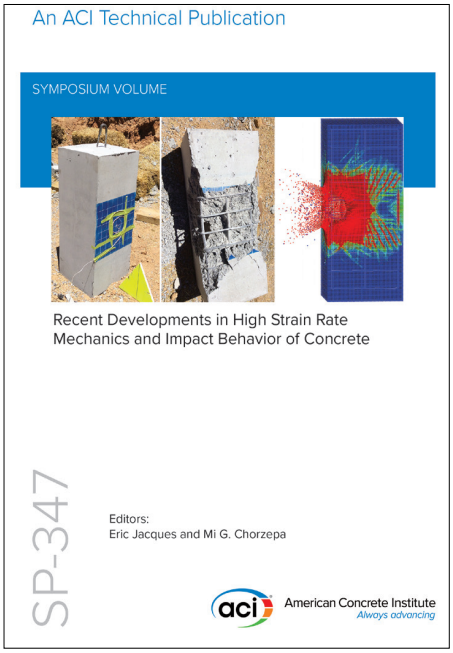

SP-347: Recent Developments in High Strain Rate Mechanics and Impact Behavior of Concrete

This Symposium Volume reports on the latest developments in the field of high-strain-rate mechanics and behavior of concrete subject to impact loads. This effort supports the mission of ACI Committee 370, Blast and Impact Load Effects, to develop and disseminate information on the design of concrete structures subjected to impact, as well as blast and other short-duration dynamic loads.

Available in PDF format: $69.50
(ACI members: $39.00) ($30.50 savings)

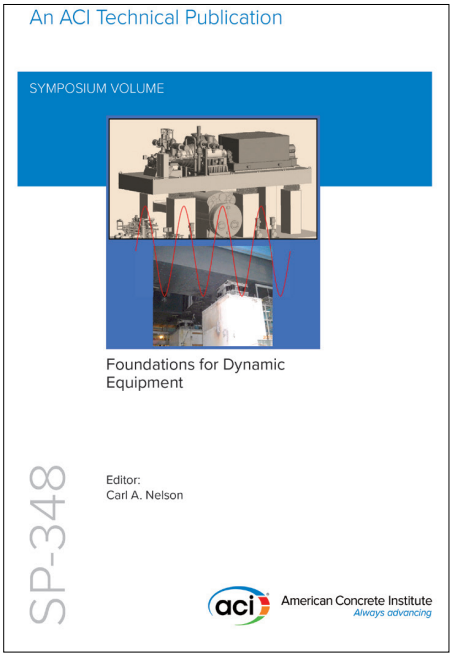

SP-348: Foundations for Dynamic Equipment

This special publication grew out of the Technical Session titled “Application of ACI 351-C Report on Dynamic Foundations,” held at the ACI Spring 2019 Convention in Québec City, Québec. Following this event, ACI Committee 351 decided to undertake a special publication with contributions from those session participants willing to develop their presentations into full-length papers. Three papers included in the current publication were contributed by these presenters and their coauthors, with six additional papers provided by others.

Available in PDF format: $69.50
(ACI members: $39.00) ($30.50 savings)

American Concrete Institute
+1.248.848.3700 • www.concrete.org

ACI STRUCTURAL JOURNAL

The American Concrete Institute (ACI) is a leading authority and resource worldwide for the development and distribution of consensus-based standards and technical resources, educational programs, and certifications for individuals and organizations involved in concrete design, construction, and materials, who share a commitment to pursuing the best use of concrete.

Individuals interested in the activities of ACI are encouraged to explore the ACI website for membership opportunities, committee activities, and a wide variety of concrete resources. As a volunteer member-driven organization, ACI invites partnerships and welcomes all concrete professionals who wish to be part of a respected, connected, social group that provides an opportunity for professional growth, networking, and enjoyment.

American Concrete Institute